From
Large Polycyclic Aromatic Hydrocarbons
to
Extended Aromate-Rich Networks

Dissertation zur Erlangung des Grades
"Doktor der Naturwissenschaften"
am Fachbereich Chemie, Pharmazie und Geowissenschaften
der Johannes Gutenberg-Universität Mainz

Matthias Georg Schwab
geboren in Münster/Westfalen
Mainz im Jahr 2011

Für die Meinen.

„Ich Bin, Was da ist“

„Ich bin alles, Was ist, Was war, und Was seyn wird,
Kein sterblicher Mensch hat meinen Schleyer aufgehoben“

„Er ist einzig von ihm selbst,
und diesem Einzigen sind alle Dinge ihr Daseyn schuldig“

Friedrich Schiller

Contents

Index of Abbrevations

2D-WAXS	two-dimensional wide-angle X-ray scattering
BET	*Brunauer-Emmett-Teller*
BJH	*Barret-Joyner-Halenda*
COF	covalent-organic framework
COSY	correlation spectroscopy (NMR)
CP	cross-polarization (NMR)
d	doublet (NMR)
DCM	dichloromethane
DFT	density functional theory
DLS	dynamic light scattering
DMA	*N,N*-dimethylacetamide
DMF	*N,N*-dimethylformamide
DMSO	dimethyl sulfoxide
DSC	differential scanning calorimetry
ECA	elemental combustion analysis
EDLC	electrochemical double-layer capacitor
EDX	energy-dispersive X-ray spectroscopy
FD	field desorption
FET	field-effect transistor
FTIR	*Fourier* transform infrared spectroscopy
GNR	graphene nanoribbon

GPC	analytical gel permeation chromatography
h	hour
HBC	hexa-*peri*-hexabenzocoronene
HCP	hypercrosslinked polymer
HOMO	highest occupied molecular orbital
HOPG	highly ordered pyrolytic graphite
HPLC	high performance liquid chromatography
HRTEM	high resolution transition electron microscopy
LC	liquid crystal
LED	light emitting diode
LUMO	lowest unoccupied molecular orbital
MALDI-TOF	matrix-assisted laser desorption/ionization time-of-flight
MAS	magic angle spinning
min	minute
MOF	metal-organic framework
MPV	micropore volume
MS	mass spectroscopy
NEMC	nitrogen-enriched mesoporous carbon
NLDFT	non-local density functional theory
NMP	*N*-methylpyrrolidone
NMR	nuclear magnetic resonance
NOESY	nuclear *Overhauser* enhancement spectroscopy
o-DCB	1,2-dichlorobenzene
PAH	polycyclic aromatic hydrocarbon
PIFA	phenyliodine(III) bis(trifluoroacetate)
PIM	polymer of intrinsic microporosity
PL	photoluminescence

POM	polarized optical microscopy
PPP	poly(*para*-phenylene)
PS	poly(styrene)
PV	pore volume
rGPC	recycling gel permeation chromatography
RT	room temperature
s	singlet (NMR)
SEM	scanning electron microscopy
SSNMR	solid state nuclear magnetic resonance
SSUV	solid state ultraviolet-visible absorption spectroscopy
STM	scanning tunneling microscopy
TBAF	tetra-*n*-butyl ammonium fluoride
TCB	1,2,4-trichlorobenzene
TCE	1,1,2,2-tetrachloroethane
TCNQ	7,7,8,8-tetracyanoquinodimethane
TEM	transmission electron microscopy
THF	tetrahydrofuran
TGA	thermogravimetric analysis
TON	turn over number
TLC	thin layer chromatography
TMS	trimethylsilyl
TOF	time-of-flight
UHV	ultra-high vacuum
UV	ultraviolet
UV-vis	ultraviolet-visible absorption spectroscopy
XPS	X-ray photoelectron spectroscopy

1 Introduction

1.1 Polycyclic Aromatic Hydrocarbons

One of the most abundant and thermodynamic most stable allotropes of the sixth element carbon is graphite. In this modification, every carbon atom is connected to three of its neighbors through σ-bonds leading to a hexagonal pattern (Figure 1-1). The sp^2-hybridization of the carbon atoms induces the planar geometry of the carbon sheets which are arranged in a layered fashion. The fourth valence electron of carbon is available for an additional, delocalized bond within the extended, planar sheets. The delocalization of these electrons leads to a metallic conductivity along the layer direction. Perpendicular to the stacked sheets, the transport of charge carriers is greatly obstructed.

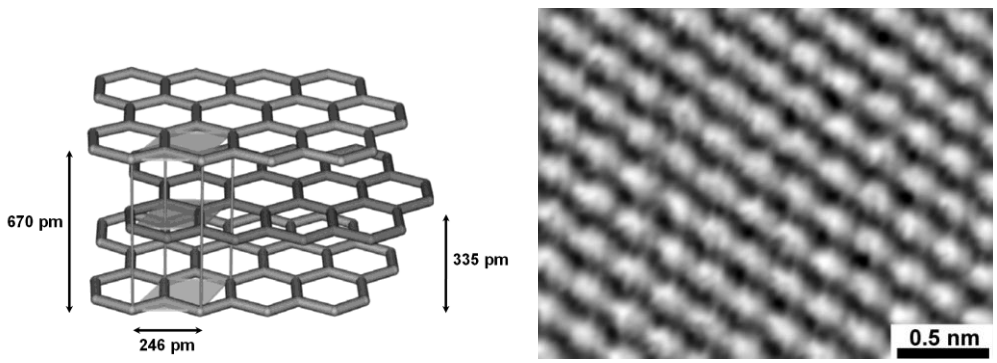

Figure 1-1: Schematic representation of a graphite lattice with characteristic distances (left) and STM image of graphite (right).

The building block of graphite, benzene, is the simplest aromatic compound and consists of six sp^2-hybridized carbon atoms that form a uniform hexagon, similar to graphite. Initially discovered in 1825 by *Faraday*,[1] the precise chemical structure remained the topic of fundamental discussions at the time.[2,3] It was in 1865 when

Kekulé expressed for the first time the principle of aromaticity[4] in his cyclic formula of benzene. The concept of the aromatic π-sextet was introduced by *Robinson* in 1925[5] with his famous "circle" notation and further refined by *Hückel* in his theory of molecular orbitals in 1931.[6] *Clar* postulated in 1964 his sextet rule which allowed for the easier prediction of the stability of larger aromatic systems.[7,8]

The periodical annelation of benzene rings constitutes the common ground of all polycyclic aromatic hydrocarbons (PAHs) often leading to extended aromaticity. PAHs constitute an extraordinarily large and diverse class of organic molecules. This is reflected by the number of 20600 possible alternating PAHs which can be constructed from four to ten benzene rings. The enormous structural diversity becomes apparent if four benzene units are directly annelated leading to seven possible structures namely triphenylene **1-1**, pyrene **1-2**, tetracene **1-3**, crysene **1-4**, tetraphene **1-5**, benzo[*de*]anthracene **1-6** and benzo[*c*]phenanthrene **1-7**, respectively (Figure 1-2).

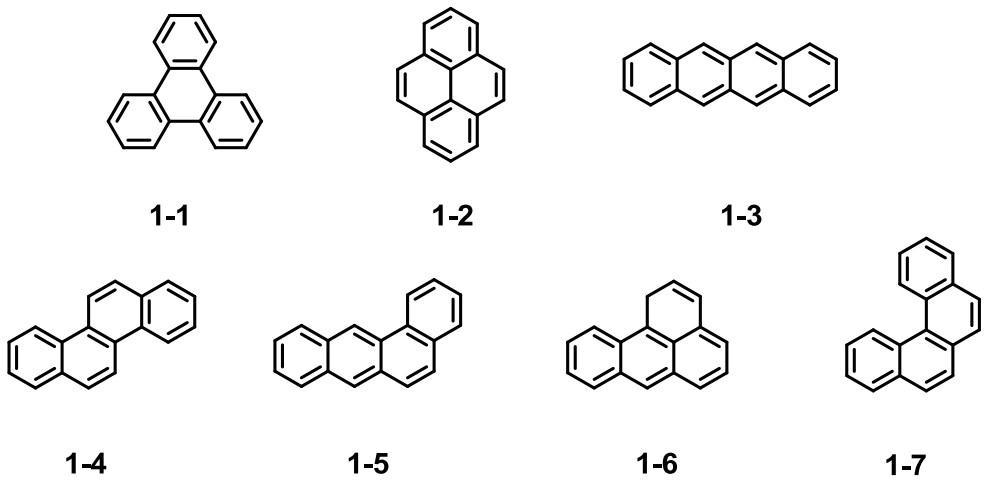

Figure 1-2: The structural diversity of PAH as exemplified by the annelation of four benzene rings.

Since their discovery as constituents of coal tar in the middle of the 19th century, PAHs have been in the focus of scientific research. This is due to their high stability, rigid planar structure and unique electronic properties. Early works on PAHs spurred the development of industrial organic chemistry, especially in the field of synthetic dyestuffs. In the meantime, PAHs have even been proven to be major constituents of interstellar matter in the universe.[9,10]

Pioneering studies by *Scholl*,[11-14] *Clar*[15-21] and *Zander*[19-21] addressed in the early 20th century fundamental aspects of PAH chemistry that lead to a number of bottom-up methodologies for the targeted synthesis of carbon-rich compounds.

With the discovery of discotic liquid crystals by *Chandrasekhar* in 1977[22] another

important field of application for PAHs began to emerge. Frequently, these disc-like structures assemble into highly oriented columnar structures if substituted with peripheral alkyl chains.[23-28] In combination with their tendency to self-orientate, the outstanding electronic characteristics of PAHs promoted their widespread use in the design of organic conductors,[28-30] solar cells,[24,31-35] photo- and electroluminescent devices,[24,36,37] as well as field-effect transistors.[24,38-41]

Graphene, a single-layer cutout of the graphite lattice can be regarded as a giant PAH. For a long time it was believed that the isolation of free-standing graphene would be extremely difficult if not impossible. Early works regarding the preparation of atomically thin carbon films can be traced back until 1948 when *Ruess* and *Vogt* obtained the first transition electron micrographs of few-layer graphene flakes.[42] In 1962 *Boehm* also reported the isolation of ultrathin carbon foils.[43] Ever since, the question regarding the exploitation of the valuable electronic properties of graphene has been raised. In the year 2004, *de Heer* described the fabrication of ultrathin epitaxial graphite and the two-dimensional electron gas properties of this material.[44] In the same year *Novoselov* and *Geim* published their groundbreaking experiments regarding the electric field effect in graphene that was obtained by a microexfoliation scotch tape approach.[45,46] The two researchers received the Nobel Prize 2010 in physics for this achievement.

Current chemical research is directed towards the bottom-up fabrication of this carbon modification *via* synthetic approaches.[47,48] In this respect, large well-defined nanographenes[49,50] and graphene nanoribbons (GNRs)[51-53], one- and two-dimensional cutouts from the parent graphene lattice, fill the gap between smaller aromatic molecules and extended sheets.

Besides the aforementioned practical importance of PAHs, fundamental questions like the degree, limitation and effect of aromaticity remain the topic of scientific controversy until today. If PAHs are considered as smaller model compounds for graphite they can be indeed applied to fundamental studies.[2,3,54-58]

It has to be noted that due to mutagenic and carcinogenic properties of some PAHs they are also of major concern as pollutants if spread in atmosphere and environment.[59]

1.2 Synthetic Approaches to PAHs

Smaller PAH like naphthalene, anthracene or phenanthrene can be often isolated by distillative separation of mixtures, either from coal tar[60,61] or the side-products from the catalytic hydrocracking of petroleum.[62-64] Even compounds which are only present in minor amounts in the crude feedstock are thus accessible due to the industrial scale of the process.

First fundamental contributions to the direct synthesis and characterization of PAHs made use of relatively vigorous reaction conditions under high temperature and pressure.[12-21] Modern organic synthesis is however directed towards milder methods offering better regioselectivity and higher yields. In this part several standard reactions will be briefly introduced.

1.2.1 Friedel-Crafts-type Reactions

The classic *Haworth* synthesis of phenanthrenes[65-68] is initated by a *Friedel-Crafts* condensation of naphthalene **1-8** with succinic anhydride **1-9** to yield the keto-acid **1-10** (Figure 1-3). A first *Clemmensen* reduction using zinc amalgam and hydrochloric acid followed by acid-catalyzed cyclization of the resulting carboxylic acid yields the ketone **1-12**. The keto group is reduced by a second *Clemmensen* reduction and final aromatization of this intermediate in the presence of selenium gives phenanthrene **1-14**.

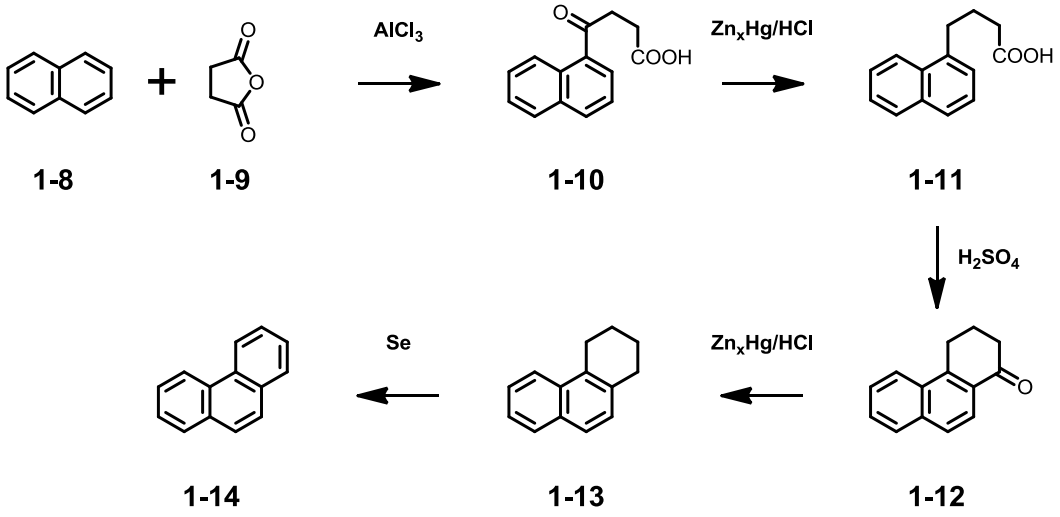

Figure 1-3: The *Haworth* synthesis of phenanthrene.

Additional examples are depicted in Figure 1-4 illustrating the versatility of the *Friedel-Crafts* acylation in the synthesis of other polycyclic ring systems.

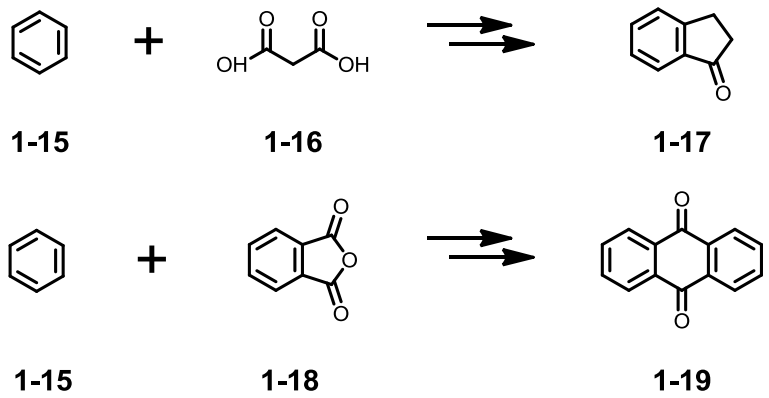

Figure 1-4: Examples of *Friedel-Crafts* acylations.

Reaction of benzene **1-15** with malonic acid **1-16** or phthalic anhydride **1-18** can be used for the build-up of indene- or anthracene-based scaffolds such as **1-17** and **1-19**, respectively. Also, substituted PAHs are easily available *via* this synthetic approach.[69]

1.2.2 Diels-Alder Cycloaddition

Both *intra*- and *inter*molecular Diels-Alder cycloaddtions[70] found numerous applications in the synthesis of PAHs. Figure 1-5 gives an example for an *intra*molecular case in the preparation of rhombus-shaped PAH **1-22** containing 54 aromatic carbon atoms.[71,72]

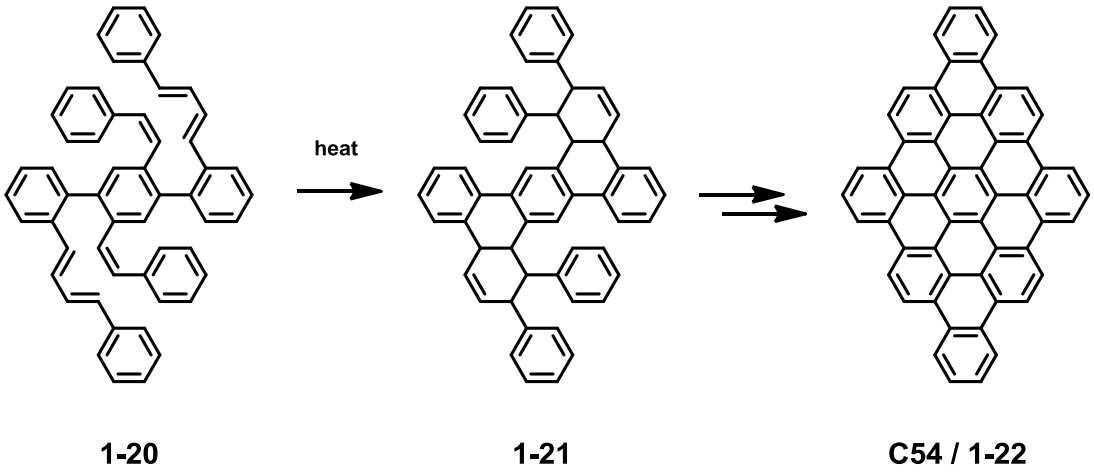

Figure 1-5: *Intra*molecular *Diels-Alder* cycloaddition during the synthesis of a rhombus-shaped PAH.

In the phenylene-vinylene derivative **1-20** the diene- and the dienophile functionalities

are topologically orientated in a way that they can react upon thermal treatment to give compound **1-21**. After a rearomatization, the resulting oligophenylene is converted to the disc **1-22** *via* oxidative cyclodehydrogenation.

The synthesis of hexaphenylbenzenes **1-25** is an example for the *inter*molecular *Diels-Alder* reaction of tetraphenylcyclopentadienones **1-23** with diphenyl acetylenes **1-24** (Figure 1-6).[27,73-78] The resulting oligophenylenes can be converted into the corresponding planarized PAH by subsequent cyclodehydrogenation. The repeated application of this [4+2] cycloaddtion has become an indispensable tool in the synthesis of large PAHs.[49,50] The reaction is driven by the elimination of carbon monoxide from the carbonyl bridged cycloaddition adduct at elevated temperatures. For this reason, high-boiling solvents such as xylenes or phenyl ether need to be used. As shown in Figure 1-6, the flexible synthetic protocol also allows for the introduction of a variety of functionalities on the periphery of the final PAH due to the possibility for substitution on both precursor compounds at early synthetic stages.

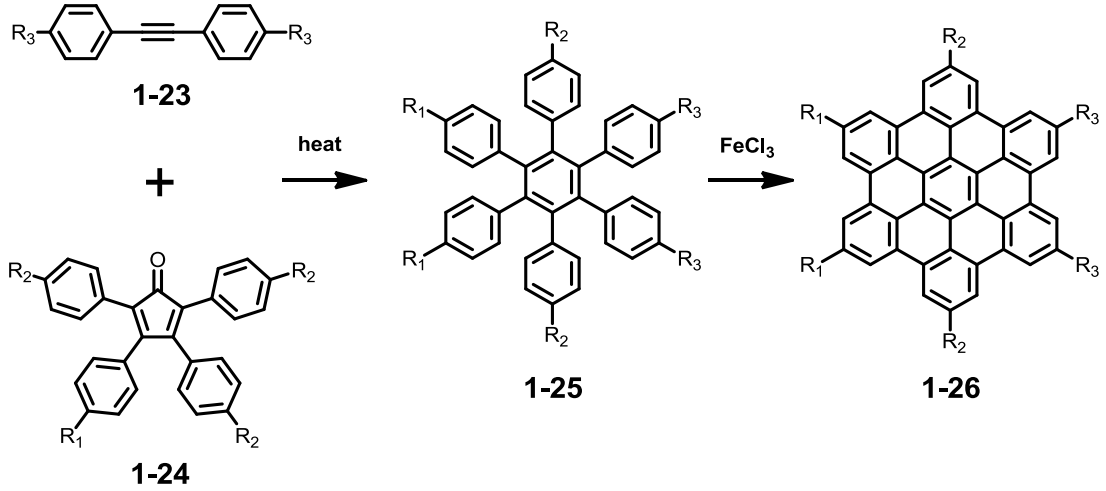

Figure 1-6: *Inter*molecular *Diels-Alder* cycloaddition during the synthesis of HBCs.

1.2.3 Photocyclization

A number of PAHs can be conveniently prepared by the photo-induced cyclization of suitable precursors. A prominent example is the synthesis of phenathrene **1-14** from stilbene **1-27** (Figure 1-7).[79]

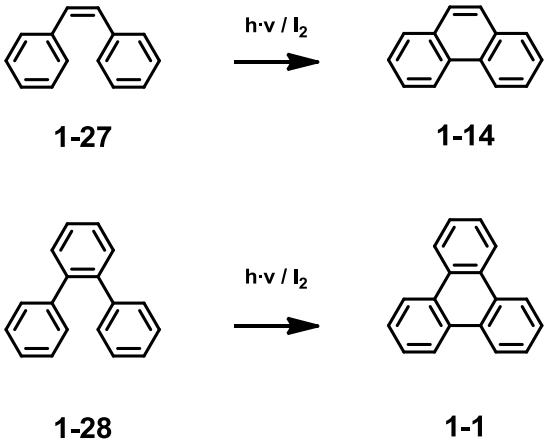

Figure 1-7: Preparation of phenanthrene and triphenylene *via* photocyclization.

Likewise, if the double bond of stilbene is replaced by an aromatic ring, an *ortho*-terphenyl **1-28** is obtained which can be photocyclized to triphenylene **1-1** (Figure 1-7).

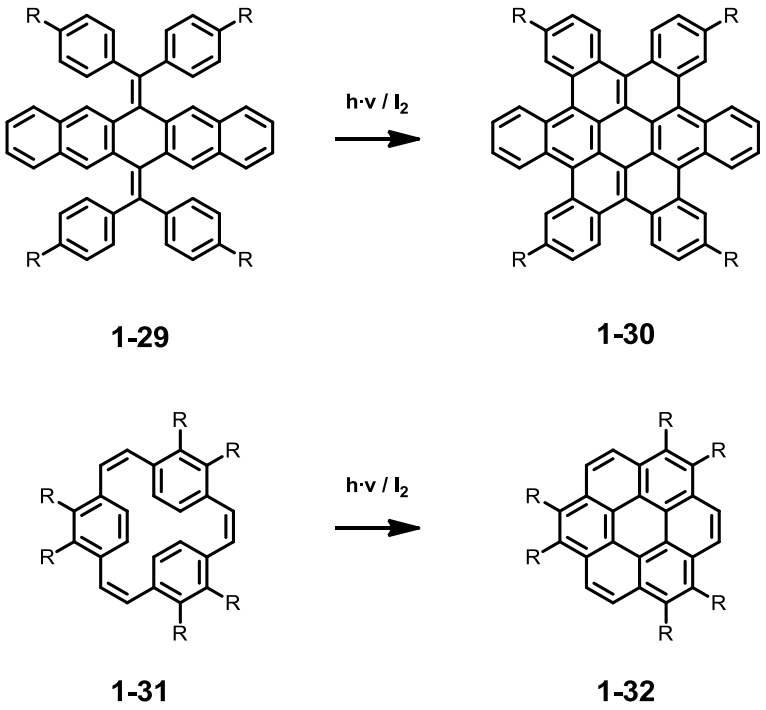

Figure 1-8: Photocyclization reactions during the synthesis of coronene derivatives.

Typical reaction conditions make use of UV radiation in the presence of a mild oxidant such as iodine. In order to suppress side-reactions, dilute solutions are needed which, however, limit the scalability of this approach.

However, photocyclization reactions have also been applied to the build-up of highly sophisticated molecules (Figure 1-8).[80,81]

As such, the decisive step in the preparation of the distorted hexa-*cata*-

hexabenzocoronone derivative **1-30** was accomplished by the photocyclization of the precursor molecule **1-29**.[80] Despite the severe steric crowding in this part of the molecule, the reaction leads to **1-30** as the exclusive reaction product.

The conversion of cyclophanes like **1-31** into coronenes **1-32** is another example for the usefulness of photocyclization reactions in the preparation of extended, substituted PAH systems (Figure 1-8).[81,82]

1.2.4 Extrusion of Heteroatoms

Based on initial works on the transformation of sulfide linkages to carbon-carbon double bonds,[83,84] the preparation of zethrene **1-37** represents an early example for the extrusion of heteroatoms in the synthesis of PAHs.[85] The thioether-bridged derivative **1-35** is prepared by reaction of **1-33** with **1-34** (Figure 1-9). Methylation leads to the intermediate **1-36**, which is transformed into the desired compound by *Stevens* rearrangement followed by *Hofmann*-type elimination.

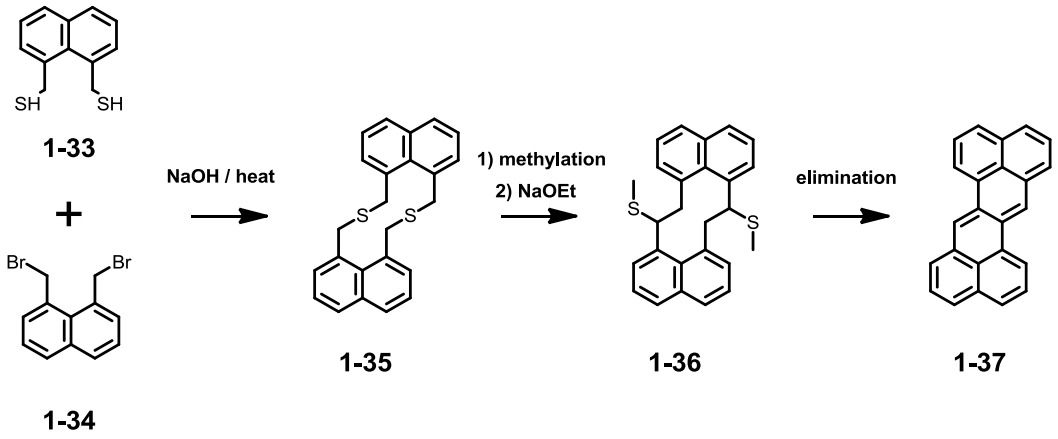

Figure 1-9: Extrusion of sulfur during the synthesis of zethrene.

The multi-step synthesis of kekulene **1-40**[86-89] also involves the extrusion of sulfur in the key sequence of the synthetic route (Figure 1-10).

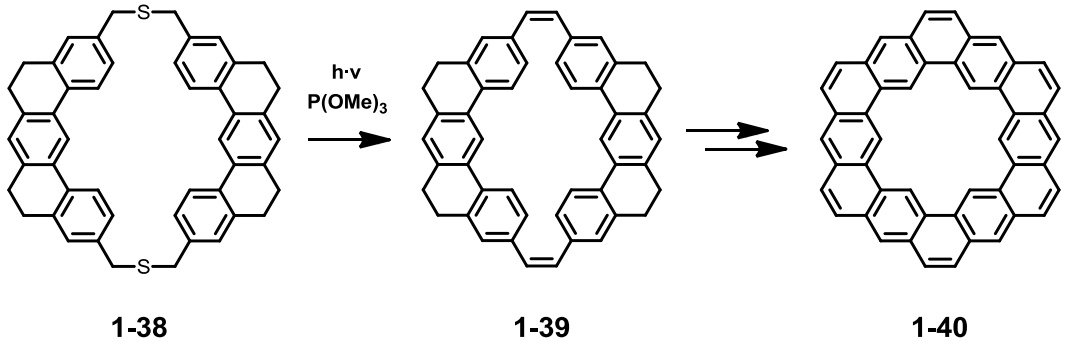

Figure 1-10: Extrusion of sulfur during the synthesis of kekulene.

The dithiaphane **1-38** is converted into the carbocyclic system **1-39**. Further synthesis ultimately leads to the fully annelated macrocycle **1-40**.

1.2.5 Cyclodehydrogenation Methods

A large variety of *intra*molecular cyclodehydrogenation methods have been developed for the conversion of oligophenylene precursors into fully fused polycyclic aromatic systems. Synthetic protocols relying on reductive as well as oxidative conditions found wide application. An example involving both processes is the synthesis of quaterrylene derivatives such as **1-43** (Figure 1-11).[90] Initial treatment of precursor **1-41** with potassium leads to the intermediate **1-42**. Subsequent reaction with a mixture of copper(II) chloride and aluminum(III) chloride yields the target molecule.

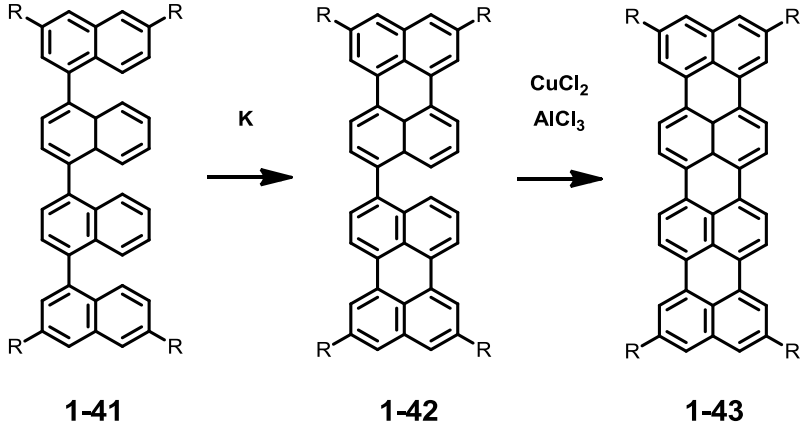

Figure 1-11: Synthesis of quaterrylene using reductive and oxidative cyclodehydrogenation.

The oxidative cyclohdeydrogenation is also known as the *Scholl* reaction[11,14,91-93] and has allowed for the synthesis of numerous PAHs. Other frequently applied oxidants are iron(III) chloride and molybdenum(V) pentachloride. HBC molecules like **1-26** are

usually prepared by this approach (Figure 1-6). The enormous potential of the oxidative cyclodehydrogenation is also evidenced by the successful synthesis of rhombus shaped PAH **1-22**[71,72] and the molecular triangle **1-44** (Figure 1-12).[94] Also, giant graphene molecules[49,50] and ribbon-type structures[51-53] are accessible *via* this route.

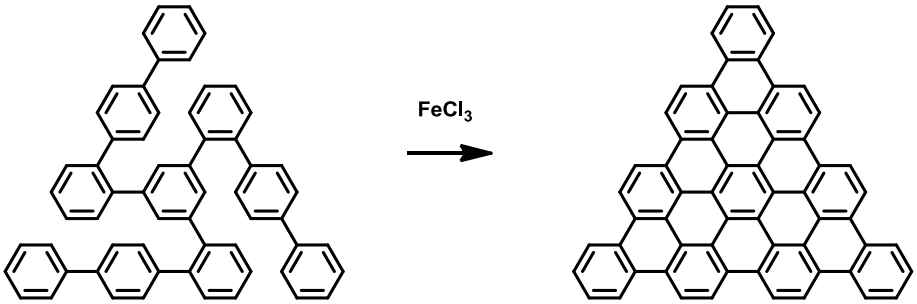

Figure 1-12: Synthesis of a molecular triangle *via* oxidative cyclodehydrogenation.

1.3 PAHs of Unusual Geometry

1.3.1 Macrocyclic PAHs

Macrocyclic PAHs exclusively constructed from directly connected aromatic units constitute an important family of compounds which has been under investigation since the pioneering works of *Staab* in the 1960s.[95-99]

Whereas in cyclic oligoarenes the ring members are connected through single bonds, direct fusion of aromatic rings gives rise to cycloarenes.

Depending on the substitution pattern on the benzene rings, different geometric shapes will result (Figure 1-13). This is exemplified for the cylohexaphenylene series where pure *ortho*-substitution results in the strained cyclo-*ortho*-hexaphenylene **1-45**.[100,101] Switching to a *meta*-pattern on the benzene units leads to cyclo-*meta*-hexaphenylene **1-46** for which a number of functionalized derivatives are known.[47,95,99,102-105] In this context, spherands such as **1-47** adopt a specific role since their endocyclic functionalization allows for the efficient complexation of guest species.[106-110] Alternating *ortho*- and *para*-connectivity leads to the triangle-shaped oligoarylene **1-48** which can be converted to the corresponding triangular PAH by cyclodehydrogenation.[111] Full *para*-subsitution will ultimately result in belt-shaped structures which are known as cyclophanes.[112]

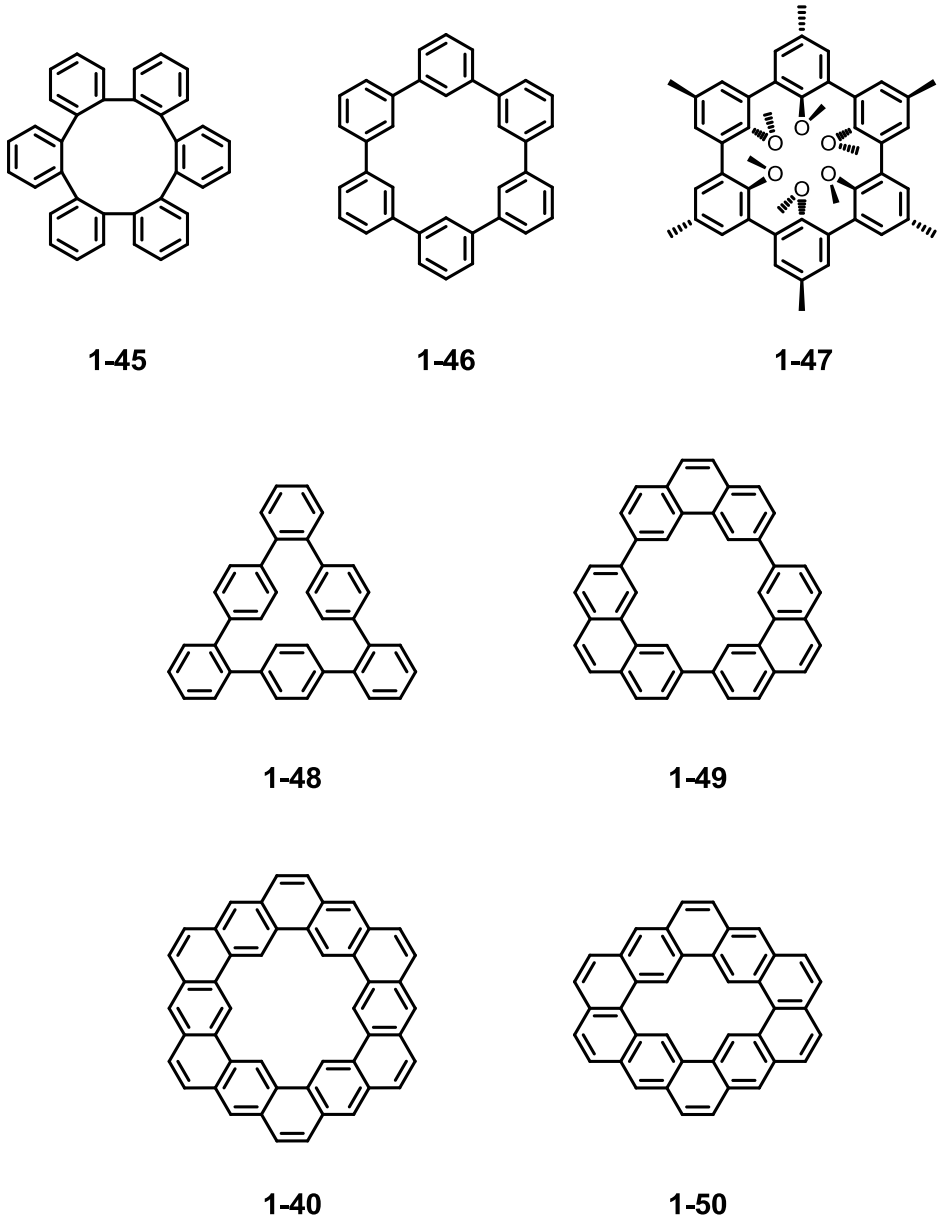

Figure 1-13: The backbone structures of representative macrocyclic PAHs.

The cyclo-3,6-trisphenanthrene macrocycle **1-49** links the cylic oligoarenes to the fully annelated cycloarenes.[96,104] In this macrocycle a high degree of conformational planarity is induced by the three phenanthrene units which are connected to each other (Figure 1-13). The nearly planar conformation of this ring system was investigated regarding liquid-crystallinity and self-assembly.[104]

Further closure of the missing bonds leads to kekulene **1-40** which was first reported in 1978 by *Staab*.[54,58,86-89] In this highly rigid PAH, the cavity of the macrocycle is surrounded by twelve benzene units which are angularly and linearly annelated. For this compound, 200 structures with different arrangements of double and single bonds can be formulated which is of interest with regard to π-electron delocalization and

fundamental questions regarding super-aromaticity.[87,113] The nature of kekulene remains controversial to the present day. Later, a smaller homologue of kekulene, macrocycle **1-50**, was also described which encloses ten benzene units in its cyclic backbone.[114]

1.3.2 Nitrogen-Containing Macrocycles

Nitrogen-containing macrocycles can be considered a special class of macrocyclic PAHs and have been the focus of synthetic chemistry for a long time. Their ability to sequestrate guest species in their cavity is certainly the most widely examined feature. In particular, lone electron pairs of pyridinium-, imine-, and amine-type nitrogen as well as pyrrole-type moieties are able to complex guest species such as metal cations through a number of non-covalent interactions.

The importance of these macrocycles is evidenced by porphyrins (**1-51**)[115-117] and phthalocyanines (**1-52**)[117] which occur in nature and are essential for life (Figure 1-14). But these macrocycles also represent an important class of compounds both in organic chemistry and material science. Due to their extended π-systems which are delocalized over the macrocycle they are intensively colored and are thus used in artificial organic pigments and dye-sensitized solar cells.[118] The metal-complexing ability of their tetraaza cavity makes them also interesting building blocks for host-guest systems and supramolecular assemblies.[116,119]

However, only few nitrogen-containing macrocycles with a hexagonal-planar arrangement of the nitrogen atoms and an 18-membered cavity have been reported. Due to their ring shaped structure these compounds are termed torands.[120,121] Examples of toroidal macrocycles involve a number of conjugated cyclic *Schiff* bases which are derived from the parent hexa[18]azaannulene system (**1-53**).[120,122-125]

In general, their synthesis can be accomplished through [2+2] template-assisted cyclocondensations between aromatic dialdehydes and diamines. Depending on the choice of the precursors, pyridine[122-125] (**1-54**) or 1,10-phenanthroline (**1-55**)[120] will contribute to the six-fold binding geometry of the cyclic ligand. Nevertheless, significant deviations from planarity are frequently encountered which prevent an efficient face-to-face packing of these molecules in the solid state.[124,125]

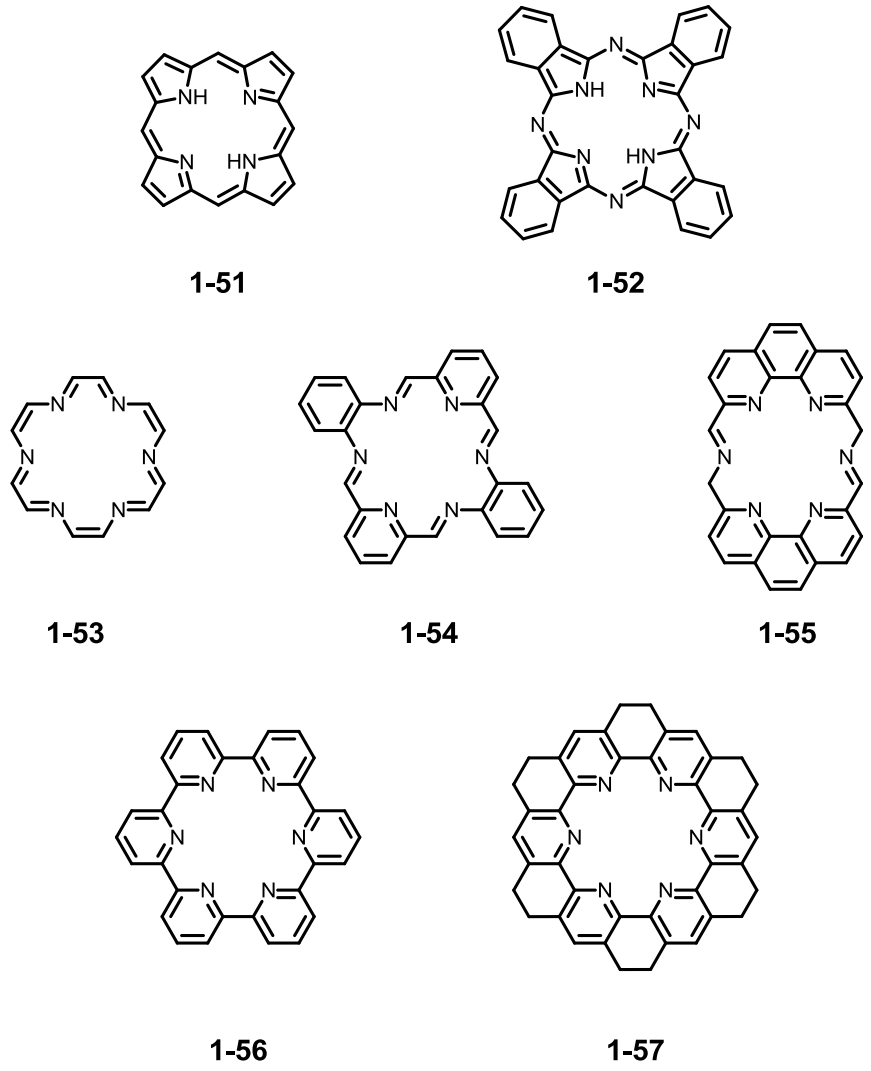

Figure 1-14: The backbone structures of representative nitrogen-containing macrocyclic PAHs.

Cyclosexipyridine (**1-56**)[126,127] is a hexaaza macrocycle in which the aromatic units are connected through aryl-aryl bonds. Its six nitrogen atoms are directed towards the centre of the cavity. Due to their poor solubility only sparse analytical information has been available about these cycles.

Additional fusion of the six pyridine units of **1-56** through ethyl linkages further increases both rigidity and planarity.[128-131] By this approach, dodecahydro-hexaazakekulene (**1-57**)[128] and its derivatives[129-131] were obtained which represent a class of fully planar macrocycles (Figure 1-14).

1.3.3 Graphene Nanoribbons

Graphene nanoribbons (GNRs) are two-dimensional cutouts from graphene that exhibit a geometric size anisotropy induced by a large aspect ratio of length over width. Currently, various physical approaches are investigated for their top-down fabrication making use of lithographic patterning[132-134] or mechanical exfoliation from parent graphene.[135] Due to their unique electronic properties GNRs are believed to hold great potential for numerous applications in the emerging field of carbon-based semiconductor technology [132,135-142]

From a chemical point of view, the easiest way to build GNRs following a bottom-up approach is the repeated linear annelation of benzene rings leading to a class of polymers referred to as poly(acenes) (**1-58**).[143,144] However, the synthesis of the higher acenes represents a major challenge both in organic and polymer chemistry.

As only one electron sextet can be assigned to these linear molecules according to *Clar*'s rule,[8] they are highly unstable and thus need to be stabilized either by interrupting the conjugation[143,144] or stabilizing substituents.[145-147]

Early works on stable, albeit heteroatom-containing ladder-type polymers can be traced back until the 1960s. Examples by *Stille*[148-150] and *Marvel*[151,152] reflect synthetic approaches of that time to obtain rigid macromolecules adopting structural parameters of graphite. Aromate-rich structures like **1-59**[149] and **1-60**[152] were obtained by polycondensation reactions under harsh synthetic conditions (Figure 1-16).

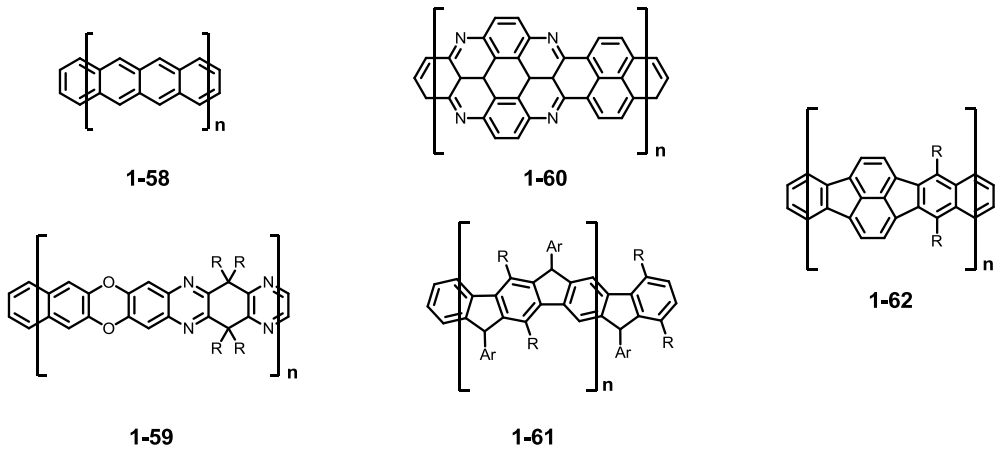

Figure 1-15: Early examples of ladder- and ribbon type polymers.

Due to the lack of solubilizing side-chains insoluble and infusible polymeric materials were frequently obtained which greatly limited their characterization. However, the

development towards multi-stranded polyaromatic ribbons such as **1-60** can already be seen from these early contributions.[153] By applying the *Diels-Alder* cycloaddition the construction of polymers with backbones composed of all-carbon five- and six-membered rings was achieved as illustrated by polymer **1-61**.[153-155] Transition-metal catalyzed aryl-aryl coupling and subsequent ring-closure lead to rod-like macromolecules such as **1-62**.[153,154,156]

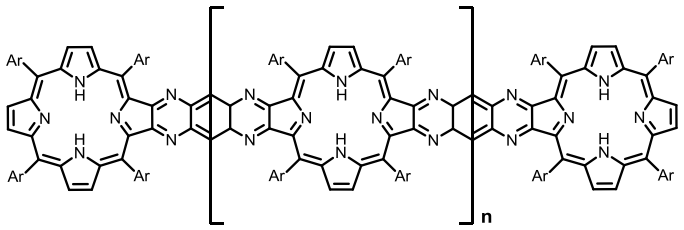

1-63

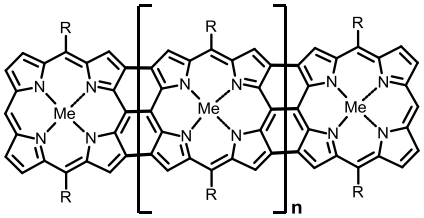

1-64

Figure 1-16: Examples of conjugated porphyrin arrays.

Fully conjugated porphyrin arrays were reported by *Crossley* (**1-63**)[157] and *Osuka* (**1-64**) (Figure 1-16).[158-160] Whereas the macrocyclic units were fused through pyrazine rings in the first example complete lateral annelation was realized in the second case. Their extended conjugation in combination with the metal chelating ability of the porphyrin cavity suggests the potential use of these nanoscale ribbons as molecular wires. Structure-wise, these porphyrin tapes bridge the gap between the aforementioned single-stranded polymers and laterally extended, fully fused GNRs.

In order to overcome solubility problems often obstructing synthesis of high-molecular weight species, *Müllen* developed a synthetic route that comprises two steps. Firstly, well-soluble dendronized poly(*para*-phenylene) precursors are synthesized by *Diels-Alder* cycloaddition[51,53,75] or palladium-catalyzed aryl-aryl coupling.[52]

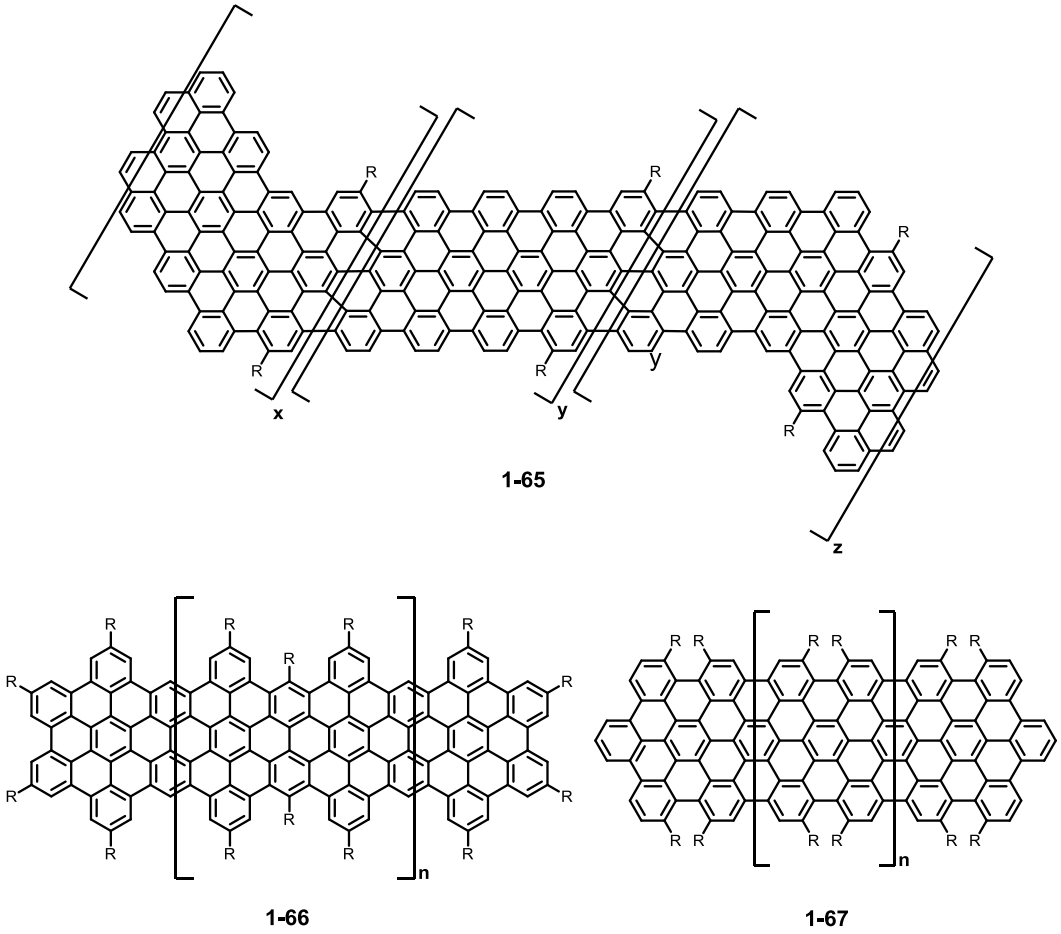

Figure 1-17: Examples of laterally extended graphene nanoribbons obtained by *intra*molecular cyclodehydrogenation of oligophenylene precursors.

In these precursors, the phenyl rings adopt a close spatial arrangement which is similar to the topology of the target molecule. In a second step, planarized GNRs are obtained through oxidative *intra*molecular cyclodehydrogenation of the oligophenylene precursor. By this synthetic strategy, a number of ribbon-type structures have been synthesized which differ in their shape, periphery and lateral extension. Initial attempts resulted in kinked structures such as **1-65**[51] due to several possible conformations of the precursor polymer (Figure 1-17).

Application of the *Diels-Alder* reaction in a repetitive manner using rigid building blocks lead however to a series of well-defined graphene stripes **1-66**[53] which were characterized regarding their self-assembly on surfaces. The *Suzuki-Miyaura* polycondensation of large dendronized monomers was used for the synthesis of nanoribbon **1-67**[52] consisting of up to 20 repeat units. For this graphitic molecule, high efficiency of the cyclodehydrogenation could be proven and the compound was studied by electron and scanning tunneling microscopy.

Whereas all examples described above concern the solution-based synthesis of GNRs,

a very recent trend addresses the surface-assisted preparation of extended graphene structures under STM control and UHV conditions.[47,48]

By this approach, the chevron-type nanoribbon **1-68**[48] could be prepared as well as the linear fused poly(anthracyl) derivative **1-69**.[48] It has to be noted, that even though this technique is situated at the edge of synthetic polymer chemistry, classical radical reaction mechanisms were found to be still valid under this exotic synthetic environment (Figure 1-18). Also, the problem of solubility is efficiently circumvented following the surface concept.

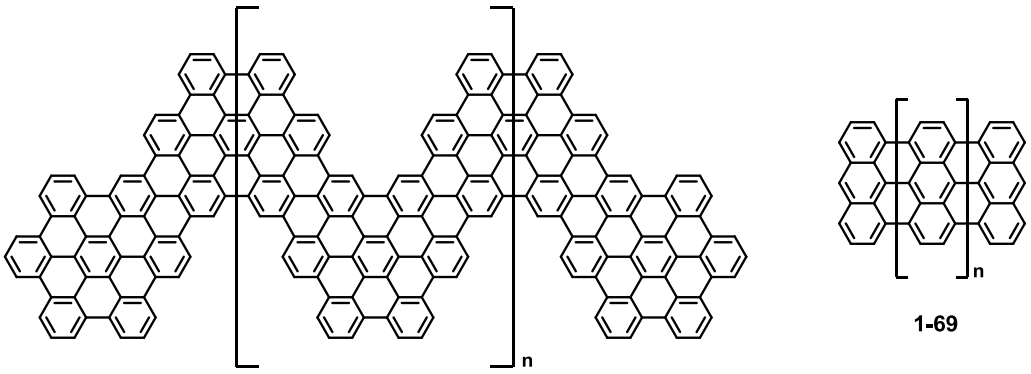

1-68 **1-69**

Figure 1-18: Examples of nanoribbons obtained by surface-assisted polymerization and cyclodehydrogenation.

1.4 Supramolecular Properties of PAHs

Supramolecular structures[24,116,161,162] emerge from the spontaneous association of molecules due to non-covalent interactions such as hydrogen-bonds, *van der Waals* or *π*-*π* interactions between them. According to *Lehn* supramolecular chemistry can be regarded "*the chemistry beyond the molecule, bearing on organized entities of higher complexity that result from the association of two or more chemical species held together by intermolecular forces*".[163]

In particular, two- and three-dimensional non-covalent assemblies of *π*-conjugated systems are intensively studied in nanoscience due to the growing interest in molecular electronics. This term refers to electronic devices which either make use of the bulk properties of self-assembled thin films or rely on the individual application of single molecules.

For discotic PAHs several applications in organic electronic devices have been demonstrated and could not have been realized without the intrinsic capacity of the

underlying molecules to self-organize.[24,31-41] Also, monolayers of PAHs could be used in the future for molecular data storage by writing information into highly ordered superstructures.[164,165]

1.4.1 Discotic Liquid Crystals

Liquid crystalline (LC) phases are systems which are characterized by a high degree of structural order on the microscopic scale. The LC mesophase is a state of matter, which lies between the crystalline and the isotropic liquid phase comprising characteristics of both (Figure 1-19). On the one hand, properties of a liquid such as deformability and mobility are encountered. However, also typical crystalline features like short- to medium-range order as well as optical and electrical anisotropy manifest themselves in the LC state.

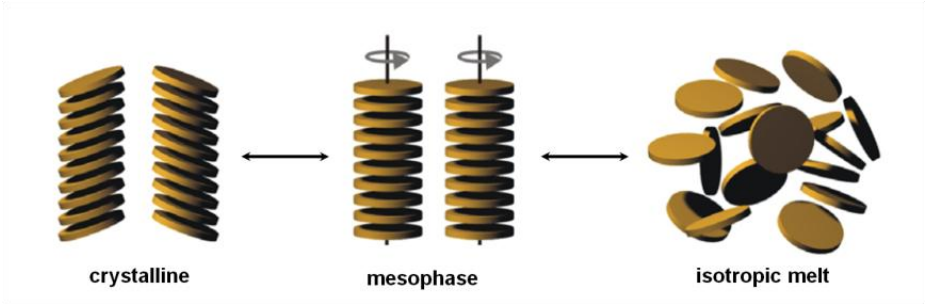

Figure 1-19: Schematic representation of different phases of discotic liquid crystals.

Discotic liquid crystalline materials are typically composed of a central disc-like rigid core that is substituted with aliphatic alkyl chains on the periphery.[23-25] Figure 1-20 illustrates the chemical diversity which has been developed since the discovery of these materials in the 1970s.[22]

Among others, substituted HBC molecules (**1-26**),[26] hexa-alkanoyloxy-benzenes **1-70**,[22] hexa-substituted triphenylenes **1-71**[166-168] and dibenzopyrenes **1-72**[169] as well as perylene derivatives **1-73**[170] were found to exhibit strong *inter*molecular packing interactions. Also, macrocyclic mesogens based on porphyrin (**1-51**) and phthalocyanine (**1-52**) motifs can form LC phases.[116]

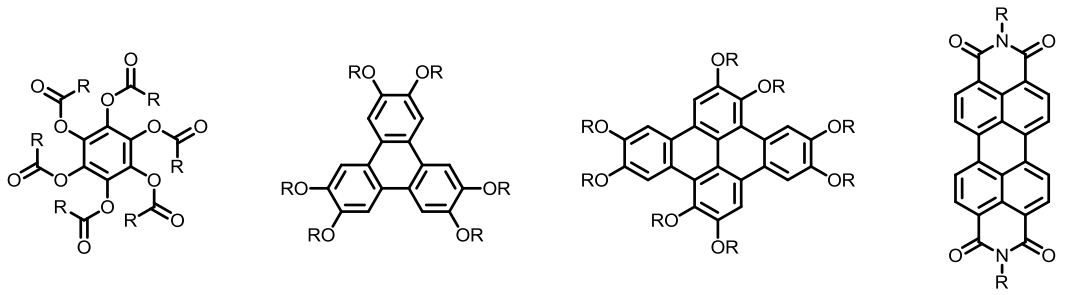

1-70 **1-71** **1-72** **1-73**

Figure 1-20: The structures of representative discotic mesogens.

The thermotropic phase behavior of discotic mesogens can be investigated using a variety of analytical techniques.

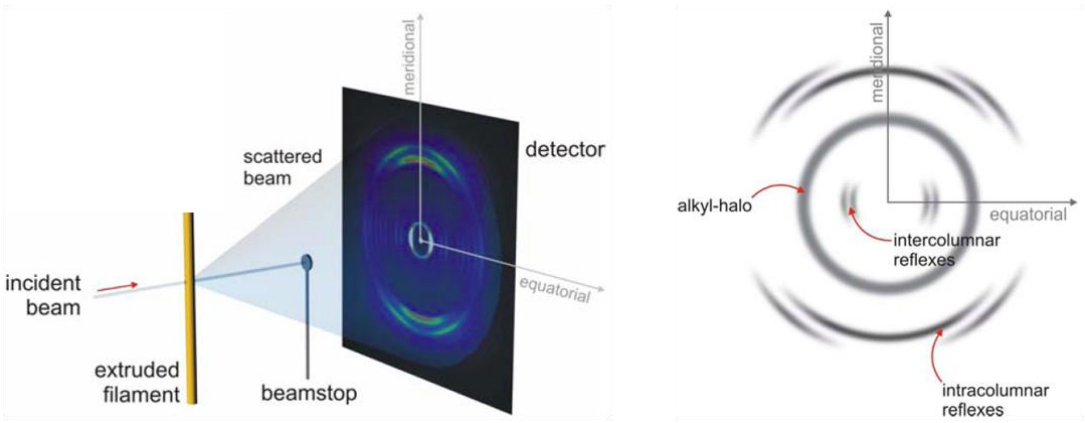

Figure 1-21: Two-dimensional wide angle X-ray scattering (2D-WAXS). Experimental setup (left) and typical diffraction pattern observed for a discotic liquid crystal (right).[26]

Phase transition temperatures and the corresponding enthalpies may be derived from differential scanning calorimetry (DSC). By applying polarized optical microscopy (POM), the birefringence of LC materials can be used to further elucidate the type of mesophase. An insight into the supramolecular organization can be obtained by temperature-dependent two-dimensional wide-angle X-ray scattering (2D-WAXS).[26,171] Therefore, a fiber is extruded as depicted in Figure 1-21. The beam hits the fiber resulting in reflections in the fiber direction (meridional) and perpendicular to the fiber direction (equatorial). A representative diffraction pattern for which important structural parameters are schematically indicated can be seen in Figure 1-21. It has however to be taken into account that the shear profile during the extrusion process significantly affects the orientation of the discotic molecules.

1.4.2 Monolayers of PAHs

Regarding self-assembly of PAHs on surfaces, their stiff and flat shape facilitates the study of molecule-substrate interactions. Scanning tunneling microscopy (STM) has become a versatile technique in exploring organic surfaces on different length scales and in various environments (Figure 1-22).[172,173] STM provides an image of the tunneling current in a plane across a conductive sample leading to a topographical map. More precisely, rather than measuring a physical topography, the atomically fine STM tip probes point by point the probability of tunneling between tip and surface while scanning.

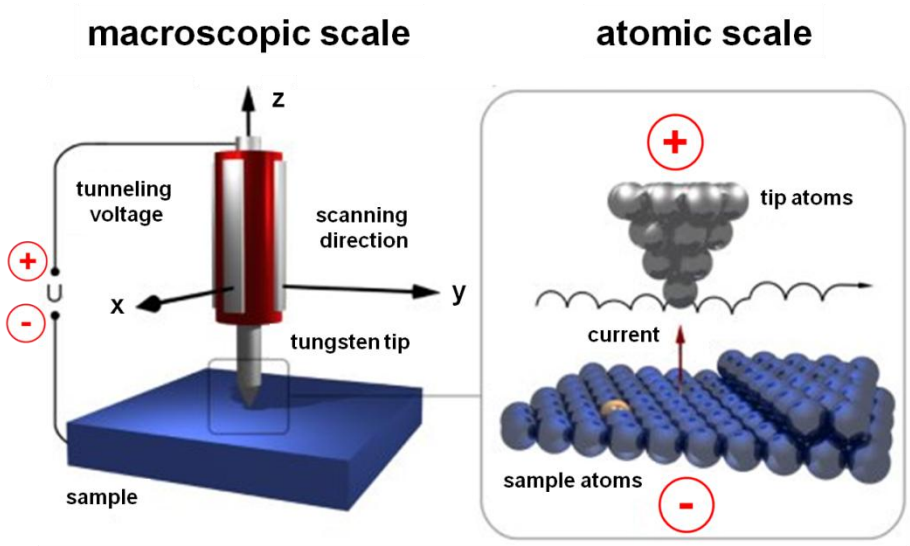

Figure 1-22: Scanning tunneling microscopy (STM). Working principle on the macroscopic (left) and atomic level (right).

Thereby the visualization of extended monolayers on a submolecular level,[161] the manipulation of single molecules[164,174] as well as the *in-situ* observation of chemical reactions[47,48] and catalytic processes[175] can be achieved.

Initial works on PAHs were carried out on thin films which were produced *via* ultra-high vacuum (UHV) sublimation[176]. This approach requires organic compounds that vaporize without decomposition, but for potential applications they must also exhibit strong intermolecular binding forces.

Non-substituted HBC molecules (**1-26**, Figure 1-23A)[177] as well as the rhombus shaped PAH **1-22**[72] (Figure 1-23B) could be visualized by this technique and were investigated with respect to the multiple interactions between molecule and surface that drive the molecular self-organization.

A different approach, which is simpler and more aimed towards practical and technological applications, relies on the processing of suitable compounds from the liquid phase.[161] This methodology takes advantage of the tendency of PAHs to spontaneously physisorb from solution on the basal plane of flat solid surfaces such as highly ordered pyrolitic graphite (HOPG) or molybdenite (MoS_2).

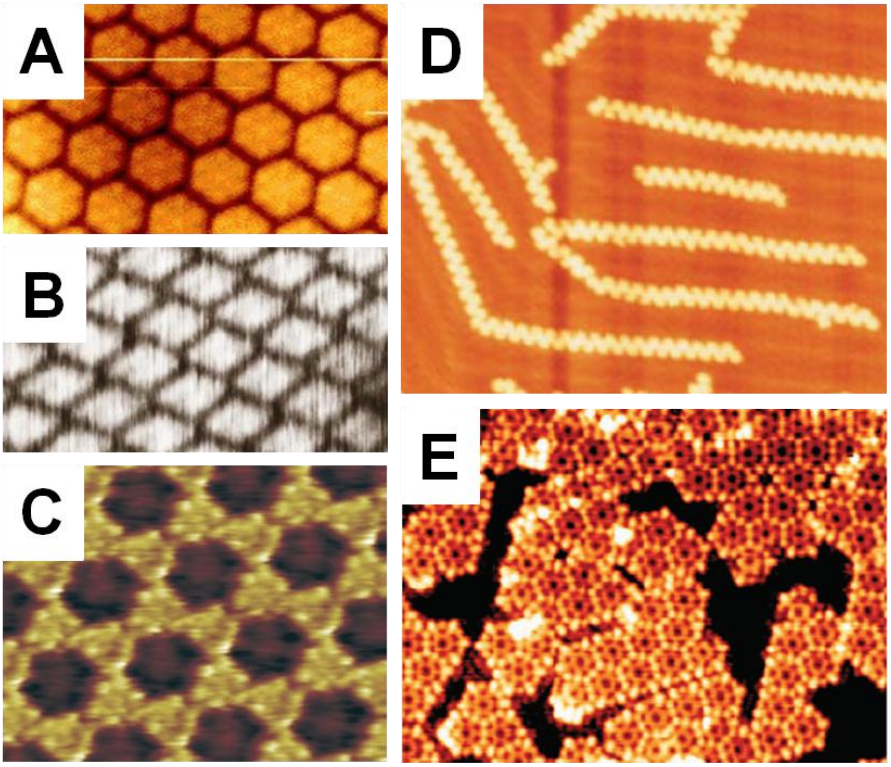

Figure 1-23: STM images of sublimed non-substituted HBC **1-26** (**A**)[177] and rhombus-shaped PAH **1-22** (**B**),[72] visualization of the molecular triangle **1-44** on the liquid-solid interface (**C**)[94] and surface-assisted synthesis of graphene nanoribbons **1-68** (**D**)[48] and porous graphene networks formed by hexa-iodinated **1-46** (**E**)[47] under STM control.

However, the complex interplay of molecule-molecule, molecule-surface and molecule-solvent interactions will greatly affect the final self-assembly in each individual case. For this approach to be practicable, the molecules need to be substituted with peripheral alkyl chains to ensure for sufficient solubility. Furthermore, the alkyl chain interdigitation has been recognized as a driving force for the efficient formation of monolayers.[178] Figure 1-23C shows a STM image of the molecular triangle **1-44**.[94]
The molecules assemble in a regular pattern that ensures maximum contact of the alkyl chains. The unique triangular geometry of this PAH is clearly seen.
As mentioned previously, the STM technique is not limited to the simple visualization of molecules on surfaces but can be used as a tool to observe and control chemical

reactions on surfaces at the atomic level. In the context of PAHs, recent works towards graphene-based molecular devices made use of the STM to study the growth of extended GNRs (Figure 1-23D)[48] and graphene networks (Figure 1-23E)[47] from molecular precursors, respectively. The chevron-type nanoribbons **1-68** were obtained after UHV deposition of a suitable functionalized precursor. Both, the metal-assisted radical polymerization and the subsequent cyclodehydrogenation could be closely monitored. The same holds for the surface polymerization of a hexa-iodinated cyclo-*meta*-hexaphenylene **1-46** from which a porous graphene network was fabricated under STM control.

1.5 Three-dimensional Microporous Polymer Networks

Another important class of aromate-rich materials are microporous polymer networks. In contrast to the one-dimensional nature of PAHs and nanographenes and the two-dimensionality of parent graphene discussed above, such materials are highly crosslinked three-dimensional structures. In the recent past, organic materials[179-183] that are additionally characterized by a high degree of porosity have found considerable interest which is due to a number of potential applications in various fields of polymer and material science.

Polymers hold a number of advantages in comparison to other microporous materials such as carbons,[184] zeolites and metal-organic frameworks (MOFs). In general, they can be precisely tailored by means of chemical synthesis. This holds for the systematic variation of structural features as well as the incorporation of functional groups for specific applications. Moreover, many polymers exhibit excellent chemical resistivity and thermal robustness. Being composed of light elements they often possess low densities. Also, scalability and pricing are important factors from a economical point of view.

Microporous organic polymers may be divided into hypercrosslinked polymers (HCPs), polymers of intrinsic microporosity (PIMs) and covalent organic frameworks (COFs). HCPs and PIMs are typically amorphous in nature, on the contrary a high degree of order is found for COF materials. The latter are typically prepared under thermodynamic control whereas the synthesis of HCPs and PIMs is irreversibly governed by kinetic control. Nevertheless, all three material classes share one common chemical feature which is the predominance of rigid aromatic structure motifs.

Typically, the specific surface area of HCPs varies between 500 and 2500 m^2/g as determined from multilayer-based *Brunauer-Emmet-Teller* (BET) theory. An

exceptionally high value of 5600 m^2/g has been claimed for a material that was obtained by multiple *Yamamoto* cross-coupling of a spiro bifluorene derivative.[185,186]
For PIMs, either linear or crosslinked, a maximum BET surface area of 1100 m^2/g has been reported.[187] Due to their high degree of structural order and the absence of defects, the BET surface area of COF materials often exceeds the values of HCPs and PIMs and can amount up to 4200 m^2/g.[188]

1.5.1 Hypercrosslinked Polymers

The generation of microporosity within a hypercrosslinked polymer (HCP) is achieved through extensive crosslinking of polymer chains in an expanded state. For this reason, the solvent used must be as thermodynamically compatible with the precursors as possible in order to prevent it to be rejected from the crosslinked material at an early stage. After synthesis, permanent porosity is conserved due to numerous rigid crosslinking points which prevent the structural collapse of the polymer. In the dry state HCPs can be thought of as similar to a rigid sponge.
The multiple *Friedel-Crafts* alkylation has been well-established for the build-up of HCPs and was first reported as a versatile crosslinking reaction in 1969.[189,190] Following this approach, polymeric precursors such as swollen poly(styrene)[191-193] and poly(chloromethylstyrene)[191,193-195] were used for the build-up of various HCPs (**1-74**). Using the same synthetic procedure, it was also demonstrated that functionalized aromatic benzyl chlorides can be used for the build-up of the network in a stepwise fashion (Figure 1-24).[191,196-198]
Hypercrosslinking of poly(aniline) (**1-75**) [199,200] or poly(pyrrole) (**1-76**)[201] through multiple *N*-alkylation is a closely related process for the synthesis of nitrogen-rich HCPs. Linear polymer chains act as precursors for the formation of network structures with high degrees of porosity. In this case, polyfunctional alkyl halides serve as crosslinking points (Figure 1-24).
Transition-metal catalyzed aryl-aryl coupling reactions such as the *Sonogashira-Hagihara* (**1-77**),[202-207] the *Glaser* (**1-78**),[208] the *Suzuki-Miyaura*,[207] the *Yamamoto* (**1-79**),[185,186,209] or the *Buchwald-Hartwig*[200] reaction are also efficient methods for the synthesis of microporous polymer networks. By this approach, fully conjugated HCP structures can be obtained.

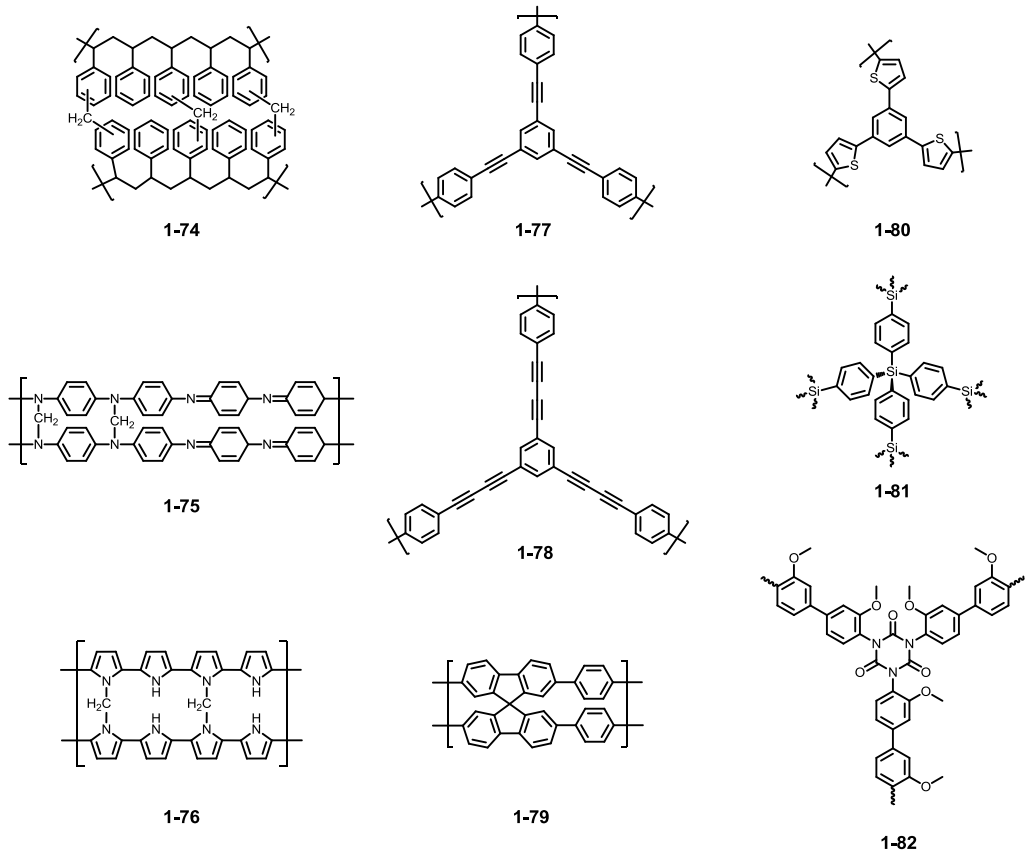

Figure 1-24: Examples of hypercrosslinked polymer networks.

Via the oxidative polymerization of thiophenes (**1-80**)[210] and thiophene-decorated porphyrines[211] microporous poly(thienylene arylene) networks were synthesized.

The crosslinking of organolithium compounds with silanes is another method that gives rise to microporous organic-inorganic hybrid networks (**1-81**).[212] Trimerization of aryl isocyanates leads to poly(isocyanurate) networks (**1-82**).[213]

1.5.2 Polymers of Intrinsic Microporosity

Polymers of intrinsic microporosity (PIMs)[214-216] represent another class of disordered microporous polymers. Their synthesis is based on the ladder-type assembly of sterically demanding building blocks to form either polymer chains[217-225] or networks (Figure 1-25).[187,226-231]

Due to the contorted geometry of the macromolecules, PIMs cannot pack efficiently in the solid state so that a high fraction of free volume is retained.[215] Subunits containing spiro centers are frequently used to induce kinks and twists within the repeat unit of the polymer framework. Thus, the molecular structure of PIMs resembles a basket of large shards of broken glass.

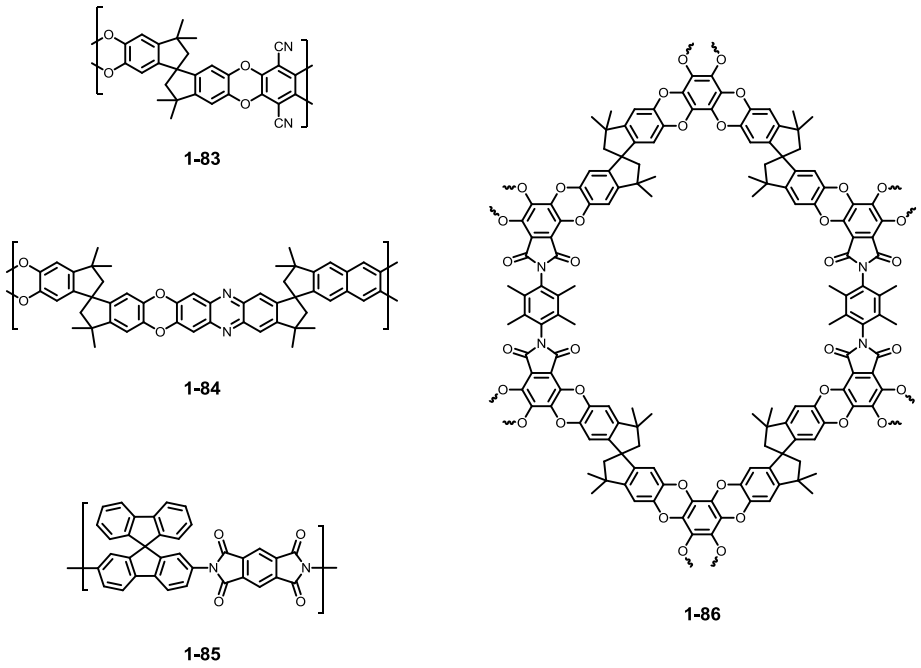

Figure 1-25: Examples of polymers of intrinsic microporosity.

If the double aromatic nucleophilic substitution between bis(catechols) and aryl halides is applied polymers that are connected through dibenzodioxane units will result (**1-83** and **1-84**). Also, poly(amide) and poly(imide) chemistry (**1-85**) was used for the synthesis of linear PIM systems.[220,223-225] Unlike their highly crosslinked counterparts, linear PIM systems are easily dissolved so that they can be processed from solution. In contrast, three-dimensional PIM systems like **1-86** are obtained as insoluble and infusible solids (Figure 1-25).

1.5.3 Covalent Organic Frameworks

Covalent organic frameworks (COFs)[232] are crystalline porous organic materials of either two-dimensional[233-244] or three-dimensional[188,237,245] order. The reversibility of the bond forming reaction is often considered the key requisite for the build-up of polymer networks with regular porosity.

In many cases, self-condensation and co-condensation reactions of aryl boronic acids are used for the synthesis of COFs leading to network structures that are interconnected through boroxine rings[188,233,234,236,243,246] or boronate esters,[188,233-235,237-239,246] respectively (**1-87** and **1-88**). Also, borosilicate cages have been successfully adopted as crosslinking units (Figure 1-26).[237]

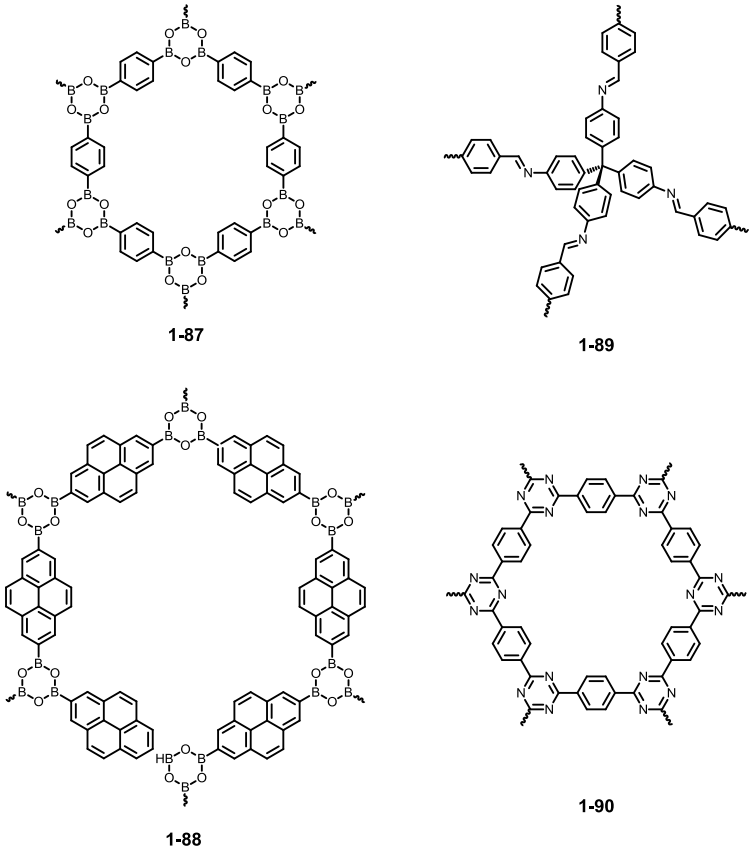

Figure 1-26: Examples of covalent organic frameworks.

More recently, an imine-linked COF (**1-89**) was prepared by crosslinking aromatic bis(aldehydes) with a tetrafunctional aromatic amine.[245] Highly ordered materials with sheet-like structures were also obtained *via* the trimerization of aromatic nitrile monomers under ionothermal conditions (**1-90**).[240-242,244]

1.6 Assessment of Porosity

The physisorption of nitrogen at a temperature of 77 K is the most widely applied tool for the determination of the surface area, pore volume and pore size distribution of a porous analyte.[247-249] The technique allows precise, non-destructive analysis of porous materials and can be extended to other gases such as argon or carbon dioxide.[248,249]

At the origin of physisorption are *van der Waals* forces with interaction energies ranging between 5 - 20 kJ/mol. They result from randomly induced dipole moments between the gaseous adsorptive and the surface of the adsorbent. Characteristic of physisorption is the formation of multilayers of the adsorbate on the surface (Figure 1-27).

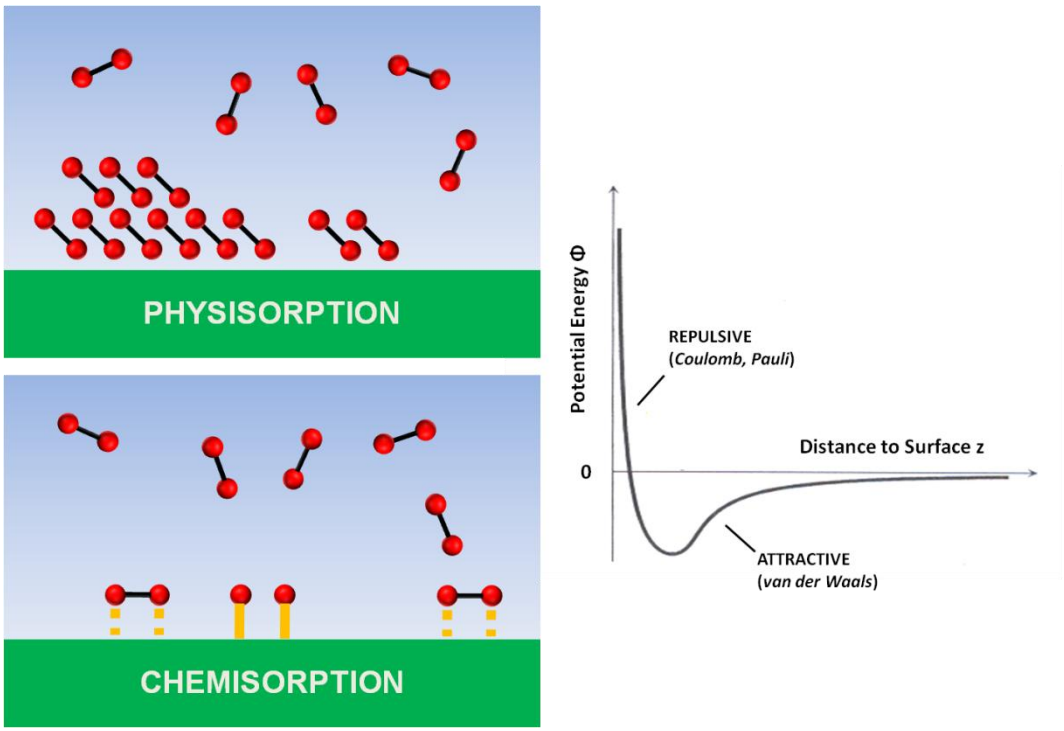

Figure 1-27: Schematic representation of physisorption and chemisorptions (left), course of the potential energy a as function of the surface distance for physisorption.

Repulsive forces prevent the gas molecules however to directly contact the surface as this is seen in chemisorption (Figure 1-27). This adsorption phenomenon is based on the formation of stronger chemical bonds between the surface and the adsorbed species. The binding energies are typically higher than 20 kJ/mol. Due to the weak interaction forces, physisorption in contrast can only be observed at low temperatures. Also, increasing relative pressures will make the physisorptive addition of gas molecules to the surface more favorable.

According to IUPAC, porous materials are divided into three classes depending on the pore size (Figure 1-28).[250] All materials with pore diameter below 2.0 nm are classified as microporous. Apart from the aforementioned microporous polymer networks, which can be either amorphous (HCPs, PIMs) or highly ordered (COFs), other examples involve crystalline zeolites such as ZSM-5,[251,252] metal-organic frameworks (MOFs)[253,254] and carbon materials.[184,255] Microporous materials generally possess high specific surface areas and an enhanced inner pore volume.

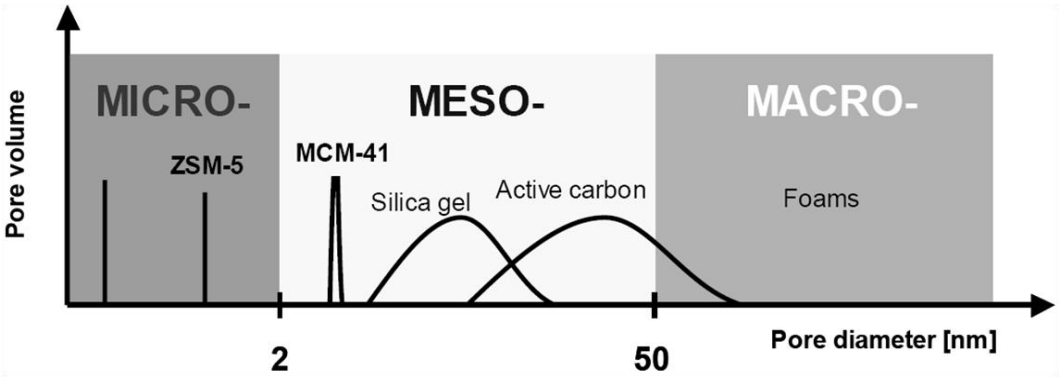

Figure 1-28: IUPAC classification of porous materials with respect to the pore diameter.[250]

Pore diameters between 2.0 and 50.0 nm are assigned to mesoporous materials. Larger pore dimensions than in the case of microporous materials promote transport processes through the material. Silica gel and activated carbons are examples of typical disordered mesoporous materials which lack a defined pore size distribution. Therefore, a number of synthetic approaches have been developed making ordered mesoporous oxide materials such as MCM-41[256] or SBA-15[257] easily accessible.

These templates can then be used to assist in the preparation of other ordered mesoporous materials.[258] The upper limit of the IUPAC scale is covered by macroporous materials with pore diameters larger than 50.0 nm. Foams and materials prepared by mechanical treatment are representative members of the macroporous family.[259]

On the one hand the open porosity of these materials is fully accessible to guest molecules but the overall porosity is significantly lower than for micro- or mesoporous materials.

The different types of porosity also result in different types of adsorption. The amount of adsorbed gas volume as a function of pressure at a constant temperature is called adsorption isotherm. Figure 1-29 illustrates six different isotherms which have been classified by IUPAC according to their characteristic shapes. Isotherms of type I and type IV are typically encountered when dealing with microporous and mesoporous materials, respectively.[250]

For the interpretation of adsorption isotherms two main methods are applied on a routine basis. On the one hand, the *Brunauer-Emmett-Teller* (BET) theory which takes multilayer adsorption into account can be used to calculate the specific surface area of a sample.[248,260] On the other hand the computational procedure developed by *Barrett*, *Joyner* and *Halenda* (BJH) is frequently applied to the evaluation of pore size distributions.[248,261]

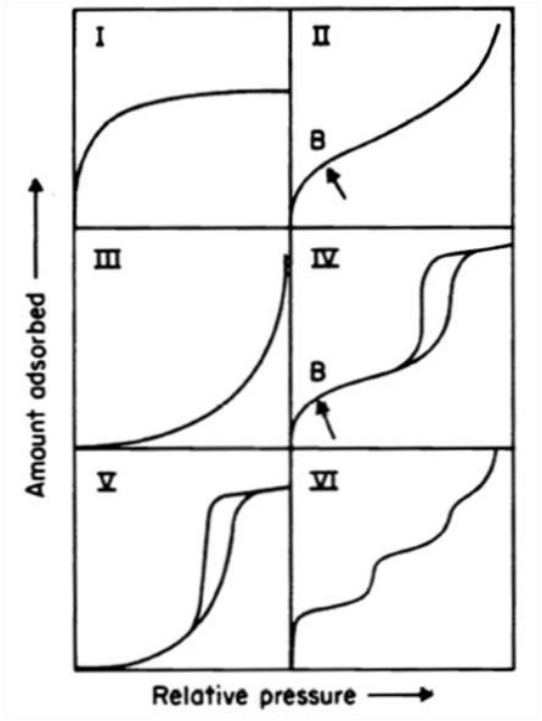

Figure 1-29: Classification of sorption isotherms according to IUPAC.[250]

Pore volumes are conveniently calculated by converting the adsorbed gas volume at a give relative pressure p/p_0 into the corresponding liquid volume. Typically, the micropore volume (MPV) is determined at $p/p_0 = 0.1$ whereas the overall pore volume (PV) is obtained at $p/p_0 = 0.8$.

1.7 Application of Microporous Polymers

Early applications of microporous polymers are found in the field of chromatography. In this regard, HCPs are well-developed and are being commercially used for separation problems and removal of specific components from complex mixtures. Hence, hypercrosslinked poly(styrene) has been used as a stationary phase in high pressure liquid chromatography (HPLC).[262,263] The targeted generation of bimodal pore size distributions is a significant advantage of microporous polymers, as larger macropores promote transport and diffusion processes towards smaller micropores.[193,194] Furthermore, chromatographic applications benefit from the relatively low cost and high stability of HCPs.

The combination of high specific surface area and enhanced microporosity is often considered the key requisite for high gas uptake capacities. Consequently, various HCPs, PIMs and COFs have been evaluated as gas storage materials for

hydrogen,[187,228,230,231,246,264,265] methane,[265] carbon dioxide[265] and ammonia.[266]

Microporous and highly selective gas separation membranes were casted from soluble PIM materials that showed promising results for the separation of commercially important gas pairs such as carbon dioxide/nitrogen or carbon dioxide/methane.[219-221] Also, liquid phase adsorption of various dyes and phenolics was demonstrated for HCP,[205] PIM[218,267] and COF materials.[242]

Catalysis represents another field of application where high surface areas and enhanced pore volumes are beneficial. Crosslinked PIMs containing metallophthalocyanines and metalloporphyrins were used for redox processes such as the decomposition of hydrogen peroxide, the oxidation of cyclohexene, and the oxidation of hydroquinone.[229]

Additionally, the surface area of microporous polymers may be used for the accommodation of catalytic guest species. For example, the efficient hydrogenation of alkynes to alkanes was achieved under catalysis of palladium clusters that were imbedded within the matrix of a microporous poly(thienylene arylene) HCP.[210] Iron-impregnated poly(isocyanurate) HCPs were highly active and selective in oxidizing benzyl alcohol to benzaldehyde under mild conditions.[213] Palladium nanoparticles were also incorporated within a triazine-based COF and the resulting material was found a suitable catalyst for the oxidation of glycerol.[268] The selective oxidation of methane to methanol was achieved by application of the same material upon impregnation with platinum.[269]

Future applications of microporous organic polymers may involve the field of organic electronics. In principle two interconnected phases exist in these materials - the polymer itself and empty space that can be filled with a second material. Conjugated HCPs[202,207] and COFs[235,236] were recently studied with respect to fluorescence characteristics[202,207] and photo current generation.[236] The *in-situ* formation of a COF was used for surface patterning and monitored by STM.[243]

1.8 Bibliography

(1) Faraday, M. *Phil. Trans. R. Soc. London* **1825**, 440.
(2) Randić, M. *Chem. Rev.* **2003**, *103*, 3449-3606.
(3) Balaban, A. T.; Schleyer, P. v. R.; Rzepa, H. S. *Chem. Rev.* **2005**, *105*, 3436-3447.
(4) Kekulé, A. *Bull. Soc. Chim. Fr.* **1865**, *3*, 98.
(5) Armit, T. W.; Robinson, R. *J. Chem. Soc., Trans.* **1925**, *127*, 1604 - 1618.
(6) Hückel, E. *Z. Phys.* **1931**, *70*, 204 - 286.
(7) Clar, E. *Polycyclic Hydrocarbons*; Academic Press and Springer: London and Berlin, **1964**.
(8) Clar, E. *The Aromatic Sextet*; J. Wiley & Sons: London, **1972**.
(9) Hendel, W.; Khan, Z. H.; Schmidt, W. *Tetrahedron* **1986**, *42*, 1127-1134.
(10) Henning, T.; Salama, F. *Science* **1998**, *282*, 2204-2210.
(11) Scholl, R.; Mansfeld, J. *Ber. Dtsch. Chem. Ges.* **1910**, *43*, 1734-1746.
(12) Scholl, R.; Seer, C.; Weitzenböck, R. *Ber. Dtsch. Chem. Ges.* **1910**, *43*, 2202-2209.
(13) Scholl, R.; Seer, C. *Ber. Dtsch. Chem. Ges.* **1911**, *44*, 1233-1249.
(14) Scholl, R.; Seer, C. *Liebigs Ann. Chem.* **1912**, *394*, 111-177.
(15) Clar, E. *Ber. Dtsch. Chem. Ges.* **1929**, *62*, 350-359.
(16) Clar, E.; John, F.; Hawran, B. *Ber. Dtsch. Chem. Ges.* **1929**, *62*, 940-950.
(17) Clar, E.; Wallenstein, H.; Avenarius, R. *Ber. Dtsch. Chem. Ges.* **1929**, *62*, 950-955.
(18) Clar, E. *Ber. Dtsch. Chem. Ges.* **1929**, *62*, 1574-1582.
(19) Clar, E.; Zander, M. *J. Chem. Soc.* **1957**, *1957*, 4616-4619.
(20) Clar, E.; Zander, M. *J. Chem. Soc.* **1958**, *1958*, 1577-1579.
(21) Clar, E.; Ironside, C. T.; Zander, M. *Tetrahedron* **1959**, *6*, 358-363.
(22) Chandrasekhar, S.; Sadashiva, B. K.; Suresh, K. A. *Pramana* **1977**, *9*, 471-480.
(23) Chandrasekhar, S.; Prasad, S. K. *Contemp. Phys.* **1999**, *40*, 237 - 245.
(24) Laschat, S.; Baro, A.; Steinke, N.; Giesselmann, F.; Hägele, C.; Scalia, G.; Judele, R.; Kapatsina, E.; Sauer, S.; Schreivogel, A. *Angew. Chem. Int. Ed.* **2007**, *46*, 4832-4887.
(25) Kumar, S. *Liq. Cryst.* **2009**, *36*, 607–638.
(26) Pisula, W.; Tomovic, Z.; Simpson, C.; Kastler, M.; Pakula, T.; Müllen, K. *Chem. Mater.* **2005**, *17*, 4296-4303.
(27) Wasserfallen, D.; Kastler, M.; Pisula, W.; Hofer, W. A.; Fogel, Y.; Wang, Z.; Müllen, K. *J. Am. Chem. Soc.* **2006**, *128*, 1334-1339.
(28) Feng, X.; Marcon, V.; Pisula, W.; Hansen, M. R.; Kirkpatrick, J.; Grozema, F.; Andrienko, D.; Kremer, K.; Müllen, K. *Nat. Mater.* **2009**, *8*, 421-426.
(29) Gama, V.; Henriques, R. T.; Bonfait, G.; Almeida, M.; Meetsma, A.; Van Smaalen, S.; De Boer, J. L. *J. Am. Chem. Soc.* **1992**, *114*, 1986-1989.
(30) van de Craats, A. M.; Warman, J. M.; Fechtenkötter, A.; Brand, J. D.; Harbison, M. A.; Müllen, K. *Adv. Mater.* **1999**, *11*, 1469-1472.
(31) Hiramoto, M.; Kishigami, Y.; Yokoyama, M. *Chem. Lett.* **1990**, *19*, 119-122.
(32) Schmidt-Mende, L.; Fechtenkötter, A.; Müllen, K.; Moons, E.; Friend, R. H.; MacKenzie, J. D. *Science* **2001**, *293*, 1119.
(33) Schmidtke, J. P.; Friend, R. H.; Kastler, M.; Müllen, K. *J. Chem. Phys.* **2006**, *124*, 174704.
(34) Hesse, H. C.; Weickert, J.; Al-Hussein, M.; Dössel, L.; Feng, X.; Müllen, K.; Schmidt-Mende, L. *Sol. Energy Mater. Sol. Cells* **2009**.
(35) Wong, W. W. H.; Ma, C.-Q.; Pisula, W.; Yan, C.; Feng, X.; Jones, D. J.; Müllen, K.; Janssen, R. A. J.; Bäuerle, P.; Holmes, A. B. *Chem. Mater.* **2009**, *22*, 457-466.
(36) Debad, J. D.; Morris, J. C.; Magnus, P.; Bard, A. J. *J. Org. Chem.* **1997**, *62*, 530-537.
(37) Holtrup, F. O.; Müller, G. R. J.; Quante, H.; de Feyter, S.; de Schryver, F. C.; Müllen, K. *Chem. Eur. J.* **1997**, *3*, 219-225.
(38) van de Craats, A.; Stutzmann, N.; Bunk, O.; Nielsen, M.; Watson, M.; Müllen, K.; Chanzy, H.; Sirringhaus, H.; Friend, R. *Adv. Mater.* **2003**, *15*, 495-499.
(39) Pisula, W.; Menon, A.; Stepputat, M.; Lieberwirth, I.; Kolb, U.; Tracz, A.; Sirringhaus, H.; Pakula, T.; Müllen, K. *Adv. Mater.* **2005**, *17*, 684-689.
(40) Allard, S.; Forster, M.; Souharce, B.; Thiem, H.; Scherf, U. *Angew. Chem. Int. Ed.* **2008**, *47*, 4070-4098.
(41) Wong, W. W. H.; Singh, T. B.; Vak, D.; Pisula, W.; Yan, C.; Feng, X.; Williams, E. L.; Chan, K. L.; Mao, Q.; Jones, D. J.; Ma, C. Q.; Müllen, K.; Bäuerle, P.; Holmes, A. B. *Adv. Funct. Mater.* **2010**, *20*, 927-938.
(42) Ruess, G.; Vogt, F. *Monatsh. Chem.* **1948**, *78*, 222-242.
(43) Boehm, H. P.; Clauss, A.; Fischer, G. O.; Hofmann, U. *Z. Naturforschg.* **1962**, *17b*, 150-153.
(44) Berger, C.; Song, Z.; Li, T.; Li, X.; Ogbazghi, A. Y.; Feng, R.; Dai, Z.; Marchenkov, A. N.; Conrad, E. H.; First, P. N.; de Heer, W. A. *J. Phys. Chem. B* **2004**, *108*, 19912-19916.
(45) Novoselov, K. S.; Geim, A. K.; Morozov, S. V.; Jiang, D.; Zhang, Y.; Dubonos, S. V.; Grigorieva, I. V.; Firsov, A. A. *Science* **2004**, *306*, 666.
(46) Geim, A. K. *Science* **2009**, *324*, 1530-1534.

(47) Bieri, M.; Treier, M.; Cai, J.; Aït-Mansour, K.; Ruffieux, P.; Gröning, O.; Gröning, P.; Kastler, M.; Rieger, R.; Feng, X.; Müllen, K.; Fasel, R. *Chem. Commun.* **2009**, *2009*, 6919-6921.
(48) Cai, J.; Ruffieux, P.; Jaafar, R.; Bieri, M.; Braun, T.; Blankenburg, S.; Muoth, M.; Seitsonen, A. P.; Saleh, M.; Feng, X.; Müllen, K.; Fasel, R. *Nature* **2010**, *466*, 470-473.
(49) Simpson, C. D.; Mattersteig, G.; Martin, K.; Gherghel, L.; Bauer, R. E.; Räder, H. J.; Müllen, K. *J. Am. Chem. Soc.* **2004**, *126*, 3139-3147.
(50) Simpson, C. D.; Brand, J. D.; Berresheim, A. J.; Przybilla, L.; Räder, H. J.; Müllen, K. *Chem. Eur. J.* **2002**, *8*, 1424-1429.
(51) Wu, J.; Gherghel, L.; Watson, M. D.; Li, J.; Wang, Z.; Simpson, C. D.; Kolb, U.; Müllen, K. *Macromolecules* **2003**, *36*, 7082-7089.
(52) Yang, X.; Dou, X.; Rouhanipour, A.; Zhi, L.; Räder, H. J.; Müllen, K. *J. Am. Chem. Soc.* **2008**, *130*, 4216-4217.
(53) Fogel, Y.; Zhi, L.; Rouhanipour, A.; Andrienko, D.; Räder, H. J.; Müllen, K. *Macromolecules* **2009**, *42*, 6878-6884.
(54) Aihara, J. *J. Am. Chem. Soc.* **1992**, *114*, 865-868.
(55) Dias, J. R. *Thermochim. Acta* **1987**, *122*, 313-337.
(56) Watson, M. D.; Fechtenkötter, A.; Müllen, K. *Chem. Rev* **2001**, *101*, 1267-1300.
(57) Rieger, R.; Müllen, K. *J. Phys. Org. Chem.* **2010**, *23*, 315-325.
(58) Jiao, H.; Schleyer, P. v. R. *Angew. Chem. Int. Ed.* **1996**, *35*, 2383-2386.
(59) Luch, A. *Imperial College Press: London* **2005**.
(60) Lang, K. F.; Kalowy, J.; Buffleb, H. *Chem. Ber. Recl.* **1962**, *95*, 1052-1053.
(61) Lang, K. F.; Buffleb, H.; Kalowy, J. *Chem. Ber. Recl.* **1964**, *97*, 494-497.
(62) Lang, K. F.; Buffleb, H. *Chem. Ber. Recl.* **1962**, *95*, 1049-1051.
(63) Lang, K. F.; Buffleb, H.; Zander, M. *Angew. Chem.* **1963**, *75*, 170-170.
(64) Sullivan, R. F.; Boduszynski, M. M.; Fetzer, J. C. *Energy & Fuels* **1989**, *3*, 603-612.
(65) Haworth, R. D. *J. Chem. Soc.* **1932**, *1932*, 1125-1133.
(66) Haworth, R. D.; Bolam, F. M. *J. Chem. Soc.* **1932**, *1932*, 2248-2251.
(67) Haworth, R. D.; Mavin, C. R. *J. Chem. Soc.* **1932**, *1932*, 2720-2723.
(68) Haworth, R. D.; Mavin, C. R.; Sheldrick, G. *J. Chem. Soc.* **1934**, *1934*, 454 - 461.
(69) Menicagli, R.; Piccolo, O. *J. Org. Chem.* **1980**, *45*, 2581-2585.
(70) Diels, O.; Alder, K. *Justus Liebigs Ann. Chem.* **1928**, *460*, 98-122.
(71) Müller, M.; Mauermann-Düll, H.; Wagner, M.; Enkelmann, V.; Müllen, K. *Angew. Chem. Int. Ed.* **1995**, *34*, 1583-1586.
(72) Müller, M.; Petersen, J.; Strohmaier, R.; Günther, C.; Karl, N.; Müllen, K. *Angew. Chem. Int. Ed.* **1996**, *35*, 886-888.
(73) Ogliaruso, M. A.; Romanelli, M. G.; Becker, E. I. *Chem. Rev.* **1965**, *65*, 261-367.
(74) Iyer, V. S.; Wehmeier, M.; Brand, J. D.; Keegstra, M. A.; Müllen, K. *Angew. Chem. Int. Ed.* **1997**, *36*, 1604-1607.
(75) Shifrina, Z. B.; Averina, M. S.; Rusanov, A. L.; Wagner, M.; Müllen, K. *Macromolecules* **2000**, *33*, 3525-3529.
(76) Dilthey, W.; Hurtig, G. *Ber. Dtsch. Chem. Ges.* **1934**, *67*, 2004-2007.
(77) Dilthey, W.; Quint, F. *J. Prakt. Chem.* **1930**, *128*, 139-149.
(78) Dilthey, W.; Schommer, W. *J. Prakt. Chem.* **1933**, *136*, 293-298.
(79) Mallory, F. B.; Wood, C. S.; Gordon, J. T.; Lindquist, L. C.; Savitz, M. L. *J. Am. Chem. Soc.* **1962**, *84*, 4361-4362.
(80) Xiao, S.; Myers, M.; Miao, Q.; Sanaur, S.; Pang, K.; Steigerwald, M. L.; Nuckolls, C. *Angew. Chem. Int. Ed.* **2005**, *44*, 7390-7394.
(81) Rieger, R.; Kastler, M.; Enkelmann, V.; Müllen, K. *Chem. Eur. J.* **2008**, *14*, 6322-6325.
(82) Otsubo, T.; Gray, R.; Boekelheide, V. *J. Am. Chem. Soc.* **1978**, *100*, 2449-2456.
(83) Mitchell, R. H.; Boekelheide, V. *J. Am. Chem. Soc.* **1974**, *96*, 1547-1557.
(84) Haenel, M.; Staab, H. A. *Chem. Ber.* **1973**, *106*, 2203-2216.
(85) Kemp, W.; Storie, I. T.; Tulloch, C. D. *J. Chem. Soc., Perkin Trans. 1* **1980**, *1980*, 2812-2817.
(86) Diederich, F.; Staab, H. A. *Angew. Chem. Int. Ed.* **1978**, *17*, 372-374.
(87) Krieger, C.; Diederich, F.; Schweitzer, D.; Staab, H. A. *Angew. Chem. Int. Ed.* **1979**, *18*, 699-701.
(88) Staab, H. A.; Diederich, F. *Chem. Ber.* **1983**, *116*, 3487-3503.
(89) Staab, H. A.; Diederich, F.; Krieger, C.; Schweitzer, D. *Chem. Ber.* **1983**, *116*, 3504-3512.
(90) Koch, K. H.; Müllen, K. *Chem. Ber.* **1991**, *124*, 2091-2100.
(91) Rempala, P.; Kroulík, J.; King, B. T. *J. Am. Chem. Soc.* **2004**, *126*, 15002-15003.
(92) King, B. T.; Kroulik, J.; Robertson, C. R.; Rempala, P.; Hilton, C. L.; Korinek, J. D.; Gortari, L. M. *J. Org. Chem.* **2007**, *72*, 2279-2288.
(93) Di Stefano, M.; Negri, F.; Carbone, P.; Müllen, K. *Chem. Phys.* **2005**, *314*, 85-99.
(94) Feng, X.; Wu, J.; Ai, M.; Pisula, W.; Zhi, L.; Rabe, J. P.; Müllen, K. *Angew. Chem. Int. Ed.* **2007**, *46*, 3033-3036.
(95) Staab, H. A.; Binnig, F. *Tetrahedron Lett.* **1964**, *5*, 319-321.
(96) Staab, H. A.; Bräunling, H. *Tetrahedron Lett.* **1965**, *6*, 45-49.
(97) Meyer, H.; Staab, H. A. *Liebigs Ann. Chem.* **1969**, *724*, 30-33.
(98) Staab, H. A.; Binnig, F. *Chem. Ber.* **1967**, *100*, 889-892.

(99) Staab, H. A.; Binnig, F. *Chem. Ber.* **1967**, *100*, 293-305.
(100) Wittig, G.; Rümpler, K. D. *Liebigs Ann. Chem.* **1971**, *751*, 1-16.
(101) Song, Q.; Lebeis, C. W.; Shen, X.; Ho, D. M.; Pascal, R. A. *J. Am. Chem. Soc.* **2005**, *127*, 13732-13737.
(102) Bräunling, H.; Binnig, F.; Staab, H. A. *Chem. Ber.* **1967**, *100*, 880-888.
(103) Irngartinger, H.; Leiserowitz, L.; Schmidt, G. M. J. *Chem. Ber.* **1970**, *103*, 1132-1156.
(104) Pisula, W.; Kastler, M.; Yang , C.; Enkelmann, V.; Müllen, K. *Chem. Asian J.* **2007**, *2*, 51-56.
(105) Blankenburg, S.; Bieri, M.; Fasel, R.; Müllen, K.; Pignedoli, C. A.; Passerone, D. *Small* **2010**, *6*, 2266-2271.
(106) Cram, D. J.; Kaneda, T.; Helgeson, R. C.; Lein, G. M. *J. Am. Chem. Soc.* **1979**, *101*, 6752-6754.
(107) Cram, D. J.; Lein, G. M.; Kaneda, T.; Helgeson, R. C.; Knobler, C. B.; Maverick, E.; Trueblood, K. N. *J. Am. Chem. Soc.* **1981**, *103*, 6228-6232.
(108) Cram, D. J.; Kaneda, T.; Helgeson, R. C.; Brown, S. B.; Knobler, C. B.; Maverick, E.; Trueblood, K. N. *J. Am. Chem. Soc.* **1985**, *107*, 3645-3657.
(109) Trueblood, K. N.; Maverick, E. F.; Knobler, C. B. *Acta Crystallogr., Sect. B: Struct. Sci* **1991**, *47*, 389-398.
(110) Knobler, C. B.; Maverick, E.; Trueblood, K. N. *J. Inclusion Phenom. Mol. Recognit. Chem.* **1992**, *12*, 341-360.
(111) Treier, M.; Pignedoli, C. A.; Laino, T.; Rieger, R.; Müllen, K.; Passerone, D.; Fasel, R. *Nat. Chem.* **2011**, *3*, 61-67.
(112) Tahara, K.; Tobe, Y. *Chem. Rev.* **2006**, *106*, 5274-5290.
(113) Aihara, J. *Bull. Chem. Soc. Jpn.* **1976**, *49*, 1429-1430.
(114) Funhoff, D. J. H.; Staab, H. A. *Angew. Chem. Int. Ed.* **1986**, *25*, 742-744.
(115) Jasat, A.; Dolphin, D. *Chem. Rev.* **1997**, *97*, 2267-2340.
(116) Beletskaya, I.; Tyurin, V. S.; Tsivadze, A. Y.; Guilard, R.; Stern, C. *Chem. Rev.* **2009**, *109*, 1659-1713.
(117) Elemans, J.; van Hameren, R.; Nolte, R.; Rowan, A. *Adv. Mater.* **2006**, *18*, 1251-1266.
(118) Bessho, T.; Zakeeruddin, S. M.; Yeh, C. Y.; Diau, E. W. G.; Grätzel, M. *Angew. Chem. Int. Ed.* **2010**, *49*, 6646-6649.
(119) Spillmann, H.; Kiebele, A.; Stöhr, M.; Jung, T. A.; Bonifazi, D.; Cheng, F.; Diederich, F. *Adv. Mater.* **2006**, *18*, 275-279.
(120) Bell, T. W.; Firestone, A.; Guzzo, F.; Hu, L. Y. *J. Inclusion Phenom. Macrocyclic Chem.* **1987**, *5*, 149-152.
(121) Bell, T. W.; Cragg, P. J.; Drew, M. G. B.; Firestone, A.; Kwok, A. D. I.; Liu, J. I. A.; Ludwig, R. T.; Papoulis, A. T. *Pure Appl. Chem.* **1993**, *65*, 361-361.
(122) Drew, M. G. B.; de O. Cabral, J.; Cabral, M. F.; Esho, F. S.; Nelson, S. M. *J. Chem. Soc., Chem. Commun.* **1979**, *1979*, 1033 - 1035.
(123) Bell, T. W.; Guzzo, F. *J. Am. Chem. Soc.* **1984**, *106*, 6111-6112.
(124) Bell, T. W.; Guzzo, F.; Drew, M. G. B. *J. Am. Chem. Soc.* **1991**, *113*, 3115-3122.
(125) Benetollo, F.; Bombieri, G.; De Cola, L.; Polo, A.; Smailes, D. L.; Vallarino, L. M. *Inorg. Chem.* **1989**, *28*, 3447-3452.
(126) Newkome, G. R.; Lee, H. W. *J. Am. Chem. Soc.* **1983**, *105*, 5956-5957.
(127) Toner, J. L. *Tetrahedron Lett.* **1983**, *24*, 2707-2710.
(128) Ransohoff, J. E. B.; Staab, H. A. *Tetrahedron Lett.* **1985**, *26*, 6179-6182.
(129) Bell, T. W.; Firestone, A. *J. Am. Chem. Soc.* **1986**, *108*, 8109-8111.
(130) Bell, T. W.; Cragg, P. J.; Drew, M. G. B.; Firestone, A.; Kwok, D. I. A. *Angew. Chem. Int. Ed.* **1992**, *31*, 345-347, 348-350.
(131) Boguslavsky, L.; Bell, T. W. *Langmuir* **1994**, *10*, 991-993.
(132) Han, M. Y.; Özyilmaz, B.; Zhang, Y.; Kim, P. *Phys. Rev. Lett.* **2007**, *98*, 206805.
(133) Özyilmaz, B.; Jarillo-Herrero, P.; Efetov, D.; Kim, P. *Appl. Phys. Lett.* **2007**, *91*, 192107.
(134) Kosynkin, D. V.; Higginbotham, A. L.; Sinitskii, A.; Lomeda, J. R.; Dimiev, A.; Price, B. K.; Tour, J. M. *Nature* **2009**, *458*, 872-876.
(135) Li, X.; Wang, X.; Zhang, L.; Lee, S.; Dai, H. *Science* **2008**, *319*, 1229-1232.
(136) Chen, Z.; Lin, Y. M.; Rooks, M. J.; Avouris, P. *Physica E* **2007**, *40*, 228-232.
(137) Barone, V.; Hod, O.; Scuseria, G. E. *Nano Lett.* **2006**, *6*, 2748-2754.
(138) Yang, L.; Park, C.-H.; Son, Y.-W.; Cohen, M. L.; Louie, S. G. *Phys. Rev. Lett.* **2007**, *99*, 186801.
(139) Radovic, L. R.; Bockrath, B. *J. Am. Chem. Soc.* **2005**, *127*, 5917-5927.
(140) Oeiras, R. Y.; Araújo-Moreira, F. M.; da Silva, E. Z. *Phys. Rev. B* **2009**, *80*, 73405.
(141) Enoki, T.; Kobayashi, Y.; Fukui, K. I. *Int. Rev. Phys. Chem.* **2007**, *26*, 609-645.
(142) Jia, X.; Hofmann, M.; Meunier, V.; Sumpter, B. G.; Campos-Delgado, J.; Romo-Herrera, J. M.; Son, H.; Hsieh, Y. P.; Reina, A.; Kong, J. *Science* **2009**, *323*, 1701.
(143) Sastri, V. R.; Schulman, R.; Roberts, D. C. *Macromolecules* **1982**, *15*, 939-947.
(144) Horn, T.; Wegener, S.; Müllen, K. *Macromol. Chem. Phys.* **1995**, *196*, 2463-2474.
(145) Kaur, I.; Stein, N. N.; Kopreski, R. P.; Miller, G. P. *J. Am. Chem. Soc.* **2009**, *131*, 3424-3425.
(146) Kaur, I.; Jazdzyk, M.; Stein, N. N.; Prusevich, P.; Miller, G. P. *J. Am. Chem. Soc.* **2010**, *132*, 1261-1263.
(147) Zade, S. S.; Bendikov, M. *Angew. Chem. Int. Ed.* **2010**, *49*, 4012-4015.
(148) Stille, J. K.; Harris, F. W.; Rakutis, R. O.; Mukamal, H. *J. Polym. Sci. B, Polym. Lett.* **1966**, *4*, 791-793.
(149) Stille, J. K.; Freeburger, M. E. *J. Polym. Sci. B, Polym. Lett.* **1967**, *5*, 989-992.
(150) Imai, K.; Kurihara, M.; Mathias, L.; Wittmann, J.; Alston, W. B.; Stille, J. K. *Macromolecules* **1973**, *6*, 158-162.
(151) de Schryver, F.; Marvel, C. S. *J. Polym. Sci. A, Polym. Chem.* **1967**, *5*, 545-552.

(152) Kellman, R.; Marvel, C. S. *J. Polym. Sci. A, Polym. Chem.* **1975**, *13*, 2125-2131.
(153) Sakamoto, J.; van Heijst, J.; Lukin, O.; Schlüter, A. D. *Angew. Chem. Int. Ed.* **2009**, *48*, 1030-1069.
(154) Berresheim, A. J.; Müller, M.; Müllen, K. *Chem. Rev.* **1999**, *99*, 1747-1786.
(155) Löffler, M.; Schlüter, A.-D.; Geßler, K.; Saenger, W.; Toussaint, J.-M.; Brédas, J. L. *Angew. Chem. Int. Ed.* **1994**, *33*, 2209-2212.
(156) Scherf, U.; Müllen, K. *Makromol. Chem., Rapid Commun.* **1991**, *12*, 489-497.
(157) Crossley, M. J.; Burn, P. L. *J. Chem. Soc., Chem. Commun.* **1991**, 1569-1571.
(158) Tsuda, A.; Furuta, H.; Osuka, A. *Angew. Chem. Int. Ed.* **2000**, *39*, 2549-2552.
(159) Tsuda, A.; Osuka, A. *Science* **2001**, *293*, 79-82.
(160) Ikeda, T.; Aratani, N.; Osuka, A. *Chem. Asian J.* **2009**, *4*, 1248-1256.
(161) Elemans, J.; Lei, S.; de Feyter, S. *Angew. Chem. Int. Ed.* **2009**, *48*, 7298-7332.
(162) Hoeben, F. J. M.; Jonkheijm, P.; Meijer, E. W.; Schenning, A. *Chem. Rev.* **2005**, *105*, 1491-1546.
(163) Lehn, J.-M. *VCH: Weinheim* **1995**.
(164) Liljeroth, P.; Repp, J.; Meyer, G. *Science* **2007**, *317*, 1203-1206.
(165) Hirjibehedin, C. F.; Lin, C. Y.; Otte, A. F.; Ternes, M.; Lutz, C. P.; Jones, B. A.; Heinrich, A. J. *Science* **2007**, *317*, 1199-1203.
(166) Adam, D.; Schuhmacher, P.; Simmerer, J.; Häussling, L.; Siemensmeyer, K.; Etzbachi, K. H.; Ringsdorf, H.; Haarer, D. *Nature* **1994**, *371*.
(167) Henderson, P.; Kumar, S.; Rego, J. A.; Ringsdorf, H.; Schuhmacher, P. *J. Chem. Soc., Chem. Commun.* **1995**, *1995*, 1059-1060.
(168) Kumar, S. *Liq. Cryst.* **2005**, *32*, 1089-1113.
(169) Kumar, S.; Naidu, J. J.; Rao, D. S. S. *J. Mater. Chem.* **2002**, *12*, 1335-1341.
(170) Müller, G. R. J.; Meiners, C.; Enkelmann, V.; Geerts, Y.; Müllen, K. *J. Mater. Chem.* **1998**, *8*, 61-64.
(171) Fischbach, I.; Pakula, T.; Minkin, P.; Fechtenkötter, A.; Müllen, K.; Spiess, H. W.; Saalwächter, K. *J. Phys. Chem. B* **2002**, *106*, 6408-6418.
(172) Binnig, G.; Rohrer, H. *Helv. Phys. Acta* **1982**, *55*, 726–735.
(173) Samori, P.; Rabe, J. P. *J. Phys. Condens. Matter* **2002**, *14*, 9955–9973.
(174) Lafferentz, L.; Ample, F.; Yu, H.; Hecht, S.; Joachim, C.; Grill, L. *Science* **2009**, *323*, 1193.
(175) Hulsken, B.; Van Hameren, R.; Gerritsen, J. W.; Khoury, T.; Thordarson, P.; Crossley, M. J.; Rowan, A. E.; Nolte, R. J. M.; Elemans, J.; Speller, S. *Nat. Nanotechnol.* **2007**, *2*, 285-289.
(176) Forrest, S. R. *Chem. Rev.* **1997**, *97*, 1793-1896.
(177) Ruffieux, P.; Gröning, O.; Fasel, R.; Kastler, M.; Wasserfallen, D.; Müllen, K.; Gröning, P. *J. Phys. Chem. B* **2006**, *110*, 11253-11258.
(178) Rabe, J. P.; Buchholz, S. *Science* **1991**, *253*, 424-427.
(179) Budd, P. M. *Science* **2007**, *316*, 210-211.
(180) Cooper, A. I. *Adv. Mater.* **2009**, *21*, 1291 - 1295.
(181) Germain, J.; Fréchet, J. M. J.; Svec, F. *Small* **2009**, *5*, 1098 - 1111.
(182) Maly, K. E. *J. Mater. Chem.* **2009**, *19*, 1781-1787.
(183) Jiang, J. X.; Cooper, A. I. *Top. Curr. Chem.* **2010**, *293*, 1-33.
(184) Lee, J.; Kim, J.; Hyeon, T. *Adv. Mater.* **2006**, *18*, 2073-2094.
(185) Ben, T.; Ren, H.; Ma, S.; Cao, D.; Lan, J.; Jing, X.; Wang, W.; Xu, J.; Deng, F.; Simmons, J. M. *Angew. Chem. Int. Ed.* **2009**, *48*, 9457-9460.
(186) Trewin, A.; Cooper, A. I. *Angew. Chem. Int. Ed.* **2010**, *49*, 1533-1535.
(187) Ghanem, B. S.; Msayib, K. J.; McKeown, N. B.; Harris, K. D. M.; Pan, Z.; Budd, P. M.; Butler, A.; Selbie, J.; Book, D.; Walton, A. *Chem. Commun.* **2007**, *2007*, 67-69.
(188) El-Kaderi, H. M.; Hunt, J. R.; Mendoza-Cortes, J. L.; Cote, A. P.; Taylor, R. E.; O'Keeffe, M.; Yaghi, O. M. *Science* **2007**, *316*, 268-272.
(189) Davankov, V. A.; Rogozhin, S. V.; Tsyurupa, M. P. *USSR Pat., 299165* **1969**.
(190) Davankov, V. A.; Rogozhin, S. V.; Tsyurupa, M. P. *US Pat., 3729457* **1973**.
(191) Tsyurupa, M. P.; Davankov, V. A. *React. Funct. Polym.* **2002**, *53*, 193-203.
(192) Tsyurupa, M. P.; Davankov, V. A. *React. Funct. Polym.* **2006**, *66*, 768-779.
(193) Schwab, M. G.; Senkovska, I.; Rose, M.; Klein, N.; Koch, M.; Pahnke, J.; Jonschker, G.; Schmitz, B.; Michael, H.; Kaskel, S. *Soft Matter* **2009**, *5*, 1055-1059.
(194) Ahn, J. H.; Jang, J. E.; Oh, C. G.; Ihm, S. K.; Cortez, J.; Sherrington, D. C. *Macromolecules* **2006**, *39*, 627-632.
(195) Germain, J.; Hradil, J.; Fréchet, J. M. J.; Svec, F. *Chem. Mater.* **2006**, *18*, 4430-4435.
(196) Wood, C. D.; Tan, B.; Trewin, A.; Niu, H.; Bradshaw, D.; Rosseinsky, M. J.; Khimyak, Y. Z.; Campbell, N. L.; Kirk, R.; Stöckel, E.; Cooper, A. I. *Chem. Mater.* **2007**, *19*, 2034-2048.
(197) Wood, C. D.; Tan, B.; Trewin, A.; Su, F.; Rosseinsky, M. J.; Bradshaw, D.; Sun, Y.; Zhou, L.; Cooper, A. I. *Adv. Mater.* **2008**, *20*, 1916-1921.
(198) Schwab, M. G.; Lennert, A.; Pahnke, J.; Jonschker, G.; Koch, M.; Senkovska, I.; Rehahn, M.; Kaskel, S. *J. Mater. Chem.* **2011**, *21*, 2131-2135.
(199) Germain, J.; Fréchet, J. M. J.; Svec, F. *J. Mater. Chem.* **2007**, *17*, 4989-4997.
(200) Germain, J.; Svec, F.; Fréchet, J. M. J. *Chem. Mater.* **2008**, *20*, 7069-7076.
(201) Germain, J.; Fréchet, J. M. J.; Svec, F. *Chem. Commun.* **2009**, *2009*, 1526-1528.
(202) Jiang, J. X.; Su, F.; Trewin, A.; Wood, C. D.; Campbell, N. L.; Niu, H.; Dickinson, C.; Ganin, A. Y.; Rosseinsky, M. J.; Khimyak, Y. Z.; Cooper, A. I. *Angew. Chem. Int. Ed.* **2007**, *46*, 8574-8578.

(203) Jiang, J. X.; Su, F.; Trewin, A.; Wood, C. D.; Niu, H.; Jones, J. T. A.; Khimyak, Y. Z.; Cooper, A. I. *J. Am. Chem. Soc.* **2008**, *130*, 7710-7720.
(204) Jiang, J. X.; Trewin, A.; Su, F.; Wood, C. D.; Niu, H.; Jones, J. T. A.; Khimyak, Y. Z.; Cooper, A. I. *Macromolecules* **2009**, *42*, 2658-2666.
(205) Dawson, R.; Laybourn, A.; Clowes, R.; Khimyak, Y. Z.; Adams, D. J.; Cooper, A. I. *Macromolecules* **2009**, 675-683.
(206) Stöckel, E.; Wu, X.; Trewin, A.; Wood, C. D.; Clowes, R.; Campbell, N. L.; Jones, J. T. A.; Khimyak, Y. Z.; Adams, D. J.; Cooper, A. I. *Chem. Commun.* **2009**, *2009*, 212-214.
(207) Weber, J.; Thomas, A. *J. Am. Chem. Soc.* **2008**, *130*, 6334-6335.
(208) Jiang, J. X.; Su, F.; Niu, H.; Wood, C. D.; Campbell, N. L.; Khimyak, Y. Z.; Cooper, A. I. *Chem. Commun.* **2008**, *2008*, 486-488.
(209) Schmidt, J.; Werner, M.; Thomas, A. *Macromolecules* **2009**, *42*, 4426-4429.
(210) Schmidt, J.; Weber, J.; Epping, J. D.; Antonietti, M.; Thomas, A. *Adv. Mater.* **2009**, *21*, 702-705.
(211) Xia, J.; Yuan, S.; Wang, Z.; Kirklin, S.; Dorney, B.; Liu, D. J.; Yu, L. *Macromolecules* **2010**, *43*, 3325-3330.
(212) Rose, M.; Böhlmann, W.; Sabo, M.; Kaskel, S. *Chem. Commun.* **2008**, 2462-2464.
(213) Zhang, Y.; Riduan, S. N.; Ying, J. Y. *Chem. Eur. J.* **2008**.
(214) McKeown, N. B.; Budd, P. M.; Msayib, K. J.; Ghanem, B. S.; Kingston, H. J.; Tattershall, C. E.; Makhseed, S.; Reynolds, K. J.; Fritsch, D. *Chem. Eur. J.* **2005**, *11*, 2610-2620.
(215) Budd, P. M.; McKeown, N. B.; Fritsch, D. *J. Mater. Chem.* **2005**, *15*, 1977-1986.
(216) McKeown, N. B.; Budd, P. M. *Chem. Soc. Rev.* **2006**, *35*, 675-683.
(217) Budd, P. M.; Ghanem, B. S.; Makhseed, S.; McKeown, N. B.; Msayib, K. J.; Tattershall, C. E. *Chem. Commun.* **2004**, *2004*, 230-231.
(218) Budd, P. M.; Elabas, E. S.; Ghanem, B. S.; Makhseed, S.; McKeown, N. B.; Msayib, K. J.; Tattershall, C. E.; Wang, D. *Adv. Mater.* **2004**, *16*, 456-458.
(219) Budd, P. M.; Msayib, K. J.; Tattershall, C. E.; Ghanem, B. S.; Reynolds, K. J.; McKeown, N. B.; Fritsch, D. *J. Membr. Sci.* **2005**, *251*, 263-269.
(220) Ghanem, B. S.; McKeown, N. B.; Budd, P. M.; Selbie, J. D.; Fritsch, D. *Adv. Mater.* **2008**, *20*, 2766–2771.
(221) Ghanem, B. S.; McKeown, N. B.; Budd, P. M.; Fritsch, D. *Macromolecules* **2008**, *41*, 1640-1646.
(222) Carta, M.; Msayib, K. J.; Budd, P. M.; McKeown, N. B. *Org. Lett.* **2008**, *10*, 2641-2643.
(223) Weber, J.; Su, Q.; Antonietti, M.; Thomas, A. *Macromol. Rapid Commun.* **2007**, *28*, 1871-1876.
(224) Weber, J.; Antonietti, M.; Thomas, A. *Macromolecules* **2008**, *41*, 2880-2885.
(225) Ritter, N.; Antonietti, M.; Thomas, A.; Senkovska, I.; Kaskel, S.; Weber, J. *Macromolecules* **2009**, *42*, 8017–8020.
(226) McKeown, N. B.; Makhseed, S.; Budd, P. M. *Chem. Commun.* **2002**, *2002*, 2780-2781.
(227) McKeown, N. B.; Hanif, S.; Msayib, K.; Tattershall, C. E.; Budd, P. M. *Chem. Commun.* **2002**, *2002*, 2782-2783.
(228) McKeown, N. B.; Budd, P. M.; Book, D. *Macromol. Rapid Commun.* **2007**, *28*, 995-1002.
(229) Mackintosh, H. J.; Budd, P. M.; McKeown, N. B. *J. Mater. Chem.* **2008**, *18*, 573-578.
(230) Makhseed, S.; Samuel, J. *Chem. Commun.* **2008**, *2008*, 4342-4344.
(231) Makhseed, S.; Samuel, J.; Bumajdad, A.; Hassan, M. *J. Appl. Polym. Sci.* **2008**, *109*, 2591-2597.
(232) Mastalerz, M. *Angew. Chem. Int. Ed.* **2008**, *47*, 445-447.
(233) Coté, A. P.; Benin, A. I.; Ockwig, N. W.; O'Keeffe, M.; Matzger, A. J.; Yaghi, O. M. *Science* **2005**, *310*, 1166-1170.
(234) Côté, A. P.; El-Kaderi, H. M.; Furukawa, H.; Hunt, J. R.; Yaghi, O. M. *J. Am. Chem. Soc.* **2007**, *129*, 12914-12915.
(235) Wan, S.; Guo, J.; Kim, J.; Ihee, H.; Jiang, D. *Angew. Chem. Int. Ed.* **2008**, *47*, 8826-8830.
(236) Wan, S.; Guo, J.; Kim, J.; Ihee, H.; Jiang, D. *Angew. Chem. Int. Ed.* **2009**, *48*, 5439 - 5442.
(237) Hunt, J. R.; Doonan, C. J.; LeVangie, J. D.; Co te, A. P.; Yaghi, O. M. *J. Am. Chem. Soc.* **2008**, *130*, 11872-11873.
(238) Tilford, R. W.; Gemmill, W. R.; zur Loye, H. C.; Lavigne, J. J. *Chem. Mater.* **2006**, *18*, 5296-5301.
(239) Tilford, R. W.; Mugavero Iii, S. J.; Pellechia, P. J.; Lavigne, J. J. *Adv. Mater.* **2008**, *20*, 2741-2746.
(240) Kuhn, P.; Antonietti, M.; Thomas, A. *Angew. Chem. Int. Ed.* **2008**, *47*, 3450-3453.
(241) Kuhn, P.; Thomas, A.; Antonietti, M. *Macromolecules* **2009**, *42*, 319-326.
(242) Kuhn, P.; Krüger, K.; Thomas, A.; Antonietti, M. *Chem. Commun.* **2008**, *2008*, 5815-5817.
(243) Zwaneveld, N. A. A.; Pawlak, R.; Abel, M.; Catalin, D.; Gigmes, D.; Bertin, D.; Porte, L. *J. Am. Chem. Soc.* **2008**, *130*, 6678-6679.
(244) Bojdys, M. J.; Jeromenok, J.; Thomas, A.; Antonietti, M. *Adv. Mater.* **2010**, *22*, 2202-2205.
(245) Uribe-Romo, F. J.; Hunt, J. R.; Furukawa, H.; Klöck, C.; O'Keeffe, M.; Yaghi, O. M. *J. Am. Chem. Soc.* **2009**, *131*, 4570-4571.
(246) Han, S. S.; Furukawa, H.; Yaghi, O. M.; Goddard, W. A. *J. Am. Chem. Soc.* **2008**, *130*, 11580-11581.
(247) Sing, K. S. W. *J. Porous Mater.* **1995**, *2*, 5-8.
(248) Rouquerol, F.; Rouquerol, J.; Sing, K. *Adsorption by Powders and Porous Solids. Principles, Methodology and Applications*; Academic Press: New York, **1999**.
(249) Lowell, S.; Shields, J. E.; Thomas, M. A.; Thommes, M. *Characterization of Porous Solids and Powders: Surface Area, Pore Size, and Density*; Kluwer Academic Publishers: Dordrecht, **2004**.

(250) Sing, K. S. W.; Everett, D. H.; Haul, R. A. W.; Moscou, L.; Pierotti, R. A.; Rouquerol, J.; Siemieniewska, T. *Pure Appl. Chem.* **1985**, *57*, 603–619.
(251) Weitkamp, J. *Solid State Ion.* **2000**, *131*, 175-188.
(252) Ma, Y.; Tong, W.; Zhou, H.; Suib, S. L. *Microporous Mesoporous Mater.* **2000**, *37*, 243-252.
(253) Eddaoudi, M.; Kim, J.; Rosi, N.; Vodak, D.; Wachter, J.; O'Keeffe, M.; Yaghi, O. M. *Science* **2002**, *295*, 469-472.
(254) Kitagawa, S.; Kitaura, R.; Noro, S. *Angew. Chem. Int. Ed.* **2004**, *43*, 2334-2375.
(255) Celzard, A.; Albiniak, A.; Jasienko-Halat, M.; Mareché, J. F.; Furdin, G. *Carbon* **2005**, *43*, 1990-1999.
(256) Kresge, C. T.; Leonowicz, M. E.; Roth, W. J.; Vartuli, J. C.; Beck, J. S. *Nature* **1992**, *359*, 710-712.
(257) Zhao, D.; Feng, J.; Huo, Q.; Melosh, N.; Fredrickson, G. H.; Chmelka, B. F.; Stucky, G. D. *Science* **1998**, *279*, 548.
(258) Schüth, F. *Angew. Chem. Int. Ed.* **2003**, *42*, 3604-3622.
(259) Yuan, Z. Y.; Su, B. L. *J. Mater. Chem.* **2006**, *16*, 663-677.
(260) Brunauer, S.; Emmett, P. H.; Teller, E. *J. Am. Chem. Soc.* **1938**, *60*, 309-319.
(261) Barrett, E. P.; Joyner, L. G.; Halenda, P. P. *J. Am. Chem. Soc.* **1951**, *73*, 373-380.
(262) Penner, N.; Nesterenko, P.; Ilyin, M.; Tsyurupa, M.; Davankov, V. *Chromatographia* **1999**, *50*, 611-620.
(263) Penner, N. A.; Nesterenko, P. N.; Rybalko, M. A. *J. Anal. Chem.* **2001**, *56*, 934-939.
(264) McKeown, N. B. *Angew. Chem. Int. Ed.* **2006**, *45*, 1804-1807.
(265) Furukawa, H.; Yaghi, O. M. *J. Am. Chem. Soc.* **2009**, *131*, 8875-8883.
(266) Doonan, C. J.; Tranchemontagne, D. J.; Glover, T. G.; Hunt, J. R.; Yaghi, O. M. *Nat. Chem.* **2010**, *2*, 235-238.
(267) Maffei, A. V.; Budd, P. M.; McKeown, N. B. *Langmuir* **2006**, *22*, 4225-4229.
(268) Chan-Thaw, C. E.; Villa, A.; Katekomol, P.; Su, D.; Thomas, A.; Prati, L. *Nano Lett.* **2010**, *10*, 537–541.
(269) Palkovits, R.; Antonietti, M.; Kuhn, P.; Thomas, A.; Schüth, F. *Angew. Chem. Int. Ed.* **2009**, *48*, 6909-6912.

2 Objectives and Motivation

The Nobel Prize 2010 in chemistry has been awarded to three scientists that promoted the development of modern aryl chemistry by the introduction of palladium-catalyzed cross-coupling reactions. The works of *Heck*, *Suzuki* and *Negishi* along with valuable contributions from other chemists made the synthesis of countless compounds *via* straightforward synthetic routes possible. As a consequence, the library of molecules and polymers has significantly grown in number since. The common ground of this study is the development of novel synthetic strategies to extended one-, two- and three-dimensional aromate-rich systems for which a number of applications are envisaged.

The point of departure is the synthesis and characterization of highly symmetric macrocyclic PAHs for which various aspects of supramolecular chemistry will be investigated. The versatility of the *Yamamoto* macrocyclization will be demonstrated on the basis of a set of cyclic trimers that exhibit a rich supramolecular chemistry.

Secondly, the development of chemical approaches to highly shape-anisotropic graphene nanoribbons (GNRs) and related nanographene molecules shall be discussed. Also in this case, aryl-aryl coupling was indispensable to the bottom-up fabrication of dendronized monomers, polymers and model compounds. The relevance of structural tailoring in the field of well-defined graphene materials will be at the heart of this chapter.

Lastly, novel pathways towards the synthesis of extended three-dimensional networks that are dominated by nitrogen-rich motifs will be presented. If porous, these materials hold a great potential in the fields of gas and energy storage as well as for applications in catalysis. On the other hand conjugated networks can be used as a novel class of organic semiconductors.

2.1 Macrocycles

Self-assembly, metal complexation and liquid-crystallinity are at the heart of the first part which is dedicated to the synthesis of novel macrocyclic PAHs through a nickel-mediated *Yamamoto* macrocyclization.[1,2] The resulting macrocycles are nearly planar, shape-persistent and highly symmetric which is a consequence of the assembly of monomers whose reactive sites include ideal angles of 120 ° (Figure 2-1). Furthermore, the high structural rigidity of the building blocks should increase the overall yield as the entropy loss is partially compensated prior to the cyclization reaction.

A synthetic approach is always especially valuable if the design of different shapes and functionalities can be realized. In this case, multiple options are at hand without the necessity to change the successful synthetic route. Thus, a set of monomers characterized by individual shape and chemical nature have been subjected to the *Yamamoto* protocol (Figure 2-1).

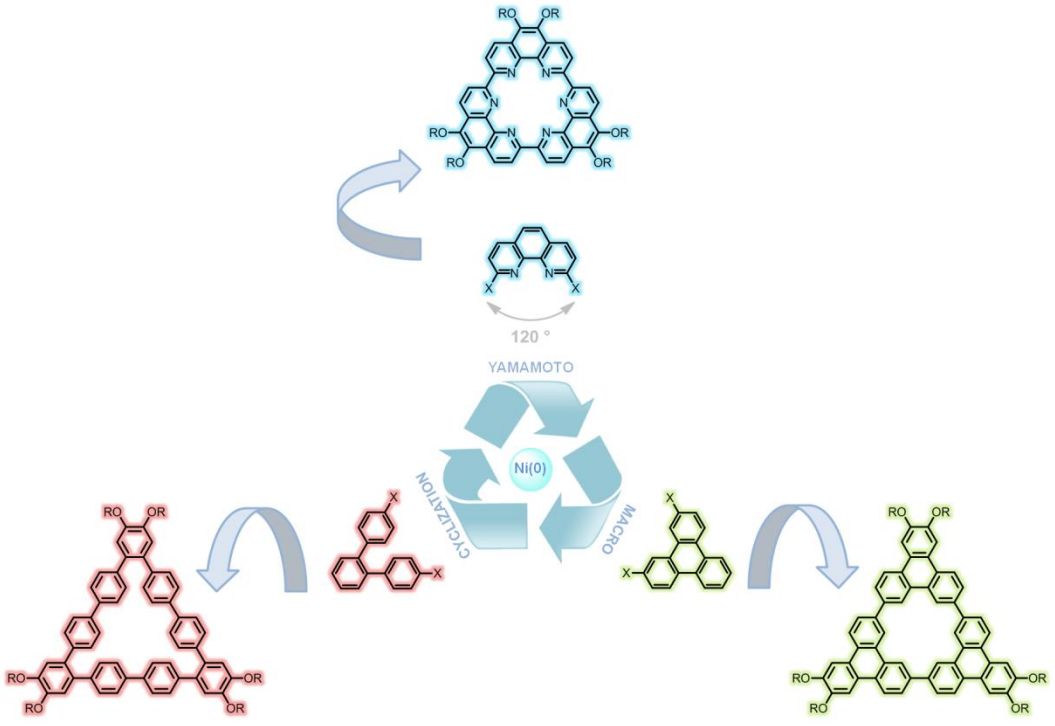

Figure 2-1: Schematic representation of the *Yamamoto* macrocyclization and chemical structures of the building units used in this study.

The introduction of binding sites through nitrogen-containing building blocks enables the formation of metal complexes. Contrary to classical examples such as porphyrins[3-5] and phthalocyanines,[5] novel macrocyclic ligands were designed which rely on pure ion-

dipole complexation and are not involved in ionic bond formation. 1,10-Phenanthroline with its strongly pre-orientated chelating site represents an ideal monomer in this context.[6-8] Upon cyclotrimerization of this molecule a hexaaza cavity will result that is in analogy to a class of nitrogen-containing macrocycles known as torands. A number of synthetic routes towards these cyclic ligands were developed during the 1980s but the supramolecular behavior was poorly investigated at the time.[9-14] Interesting questions to be solved concern the effect of the metal guest on the self-assembly and liquid crystallinity of such macrocycles. Also, the transformation of the cationic guest species by reduction is believed to open new fields of application ranging from nano-templating to molecular data storage.[15,16]

When dealing with conjugated macrocycles the electronic properties represent another field of paramount importance. The introduction of directly linked triphenylene units into a highly symmetric macrocyclic ring system should thus strongly influence the optoelectronic properties as compared to the single chromophore.[17-21] The same is true for the liquid-crystallinity as substituted triphenylene derivatives can act as discotic mesogens by themselves.[22-24]

The high tolerance of the novel *Yamamoto* protocol towards flexible building blocks will be exemplified on the basis of *ortho*-terphenyl monomers. The cyclotrimerization of such precursros should enable new pathways towards the straightforward synthesis of cylic oligoarenes. Little is known so far about the supramolecular properties of these macrocycles and only few reports address their *inter*molecular self-organization.[25,26]

2.2 Graphene Nanoribbons

The focus of the second part of this work is devoted to the development of chemical pathways to the synthesis of graphene nanoribbons (GNRs).

GNRs are known as two-dimensional stripe-like cutouts of graphene that are characterized by their high aspect ratio.[27-34] These materials are predicted to exhibit electronic properties that make them attractive candidates for the fabrication of yet smaller carbon-based electronic devices and integrated circuits.[28,35,36] In fact, GNRs are needed to “open” the band gap of graphene which itself is a semi-metallic, zero band gap material.

It has been demonstrated that both width and periphery of GNRs strongly govern the electronic properties of the material (Figure 2-2).[27-29] For example, semiconductor behavior is to be expected for armchair-type GNRs with widths below 5.0 nm whereas the metallic character increases at higher lateral extension.[30,37,38] At the same time the edge structure of the GNR will have a strong impact on the electronic characteristics of

the material. Computational simulations predict that GNRs exhibiting nonbonding *π*-electron states localized at zigzag edges may give rise to unconventional magnetic behavior.[33,34,39] The precise control of the morphology on the edges is thus decisive for practical purposes (Figure 2-2).[31-34]

These properties can, however, only be exploited if new methods for the reliable production of well-defined GNRs with a lateral extension on the single nanometer regime are developed. Traditional lithographic tools used for the "cutting" of GNRs from graphene flakes cannot reach the chemical accuracy that is required.[30,32,36,40] The same holds for the longitudinal "unzipping" of carbon nanotubes[41-43] or the surfactant-assisted extraction of GNRs from graphene dispersions.[38] In addition, the reproducibility of these methods still needs to be enhanced for a possible large-scale application.

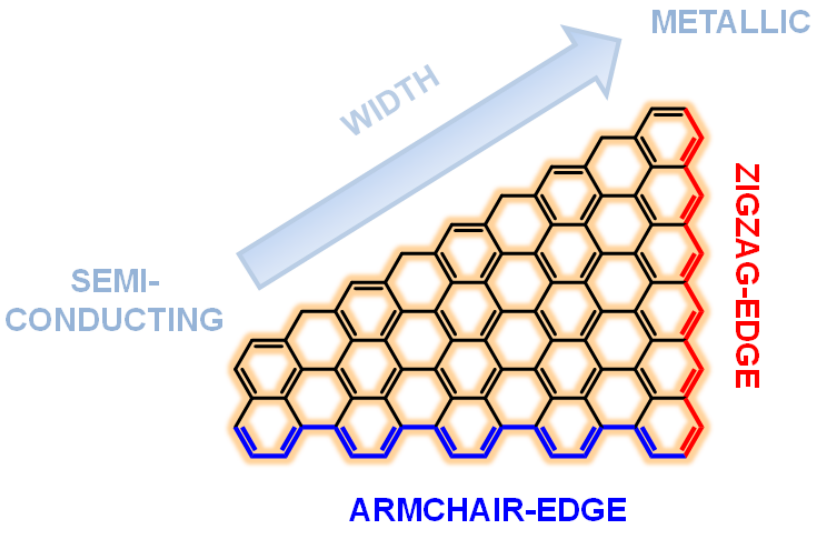

Figure 2-2: Schematic representation of different edge structures and dependency of the electronic properties on the width of the GNR.

Thus, the synthetic bottom-up fabrication of GNRs constitutes a promising alternative pathway which offers several distinct advantages. Through chemical synthesis, the desired information on geometry, width, length, edge structure and mass of the repeating unit can be chemically "written" into the graphene material.[44-46] Furthermore, in analogy to inorganic semiconductors, doping can be easily achieved *via* the introduction of heteroatoms such as boron or nitrogen in defined quantities and at precise positions.[47,48] This would allow for further tuning of the electronic properties.

The concept towards the synthetic build-up of defined GNRs presented herein is based on two steps. Firstly, laterally extended poly(*para*-phenylene) precursors are produced by transition-metal mediated polycondensation of large functionalized monomers. Two classical synthetic protocols will be applied in this work, namely the *Suzuki-Miyaura*[49,50]

and the *Yamamoto*[1,2] cross-coupling reaction. Benefits and drawbacks of both methods will be examined in this study.

At this point of the synthetic route, well-defined structures are obtained, in which the benzene rings are arranged in a fashion that is similar to the targeted graphene framework. Importantly, many carbon-carbon bonds are already formed in these structures which do not have to be established in the following step. This stage consists in the planarization of the polymeric precursors to the final GNRs which shall be achieved by *intra*molecular oxidative cyclodehydrogenation. In order to be able to closely follow the graphitization reaction on a smaller scale, the preparation of model compounds which exactly reflect the topology of the benzene units in the GNR precursors constitutes another objective.

The described route can in principle be applied to solution- and surface-assisted procedures. In the first case, the solubility of the polymeric precursors needs to be assured by substitution with a high number of alkyl chains. For the second case, non-substituted rigid building blocks are needed.[51] The two different approaches have in common that highly reactive and accessible functional sites need to be introduced in order to guarantee for an efficient polymerization. Within the experimental scope of these investigations, both methods will be discussed. Since only few synthesis-based examples, either in solution or on surfaces, have been reported for the production of GNRs, the present study represents virgin soil. Nevertheless, stronger chemical contributions to the rising field of graphene are needed if the promising material properties are to be fully exploited in the future.

2.3 Networks

In the final chapter, the third dimension of space will be addressed in the context of highly microporous polymer networks and carbon materials derived thereof. The generation of strongly reticulated frameworks mainly composed of aromatic rings offers a strategy for the development of novel porous materials which add to the traditional portfolio dominated by carbons,[52] zeolites[53,54] and metal-organic frameworks (MOFs).[55,56]

In a microporous polymer, the pore itself can no longer be regarded as a cavity that is defined by its walls, but is best described as an increased *inter*chain distance that is permanently fixed through extensive crosslinking.[57,58] Nowadays, most synthetic approaches towards microporous polymers rely on metal-catalyzed reaction protocols that lead to a significant contamination of the final material with inorganic remains and by-products.[59-70] Also, pricing and scalability are often limiting factors. It remains a great

challenge to synthesize novel microporous polymers with a rational design at the molecular level using cheap and straightforward processes. This would allow for the development of potential fields of application ranging from gas storage and purification to catalysis which could benefit from the tunability and variety of polymeric materials.

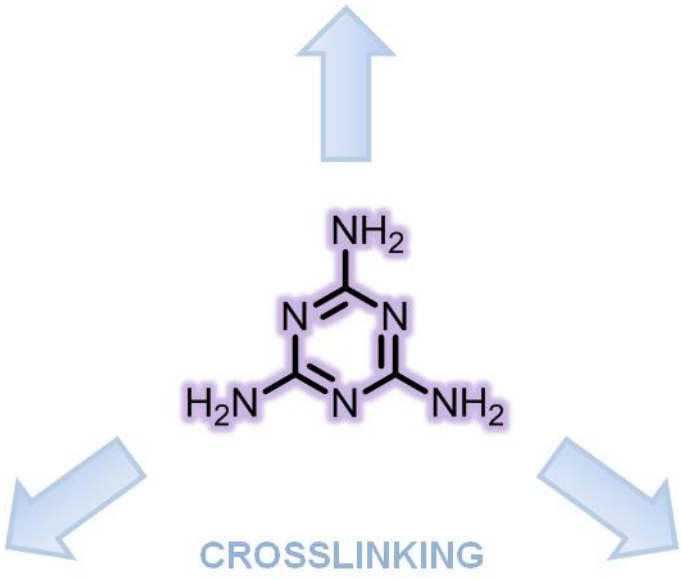

Figure 2-3: The role of melamine as a crosslinker.

Melamine, a large-scale synthetic chemical, represents an ideal crosslinker for the preparation of microporous polymer materials that simultaneously benefit from intrinsically high nitrogen contents (Figure 2-3). Therefore, a new one-pot condensation approach based on melamine has been developed that overcomes the aforementioned limitations and gives access to a novel class of microporous poly(aminal) networks. Classical *Schiff* base chemistry (Figure 2-4) which dates back to the 19th century[71-73] was further used for the synthesis of porous and non-porous poly(azomethine) networks which shall be evaluated as a novel class of fully organic photocatalysts for the production of hydrogen from water. In this respect, understanding and tailoring of the electronic properties of organic semiconductor networks are important issues to be addressed. The reversibility of the *Schiff* base formation of primary amines and aldehydes also allowed for the build-up of three-dimensional interconnected polymer structures. These materials are among the few examples of porous imine-linked polymers.[74,75]

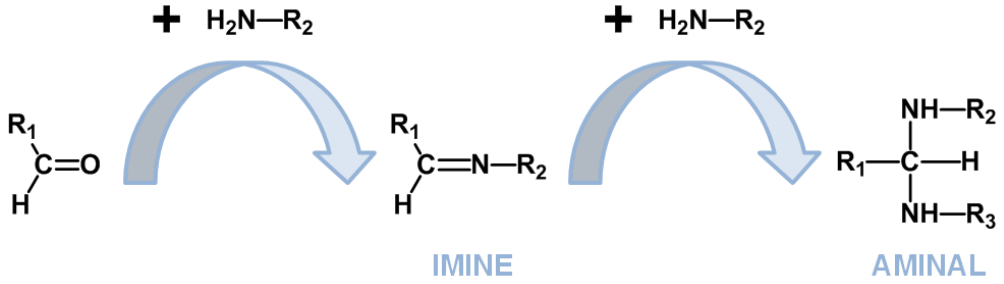

Figure 2-4: Fundamental reaction steps of *Schiff* base chemistry.

Furthermore, the aspect of morphology during the preparation of microporous polymer networks has not been addressed by the scientific community so far. The extensive crosslinking of monomers inevitably results in the formation and precipitation of highly insoluble polymeric structures.[76] Thus, emulsion-templating will be examined as a possible tool for the control of the synthetic process and the bulk morphological properties of the final material.

Lastly, the controlled pyrolysis of nitrogen-rich polymer networks should give rise to interesting carbon materials for which applications in charge storage and catalysis are envisaged. It remains to be answered whether the primary porosity of the polymeric precursor has an impact on the structural and textural properties of the final carbon. Also, the progressive transformation of the embedded nitrogen sites as a function of pyrolysis temperature will be presented.

2.4 Bibliography

(1) Yamamoto, T. *Progr. Polym. Sci.* **1992**, *17*, 1153-1205.
(2) Yamamoto, T. *Bull. Chem. Soc. Jpn.* **1999**, *72*, 621-638.
(3) Jasat, A.; Dolphin, D. *Chem. Rev.* **1997**, *97*, 2267-2340.
(4) Beletskaya, I.; Tyurin, V. S.; Tsivadze, A. Y.; Guilard, R.; Stern, C. *Chem. Rev.* **2009**, *109*, 1659-1713.
(5) Elemans, J.; van Hameren, R.; Nolte, R.; Rowan, A. *Adv. Mater.* **2006**, *18*, 1251-1266.
(6) Sammes, P. G.; Yahioglu, G. *Chem. Soc. Rev.* **1994**, *23*, 327-334.
(7) Accorsi, G.; Listorti, A.; Yoosaf, K.; Armaroli, N. *Chem. Soc. Rev.* **2009**, *38*, 1690-1700.
(8) Bencini, A.; Lippolis, V. *Coord. Chem. Rev.* **2010**, *254*, 2096-2180.
(9) Newkome, G. R.; Lee, H. W. *J. Am. Chem. Soc.* **1983**, *105*, 5956-5957.
(10) Toner, J. L. *Tetrahedron Lett.* **1983**, *24*, 2707-2710.
(11) Ransohoff, J. E. B.; Staab, H. A. *Tetrahedron Lett.* **1985**, *26*, 6179-6182.
(12) Bell, T. W.; Firestone, A. *J. Am. Chem. Soc.* **1986**, *108*, 8109-8111.
(13) Bell, T. W.; Cragg, P. J.; Drew, M. G. B.; Firestone, A.; Kwok, D. I. A. *Angew. Chem. Int. Ed.* **1992**, *31*, 345-347, 348-350.
(14) Boguslavsky, L.; Bell, T. W. *Langmuir* **1994**, *10*, 991-993.
(15) Liljeroth, P.; Repp, J.; Meyer, G. *Science* **2007**, *317*, 1203-1206.
(16) Hirjibehedin, C. F.; Lin, C. Y.; Otte, A. F.; Ternes, M.; Lutz, C. P.; Jones, B. A.; Heinrich, A. J. *Science* **2007**, *317*, 1199-1203.
(17) Saleh, M.; Park, Y. S.; Baumgarten, M.; Kim, J. J.; Müllen, K. *Macromol. Rapid Commun.* **2009**, *30*, 1279-1283.
(18) Qin, T.; Zhou, G.; Scheiber, H.; Bauer, R. E.; Baumgarten, M.; Anson, C. E.; List, E. J. W.; Müllen, K. *Angew. Chem. Int. Ed.* **2008**, *47*, 8292-8296.
(19) Wendorff, J. H.; Christ, T.; Glüsen, B.; Greiner, A.; Kettner, A.; Sander, R.; Stümpflen, V.; Tsukruk, V. V. *Adv. Mater.* **1997**, *9*, 48-52.
(20) Seguy, I.; Destruel, P.; Bock, H. *Synth. Met.* **2000**, *111-112*, 15-18.
(21) Hao, Q.; Xie, X.; Lei, W.; Xia, M.; Wang, F.; Wang, X. *J. Phys. Chem. C* **2010**, *114*, 9608-9617.
(22) Adam, D.; Schuhmacher, P.; Simmerer, J.; Häussling, L.; Siemensmeyer, K.; Etzbachi, K. H.; Ringsdorf, H.; Haarer, D. *Nature* **1994**, *371*.
(23) Henderson, P.; Kumar, S.; Rego, J. A.; Ringsdorf, H.; Schuhmacher, P. *J. Chem. Soc., Chem. Commun.* **1995**, *1995*, 1059-1060.
(24) Kumar, S. *Liq. Cryst.* **2005**, *32*, 1089-1113.
(25) Pisula, W.; Kastler, M.; Yang , C.; Enkelmann, V.; Müllen, K. *Chem. Asian J.* **2007**, *2*, 51-56.
(26) Rahman, M. J.; Yamakawa, J.; Matsumoto, A.; Enozawa, H.; Nishinaga, T.; Kamada, K.; Iyoda, M. *J. Org. Chem.* **2008**, *73*, 5542-5548.
(27) Barone, V.; Hod, O.; Scuseria, G. E. *Nano Lett.* **2006**, *6*, 2748-2754.
(28) Chen, Z.; Lin, Y. M.; Rooks, M. J.; Avouris, P. *Physica E* **2007**, *40*, 228-232.
(29) Yang, L.; Park, C.-H.; Son, Y.-W.; Cohen, M. L.; Louie, S. G. *Phys. Rev. Lett.* **2007**, *99*, 186801.
(30) Han, M. Y.; Özyilmaz, B.; Zhang, Y.; Kim, P. *Phys. Rev. Lett.* **2007**, *98*, 206805.
(31) Oeiras, R. Y.; Araújo-Moreira, F. M.; da Silva, E. Z. *Phys. Rev. B* **2009**, *80*, 73405.
(32) Jia, X.; Hofmann, M.; Meunier, V.; Sumpter, B. G.; Campos-Delgado, J.; Romo-Herrera, J. M.; Son, H.; Hsieh, Y. P.; Reina, A.; Kong, J. *Science* **2009**, *323*, 1701.
(33) Radovic, L. R.; Bockrath, B. *J. Am. Chem. Soc.* **2005**, *127*, 5917-5927.
(34) Enoki, T.; Kobayashi, Y.; Fukui, K. I. *Int. Rev. Phys. Chem.* **2007**, *26*, 609-645.
(35) Schwierz, F. *Nat. Nanotechnol.* **2010**, *5*, 487-496.
(36) Wei, Z.; Wang, D.; Kim, S.; Kim, S. Y.; Hu, Y.; Yakes, M. K.; Laracuente, A. R.; Dai, Z.; Marder, S. R.; Berger, C. *Science* **2010**, *328*, 1373-1376.
(37) Yang, L.; Park, C. H.; Son, Y. W.; Cohen, M. L.; Louie, S. G. *Phys. Rev. Lett.* **2007**, *99*, 186801.
(38) Li, X.; Wang, X.; Zhang, L.; Lee, S.; Dai, H. *Science* **2008**, *319*, 1229-1232.
(39) Konishi, A.; Hirao, Y.; Nakano, M.; Shimizu, A.; Botek, E.; Champagne, B.; Shiomi, D.; Sato, K.; Takui, T.; Matsumoto, K.; Kurata, H.; Kubo, T. *J. Am. Chem. Soc.* **2010**, *132*, 11021-11023.
(40) Özyilmaz, B.; Jarillo-Herrero, P.; Efetov, D.; Kim, P. *Appl. Phys. Lett.* **2007**, *91*, 192107.
(41) Kosynkin, D. V.; Higginbotham, A. L.; Sinitskii, A.; Lomeda, J. R.; Dimiev, A.; Price, B. K.; Tour, J. M. *Nature* **2009**, *458*, 872-876.
(42) Sinitskii, A.; Dimiev, A.; Kosynkin, D. V.; Tour, J. M. *ACS Nano* **2010**, *4* 5405-5413.
(43) Shimizu, T.; Haruyama, J.; Marcano, D. C.; Kosinkin, D. V.; Tour, J. M.; Hirose, K.; Suenaga, K. *Nat. Nanotechnol.* **2011**, *6*, 45-50.
(44) Wu, J.; Gherghel, L.; Watson, M. D.; Li, J.; Wang, Z.; Simpson, C. D.; Kolb, U.; Müllen, K. *Macromolecules* **2003**, *36*, 7082-7089.
(45) Yang, X.; Dou, X.; Rouhanipour, A.; Zhi, L.; Räder, H. J.; Müllen, K. *J. Am. Chem. Soc.* **2008**, *130*, 4216-4217.
(46) Fogel, Y.; Zhi, L.; Rouhanipour, A.; Andrienko, D.; Räder, H. J.; Müllen, K. *Macromolecules* **2009**, *42*, 6878-6884.

(47) Li, X.; Wang, H.; Robinson, J. T.; Sanchez, H.; Diankov, G.; Dai, H. *J. Am. Chem. Soc.* **2009**, *131*, 15939-15944.
(48) Wang, X.; Li, X.; Zhang, L.; Yoon, Y.; Weber, P. K.; Wang, H.; Guo, J.; Dai, H. *Science* **2009**, *324*, 768-771.
(49) Miyaura, N.; Suzuki, A. *Chem. Rev.* **1995**, *95*, 2457-2483.
(50) Suzuki, A. *J. Organomet. Chem.* **1999**, *576*, 147-168.
(51) Cai, J.; Ruffieux, P.; Jaafar, R.; Bieri, M.; Braun, T.; Blankenburg, S.; Muoth, M.; Seitsonen, A. P.; Saleh, M.; Feng, X.; Müllen, K.; Fasel, R. *Nature* **2010**, *466*, 470-473.
(52) Lee, J.; Kim, J.; Hyeon, T. *Adv. Mater.* **2006**, *18*, 2073-2094.
(53) Weitkamp, J. *Solid State Ion.* **2000**, *131*, 175-188.
(54) Ma, Y.; Tong, W.; Zhou, H.; Suib, S. L. *Microporous Mesoporous Mater.* **2000**, *37*, 243-252.
(55) Eddaoudi, M.; Kim, J.; Rosi, N.; Vodak, D.; Wachter, J.; O'Keeffe, M.; Yaghi, O. M. *Science* **2002**, *295*, 469-472.
(56) Kitagawa, S.; Kitaura, R.; Noro, S. *Angew. Chem. Int. Ed.* **2004**, *43*, 2334-2375.
(57) Germain, J.; Fréchet, J. M. J.; Svec, F. *Small* **2009**, *5*, 1098 - 1111.
(58) Jiang, J. X.; Cooper, A. I. *Top. Curr. Chem.* **2010**, *293*, 1-33.
(59) Jiang, J. X.; Su, F.; Trewin, A.; Wood, C. D.; Campbell, N. L.; Niu, H.; Dickinson, C.; Ganin, A. Y.; Rosseinsky, M. J.; Khimyak, Y. Z.; Cooper, A. I. *Angew. Chem. Int. Ed.* **2007**, *46*, 8574-8578.
(60) Jiang, J. X.; Su, F.; Trewin, A.; Wood, C. D.; Niu, H.; Jones, J. T. A.; Khimyak, Y. Z.; Cooper, A. I. *J. Am. Chem. Soc.* **2008**, *130*, 7710-7720.
(61) Jiang, J. X.; Trewin, A.; Su, F.; Wood, C. D.; Niu, H.; Jones, J. T. A.; Khimyak, Y. Z.; Cooper, A. I. *Macromolecules* **2009**, *42*, 2658-2666.
(62) Dawson, R.; Laybourn, A.; Clowes, R.; Khimyak, Y. Z.; Adams, D. J.; Cooper, A. I. *Macromolecules* **2009**, 675-683.
(63) Stöckel, E.; Wu, X.; Trewin, A.; Wood, C. D.; Clowes, R.; Campbell, N. L.; Jones, J. T. A.; Khimyak, Y. Z.; Adams, D. J.; Cooper, A. I. *Chem. Commun.* **2009**, *2009*, 212-214.
(64) Weber, J.; Thomas, A. *J. Am. Chem. Soc.* **2008**, *130*, 6334-6335.
(65) Jiang, J. X.; Su, F.; Niu, H.; Wood, C. D.; Campbell, N. L.; Khimyak, Y. Z.; Cooper, A. I. *Chem. Commun.* **2008**, *2008*, 486-488.
(66) Schmidt, J.; Werner, M.; Thomas, A. *Macromolecules* **2009**, *42*, 4426-4429.
(67) Ben, T.; Ren, H.; Ma, S.; Cao, D.; Lan, J.; Jing, X.; Wang, W.; Xu, J.; Deng, F.; Simmons, J. M. *Angew. Chem. Int. Ed.* **2009**, *48*, 9457-9460.
(68) Trewin, A.; Cooper, A. I. *Angew. Chem. Int. Ed.* **2010**, *49*, 1533-1535.
(69) Kuhn, P.; Antonietti, M.; Thomas, A. *Angew. Chem. Int. Ed.* **2008**, *47*, 3450-3453.
(70) Kuhn, P.; Thomas, A.; Antonietti, M. *Macromolecules* **2009**, *42*, 319-326.
(71) Schiff, H. *Liebigs Ann. Chem.* **1864**, *131*, 118-119.
(72) Layer, R. W. *Chem. Rev.* **1963**, *63*, 489-510.
(73) Tidwell, T. T. *Angew. Chem. Int. Ed.* **2008**, *47*, 1016-1020.
(74) Uribe-Romo, F. J.; Hunt, J. R.; Furukawa, H.; Klöck, C.; O'Keeffe, M.; Yaghi, O. M. *J. Am. Chem. Soc.* **2009**, *131*, 4570-4571.
(75) Pandey, P.; Katsoulidis, A. P.; Eryazici, I.; Wu, Y.; Kanatzidis, M. G.; Nguyen, S. B. T. *Chem. Mater.* **2010**, *22*, 4974–4979.
(76) Odian, G. G. *Principles of Polymerization*; J. Wiley & Sons: Hoboken, **2004**.

3 Triangular Macrocycles via Yamamoto Cyclotrimerization

3.1 Introduction

With the toolbox of modern aryl-aryl cross-coupling reactions at hand, alternative pathways for the construction of novel C_3 symmetric macrocycles can be thought of. Instead of assembling the cyclic system from two or more complementarily functionalized monomers,[1-3] cyclotrimerization of suitable precursors would significantly shorten the synthetic route and thereby enhance the overall yield. Moreover, the resulting triangular geometries are less frequently encountered and induce interesting structure motifs to self-assembled bulk systems and monolayers.

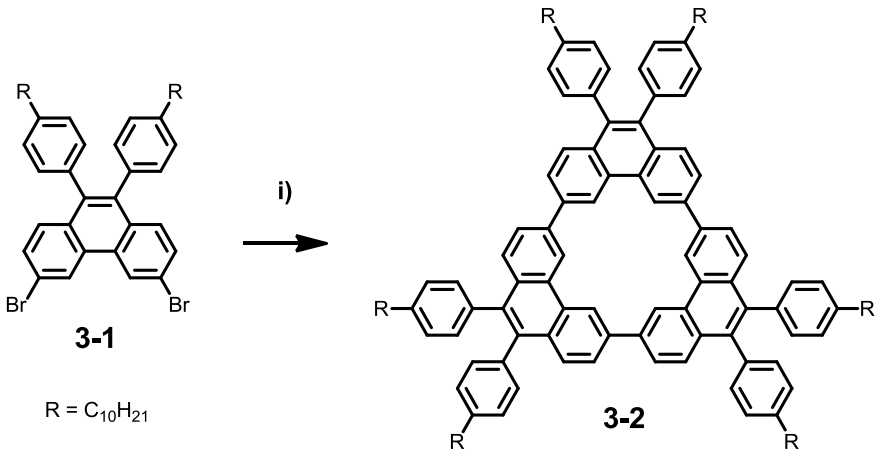

Figure 3-1: Examples of a macrocycle synthesis through cyclotrimerization; conditions: i) bis(cycloocta-(1,5)-diene)nickel(0), cycloocta-(1,5)-diene, 2,2'-bipyridine, toluene/DMF, 80 °C, 12 %.

The prerequisite for a cyclotrimerization is a suitable substitution pattern on the monomers; ideally the functional groups include a fixed angle of 120 ° as for phenanthrene derivative **3-1** (Figure 3-1). A successful formation of macrocycles such as **3-2** *via* this approach has only scarcely been reported in the literature and was

exclusively applied to the build-up of pure C/H-containing systems. Examples involve the copper(II) mediated reaction of *Grignard* reagents derived from biphenyl,[4] *ortho*-terphenyl[5] and phenanthrene[6,7] and the more recent nickel(0) mediated coupling of functionalized phenanthrens[8,9] using the *Yamamoto* protocol. Also, the trimerization of *Lipshutz* cuprates in the presence of duroquinone has been reported.[10] In this chapter, the *Yamamoto* method was chosen for the synthesis of a series of functional macrocycles from new building blocks including 1,10-phenanthroline, triphenylene and *ortho*-terphenyl.

3.2 Cyclo-2,9-tris-1,10-phenanthrolines

Based on the above considerations, 1,10-phenanthroline[11-13] was identified as a structural motif that would yield upon cyclotrimerization a novel hexaaza macrocycle of intrinsic rigidity and planarity. The chelating ability of 1,10-phenanthroline makes it a frequently used bidentate ligand in coordination chemistry.[11-13] Transition metal cations such as ruthenium(II)[14] and members of the lanthanide series[15] easily form complexes with the ligand in aqueous solutions and have been extensively studied with respect to their photophysical properties. 1,10-phenanthroline is a weak base with a protonation constant of log K = 4.95.[16] It is expected that the binding of a 1,10-phenanthroline surrounded cavity will be unique as it is based on pure ion dipole interactions. Six inward-pointing nitrogen donor atoms being held juxtaposed are expected to induce strong metal binding. A neutral cyclic ligand is in contrast to porphyrins and phthalocyanines which are typically deprotonated at the pyrrole site upon metal sequestration.[17-19]

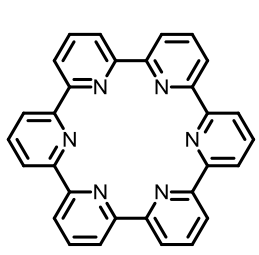

3-3

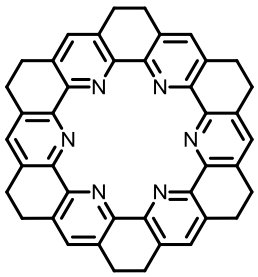

3-4

Figure 3-2: The backbone structure of cyclosexipyridine **3-3** and dodecahydro-hexaazakekulene **3-4**.

Previous investigations on related macrocycles (also termed torands) such as cyclosexipyridine **3-3**[20,21] and dodecahydro-hexaazakekulene **3-4**[22-25] were frequently

obstructed by the poor solubility in combination with the extremely high polarity of the hexaaza cavity.[20-25] The understanding of torands is so far limited to studies concerning their organization in the crystalline state[24,26-28] and in thin films.[25] Liquid-crystallinity that can be anticipated from their flat doughnut-like geometry as well as self-assembly on surfaces remain thus important issues to be explored. The same holds for the impact of a metal guest on the molecular self-organization. Thus, in order to guarantee for processability on the one hand and the desired phase forming behavior on the other hand, the substitution of the targeted 1,10 phenanthroline macrocycle with solubilizing side chains needs to be assured in the present case. By this, the detailed elucidation of the two- and three-dimensional self-assembly behavior of toroidal macrocycles should be possible for the very first time.

3.2.1 Synthetic Procedures

On the basis of synthetic works by *Dr. M. Takase* (MPI-P Mainz, Germany), a five-step synthetic route from 1,10-phenanthroline **3-5** lead to the target 2,9-dichloro-5,6-dialkoxy-1,10-phenanthroline precursors **3-10a-c** & **3-11** (Figure 3-3).[29,30]

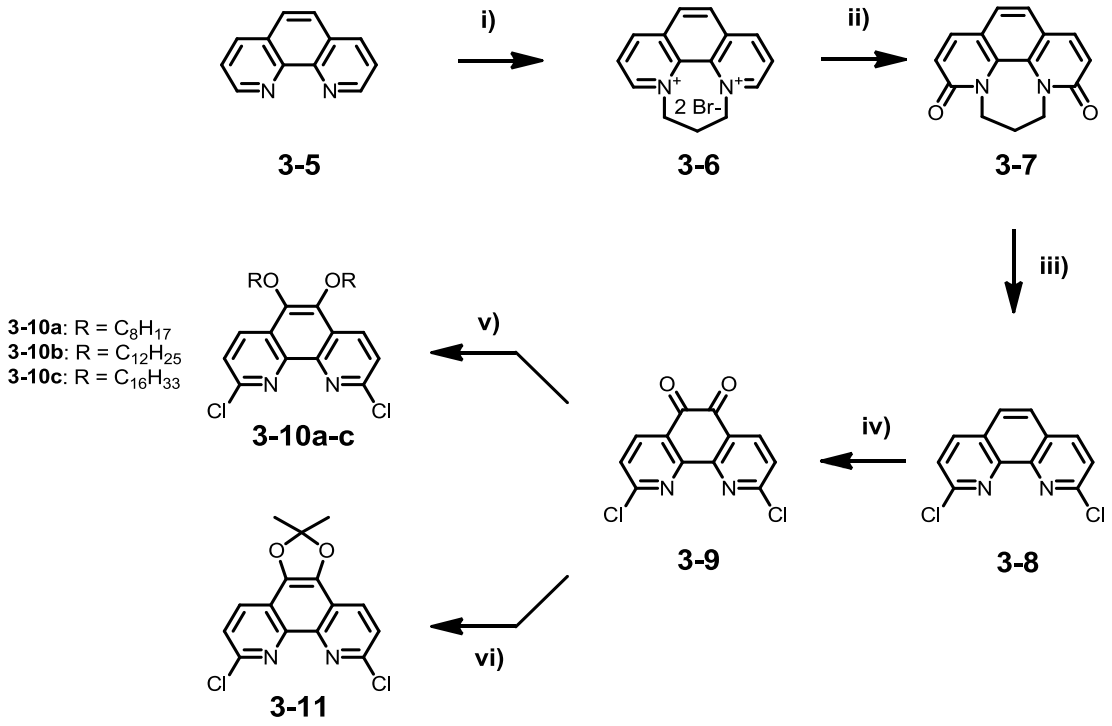

Figure 3-3: Synthetic route to the precursors **3-10a-c** and **3-11**; conditions: i) 1,3-dibromopropane, 120 °C, 95 %; ii) $K_3Fe(CN)_6$, NaOH, - 10 °C, 41 %; iii) $POCl_3$, PCl_5, reflux, 82 %; iv) H_2SO_4, HNO_3, KBr, 80 °C, 88 %; v) TBAB, $Na_2S_2O_4$, H_2O/THF, alkyl bromide, KOH, 40 °C, 60 - 70 %; vi) 2-nitropropane, K_2CO_3, H_2O/MeCN, 55 °C, 65 %.

As mentioned above, the ideal 120 ° substitution pattern of the halogen functionalities in the 2,9-position is required for high selectivity towards macrocycle formation.[8] Moreover, good solubility can be expected from the alkoxy chains in the peripheral 5,6-position. As it is known that the chlorine group of 2-chloropyridine is strongly activated by the electron-withdrawing effect of the neighboring nitrogen, an enhanced reactivity in aryl-aryl coupling can also be expected for the analogous 2,9-dichloro-1,10-phenanthrolines.

The introduction of halogens into the 2,9-[29,30] and 4,7-positions[31,32] of 1,10-phenathroline **3-5** is best achieved by chlorination or bromination of the corresponding 2,9- and 4,7-diones. In a first step, the *N*,*N*'-annelated bis-quaternary salt **3-6** was prepared in nearly quantitative yield by double-alkylation with 1,3-dibromopropane. In the literature, nitrobenzene is used as reaction medium. It was however found, that the reaction also works in the absence of this high-boiling and toxic solvent. Running the alkylation in pure 1,3-dibromopropane leads to the precipitation of the product in high purity during the course of the reaction. Excess alkane can be easily recycled.

The low-yield synthesis of diketone **3-7** was found the bottleneck in the synthetic route towards **3-10a-c** and **3-11**. The oxidation can be accomplished by treatment with potassium ferricyanide under alkaline conditions.[29] The reaction is highly sensitive towards temperatures above 0 °C so that intense cooling has to be assured throughout the whole synthetic and workup procedure. Due to the moderate solubility of potassium ferricyanide large liquid volumes are necessary which limit the scale-up of the reaction. A part of the crude product could be directly collected by filtration. Subsequent removal of the aqueous phase and *Soxhlet* extraction of the inorganic residue with THF yielded additional 15 to 20 % of **3-7**, thus increasing the total yield of the reaction to 41 %.

In view of the low-yielding and tedious oxidation step towards **3-7** it is surprising that no alternative synthetic protocols for the synthesis of 2,9-dihalo-1,10-phenanthrolines are reported in the literature. However, for the preparation of structurally related 2-chloroquinolines **3-14** from parent quinoline **3-12**, an efficient route via the intermediate *N*-oxide **3-13** is known.[33,34] *N*-oxidation is achieved by treatment with *meta*-chloroperbenzoic acid followed by reaction with phosphoryl chloride in the presence of *N*,*N*-diisopropylethylamine. Due to the structural similarity, analogous reaction conditions were tested for 1,10-phenanthroline **3-5**. The desired product was however only detected in trace amounts by FD mass spectroscopy and thin-layer chromatography. Further attempts varying reaction temperature and time did not result in the formation of **3-8** so that the aforementioned synthetic route via 2,9-dione **3-7** had to be used.

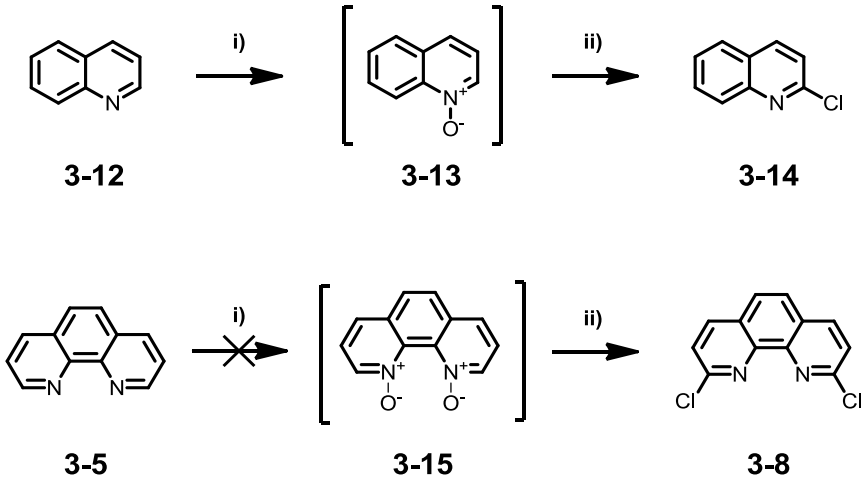

Figure 3-4: Attempted alternative route to 2,9-dichloro-1,10-phenanthroline **3-8**; conditions: i) mCPBA, RT, 61 %; ii) $POCl_3$, DIPEA, RT, 38 %.

Treatment of crude dione **3-7** with phosphoryl chloride afforded 2,9-dichloro-1,10-phenanthroline **3-8** in 82 % yield which could be easily separated from the triple-chlorinated by-product by column chromatography.

For the second oxidation towards 2,9-dichloro-1,10-phenanthrolin-5,6-dione **3-9** treatment of **3-8** with a mixture of concentrated nitric and sulphuric acid in the presence of bromine gave the target compound.[30] The yield of this step was 88 %.

A novel reaction protocol had to be established for the synthesis of the unreported 5,6-dialkoxy derivatives **3-10a-c**. As the low stability for 5,6-dihydroxy-1,10-phenanthrolines has been mentioned previously,[35] a one-pot reduction-etherification approach was used. Firstly, the diketone **3-9** was reduced by treatment with sodium dithionite followed by *in-situ* transformation of the hydroxyl groups to the corresponding alkoxy derivative under *Williamson* conditions. By this, the octyloxy **3-10a**, dodecyloxy **3-10b** and hexadecyloxy **3-10c** derivative were prepared in 60 - 70 % yield, respectively. The compounds showed enhanced solubility in various polar and non-polar solvents and mixtures thereof.

Alternatively, the dione function can be subsequently converted by reacting **3-9** with 2-nitropropane under basic conditions.[36] The resulting ketal **3-11** was obtained in 65 % yield and exhibited equally good solubility as compared to the alkoxy series **3-10a-c**.

Despite of its long dodecyloxy chains, 2,9-dichloro-5,6-bis(dodecyloxy)-1,10-phenanthroline **3-10b** readily crystallizes reflecting the underlying tendency towards aggregation of the planar 1,10-phenanthroline core. Pale yellow needle-like crystals were obtained whose crystal structure was elucidated by X-ray diffraction analysis. Figure 3-5 shows the packing in the crystal corresponding to the triclinic, space group

P-1. It can be clearly seen how the alkoxy chains are arranged in a parallel fashion forming an individual aliphatic microphase.

The unit cell contains two 1,10-phenanthroline units which are pointing towards each other thus maximizing the overlap of four alkoxy chains within the interspace. Remarkably, one of the two dodecyloxy chains has to adapt a kinked conformation in order to avoid steric repulsion from the neighboring chain.

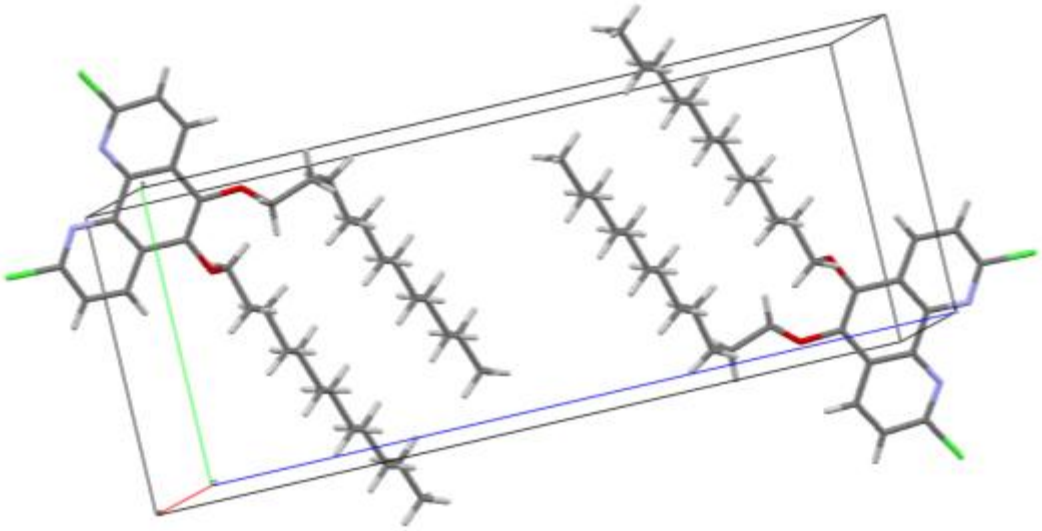

Figure 3-5: Crystal structure of 2,9-dichloro-5,6-bis(dodecyloxy)-1,10-phenanthroline **3-10b**.

The fully planarized 1,10-phenanthroline cores form themselves pillars in which they are arranged face-to-face with an *inter*molecular spacing of 3.41 Å.

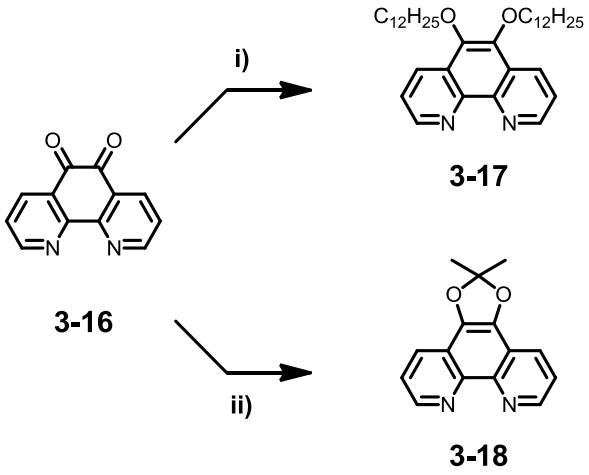

Figure 3-6: Synthetic route to the model compounds **3-17** and **3-18**; conditions: i) TBAB, $Na_2S_2O_4$, H_2O/THF, then R–Br, KOH, 40 °C, 59 %; ii) 2-nitropropane, TBAH, MeCN, 60 °C, 61 %.

Starting from commercially available 1,10-phenanthroline-5,6-dione **3-16** two model compounds were synthesized using similar reaction conditions as previously described. By this approach, the non-functionalized 5,6-bis(dodecyloxy)-1,10-phenanthroline **3-17** and 2,2-dimethyl-[1,3]dioxolo[4,5-f][1,10]phenanthroline **3-18** were prepared in comparable yields.

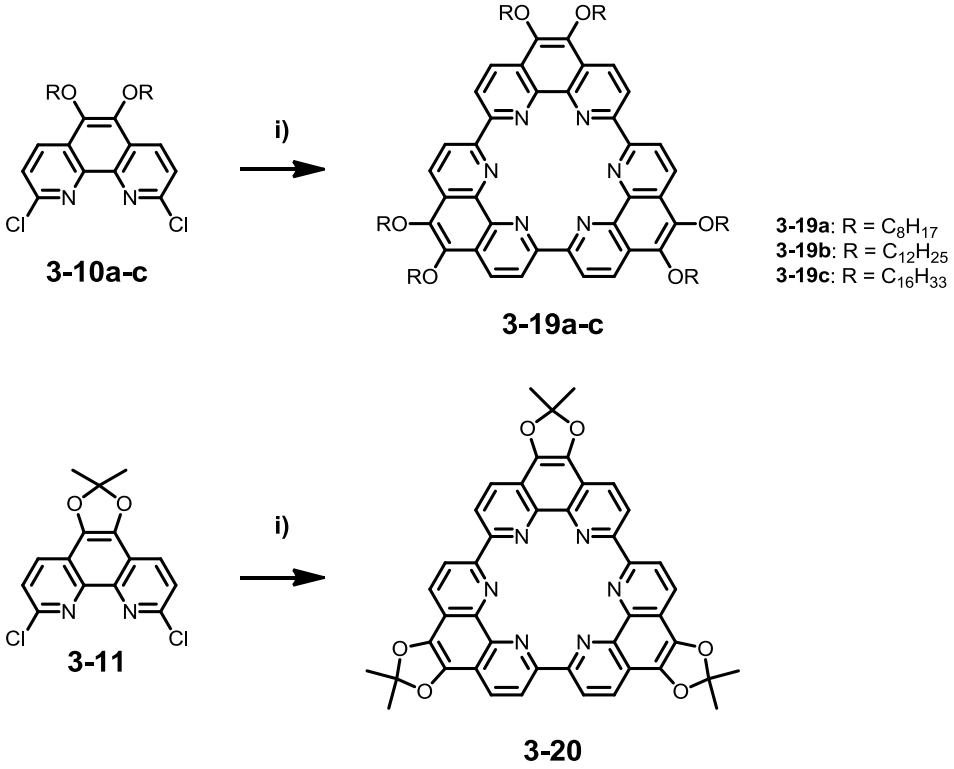

Figure 3-7: Synthetic route to the macrocycles **3-19a-c** and **3-20**; conditions: i) bis(cycloocta-(1,5)-diene)nickel(0), cycloocta-(1,5)-diene, 2,2'-bipyridine, toluene/DMF, 60 °C, 15 - 20 %.

For the cyclotrimerization reaction of the precursors **3-10a-c** and **3-11** towards the macrocycles **3-19a-c** and **3-20**, respectively, a standard *Yamomoto* protocol[37,38] was used in a overall 3/1 mixture of toluene/DMF. The catalyst was prepared under glove-box conditions from a stoichiometric mixture of bis(cyclooctadiene)nickel(0), 1,5-cyclooctadiene and 2,2'-bipyridine in toluene/DMF. The deep-purple catalyst solution was subsequently activated at 60 °C for 30 minutes in the dark.

In macrocycle synthesis, it is well-known that oligomerization will inevitably occur as a side-reaction if too high precursor concentrations are used.[1-3] Therefore, the concentration was set to $8 \cdot 10^{-3}$ M for all experiments and the precursor solution in toluene was added drop-wise in order to guarantee for *pseudo*-dilution conditions. Typically, the reaction was run at 60 °C for three days in the dark. Quenching and decomposition of nickel residues was achieved by dropping the reaction mixture into

dilute methanolic hydrochloric acid. The crude products were extracted with diethyl ether and pre-purified using standard column chromatography on silica. However, due to the high intrinsic polarity of the macrocycle the final purification of these compounds was only achievable by recycling gel permeation chromatography (rGPC).

During the purification procedure, the macrocycles could be easily identified by their intense turquoise (**3-19a-c**) and yellow (**3-20**) luminescence upon excitation with a UV lamp operating at 366 nm. All compounds displayed high solubility in polar aprotic solvents like DCM, THF and ethyl acetate. Still, they were poorly soluble in non-polar solvents such as alkanes and could be precipitated into alcohols.

The overall yield of the macrocycle formation varied between 15 and 20 %. Analysis of the reaction mixtures by FD and MALDI-TOF mass spectroscopy indicated that the major side-reaction of this *Yamamoto* cyclotrimerization is dehalogenation. This commonly observed phenomenon resulted in the presence of non-functionalized monomeric and dimeric species in the corresponding mass spectra and accounts for the moderate yield of the reaction. On the other hand, no evidence was found for the formation of higher macrocycles or polymeric products under the applied reaction conditions. This finding suggests a highly favored pathway towards cyclotrimerization *via* a cascade of *inter*- and *intra*molecular *Yamamoto* coupling events. In Figure 3-8, the corresponding reaction sequence is depicted.

The proposed mechanism relies on the fundamental reaction steps of organometallic chemistry.[39,40] The activation of the zerovalent nickel catalyst bis(cyclooctadiene)nickel(0) (**Ni(COD)$_2$**) is achieved *via* the replacement of one 1,5-cyclooctadiene (**COD**) ligand by the auxiliary ligand 2,2'-bipyridine (**bipy**). In the next step, oxidative addition of the 1,10-phenanthroline unit (**E**) to the activated complex **C-I** results in the insertion of the nickel atom into the carbon-chlorine bond leading to the formation of Ni(II) complex **C-II**.[41-43] Two of these species disproportionate to yield the complex **C-III** in which the two aryl units are already brought into close proximity.[42] The formation of complex **C-IV** in stoichiometric amounts is the reason for the consumption of the catalyst during the course of the reaction as this species further degrades to nickel(II) chloride.

The subsequent reductive elimination of complex **C-III** yields the desired coupling product (**D**) and at the same time liberates the activated complex **C-I** that re-enters the catalytic cycle. For the formation of the open trimeric 1,10-phenanthroline species an analogous *inter*molecular reaction sequence involving the monomer and dimer can be expected. For the last step of the cyclotrimerization, however, that is the closure of the open trimer to the final macrocycle, an *intra*molecular coupling is necessary.

Once the trimer is coordinated to the metal centre, its rigid molecular backbone along with the ideal binding angles of 120 ° assists in the coordination of its second end to the same nickel site.

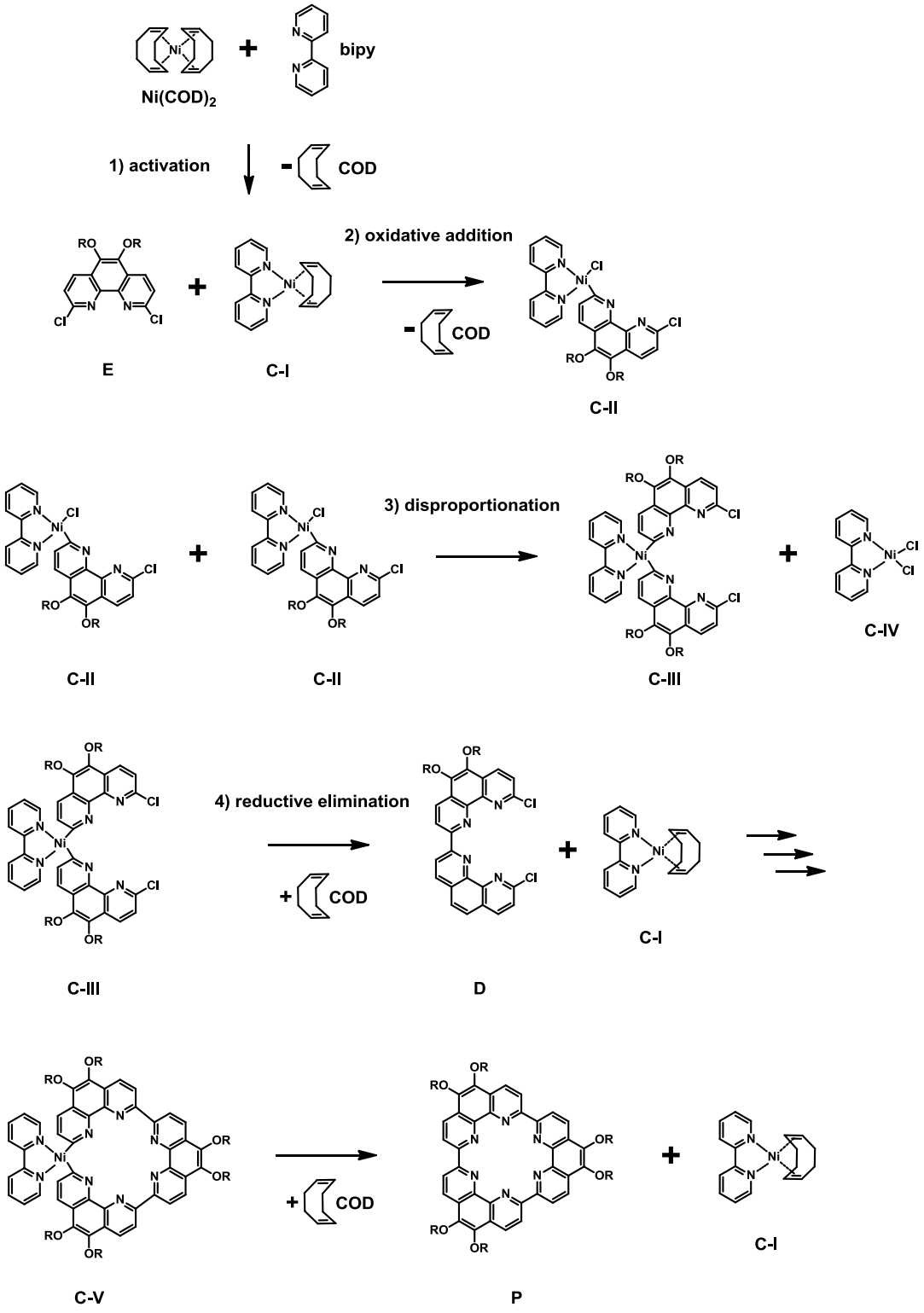

Figure 3-8: Proposed reaction mechanism during the formation of the cyclo-2,9-tris-1,10-phenanthroline macrocycles involving *inter*- and *intra*molecular coupling steps.

Already in **C-V** the shape of the final product is predefined by the geometry of the complex and the macrocycle (**P**) is then formed upon reductive elimination.

As it will be discussed in the next chapter, the Na^+ complexes of **3-19a-c** and **3-20** were used as a reference for all experiments and were also subjected to NMR analysis of the macrocycles following synthesis and purification.

The successful build-up of the cyclo-2,9-tris-1,10-phenanthrolines was confirmed by ^1H, ^{13}C and ^1H-^{13}C-COSY NMR spectroscopy in DCM-d_2 at room temperature. As shown for **3-19b-Na** in Figure 3-9, two characteristic doublets from the AB spin system on the 1,10-phenanthroline backbone are found at δ = 8.98 ppm (H_a) and δ = 8.75 ppm (H_b) in the ^1H NMR spectrum. The *alpha*-protons of the dodecyloxy chains give rise to a triplet at δ = 4.37 ppm. The resonances of the well-resolved alkyl chain are found in the region between δ = 2.10 ppm and δ = 0.80 ppm.

Correlation of the ^1H resonances to the signals of the spin-echo ^{13}C spectrum unambiguously proves the presence of the desired cyclic trimer and the absence of non-cyclic by-products. Comparison of the ^1H NMR spectrum of **3-19b-Na** to that of precursor **3-10b** reveals a downfield shift of 0.46 ppm for H_a and 1.13 ppm for H_b further illustrating the successful macrocycle formation.

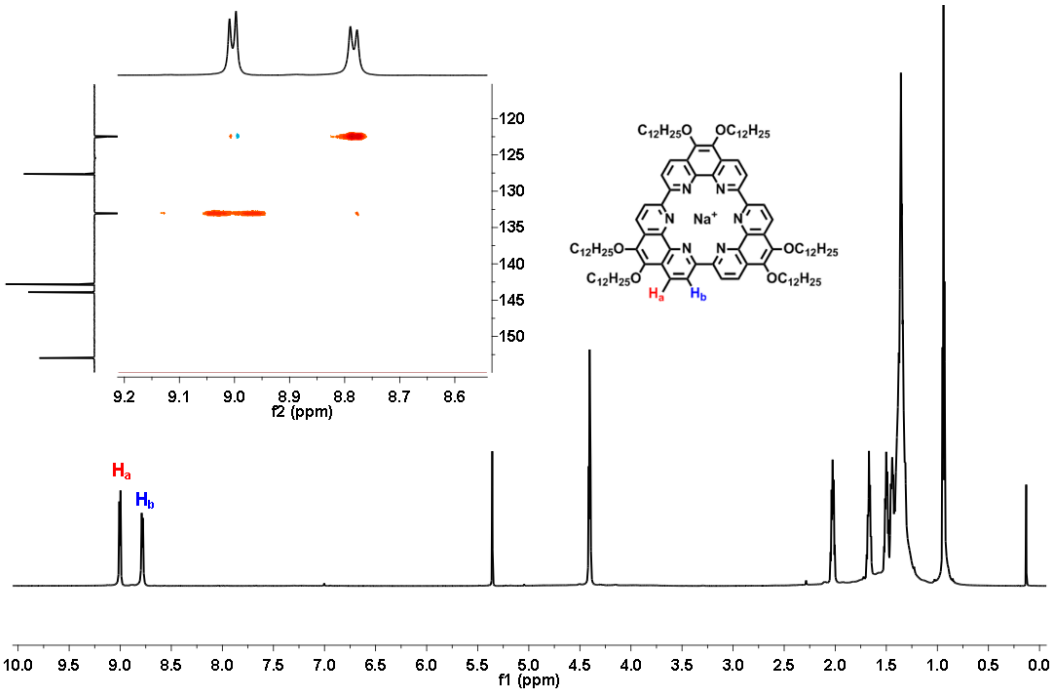

Figure 3-9: ^1H NMR spectrum of macrocycle **3-19b-Na** in DCM-d_2 at 25 °C. The inset shows the ^1H,^{13}C-COSY NMR spectrum of the aromatic region of the compound.

The UV-vis absorption spectra for **3-19b-Na** and **3-20-Na** were recorded in DCM and compared to the data obtained for the corresponding monomeric model compounds **3-17** and **3-18**, respectively. The concentration for the experiments was set to $1 \cdot 10^{-5}$ M. The rigidity of both macrocycles and model compounds is reflected by an enhanced degree of fine structure in the corresponding spectra that is frequently encountered in the spectroscopic analysis of PAHs.[44,45] These compounds exhibit a high number of possible transitions from the ground state level into higher unoccupied degenerated molecular orbitals. The consequence are numerous absorption bands that can reveal valuable details about the electronic nature of the investigated compounds.[45,46]

Compared to the absorption spectrum of pristine 1,10-phenanthroline **3-5**, essentially containing two major absorptions at 205 nm and 263 nm,[44] the signals of the model compounds **3-17** and **3-18** and the macrocycles **3-19b-Na** and **3-20-Na** are shifted to higher wavelengths. Firstly, this is a result of the electron-donating alkoxy chains on the periphery of the compounds. On the other hand, the increased conjugation of the two macrocycles shows up as an additional bathochromic shift.

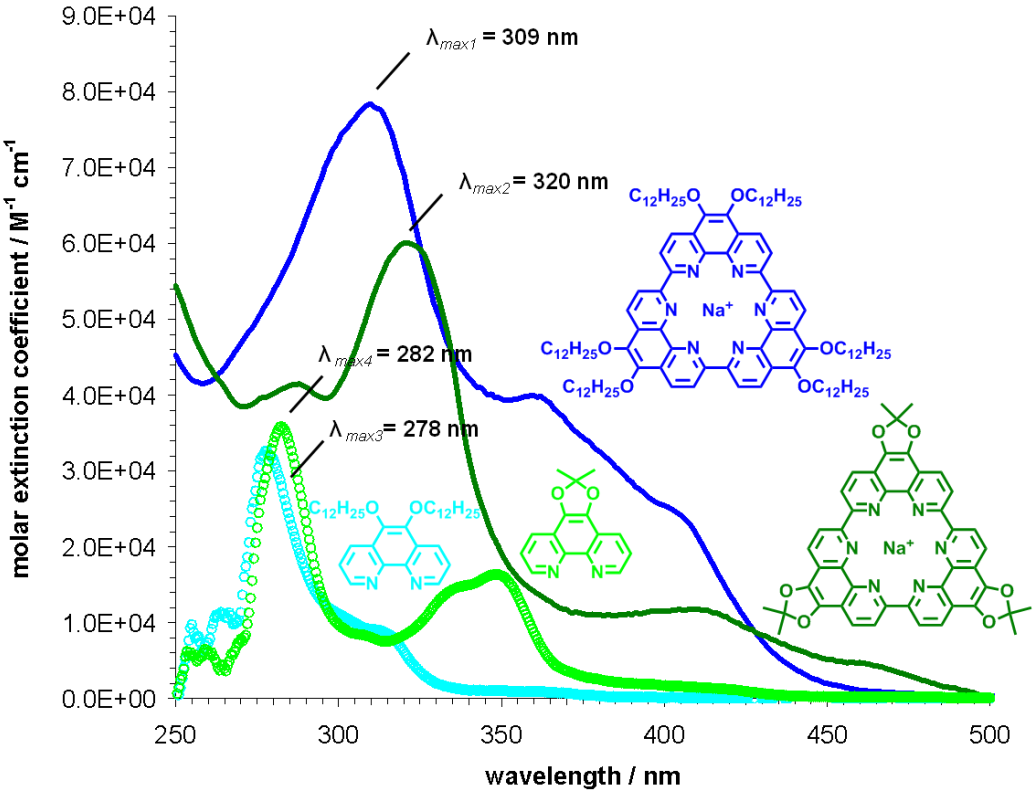

Figure 3-10: UV-vis spectra of macrocycles **3-19b-Na** and **3-20-Na** and the corresponding model compounds **3-17** and **3-18** in DCM at 10^{-5} M (right).

The spectrum of **3-19b-Na** contains a broad absorption maximum centered at λ_{max1} = 309 nm (ε = 78313 $M^{-1}cm^{-1}$) and two minor resolved peaks at 359 nm and 403 nm. The spectrum of **3-20-Na** is similar in structure, but the signals are red-shifted as compared to **3-19b-Na**. The main absorption is located at λ_{max2} = 320 nm (ε = 60044 $M^{-1}cm^{-1}$) with two shoulders at 409 nm and 459 nm, respectively. This finding might be explained by the three ketal groups of **3-20-Na** which further decrease the conformational freedom of the macrocycle and enhance the overall rigidity. Whereas the dodecyloxy chains of **3-19b-Na** freely rotate, the distance between the two oxygen atoms of **3-20-Na** is fixed leading to an enhanced contribution of the 1,3-dioxolane unit to the aromatic system. Concentration-dependent absorption spectra recorded in cyclohexane showed a linear relationship between the concentration and absorbance in the range between $2 \cdot 10^{-4}$ M and $3 \cdot 10^{-6}$ M indicating no self-assembly under these conditions. This is in contrast to other planar PAHs and macrocycles for which significant π-π-interactions were documented in the past. [1,47]

The higher degree of conjugation and symmetry of the macrocycles is illustrated by comparison to the spectra of the two model compounds **3-17** and **3-18**, respectively. The absorption maxima are found at λ_{max3} = 278 nm (ε = 32629 $M^{-1}cm^{-1}$) in the case of **3-17** and at λ_{max4} = 288 nm (ε = 35487 $M^{-1}cm^{-1}$) for **3-18**. The smaller π-conjugated systems result in strong hypsochromic shifts of 31 nm for both model compounds. Additionally, the lower molar extinction coefficients can be attributed to their higher dipole moment as compared to the C_3 symmetric macrocycles.[12] Also, the absorption arises from individual molecules whereas three chromophores are connected in the conjugated macrocycles.

DFT calculations (B3LYP, 6-311G**) revealed an energy value for the HOMO of macrocycle **3-19b** of - 5.34 eV and a LUMO value of - 1.67 eV. The resulting energy gap of 3.67 eV is in good agreement with the π-π^* transition of the conjugated system deduced from the UV-vis spectrum.[12]

3.2.2 Metal Complexation

Analysis by MALDI-TOF spectroscopy revealed that the as-synthesized macrocycles **3-19a-c** and **3-20** are typically found as mixtures of various alkaline metal complexes (Figure 3-11).

In all cases, the Li^+, Na^+ and K^+ complexes were detected with the Na^+ and K^+ adduct showing the strongest peak intensity. Small quantities of the Li^+ complex and the protonated species were also found with the latter possibly being generated *in-situ* during the laser pulsing of the sample.

The high affinity of various hexaaza macrocycles of similar cavity size towards alkaline metal cations has been documented in the past.[21,24,26,27,48] It is reasonable to deduce that in the present case these ions were entrapped from the glassware and solvents during the reaction and workup procedure.

The high tendency towards complexation of alkaline metal cations is further reflected by the fact that preparation of the metal-free macrocycle by acid treatment was unsuccessful. On the other hand, as depicted in Figure 3-11 for **3-19b**, the Na^+ complex can be prepared in virtually quantitative yield by washing with an aqueous solution of sodium hydroxide. Therefore, this compound was chosen as the starting point for all following metal sequestration experiments.

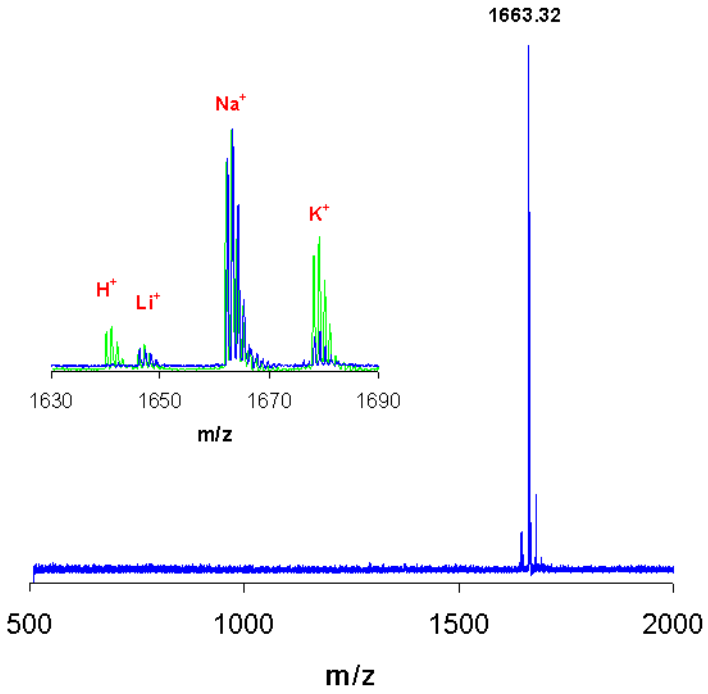

Figure 3-11: MALDI-TOF spectrum of **3-19b**, the inset shows the distribution of the different alkaline metal complexes before (green) and after (blue) treatment with NaOH (2 M).

DFT analysis (B3LYP, 6-311G**) was performed to reveal the geometrical parameters of the hexaaza cavity of the macrocycles. A distance of 5.61 Å between two opposite nitrogen atoms was found (Figure 3-12), the two nitrogen atoms of the 1,10-phenanthroline chelating site are separated by 2.88 Å. Moreover, the cyclic system adopts a propeller-like structure with a dihedral angle of 24.9 ° between two neighboring 1,10-phenanthroline units causing a slight deviation from full planarity (Figure 3-12). Theoretical calculations on related *Schiff* base macrocycles[49] as well as single crystal X-ray diffraction data on dodecahydro-hexaazakekulenes (**3-4**)[24] are in good agreement with these findings.

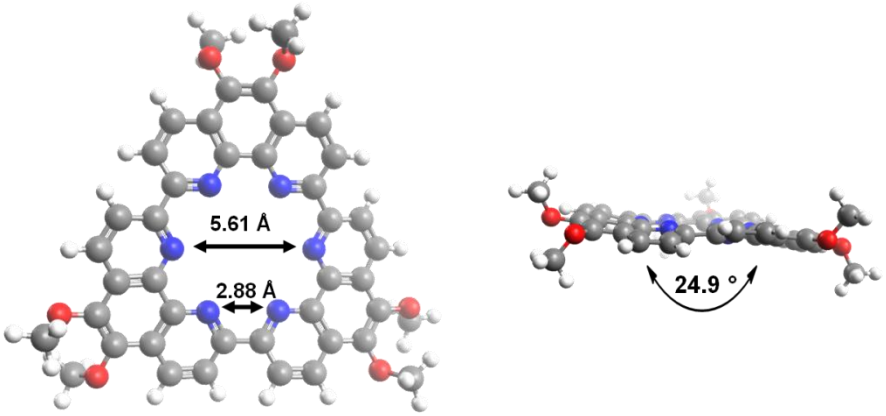

Figure 3-12: Geometric dimensions of the cavity left and side view of the propeller-like structure of macrocycle **3-19** (right) as derived from computational analysis (B3LYP, 6-311G**).

In view of these results, it can be expected that only large metal cations will be accommodated by the cyclo-2,9-tris-1,10-phenanthroline macrocycles as the geometrical match between guest and host is imperative for efficient metal binding. Indeed, the ionic diameters of Na^+ (2.04 to 2.36 Å) and K^+ (2.76 to 3.02 Å) are among the highest if hexa-fold coordination is assumed.[50]

The hexaaza cavity of macrocycles **3-19a-c** and **3-20** is unique as it does not rely on deprotonation but on a weaker binding of the guest species *via* ion-dipole interactions. As a result, the exchange of the metal species should be facilitated. For potential applications of self-assembled macrocycles in molecular data storage based on reversible reductive switching,[51,52] the complexation of metal cations other than alkaline and alkaline earth would be highly desirable. Due to their ns^1 and ns^2 electron configuration they exhibit extremely low standard electrode potentials making a reduction to the neutral species difficult. In contrast, transition and heavy metal cations are usually characterized by a high number of *d*- and *f*-electrons and a significantly more positive standard electrode potential allowing for the easy reduction of the cation to its neutral state. When transferred to the bulk state, the concept could be also used for the fabrication of nanoscale metallic wires. In this case, a self-assembled column of the cyclo-2,9-tris-1,10-phenanthroline macrocycle containing the metal guest would represent a molecular template. Upon reduction of the cationic species the question arises as to what degree the dimensions of the molecular channel will be conferred to the metallic nanostructure that is formed in this step.

Hence, the metal complexing ability of **3-19b-Na** was studied in detail as a function of the ionic diameter of various metal cations. Successful sequestration was observed for a number of large transition metal cations including Pb^{2+} (2.38 to 2.58 Å), Ag^+ (2.30 to 2.56 Å), Cd^{2+} (1.90 to 2.10 Å), Zn^{2+} (1.50 to 1.80 Å) and

Cu^{2+} (1.46 to 1.48 Å) as qualitatively evidenced by MALDI-TOF spectroscopy. The diameters given are valid for hexa-fold coordination.[50]

For the synthesis of the complexes, two preparative methods were developed. Mixing of a DCM solution of **3-19b-Na** with methanolic silver triflate, copper acetate and cadmium acetate solution resulted in the formation of **3-19b-Ag**, **3-19b-Cu** and **3-19b-Cd**, respectively.

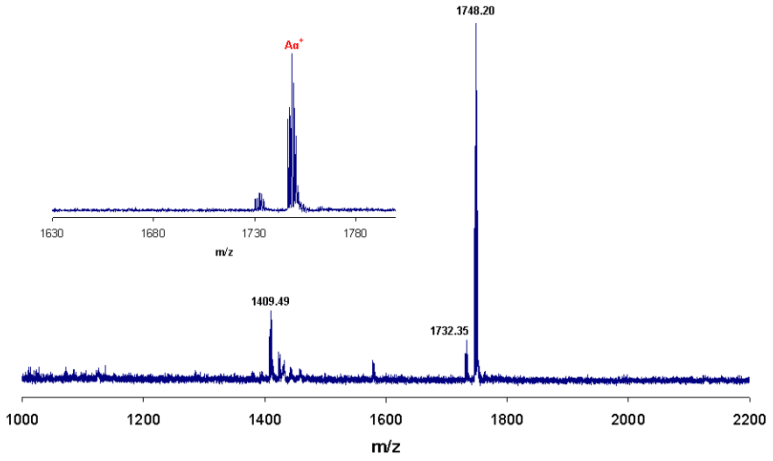

Figure 3-13: MALDI-TOF spectrum of **3-19b-Ag**, the inset shows the main peak region of the complex.

On the other hand, treatment of the same macrocycle solution with aqueous zinc chloride and lead acetate was used for the synthesis of **3-19b-Zn** and **3-19b-Pb**. Alternatively the Zn^{2+} complex is also accessible *via* the first approach using zinc acetate as the metal source.

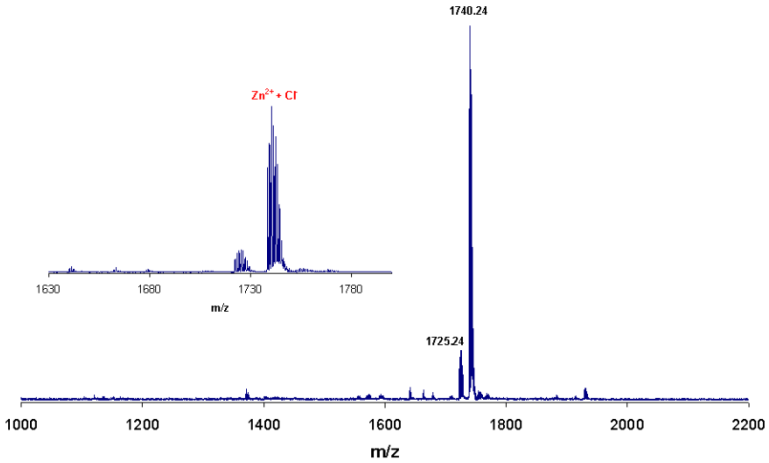

Figure 3-14: MALDI-TOF spectrum of **3-19b-Zn**, the inset shows the main peak region of the complex.

MALDI-TOF spectroscopy was used to monitor the success of the complex formation. In all resulting spectra the complete disappearance of the initial Na^+ peak of **3-19b-Na** was observed.

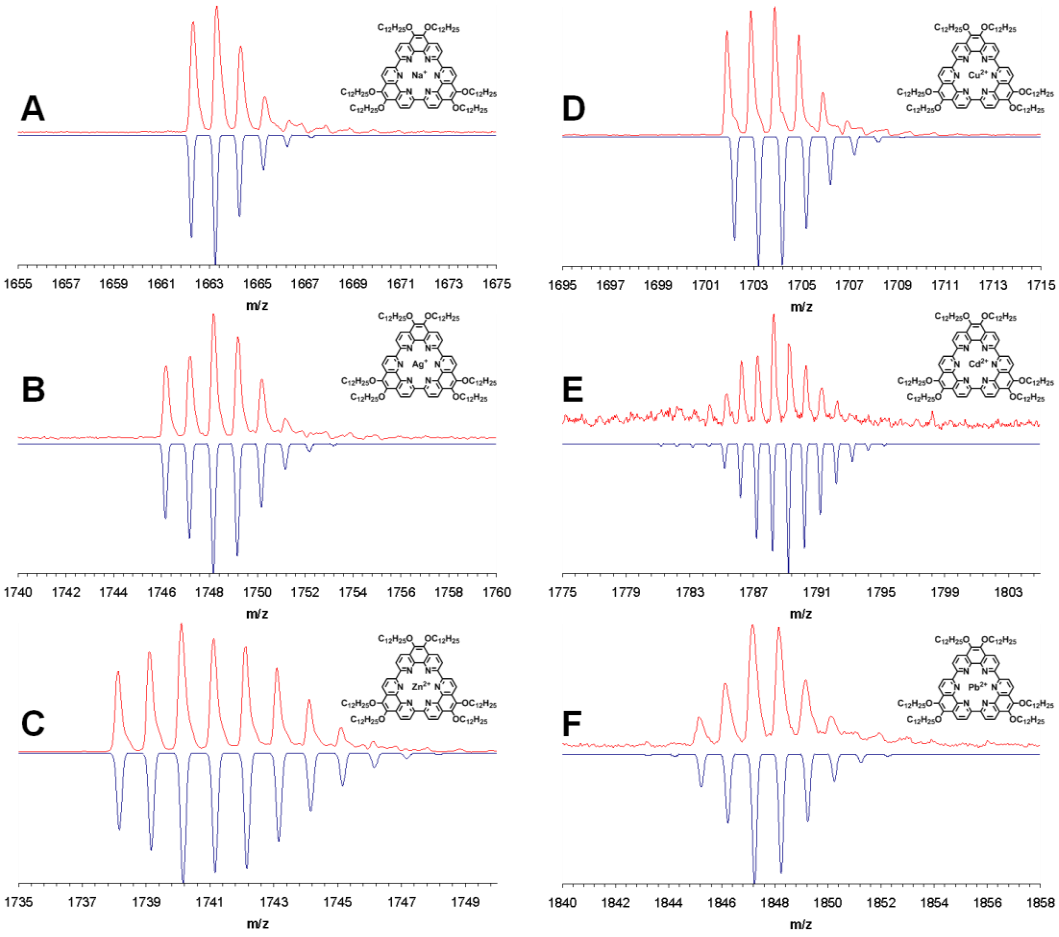

Figure 3-15: Comparison between experimental (red) and theoretically calculated (blue) isotopic pattern of parent **3-19b-Na** (**A**), **3-19b-Ag** (**B**), **3-19b-Zn** (**C**), **3-19b-Cu** (**D**), **3-19b-Cd** (**E**) and **3-19b-Pb** (**F**).

For **3-19b-Ag** and **3-19b-Cu** the corresponding 1:1 adducts were detected as exclusive species, which is shown for **3-19b-Ag** in Figure 3-13.

However, for **3-19b-Zn**, **3-19b-Cd** and **3-19b-Pb** the participation of water and counter-ions in the complex formation was observed. This is shown in Figure 3-14 for **3-19b-Zn**, where the target peak corresponds to the combined mass of the macrocycle, the zinc cation and one chlorine counter-anion, which originates from the metal salt.

The isotopic distribution of the metal complex can be used as a fingerprint tool for proving the formation of the desired metal complex. Figure 3-15 summarizes the corresponding data and illustrates how the isotopic multiplicity of zinc and cadmium leads to a significant splitting of the signal.

The metal sequestration of **3-19b-Ag** was then studied by ^{1}H NMR analysis of the Ag^{+} complex in TCE-d_2.[53] Compared to **3-19b-Na** an overall line broadening can be observed in the case of **3-19b-Ag**. This is particularly pronounced for the two doublets corresponding to the aromatic protons of the macrocycle which are not resolved for **3-19b-Ag** even at high temperatures. Additionally the two signals are shifted from δ = 8.98 ppm to δ = 8.59 ppm and from δ = 8.79 ppm to δ = 8.26 ppm, respectively. The signal corresponding to the *alpha*-protons of the dodecyloxy chain are less affected by this phenomenon, as the high-field shift is only 0.01 ppm with the triplet remaining partially resolved.

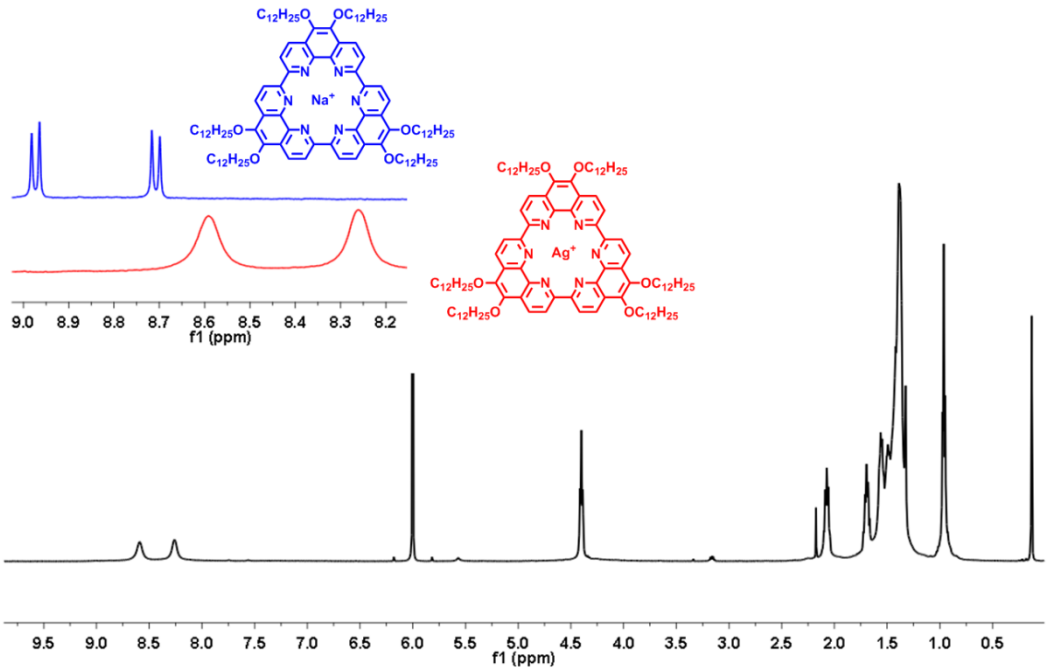

Figure 3-16: ^{1}H NMR spectrum of **3-19b-Ag** in TCE-d_2. The inset shows a comparison between the aromatic region of parent **3-19b-Na** and **3-19b-Ag**.

Further experiments were carried out to examine a possible re-exchange of the Ag^{+} species by a Na^{+} cation. As illustrated by the metal complexation experiments discussed above, the cavity readily exchanges sodium for larger, electron-rich transition metal cations. In order to make the opposite pathway thermodynamically favorable, the Ag^{+} cation needs to be irreversibly removed from the chemical equilibrium.

This was achieved by addition of excess sodium borohydride or hydrazine to a solution of **3-19b-Ag** resulting in the formation of **3-19b-Na** and the precipitation of colloidal silver nanoparticles. As shown in Figure 3-17, the reduction experiment can be easily monitored under UV radiation (366 nm).

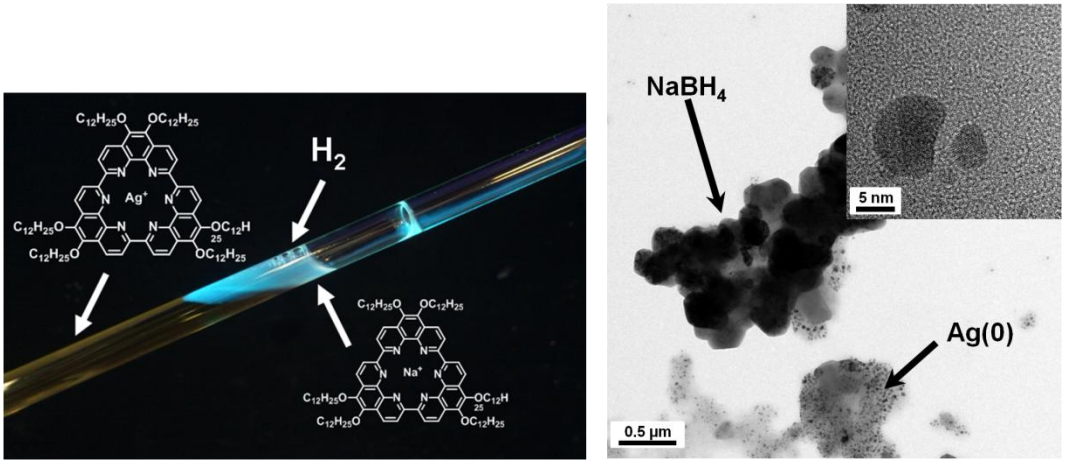

Figure 3-17: The reduction of **3-19b-Ag** with sodium borohydride under 366 nm UV radiation (left), TEM micrograph of the resulting precipitate (right). The inset shows a magnification of single silver nanoparticles.

Upon mixing the reducing agent with the macrocycle solution an instant reappearance of the turquoise fluorescence of the Na^+ complex **3-19b-Na** is observed along with the evolution of hydrogen gas.^{1}H NMR measurements and MALDI-TOF analysis were used to prove the quantitative transformation of **3-19b-Ag** into the Na^+ complex. Electron microscopy and the corresponding energy dispersive X-ray (EDX) spectrum indicated that the precipitate is predominantly composed of small silver particles (5.0 - 20.0 nm in diameter) and larger crystallites of sodium borohydride (several hundred nm in diameter). Alternatively, the Ag^+ guest can also be successfully removed by addition of excess sodium bromide to a solution of **3-19b-Ag**. It is known that silver halides display extremely poor solubility in most solvents leaving only minor amounts of silver cations unbound. However, whereas the reduction of silver by sodium borohydride and hydrazine occurred instantly, the formation of silver bromide proceeded much slower and was only complete after several weeks as evidenced by ^{1}H NMR analysis.

The straightforward reducibility of the metal guest that was documented by these experiments is of great relevance for the envisaged application of the macrocyclic metal complexes in molecular data storage and in the formation of metallic nanostructures. It provides a proof of concept to the question whether the cation within the hexaaza cavity can be reached by the reducing or precipitating agent and proves that the metal guest only loosely binds to the 1,10-phenanthroline moieties of the ring system.

In the next step, a qualitative analysis of the metal exchange capability was performed on the basis of titration experiments that were monitored by fluorescence spectroscopy. A preliminary qualitative experiments with a UV lamp operating at 366 nm indicated,

that replacing the metal guest is always accompanied by pronounced changes of the luminescence of the cyclo-2,9-tris-1,10-phenanthroline macrocycles.

It was demonstrated before, that the addition of silver triflate and zinc acetate results in the formation of well-defined complexes as evidenced by the corresponding MALDI-TOF spectra. Furthermore, in analogy to the macrocycle, both metal salts are well-soluble in THF. By choosing a common solvent, polarity effects or solvent-induced quenching can be excluded. Additionally, anhydrous metal salts were chosen in order to avoid a possible interference from water of crystallization. In order to minimize the influence of dilution, aliquots of a 10^{-4} M solution of the metal salt were dosed to a 10^{-5} M solution of **3-19b-Na**. If equimolar amounts of macrocycle and salt are present the overall dilution is limited to 10.0 % by this procedure. All experiments were performed *in-situ* within a fluorescence cuvette and the excitation wavelength was set to the absorption maximum of 310 nm. This value was determined by preliminary UV-vis measurements of **3-19b-Na** which are depicted in Figure 3-10.

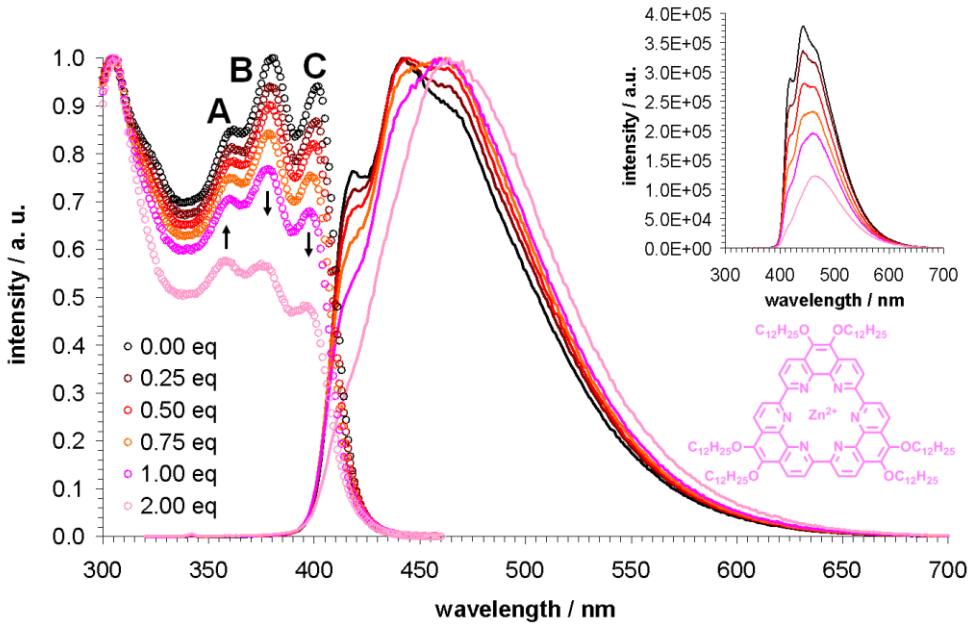

Figure 3-18: Fluorescence excitation and emission spectra of **3-19b-Na** upon titration with zinc acetate

The fluorescence spectrum of **3-19b-Na** shows a broad emission between 380 nm and 650 nm with the maximum located at 444 nm. A minor peak is resolved at 420 nm and a shoulder is found at 467 nm. The vibronic fine structure of the emission spectrum is mirrored by the corresponding excitation spectrum. This contains, in addition to the main absorption at 310 nm, three well-resolved bands at 362 nm (**A**), 380 nm (**B**) and 402 nm (**C**), respectively. The structure of fluorescence excitation and UV-vis

absorption spectrum as well as the location of the main bands was found to be identical which proves a high purity of the material.

The step-wise addition of zinc acetate to the parent solution of **3-19b-Na** was followed by a progressive bathochromic shift of the emission maximum to a final value of 460 nm after the addition of one equivalent of zinc acetate (Figure 3-18).

Formation of the zinc adduct was also accompanied by an overall broadening of the emission spectrum. At the beginning of the titration the aforementioned fine structure was partially conserved (in particular the peak at 420 nm) but progressively vanishes into a featureless emission towards the end of the experiment. At the same time a continuous decline of the overall photoluminescence was observed. The initial value was decreased by approximatively 50 % after addition of one equivalent of zinc acetate to the solution of **3-19b-Na** (see inset of Figure 3-18). Apart from a minor effect due to dilution, the major intensity decrease can be ascribed to the exchange of the cationic guest species within the cavity of the macrocycle.

A closer look on the evolution of the normalized fluorescence excitation spectra during the titration also reveals significant transformations (Figure 3-18). Whereas the location of the bands remains mostly unaffected, the relative intensities of the three signals are changed during the course of the experiment. Both bands, **B** and **C**, decrease progressively whereas band **A** grows in its relative signal strength.

The migration of the emission band upon progressive titration with a metal source has been extensively described in the past and the corresponding cyclic[53-55] and non-cyclic ligands[56,57] were thus applied as sensors for the detection of specific metal cations in solution. In contrast, the instant and complete replacement of a metal guest by another cation as in the case of the cyclo-2,9-tris-1,10-phenanthroline macrocycles is a unique feature. For the structurally related torands discussed above, the exchange of the metal guest is also possible but the cavity needs to be “emptied” by an intermediate acid treatment.[22-25] It can be assumed that the non-ionic binding of the hexaaza cavity of **3-19b** is at the heart of the selective exchange of the metal guest that is accompanied by a characteristic evolution of the optical spectra.

In a second experiment, it could be proven that also the titration with silver triflate results in a similar behavior (Figure 3-19). The addition of this salt resulted in a much stronger bathochromic shift of the main emission peak from 444 nm to 474 nm after the addition of two equivalents.

In contrast to **3-19b-Zn**, the formation of the Ag^+ macrocycle seems to be not quantitative once equimolar amounts of macrocycle and salt are mixed. Only the addition of an excess resulted in the formation of the Ag^+ complex which was revealed by MALDI-TOF measurements of the corresponding solutions. Compared to the

previous case, the decrease in luminescence is much stronger as the intensity drops by nearly 90 % after addition of one equivalent. For the silver titration, the fluorescence excitation spectra are also considerably affected by the experiment. The change in relative signal strength is even more pronounced as for dosing with zinc, since band **B** and **C** are no longer resolved. At the expense of the other two main absorptions, **A** becomes the strongest signal after full conversion of **3-19b-Na** to the Ag^+ complex **3-19b-Ag**.

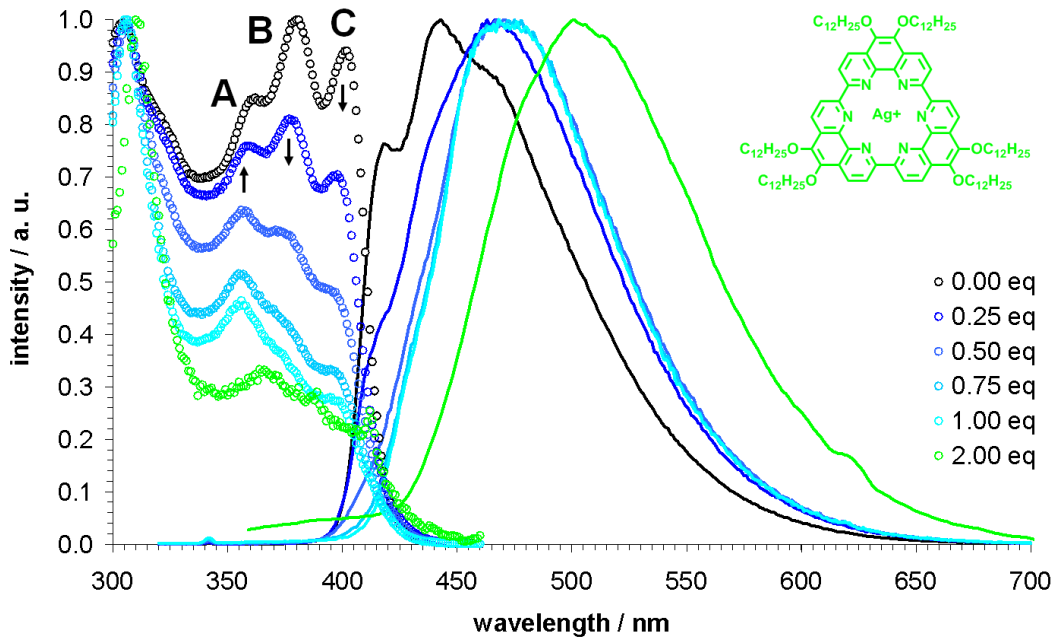

Figure 3-19: Fluorescence excitation and emission spectra of **3-19b-Na** upon titration with silver triflate.

In view of the fact that both Na^+ and Ag^+ are similar in size and possess the same charge it appears that the driving force for the instant displacement of the alkaline metal species must arise from the different electron shell configuration of the Ag^+ cation. Taking into account the reducibility of this metal guest the macrocycle could serve as a recyclable template for the preparation of metallic nanostructures from solution as it will be discussed in the next section.

3.2.3 Self-Assembly from Solution

The self-assembly of discotic molecules to form self-assembled structures of different morphologies from solution is an attractive route towards active materials for supramolecular electronics.[58,59] Herein, nanoscale fibers, tubular structures and ribbons

formed by macrocycles adopt an important role as they can provide strongly orientated charge- and ion-transporting pathways.[19,60-62]

As mentioned previously, the cyclo-2,9-tris-1,10-phenanthroline macrocycles and their corresponding metal complexes benefit from an excellent solubility in polar solvents for which their extensive alkyl chain substitution accounts. However, controlled precipitation was achieved by slow dropping of a THF solution of **3-19b-Na** into ethanol. Upon standing, a voluminous yellow precipitate slowly formed (inset Figure 3-20) which could be collected by centrifugation and was subjected to electron microscopy investigation. These experiments have been carried out in cooperation with *Dr. D. Wu* (MPI-P Mainz, Germany).

The SEM analysis revealed that the precipitate was composed of fiber-like aggregates for which typical micrographs are depicted in Figure 3-20. As it can be clearly seen, the fibers are of very homogenous nature. They all exhibit similar geometric dimensions, in particular their diameter is uniform and ranges between 180 nm and 200 nm. In some cases they reach considerable longitudinal extensions of up to 10 microns illustrating a high tendency towards self-organization from solution for **3-19b-Na**.

With the aim to evaluate a possible formation of metallic nanostructures *via* chemical reduction it was then decided to transfer the precipitation protocol to a surface-confined environment. The Ag^+ complex **3-19b-Ag** was chosen for these experiments since it exhibited good chemical reducibility as proven by the NMR investigations discussed above.

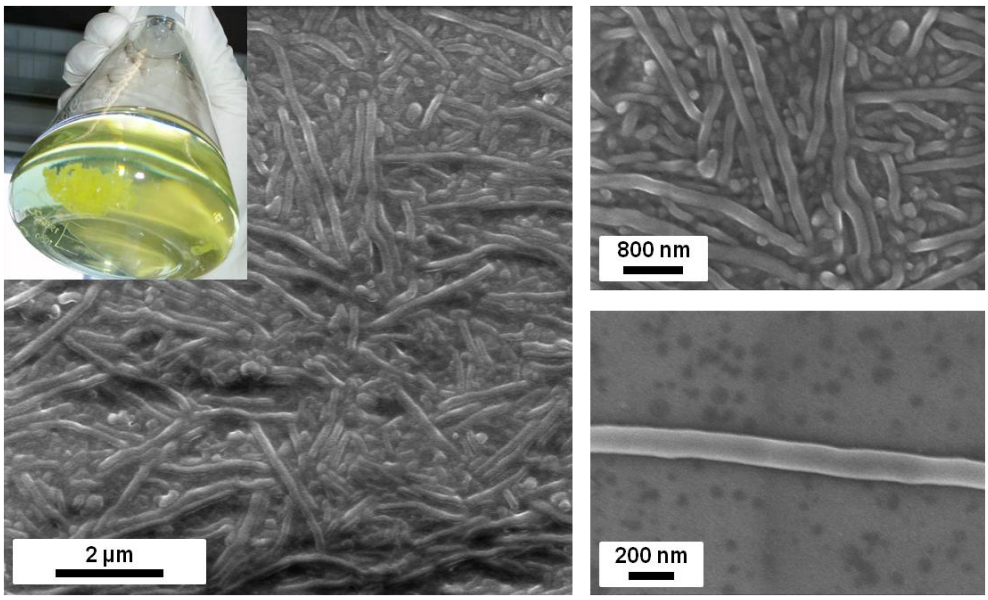

Figure 3-20: SEM analysis of fiber-like aggregates obtained by controlled precipitation of **3-19b-Na**; the inset shows a photograph of the yellow precipitate.

Among the tested reducing reagents, hydrazine appeared the most suitable one since the typical by-products of its oxidation are nitrogen and water. The supramolecular structures are thus not contaminated by inorganic remains as this would be the case for sodium borohydride. Furthermore, hydrazine vapors can be easily formed by simple heating of its solutions thus allowing for solvent-free reductions. Also, aqueous hydrazine solutions can be fully evaporated.

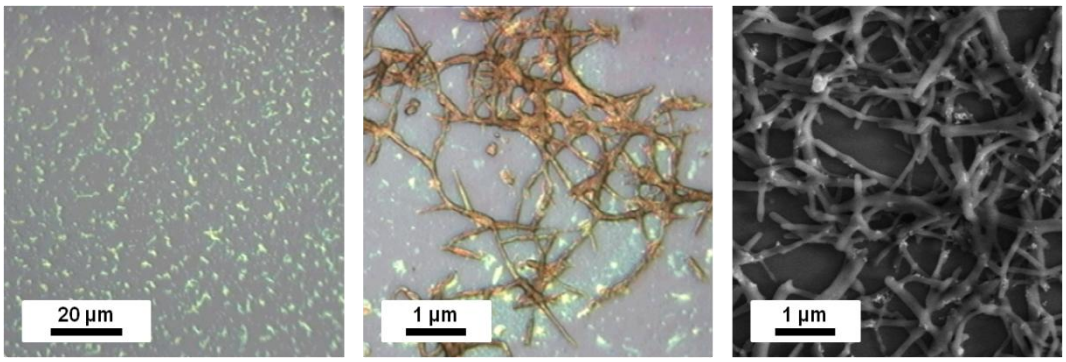

Figure 3-21: POM image of **3-19b-Ag** fibers obtained by dropcasting prior to reduction (left); POM (middle) and SEM image (right) of the aggregates after treatment with hydrazine.

In cooperation with *S. Wang* (MPI-P Mainz, Germany), the self-assembly from solution was studied for **3-19b-Ag**. It was found that fibers of the macrocycle could also be formed directly on a silicon wafer by dropcasting of ethanolic THF solutions containing the metal complex.

The same fiber-like structures which were seen for the Na^+ complex **3-19b-Na** could be also detected for **3-19b-Ag** (Figure 3-21). The POM images obtained reveal the homogenous coverage of the substrate with birefringent fibers reaching longitudinal dimensions on the micrometer scale. Hence, the reduction was attempted by two methods. The first consisted in immersing the substrate decorated with **3-19b-Ag** into a gas chamber containing a saturated hydrazine atmosphere at a temperature of 60 °C. The second reduction protocol was carried out by direct deposition and slow evaporation of an aqueous hydrazine solution on top of the self-assembled film of macrocycle **3-19b-Ag**. However, only in the second case significant changes of the fibers upon exposure to hydrazine could be detected. The contrast seen in the corresponding POM image (Figure 3-21) is significantly increased. Whereas the nanostructures show strong birefringence prior to reduction, an indication for an enhanced molecular orientation, the fibers appear brownish after the hydrazine treatment. This might indicate the successful formation of metallic silver nanostructures. From the corresponding SEM image, no definite answer regarding the

internal nature of the fibers can be drawn. It will be therefore necessary to further evaluate the fibers by TEM analysis which will provide a cross-sectional view of the aggregates.

3.2.4 Self-Assembly in the Bulk Phase

In principle, the arrangement of rigid macrocyclic mesogens in a polymolecular stack results in the formation of tubular superstructures as observed for macrocyclic polyethers[63] and polyamines,[64] phthalocyanines[65,66] and various shape-persistent phenylene-ethynylene macrocycles.[67,68] It can be expected that the presence of *intra*annular aza or oxo coordination sites furthermore enables the formation of molecular channels holding promise for the transport of ions, charges and small molecules.[65] Useful applications involve membranes containing ion-selective channels,[69] amphiphilic metallomesogens with enhanced charge-carrier mobilities for high-performance organic field effect transistors[70] and conducting wires.[65,71]

Again, the cyclo-2,9-tris-1,10-phenanthroline macrocycles adopt a special role due to the ion-dipole-type metal binding which has been discussed in the previous chapter. This characteristic feature allows for the fast and quantitative exchange and reduction of the metal guest.

In cooperation with *A. Mavrinskiy* and *Dr. W. Pisula* (MPI-P Mainz, Germany) the supramolecular organization of **3-19a-c-Na** and the transition metal complexes of **3-19b** in the bulk state were studied in detail by two-dimensional wide-angle X-ray scattering (2D-WAXS).[66-68,72] The patterns were recorded for mechanically extruded fibers obtained by a setup described elsewhere.[73] The extrusion process leads to a strong pre-organization of the disc-like molecules which is reflected by the collected experimental data.

The measurements indicated an overall liquid crystalline hexagonal columnar arrangement of the macrocycles and a coaxial orientation of the discs in the stacks. The *inter*columnar distance a_{hex} increased successively with the length of the alkoxy chains from a_{hex} = 3.32 nm (**3-19a-Na**), a_{hex} = 3.75 nm (**3-19b-Na**) to a_{hex} = 4.22 nm (**3-19c-Na**) (Figure 3-22). The rather isotropic small-angle reflections related to intercolumnar correlations and the lack of higher-order reflections revealed poor macroscopic orientation of the macrocycles along the extrusion direction.

An *intra*columnar disc *π*-stacking of p = 0.37 nm was only observed for **3-19a-Na** which is the derivative with the shortest alkyl chains of this series (Figure 3-22). Probably, the long chains for **3-19b-Na** and **3-19c-Na** hindered pronounced interactions between the molecules resulting in a so-called disordered columnar phase. The discotic liquid

crystalline organization of **3-19a-c-Na** is in accordance with 2D-WAXS results obtained for other macrocyclic mesogens and suggests the presence of molecular channels within the liquid-crystalline phase.[66-68,72]

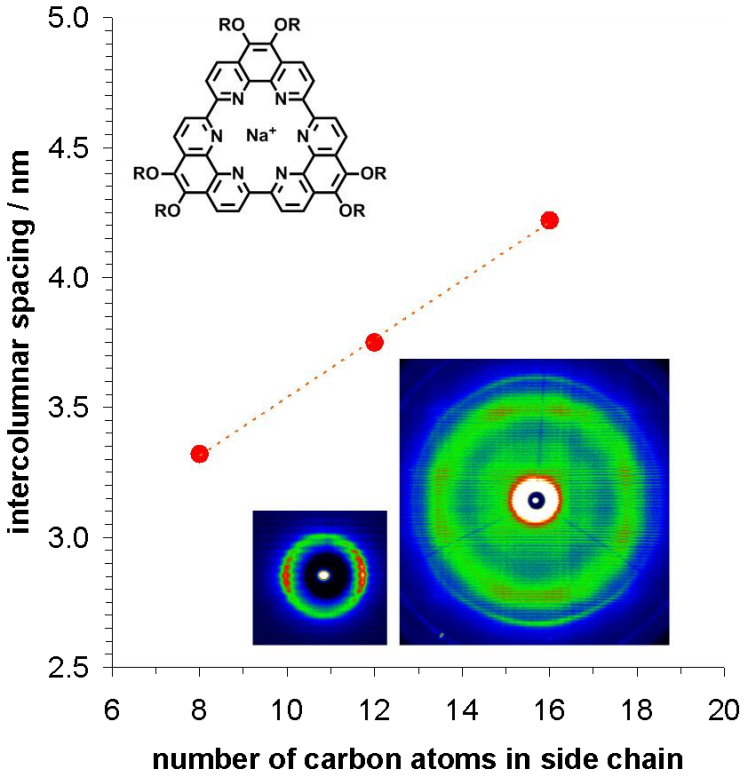

Figure 3-22: Linear relationship found between alkoxy chain length and intercolumnar spacing, the inset shows the 2D-WAXS pattern of **3-19b-Na** (30 °C).

The overall moderate tendency of the Na^+ complexes to self-assemble gave however motivation to examine a possible stabilization of the mesophase by large, electron-rich transition metal cations and different counterions. In the following, the Ag^+ and Pb^{2+} complexes **3-19b-Ag** and **3-19b-Pb** were investigated by temperature-dependent 2D-WAXS experiments. For these two transition metal species the actual ionic diameters can be expected between 2.30 Å to 2.56 Å for Ag^+ and between 2.38 and 2.58 Å for Pb^{2+}.[50] In the corresponding complexes triflate and acetate, most probably sandwiched in between neighboring macrocycles,[74] counterbalance the positive charges as they originate from the salts which were used as metal source. Various studies have also addressed the impact of the anionic species on the organization of metallomesophases.

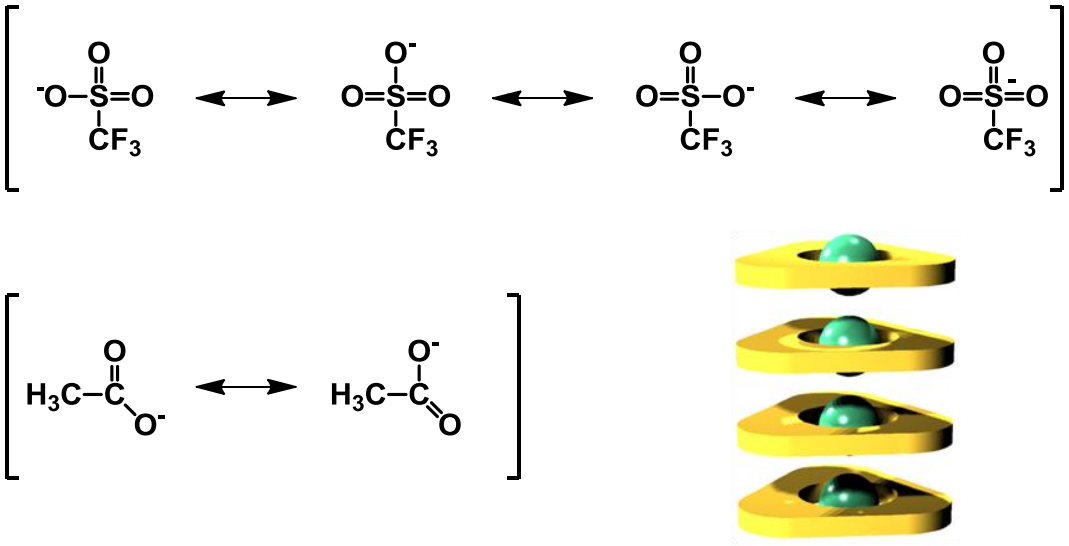

Figure 3-23: Mesomeric stabilization of the triflate and acetate anion; schematic illustration of the molecular packing of the metal complexes after annealing, the stabilizing metal guest is indicated as a green sphere.

Based on *Pearson*'s HSAB concept[75] it was recently found that hard anions slightly stabilize or even destabilize the mesophase. In contrast, soft anions can efficiently improve the mesomorphic properties of liquid-crystalline crown ether derivatives.[76-78] In this respect, hydroxide, fluorine and chlorine represent hard bases due to their small size and low polarizability. On the other hand, larger, electron-rich anions such as iodine or thiocyanate are classified as soft bases. In the present case, the hydroxide counterion of **3-19b-Na** can be regarded as hard, whereas triflate (**3-19b-Ag**) and acetate (**3-19b-Pb**) are of much softer character. This can be ascribed to their increased size and the high delocalization of the negative charge through mesomeric stabilization (Figure 3-23). Consequently, such electron-rich anions can also act as axial bridging agents between individual metal centers thus further stabilizing supramolecular architectures.[79-81] This is again in contrast to the role of the hard bases discussed above.

As it can be seen in Figure 3-24 (**3-19b-Ag**) and Figure 3-25 (**3-19b-Pb**) both metal complexes exhibit a hexagonal columnar organization after extrusion of the filaments. The patterns recorded at ambient temperature are dominated by the amorphous halo which is caused by the disordered dodecyloxy chains and a low supramolecular organization. This additionally manifests in very weak meridional reflections typical of a disordered *intra*columnar packing. In general, the packing still appears to be rather weak as observed already in the case of **3-19b-Na**.

The two samples were then subjected to an annealing procedure with a maximum temperature of 150 °C in each case. It has to be noted that all compounds did not show

phase transitions in the DSC scans but the higher molecular mobility at elevated temperatures was expected to result in an improved packing.

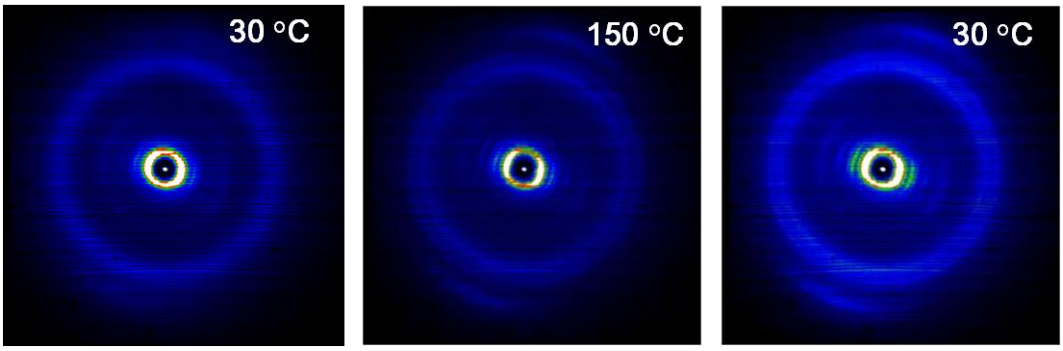

Figure 3-24: Temperature-dependent 2D-WAXS patterns of **3-19b-Ag**.

As it can be seen in Figure 3-23 and in Figure 3-25, the self-organization of the macrocycles was strongly increased by this treatment. At a temperature of 150 °C sharp meridional reflexes are well-resolved in the pattern of **3-19b-Ag** which indicate an improvement in molecular packing within the stacks (Figure 3-24).

Additional higher order reflections in the equatorial plane of the pattern also confirm an enhancement of the overall hexagonal columnar organization. Importantly, the high degree of order is preserved upon cooling to 30 °C as seen by the prevalence of the high-order reflections. The *inter*columnar and *intra*columnar parameters of the mesophase can be further used as a descriptor which illustrates the improved order of **3-19b-Ag** as compared to the Na^+ complex **3-19b-Na**. The Ag^+ complex exhibits an *inter*columnar separation of a_{hex} = 3.02 nm and a typical *intra*molecular stacking distance of p = 0.35 nm, which is indicative of strong *π*-*π*-interactions within the columns. In contrast, the stacks of **3-19b-Na** exhibit a much larger *inter*columnar distance of a_{hex} = 3.75 nm despite the identical length of the alkoxy chain. One can also attribute the smaller *inter*columnar distance for **3-19b-Ag** to the crystallization and therefore more pronounced interdigitation of the lateral substituents. Moreover, no significant face-to-face interactions were found between the macrocycles of individual columns for **3-19b-Na**.

Concerning the bulk organization of **3-19b-Pb**, the metal guest was also found to efficiently help in the columnar arrangement of the cyclic metal complexes. However, the improvement of the molecular order occurred at a lower temperature in this case as it can be seen when comparing the patterns obtained at 110 °C and 150 °C, respectively (Figure 3-25). In analogy to **3-19b-Ag** pronounced meridional reflexes were observed at 110 °C proving the presence of a well-organized hexagonal columnar

mesophase. Further increase of the temperature to 150 °C leads however to a decrease of the molecular order. Nevertheless, the samples preserved a certain degree of ordering after the heating cycle. The self-organization is not as high as for **3-19b-Ag** but the patterns allow for the determination of the packing parameters which are a_{hex} = 3.10 nm and p = 0.37 nm.

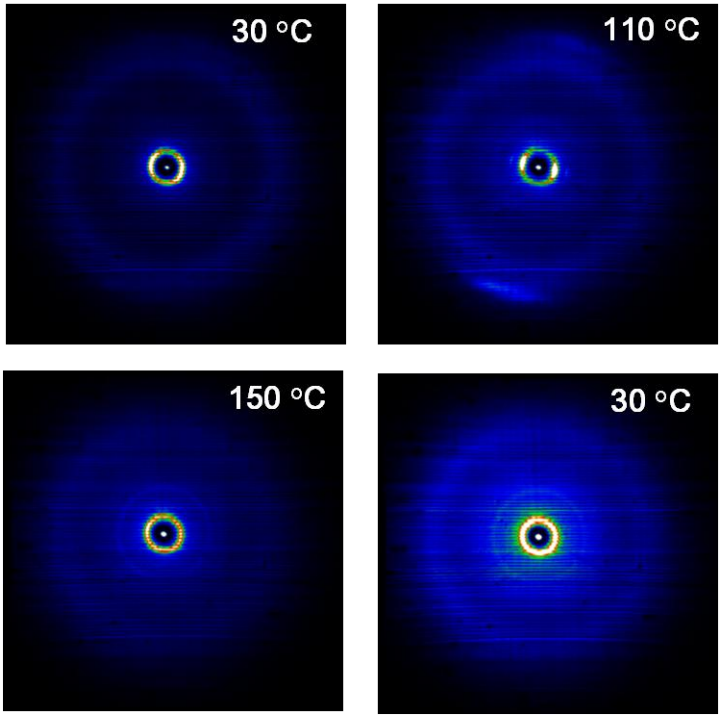

Figure 3-25: Temperature-dependent 2D-WAXS patterns of **3-19b-Pb**.

In summary, the 2D-WAXS experiments illustrate the ability of the cyclo-2,9-tris-1,10-phenanthrolines to self-assemble into hexagonal columnar mesophases. It seems, however, that the packing tendency of the macrocycle itself is rather moderate which can be explained by the rather small continuous *π*-surface of the compound when compared to the size of the larger liquid-crystalline derivatives of coronene or HBC.[58,73,82] The significantly smaller overlap of the molecules as compared to classical discotic mesogens leads to the formation of disordered mesophases in the case of the Na^+ complexes. It was however demonstrated that large transition metal cations such as Ag^+ and Pb^{2+} along with electron-rich counterions such as triflate and acetate efficiently stabilize the mesophase and lead to an improved organization upon annealing the mesophase at elevated temperatures. This is in line with observations that have been made for liquid-crystalline crown ether derivatives and their corresponding metal complexes.[76-78]

Taking into account the possibility to reduce the transition metal guests to their neutral state as demonstrated before, the preparation of nanoscale metallic structures such as wires should be feasible. In this case the mesophase itself would constitute a template on the molecular level.

3.2.5 Self-Assembly on Surfaces

In addition to the formation of columnar mesophases in the bulk state, self-assembly of highly structured macrocycles such as **3-19a-c** into monolayers will lead to surface-confined supramolecular networks.[61,67,72] Being highly ordered, two-dimensional crystals are currently extensively investigated for surface templating at the nanoscale[83,84] as well as for host-guest chemistry[84]. In the case of metal complexes, new concepts of molecular data storage can be thought of which rely on the reversible "switching" *via* the manipulation of single molecules.[51] Scanning tunneling microscopy (STM) is a powerful tool for the structural and electronic characterization of single molecules in self-assembled monolayers on conducting substrates. The cyclo-2,9-tris-1,10-phenanthroline macrocycles and their corresponding metal complexes were thus studied in cooperation with the group of *de Feyter* (KU Leuven, Belgium).

Figure 3-26 displays the large scale and high resolution STM images of **3-19b-Na** obtained at the liquid-solid interface of 1-phenyloctane and highly ordered pyrolytic graphite (HOPG). The concentration of the macrocycle is $5.5 \cdot 10^{-4}$ for all images. The images reveal that **3-19b-Na** forms highly ordered domains which cover large areas of the substrate. The triangular molecules are arranged in the form of rows which extend over several dozen nanometers (α-phase). The rows are orientated in an alternating up-down fashion keeping the flat lying molecules at a fixed distance.

The bright features in the image can be attributed to the *π*-conjugated fused 1,10-phenanthroline cores of **3-19b-Na**. The corresponding unit cell parameters of the two-dimensional monolayer are found to be a = 2.82 ± 0.02 nm, b = 4.67 ± 0.20 nm and α = 74.0 ± 1.00 °.

The alkoxy chains of the cyclo-2,9-tris-1,10-phenanthroline macrocycles are well resolved in the high resolution STM image (Figure 3-26). It reveals that the dodecyloxy chains are compactly interdigitated and run parallel to the underlying main graphite axes. The interdigitation of lateral alkyl or alkoxy chains is a feature which has been frequently observed within self-assembled monolayers, in particular at liquid-solid interfaces. The stabilization occurs not only by means of non-covalent attraction between the chains themselves, but also by *van der Waals* interactions with the HOPG

substrate. Especially graphite surfaces have a high affinity for alkyl chains, because of the high degree of structural matching.[61,85]

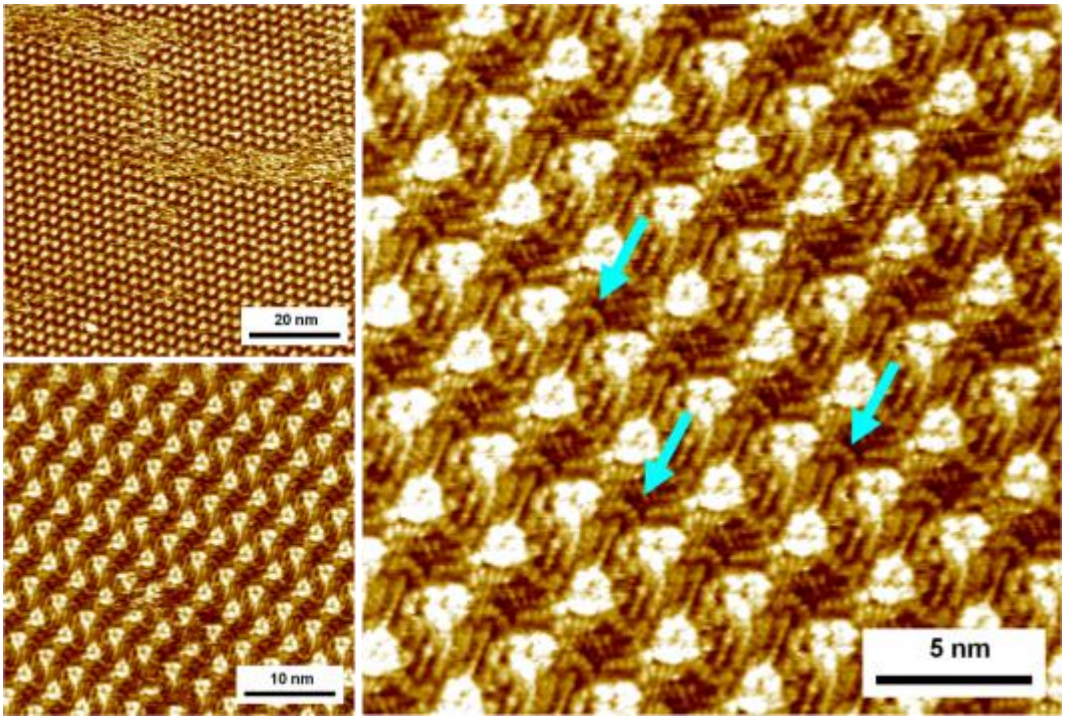

Figure 3-26: STM (left) and high-resolution STM image (right) of row-like assemblies (α-phase) of **3-19b-Na** at the liquid-solid interface. The blue arrows indicate the unusually curved alkyl chains.

As a result of the strong directing effect of the alkyl chains and their interdigitation with tails of adjacent molecules, two-dimensional network structures can be created which are solely based on *inter*molecular *van der Waals* forces. Besides that, the shape of the molecular core will also have a strong influence on the characteristics of the two-dimensional lattice. For example, the self-assembly of dehydrobenzoannulenes, exhibiting either rhombic or triangular shapes, was found to be governed by the symmetry of the molecular core. Whereas in both cases extended surface-confined networks were formed they differed despite the same alkyl chain length strongly in their unit cell parameters.[86,87]

Another characteristic feature of the high resolution STM image of **3-19b-Na** is the prevalence of curved alkoxy chains which are indicated by blue arrows in Figure 3-26 and appear at various points of the monolayer. This phenomenon results from the filling of free volume by the dynamical rearrangement of the alkoxy chains which has for example also been reported for HBC derivatives in the past.[88]

Regarding the Na^+ cation, no evidence for the metal guest could be derived from the line profile analysis which was carried out on the monolayer (Figure 3-27). The line

profile follows the linear arrangement of the macrocycles. The cavity of **3-19b-Na** appears “empty” and a depression is found at the expected position. Also, on the corresponding STM topograph triangular bowl-shaped structures are found which appear however to be unfilled (Figure 3-27). The centers of the macrocycles are separated by approximately 2.87 nm.

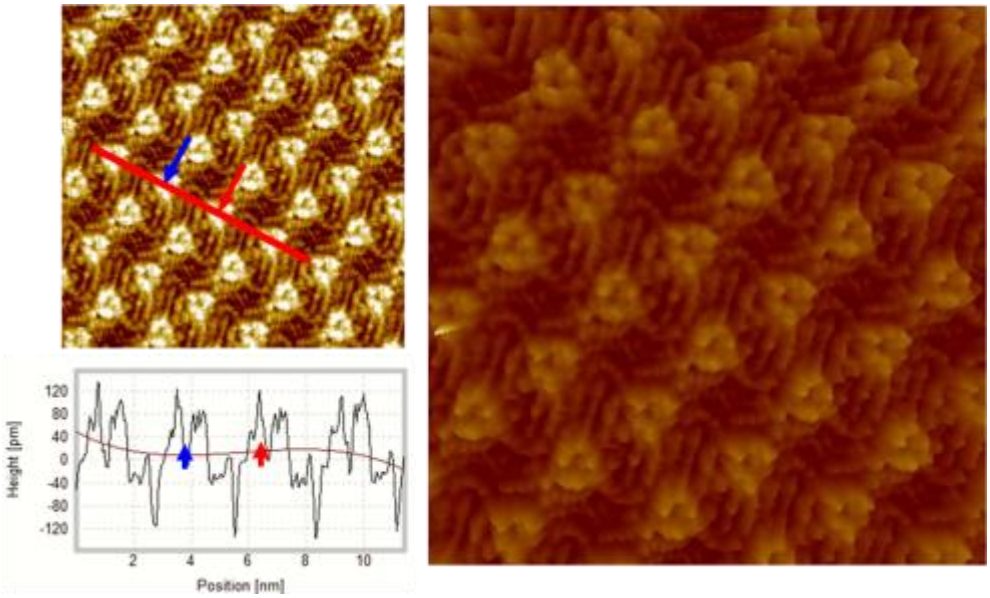

Figure 3-27: Monolayer of **3-19b-Na** (α-phase) and corresponding line profile analysis (left), STM topograph obtained from the analysis (right).

In order to analyze a possible influence of a larger metal cation on the self-assembly of the macrocycle, the Ag^+ complex **3-19b-Ag** was studied subsequently.

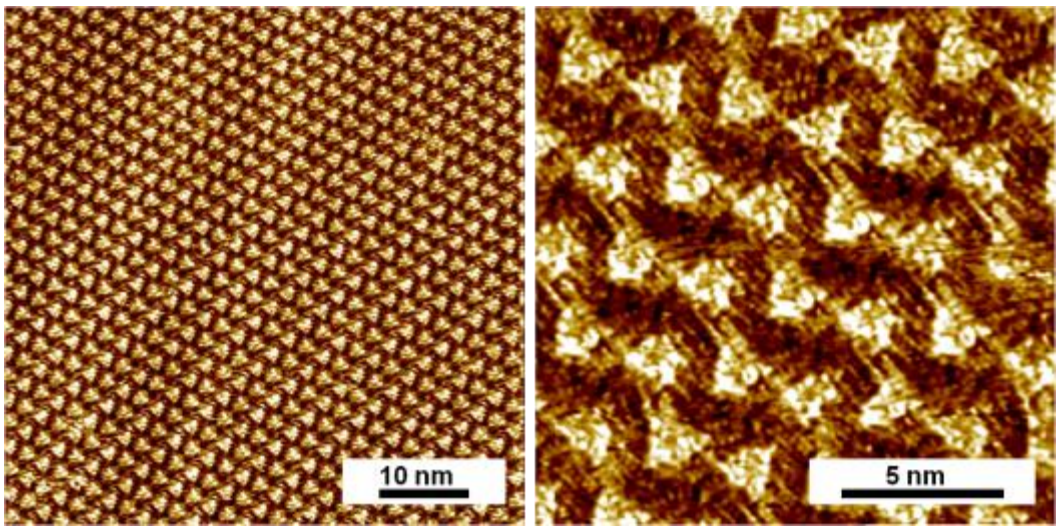

Figure 3-28: STM images of row-like assemblies (α-phase) of **3-19b-Ag** at the liquid-solid interface.

In comparison to the Na^+ cation (d = 2.04 to 2.36 Å) the ionic diameter of the Ag^+ guest is significantly larger (d = 2.30 to 2.56 Å).[50] Also, the number of electrons is increased from 10 to 46 with contributions from the d-block for the Ag^+ species. The monolayer formed by **3-19b-Ag** was investigated as before at the 1-phenyloctane/HOPG interface. Surprisingly, the macrocycle organizes in more than one pattern on the HOPG substrate.

One of the phases is a linear arrangement of molecules (α-phase) which is analogous to that observed in case of **3-19b-Na**. The similarity between the row-like assemblies is also reflected by the unit cell parameters of a = 2.73 ± 0.08 nm, b = 4.55 ± 0.10 nm and α = 76.9 ± 2.00 °. Figure 3-28 shows the large scale and high resolution STM images of the α-phase of **3-19b-Ag**.

Although the high resolution image does not resolve the side chains as clearly as in the case of **3-19b-Na** (Figure 3-26), there is sufficient indication for the presence of the curved alkoxy chains discussed previously.

Another phase, which coexists with the α-phase, is characterized by an extended porous honeycomb network. In Figure 3-29 the STM images of the β-phase of **3-19b-Ag** are shown. The period of the honeycomb structure is found to be 4.28 ± 0.03 nm. The diameter of a pore, determined from edge to edge, is 2.73 ± 0.12 nm whereas it is 3.37 ± 0.10 nm when measured from corner to corner.

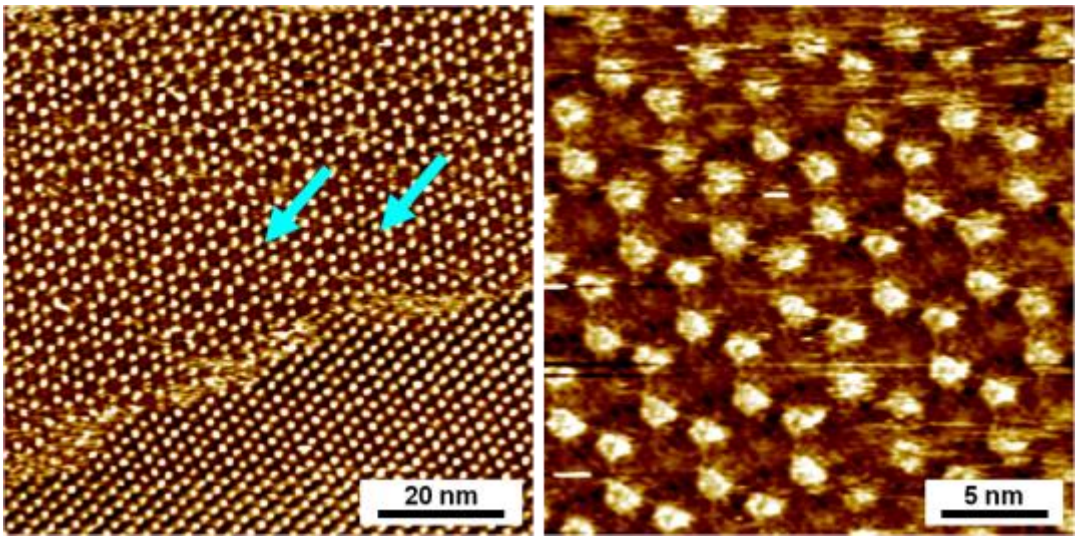

Figure 3-29: STM images of coexisting α-phase and β-phase of **3-19b-Ag** at the liquid-solid interface (left), the honeycomb network formed by the β-phase (right). The blue arrows indicate trapped molecules in the hexagonal cavities.

Even though the porous network extends over several hundred nanometers it always coexists with the tightly packed linear α-phase.

In principle, most molecules are able to form surface-confined lattices of high order and periodicity. Two-dimensional porous network structures, either based on covalent[89-92] or non-covalent bonds,[87,93-102] have attracted considerable attention only in the recent past. This is due to their ability to immobilize functional guest molecules such as large PAHs[94,99,102] and fullerenes[101] in the recurring and spatially organized network. Also, the aspect of surface patterning has been addressed by various studies.[93,101] Porous graphene layers have been recently proposed as atmospheric nanofilters.[92]

However, most of the non-covalent supramolecular surface networks known so far are based on self-assembly through *inter*molecular hydrogen bonds[93,96,97] or metal-ligand interactions.[93,98] Porous surface networks built from the weaker *van der Waals* forces are much less frequently encountered.[87,93,99,100] In these systems porosity can be either generated by *inter*molecular voids resulting from the arrangement of the molecules or by molecules that are intrinsically "porous" themselves. It is apparent that macrocycles are ideal candidates as they contain by definition a nanoscale cavity which can be precisely tailored during the synthetic strategy used for the build-up of the compound.

In this respect, the described two-dimensional lattice of **3-19b-Ag** is conceptually novel[93-95] as an inherently "porous" molecule, the cyclo-2,9-tris-1,10-phenanthroline macrocycle, forms a porous superstructure which may be further used for accommodation of a second guest other than the macrocycle itself (Figure 3-29). Indeed, the sequestration of guest species is already seen for **3-19b-Ag**. At some positions of the monolayer, indicated by blue arrows in Figure 3-30, the macrocycles are themselves trapped within the hexagonal voids which are formed by the surrounding macrocycles. The molecular dimensions of **3-19b-Ag** correspond well to the diameter of the hexagonal pores and allow for an efficient stabilization within the cavity. It should be noted again that the network already hosts the Ag^+ cations in the primary cavities. The spatial and periodic separation of individual metal centers is a prerequisite for a possible application in molecular data storage.[51,52] As these geometric dimensions are determined by the parameters of the supramolecular lattice the application of the latter to the storage of binary data *via* reduction of single metal species such as the Ag^+ guests can be envisaged. The presence of Ag^+ has been confirmed independently as described before by using a combination of NMR and MALDI-TOF spectroscopy.

At very low concentrations of the macrocycle, a third phase was discovered. In the γ-phase, an extremely close packing of **3-19b-Ag** is seen (Figure 3-30). It appears that in the γ-phase, each hexagon in the honeycomb lattice is surrounded by an outer motif of six additional molecules forming a bigger hexagonal feature. This packing is most peculiar and can be rationalized in terms of a "honeycomb@honeycomb" structural

arrangement. In Figure 3-30, the first hexagonal motif is indicated by blue circles, whereas the secondary hexagonal level is depicted by red circles. The tightly interdigitated alkyl chains are well-resolved on these images. The secondary hexagonal superlattice is interrupted by a few defect sites of which one is indicated by the yellow arrow in Figure 3-30. In this case a molecule from the outer hexagonal motif (red circles) is missing. If the metal guest of **3-19b-Ag** is again taken into account, three different types of pores coexist in the γ-phase.

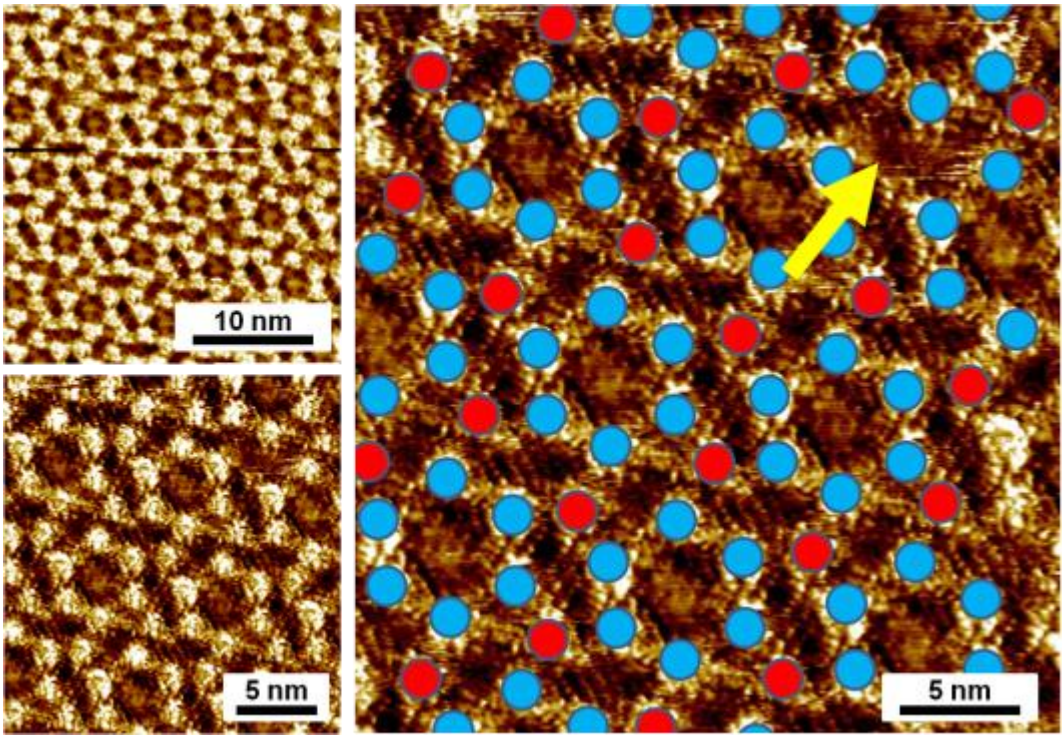

Figure 3-30: STM images of the γ-phase of **3-19b-Ag** at the liquid-solid interface (left), analysis of the honeycomb@honeycomb arrangement of the γ-phase (right). The yellow arrow indicates a defect site.

The line profile analysis (Figure 3-31) performed on the α-phase of **3-19b-Ag** gave similar results as in the previous case. Even though the triangular shape of the cyclo-2,9-tris-1,10-phenanthroline macrocycle is well-resolved *via* STM topography, the cavity of the compound still appears “empty”. However, the depression seen in the cross-section profile is less pronounced as for **3-19b-Na** which might be indeed an effect of the larger diameter of the Ag^+ cation. A distance of 2.66 nm was found between two individual cavities.

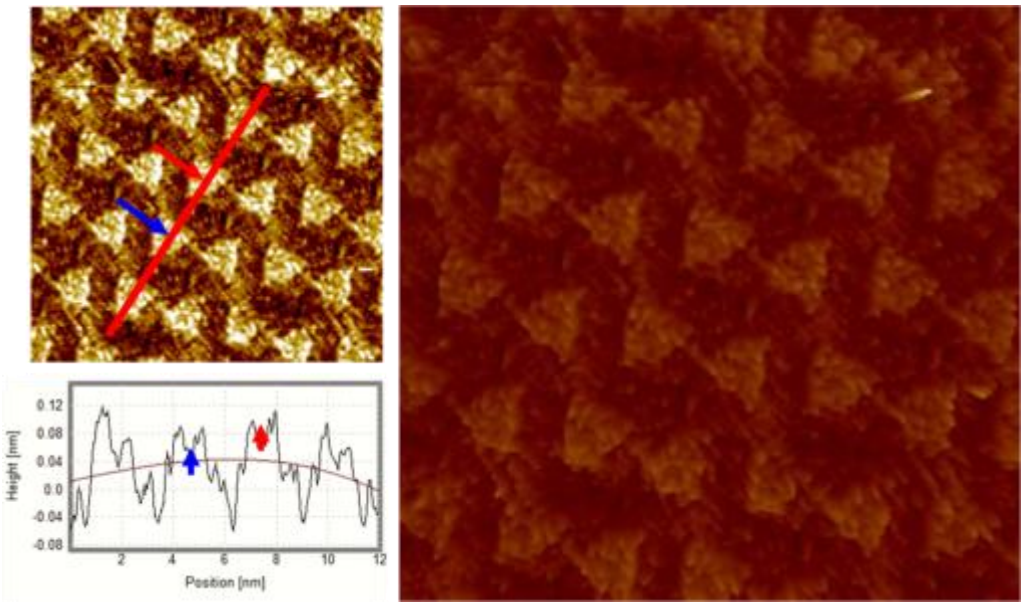

Figure 3-31: Monolayer of **3-19b-Ag** (α-phase) and corresponding line profile analysis (left), STM topograph obtained from the analysis (right).

An additional series of STM measurements was then carried out on **3-19b-Pb**. The Pb^{2+} cation is still larger in size than the metal guests in the two previous cases and is characterized by its high number of 80 electrons (compared to 10 for Na^{+} and 46 for Ag^{+}). Contrary to **3-19b-Ag** with its three different polymorphs, only the formation of the α-phase was confirmed for **3-19b-Pb**. Figure 3-32 shows the STM images of the macrocycle physisorbed at the 1-phenyloctane/HOPG interface.

It can be noticed that the molecular arrangement in the monolayer of **3-19b-Pb** is almost identical to the linear α-phases observed in case of the other two metal complexes. Consequently, the unit cell parameters are very similar and can be calculated as a = 2.81 ± 0.04 nm, b = 4.52 ± 0.07 nm and α = 75.2 ± 0.90 °.

A close look on the STM images of **3-19b-Pb** reveals a very characteristic feature which has only been observed for this metal complex. The STM analysis of adsorbed surface layers relies on the measurement of the tunnel current between tip and surface.[103,104] Consequently, bright features in STM images are attributed to electron-rich regions of molecules such as *π*-systems whereas those of lower electron density such as alkyl chains appear darker in contrast. As previously described for the other two metal complexes, one would intuitively expect the aromatic core of **3-19b-Pb** to appear brightest which can, however, not be confirmed. Unusually bright spots are seen in the centre of almost all macrocycles represented on the images (Figure 3-32). In comparison to these spots, the organic part of the molecule, even though identical to the case of **3-19b-Na** and **3-19b-Ag**, appears now significantly darker.

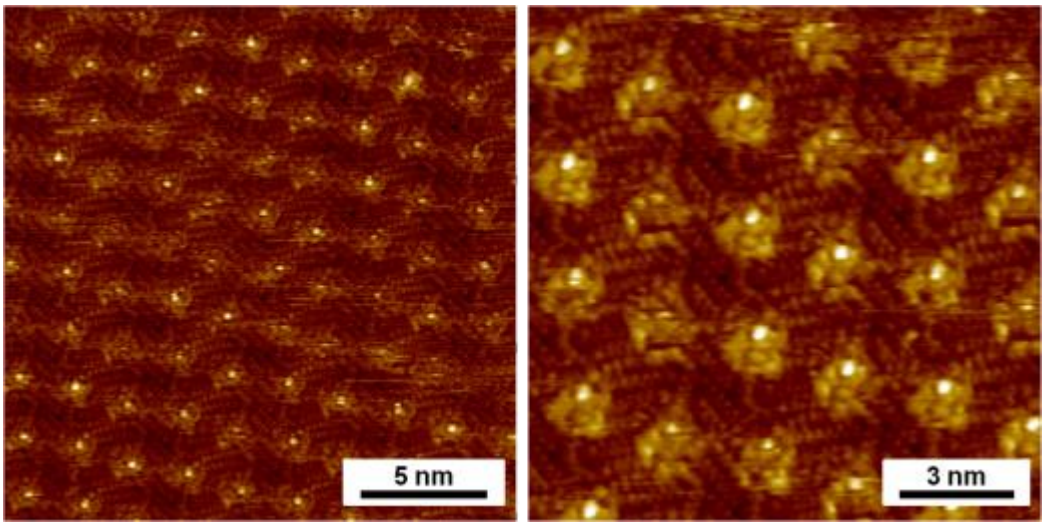

Figure 3-32: STM images of row-like assemblies (α-phase) of **3-19b-Pb** at the liquid-solid interface.

In order to gather more information on this phenomenon a line profile analysis in combination with STM topography was also carried out on **3-19b-Pb** (Figure 3-33). This analysis gave significantly different results as compared to the other two metal complexes previously investigated. It can be noticed that the cross-section across the centre of the macrocycles shows a large peak unlike in case of **3-19b-Na** and **3-19b-Ag** (Figure 3-35). The positions of the peak in the line profile analysis and the bright spot on the STM image are in accordance. The three-dimensional topographical representation reveals triangular shaped structures for which spike-type protrusion are found to be located in the centre of the cavity. It can thus be supposed that the Pb^{2+} cation has a very decisive influence on the appearance of the cyclo-2,9-tris-1,10-phenanthroline macrocycle in this case.

For the interpretation of the results found for **3-19b-Pb** previous STM investigations on another class of macrocycles are very helpful. For metal phthalocyanine complexes detailed STM investigations have been carried out regarding the influence of the metal guest on the apparent height of the central metal cation.[105-107] It was found that the predominant features of the molecular image could not be fully understood on the basis of the cyclic ligand alone. On the contrary, comparative studies on copper(II) and cobalt(II) phthalocyanines revealed a strong dependency on the metal ion valence configuration.[107] For complexes with metal ions possessing a high d-orbital contribution in molecular orbitals situated near the *Fermi* level the metal site provides the dominant tunneling pathway of the molecule.

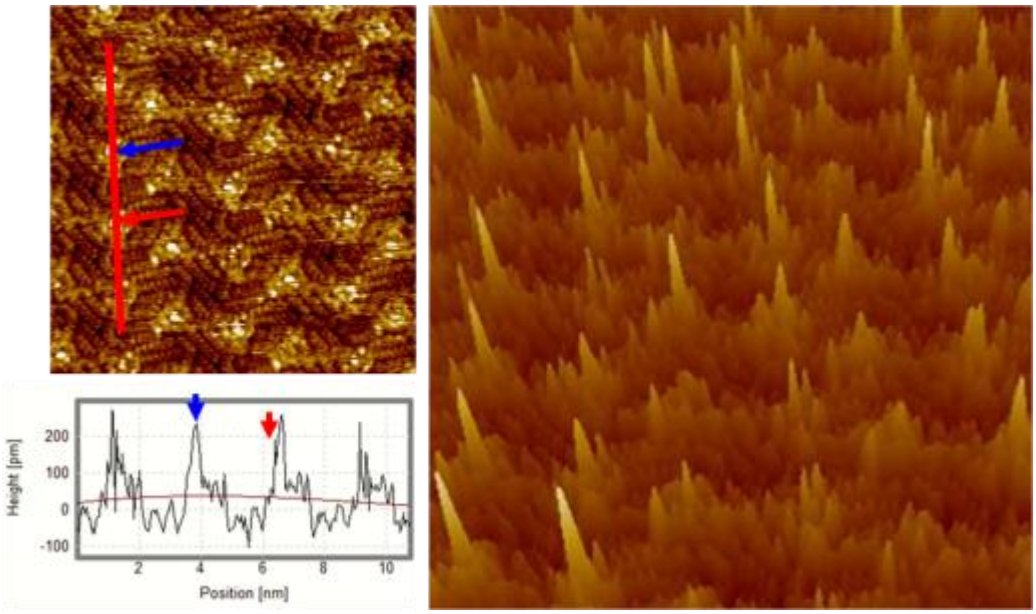

Figure 3-33: Monolayer of **3-19b-Pb** (α-phase) and corresponding line profile analysis (left), STM topograph obtained from the analysis (right).

The result is an increased STM contrast and the appearance of protrusions as observed for **3-19b-Pb**. Yet another aspect has been highlighted in studies concerning lead(II) phthalocyanines.[106] As the diameter of the metal guest exceeds the dimensions of the phthalocyanine cavity, the macrocycle adopts a non-planar, bent conformation. Also this effect might contribute to the unusual features seen in the case of **3-19b-Pb**. The assumption is further supported by single crystal X-ray analysis of a related bisbenzodipyridohexaaza[18]annulene that indicated the adoption of a distorted hexagonal pyramidal conformation with the lead(II) species located on top of the macrocycle.[26]

In summary, the STM analysis of the metal complexes of the cyclo-2,9-tris-1,10-phenanthroline macrocycle provided versatile insights into the molecular self-organization of these cyclic ligands. There are many potential future applications conceivable for the two-dimensional porous surface networks seen for **3-19b-Ag** and **3-19b-Pb**. It was found that the porous networks exhibit in principle size and shape recognition ability as they can immobilize the macrocycle itself in their pores. If the metal guest of the cavities can be addressed selectively by the STM tip, the monolayers could be further used for molecular data storage. In this respect, the monolayer serves as a template assuring for regular and precise location of the metal centers which could for example be switched by a tip-induced reduction process.

3.3 Cyclo-7,10-tris-triphenylenes

In the previous part the self-organization of the cyclo-2,9-tris-1,10-phenanthroline macrocycles **3-19a-c** both in the bulk and on surfaces has been discussed. It has been shown how the sequestration of large metal cations influences the supramolecular properties of the macrocycles. In the bulk state, 2D-WAXS experiments revealed an overall improvement of the molecular packing when large metal cations were incorporated into the mesophase. However, the weaker tendency to self-assemble in the absence of large stabilizing guests such as Ag^{+} and Pb^{2+} and their counterions suggests that the interaction between the macrocycles itself is rather weak. This might be an effect of the relatively small *π*-surface of the three 1,10-phenanthroline units that make up the ring. Investigations previously carried out on the structurally related cyclo-3,6-trisphenanthrene macrocycle **3-2** substantiate this assumption as the self-organization of this compound was also found to be moderate.[8] This can be rationalized in terms of the virtually identical molecular dimensions of 1,10-phenanthroline and phenanthrene.

It can thus be expected that increasing the size of the *π*-system will induce stronger interactions between neighboring macrocycles. Based on the previously described *Yamamoto* cyclotrimerization approach, the introduction of the triphenylene motif offers a convenient way to study the influence of an extended aromatic core on the aforementioned parameters. At the same time the overall C_3 geometry of the molecules can be conserved facilitating comparative studies. In contrast to 1,10-phenanthroline and phenanthrene, triphenylene is a fully benzenoid PAH. The highly symmetric molecule contains four fused benzene units and shows particular chemical stability due to the presence of 6n *π* electrons. Initially isolated from the pyrolytic products of benzene,[108] it was later synthesized for the first time by the aldol trimerization of cyclohexanone.[109] Nowadays, its chemistry is well developed and various strategies for the build-up of substituted triphenylenes are available.[110,111]

Monomeric derivatives received considerable interest, when their liquid-crystalline nature was first reported[112] spurring research on applications of 2,3,6,7,10,11-hexa-substituted triphenylene mesogens in particular.[113-117] Liquid-crystallinity is promoted by the strong *π*-packing of the planarized triphenylene core and *van der Waals* interactions of lateral side chains. But also polymers[114,118,119] and some dendrimers[120-122] based on triphenylene are known to exhibit strong self-assembly behavior. Surprisingly, only few macrocycles containing triphenylene have been

reported[78,123-126] and were investigated with respect to aggregation in solution and in the bulk state.

In addition to the self-assembly of a C_3 symmetric cyclo-7,10-tris-triphenylene macrocycle, the optical properties of such a conjugated ring system also need to be addressed. Triphenylene as a blue-emitter has recently been investigated in the field of organic electronics.[118-120,127,128] The molecule is also known to emit phosphorescence.[117,129] The direct covalent linkage of three triphenylene fluorophores in a conjugated macrocycle raises the question to which degree the three units commute with each other and which impact the intrinsic self-assembly has on the optical properties.

3.3.1 Synthetic Procedures

The functionalized triphenylene **3-25** was built from commercially available 4,5-dibromobenzene-1,2-diol **3-21** by adopting a literature-known synthetic procedure for the analogous alkyl-derivatives (Figure 3-34).[130] The alkoxy triphenylene **3-25** is however not reported so far. Etherification of the two hydroxyl functions was achieved by treatment of **3-21** with 1-bromododecane in DMF in the presence of sodium hydroxide.[131] The yield for the synthesis of the 1,2-dibromo-4,5-bis(dodecyloxy)benzene **3-22b** was 83 %.

A double *Suzuki-Miyaura* coupling of **3-22b** with commercially available phenyl boronic acid yielded the functionalized *ortho*-terphenyl **3-23** in 87 %. The oxidative photocyclization towards triphenylene **3-24** was accomplished by exposure of **3-23** to 300 nm (40 W) UV light under the oxidizing effect of iodine. Propylene oxide was added to the reaction mixture as scavenger of the reaction by-product hydriodic acid.[110,111,132] In this way, ether cleavage by hydriodic acid is suppressed. The reaction slowly proceeded at room temperature, so that an extended reaction time of two days had to be applied. However, the conversion towards **3-24** was easily monitored by the progressive disappearance of the purple colour of the mixture due to the consumption of iodine. 2,3-Bis(dodecyloxy)triphenylene **3-24** was obtained in 73 % yield and purified by repeated recrystallization from toluene. The final bromination in the 3,7-position was then achieved by treatment with bromine in the presence of catalytic amounts of iron and iodine. The triply brominated by-product of this reaction could be fully removed by standard column chromatography and 7,10-dibromo-2,3-bis(dodecyloxy)triphenylene **3-25** was isolated in 66 % yield.

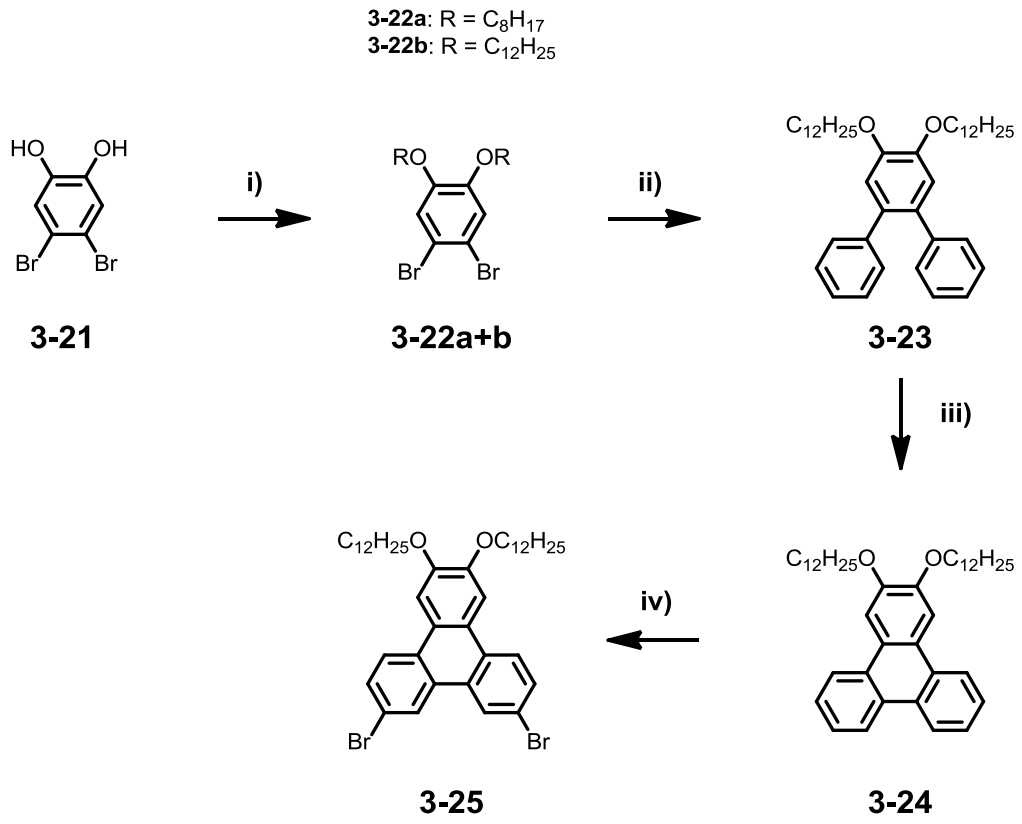

Figure 3-34: Synthetic route to the precursor **3-25**; conditions: i) alkyl bromide, NaOH, 100 °C, 80 - 85 %; ii) phenylboronic acid, $Pd(PPh_3)_4$, K_2CO_3, dioxane, 100 °C, 87 %; iii) hν, I_2, propylene oxide, toluene, 73 %; iv) Br_2, Fe/I_2, - 5 °C, 66%.

The described synthetic sequence allowed for the efficient preparation of the precursor on gram scale which is in contrast to the aforementioned yield-limitating steps encountered during the synthesis of the 1,10-phenanthroline precursors **3-10a**-**c** and **3-11**, respectively.

The cyclotrimerization reaction of triphenylene **3-25** towards the cyclo-7,10-tris-triphenylene macrocycle **3-26** was achieved following identical *Yamomoto* conditions as previously described for the synthesis of macrocycles **3-19a**-**c** and **3-20**.

Again, the reaction was run in an overall 3/1 mixture of toluene/DMF at 60 °C using the same concentration of the precursor compound. After slow addition of **3-25** to the activated catalyst solution, the reaction occurred however significantly faster than in the case of the cyclo-2,9-tris-1,10-phenanthroline macrocycles. This was evidenced by an intense blue luminescence of the reaction mixture that evolved shortly after starting the cyclotrimerization and which was in contrast to the weak purple luminescence of triphenylene **3-25**. Monitoring of the reaction by thin-layer chromatography indicated almost full consumption of **3-25** after only one hour reaction time. The reaction was

however allowed to proceed for 12 hours after what it was stopped by quenching in dilute methanolic hydrochloric acid.

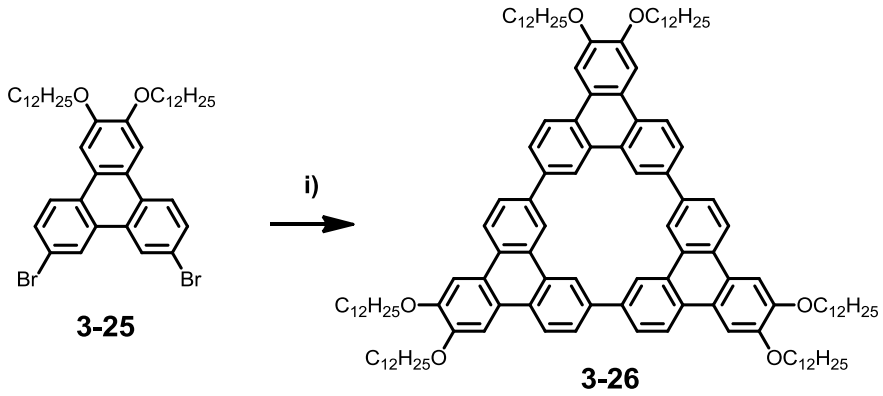

Figure 3-35: Synthetic route to macrocycle **3-26**; conditions: i) bis(cycloocta-(1,5)-diene)nickel(0), cycloocta-(1,5)-diene, 2,2'-bipyridine, toluene/DMF, 60 °C, 21 %.

Following preliminary column chromatography, **3-26** was then subjected to recycling gel permeation chromatography (rGPC) to yield the macrocycle in 27 % yield.

Figure 3-36 contains the recorded MALDI-TOF spectrum of **3-26**, which clearly indicated the successful build-up of the macrocycle. In addition to the target mass at 1783.39 g/mol, a second peak is seen at 3565.71 g/mol corresponding to the dimer of the macrocycle resulting from aggregation.

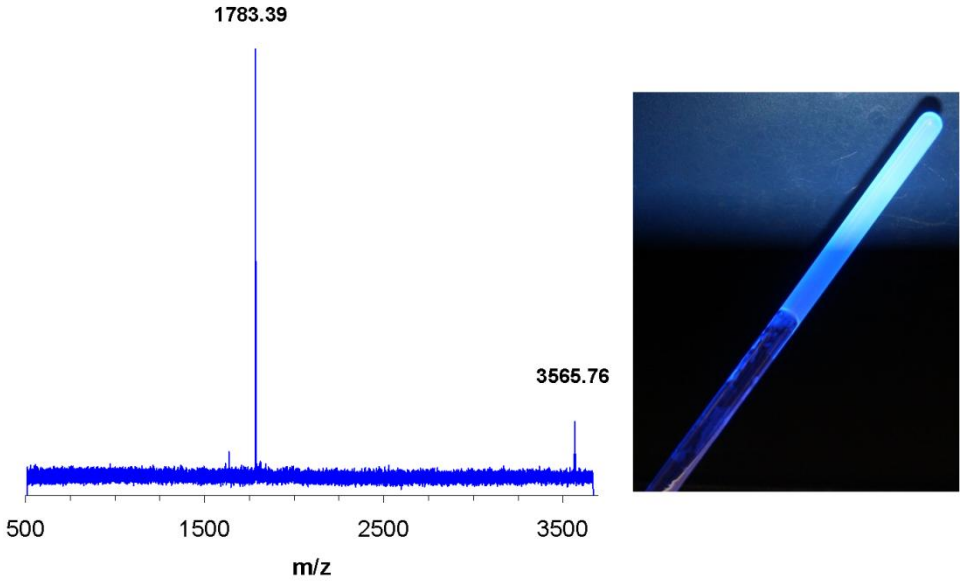

Figure 3-36: MALDI-TOF spectrum of **3-26** (left) and photograph showing luminescence and gel formation of the macrocycle (right).

As in the case of the cyclo-2,9-tris-1,10-phenanthroline macrocycles **3-19a-c** and **3-20**, MALDI-TOF analysis of the crude product also revealed the presence of the dehalogenated monomer and dimer as side-products of the reaction, respectively. These account for the moderate yield of the macrocyclization but were fully removed during the work-up procedure. The reaction mechanism discussed for **3-19a-c** and **3-20** can be also expected for the cyclotrimerization of the functional triphenylene **3-25**. Already during handling and purification of cyclo-7,10-tris-triphenylene **3-26** a strong aggregation tendency became evident. Hence, upon concentrating solutions of **3-26**, turbidity appeared long before visible precipitation could be observed. This might be due to the formation of larger aggregates in solution whose size is subject to scattering effects. Further evidence for a pronounced *inter*molecular interaction of the molecules was given by gel formation that instantly set in for concentrated solutions of **3-26** (Figure 3-36). Regarding the optical properties transparent solutions of **3-26** show a pale bluish luster when exposed to sunlight.

The ^{1}H NMR spectrum of **3-26** recorded in THF-d_8 at 25 °C is in agreement with the highly symmetric structure of the macrocycle (Figure 3-37).

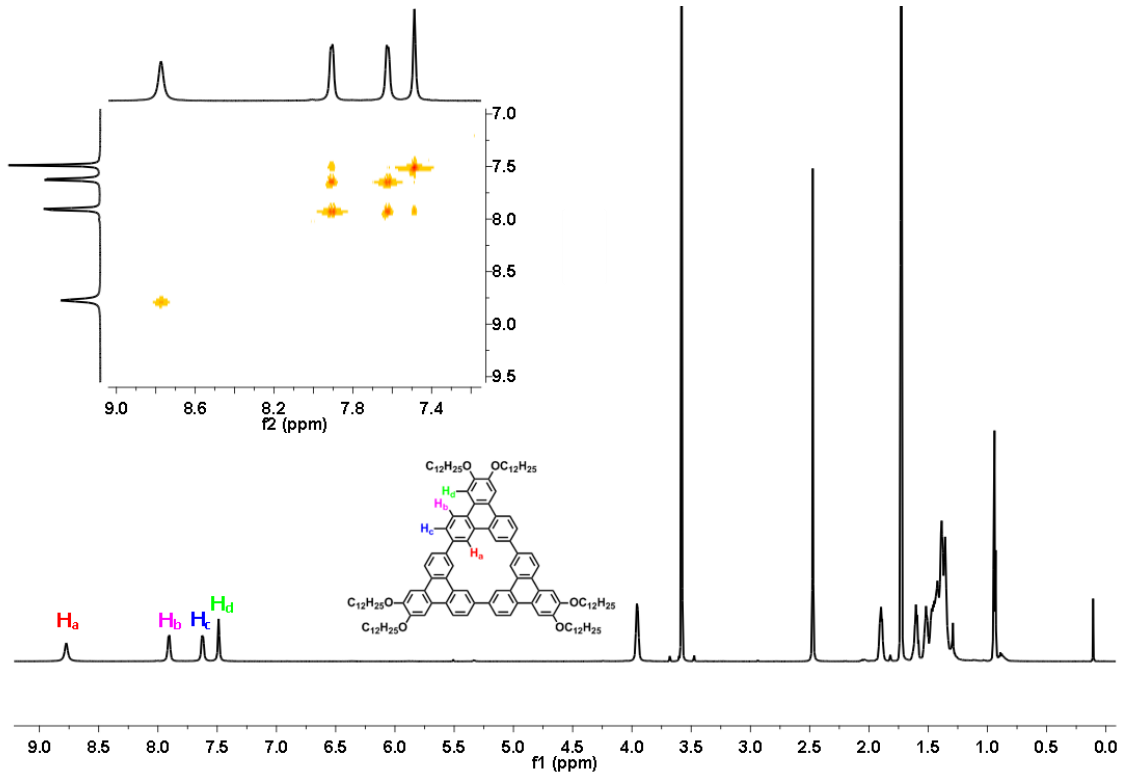

Figure 3-37: ^{1}H NMR spectrum of macrocycle **3-26** in THF-d_8 at 25 °C; the inset shows the ^{1}H,^{1}H-COSY NMR spectrum of the aromatic region of the compound with the peak assignment in THF-d_8 at 25 °C.

For the peak assignment of the protons on the aromatic core it was necessary to apply ^{1}H,^{1}H-COSY NMR spectroscopy.

Thus, the singlet at δ = 8.77 ppm can be assigned to the isolated protons pointing to the cavity of the macrocycle (H_a). The two doublets at δ = 7.90 ppm (H_b) and δ = 7.63 ppm (H_c) originate from the AB system on the triphenylene backbone. The exact identification of both protons is possible with the help of the additional cross signal of the doublet at δ = 7.90 ppm (H_b) with the singlet at δ = 7.49 ppm (H_d). Due to the rigid conformation of the triphenylene unit H_b and H_d are in close spatial contact making the coupling over five bonds possible (Figure 3-37).

3.3.2 Self-Assembly in Solution

Changing from THF-d_8 to polar non-coordinating solvents such as $CHCl_3$-d_1 or TCE-d_2 resulted in ^{1}H NMR spectra of the macrocycle **3-26** which were dominated by broad signals. They generally lacked the fine structure which was expected from the symmetry of the compound. The lower signal resolution could, however, be improved by heating of the sample. This is shown in Figure 3-38 in which the spectra recorded in TCE-d_2 at temperatures between 25 and 110 °C are depicted.

At the same time, the experiment revealed a progressive downfield shift of almost 0.45 ppm for the aromatic proton signals of the macrocycle indicating the presence of aggregates in solution. The *alpha*-protons of the dodecyloxy chains were however affected much less by temperature.

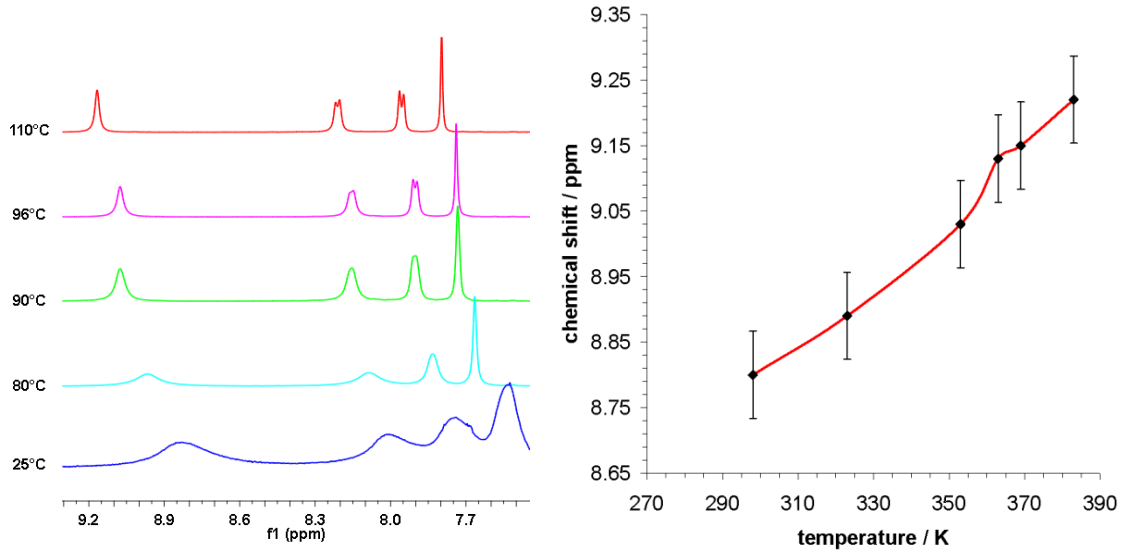

Figure 3-38: ^{1}H NMR spectra of **3-26** in TCE-d_2 at various temperatures (left) and graphical representation of the temperature-dependency (right).

The strong-temperature dependency of the signals in the ^{1}H NMR gave motivation to investigate the solution aggregation properties in more detail. Temperature- and concentration-dependent NMR experiments are known to be an effective method which allows for the elucidation of the association constant of disc-like aromatic systems in solution.[1,47,133] The underlying theory is based on the observation that the chemical shift of a particular proton in a polymolecular stack is different from that of the single molecule. In discotic PAHs the aromatic protons experience the ring current of the next disc in a stack leading to strong resonance shifts. Increasing the temperature as well as lowering the concentration will decrease the size of the aggregates and result in de-shielding of the NMR signal.

A dilution series from $8 \cdot 10^{-3}$ M to $7 \cdot 10^{-5}$ M was thus performed in TCE-d_2 at 80 °C and the chemical shift plotted as a function of concentration resulting in a typical sigmoidal curve (Figure 3-39).

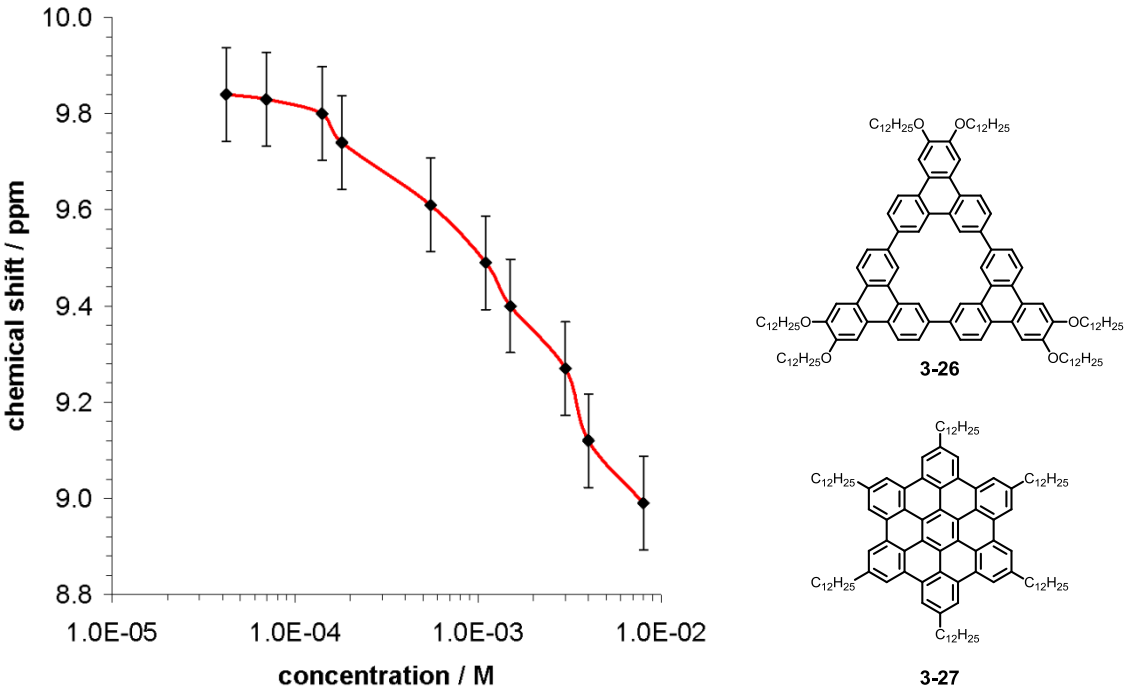

Figure 3-39: Graphical representation of the concentration-dependency of macrocycle **3-26** (left) and chemical structures of **3-26** and hexadodecyl-substituted HBC **3-27** (right).

For the analysis, an attenuated K model was used,[1,133] which is based on the assumption that the association constant for i-mer formation can be expressed as:

$$K_i = 1/i \cdot K_A$$

Herein, K_A is the association constant for the system. For the calculation of K_A two equations need to be solved iteratively:

$$L = x\,[1 + \tau(e^{x}-1)]$$

$$\alpha = 1 / [1 + \tau(e^{x}-1)]$$

Furthermore, the two variables x and L can be written as:

$$x = K_A\,[A] \text{ and } L = K_A C_T$$

wherein [A] defines the concentration of the monomeric species and C_T the total concentration of the molecule. The factor τ represents the preference for dimer formation over higher oligomers. The computational analysis of the NMR data was performed in cooperation with *Lei Dou* (Technical University Darmstadt, Germany).
For macrocycle **3-26**, an association constant K_A of 444 L/mol was calculated. This value is only slightly lower than the one known for hexadodecyl-substituted HBC derivatives (457 L/mol)[47] indicating strong *π*-stacking for the cyclic triphenylene trimer. Indeed, the number of benzene rings is 12 for macrocycle **3-26** and 13 for HBC derivative **3-27** reflecting the similar size of the total *π*-surface of both discs. Also, due to the symmetrical substitution pattern of the side-chains no dipolar contribution to the packing behavior is to be expected. For phenylene-ethynylene macrocycles of similar size but smaller aromatic core, much lower values of 20 - 50 L/mol have been obtained in chlorinated solvents.[1] The cyclo-2,9-tris-1,10-phenanthroline macrocycles **3-19a-c** discussed in the previous chapter did not exhibit any solution behavior further illustrating the importance of an extended aromatic system for solution aggregation.

3.3.3 Self-Assembly in the Bulk Phase

In the next step, the impact of core planarity and architecture on the thermotropic behavior and the long-range self-assembly in the solid state were investigated. Compared to the cyclo-2,9-tris-1,10-phenanthroline macrocycles **3-19a-c**, the effect of the larger *π*-surface was of particular interest in the case of **3-26**.
Also, monomeric alkyl-substituted triphenylenes have been widely studied in the field of discotic liquid crystals owing to the formation of mesophases that are generally characterized by a high degree of organization.[113,115,116,134,135] Their structural perfection

arises from the highly symmetric, disc-like backbone of triphenylenes readily promoting their liquid-crystallinity when decorated with peripheral alkyl chains.

Hence, the bulk phase properties of the macrocyclic homologue **3-26** were determined by 2D-WAXS experiments and correlated to results from the thermal analysis by DSC (Figure 3-40). These measurements were carried out with the help of *A. Mavrinskiy* and *Dr. W. Pisula* (MPI-P Mainz, Germany).

The DSC trace recorded in a temperature regime between - 100 °C and 200 °C shows two pronounced phase transitions (Figure 3-40) which are fully reversible. Upon second heating, two endothermic peaks are detected at 64.3 °C and 109.1 °C. They are found to reappear as exothermic transitions at 55.5 °C and 103.6 °C, respectively. The offset of 7.9 °C and 5.5 °C is a frequently observed phenomenon which is related to the kinetic process of the phase transformation.

Above the phase transition temperature of 109.1 °C macrocycle **3-26** forms a typical liquid crystalline (LC) columnar organization. The equatorial reflections in the corresponding 2D pattern (Figure 3-41) indicate that the molecules pack in columnar structures, which are assembled within a hexagonal unit cell defined by a parameter of a_{hex} = 3.55 nm.

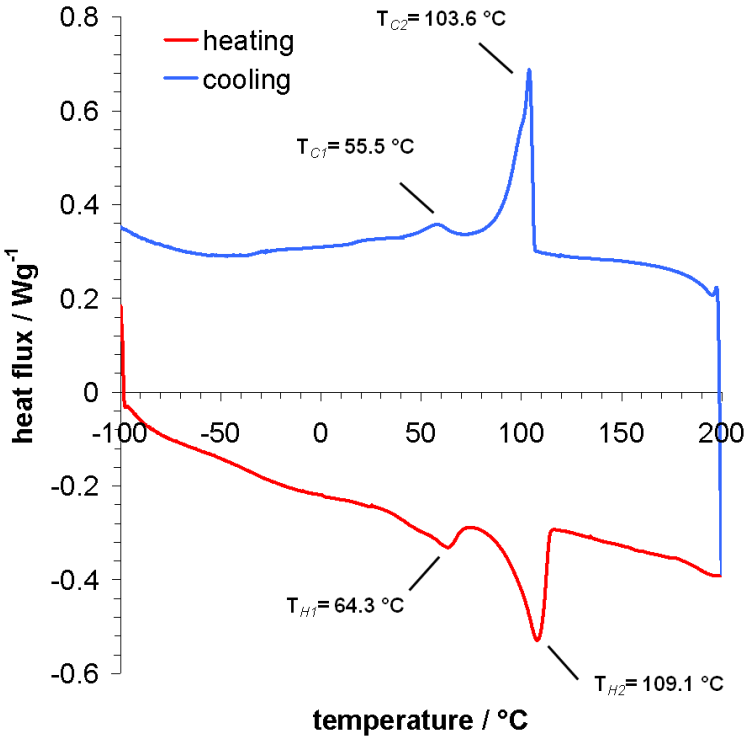

Figure 3-40: DSC trace of macrocycle **3-26** upon second heating (red) and cooling (blue).

In the columns, the macrocycles stack on top of each other with a π-stacking distance of p = 0.35. The molecular plane is arranged orthogonal to the columnar axis.

Characteristic for the LC phase, an amorphous halo appears which can be attributed to the disordered dodecyloxy chains (Figure 3-41).
Cooling down the sample to 30 °C, this halo remains unaffected, while the columnar arrangement changes to a rectangular unit cell with a_{rt} = 2.96 nm and b_{rt} = 2.03 nm.

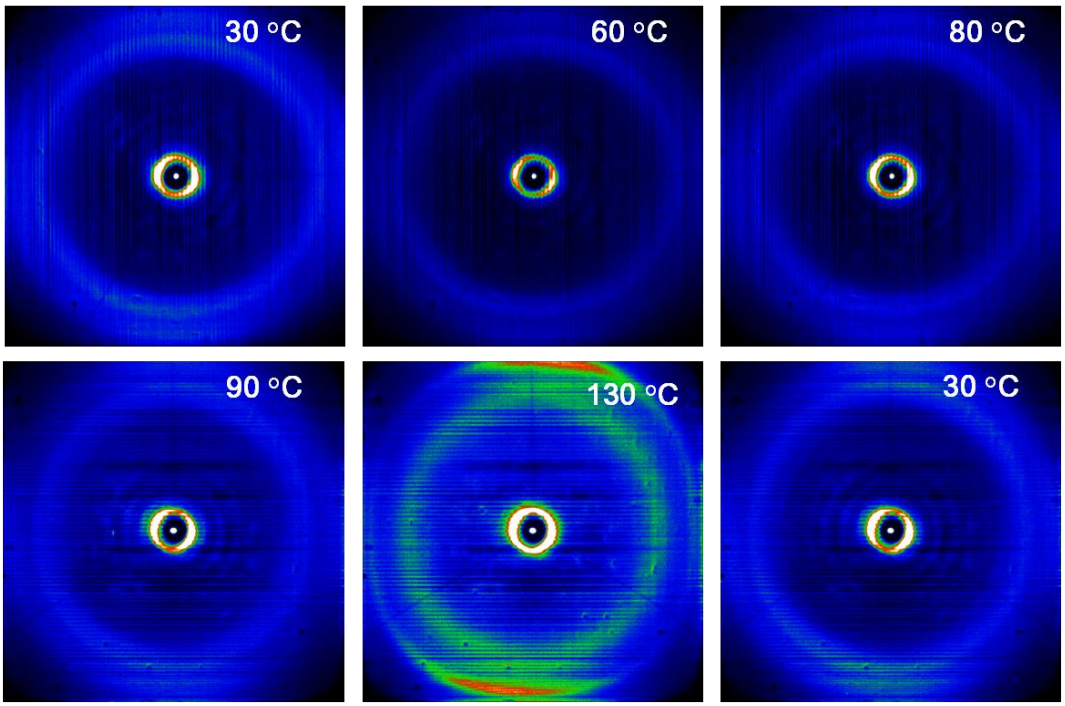

Figure 3-41: Temperature-dependent 2D-WAXS patterns of **3-26**.

Interestingly, at this temperature the meridional reflections fade away due to increased *intra*columnar disorder. One reason might be the steric hindrance of the side chains because of a cofacial molecular packing.

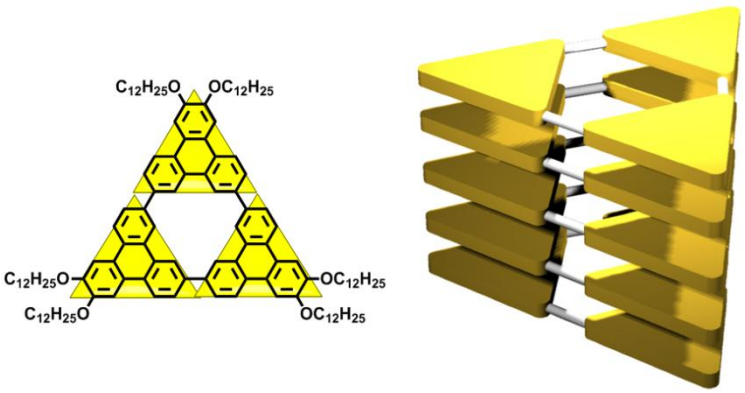

Figure 3-42: Schematic illustration of the proposed molecular packing in columnar structures by **3-26** at 130 °C. Due to simplicity, side chains are omitted.

When these results are compared to the previously reported data of 2,3,6,7,10,11-hexakis(dodecyloxy)triphenylene[135] the high *inter*molecular packing forces governing the bulk properties of **3-26** become apparent. For the monomeric triphenylene containing an identical number of dodecyloxy chains the transition to the hexagonal columnar mesophase occurred at a much lower temperature of 55 °C and the clearing point was reached at 63 °C.[135] Heating of the macrocycle to temperatures of 400 - 450 °C did not lead to the isotropization of the sample and was ultimately limited by the thermal decomposition of **3-26**. A similar liquid-crystalline phase width has only been reported for the closely related cyclo-3,6-trisphenanthrene macrocycle **3-2**[8] and can be ascribed to the fully planarized aromatic core of **3-26**. With respect to **3-2** and **3-19a-c** the overall tendency to self-organize is remarkably higher for this macrocycle due to the extended geometry of the triphenylene units.

3.3.4 Self-Assembly on Surfaces

STM investigations regarding the two-dimensional self-assembly of cyclo-7,10-tris-triphenylene **3-26** were carried out at the 1-phenyloctane/HOPG interface in the group of *de Feyter* (KU Leuven, Belgium).

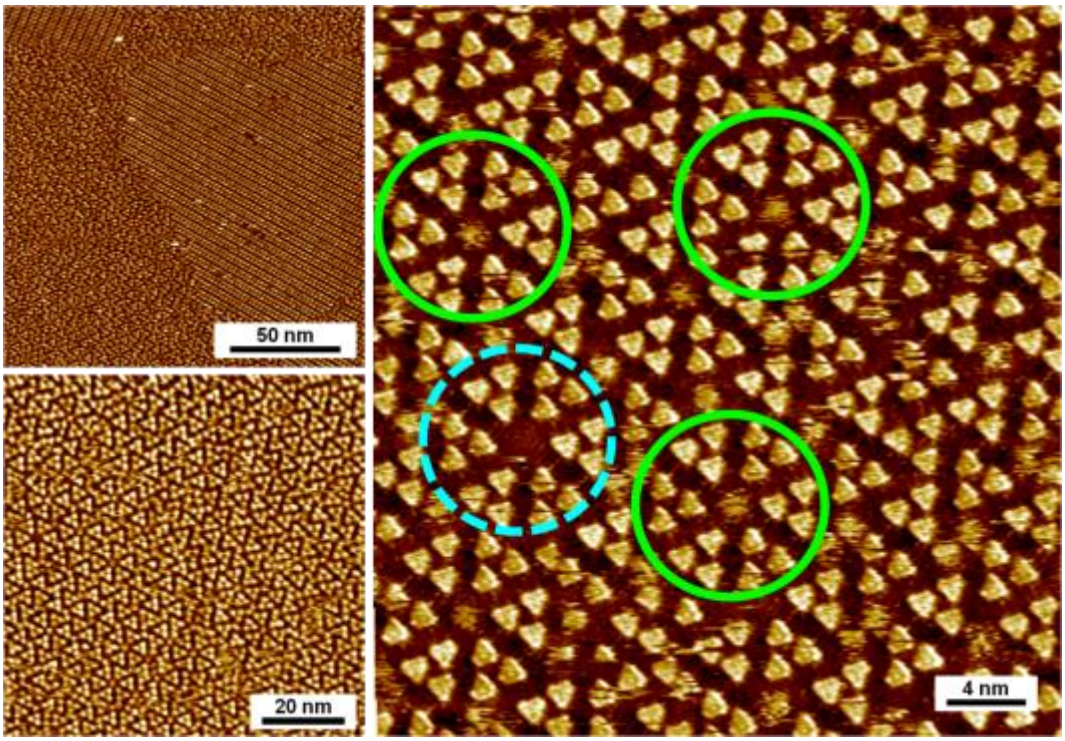

Figure 3-43: STM images of coexisting T-phase and L-phase of **3-26** at the liquid-solid interface (top left), STM image (bottom left) and analysis of the honeycomb network formed by the T-phase (right).

Figure 3-43 contains a large-scale STM image of **3-26** physisorbed on the surface of HOPG. As it can be seen, the C_3 symmetric macrocycles form two different types of patterns on the surface namely a random triangular phase (T-phase) and a highly ordered lamellar phase (L-phase). Both phases extend over several hundred nanometers.

In the T-phase, the molecules typically appear as triplets forming triangle shaped features (composed of three macrocycles) which appear to be scattered randomly over the surface.

The peripheral alkoxy chains of the triplets are tightly interdigitated and orientated parallel to each other. However, within the triplets, all alkoxy chains cannot adsorb to the surface for steric reasons. It can be deduced that these alkoxy chains must thus be pointing to the solution phase. Interestingly, in some regions of the T-phase, six of the triplets (thus comprising 18 macrocycles in total) come together to form a hexagonal void. The approximate pore size determined from corner to corner equals 3.91 ± 0.10 nm. The inner part of the hexagonal pores appears fuzzy and might be filled with entrapped solvent molecules. This situation is indicated by the green circles in Figure 3-43, whereas the blue circle depicts an empty pore. The molecular arrangement of the T-phase allows at least for a partial translation of the tris-fold symmetry of the cyclo-7,10-tris-triphenylene macrocycle into a hexagonal pattern. The self-assembly of **3-26** in the T-phase is furthermore another example for a two-dimensional porous network structure[87,89-102] which has been discussed for the β- and γ-phase of the cyclo-2,9-tris-1,10-phenanthroline macrocycle **3-19b-Ag** in detail previously. The high potential of these two-dimensional crystals has been highlighted by studies that addressed host-guest interactions[94,99,101,102] or the patterning of surfaces on the molecular level.[93,101]

Figure 3-44 gives the STM images of the L-phase of macrocycle **3-26**. In this polymorph of the cyclo-7,10-tris-triphenylene macrocycle, the molecules are arranged in a row-like fashion. The rows are formed by “dimeric” species in which two macrocycles are orientated anti-parallel to each other. The dodecyloxy chains within this monolayer can be divided into two oriented groups which has consequences regarding the original molecular symmetry.

Those alkoxy chains located in the regions of darker contrast in between of the rows appear strongly orientated and a tight interdigitation of chains from neighboring molecules can be interfered from the images. In this case, the side chains adopt a conformation which is comparable to their orthogonal anchoring on the triangular backbone of the molecule. Within the rows the chains need to adopt a different conformation due to the steric crowding caused by the orientation of the triangular backbones.

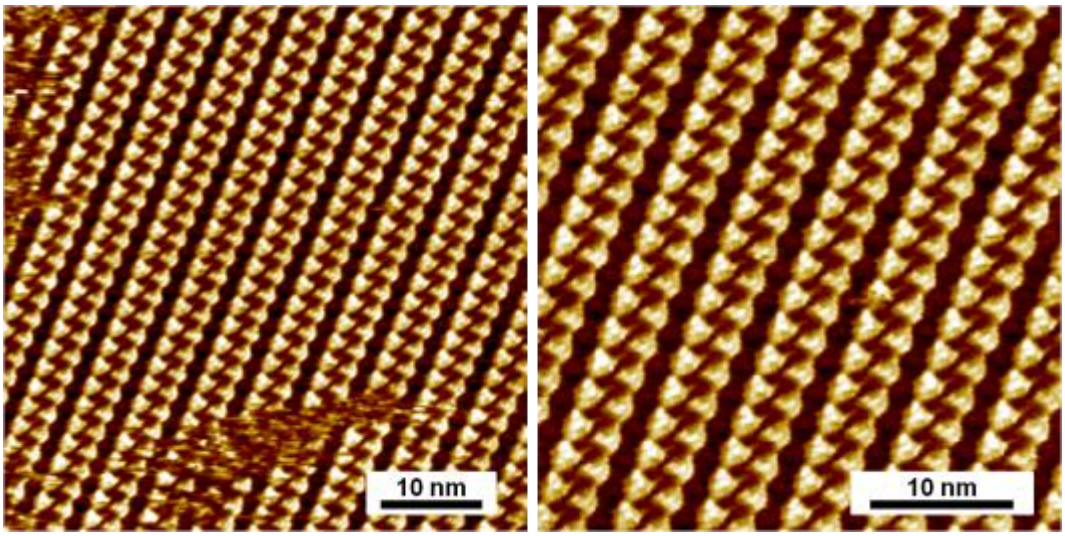

Figure 3-44: STM images of the L-phase of **3-26** at the liquid-solid interface.

By comparison of the results obtained for macrocycle **3-26** to previous STM studies on monomeric hexadodecyloxy- (**3-28**) and hexatetradecyloxy-substituted triphenylenes (**3-29**) interesting similarities can be drawn (Figure 3-45).[136-138]

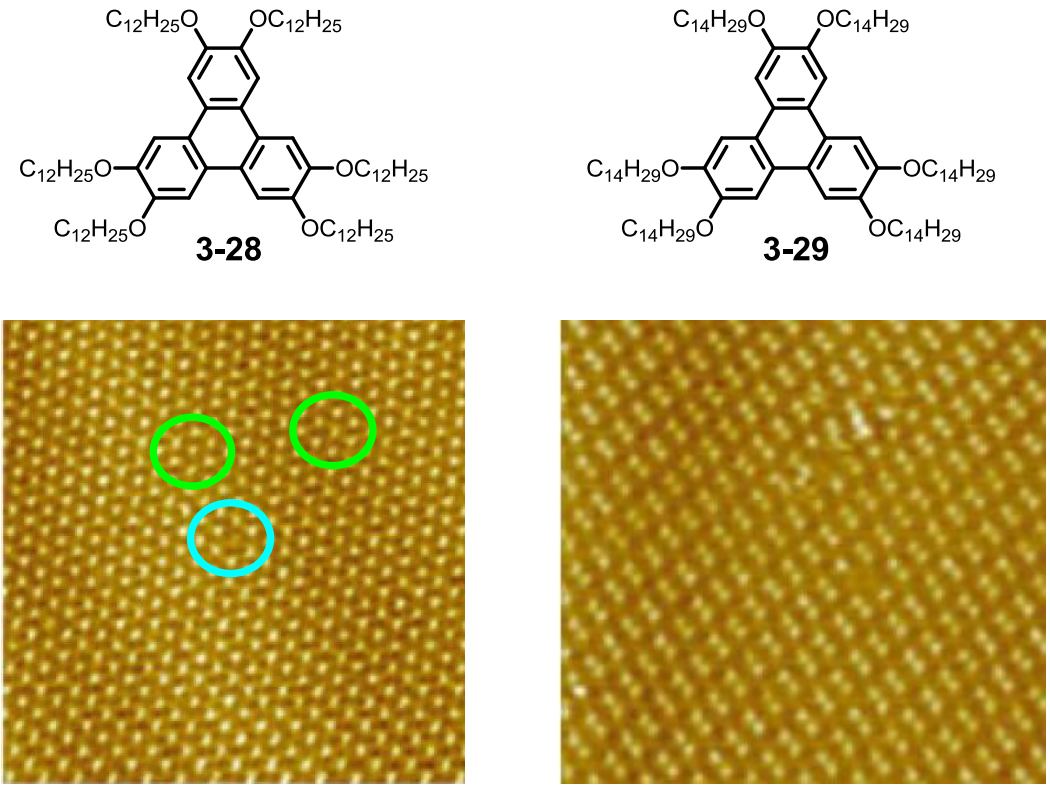

Figure 3-45: STM images from previous studies on the monolayers formed by the hexa-substituted triphenylenes **3-28** (left) and **3-29** (right).[137]

For 2,3,6,7,10,11-hexakis(dodecyloxy)triphenylene **3-28** a monolayer was found that closely resembles the T-phase of the macrocycle in the present case. In the unit cell of **3-28**, seven triphenylenes form an approximate hexagon with the seventh molecule located in the center (green circles in Figure 3-45). Some cavities remain however unfilled (blue circle in Figure 3-45). In the T-phase of **3-26** the triplets of the macrocycle (composed of three molecules) behave indeed like the single triphenylenes and do also self-assemble in hexagonal patterns (Figure 3-43). The similarity can be explained by the common triangular shape of both the triplets and the triphenylenes which additionally exhibit a similar substitution pattern of the alkoxy chains.

Another remarkable observation is made when comparing the organization of the L-phase of macrocycle **3-26** to the two-dimensional lattice formed by 2,3,6,7,10,11-hexakis(tetradecyloxy)triphenylene **3-29**. With two additional methylene units on the alkoxy chains, the whole arrangement of the triphenylene changes drastically. A characteristic dimer structure is persistent over a large area as it can be seen in Figure 3-45. From a structural viewpoint these row-like assemblies are identical to the L-phase of **3-26** (Figure 3-44) besides the fact that they are formed by monomeric triphenylenes. Still, they adopt the same anti-parallel orientation in the rows as discussed above for the cyclic trimer. Again, the identical symmetry of **3-26** and **3-29** can be used to explain the striking similarities.

3.3.5 Optical Spectroscopy

Prior to the analysis of the optoelectronic properties of the cyclo-7,10-tris-triphenylene macrocycle **3-26** a computational analysis was performed (B3LYP, 6-311G**). Concerning the geometry of macrocycle **3-26** the decrease in conformational freedom results in the expected planarization of the three triphenylene units (Figure 3-46). As a consequence of their coplanar arrangement the molecular orbitals symmetrically extend over the ring system of **3-26**.

It is known that triphenylene **1-1** belongs to the family of alternant hydrocarbons for which $S_0 \leftrightarrow S_1$ transitions are partially forbidden. Consequently, highly structured spectra result both in absorption and emission revealing information on the electronic structure of the molecules. This is exemplified by the electronic spectra of non-substituted triphenylene (Figure 3-47 and Figure 3-48).

According to *Clar,* the bands of absorption spectra of polycyclic aromatic hydrocarbons (PAHs) can be classified as *α*-, *β*-, and *p*-bands, respectively.[45,46] They originate from S_0 ground state excitation into higher orbitals with their transition probabilities governed by the *Franck-Condon* factors.

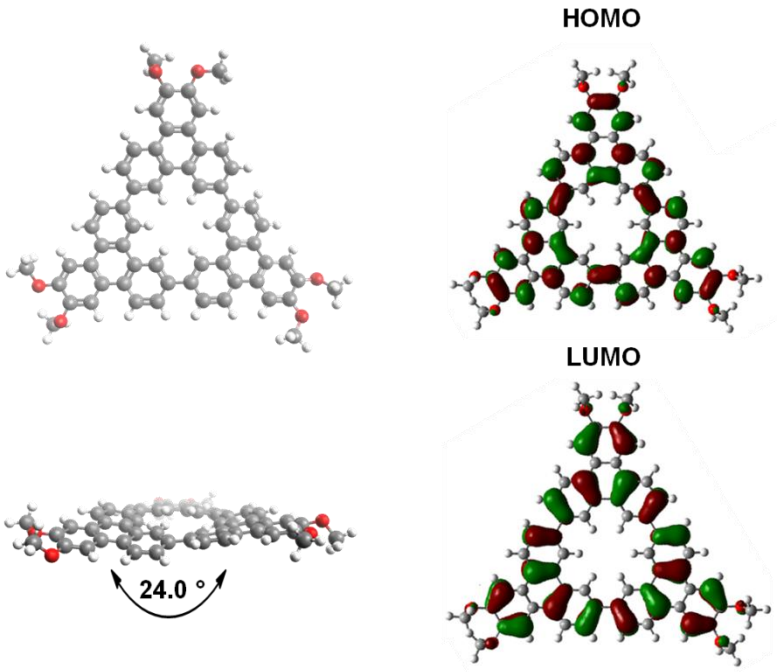

Figure 3-46: Conformation of macrocycle **3-26** as derived from computational analysis (left), wave functions of the HOMO und LUMO of the macrocycle (B3LYP, 6-311G**).

As it can be seen in Figure 3-47, these bands manifest in the spectrum of parent triphenylene at $\lambda_{\beta 1}$ = 257 nm, λ_{p1} = 284 nm and $\lambda_{\alpha 1}$ = 341 nm, respectively, and are also mirrored in the corresponding emission spectrum depicted in Figure 3-48.[45,117,139,140] Comparison to the spectrum of the model compound 2,3-bis(dodecyloxy)triphenylene **3-24** indicates a bathochromic shift of 20 nm for the absorption maximum at $\lambda_{\beta 2}$ = 277 nm. This migration of the band can be attributed to the electron-donating alkoxy chains in the 2,3-position. They are known to delocalize the π-system of an aromatic ring by means of the *z*-components of their *p*-orbitals. In general, the vibronic fine structure is less resolved due to the reduced symmetry of **3-24** compared to parent triphenylene. Nevertheless, the non-resolved shoulder at λ_{p1} = 298 nm can be attributed to the *p*-band whereas results for related alkoxy-decorated triphenylenes justify the interpretation of the minor peak at $\lambda_{\alpha 2}$ = 356 nm as α-band. The decreased symmetry of **3-24** is in accordance with an increase of the α-band intensity as this transition results from symmetry-forbidden transitions (Figure 3-47).[46]

The impact of the conjugated cyclic arrangement of three alkoxy-substituted triphenylene units is seen in the absorption spectrum of macrocycle **3-26**. From the graphical representation of the wave functions (Figure 3-46) an increased conjugation is to be expected as the HOMO and LUMO levels continuously comprise the cyclic backbone. The absorption of macrocycle **3-26** covers the wavelength regime from

250 nm to 450 nm reflecting the pronounced electronic communication between the three triphenylene units.

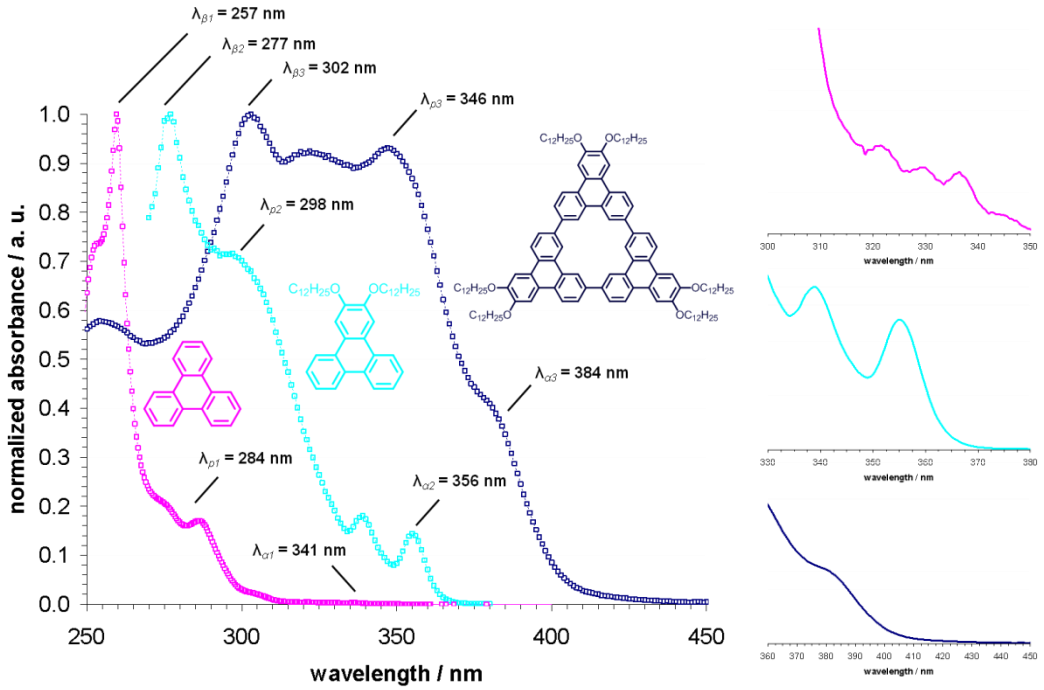

Figure 3-47: UV-vis absorption spectra of triphenylene **1-1**, model compound **3-24** and macrocycle **3-26** in chloroform at 10^{-5} M (left) and magnification of the α-bands of the three compounds (right). For better comparison, all spectra are normalized to the absorption maximum.

Hence, the red-shift of 25 nm for the β-band at $\lambda_{\beta 3}$ = 302 nm can be attributed to the extended conjugation that is in contrast to the monomeric model compound **3-24** and parent triphenylene **1-1**. With respect to the spectrum of **3-24**, the signal located at λ_{p3} = 346 nm can be identified as *p*-band, while the α-band is no longer resolved but can be possibly ascribed to the intense shoulder at $\lambda_{\alpha 3}$ = 384 nm (Figure 3-47).

In general, the vibronic fine structure of the spectrum of **3-26** is significantly blurred compared to the monomeric triphenylenes discussed above. However, the absorption of the cyclo-7,10-tris-triphenylene macrocycle **3-26** preserves the characteristic features discussed for the monomeric species.

Remarkably, the α- and *p*-band intensity of **3-24** and **3-26** is strongly increased as compared to the spectrum of parent triphenylene. As both compounds contain a substituted triphenylene system, their symmetry is lowered. Thus, both processes become more favorable resulting in higher band intensities.[45]

The luminescence was subsequently studied in order to further investigate the correlation between macrocycle **3-26** and its building unit triphenylene (Figure 3-48).

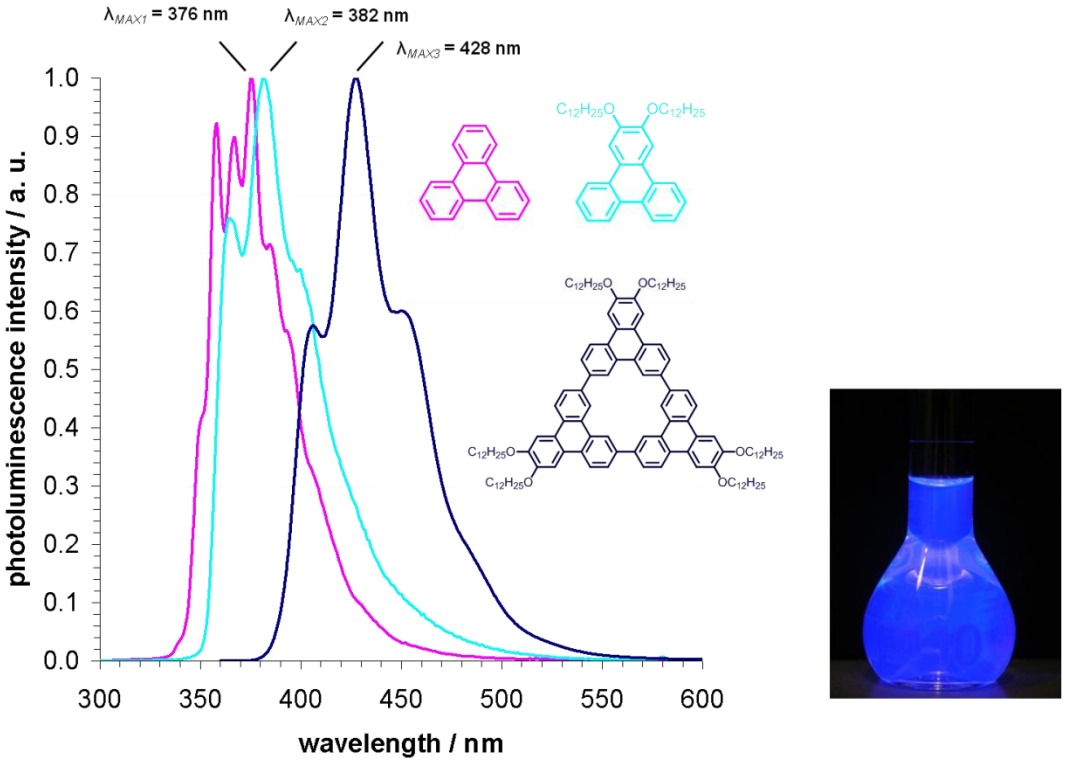

Figure 3-48: Normalized fluorescence emission spectra of triphenylene **1-1**, model compound **3-24** and macrocycle **3-26** in chloroform at 10^{-5} M (right).

The emission of triphenylene is composed of several distinct bands with the maximum located at λ_{MAX1} = 376 nm. The fine structure is significantly smeared out when looking at the fluorescence of model compound **3-26** for which the maximum is found at λ_{MAX2} = 382 nm. Again, this effect can be attributed to the substitution with the dodecyloxy chains accounting for the bathochromic shift.

The fluorescence spectrum of the cyclo-7,10-tris-triphenylene macrocycle **3-26** shows a strongly symmetric emission with the maximum located at λ_{MAX3} = 428 nm and two minor peaks at λ_i = 407 nm and λ_{ii} = 452 nm. As mentioned previously, the compound exhibits a strong blue luminescence, which is close to the ideal value for pure blue emission between 440 nm and 450 nm.[141,142] The fine structure of the emission spectrum is fully conserved upon lowering the concentration down to 10^{-8} M indicative for the absence of aggregates at high dilution (Figure 3-49).

This is in accordance with the findings from the above discussed concentration-dependent ^{1}H NMR experiments which revealed strong self-assembly in solution only at elevated concentrations (Figure 3-39). Interestingly, indications for the presence of aggregates were found by time-dependent fluorescence measurements carried out in toluene at a concentration of $1 \cdot 10^{-5}$ M (Figure 3-50). This concentration corresponds to the lower limit of the concentration-dependent NMR analysis.

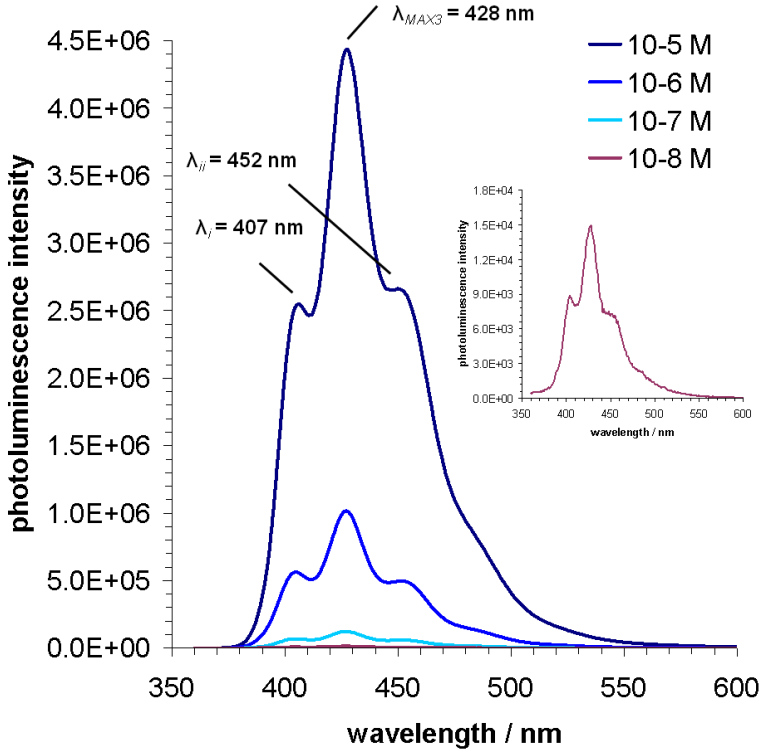

Figure 3-49: Concentration-dependent fluorescence emission spectra of macrocycle **3-26**, the inset shows the spectrum at the lowest concentration of 10^{-8} M.

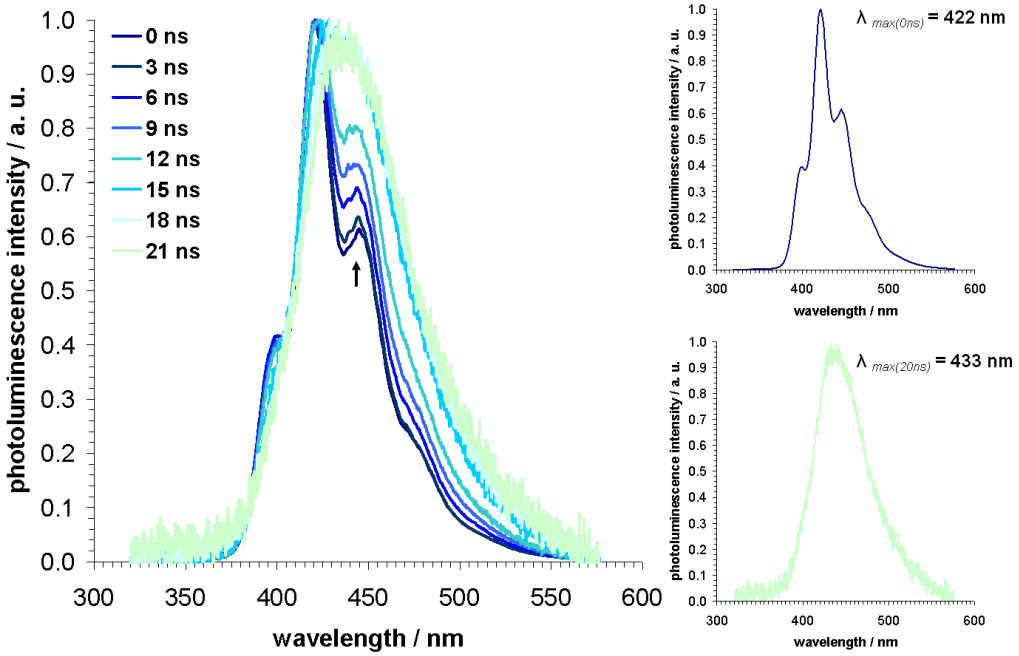

Figure 3-50: Time-dependent fluorescence emission spectra of macrocycle **3-26** in toluene at 10^{-5} M (left), the corresponding spectra after 0 and 20 ns (right).

As it can be seen for the emission spectra recorded up to 12 ns after excitation the original character of the spectrum is mostly preserved. The spectrum exhibits three main peaks and a non-resolved shoulder at high wavelengths. As indicated in Figure 3-50, the intensity of the secondary maximum at λ_{ii} = 444 nm progressively grows with time. The situation greatly changes for the spectra obtained in the time regime between 12 ns and 20 ns. In this case, the pronounced fine structure is lost at the expense of a featureless, continuous emission. Also, the maximum is shifted from its original value at $\lambda_{MAX(0ns)}$ = 422 nm to a new value at $\lambda_{MAX(20ns)}$ = 432 nm. It can be supposed that this component of the fluorescence of macrocycle **3-26** originates from aggregates that are present at this concentration. Both, the featureless character and the bathochromic shift are in line with this assumption.

3.4 Cyclo-*nona*-phenylene

Cyclic oligoarylenes have attracted considerable attention due to their unique cyclic structures which are always of high symmetry.[10] Furthermore, these shape-persistent macrocycles exhibit interesting optoelectronic properties and their cavities could be applied to host-guest chemistry. Enhanced thermal-, light-, and air-stability facilitate the handling of these compounds. Early works relied on the $CuCl_2$-mediated assembly of *Grignard* derivatives to yield cyclic penta-,[143,144] hexa[144,145], octa-,[145] nona-[5] and decaphenylenes[143] in moderate yields. Later on, alternative synthetic protocols allowed for the synthesis of still larger macrocycles such as dodeca-[146,147] and tetraicosaphenylene[146] which were obtained by *Suzuki-Miyaura* cross-coupling of two half-cycles. Also, the electron-transfer oxidation of *Lipshutz* cuprates has been demonstrated to yield *nona*- and *dodeca*-phenylenes.[10]

Surprisingly, the supramolecular properties of such cyclic oligoarylenes are poorly examined and only few reports address mesophase behavior[8] or nanostructure formation from solution.[10] Recently, the surface-supported growth of porous graphene from hexa-iodinated cyclohexa-*meta*-phenylene under STM control[90,92] opened a new field of application for these cyclic systems. Further properties of this interesting class of compounds are however yet to be elucidated. Therefore, new straightforward synthetic approaches are needed which circumvent the tedious and low-yield preparations reported in the past. It has been shown in the previous parts that the *Yamamoto* cyclotrimerization constitutes a versatile tool for the build-up of novel C_3 symmetric macrocycles in satisfying yields. It is however unclear, to what degree conformational freedom of the precursors is tolerated. Therefore, the synthesis of cyclo-*nona*-phenylene from a kinked *ortho*-terphenyl was envisaged.

3.4.1 Synthetic Procedures

The synthesis of the precursor was based on a straightforward approach starting from 1,2-dibromo-4,5-bis(octyloxy)benzene **3-22a** (Figure 3-51). Two-fold *Suzuki-Miyaura* coupling with 4-(trimethylsilyl)phenylboronic acid lead to the *ortho*-terphenyl **3-30** in 97 %. In the next step, treatment with *N*-bromosuccinimide in the presence of potassium bromide was used for the exchange of the TMS-group to bromine. 4,4''-dibromo-4',5'-bis(octyloxy)-1,1':2',1''-terphenyl **3-31** was obtained in 75 %.

For the synthesis of macrocycle **3-32**, the *ortho*-terphenyl was then subjected to the same experimental protocol which was successfully used for the previous cyclotrimerization reactions.

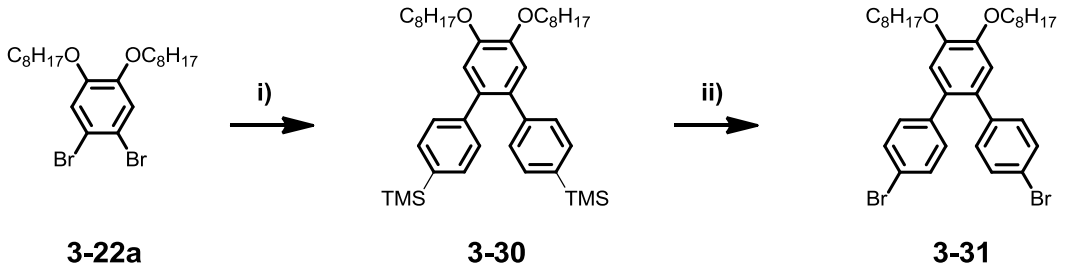

Figure 3-51: Synthetic route to the precursor **3-31**; conditions: i) 4-(trimethylsilyl)phenylboronic acid, $Pd(PPh_3)_4$, K_2CO_3, dioxane, 100 °C, 97 %; ii) NBS, NaBr, MeOH/THF, 45 °C, 75 %.

Thus, the reaction was run in an overall 3/1 mixture of toluene/DMF at 60 °C after slow addition of **3-31** to the activated catalyst solution. After stopping the reaction a strong blue luminescence was detected upon irradiation with an UV hand lamp. This was a first indication that the macrocycle formation was successful since the precursor **3-31** did not show any fluorescence behavior. After quenching in dilute methanolic hydrochloric acid and pre-purification on a regular silica column the macrocycle was passed to rGPC to yield **3-32** in 22 % as a white solid.

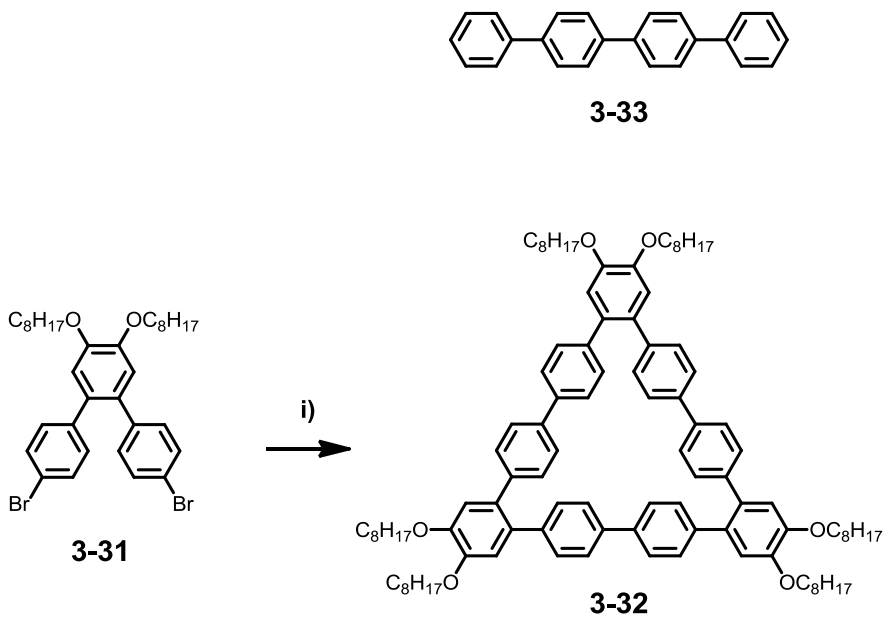

Figure 3-52: Synthetic route to macrocycle **3-32** and structure of model compound **3-33**; conditions: i) bis(cycloocta-(1,5)-diene)nickel(0), cycloocta-(1,5)-diene, 2,2'-bipyridine, toluene/DMF, 60 °C, 22 %.

Dehalogenation during the cyclotrimerization reaction lead to the formation of non-functionalized monomer and dimer species which were detected in the reaction mixture by FD and MALDI-TOF mass spectroscopy. For this reason the yield was found to

range on the same level as for the cyclo-2,9-tris-1,10-phenanthroline macrocycles **3-19a-c** and **3-20** as well as the cyclo-7,10-tris-triphenylene macrocycle **3-26**.

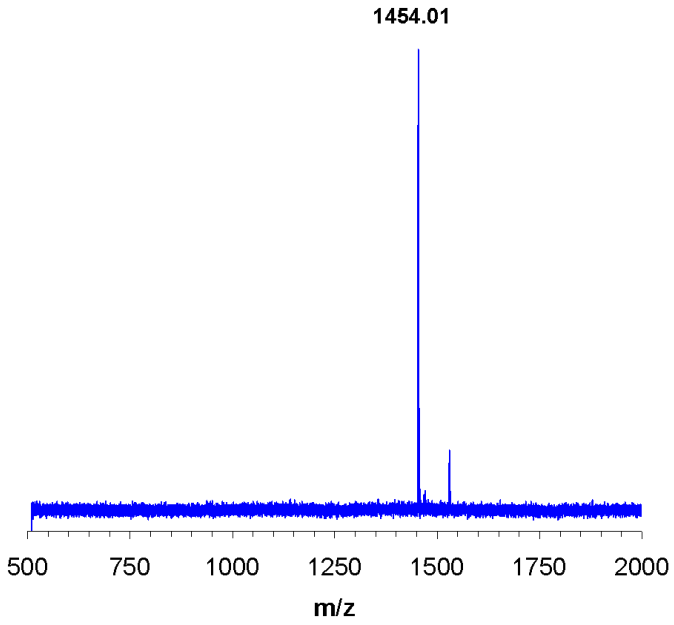

Figure 3-53: MALDI-TOF spectrum of macrocycle **3-32**.

Figure 3-53 depicts the MALDI-TOF spectrum of the cyclo-*nona*-phenylene **3-32** illustrating the successful formation and isolation of the desired compounds.

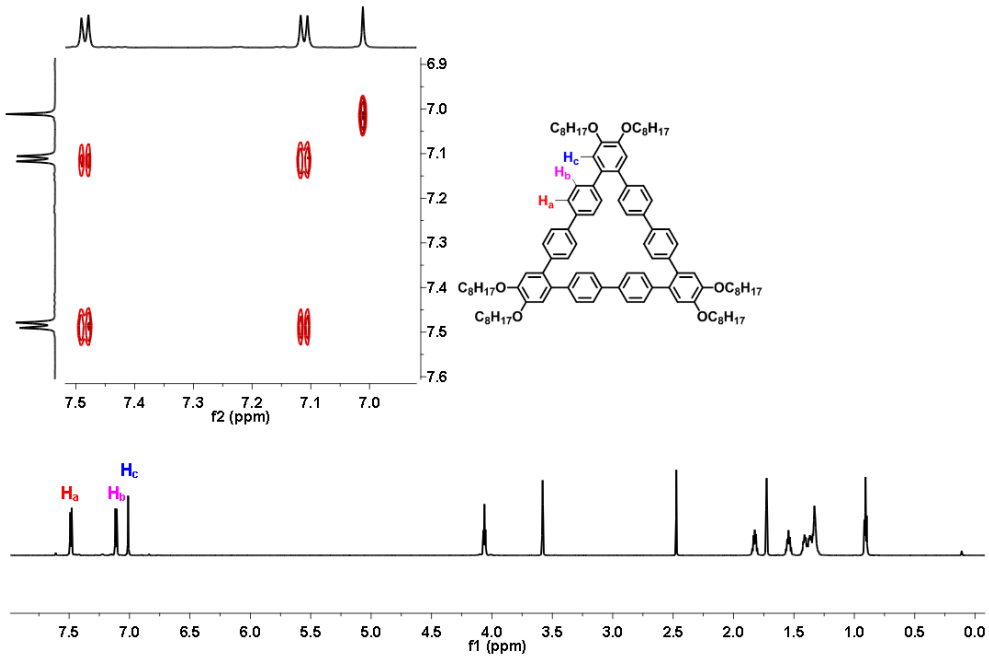

Figure 3-54: ^{1}H NMR spectrum of macrocycle **3-32** in THF-d_8. The inset shows the ^{1}H,^{1}H-COSY NMR spectrum of the aromatic region of the compound.

Also, the isotopic composition of the target peak was in perfect accordance with the expected pattern.

Furthermore, the ^{1}H NMR spectrum of macrocycle **3-32** recorded in THF-d_8 at 25 °C is in agreement with the highly symmetric nature of the compound (Figure 3-54).

Two doublets originating from H_a and H_b are found at δ = 7.49 ppm and δ = 7.12 ppm, respectively. The singlet at δ = 7.01 ppm is attributed to proton H_c.[10] The corresponding ^{1}H,^{1}H-COSY NMR spectrum is in accordance with this peak assignment.

3.4.2 Optical Spectroscopy

In the next step, a computational analysis was performed on macrocycle **3-32** in order to obtain information on conformation and electronic structure of the compound (B3LYP, 6-311G**). The steric repulsion among the twelve inner hydrogen atoms surrounding the cavity of cyclo-*nona*-phenylene **3-32** prevents a fully planar conformation of the ring. As clearly seen from the pictures in Figure 3-55, the molecule adopts an alternating arrangement of the aromatic units with torsion angles of 48.5 ° and 62.8 ° between neighboring rings, respectively. This value is much higher than in the case of linear oligoarylenes such as *para*-terphenyl or *para*-quaterphenyl **3-33** (Figure 3-52) for which the corresponding dihedral angle was found to be 37.2 ° as a consequence of the higher conformational freedom (B3LYP, 6-311G**).

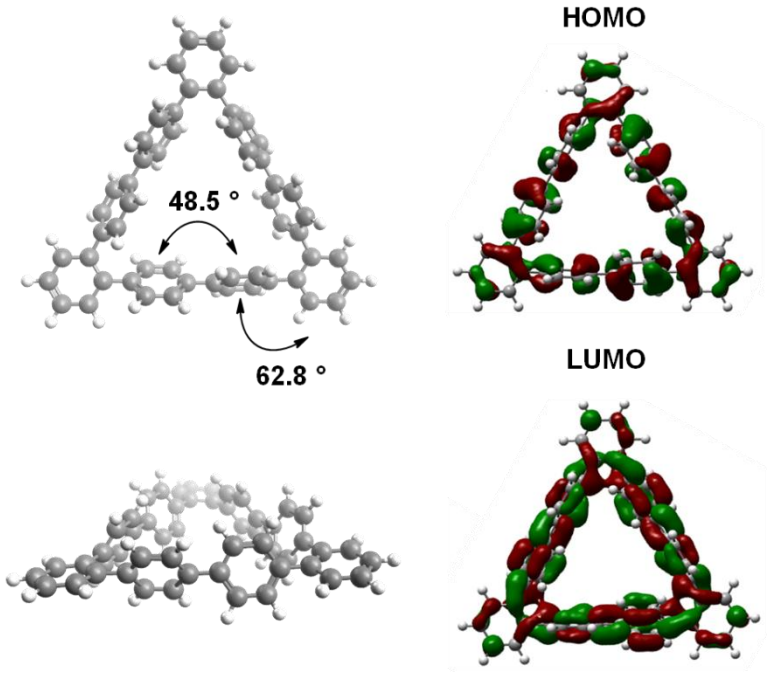

Figure 3-55: Conformation of macrocycle **3-32** derived from computational analysis (left), wave functions of the HOMO und LUMO of the macrocycle (B3LYP, 6-311G**).

The graphical representation of the HOMO and LUMO levels of **3-32** indicate that the three *ortho*-substituted benzene units that make up the corners of the triangular backbone hamper the conjugation along the cycle due the unfavorable geometric situation at these sites.

In the following step, the optoelectronic properties of macrocycle **3-32** and model compound *para*-quaterphenyl **3-33** were then studied by means of electronic spectroscopy. The UV-vis spectrum of macrocycle **3-32** is shown in Figure 3-56 and is dominated by a featureless absorption with the maximum located at λ_{max1} = 302 nm. For model compound **3-33** the absorption curve exhibits a similar course but is however slightly hypsochromically shifted by 10 nm. The absorption peak is found at λ_{max2} = 292 nm for this molecule. Taking into account the progressive displacement of the main absorption band known for linear oligoarylenes[148,149] the observed shift of macrocycle **3-32** with respect to *para*-quaterphenyl **3-33** would be expected to be more pronounced if the conjugation actually extended over the linear sides of the triangle.

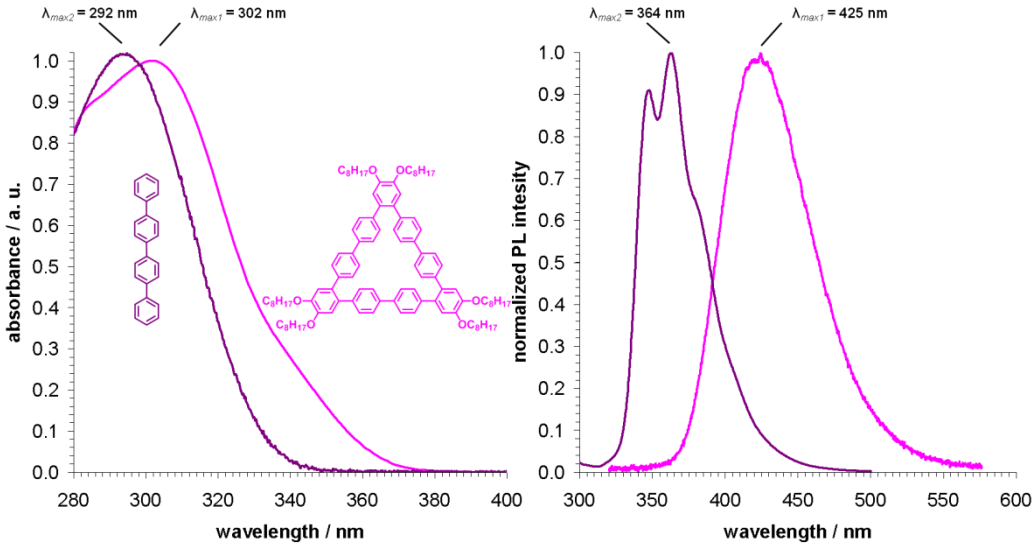

Figure 3-56: Normalized UV-vis absorption (left) and fluorescence emission spectrum (right) of macrocycle **3-32** and model compound **3-33** in toluene at 10^{-5} M.

In fact, the absorption maximum of the non-substituted cyclo-*nona*-phenylene was even detected at smaller wavelengths than the one of model compound **3-33** in the past.[5] This was ascribed to the aforementioned alternating arrangement of the benzene rings that is confirmed by the computational analysis (Figure 3-55). The bathochromic shift of **3-32** with respect to **3-33** in the present case can thus be attributed to the electron-donating effect of the octyloxy substituents.

The corresponding fluorescence emission spectra of cyclo-*nona*-phenylene **3-32** and *para*-quaterphenyl **3-33** are depicted in Figure 3-56. Whereas the spectrum of *para*-quaterphenyl **3-33** shows a vibronic fine structure with the maximum at λ_{max2} = 364 nm, the emission of the cyclo-*nona*-phenylene macrocycle is again of featureless nature peaking in the blue region of the optical spectrum at λ_{max1} = 425 nm. The effect of a larger π-conjugated system for macrocycle **3-32** is now clearly seen by the wavelength shift of 61 nm with respect to the emission maxima of *para*-quaterphenyl **3-33**. It might originate from an improved geometric conformation that the macrocycle adopts upon excitation and that is in contrast to the unfavorable arrangement of the aromatic units in the ground state discussed above.[141]

When compared to the data of the cyclo-7,10-tris-triphenylene macrocycle **3-26** the strong influence of planarization induced by closing of the bond in the 2,2''-position of *ortho*-terphenyl is apparent. The triphenylene units of **3-26** are locked to fixed positions and strongly communicate as seen from the analysis of the electronic spectra and the data obtained by computational modeling. Also, the symmetric absorption and emission spectra exhibit a strong degree of vibronic patterning originating from the intrinsic rigidity of the ring system that is consequently little affected by excitation (Figure 3-47 and Figure 3-48). In contrast, the benzene rings of **3-32** are not annelated leading to a high number of vibronic states that cause featureless curves both in absorption and emission. Whereas the absorption maximum of the cyclo-*nona*-phenylene **3-32** is significantly shifted hypsochromically with respect to the cyclo-7,10-tris-triphenylene macrocycle **3-26**, the corresponding emission maxima are found at similar wavelengths thus suggesting an similar degree of conjugation for **3-32** in the excited state.

3.4.3 Self-Assembly in the Bulk Phase

The thermal properties of macrocycle **3-32** were then studied by DSC analysis. The scans comprise two reversible peaks during the cooling/heating cycle (Figure 3-57).

By application of polarized optical microscopy (POM), the peak at 176.7 °C observed upon second heating can be correlated to the isotropization temperature. Cooling down a thin film of cyclo-*nona*-phenylene **3-32** from the isotropic melt leads to a characteristic crystalline optical texture which is seen in Figure 3-58. This texture consists of highly birefringent, micrometer long crystals which are formed directly below a temperature of 153.5 °C and remain unchanged even at temperatures below the phase transition at -16.3 °C.

Both phases seen in the DSC diagram can thus be assigned as crystalline which is in agreement with the structural study based on 2D-WAXS measurements of extruded

fibers of macrocycle **3-32** performed in cooperation with *A. Mavrinskiy* and *Dr. W. Pisula* (MPI-P Mainz, Germany).

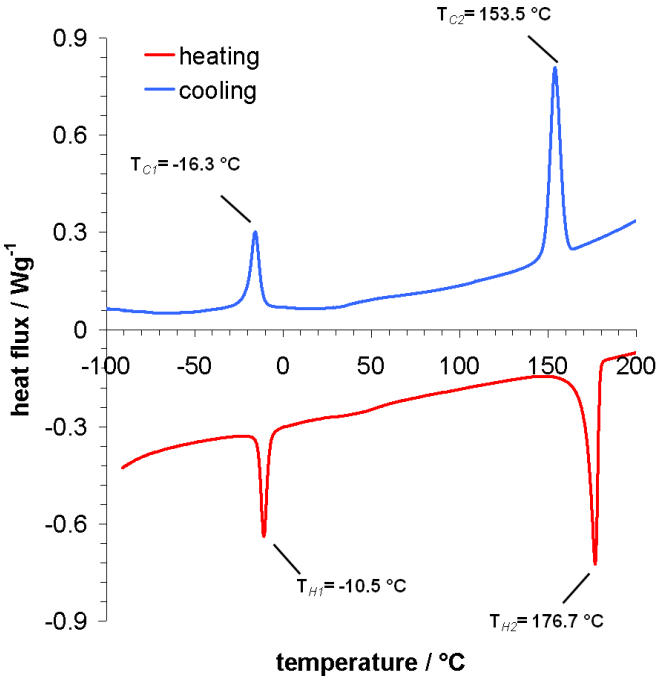

Figure 3-57: DSC trace of macrocycle **3-32** upon second heating (red) and cooling (blue).

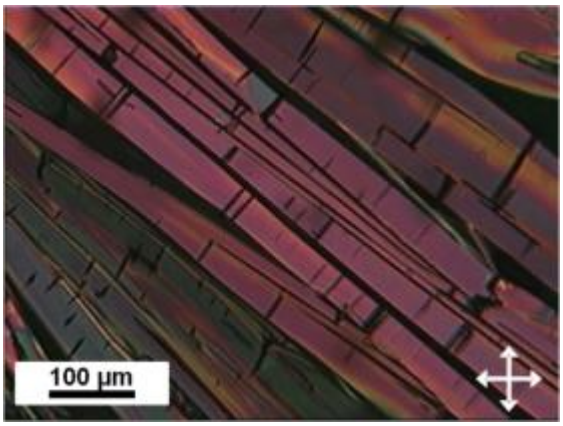

Figure 3-58: Optical microscopy image of macrocycle **3-32** recorded between cross-polarizers at 30 °C after crystallization from the isotropic melt.

At 30 °C, prior to the first heating, the pattern of **3-32** shows an amorphous halo which is attributed to disordered alky side chains (Figure 3-59). Furthermore, a small-angle equatorial reflection is observed which is correlated to one-dimensional columnar structures aligned along the fiber axis. The columnar arrangement is described by a square unit cell defined by a_{sq} = 2.82 nm as the parameter. The columns consist of macrocycle **3-32** stacked on top of each other. Since the benzene rings are out-of-

plane rotated within the ring system (Figure 3-55), *π*-stacking as the driving force for the self-assembly can be neglected.

This is evidenced by the lack of meridional reflections characteristic for molecular packing which indicates pronounced disorder within the columns. It is reasonable to deduce that the columnar superstructures are formed due to a local microphase separation between the rigid aromatic cycle core and the peripheral flexible alkyl chains. Heating of the macrocycle to 90 °C resulted in an increased degree of order as evidenced by the appearance of a large number of new reflections in the corresponding pattern (Figure 3-59).

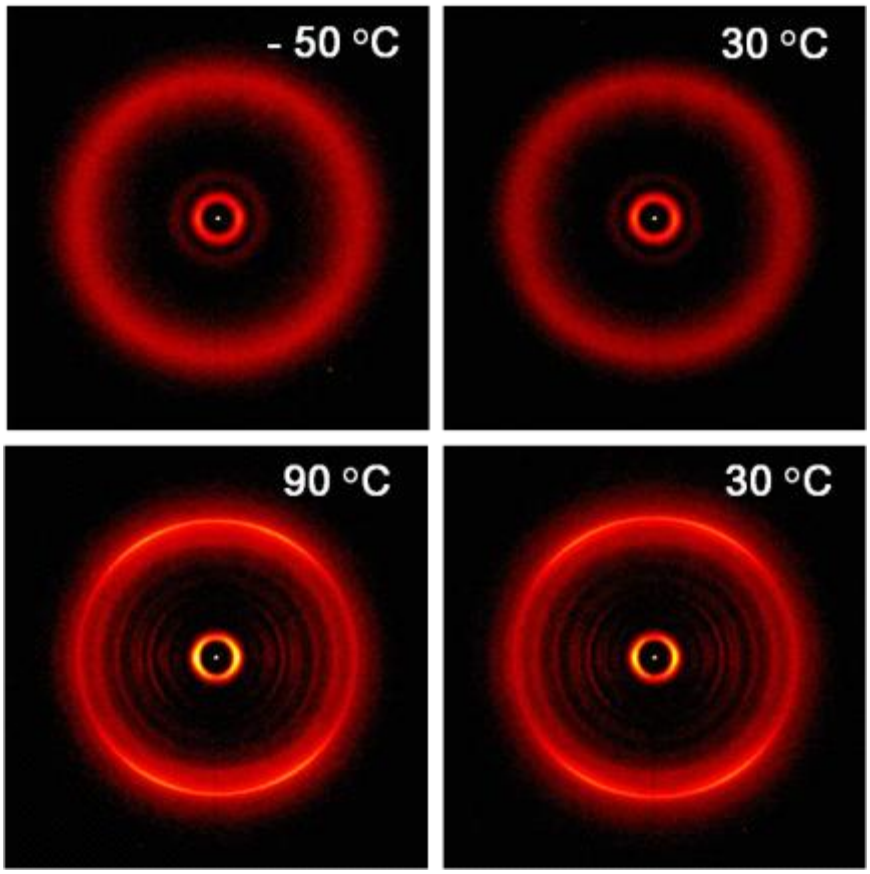

Figure 3-59: Temperature-dependent 2D-WAXS patterns of macrocycle **3-32**.

Interestingly, crystallinity remains stable after cooling back the sample to 30 °C. The higher order can be correlated to the increased mobility and subsequent rearrangement of the side chains at higher temperatures.

Before annealing, the amorphous halo in the pattern indicates disordered alkyl substituents. After annealing, however, this halo turns into a sharp isotropic reflection.

Additionally, the *intra*columnar ordering is enhanced as suggested by the new meridional reflection which corresponds to a spacing of p = 0.43 nm (Figure 3.59). This

unusually large *inter*molecular distance originates from the out-of-plane rotated benzene rings within the backbone of the macrocycle which prevent a closer contact of the molecules (Figure 3-60).

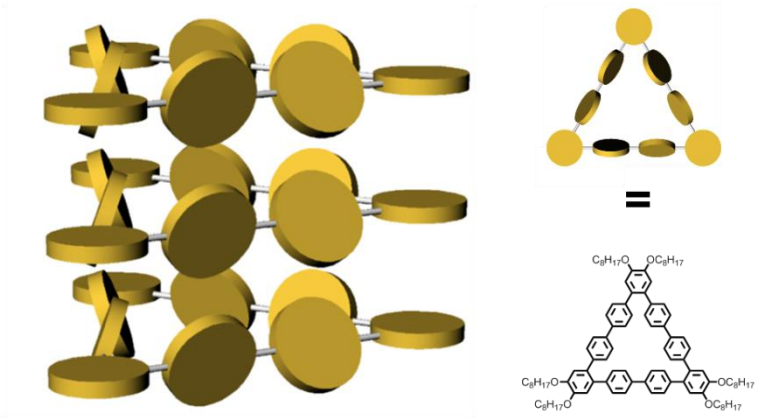

Figure 3-60: Schematic illustration of the *intra*columnar packing of **3-32** at 30 °C after annealing. Side chains are omitted for clarity, the molecular rotation is random.

With respect to the enhanced liquid-crystallinity seen for the geometry-related cyclo-7,10-tris-triphenylene macrocycle **3-26** the influence of a flat molecular core is evident. Still, the observed bulk phase properties of **3-32** cannot solely be rationalized on the basis of the aromatic units of the macrocycle. It has also to be considered that the octyloxy chains of **3-32** are shorter as compared to the dodecyloxy chains of **3-26**. It is well-accepted that the driving force for the self-assembly of mesogens in the bulk state is the microphase separation between the hard aromatic core and the soft alkyl chain corona. The weaker *π*-*π*-interactions between neighboring molecules additionally support the self-organization into highly ordered structures.[134,150,151]

The influence of both factors is apparently decreased in the case of cyclo-*nona*-phenylene **3-32**. On the one hand, the molecule is not planar; on the other hand the side chains are relatively short. For propeller-shaped hexaphenylbenzene **3-34** it has been demonstrated in the past that an extensive substitution with alkyl chains can compensate the non-planar arrangement of the aromatic rings leading to LC behavior (Figure 3-61).[82] Upon oxidative cyclodehydrogenation to the corresponding hexa-substituted HBC **3-27** which is characterized by its extended aromatic core the temperature range of the columnar mesophase could be further increased.[82] However, the number of twisted benzene units is smaller than in the case of cyclo-*nona*-phenylene **3-32** but it is likely that closing of the *ortho*-terphenyl-type corners of macrocycle **3-32** to the triphenylene groups of the hypothetical octyloxy-substituted cyclo-7,10-tris-triphenylene macrocycle **3-35** would regenerate the LC character

despite the shorter alkoxy chain length (Figure 3-61). The application of a threefold photo-induced cyclization would be a suitable tool for the conversion of the twisted macrocycle **3-32** into the planarized derivative **3-35**.

This assumption is also based on studies regarding liquid-crystalline crown ether derivatives. For these compounds a significantly higher self-organization was confirmed upon cycloaromatization of *ortho*-terphenyl containing lateral units to the corresponding triphenylenes.[78]

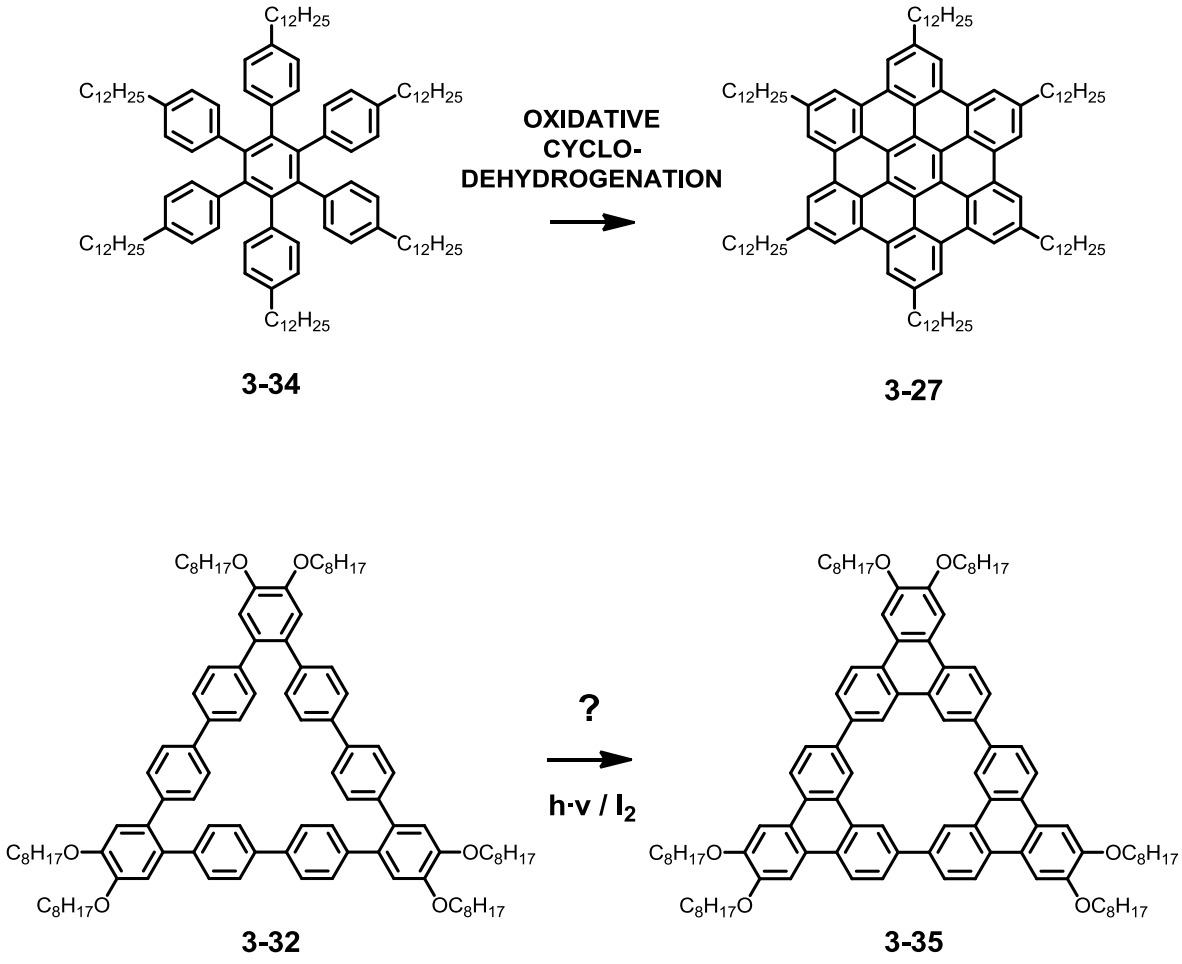

Figure 3-61: Analogy between the planarization of hexaphenylbenzene **3-34** to HBC **3-27** and the hypothetic conversion of the twisted cylclo-*nona*-phenylene **3-32** to the corresponding cyclo-7,10-tris-triphenylene **3-35**.

3.5 Summary

This chapter was an exploration of the multifold self-assembly of a series of novel conjugated macrocycles. It has been demonstrated that the *Yamamoto* cyclotrimerization is a versatile tool in the preparation of macrocycles which are characterized by a common C_3 symmetry. Monomers of different chemical and structural nature were successfully converted into the corresponding cyclic trimers. The resulting disc-like molecules all display a strong tendency to self-organize in solution, on surfaces and in the bulk state.

The metal sequestration of the cyclo-2,9-tris-1,10-phenanthroline macrocycles was investigated by various methods and revealed a preference of the hexaaza cavity for large alkaline and transition metal cations. The unique ion-dipole binding between cavity and metal cation made the straightforward preparation of a series of metal complexes possible. It was found that the presence of metal guest species in combination with stabilizing counterions can efficiently support the three-dimensional self-assembly of the liquid-crystalline state. This finding can be quantified by the improved packing parameters derived from 2D-WAXS analysis.

Moreover, the metal cation has a strong influence on the nature of the monolayer which is formed by the macrocyclic host as evidenced by extensive STM studies on a set of metal complexes. For Na^+ as the cationic guest species only a single row-like pattern was observed. In contrast, the sequestration of Ag^+ and Pb^{2+} leads to the formation of two-dimensional porous superstructures of high complexity. For the first time a nanoporous lattice was discovered for a molecule which is “intrinsically” porous and contains at the same time a cationic metal guest. These results should enable new applications of surface patterning and molecular data storage. For binary data storage two major criteria are fulfilled by these monolayers: The periodic and regular arrangement of the metal centers and the possibility to switch them by means of reduction. The possibility to convert the metal guest to its neutral state has been successfully demonstrated for the solution case.

Focus then turned to a triphenylene macrocycle in which the aromatic units are directly linked to each other. It was found that these molecular triangles also exhibit a rich supramolecular chemistry for which their increased π-surface is likely to account. The underlying characteristics of monomeric triphenylene are both reflected by the strong *inter*molecular attraction that was documented in solution as well as by the pronounced liquid-crystalline behavior of the macrocycle in the bulk state. Analysis of monolayers which are readily adopted by the macrocyclic compound *via* STM revealed that the

molecular triangle composed of three triphenylenes behaves as a giant triphenylene itself. Concerning the optoelectronic properties, the effect of increased conjugation along the cyclic backbone has been presented. The macrocycle exhibits a strong blue luminescence with the emission maximum close to the optimum value.

A cyclic oligoarylene consisting of nine benzene rings was prepared with the motivation to investigate the tolerance of the *Yamamoto* macrocyclization to somewhat more flexible precursors. The successful synthesis opens up new possibilities for precursor design as the only requirement for the selective formation of C_3 symmetric macrocycles *via* this methodology is the confinement of the halogen functions to an angle of 120 °. The study of the bulk supramolecular properties of this compound constitutes the first detailed example for this family of macrocycles. In contrast to the structurally closely related cyclo-7,10-tris-triphenylene macrocycle, the twisted nature of the cyclo-*nona*-phenylene macrocycle along with its relatively short alkoxy chains prevented access to the mesophase for this compound.

3.6 Bibliography

(1) Zhao, D.; Moore, J. S. *Chem. Commun.* **2003**, *2003*, 807-818.
(2) Zhang, W.; Moore, J. S. *Angew. Chem. Int. Ed.* **2006**, *45*, 4416-4439.
(3) Grave, C.; Schlüter, A. D. *Eur. J. Org. Chem.* **2002**, *2002*, 3075-3098.
(4) Bräunling, H.; Binnig, F.; Staab, H. A. *Chem. Ber.* **1967**, *100*, 880-888.
(5) Meyer, H.; Staab, H. A. *Liebigs Ann. Chem.* **1969**, *724*, 30-33.
(6) Staab, H. A.; Bräunling, H. *Tetrahedron Lett.* **1965**, *6*, 45-49.
(7) Staab, H. A.; Meissner, U. E.; Meissner, B. *Chem. Ber.* **1976**, *109*, 3875-3885.
(8) Pisula, W.; Kastler, M.; Yang , C.; Enkelmann, V.; Müllen, K. *Chem. Asian J.* **2007**, *2*, 51-56.
(9) Zhang, J.; Wang, X.; Su, Q.; Zhi, L.; Thomas, A.; Feng, X.; Su, D. S.; Schlögl, R.; Müllen, K. *J. Am. Chem. Soc.* **2009**, *131*, 11296–11297.
(10) Rahman, M. J.; Yamakawa, J.; Matsumoto, A.; Enozawa, H.; Nishinaga, T.; Kamada, K.; Iyoda, M. *J. Org. Chem.* **2008**, *73*, 5542-5548.
(11) Sammes, P. G.; Yahioglu, G. *Chem. Soc. Rev.* **1994**, *23*, 327-334.
(12) Accorsi, G.; Listorti, A.; Yoosaf, K.; Armaroli, N. *Chem. Soc. Rev.* **2009**, *38*, 1690-1700.
(13) Bencini, A.; Lippolis, V. *Coord. Chem. Rev.* **2010**, *254*, 2096-2180.
(14) Campagna, S.; Puntoriero, F.; Nastasi, F.; Bergamini, G.; Balzani, V. *Top. Current. Chem.* **2007**, *280*, 117-214.
(15) Quici, S.; Cavazzini, M.; Marzanni, G.; Accorsi, G.; Armaroli, N.; Ventura, B.; Barigelletti, F. *Inorg. Chem.* **2005**, *44*, 529-537.
(16) Anderegg, G. *Helv. Chim. Acta* **1963**, *46*, 2397-2410.
(17) Jasat, A.; Dolphin, D. *Chem. Rev.* **1997**, *97*, 2267-2340.
(18) Beletskaya, I.; Tyurin, V. S.; Tsivadze, A. Y.; Guilard, R.; Stern, C. *Chem. Rev.* **2009**, *109*, 1659-1713.
(19) Elemans, J.; van Hameren, R.; Nolte, R.; Rowan, A. *Adv. Mater.* **2006**, *18*, 1251-1266.
(20) Newkome, G. R.; Lee, H. W. *J. Am. Chem. Soc.* **1983**, *105*, 5956-5957.
(21) Toner, J. L. *Tetrahedron Lett.* **1983**, *24*, 2707-2710.
(22) Ransohoff, J. E. B.; Staab, H. A. *Tetrahedron Lett.* **1985**, *26*, 6179-6182.
(23) Bell, T. W.; Firestone, A. *J. Am. Chem. Soc.* **1986**, *108*, 8109-8111.
(24) Bell, T. W.; Cragg, P. J.; Drew, M. G. B.; Firestone, A.; Kwok, D. I. A. *Angew. Chem. Int. Ed.* **1992**, *31*, 345-347, 348-350.
(25) Boguslavsky, L.; Bell, T. W. *Langmuir* **1994**, *10*, 991-993.
(26) Drew, M. G. B.; de O. Cabral, J.; Cabral, M. F.; Esho, F. S.; Nelson, S. M. *J. Chem. Soc., Chem. Commun.* **1979**, *1979*, 1033 - 1035.
(27) Bell, T. W.; Guzzo, F.; Drew, M. G. B. *J. Am. Chem. Soc.* **1991**, *113*, 3115-3122.
(28) Benetollo, F.; Bombieri, G.; De Cola, L.; Polo, A.; Smailes, D. L.; Vallarino, L. M. *Inorg. Chem.* **1989**, *28*, 3447-3452.
(29) Yamada, M.; Nakamura, Y.; Kuroda, S.; Shimao, I. *Bull. Chem. Soc. Jpn.* **1990**, *63*, 2710-2712.
(30) Yamada, M.; Tanaka, Y.; Yoshimoto, Y.; Kuroda, S.; Shimao, I. *Bull. Chem. Soc. Jpn.* **1992**, *65*, 1006-1011.
(31) Schmittel, M.; Ammon, H. *Eur. J. Org. Chem.* **1998**, *1998*, 785-792.
(32) Koning, B.; de Boer, J. W.; Meetsma, A.; Kellogg, R. M. *Arkivoc* **2004**, *2*, 189-205.
(33) Ulven, T.; Frimurer, T. M.; Receveur, J. M.; Little, P. B.; Rist, O.; Norregaard, P. K.; Hogberg, T. *J. Med. Chem.* **2005**, *48*, 5684-5697.
(34) Frimurer, T. M.; Ulven, T.; Hogberg, T.; Norregaard, P. K.; Little, P. B.; Receveur, J. M. *Int. Pat. Appl. WO 03/087045 A1* **2003**.
(35) Yamamoto, T.; Saitoh, Y.; Anzai, K.; Fukumoto, H.; Yasuda, T.; Fujiwara, Y.; Choi, B. K.; Kubota, K.; Miyamaes, T. *Macromolecules* **2003**, *36*, 6722-6729.
(36) Frey, J.; Kraus, T.; Heitz, V.; Sauvage, J. P. *Chem. Eur. J.* **2007**, *13*, 7584-7594.
(37) Yamamoto, T. *Progr. Polym. Sci.* **1992**, *17*, 1153-1205.
(38) Yamamoto, T. *Bull. Chem. Soc. Jpn.* **1999**, *72*, 621-638.
(39) Yamamoto, T.; Wakabayashi, S.; Osakada, K. *J. Organomet. Chem.* **1992**, *428*, 223–237.
(40) Yamamoto, T.; Maruyama, T.; Zhou, Z. H.; Ito, T.; Fukuda, T.; Yoneda, Y.; Begum, F.; Ikeda, T.; Sasaki, S. *J. Am. Chem. Soc.* **1994**, *116*, 4832-4845.
(41) Parshall, G. W. *J. Am. Chem. Soc.* **1974**, *96*, 2360-2366.
(42) Yamamoto, T.; Kohara, T.; Yamamoto, A. *Bull. Chem. Soc. Jpn.* **1981**, *54*, 1720-1726.
(43) Zhou, Z.-h.; Yamamoto, T. *J. Organomet. Chem.* **1991**, *414*, 119-127.
(44) Henry, M. S.; Hoffman, M. Z. *J. Phys. Chem.* **1979**, *83*, 618-625.
(45) Rieger, R.; Müllen, K. *J. Phys. Org. Chem.* **2010**, *23*, 315-325.
(46) Clar, E. *The Aromatic Sextet*; J. Wiley & Sons: London, **1972**.
(47) Wu, J.; Fechtenkötter, A.; Gauss, J.; Watson, M. D.; Kastler, M.; Fechtenkötter, C.; Wagner, M.; Müllen, K. *J. Am. Chem. Soc.* **2004**, *126*, 11311-11321.
(48) Bell, T. W.; Guzzo, F. *J. Am. Chem. Soc.* **1984**, *106*, 6111-6112.
(49) Honeybourne, C. L. *Tetrahedron* **1973**, *29*, 1549-1557.

(50) Shannon, R. D. *Acta Crystallogr., Sect. A* **1976**, *32*, 751-767.
(51) Liljeroth, P.; Repp, J.; Meyer, G. *Science* **2007**, *317*, 1203-1206.
(52) Hirjibehedin, C. F.; Lin, C. Y.; Otte, A. F.; Ternes, M.; Lutz, C. P.; Jones, B. A.; Heinrich, A. J. *Science* **2007**, *317*, 1199-1203.
(53) Jousselme, B.; Blanchard, P.; Levillain, E.; Delaunay, J.; Allain, M.; Richomme, P.; Rondeau, D.; Gallego-Planas, N.; Roncali, J. *J. Am. Chem. Soc.* **2003**, *125*, 1363-1370.
(54) Baxter, P. N. W. *J. Org. Chem.* **2004**, *69*, 1813-1821.
(55) Tian, L.; Wang, C.; Dawn, S.; Smith, M. D.; Krause, J. A.; Shimizu, L. S. *J. Am. Chem. Soc.* **2009**, *131*, 17620-17629.
(56) Huang, J. H.; Wen, W. H.; Sun, Y. Y.; Chou, P. T.; Fang, J. M. *J. Org. Chem.* **2005**, *70*, 5827-5832.
(57) Fu, Y.; Li, H.; Hu, W. *Eur. J. Org. Chem.* **2007**, *2007*, 2459-2463.
(58) Simpson, C. D.; Wu, J.; Watson, M. D.; Müllen, K. *J. Mater. Chem.* **2004**, *14*, 494-504.
(59) Pisula, W.; Menon, A.; Stepputat, M.; Lieberwirth, I.; Kolb, U.; Tracz, A.; Sirringhaus, H.; Pakula, T.; Müllen, K. *Adv. Mater.* **2005**, *17*, 684-689.
(60) Grimsdale, A. C.; Müllen, K. *Angew. Chem. Int. Ed.* **2005**, *44*, 5592-5629.
(61) Elemans, J. A. A. W.; Lei, S.; de Feyter, S. *Angew. Chem. Int. Ed.* **2009**, *48*, 7298-7332.
(62) MacLachlan, M. J. *Pure Appl. Chem.* **2006**, *78*, 873.
(63) Behr, J. P.; Lehn, J. M.; Dock, A. C.; Moras, D. *Nature* **1982**, *295*, 526-527.
(64) Lehn, J. M.; Malthête, J.; Levelut, A. M. *J. Chem. Soc., Chem. Commun.* **1985**, *1985*, 1794-1796.
(65) van Nostrum, C. F.; Nolte, R. J. M. *Chem. Commun.* **1996**, *1996*, 2385-2392.
(66) Van der Pol, J. F.; Neeleman, E.; Van Miltenburg, J. C.; Zwikker, J. W.; Nolte, R. J. M.; Drenth, W. *Macromolecules* **1990**, *23*, 155-162.
(67) Fischer, M.; Lieser, G.; Rapp, A.; Schnell, I.; Mamdouh, W.; de Feyter, S.; de Schryver, F. C.; Höger, S. *J. Am. Chem. Soc.* **2004**, *126*, 214-222.
(68) Zhao, D.; Moore, J. S. *J. Org. Chem.* **2002**, *67*, 3548-3554.
(69) Beginn, U.; Zipp, G.; Mourran, A.; Walther, P.; Möller, M. *Adv. Mater.* **2000**, *12*, 513-516.
(70) Chen, Y.; Su, W.; Bai, M.; Jiang, J.; Li, X.; Liu, Y.; Wang, L.; Wang, S. *J. Am. Chem. Soc.* **2005**, *127*, 15700-15701.
(71) van Nostrum, C. F.; Picken, S. J.; Nolte, R. J. M. *Angew. Chem. Int. Ed.* **1994**, *33*, 2173-2175.
(72) Schmaltz, B.; Rouhanipour, A.; Räder, H. J.; Pisula, W.; Müllen, K. *Angew. Chem. Int. Ed.* **2009**, *48*, 720-724.
(73) Pisula, W.; Tomovic, Z.; Simpson, C.; Kastler, M.; Pakula, T.; Müllen, K. *Chem. Mater.* **2005**, *17*, 4296-4303.
(74) Bell, T. W.; Cragg, P. J.; Drew, M. G. B.; Firestone, A.; Kwok, D. I. A. *Angew. Chem. Int. Ed.* **1992**, *31*, 348-350.
(75) Pearson, R. G. *J. Am. Chem. Soc.* **1963**, *85*, 3533-3539.
(76) Percec, V.; Johansson, G.; Heck, J.; Ungarb, G.; Battyb, S. V. *J. Chem. Soc., Perkin Trans. 1* **1993**, 1411-1420.
(77) Kaller, M.; Tussetschläger, S.; Fischer, P.; Deck, C.; Baro, A.; Giesselmann, F.; Laschat, S. *Chem. Eur. J.* **2009**, *15*, 9530-9542.
(78) Kaller, M.; Deck, C.; Meister, A.; Hause, G.; Baro, A.; Laschat, S. *Chem. Eur. J.* **2010**, *16*, 6326-6337.
(79) Stehr, J.; Fischer, R. D. *J. Organomet. Chem.* **1992**, *430*, C1-C4.
(80) Schlecht, S.; Magull, J.; Fenske, D.; Dehnicke, K. *Angew. Chem. Int. Ed.* **1997**, *36*, 1994-1995.
(81) Wu, Y. Y.; Chen, J. D.; Liou, L. S.; Wang, J. C. *Inorg. Chim. Acta* **2002**, *336*, 71-79.
(82) Herwig, P.; Kayser, C. W.; Müllen, K.; Spiess, H. W. *Adv. Mater.* **1996**, *8*, 510-513.
(83) Grill, L.; Dyer, M.; Lafferentz, L.; Persson, M.; Peters, M. V.; Hecht, S. *Nat. Nanotechnol.* **2007**, *2*, 687-691.
(84) Hannes, S.; Kiebele, A.; Meike, S.; Jung, T. A.; Davide, B.; Cheng, F.; Francois, D. *Adv. Mater.* **2006**, *18*, 275-279.
(85) Rabe, J. P.; Buchholz, S. *Science* **1991**, *253*, 424-427.
(86) Tahara, K.; Johnson, C. A.; Fujita, T.; Sonoda, M.; de Schryver, F. C.; de Feyter, S.; Haley, M. M.; Tobe, Y. *Langmuir* **2007**, *23*, 10190-10197.
(87) Furukawa, S.; Uji-i, H.; Tahara, K.; Ichikawa, T.; Sonoda, M.; de Schryver, F. C.; Tobe, Y.; de Feyter, S. *J. Am. Chem. Soc.* **2006**, *128*, 3502-3503.
(88) Stabel, A.; Herwig, P.; Müllen, K.; Rabe, J. P. *Angew. Chem. Int. Ed.* **1995**, *34*, 1609-1611.
(89) Zwaneveld, N. A. A.; Pawlak, R.; Abel, M.; Catalin, D.; Gigmes, D.; Bertin, D.; Porte, L. *J. Am. Chem. Soc.* **2008**, *130*, 6678-6679.
(90) Bieri, M.; Treier, M.; Cai, J.; Aït-Mansour, K.; Ruffieux, P.; Gröning, O.; Gröning, P.; Kastler, M.; Rieger, R.; Feng, X.; Müllen, K.; Fasel, R. *Chem. Commun.* **2009**, *2009*, 6919-6921.
(91) Bieri, M.; Nguyen, M. T.; Gröning, O.; Cai, J.; Treier, M.; Aït-Mansour, K.; Ruffieux, P.; Pignedoli, C. A.; Passerone, D.; Kastler, M.; Müllen, K.; Fasel, R. *J. Am. Chem. Soc.* **2010**, *132*, 16669–16676.
(92) Blankenburg, S.; Bieri, M.; Fasel, R.; Müllen, K.; Pignedoli, C. A.; Passerone, D. *Small* **2010**, *6*, 2266-2271.
(93) Elemans, J.; Lei, S.; de Feyter, S. *Angew. Chem. Int. Ed.* **2009**, *48*, 7298-7332.
(94) Lei, S.; Tahara, K.; Adisoejoso, J.; Balandina, T.; Tobe, Y.; De Feyter, S. *Cryst. Eng. Commun.* **2010**, *12*, 3369-3381.
(95) Tahara, K.; Lei, S.; Adisoejoso, J.; de Feyter, S.; Tobe, Y. *Chem. Commun.* **2010**, *46*.

(96) Lackinger, M.; Griessl, S.; Heckl, W. M.; Hietschold, M.; Flynn, G. W. *Langmuir* **2005**, *21*, 4984-4988.
(97) Kampschulte, L.; Lackinger, M.; Maier, A. K.; Kishore, R. S. K.; Griessl, S.; Schmittel, M.; Heckl, W. M. *J. Phys. Chem. B* **2006**, *110*, 10829-10836.
(98) Stepanow, S.; Lingenfelder, M.; Dmitriev, A.; Spillmann, H.; Delvigne, E.; Lin, N.; Deng, X.; Cai, C.; Barth, J. V.; Kern, K. *Nat. Mater.* **2004**, *3*, 229-233.
(99) Schull, G.; Douillard, L.; Fiorini-Debuisschert, C.; Charra, F.; Mathevet, F.; Kreher, D.; Attias, A.-J. *Nano Lett.* **2006**, *6*, 1360-1363.
(100) Cnossen, A.; Pijper, D.; Kudernac, T.; Pollard, M. M.; Katsonis, N.; Feringa, B. L. *Chem. Eur. J.* **2009**, *15*, 2768-2772.
(101) Spillmann, H.; Kiebele, A.; Stöhr, M.; Jung, T. A.; Bonifazi, D.; Cheng, F.; Diederich, F. *Adv. Mater.* **2006**, *18*, 275-279.
(102) Lei, S.; Tahara, K.; Feng, X.; Furukawa, S.; de Schryver, F. C.; Müllen, K.; Tobe, Y.; de Feyter, S. *J. Am. Chem. Soc.* **2008**, *130*, 7119-7129.
(103) Binnig, G.; Rohrer, H. *Helv. Phys. Acta* **1982**, *55*, 726–735.
(104) Samori, P.; Rabe, J. P. *J. Phys. Condens. Matter* **2002**, *14*, 9955–9973.
(105) Hipps, K. W.; Lu, X.; Wang, X. D.; Mazur, U. *J. Phys. Chem.* **1996**, *100*, 11207-11210.
(106) Strohmaier, R.; Ludwig, C.; Petersen, J.; Gompf, B.; Eisenmenger, W. *J. Vac. Sci. Technol., B* **1996**, *14*, 1079-1082.
(107) Lu, X.; Hipps, K. W. *J. Phys. Chem. B* **1997**, *101*, 5391-5396.
(108) Schmidt, H.; Schultz, G. *Liebigs Ann. Chem.* **1880**, *203*, 118-137.
(109) Mannich, C. *Ber. Dtsch. Chem. Ges.* **1907**, *40*, 159-165.
(110) Buess, C. M.; Lawson, D. D. *Chem. Rev.* **1960**, *60*, 313-330.
(111) Perez, D.; Guitián, E. *Chem. Soc. Rev.* **2004**, *33*, 274-283.
(112) Billard, J.; Dubois, J. C.; Tinh, N. H.; A., Z. *Nouv. J. Chimie* **1978**, *2*, 535.
(113) Kumar, S. *Liq. Cryst.* **2004**, *31*, 1037-1059.
(114) Kumar, S. *Liq. Cryst.* **2005**, *32*, 1089-1113.
(115) Adam, D.; Schuhmacher, P.; Simmerer, J.; Häussling, L.; Siemensmeyer, K.; Etzbachi, K. H.; Ringsdorf, H.; Haarer, D. *Nature* **1994**, *371*.
(116) Henderson, P.; Kumar, S.; Rego, J. A.; Ringsdorf, H.; Schuhmacher, P. *J. Chem. Soc., Chem. Commun.* **1995**, *1995*, 1059-1060.
(117) Baunsgaard, D.; Larsen, M.; Harrit, N.; Frederiksen, J.; Wilbrandt, R.; Stapelfeldt, H. *J. Chem. Soc. Faraday Trans.* **1997**, *93*, 1893-1901.
(118) Saleh, M.; Park, Y. S.; Baumgarten, M.; Kim, J. J.; Müllen, K. *Macromol. Rapid Commun.* **2009**, *30*, 1279-1283.
(119) Hao, Q.; Xie, X.; Lei, W.; Xia, M.; Wang, F.; Wang, X. *J. Phys. Chem. C* **2010**, *114*, 9608-9617.
(120) Qin, T.; Zhou, G.; Scheiber, H.; Bauer, R. E.; Baumgarten, M.; Anson, C. E.; List, E. J. W.; Müllen, K. *Angew. Chem. Int. Ed.* **2008**, *47*, 8292-8296.
(121) McKenna, M. D.; Barberá, J.; Marcos, M.; Serrano, J. L. *J. Am. Chem. Soc.* **2005**, *127*, 619-625.
(122) Bagui, M.; Melinger, J. S.; Chakraborty, S.; Keightley, J. A.; Peng, Z. *Tetrahedron* **2009**, *65*, 1247-1256.
(123) Wang, D.; Hsu, J. F.; Bagui, M.; Dusevich, V.; Wang, Y.; Liu, Y.; Holder, A. J.; Peng, Z. *Tetrahedron Lett.* **2009**, *50*, 2147-2149.
(124) Li, J.; He, Z.; Gopee, H.; Cammidge, A. N. *Org. Lett.* **2010**, *12*, 472-475.
(125) Boden, B. N.; Abdolmaleki, A.; Ma, C. T. Z.; MacLachlan, M. J. *Can. J. Chem.* **2008**, *86*, 50-64.
(126) Boden, B. N. *Investigations of Highly Conjugated Macrocycles and Polymers for Aggregation and Chemical Sensing*; PhD Thesis: Vancouver, **2007**.
(127) Wendorff, J. H.; Christ, T.; Glüsen, B.; Greiner, A.; Kettner, A.; Sander, R.; Stümpflen, V.; Tsukruk, V. V. *Adv. Mater.* **1997**, *9*, 48-52.
(128) Seguy, I.; Destruel, P.; Bock, H. *Synth. Met.* **2000**, *111-112*, 15-18.
(129) Offen, H. W.; Hein, D. E. *J. Chem. Phys.* **1969**, *50*, 5274-5278.
(130) Meier, H.; Rose, B. *Journal Prakt. Chem.* **1998**, *340*, 536-543.
(131) Li, Z.; Lieberman, M. *Inorg. Chem.* **2001**, *40*, 932-939.
(132) Liu, L.; Yang, B.; Katz, T. J.; Poindexter, M. K. *J. Org. Chem.* **1991**, *56*, 3769-3775.
(133) Martin, R. B. *Chem. Rev.* **1996**, *96*, 3043-3064.
(134) Laschat, S.; Baro, A.; Steinke, N.; Giesselmann, F.; Hägele, C.; Scalia, G.; Judele, R.; Kapatsina, E.; Sauer, S.; Schreivogel, A. *Angew. Chem. Int. Ed.* **2007**, *46*, 4832-4887.
(135) Zemtsova, O. V.; Zheleznov, K. N. *Russ. Chem. Bull.* **2004**, *53*, 1743-1748.
(136) Askadskaya, L.; Boeffel, C.; Rabe, J. P. *Ber. Bunsen Ges. Phys. Chem.* **1993**, *97*, 517-521.
(137) Wu, P.; Zeng, Q.; Xu, S.; Wang, C.; Yin, S.; Bai, C. L. *Chem. Phys. Chem.* **2001**, *2*, 750-754.
(138) Xu, S.; Zeng, Q.; Lu, J.; Wang, C.; Wan, L.; Bai, C. L. *Surf. Sci.* **2003**, *538*, L451-L459.
(139) Becker, R. S.; Singh, I. S.; Jackson, E. A. *J. Chem. Phys.* **1963**, *38*, 2144.
(140) Meyerhoffer, S. M.; McGown, L. B. *Anal. Chem.* **1991**, *63*, 2082-2086.
(141) Baumgarten, M.; Yüksel, T. *Phys. Chem. Chem. Phys.* **1999**, *1*, 1699-1706.
(142) Vak, D.; Lim, B.; Lee, S.-H.; Kim, D.-Y. *Org. Lett.* **2005**, *7*, 4229-4232.
(143) Staab, H. A.; Binnig, F. *Chem. Ber.* **1967**, *100*, 889-892.
(144) Irngartinger, H.; Leiserowitz, L.; Schmidt, G. M. J. *Chem. Ber.* **1970**, *103*, 1132-1156.
(145) Staab, H. A.; Binnig, F. *Chem. Ber.* **1967**, *100*, 293-305.
(146) Hensel, V.; Schlüter, A. D. *Chem. Eur. J.* **1999**, *5*, 421-429.

(147) Hensel, V.; Lützow, K.; Schlüter, A. D.; Jacob, J.; Gessler, K.; Saenger, W. *Angew. Chem. Int. Ed.* **1997**, *36*, 2654-2656.
(148) Gillam, A. E.; Hey, D. H. *J. Chem. Soc.* **1939**, 1170-1177.
(149) Nijegorodov, N. I.; Downey, W. S.; Danailov, M. B. *Spectrochim. Acta, Part A* **2000**, *56*, 783-795.
(150) Hoeben, F. J. M.; Jonkheijm, P.; Meijer, E. W.; Schenning, A. *Chem. Rev.* **2005**, *105*, 1491-1546.
(151) Wu, J.; Pisula, W.; Müllen, K. *Chem. Rev.* **2007**, *107*, 718-747.

4 Synthetic Approaches towards Graphene Nanoribbons

4.1 Introduction

Graphene, an atomically thin layer from graphite,[1] has received considerable interest in physics, material science and chemistry since the recent discovery of its appealing electronic properties.[2-6] These involve superior charge carrier mobility[7] and the quantum *Hall* effect.[8,9] Moreover, its chemical robustness and material strength make graphene an ideal candidate for applications ranging from transparent conductive electrodes[10,11] to devices for charge and energy storage.[12,13]

Graphene nanoribbons (GNRs) are linear structures that are derived from the parent graphene lattice.[14-19] Their characteristic feature is high shape-anisotropy due to the increased ratio of length over width. Currently, their usage in yet smaller, flatter and faster carbon-based devices and integrated circuits is being widely discussed in material science.[20-24] In contrast to graphene, armchair-type GNRs exhibit a band gap that can be adjusted by their width.[14,21,25-27] Their length becomes relevant when GNRs are to be used in devices such as field-effect transistors (FETs) for which a minimum channel width has to be bridged.[20,21] The same holds for the potential replacement of copper or gold in nanoscale conducting pathways.[22,23] At the same time the edge structure of the GNRs will have a strong impact. Computational simulations[27-29] and experimental results on smaller nanographenes[30,31] suggest that GNRs exhibiting nonbonding π-electron states at zigzag edges could be used as active component in spintronic devices.

The reason why there are so few chemically defined GNRs is the considerable complexity that governs design, chemical preparation and processing of these structures. In the recent past, only few synthetic attempts have been published addressing the fabrication of GNRs of defined geometry, width, length, edge structure and heteroatom-content.[32-39] Based on the reaction environment the studies on the

synthetic bottom-up fabrication of GNRs can be further divided into solution-[32-38] and surface-based routes.[39-41]

For solution-based approaches using oligophenylene precursors a polymer is typically prepared in a first step which is subsequently converted into the graphitic structure by *Scholl*-type oxidative cyclodehydrogenation.[42,43] However, the design of the parent monomer must be carefully adjusted in order to guarantee for a suitable arrangement of the aromatic units upon the chemistry-assisted graphitization into the final GNR structure.[36-38]

Two different polymerization methods will be introduced in this chapter aiming at the lateral expansion as well as the maximization of the molecular weight of the polymeric oligophenylene. Regarding the bottom-up synthesis of GNRs this constitutes a major challenge as the number of repeat units directly translates into the length that is "written" into the graphene material. In this context the benefits and drawbacks of A_2B_2-type *Suzuki-Miyaura*[44-46] and *AA*-type *Yamamoto* polycondensation protocols[47,48] shall be discussed, respectively.

Laterally-extended building units were conceived in the present case which should enable access to GNRs of unprecedented width. The cyclodehydrogenation reaction which is at the heart of the synthetic approach shall be studied on the scale of the model compounds **C78** and **C84** which reflect the conformational situation of the larger polymeric precursors. Previous studies on the preparation of discotic nanographene molecules of related size such as **C54**,[49,50] **C60**,[51,52] **C72**,[53-55] **C78**,[56-60] **C96**,[61,62] **C132**[63] and **C222**[64] provide a valuable source for the understanding of the underlying chemical pathways.

Furthermore, the application of a recently developed surface-assisted protocol for the preparation of GNRs will be addressed in this chapter.[39-41,65] The design and synthesis of the oligophenylene precursors needed therefore was adopted from the strategy developed for the solution-based synthesis of the GNRs.

4.2 Polymeric Precursors via Suzuki Polycondensation

The *Suzuki-Miyaura* reaction represents a well-established cross-coupling protocol[66,67] which has been extensively used for the build-up of functional molecules and polymers.[44-46] The robust palladium(0)-mediated catalytic cycle is particularly useful for carbon-carbon bond formation between aromatic halides and arylboronic acids or their corresponding esters.

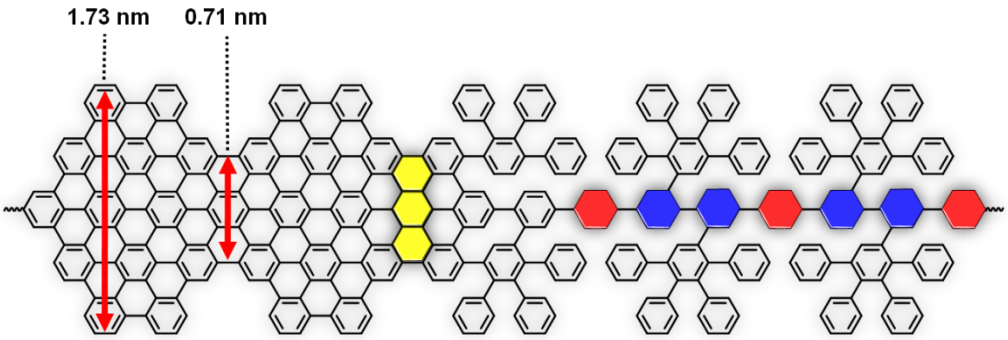

Figure 4-1: Schematic representation of *Suzuki*-based graphene nanoribbons **GNR1+2** illustrating dimensions, connectivity and overlap of the building units.

When applied as a polycondensation reaction a pair of complementarily functionalized monomers needs to be chosen. For the synthesis of GNRs *via* a *Suzuki-Miyaura* polycondensation the structural design illustrated in Figure 4-1 was envisaged.

The polymer can be rationalized as a laterally extended poly(*para*-phenylene) whose backbone chain is composed of 1,4-connected benzene rings that originate from the oligophenylene monomer (blue rings) and the diboronic acid (red rings).

The overlap between the repeat units of the final nanoribbons is achieved through three fused benzene units which are drawn as yellow rings (Figure 4-1). The GNRs possess an armchair-type edge which follows the overall saw blade periphery of the graphitic structure. The maximum diameter as derived from computational analysis is 1.73 nm and narrows down to 0.71 nm at the neck position (MMFF94s). These dimensions are significantly larger than in the case of the literature-known GNRs.[32-38]

4.2.1 Monomer Synthesis

For the synthesis of a suitable polymer precursor for the preparation of *Suzuki*-based GNRs it was decided to introduce two halogen functions on the oligophenylene unit. Polycondensation with a 1,4-functionalized diboronic acid followed by cyclodehydrogenation should then lead to the formation of the target structure depicted in Figure 4-1.

In a first reaction sequence, the synthesis of key intermediate 4,4'-dibromo-2,2'-diethynyl-1,1'-biphenyl **4-6** was achieved *via* a five-step route from commercially available 1,4-dibromo-2-nitrobenzene **4-1**. *Ullmann*-type homocoupling of **4-1** was used for the build-up of the biphenyl backbone. The reaction was achieved in the melt at 190 °C in the presence of copper powder as the reported method carried out in DMF was found to give extremely poor yields.[68] Due to the activating effect of the electron-

withdrawing nitro groups of **4-1**, the coupling only proceeded at the bromine atoms in the desired 1-position and did not result in the formation of isomeric species. The desired compound was isolated in 49 % yield. The next step consisted in the reduction of the nitro groups to yield the functionalized biphenyl **4-3**. This step was realized by hydrogenation of 4,4'-dibromo-2,2'-dinitro-1,1'biphenyl **4-2** using tin powder under acidic conditions.

Diamine **4-3** was obtained in virtually quantitative yield and directly used for the next step without further purification. Diazotation under classical *Sandmeyer* conditions followed by treatment with potassium iodide successfully lead to the synthesis of unreported 4,4'-dibromo-2,2'-diiodo-1,1'-biphenyl **4-4**. However, the mono-iodinated by-product was also observed by FD mass spectroscopy accounting for the moderate yield of 34 % in this step. The tedious separation of both products could only be achieved after two-fold column chromatography. In the next step, *Sonogashira-Hagihara* cross-coupling of **4-4** with trimethylsilyl acetylene in the presence of bis(triphenylphosphine)-palladiumchloride(II) and copper(II) iodide yielded the protected bisacetylene **4-5** in 62 %.

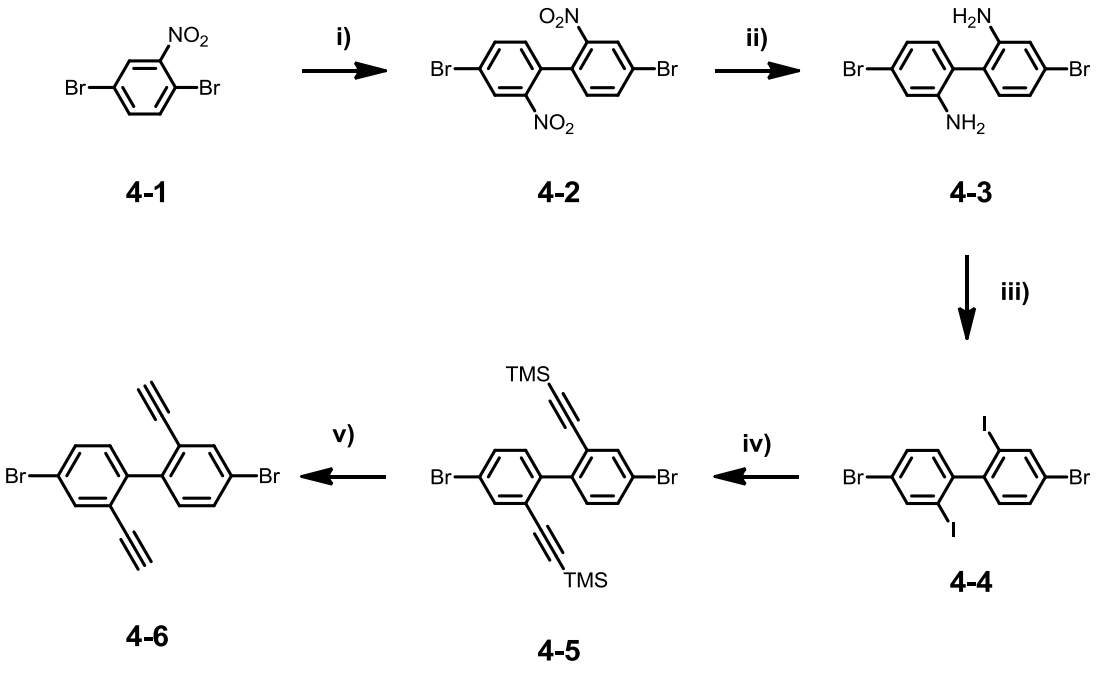

Figure 4-2: Synthetic route to 4,4'-dibromo-2,2'-diethynyl-1,1'-biphenyl **4-6**; conditions: i) copper powder, 190 °C, 49 %; ii) tin powder, HCl/EtOH, reflux, 95 %; iii) $NaNO_2$, HCl/H_2O, then KI, - 5 °C, 34 %; iv) trimethylsilyl acetylene, $Pd(PPh_3)_2Cl_2/CuI$, NEt_3; room temperature, 62 % v) K_2CO_3, THF/MeOH, room temperature, 75 %.

The difficulties for the introduction of the two acetylenes reported by others for similar biphenyls[53,55] could not be confirmed as the reaction proceeded smoothly under regular

conditions and in good yield. The reactivity of the iodine substituents was sufficiently high to run the reaction at room temperature. Thereby, a possible attack of the bromine atoms of **4-4** could be excluded. Surprisingly, the cleavage of the trimethylsilyl groups was however accompanied by significant difficulties when using the standard reagent tetra-*n*-butylammonium fluoride (TBAF). Only trace amounts of the mono-deprotected product were observed by FD mass spectroscopy. Neither increasing the equivalents of TBAF nor higher reaction temperatures lead to the target compound **4-6**. Only changing the reaction conditions using potassium carbonate as base finally resulted in the formation of 4,4'-dibromo-2,2'-diethynyl-1,1'-biphenyl **4-6** at room temperature in 70 % yield. The reaction was found to be sensitive to the solvents used and only worked well when a 1/1 mixture of THF and methanol was used. The complete removal of the protecting groups was proven by FD mass spectroscopy and the characteristic resonance of free acetylenes in the corresponding ^{1}H and ^{13}C NMR spectra.

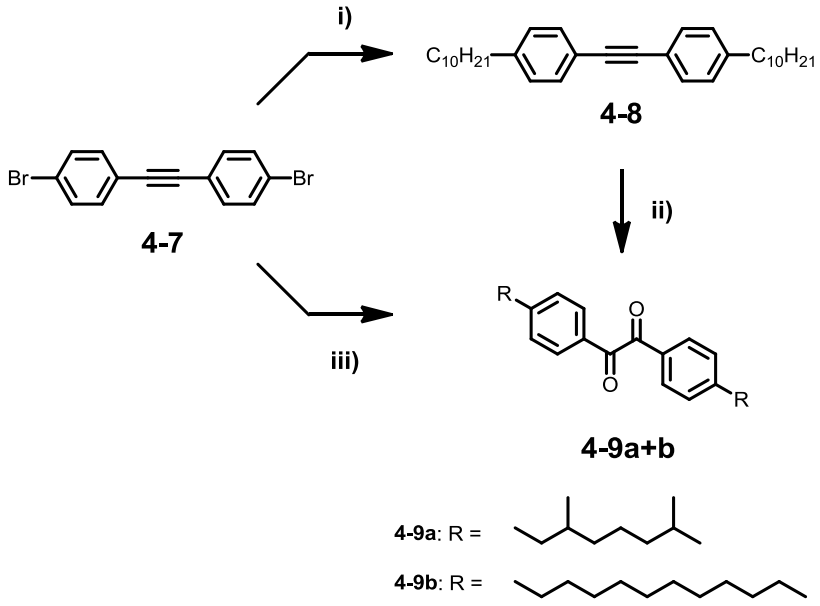

Figure 4-3: Synthetic route to the 1,2-bis(4-alkylphenyl)ethane-1,2-diones **4-9a+b**; conditions: i) alkyl magnesium bromide, $Pd(dppf)_2Cl_2$, THF, 60 °C, 95 %; ii) I_2, DMSO, 155 °C, 82 %; iii) 1-dodecene, 9-BBN, THF, then NaOH, 1,2-bis(4-bromophenyl)ethyne, $Pd(dppf)_2Cl_2$, RT, 70 %.

Diels-Alder [4+2] cyloaddtion[69] of acetylenes to tetraphenylcyclopentadienones is known to be a versatile method for the synthesis of large oligophenylene precursors.[61,70-73] By this reaction, the size of the molecule is significantly increased in one single synthetic step which is in general high-yielding. The tetraphenylcyclopentadienones **4-11a+b** were prepared according to literature-known procedures.[51,74] Figure 4-3 discloses the synthetic route to the 1,2-bis(4-

alkylphenyl)ethane-1,2-diones **4-9a+b** which are typically used for the build-up of the tetraphenylcyclopentadienone backbone. In principle, they can be decorated with any desired alkyl chain that will confer solubility to the final nanographene molecules. In the present case branched 3,7-dimethyloctyl (**4-9a**) and linear dodecyl chains (**4-9b**) were applied.

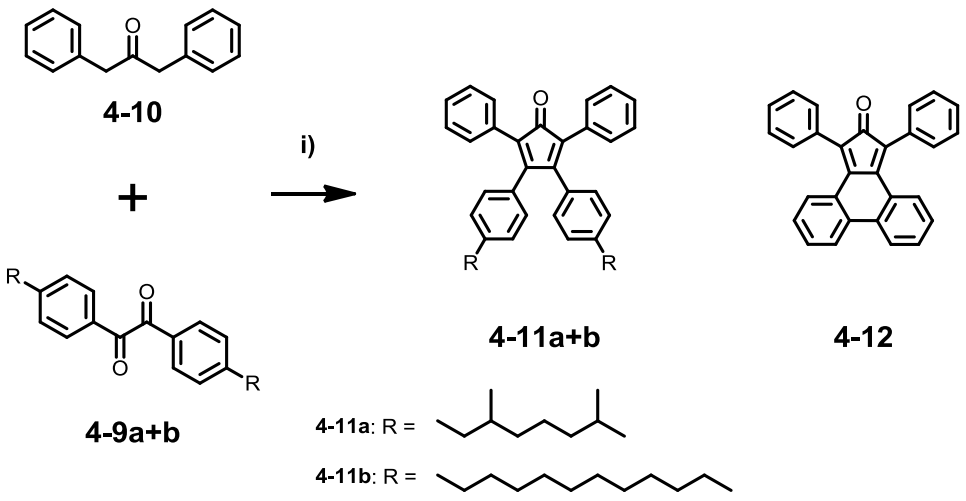

Figure 4-4: Synthetic route to the tetraphenylcyclopentadienones **4-11a+b**; conditions: i) tetra-*n*-butylammonium hydroxide, *t*-BuOH, 80 °C, 45 - 55 %.

Knoevenagel condensation with diphenylacetone **4-10** was then used to prepare the bisalkyl tetraphenylcyclopentadienones **4-11a+b**[51] in 45 - 55 % yield.

The rigid building block phencyclone **4-12** is commercially available and can be used to introduce triphenylene motifs into the lateral dendrons (Figure 4-4).[75]

With 4,4'-dibromo-2,2'-diethynyl-1,1'-biphenyl **4-6** and the tetraphenylcyclopentadienones **4-11a+b** at hand, the preparation of the oligophenylene monomer for the synthesis of the laterally extended poly(*p*ara-phenylenes) via *Suzuki* polycondensation was accessible.

Diels-Alder reaction of **4-6** and **4-11a+b** in *ortho*-xylene at 160 °C using 300 W microwave irradiation yielded the dendronized biphenyls **4-13a** and **4-13b** which differ in their alkyl chain periphery. The yield for the preparation of the oligophenylenes was 77 and 81 %, respectively. Both monomers were pre-purified using standard column chromatography. For the following A_2B_2-type polycondensation it is however imperative to remove mono-functionalized impurities as these will inevitably result in chain-termination and low molecular weights.

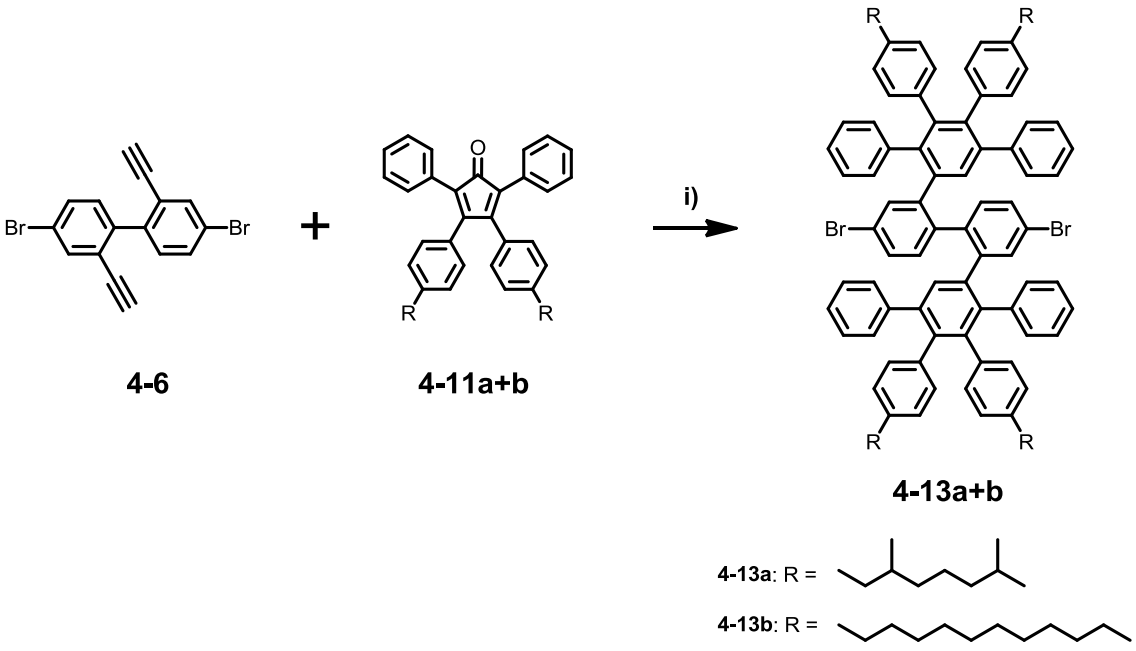

Figure 4-5: Synthetic route to the dendronized biphenyl monomers **4-13a+b**; conditions: i) *ortho*-xylene, 160 °C, µW, 300 W, 77 - 81 %.

Both monomers were therefore thoroughly purified by recycling gel permeation chromatography (rGPC).

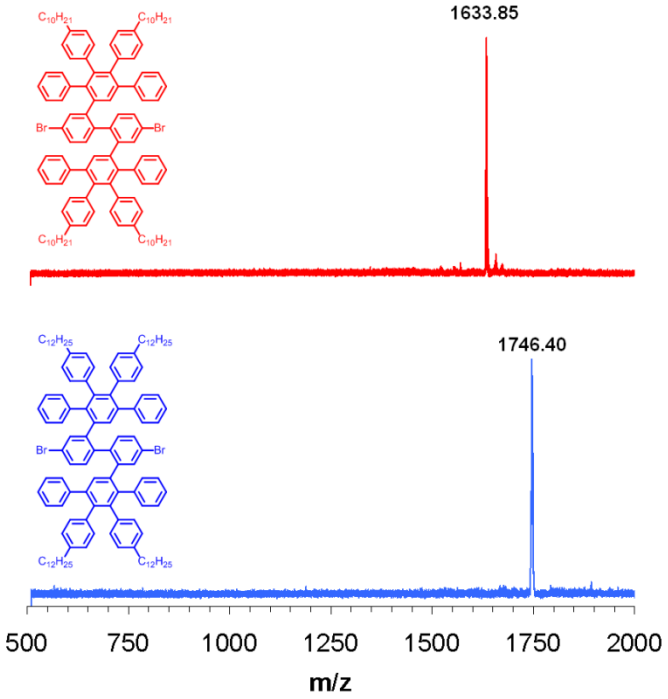

Figure 4-6: MALDI-TOF spectra of **4-13a** (top) and **4-13b** (bottom).

Their purity was confirmed by MALDI-TOF measurements and NMR analysis. The MALDI-TOF spectra of **4-13a+b** reveal the absence of mono-halogenated by-products which would act as undesired chain-terminating agents during the polycondensation process (Figure 6). The isotopic distribution corresponds to the simulated pattern and shows increased broadening due to the two naturally abundant bromine isomers.
Further evidence for the high purity was also provided by the ^{1}H NMR spectrum of monomer **4-13b** which was recorded in in TCE-d_2. At lower temperatures the signals suffered from a pronounced coalescence so that the NMR analysis had to be performed at 130 °C.

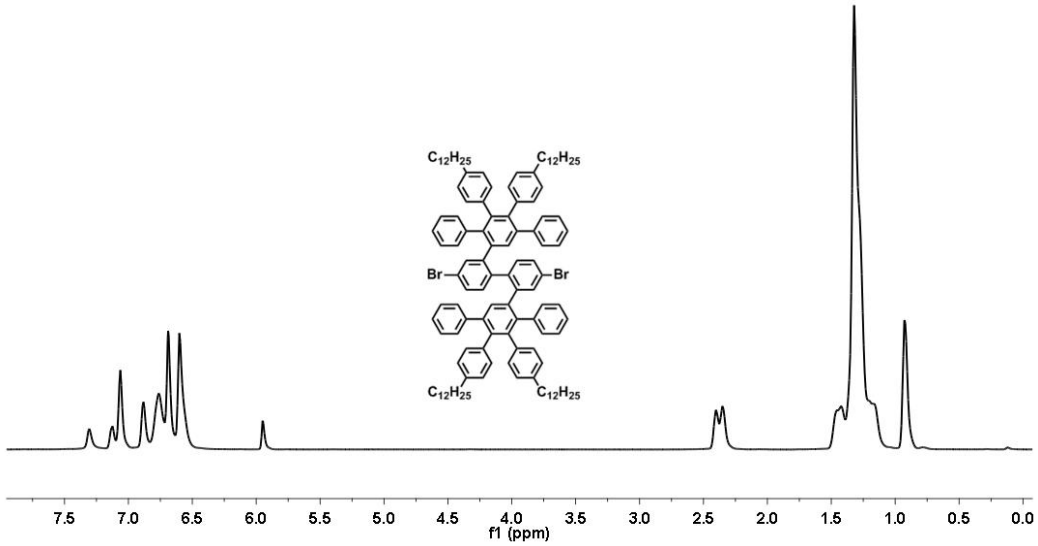

Figure 4-7: ^{1}H NMR spectrum of **4-13b** in TCE-d_2 at 130 °C.

As it can be seen in Figure 4-7 the aromatic region of the spectrum shows a complex pattern of resonances which is a result of the asymmetry of the two 2,3,4,5-tetraphenylbenzene dendrons which are attached to the biphenyl backbone. This decreased symmetry is also reflected by two individual signals originating from the *alpha*-methylene groups at δ = 2.45 ppm and δ = 2.40 ppm, respectively. A preliminary peak assignment can be achieved by simple integration of the signals. Two isolated resonances with an integral value of 2 are found at δ = 7.36 ppm and δ = 7.18 ppm. The ^{1}H,^{1}H-COSY NMR spectrum (Figure 4-8) confirms a *meta*-coupling between these two (**A**). In combination with their deep-field shift the signals can thus be attributed to protons **1** and **2**. A further cross-signal (**B**) of **2** into the broad peak at δ = 6.81 ppm allows for the identification of proton **3** which is located next to **2** on the biphenyl backbone. Additional strong cross-peaks exist between the signals at δ = 7.11 ppm and δ = 6.93 ppm (**C**) as well as within the aforementioned broad peak at

δ = 6.81 ppm (**D**). The three peaks have an integral ratio of 4:4:8 suggesting that they belong to the non-substituted phenyl rings of the dendrons. The identification of the different groups is possible taking into account the cross-signal of δ = 6.81 ppm with the shoulder of the peak located at δ = 6.65 ppm (**E**). The signals of the exposed protons (**7&14**) are typically found at higher field.

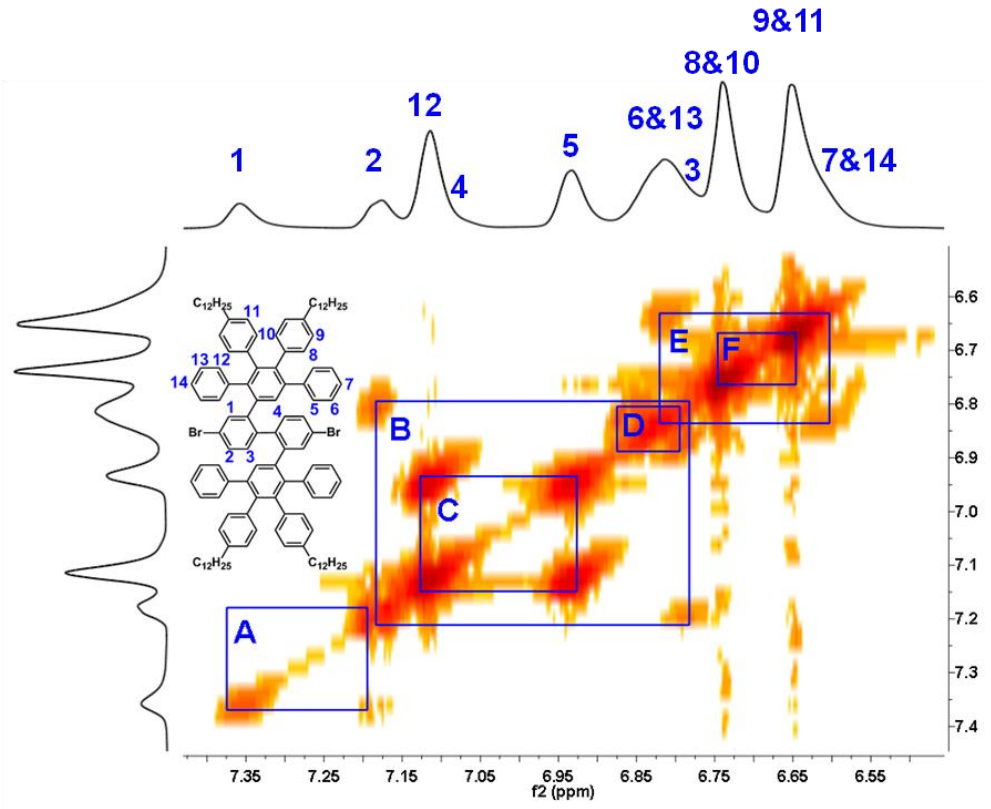

Figure 4-8: The $^{1}H,^{1}H$-COSY NMR spectrum of the aromatic region of **4-13b** in TCE-d_2 at 130 °C.

They are in close vicinity to the protons **6&13** which themselves exhibit a *meta*-coupling (**D**). The same is true for the signals of protons **5&12** which are however deep-field shifted due to the proximity of the central phenyl ring of the dendron. The remaining protons of the dodecyl-substituted phenyl rings (**8&10**, **9&11**) are unambiguously indentified by a NOESY experiment which proves their interaction with the *alpha*- and *beta*-protons of the alkyl chains. In accordance with the chemical structure an additional cross-signal (**F**) between the corresponding peaks at δ = 6.74 ppm and δ = 6.64 ppm is detected (Figure 4-8).

For the polymerization attempts the commercially available bis(pinacol) ester of 1,4-phenyldiboronic acid **4-14** was chosen. In order to guarantee for a high degree of polymerization, the same level of purity needs of course also to be assured for the second component of the polycondensation. The ester of phenylboronic acid **4-14** was applied because the purification of esters is usually easier than the parent boronic

acids due to their reduced polarity. As in the case of **4-13a** and **4-13b**, rGPC was subsequently used to further enhance the level of purity. The ^{1}H NMR spectrum of **4-14** after extended drying under reduced pressure is shown in Figure 4-9.

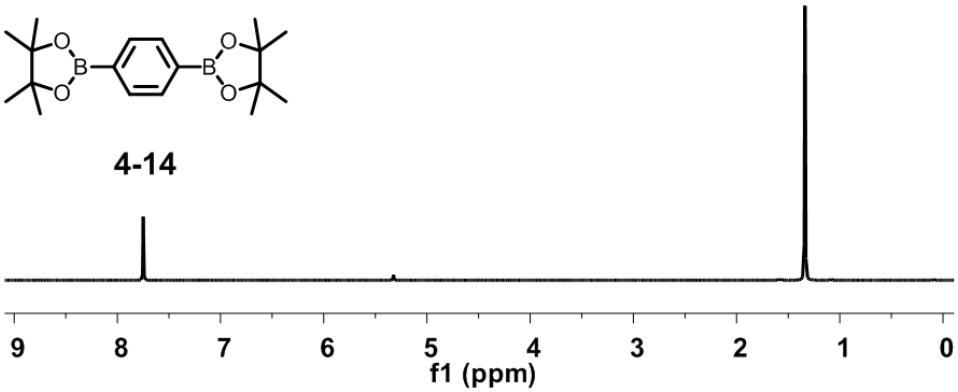

Figure 4-9: ^{1}H NMR spectrum of **4-14** in DCM-d_2 at 25 °C.

4.2.2 Model Compound

The motivation for the synthesis of a suitable model compound was the investigation of the cyclodehydrogenation on the level of a single molecule representative for the laterally extended poly(*para*-phenylenes).

Therefore, the structure of the model compound was directly derived from the repeat unit of the precursor polymers. Upon cyclodehydrogenation, a discotic nanographene with 84 aromatic carbon atoms and 14 benzene rings would be obtained which will be referred to as **C84**. Six peripheral dodecyl chains are expected to confine an enhanced solubility to the compound allowing for better characterization and a judgment regarding the suitability of the molecular design for GNR fabrication from the parent precursor polymers.

Also, the optimization of the reaction conditions for the cyclodehydrogenation of the precursor polymers should be facilitated if representative cutouts of the polymeric structure are studied on a smaller scale during preliminary experiments. In the past, the limited solubility and processability of chemically obtained GNRs constituted a major challenge rendering the evaluation of success and extend of the central graphitization reaction difficult.[32-39] This shall be circumvented by the concept of a model compound that can be more easily characterized.

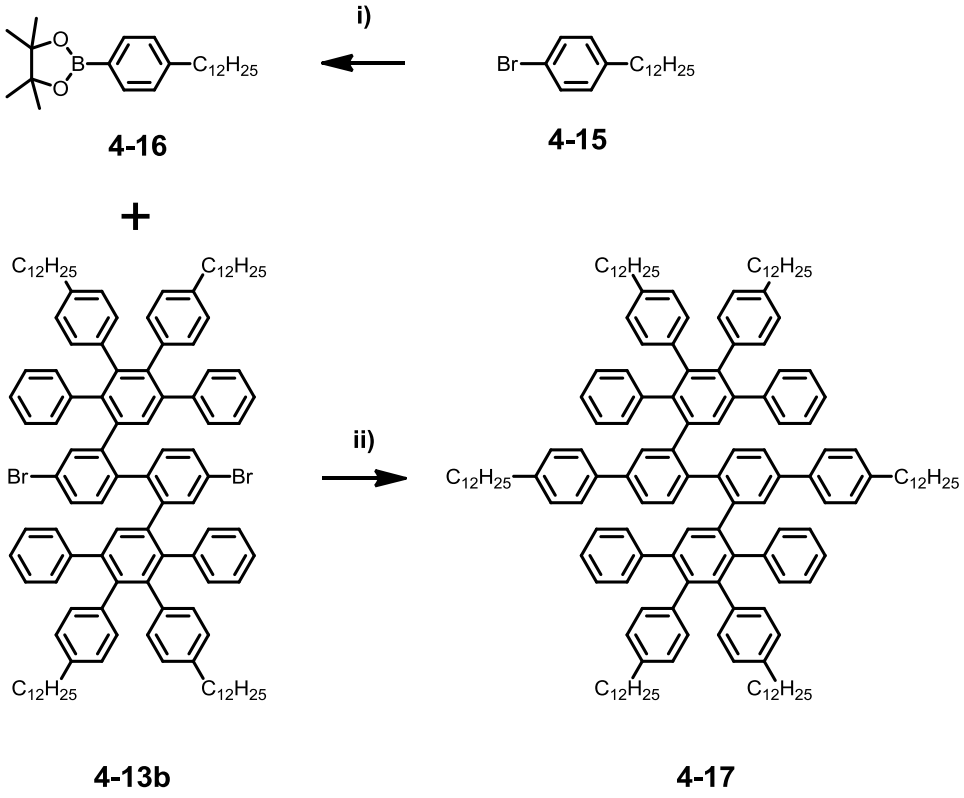

Figure 4-10: Synthesis of model compound **4-17**; conditions: i) $Pd(dppf)Cl_2$, bis(pinacolato)diboron, KOAc, dioxane, 90 °C, 83 %; ii) $Pd(Ph_3)_4$, K_2CO_3, toluene, Aliquat 336, reflux, 76 %.

As depicted in Figure 4-10, starting from monomer **4-13b**, a *Suzuki-Miyaura* cross-coupling with the pinacol ester of 4-dodecylphenylboronic acid **4-16** was employed for the build-up of model compound **4-17** (76 % yield).

4.2.3 Polymer Synthesis and Characterization

As a consequence of *Carother*s' law,[76] high number-average molecular weights M_n are only achieved *via* polycondensation at high conversion and if at the same time the stoichiometry of the functional groups is strictly maintained.

The number average degree of polymerization X_n is related to the molecular weight by the following expression in which M_0 constitutes the mass of the repeat unit:

$$X_n = \frac{M_n}{M_0}$$

The conversion of the polycondensation reaction *p* will greatly affect X_n due to the inverse proportional relationship of the two parameters:

$$X_n = \frac{1}{1-p}$$

Introducing the stoichiometric imbalance *r* which is defined as the fraction of the limiting groups [A] to the functional groups in excess [B] it can be written:

$$X_n = \frac{1+r}{1+r-2rp} \text{ with } r = \frac{[A]}{[B]}$$

If the two bifunctional monomers are present in stoichiometric amounts, thus $r = 1$, the previous equation reduces to the above *Carother*s' relationship. On the other hand, for $p = 1$, the following relation is obtained:

$$X_n = \frac{1+r}{1-r}$$

It is apparent that the purity of all reactants needs to be maximized in order to achieve a value close to unity for the stoichiometric imbalance *r*. Equally, the weighing of both monomer components has to be as precise as possible, which proves tedious for small amounts of reactant.

The polymerization of monomers **4-13a+b** with the bis(pinacol) ester of 1,4-phenyldiboronic acid **4-14** was carried out by applying standard *Suzuki-Miyaura* conditions (Figure 4-11).[45,46] Both components were placed in a *Schlenk* tube, which was then filled with toluene and a few drops of phase transfer agent *Aliquat 336*.

The concentration of the organic monomer phase was set to $1.2 \cdot 10^{-2}$ M as it is known that high concentrations are favorable for the formation of high molecular weight species during polycondensation. This is due to an enhanced probability of *inter*molecular coupling events.[77] Aqueous potassium carbonate solution (2 M) was added as a base. In order to prevent early deactivation of the catalyst, oxygen was removed *via* three freeze-pump-thaw cycles. Then, tetrakis(triphenylphosphine)palladium(0) was added to the mixture which was again degassed by three freeze-pump-thaw cycles.

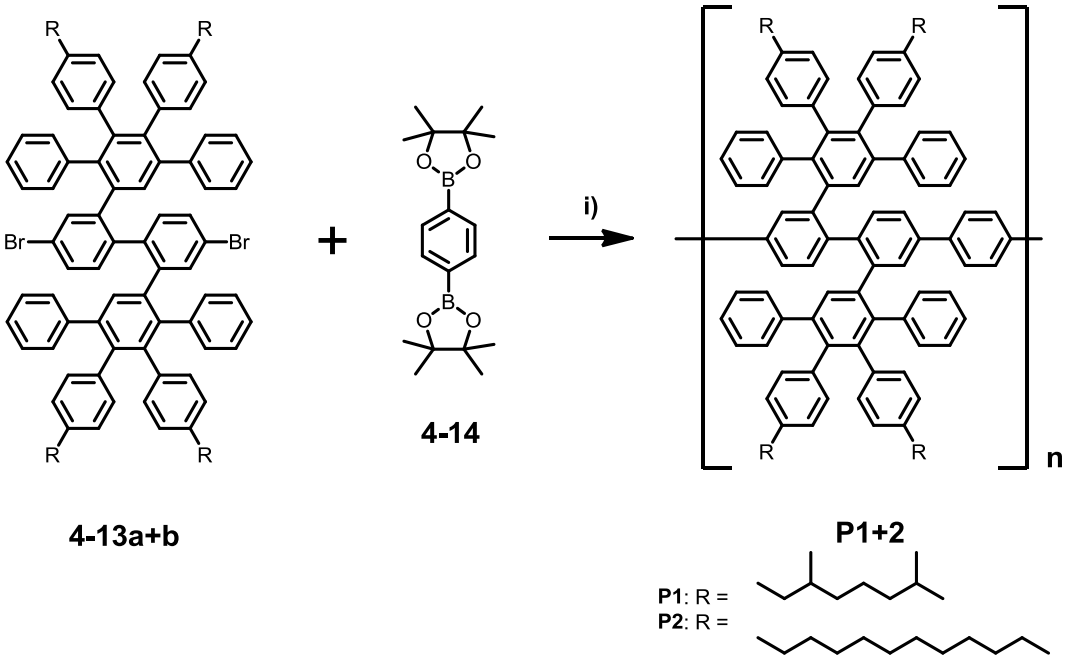

Figure 4-11: Synthesis of the laterally extended poly(*para*-phenylene) precursors **P1+2**; conditions: i) $Pd(Ph_3)_4$, K_2CO_3, toluene, Aliquat 336, reflux, 70 - 75 %.

The polymerization was then allowed to proceed for three days at reflux temperature. Afterwards, excess bromobenzene followed by excess phenylboronic acid were added as capping agents.

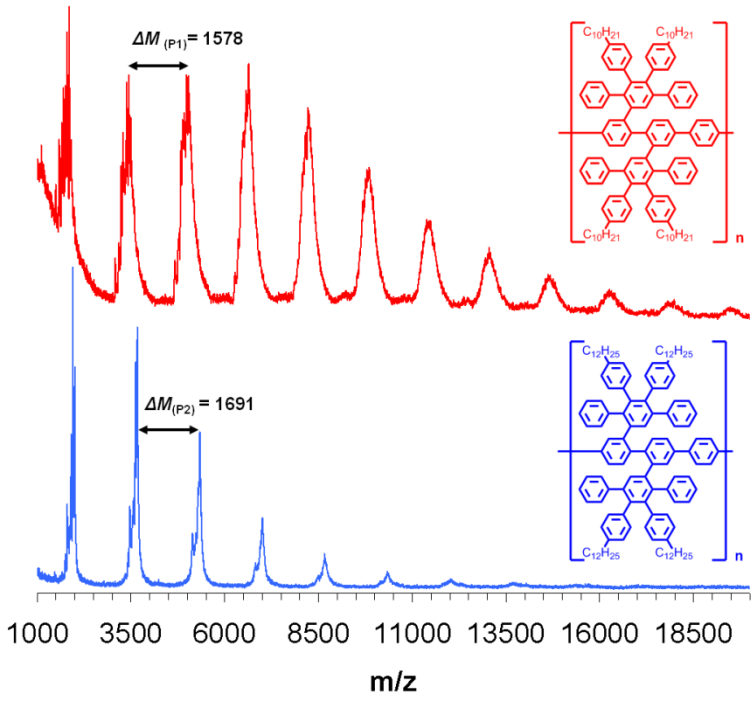

Figure 4-12: MALDI-TOF spectra of **P1** and **P2**.

The successful formation of high molecular weight species became obvious during the work-up procedure of **P1+2** since dropping of the reaction mixture into dilute methanolic hydrochloric acid lead to the instant formation of a white precipitate which was collected by filtration. The material was easily re-dissolved in DCM, filtered and re-precipitated as described above for two more times.

It is known that for *Suzuki* polycondensation reactions the average degree of polymerization rarely exceeds 20 - 30 primarily owing to the stoichiometry issue discussed above and the intrinsic insolubility of the rigid-rod polymers that are typically obtained *via* this approach.[44,45]

MALDI-TOF analysis of the well-soluble reaction products **P1+2** indicated the successful formation of polymers in both cases with molecular weights of up to 20000 g/mol corresponding to 10 - 12 repeat units (Figure 4-12). In view of the bulky oligophenylene monomer used and the steric screening of the bromine atoms these results highlight the suitability of the monomer design and the reaction conditions used. Also, the alkyl chain substitution and the twisting of the dendrons appear sufficient to prevent the reaction products from premature precipitation that would result in an undesired decrease of the molecular weight.

A regular pattern was observed with the peaks separated by a mass difference corresponding to the calculated repeat units of $\Delta M_{(P1)}$ = 1580 g/mol (**P1**) and $\Delta M_{(P2)}$ = 1693 g/mol (**P2**), respectively. Due to the considerable molecular weight of the repeat units, broad signals are obtained for which the isotopic distribution accounts. The mass of each individual peak corresponds to the calculated value even though residual functional groups seem to be still present despite the end-capping procedure.

Both spectra exhibit an exponential decline of the peak intensities which is due to the experimental setup for the MALDI-TOF measurements. Lower molecular weight species are easily desorbed by the laser pulse and reach the detector unit in larger amounts leading to saturation. Those species having higher molecular weight are less efficiently ionized and consequently do not show up with equal intensity. Even though the MALDI-TOF spectra do not reflect the effective molecular weight distribution of a polymeric sample, they are however a versatile analytical tool as absolute molecular weights can be derived.

Further analysis of the molecular weights of **P1+2** was carried out by analytical gel permeation chromatography (GPC). The GPC method relies on the relative determination of molecular weights by comparing the elution volume of the analyte to a calibration curve obtained from polymer standards of defined molecular weight. For the present analysis poly(styrene) (PS) and poly(*para*-pheylene) (PPP) were applied. The stationary phase separates based on the hydrodynamic volume of the analyte. If the

relation between size and corresponding molecular weight is known, the unknown molecular weight of the analyte can be derived with high accuracy.

However, significant conformational differences between the laterally extended poly(*para*-phenylene)s **P1+2** and the two standards PS and PPP are to be expected. Nevertheless, the GPC method can be used to compare the differences of a series of structurally related polymers. The signal of the UV-vis detector was used for the analysis. The narrow GPC curve of **P1** shows a rather continuous course with the maximum (from PS standard) located at 7000 g/mol which would correspond to an average of 3 - 4 repeat units. For **P2** a number average molecular weight of 6130 g/mol is found (Figure 4-13).

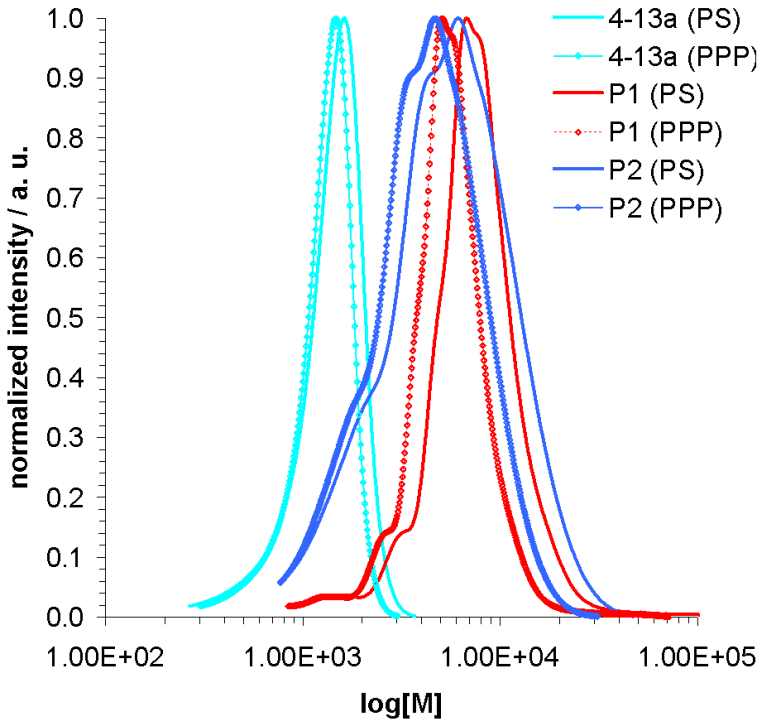

Figure 4-13: GPC traces of **P1** and **P2** and monomer **4-13a** as derived from the UV-vis signal.

In order to further validate the informative value of the chromatograms for the two polymers, monomer **4-13a** was also subjected to GPC analysis. Interestingly, the molecular weight of 1239 g/mol determined from the PS calibration curve is found in the same order of magnitude as the actual molecular weight of the molecule (1634 g/mol). The error of roughly 25 % needs to be taken into account when looking at the average molecular weights of **P1+2** which are underestimated by the GPC method.

Subsequently, the optical properties of both precursor polymers were studied and compared to those of model compound **4-17**. The UV-vis absorption spectrum of

polymer **P2** and the smaller oligophenylene **4-17** show a featureless absorption that extends to 350 nm and 390 nm, respectively (Figure 4-14).

The higher degree of conjugation for the polymeric species is reflected by the bathochromic shift of 40 nm and the higher molar extinction coefficient at wavelengths above 330 nm. A similar trend is found for the corresponding fluorescence emission spectra (Figure 4-14). For model compound **4-17** the maximum is found at 402 nm, whereas a small bathochromic shift towards a wavelength of 406 nm is observed for **P2**. Both spectra exhibit a symmetric continuous emission behavior with a slight tailing into the green region of the spectrum. No mirror effect is observed between excitation and emission of **P2**.

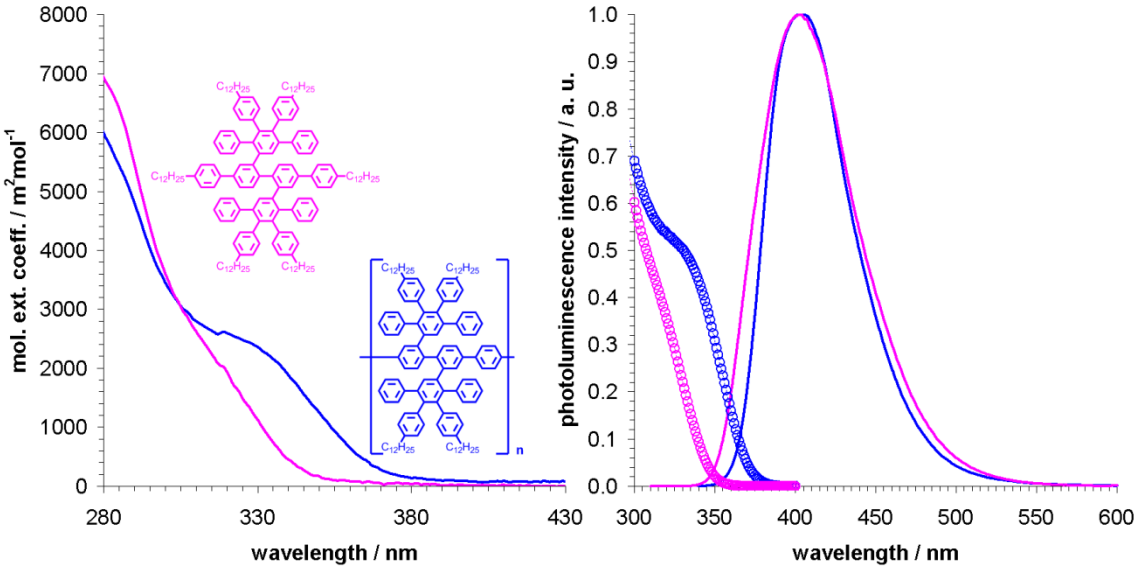

Figure 4-14: UV-vis absorption spectra of **P2** and model compound **4-17** in chloroform at 10^{-5} M (left), normalized fluorescence emission and excitation spectra of **P2** and model compound **4-17** in chloroform at 10^{-5} M (right).

The fact that the spectrum of the longer polymer **P2** exhibits only a minor bathochromic shift as compared to model compound **4-17** suggests that the conjugation along the main chain is hampered and that partial electronic decoupling of the repeat units occurs. A similar effect has been discussed for bi- and terpyrenyl compounds[78] as well as for poly(2,7-pyrenylene) in previous studies.[79] Also the strong twisting of the polymeric backbone needs to be taken into account.

4.3 Synthesis and Characterization of the C84 disc

4.3.1 Solution Cyclodehydrogenation

With model compound **4-17** at hand, various synthetic trials were performed towards the synthesis of the **C84** disc (Figure 4-15). Apart from its relevance as a model case for the targeted graphene nanoribbons, the preparation of large PAHs of high carbon/hydrogen ratio is also of interest due to the properties such low-bandgap materials exhibit. The substantial experimental and theoretic experience of the *Müllen* group allowed for the preparation of well-defined PAHs such as **C54**,[49,50] **C60**,[51,52] **C78**,[56,59,60] **C96**,[61,62] **C132**[63] and **C222**[64] *via* oxidative cyclodehydrogenation of oligophenylenes in the past.

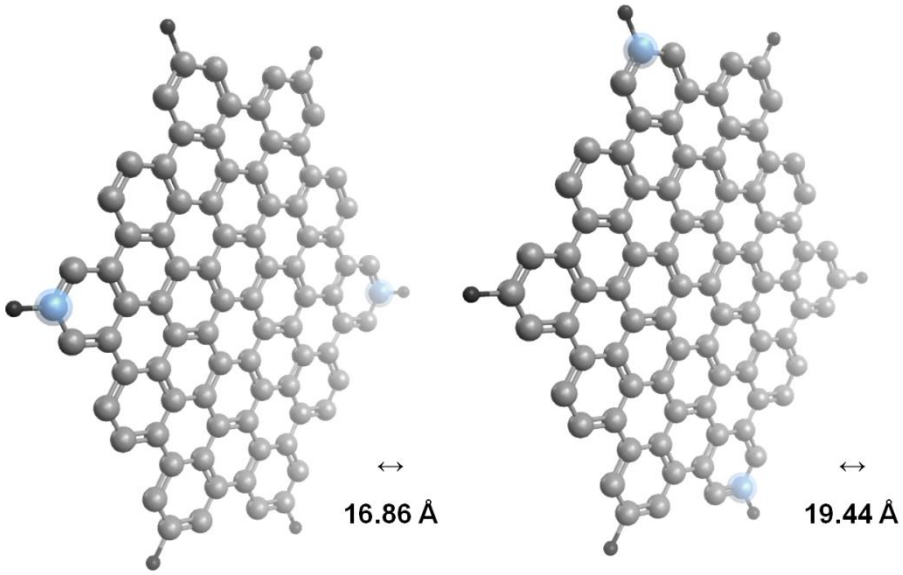

Figure 4-15: Geometric dimensions of the **C84** core as derived from computational analysis (MMFF94s).

The synthetic protocol that provided access to the aforementioned variety of large PAHs is commonly based on the planarization of suitable oligophenylenes. Most important, the targeted carbon framework of the PAH is already prepared in the well-soluble precursor compounds which, however, adopt twisted three-dimensional conformations prior to their oxidative cyclodehydrogenation. It is apparent that the graphitization step will work especially well if a high degree of planarity is already confined to the precursor molecule.[54,55] Substitution of the latter with a flexible shell of alkyl chains also guarantees for the processability of the planarized target molecules.

Due to similar size and geometry, the previous works on the structurally related **C72** disc ("supernaphthalene") carried out by *Müller*[53] and *Wasserfallen*[55] are particularly relevant to the synthesis of **C84**.

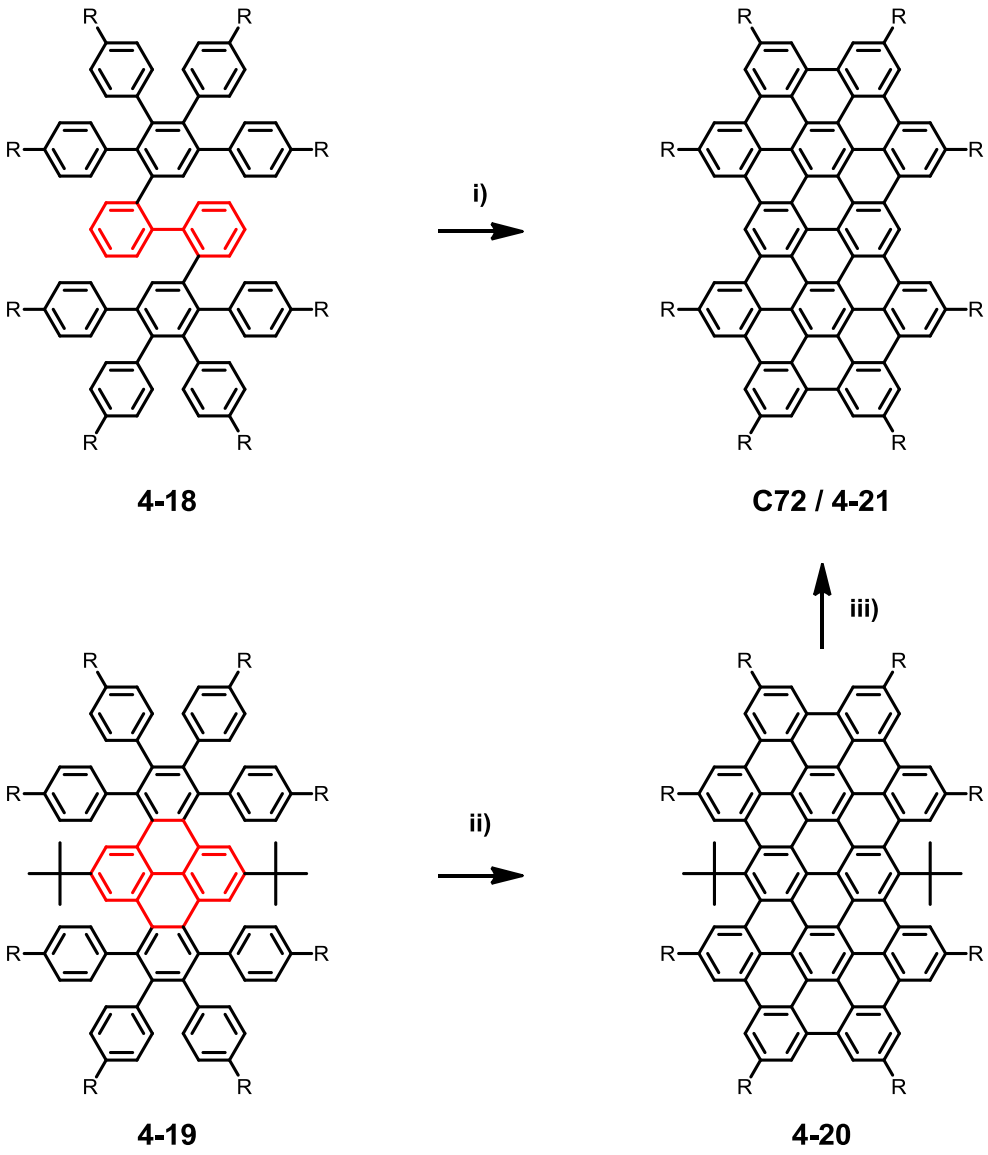

Figure 4-16: The synthetic approaches of *Müller*[53] and *Wasserfallen*[55] to the **C72** disc; conditions: i) $CuCl_2/AlCl_3$, $C_2H_2Cl_4$, 145 °C, 90 %; ii) $FeCl_3$, DCM/CH_3NO_2, RT, 85%; iii) oleum (65%), benzene, 150 °C, 95%.

In the first case, the oligophenylene precursor **4-18** was built from a biphenyl backbone to which two 2,3,4,5-tetraphenylbenzene dendrons were attached (indicated in red in Figure 4-16). This design results in a high degree of conformational freedom since the phenyl rings are able to rotate around formal single bonds. A problematic situation arises also from the twisted conformation that the central biphenyl unit will adopt in order to minimize the steric interaction of neighboring protons. As a consequence, the

oligophenylene could only be planarized to **C72** under harsh experimental conditions. Hence, treatment with a mixture of copper(II) chloride and aluminium(III) chloride in TCE at an unusually high temperature of 145 °C had to be applied for the successful preparation of the PAH *via* this route.[53]

Later on, more detailed studies lead to the development of a second synthetic approach which was improved by the introduction of a pyrene core to the precursor **4-19** (indicated in red in Figure 4-16).[54,55] This structural motif resulted in a significant pre-planarization of the molecule which strongly facilitated the subsequent cyclodehydrogenation reaction using moderate amounts of ferric chloride. Two peripheral *tert*-butyl groups efficiently prevented aggregation so that compound **4-20** could be fully characterized by NMR spectroscopy.[55] Final treatment of this PAH with oleum was used to cleave off the *tert*-butyl groups leading to the formation of **C72** (Figure 4-16). The versatility of this design concept was further applied to the synthesis of smaller ovalene-type PAHs[80] and larger GNR systems highlighting the importance of a suitable precursor geometry.[38]

The geometric and conformational situation of model compound **4-17** resembles that of precursor **4-18** which was used for the formation of **C72** according to the route of *Müller.* Also in the present case, a substituted biphenyl unit is found at the core of the molecule. However, the introduction of two additional benzene rings in the indentation of precursor **4-18** should assist in the planarization of model compound **4-17** (Figure 4-17) as well as the laterally extended poly(*para*-phenylenes) **P1+2**. In the polymer case the indentations are “filled” by the benzene ring of comonomer **4-14**.

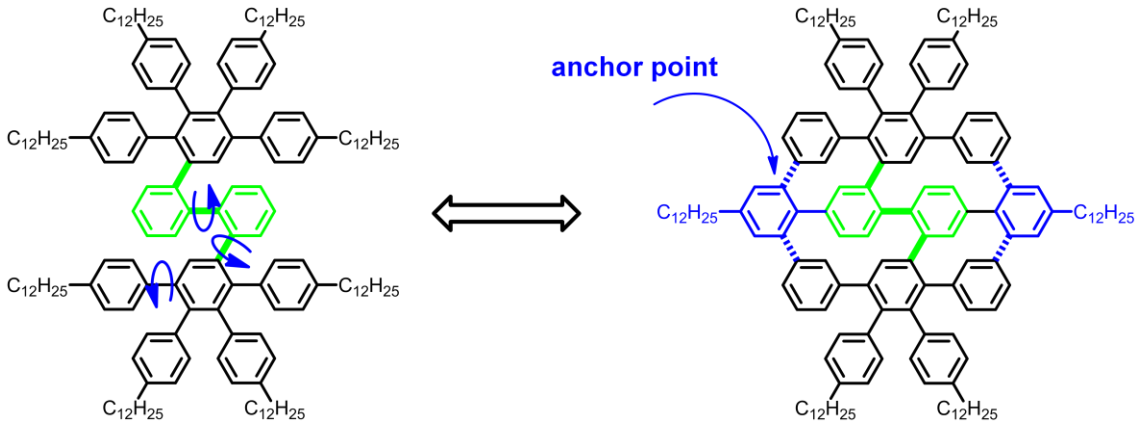

Figure 4-17: Comparison between the geometry of the **C72** precursor of *Müller*[53] and model compound **4-17** possessing additional anchor points.

As depicted in Figure 4-17, these benzene units represent additional anchor points for the attachment of the two 2,3,4,5-tetraphenylbenzene dendrons to the linear backbone

of the molecule during the planarization (indicated by the dashed blue lines). They should also counteract the aforementioned twisting of the central biphenyl core. Whereas the two dendrons rotate in the case of compound **4-18** resulting in a strongly twisted non-planar conformation, the conformational flexibility of the entire molecule is hampered and further decreased at early stages of the cyclodehydrogenation reaction as a consequence of the modified geometry of oligophenylene precursor **4-17**.

Initial attempts towards the synthesis of **C84** were carried out using moderate amounts of ferric chloride (2.00 - 3.00 bond equivalents) but resulted not in the formation of the desired compound. Only partially cyclodehydrogenated intermediates were observed by MALDI-TOF spectroscopy even after an extended reaction time of one week.

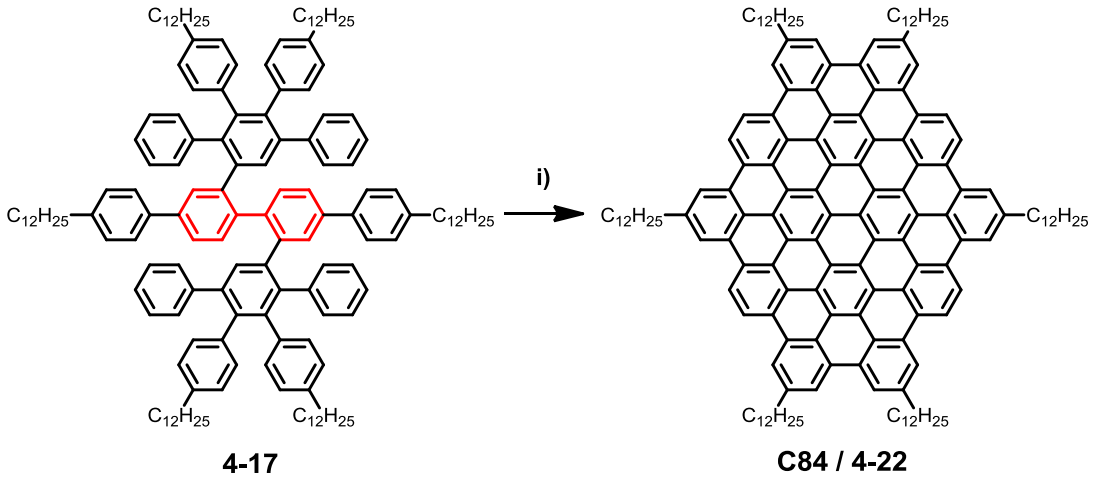

Figure 4-18: Synthesis of the **C84** disc; conditions: i) $FeCl_3$, DCM/CH_3NO_2, RT, 91%.

The amount of the oxidant had then to be progressively increased to 7.50 bond equivalents. Isolation of the PAH from this reaction was achieved by dropping of the reaction mixture into excess methanol leading to the instant precipitation of the compound. Remaining inorganic impurities and side-products were fully removed by repeated dissolution and precipitation of the compound to provide a reddish brown solid in 91 %.

In the next step, the purity of **C84** was verified by MALDI-TOF spectroscopy (Figure 4-19). The target peak was observed in the corresponding spectrum as exclusive species and no partially fused by-products were detected. The possibility for isotopic resolution of this high molecular weight compound enabled the comparison of the measured spectrum to the calculated isotopic distribution which stretches over seven mass units. The experimental data from **C84** is in perfect accordance to the theoretic pattern thus proving the presence of the desired PAH (see inset of

Figure 4-19). However, due to the severe excess of ferric chloride, chlorination of the final disc could not be fully avoided as it can be seen from the corresponding spectrum containing peaks of chlorinated species. Attempts to suppress chlorination by removal of hydrochloric acid through extended argon bubbling over the whole reaction time failed. The same holds for trials to remove the chlorine atoms *via* reductive post-treatment in the presence of samarium(II) iodide.[81] The versatility of this approach has been for example demonstrated in the reductive alkylation of α-cyano ketones.[82]

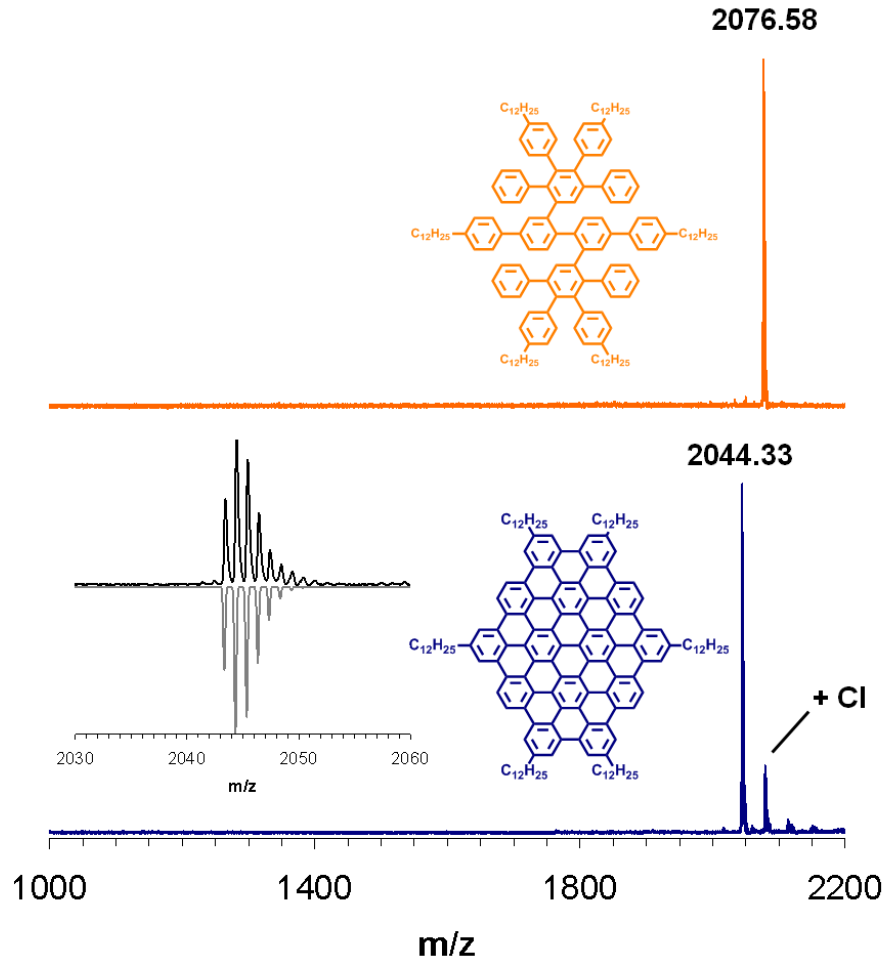

Figure 4-19: MALDI-TOF spectra of the **C84** disc and the oligophenylene precursor **4-17**; the inset shows a comparison between experimental (black) and calculated (gray) isotopic pattern of the **C84** disc.

In contrast to the analysis of **C78$_{hexa}$** which will be discussed later the NMR analysis of **C84** was not possible due to the presence of aggregates in solution.

For the planarization of extended disc-like molecules, an “outside-in” pathway has been proposed.[54] This means that the fusing of benzene rings starts at the well-accessible outer rim of the precursor and then proceeds towards the inner core of the molecule where shielding and steric crowding is strongest. In the present case, this pathway

would result in the initial formation of two **C30**-panels which are orientated perpendicular to each other as shown for intermediate **4-17i** (Figure 4-20). In fact it was proven experimentally that the smaller PAH **C30** can be prepared from a precursor that exhibits the same topology that is encountered in the two dendrons of **4-17**.[54,83]

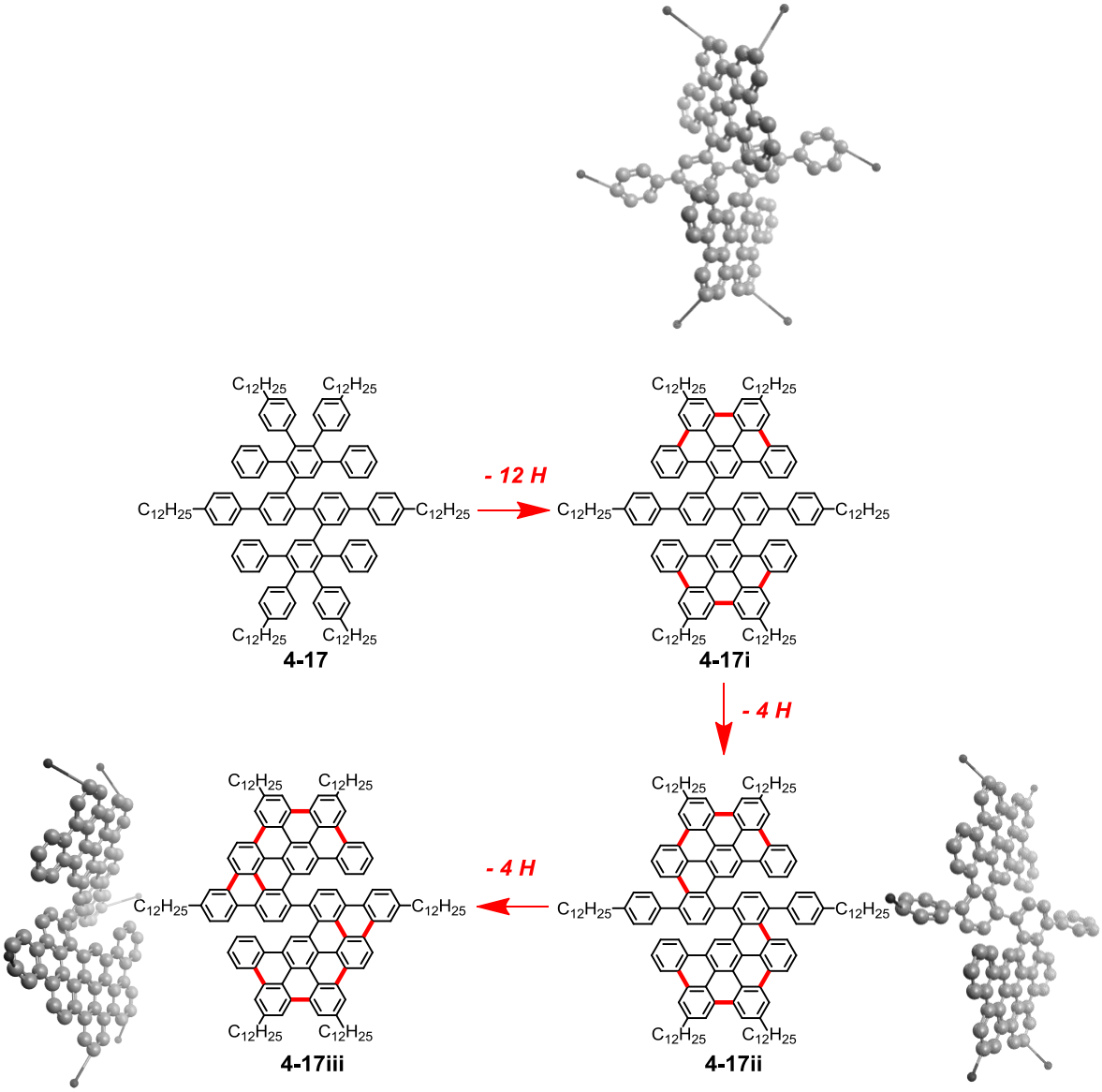

Figure 4-20: Proposed pathway for the cyclodehydrogenation of oligophenylene **4-17** to the **C84** disc and computational analysis of the possible intermediates (MMFF94s).

At this point, the steric strain due to the repulsion of neighboring hydrogen atoms can be still minimized due to the perpendicular orientation of the two panels. Further loss of four hydrogen atoms results in the build-up of two **C36**-units and compound **4-17ii**. Similar to **C30** the **C36** molecule has also been prepared as a model case from a

structurally identical oligophenylene precursor.[83] The gain in aromaticity is, however, strongly outnumbered by severe steric repulsions which might lead to a kinetic entrapping at this point of the reaction. Another hint for a pathway *via* **C36** formation is given by the fact that the partially fused species seen by MALDI-TOF spectroscopy at lower oxidant concentration have the same mass as intermediate **4-17ii**.

It is believed, that the two anchor points represented by the two peripheral benzene units will then assist in the further planarization of the molecule towards **4-17iii** *via* extension of the panels to **C42**-units. This step brings the two panels into spatial proximity that is needed for the formation of the final bonds. However, this final reaction step towards **C84** only proceeded at the maximum concentration of 7.50 bond equivalents ferric chloride. This indicates an unfavorable interplay of geometry and steric strain that has to be overcome during the graphitization reaction of **4-17**.

4.3.2 Structural Characterization

Due to the good solubility of the PAH, UV-vis analysis could be used to further study the **C84** core. Electronic spectroscopy is an important tool in the field of PAH chemistry as it provides a facile insight into the purity and optoelectronic nature of the molecules.[84] The absorption spectra of PAHs are typically composed of three main bands which are denominated as *α*-, *β*-, and *p*-bands according to the original nomenclature of *Clar*.[84,85] As a result of the larger conjugated *π*-system of PAHs the absorption is typically shifted to intermediate and long wavelengths.[84]

This is seen when comparing the location of the absorption maximum of precursor compound **4-17** at 255 nm to the spectrum of **C84**. For the PAH the main band is bathochromically shifted by more than 200 nm to a value of 473 nm as a result of the large *π*-system which has been formed during the cyclodehydrogenation reaction.

Due to its intensity and its lower wavelength in comparison to the other bands of the spectrum this prominent band can be identified as the *β*-band with a molar extinction coefficient of 6864 m^2/mol.[84,85] It typically arises from a transition involving the HOMO and the second lowest unoccupied orbital LUMO+1.[80,86]

At an order of magnitude lower a shoulder is detected at 564 nm which corresponds to the *p*-band of the PAH. This band is usually of intermediate intensity and can be assigned to a transition from the HOMO to the LUMO level.[80,86]

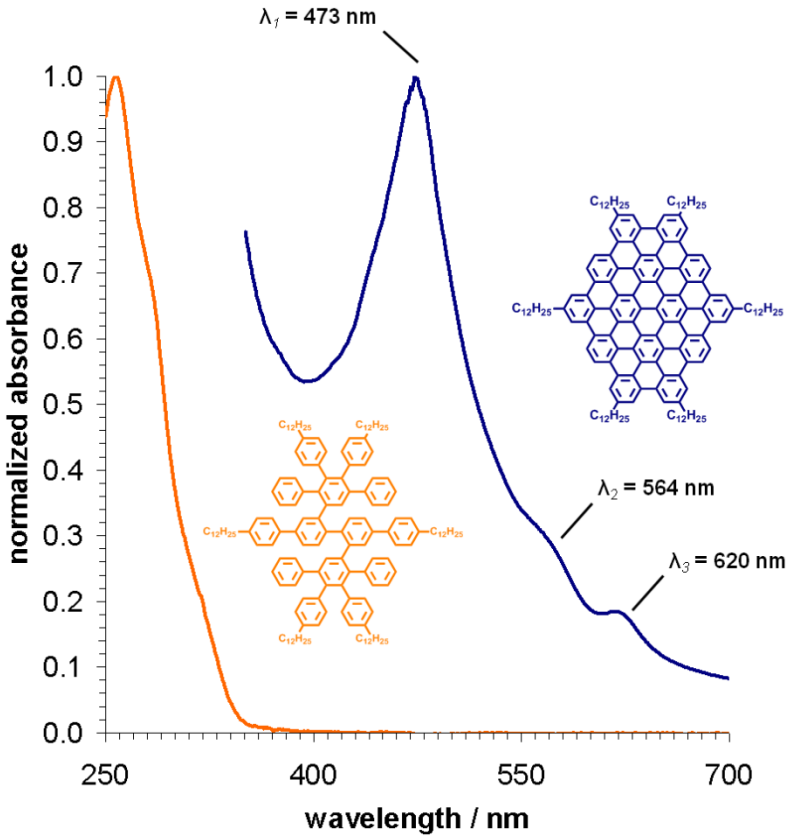

Figure 4-21: Normalized UV-vis absorption spectra of the **C84** disc and oligophenylene **4-17** in THF at $5 \cdot 10^{-6}$ M.

The small signal at 620 nm can be assigned to the *α*-band which is typically found at long wavelengths and low intensities.[85] For large PAHs, the highest wavelength absorption corresponds to the transition from the lowest vibrational energy level of the ground state to the lowest vibrational energy state of the exited state.[85] By converting the corresponding wavelength into an energy difference the HOMO–LUMO energy gap of a molecule can be easily derived. The wavelength of the *α*-band at 620 nm thus translates into a band gap of 2.0 eV.

The spectroscopic analysis of **C84** is in line with the results obtained from discs of similar size. Compared to **C72** for which the *β*-band is found at 441 nm[55] and **C78** exhibiting an absorption maximum at 445 nm[59] the corresponding value of **C84** is shifted bathochromically which is a consequence of its larger aromatic system. This finding confirms the complete cyclodehydrogenation of precursor **4-17** to the PAH because partially fused species would lead to a significant hypsochromic shift that is, however, not observed in the spectrum of **C84**.

The thermal properties of the **C84** disc were subsequently studied by DSC. In the temperature range from - 100 °C to 300 °C only one phase transition is observed upon second heating at 73.7 °C (Figure 4-22). Above this temperature level, **C84** enters the

liquid crystalline (LC) state. As evidenced by 2D-WAXS experiments performed in cooperation with *A. Mavrinskiy* and *Dr. W. Pisula* (MPI-P Mainz, Germany) on an extruded fiber, **C84** forms columnar structures in which the disc-shaped molecules are arranged perpendicular to the columnar axis.[87,88]

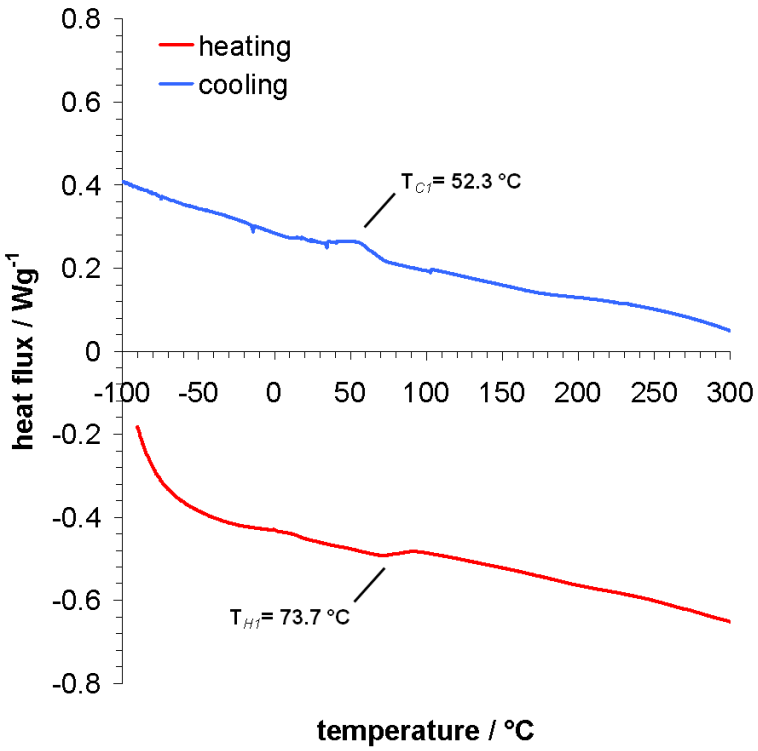

Figure 4-22: DSC trace of the **C84** disc upon second heating (red) and cooling (blue).

Strong *π*-stacking interactions are observed leading to a typical *inter*molecular separation of the disc by p = 0.35 nm as derived from the meridional reflections in the pattern (Figure 4-23).

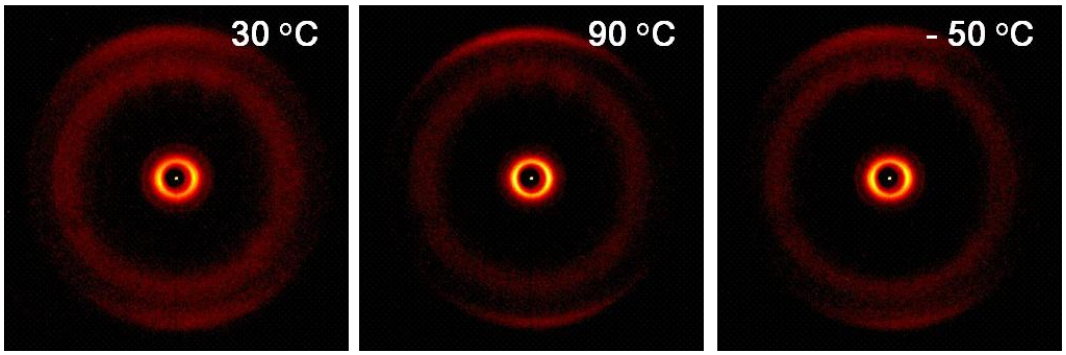

Figure 4-23: Temperature-dependent 2D-WAXS patterns of the **C84** disc.

The equatorial reflections indicate an *inter*columnar organization which is described by a hexagonal unit cell with a_{hex} = 3.20 nm as the parameter at a temperature of 90 °C. The LC organization remains unchanged for **C84** after cooling down the sample below the temperature of the phase transition. The broadening of the meridional reflections is the only evidence for a slight structural modification pointing towards a decreased *intra*columnar order. This minor change can be explained in terms of increased steric demand of the alkyl substituents. In summary, the 2D-WAXS analysis is in agreement with the behavior that is to be expected from a fully planarized PAH such as **C84**. In this respect the results along with the outcome of the spectroscopic investigation can serve as an additional prove for the successful preparation of the target molecule.

4.3.3 Surface Cyclodehydrogenation

For STM-controlled surface cyclodehydrogenation experiments in cooperation with the group of *Fasel* (EMPA Dübendorf, Switzerland) pre-planarized and non-substituted precursor compounds are needed. The reaction, transformation and manipulation of single molecules on surfaces under STM control has recently emerged as a new discipline in the field of surface science. [39-41,65,89] The selective formation of single carbon-carbon bonds *via* thermal annealing on metal substrates has been demonstrated in the transformation of hexaalkoxy-substituted hexaphenylbenzene to the corresponding HBC[89] and of cyclic oligoarylenes to triangular-shaped nanographene molecules.[65]

In view of the size of **C84** the possible formation of this PAH directly on the surface would provide valuable information regarding the suitable design of future precursor compounds. Based on the design of the solution-processable **C84** disc, an analogous compound was synthesized in two steps from 4,4'-dibromo-2,2'-diethynyl-1,1'-biphenyl **4-6**. *Diels-Alder* cyclodaddtion with phencyclone **4-12** successfully resulted in the formation of compound **4-23** which contains two rigidified triphenylene dendrons. Subsequent double *Suzuki-Miyaura* coupling of the bromine groups with phenylboronic acid was used to “close” the indentation in a similar fashion as discussed for the oligophenylene compound **4-17**. The final nanographene precursor is characterized by a molecular backbone that is solely composed of aromatic rings and does not contain a lateral alkyl substitution that is imperative for solution-based experiments.

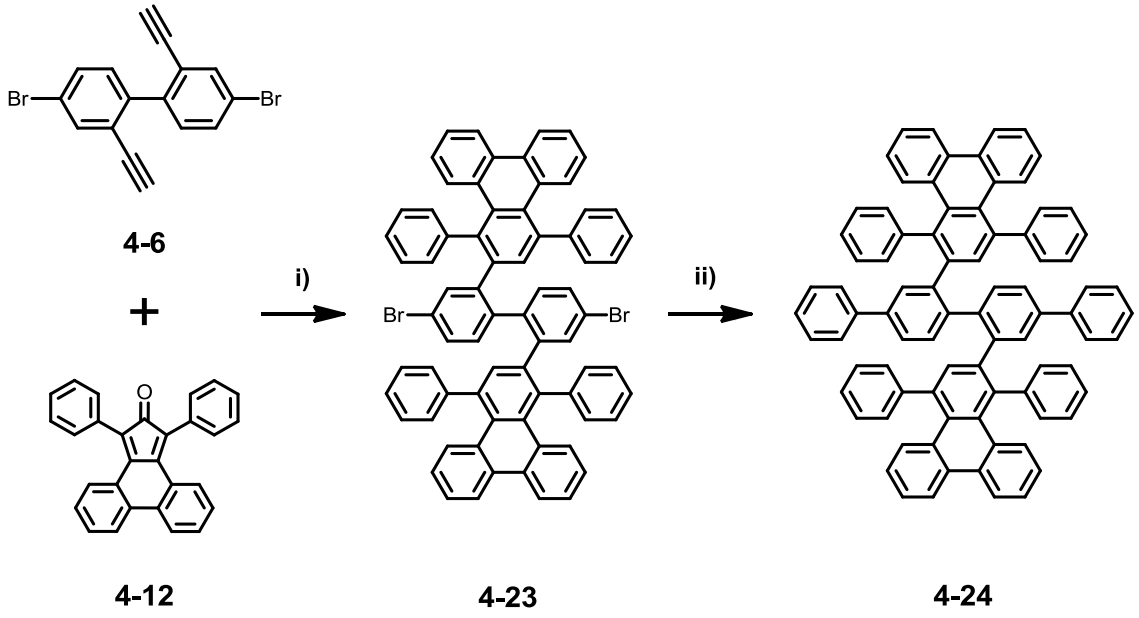

Figure **4-24**: Synthesis of the STM-precursor **4-24**; conditions: i) *ortho*-xylene, 160 °C, µW, 300 W, 81 %; ii) phenylboronic acid, $Pd(Ph_3)_4$, K_2CO_3, toluene, Aliquat 336, reflux, 61 %.

The MALDI-TOF spectrum of **4-24** is shown in Figure 4-25 and reveals the target peak of the desired compound as exclusive species. The ^{1}H NMR spectrum of the molecule had to be recorded in TCE-d_2 at elevated temperature due to enhanced coalescence of the aromatic signals. At 130 °C the signals are well-resolved and peak integration can be performed to further prove the purity of the STM precursor (Figure 4-25). Due to the similarity of the chemical environment of the protons along with their high number the exact peak assignment was not possible.

Despite its considerable molecular weight of 1063.33 g/mol, precursor **4-24** could be then successfully deposited on an Au(111) surface by means of UHV sublimation for the subsequent STM experiments. It was hoped that by thermal annealing of the molecule on the surface the formation of the fully planarized PAH would be achievable in analogy to the previously discussed cases.[65,89]

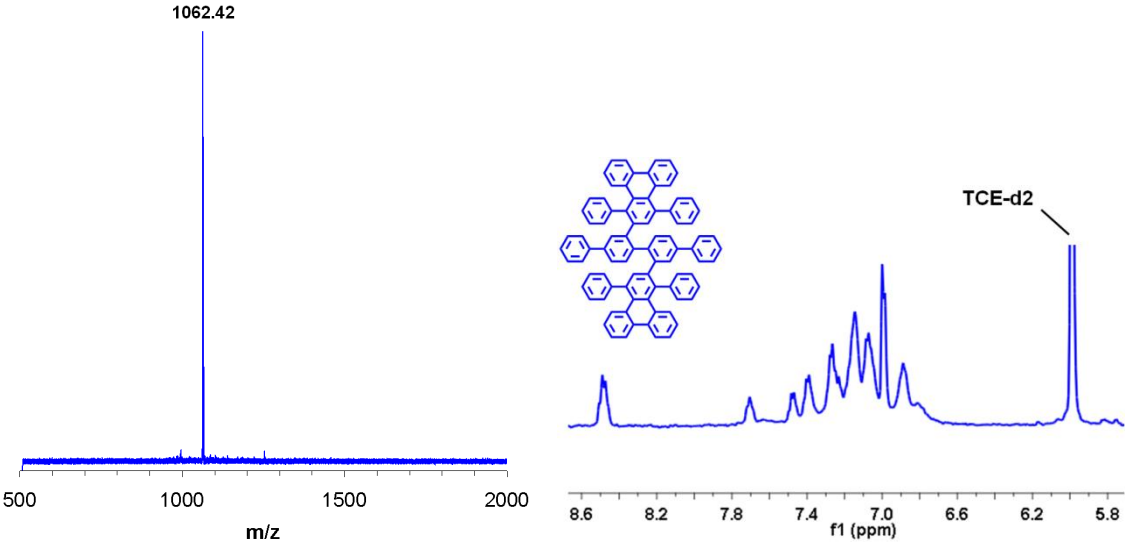

Figure 4-25: MALDI-TOF spectrum (left) and ^{1}H NMR spectrum of the aromatic region of STM- precursor **4-24** in TCE-d_2 at 130 °C (right).

As it can be seen in Figure 4-26A the gold surface is not homogenously covered and the resolution is rather low due to the mobility of the molecular species on the substrate. This makes it difficult to assign as to what degree the surface-assisted cyclodehydrogenation of **4-24** proceeded. After annealing at 200 °C, flat molecules are found at various positions of the gold substrate. Their size is in accordance with the molecular dimensions of the **C84** core.

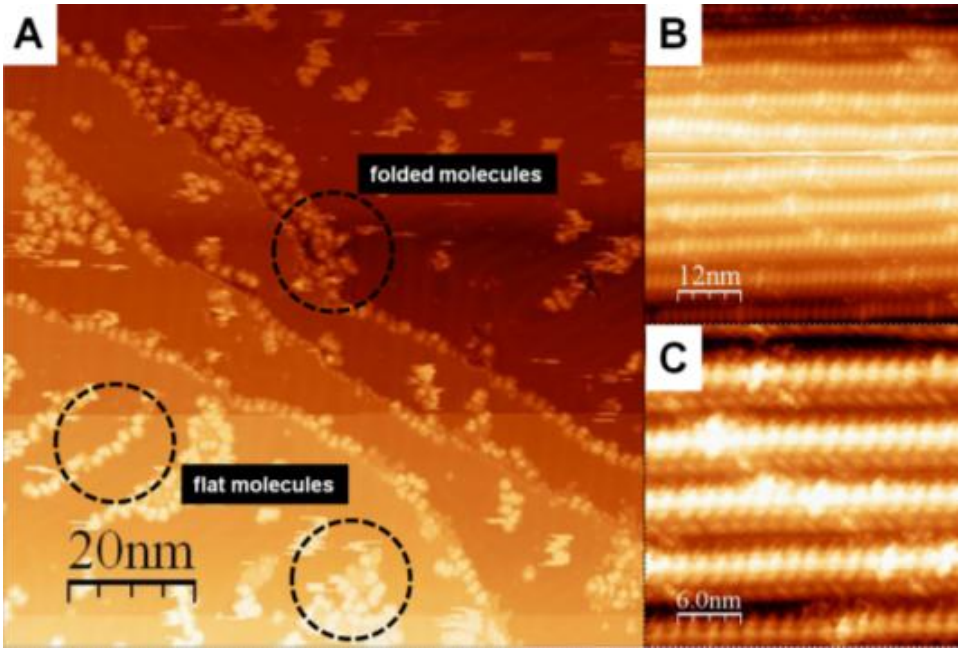

Figure 4-26: STM images of **4-24** after deposition and annealing at 200 °C on Au(111).

Nevertheless, also partially planarized or folded species are observed as indicated in Figure 4-26-A. Interestingly, the steps of the substrate are covered with a dense array of the molecules which appear to be orientated edge-on at these positions (Figure 4-26B and Figure 4-26C).

In view of these results it can be concluded that the geometry of precursor **4-24** in principle allows for the formation of **C84**. Nevertheless, the increased number of non-planarized molecules suggests that the rigidity of the two dendrons is not sufficient to completely decrease the conformational flexibility. The twisting which has been discussed for the solution case is likely to interfere with the cofacial adsorption of the molecues to the metal substrate. The introduction of anchor groups such as alkoxy or thiol functions could resolve the problem.[89] Also the aforementioned pre-planarization of the central core of **C72** *via* the introduction of a pyrene motif would be beneficial.[54,55]

4.4 Suzuki-Based Graphene Nanoribbons

After the cyclodehydrogenation series that resulted in the formation of the **C84** disc at high oxidant concentration, analogous attempts were carried out on the laterally extended poly(*para*-phenylenes) **P1+2** according to the determined experimental conditions. The products of the cyclodehydrogenation reactions on **P1** and **P2** will be referred to as **GNR1** and **GNR2** in the following paragraph, respectively.

In a typical experiment the polymeric precursor was dissolved in DCM after what the oxidant was slowly added. Based on the synthetic conditions derived from the synthesis of **C84**, the cyclodehydrogenation reactions of **P1** and **P2** were carried out in the presence of 7.50 bond equivalents of ferric chloride at room temperature. In all experiments, a black precipitate formed shortly after the start of the reaction. It was collected by filtration after 24 h and purified by washing with water and methanol.

A second oxidative treatment applied on **P1** consisted in the cyclodehydrogenation with a mixture of phenyliodine(III) bis(trifluoroacetate) (PIFA) and boron trifluoride etherate $BF_3 \cdot Et_2O$ in DCM.[90] It is known that PIFA when activated by a *Lewis* acid readily reacts with a broad range of substrates to give biaryl products in excellent yields.[91] Furthermore, it was recently applied to the synthesis of triphenylenes[42] and HBC derivatives.[43] Importantly, undesired chlorination which is frequently observed when applying ferric chloride can be ruled out by this procedure. The reactions with PIFA/ $BF_3 \cdot Et_2O$ (2.50 bond equivalents) were started at - 60 °C and the thermal level was slowly raised to room temperature after 2 h. The reaction was allowed to proceed for additional 24 h after what it was stopped by addition of methanol. The black precipitate that had formed was separated from the reaction mixture and washed as described above.

The materials obtained from the two cyclodehydrogenation protocols were completely insoluble in common organic solvents and could thus only be characterized in a powder form. This fact significantly limited the number of analytical tools available for the characterization of the two graphene nanoribbons.

It was however possible to record MALDI-TOF spectra of the materials when a solvent-free preparation with TCNQ as matrix was used. The spectrum of **GNR1** obtained from the reaction with ferric chloride contains a regular pattern (Figure 4-27). The number of detected repeat units is the same as for the precursor polymer **P1**. Further comparison to the spectrum of **P1** reveals that the signals of **GNR1** at the corresponding repeat unit are slightly shifted to a lower molecular weight which is in accordance with the expected mass loss effect of the cyclodehydrogenation reaction.

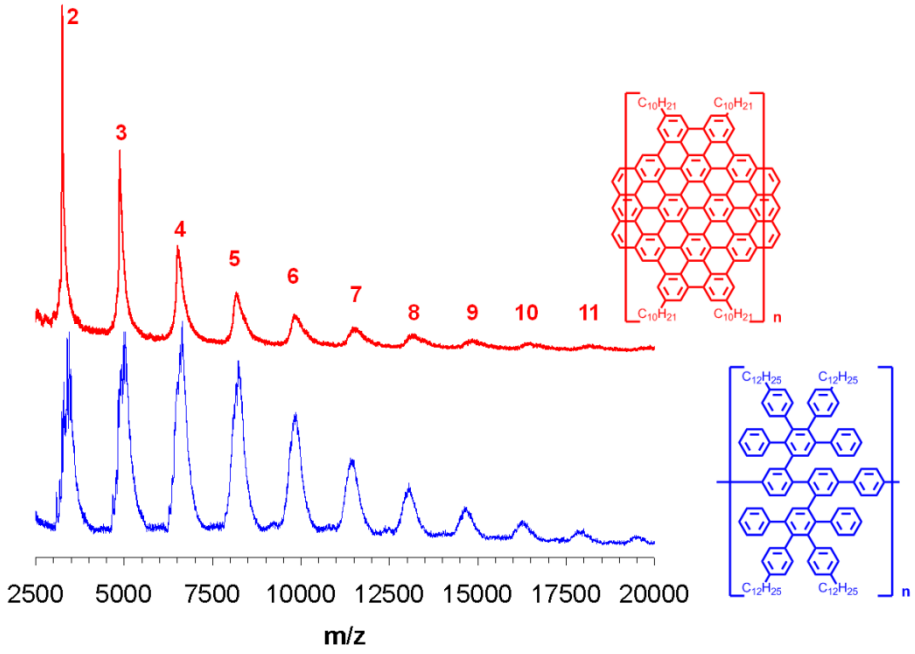

Figure 4-27: MALDI-TOF spectra of **GNR1** (red) and precursor polymer **P1** (blue) after treatment with $FeCl_3$.

At molecular weights above 10000 g/mol (corresponding to seven repeat units) the signals are however found at higher masses with respect to the spectrum of precursor **P1**. On the one hand this effect might be attributed to partial chlorination of the GNR.

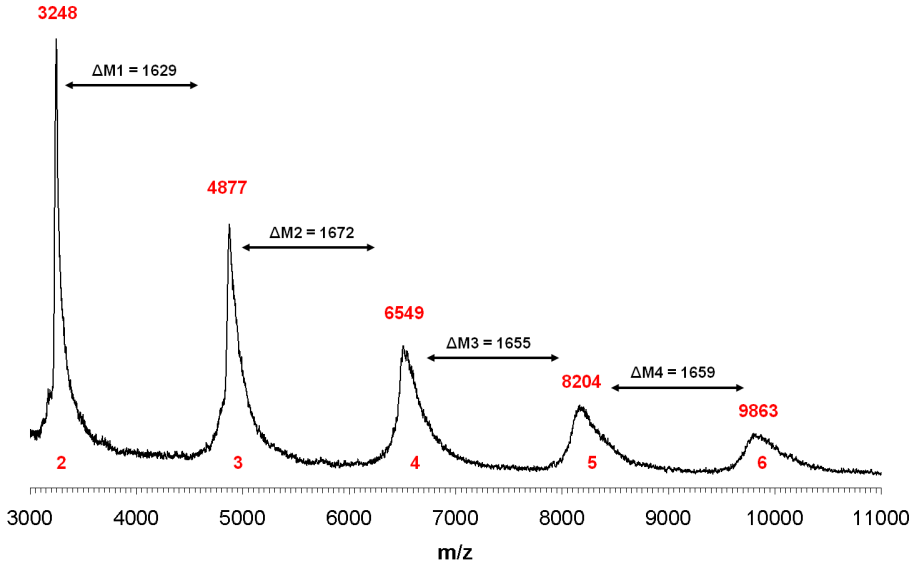

Figure 4-28: Detailed view on the MALDI-TOF spectrum of **GNR1**.

On the other hand, the large peak width in the spectrum of **GNR1** makes the determination of subtle mass changes impossible to verify (Figure 4-28).

After the cyclodehydrogenation of **P2** with ferric chloride a similar broadened pattern was observed. The smaller number of repeat units for this precursor is reflected by the spectrum of **GNR2** for which up to eight repeat units are detected by the method corresponding to molecular weights of 15000 g/mol. (Figure 4-29). Importantly, even though less resolved, a similar spectrum was also obtained after treatment of **P2** with PIFA/ $BF_3 \cdot Et_2O$ illustrating the efficiency of this alternative approach. For all peaks a small mass loss is found which remains difficult to quantify due to the broadness of the signals.

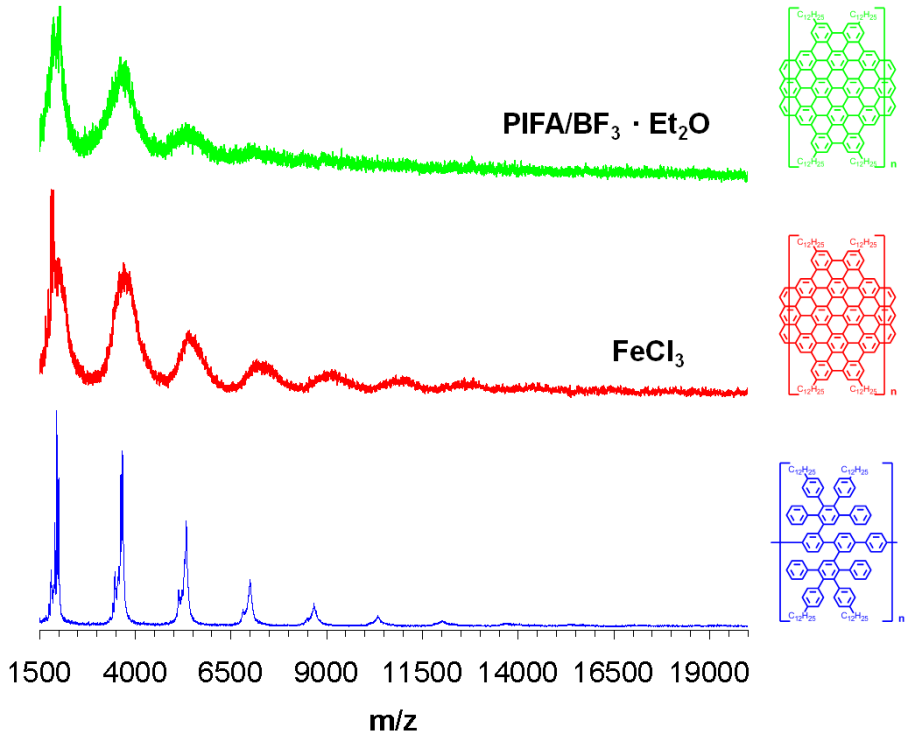

Figure 4-29: MALDI-TOF spectra of **GNR2** as obtained from oxidative treatment with PIFA/ $BF_3 \cdot Et_2O$ (top) and ferric chloride (middle). At the bottom the spectrum of precursor polymer **P2** is shown.

Further investigations on the chemical nature of the GNRs were carried out by vibrational spectroscopy. Both, FTIR and Raman spectroscopy are non-destructive spectroscopic methods for which no soluble analyte is needed.

At first view, the FTIR spectrum of **GNR2** appears simplified with respect to the spectrum of parent **P2** (Figure 4-30). The main structural features (aromatic rings, alkyl chains) are however conserved after the cyclodehydrogenation reaction. Several regions of the FTIR spectrum in which characteristic bands are located were selected with the aim to obtain information about the chemical changes upon transformation of **P2** into **GNR2**. Of particular usefulness are the traditional group frequencies which are normally applied to the spectroscopic analysis of monosubstituted benzene rings.[92]

Starting at high wavenumbers, the first relevant signal is found at 4050 cm^{-1}. This very weak band is attributed to the free rotation of benzene units.[36,92] For the detection of this signal the scan number of the FTIR spectrometer had to be increased to 2000. Despite its low intensity it is clearly observed in the spectrum of **P2** which is composed of non-annelated benzene rings. In contrast, only highly substituted aromatic rings are expected for the structure of **GNR2**. Consequently, this band is absent in the spectrum of the GNR (Figure 4-31).

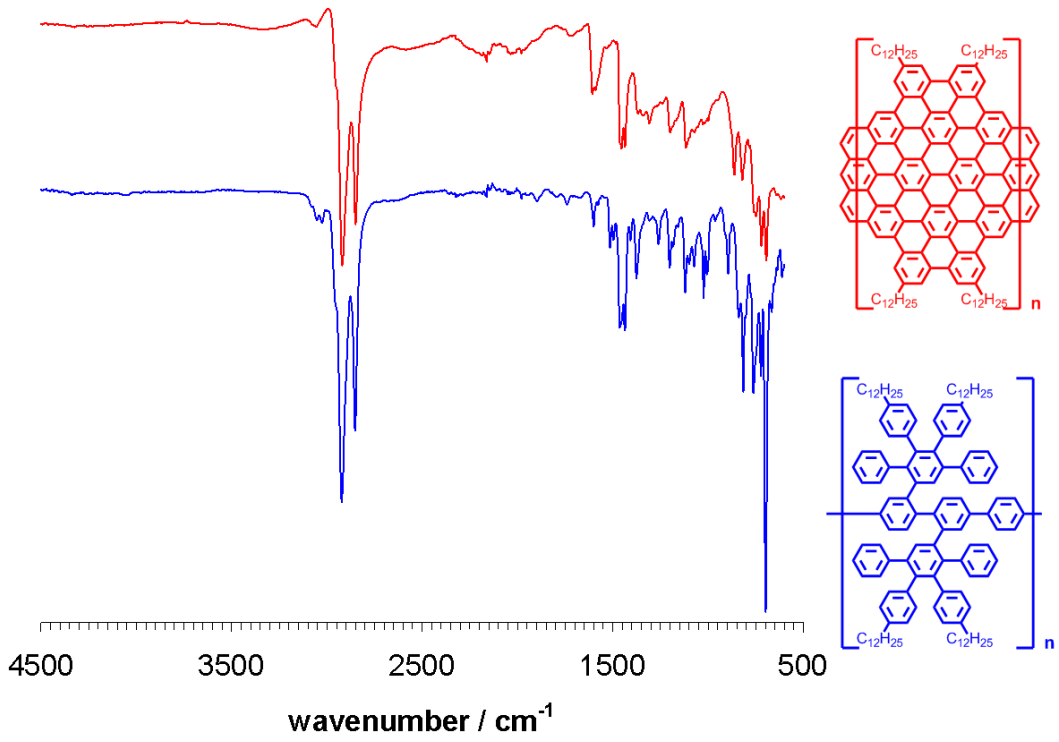

Figure 4-30: FTIR spectra of **GNR2** and precursor polymer **P2**.

The signal group composed of the bands at 3030 cm^{-1}, 3060 cm^{-1} and 3090 cm^{-1} is characteristic for C-H stretching vibrations on the backbone of aromatic rings. During the cyclodehydrogenation reaction the number of benzene-bound hydrogen atoms is strongly reduced. Thus, a decrease of these bands can be anticipated. Hence, only a broad unstructured signal is found in the spectrum of **GNR2** as compared to the well-resolved set of peaks for **P2**.[73,92]

Aliphatic C-H stretching vibrations give rise to the two strong bands at 2920 cm^{-1} and 2850 cm^{-1} in the spectrum of **P2**, respectively. Position and strength of these signals is virtually not affected by the oxidative treatment proving the conservation of the alkyl chains in the structure of **GNR2**.

Among the in-plane (900 - 1160 cm^{-1}) and out-of-plane C-H vibrations (650 - 900 cm^{-1}) two bands at 699 cm^{-1} and 764 cm^{-1} are of special importance to the analysis of the GNRs.

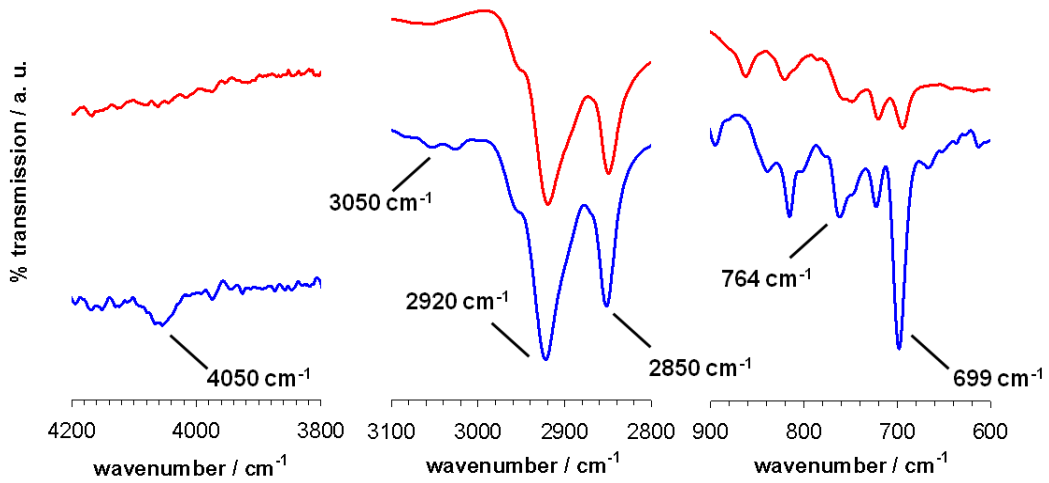

Figure 4-31: Representative regions of the FTIR spectra of **GNR2** (red) and precursor polymer **P2** (blue).

Whereas intense signals at these wavelengths are found in the spectrum of **P2** they are strongly decreased in intensity for **GNR2**. The first band originates from out-of-plane C-H vibrations of monosubstituted benzene rings as they are found at various positions among the 2,3,4,5-tetraphenylbenzene dendrons of **P2**. Successful annelation of the aromatic units leads to a strong attenuation of this band in the spectrum of **GNR2**. The same holds for the signal at 764 cm^{-1} which is almost not detected for the graphene material.

Raman spectroscopy is another versatile tool for the spectroscopic analysis of highly condensed aromatic systems.[92-95] Historically, it has played an important role in the structural characterization of graphitic materials, thus providing analytical information about defects as well as number and stacking of graphene layers.[93-95] It has recently become an important method in the characterization of nanographene species as important structural features are disclosed by the corresponding spectra.[39,92]

The most prominent features in the Raman spectra of graphitic materials are the G band or graphite-band (1580 cm^{-1}) and the D band or disorder-band (1350 cm^{-1}). Further Raman modes such as D' band or 2D bands are found at wavenumbers of about 1350 cm^{-1}, and 2700 cm^{-1}, respectively. As the D and D' bands are defect-induced Raman features they are not observed for highly crystalline graphite.[96] In the case of nanographenes or GNRs the edges of the molecules can be considered as

defect sites and thus give rise to significant D band contributions.[94,95] The same holds for regions of the GNR where the cyclodehydrogenation reaction was not quantitative. In the present case, it was found that the samples which were obtained by treatment with PIFA/ $BF_3 \cdot Et_2O$ showed in general better signal resolution than their counterparts from cyclodehydrogenation with ferric chloride. Compared to fluorescence, the intensity of the Raman signal is several orders of magnitude lower and thus strongly affected by undesired interference with luminescence. This is seen in the Raman spectrum of **GNR2** for which no flat baseline could be obtained due to the overlap with the fluorescence effect. Nevertheless, two important bands are clearly detected that prove the presence of an extended graphite-like structure. Hence, both G and D band are found for **GNR2** at 1310 cm^{-1} and 1585 cm^{-1}, respectively. This is in line with previous Raman studies on chemically fabricated GNRs.[36]

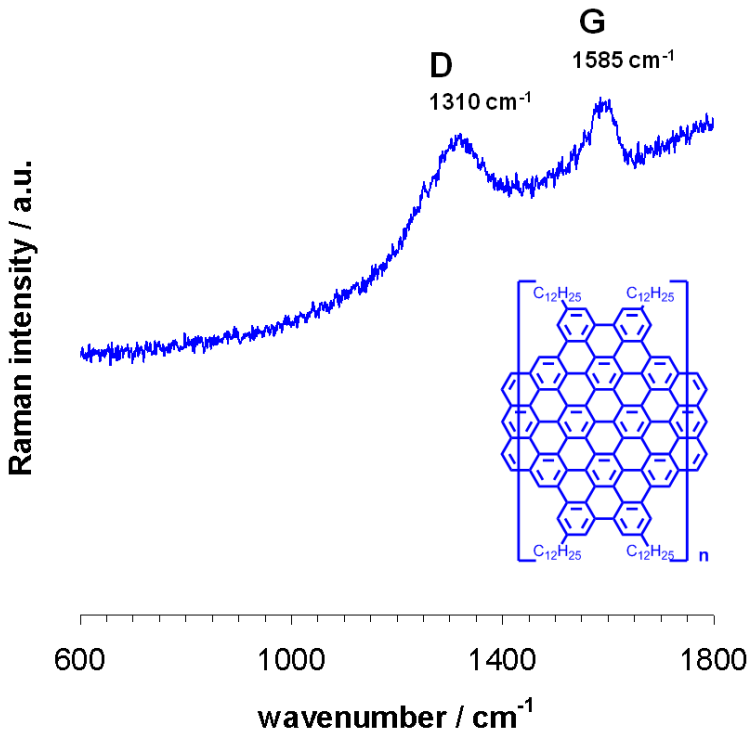

Figure 4-32: Raman spectrum of **GNR2**.

In summary, the preparation of GNR from precursor polymers derived from *Suzuki* polycondensation was demonstrated in the previous section. In a broader sense the preparation of the laterally extended poly(*para*-phenylenes) **P1+2** and their subsequent graphitization to the polymeric graphene nanoribbons **GNR1** and **GNR2** reaches the boundaries of polymer science. This refers in particular to the limited processability of the GNRs which is a consequence of their strong tendency to aggregate. Despite the difficulties regarding their characterization, analytical evidence has been presented that

supports the concept of a chemical bottom-up approach which can be used to confine those intriguing properties to the graphene material that cannot be accessed by other preparation techniques such as the lithographic[14-16,23] and sonochemcial[19] “cutting” of GNR from the graphene lattice or the oxidative “unzipping” of carbon nanotubes.[17,18,97] This refers to the control over important geometric parameters such as for example width, length and edge structure of the GNR. Also, the aspect of reproducibility provided by chemical synthesis shall be emphasized.

Further analysis of the GNRs could be provided by microscopy tools such as STM or TEM. It would be also desirable to obtain Raman spectra of higher resolution since this technique has proven its value to the analysis of graphite and graphene materials in the past.[92-95] In order to overcome the problem of fluorescence that overlaps with the low-intensity Raman signal, confocal Raman microscopy could be used. By this, the extent of the cyclodehydrogenation reaction could be quantified. Also, the thermal healing of defect sites or the possible fusion of individual GNRs to larger strips could be investigated by a combination of these analytical tools.

4.5 Polymeric Precursors *via* Yamamoto Polycondensation

It was shown in the previous part how the *Suzuki-Miyaura* protocol was successfully applied to the synthesis of the laterally extended poly(*para*-phenylenes) **P1+2** and the graphene nanoribbons **GNR1+2** derived thereof. Since the polymeric precursor is at the heart of this synthetic concept its nature and quality have a strong impact on the material properties of the final GNR. This refers primarily to the lateral dimensions of the GNR which will determine the band gap.[14,19,98] Also, subtle changes of the edge structure will for example strongly influence the magnetoelectronic properties of these ribbon-type structures.[27,28] For practical applications, a minimum length of the GNR needs to be achieved as well allowing for the filling of the active channel of a field-effect transistor or the connection of two electrodes in nanoscale integrated circuits.[20]
These parameters can, however, be tuned by careful design of the monomers and optimization of the synthetic conditions applied to the build-up of the polymeric precursor.
A critical analysis of the polymeric materials obtained by *Suzuki* polycondensation and the study regarding the **C84** disc revealed several drawbacks of this methodology which will be addressed in the following section:

- Due to the sensitivity of A_2B_2-type polycondensation reactions to stoichiometry, the equimolar presence of the two functional groups needs to be precisely controlled. In particular, accurate weighing of small amounts on the milligram scale proved to be challenging.
- Aberration from stoichiometry will result in lower molecular weights and shorter lengths of both the poly(*para*-phenylene) and the derived GNR.
- Also, the reproducibility of the polycondensation is affected by stoichiometry limiting the comparison between experimental series.
- Furthermore, only extended reaction times lead to high molecular weights as a consequence of the underlying kinetics of the polycondensation mechanism.
- The bromine atoms of the biphenyl monomer are considerably shielded which might have hampered the formation of higher molecular weights due to steric reasons. A more exposed position on the monomer backbone should facilitate polymerization.
- There is analytical evidence for the presence of undesired functional groups which cannot be fully converted *via* end-capping of the final polymers. This refers especially to the boronic acid and ester groups.

- Concerning the cyclodehydrogenation, it appears that the geometric environment of the biphenyl monomer despite the introduction of anchor points is still not ideal. For an efficient planarization of both the model compound and the polymeric precursor high amounts of oxidant were necessary.

Based on these considerations, the need for an improved synthetic system is obvious. Many transition-metal mediated aryl-aryl couplings rely on the addition of an *A*-functionalized unit to a *B*-substituted counterpart. In comparison, only a few catalytic protocols are available for efficient *AA*-type couplings. One of the most versatile methods for the build-up of polymers with a stiff aromatic backbone is the nickel(0) mediated *Yamamoto* dehalogenation polycondensation.[47,48] In fact, many pioneering works on poly(*para*-phenylene)s and related compounds[99-103] were accomplished *via* this method and numerous other conjugated polymers have been prepared accordingly.[104] Therefore, the *Yamamoto* protocol appeared a promising tool for the synthesis of high-molecular weight polymeric precursors for GNRs as well. The following points summarize the motivation and possible advantages:

- For an *AA*-type polymerization system, only one bifunctionalized component is needed. For this reason, the precise weighing of two components is circumvented. It can be anticipated that this will result in higher molecular weights and an increase of the GNR length.
- As such, the reproducibility of the polymerization related to this aspect can also be guaranteed. This is one of the major advantages of the chemical approach towards GNR synthesis.
- The addition of new monomer to the growing polymer chain occurs in a step-wise manner, only *AA*-type monomer and *AA*-functionalized chain-ends are present in the reaction mixture.
- It is known, that the dehalogenation mechanism mostly leads to non-functionalized chain ends if the reaction is quenched.
- Inorganic nickel residues are easily decomposed by acid treatment of the polymer after reaction. The purity of the graphene material if applied as active component in electronic devices is crucial.
- A new molecular design regarding both model compound and monomer has to be established in order to guarantee for an easier graphitization of the oligophenylene scaffold. Still, structural analogy would be highly desirable in

order to make comparison between the *Suzuki-Miyaura* and the *Yamamoto* approach possible.

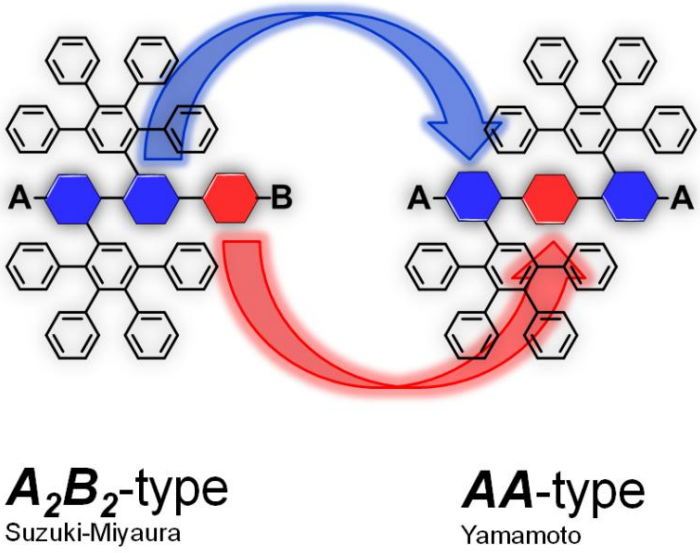

Figure 4-33: Schematic representation illustrating the design of a suitable *AA*-type monomer (*Yamamoto*) on the basis of an A_2B_2-type system (*Suzuki-Miyaura*).

For the *Yamamoto* polymerization, however, fully symmetric monomers are needed; else a statistical head-tail mixture will result. As depicted in Figure 4-33, the repeat unit of the *Suzuki-Miyaura* system had to be transformed into a new monomer for the *Yamamoto* approach. This can be done, by "inserting" the benzene ring (red) originating from the *BB*-type monomer into the biphenyl unit (blue) of the new *AA*-type monomer. By this, the monomer backbone is extended to a *para*-terphenyl with the 2,3,4,5-tetraphenylbenzene dendrons attached to its two peripheral benzene rings. Another benefit from this modification is the fact that the two halogen functions are now better accessible as the steric shielding by neighboring benzene rings is reduced in the case of the *para*-terphenyl geometry.

As discussed previously, the connection pattern of repeat unit constitutes an important aspect in the synthesis of GNRs. The periphery will have a strong influence on the final character of the material and can be used to efficiently tune the electronic properties.[14,19,27,28,98] For steric reasons, the *Suzuki-Miyaura* system only allowed for *para*-connection of the two monomers. In the case of the *Yamamoto* approach, also a *meta*-functionalized oligophenylene monomer can be thought of.

As schematically depicted in Figure 4-34, the fusing of two repeat units is achieved by four benzene rings in the case of *para*-connected **GNR3**. The width of the nanoribbon varies between 1.73 nm and 1.22 nm (MMFF94s). With respect to previously discussed

GNR1+2, the “neck” is expanded by one benzene unit even though the saw blade structure is still maintained.

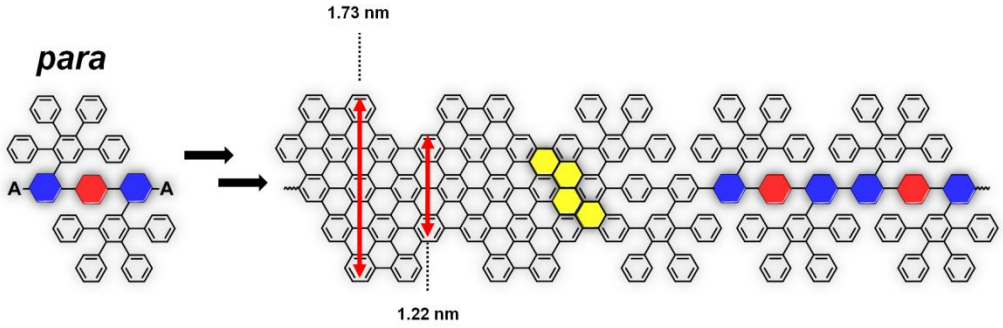

Figure 4-34: Schematic representation of *Yamamoto*-based graphene nanoribbons **GNR3** illustrating dimensions, *para*-connectivity and overlap of the building units.

These structural parameters greatly change when a *meta*-functionalization as in the case of **GNR4** is chosen (Figure 4-35). The different connectivity of the building units leads to an enhanced overlap *via* six aromatic rings. The *π*-surface of the resulting GNRs is greatly increased further illustrating the power of controlling the structural parameters of graphene materials by precise chemical tailoring.

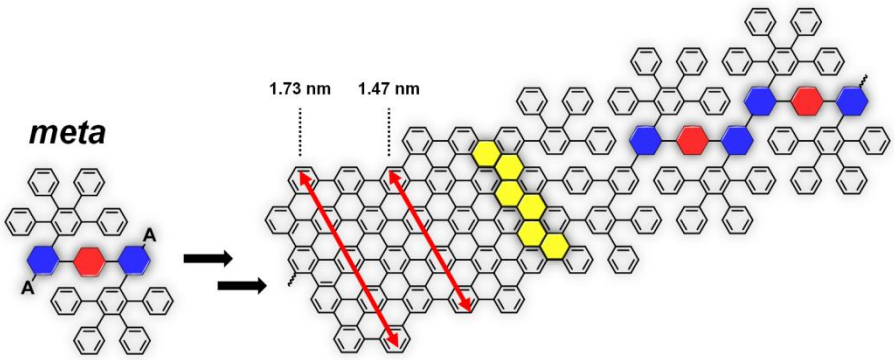

Figure 4-35: Schematic representation of *Yamamoto*-based graphene nanoribbons **GNR4** illustrating dimensions, *meta*-connectivity and overlap of the building units.

Due to the induced kink, the armchair-periphery of the molecule is significantly smoothened as compared to **GNR1+2** and **GNR3** resulting in a maximum lateral extension of 1.73 nm and a minimum value of only 1.47 nm (MMFF94s).

4.5.1 Monomer Synthesis

The synthesis of the *para*-functionalized bisacetylene **4-31** was started from commercially available 1,4-phenyldiboronic acid **4-25** and 1-bromo-4-chloro-2-nitrobenzene **4-26**. Gram-scale *Suzuki-Miyaura* coupling of both components yielded the functionalized *para*-terphenyl **4-27** in 88 % (Figure 4-36).[105] The desired compound precipitated during the course of the reaction. The work-up and purification procedure could thus be significantly shortened. Subsequently, the two nitro-groups were converted into the corresponding amine functions by reduction with hydrogen gas in the presence of carbon-supported palladium(0). An analogous reduction protocol using tin/hydrochloric acid as used for the preparation of **4-3** was not applicable due to the limited solubility of **4-27**.

Also in this case, the hydrogenation had to be started heterogeneously. The reaction mixture turned however homogeneous as **4-28** exhibits enhanced solubility in comparison to **4-27**. The unstable diamine **4-28** had to be used as obtained and was quickly converted into 4,4''-dichloro-2,2''-diiodo-1,1':4',1''-terphenyl **4-29** by double *Sandmeyer* reaction. Compound **4-29** was isolated in 39 % yield which is appreciable in view of the aqueous environment typically used for this reaction. As for the synthesis of biphenyl **4-4**, the loss of one iodine atom was also observed in this case by FD mass spectroscopy. Two-fold *Sonogashira-Hagihara* cross-coupling with trimethylsilyl acetylene in the presence of bis(triphenylphosphine)palladiumchloride(II) and copper iodide gave the protected bisacetylene **4-30** in good yield (90 %). However, the deprotection of this compound could only be achieved by the aforementioned method using potassium carbonate as base. Remaining impurities of mono-substituted by-product could be fully removed by final column chromatography of **4-31** as the polarity difference between mono- and bisacetylene was found to be strongly increased after the deprotection step.

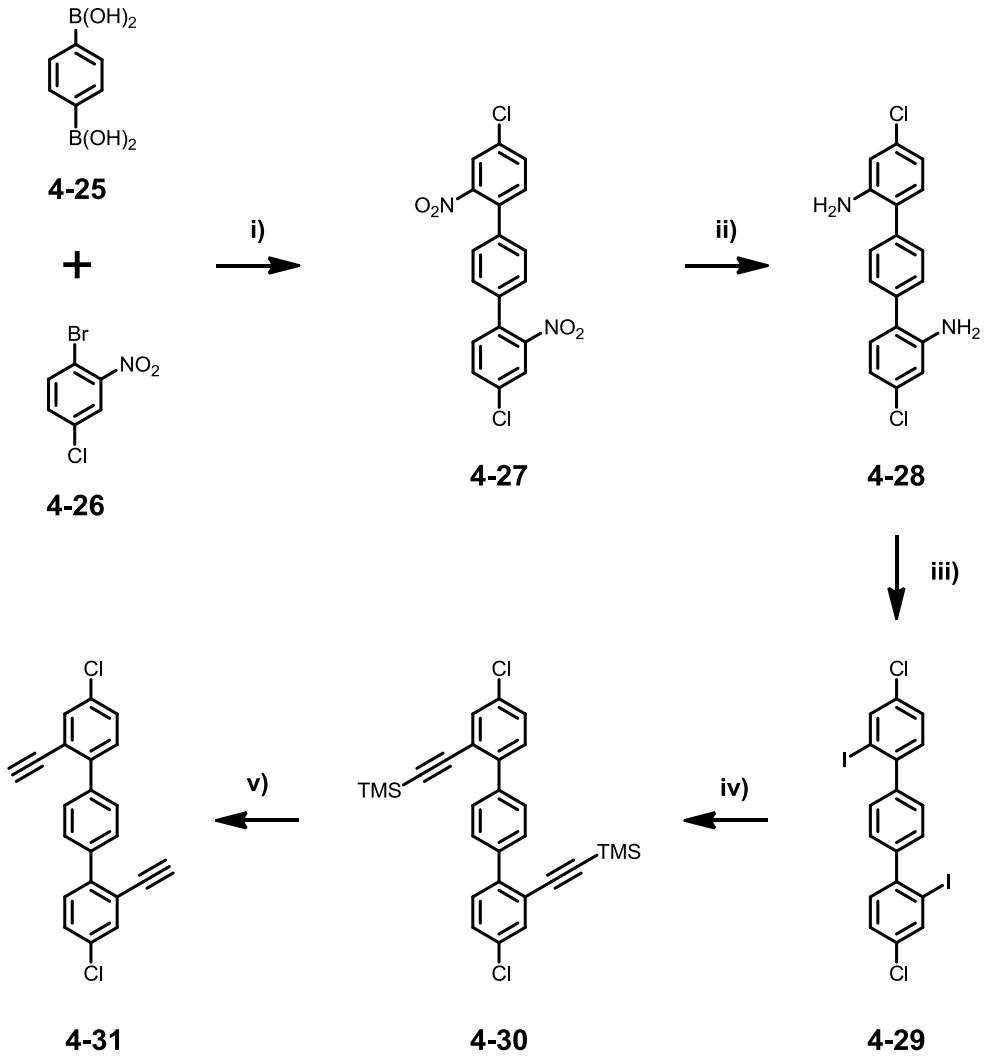

Figure 4-36: Synthetic route to the *para*-functionalized bisacetylene **4-31**; conditions: i) $Pd(PPh_3)_4$, K_2CO_3, dioxane, 100°C, 88 %; ii) H_2, Pd/C, RT, 92 %; iii) $NaNO_2$, HCl/H_2O, then KI, - 5 °C, 39 %; iv) trimethylsilyl acetylene, $Pd(PPh_3)_2Cl_2$/CuI, NEt_3; room temperature, 90 % v) K_2CO_3, THF/MeOH, room temperature, 64 %.

The *meta*- functionalized bisacetylene **4-36** was prepared in a similar fashion using a closely related synthetic sequence (Figure 4-37). It was however found that the initial *Suzuki-Miyaura* reaction worked also well in the presence of free amine groups. By coupling 2-bromo-4-chloroaniline **4-32** instead of the nitro derivative to the bis(pinacol) ester of 1,4-phenyldiboronic acid **4-14**, the low solubility observed for **4-27** could be avoided. Hence, 5,5''-dichloro-[1,1':4',1''-terphenyl]-2,2''-diamine **4-33** was prepared in 79 %. As the compound changed in color in the dry state, it was directly converted into **4-34** with the yield of this step being 42 %. This compound was then transformed into target compound **4-36** using identical synthetic conditions as described above (Figure 4-37).

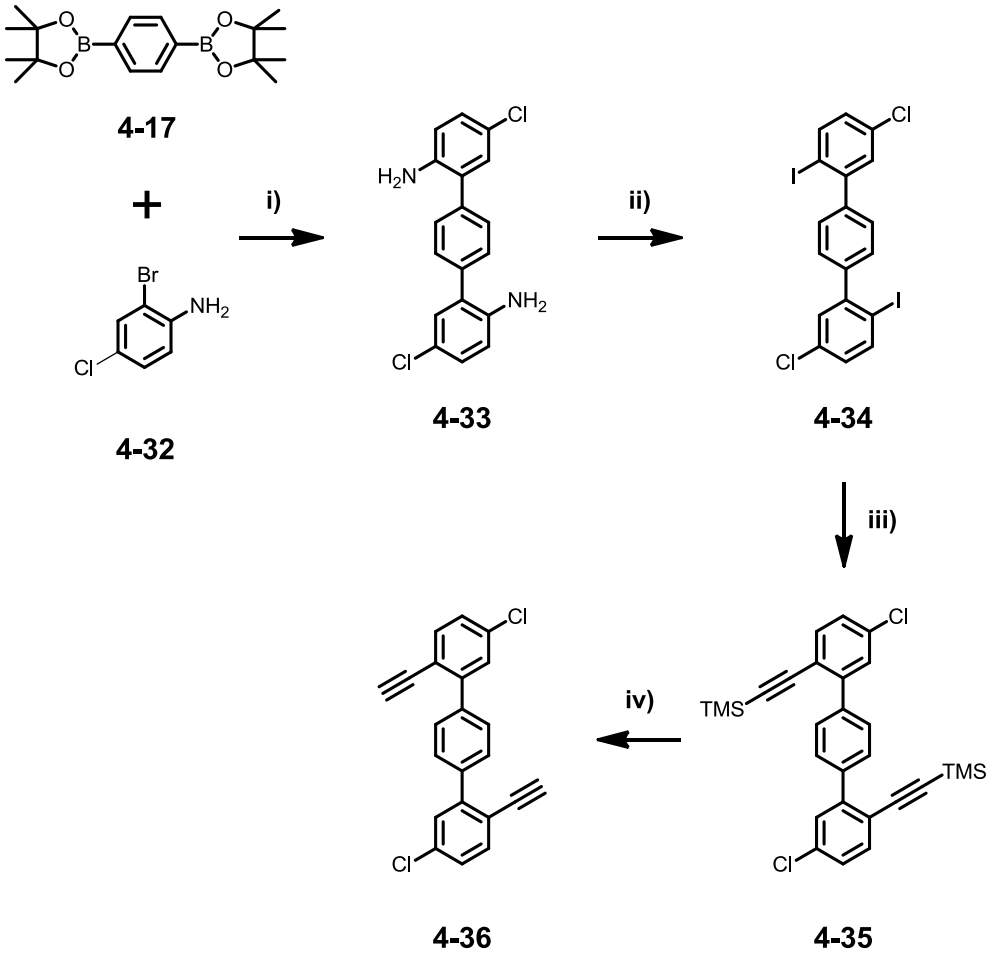

Figure 4-37: Synthetic route to the *meta*-functionalized bisacetylene **4-36**; conditions: i) $Pd(PPh_3)_4$, K_2CO_3, dioxane, 100°C, 79 %; ii) $NaNO_2$, HCl/H_2O, then KI, - 5 °C, 42 %; iii) trimethylsilyl acetylene, $Pd(PPh_3)_2Cl_2$/CuI, NEt_3; room temperature, 85 % iv) K_2CO_3, THF/MeOH, room temperature, 68 %.

Both functionalized *para*-terphenyls showed a strong tendency to crystallize which can be attributed to the rigid nature of the molecules and the two peripheral ethinyl groups for which a high packing tendency is known. Suitable needle-like crystals for X-ray diffraction analysis were obtained from slow evaporation of DCM solutions containing the compounds. From the crystal structures it can be derived that **4-31** is arranged in the $P2_1/n$ monoclinic phase (Figure 4-38). On the contrary, **4-36** belongs to the *P1* triclinic space group (Figure 4-39).

The torsion between the peripheral benzene rings and the central ring is clearly seen from the two crystal structures. The corresponding angle amounts to 45.5 ° in the case of **4-31** and to 46.5 ° for **4-36**.

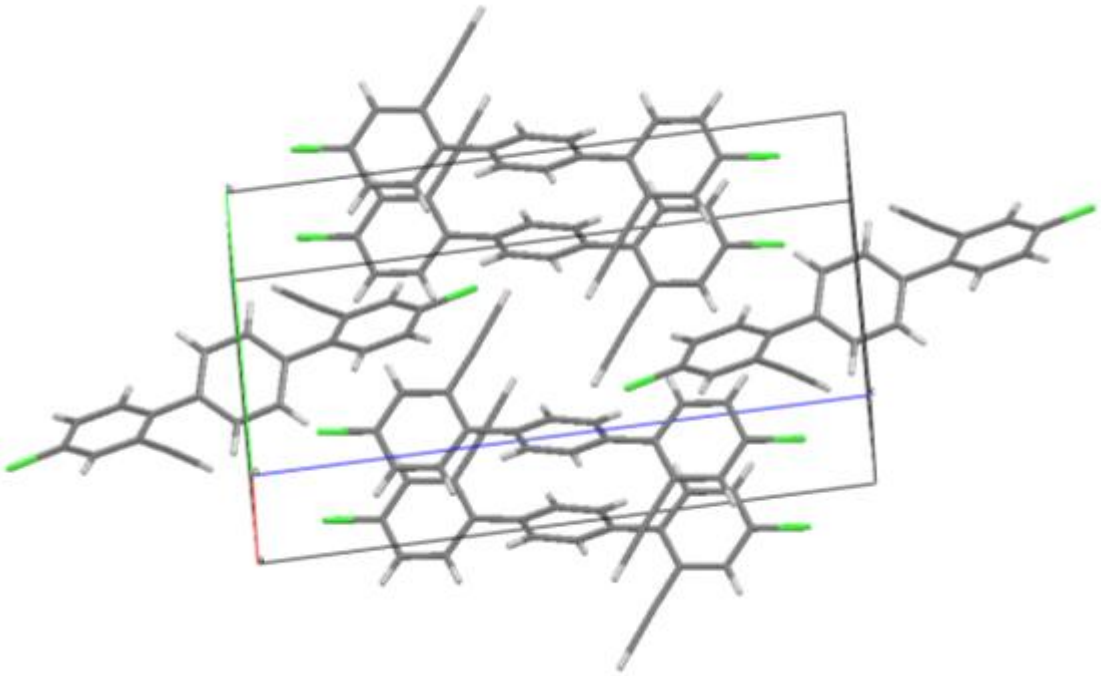

Figure 4-38: Crystal structure of 4,4"-dichloro-2,2"-diethynyl-1,1':4',1"-terphenyl **4-31**.

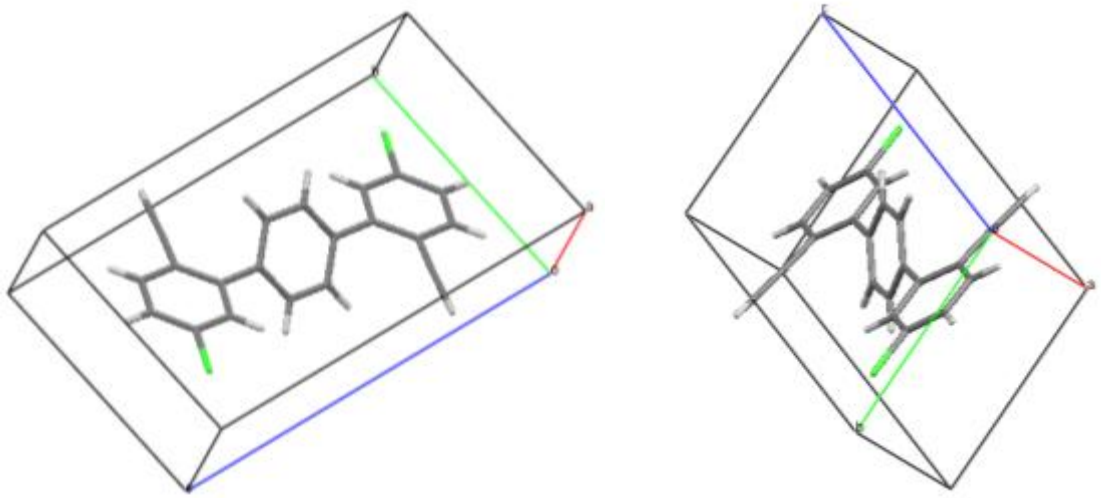

Figure 4-39: Crystal structure of 5,5"-dichloro-2,2"-diethynyl-1,1':4',1"-terphenyl **4-36**.

In the final step, *Diels-Alder* reaction of **4-31** and **4-36** with dodecyl-functionalized tetraphenylcyclopentadienone **4-11b** was used for the preparation of the corresponding oligophenylene monomers **4-37** and **4-38**, respectively (Figure 4-40). The reactions were carried out under 300 W microwave irradiation in *ortho*-xylene at 160 °C.

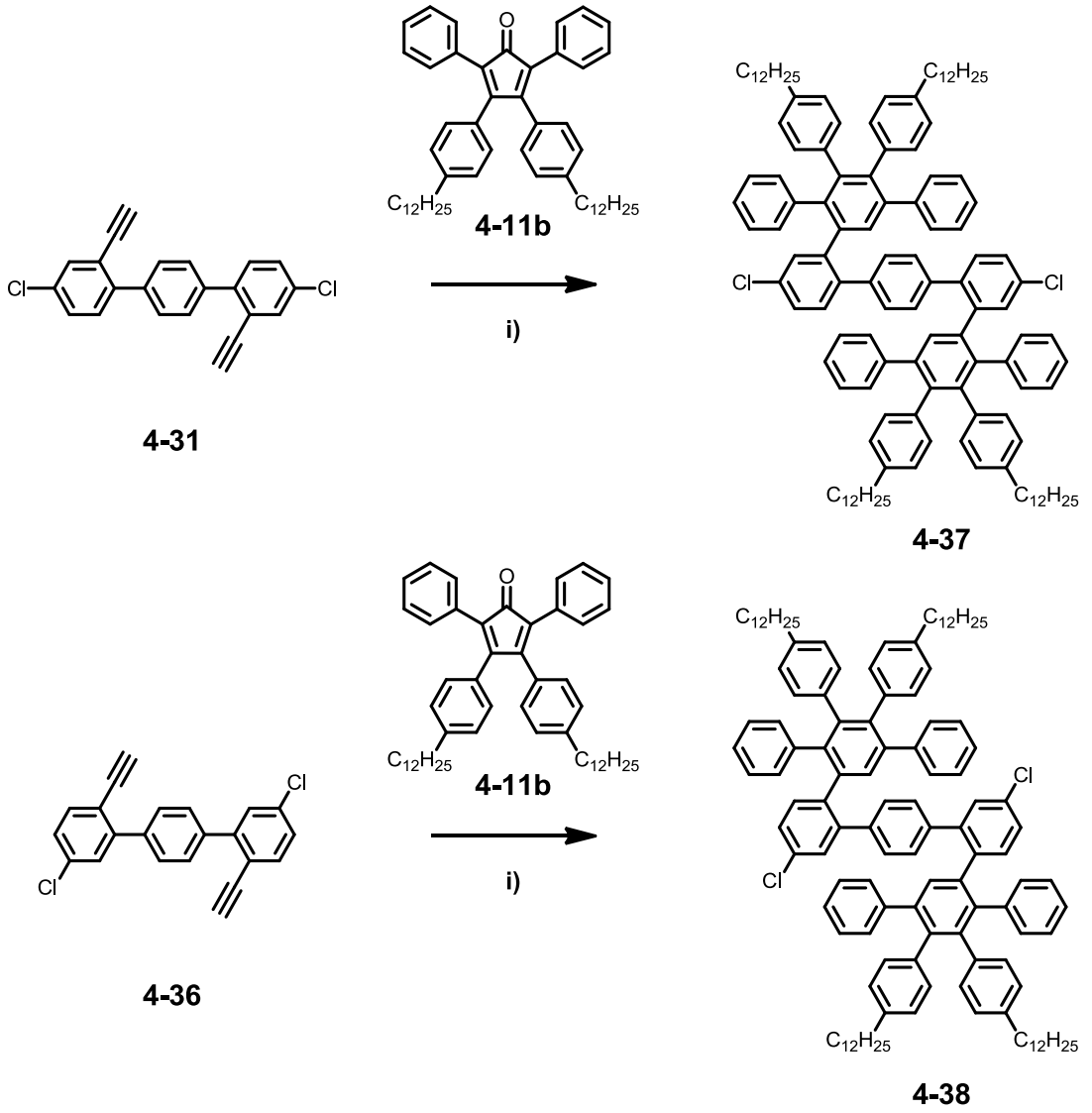

Figure 4-40: Synthetic route to the dendronized *para*-terphenyl monomers **4-37** and **4-38**; conditions: i) *ortho*-xylene, 160 °C, µW, 300 W, 74 - 85 %.

The two dendronized terphenyl monomers **4-37** and **4-38** were passed to rGPC and isolated as colorless oils that solidified upon standing. The yield was 74 % and 85 %, respectively. NMR and MALDI-TOF spectroscopy was used for the assessment of the purity of the two compounds. For both monomers, the target mass was detected as exclusive peak reflecting the high degree of purity. The presence of the sodium and potassium adduct results from the sample preparation.

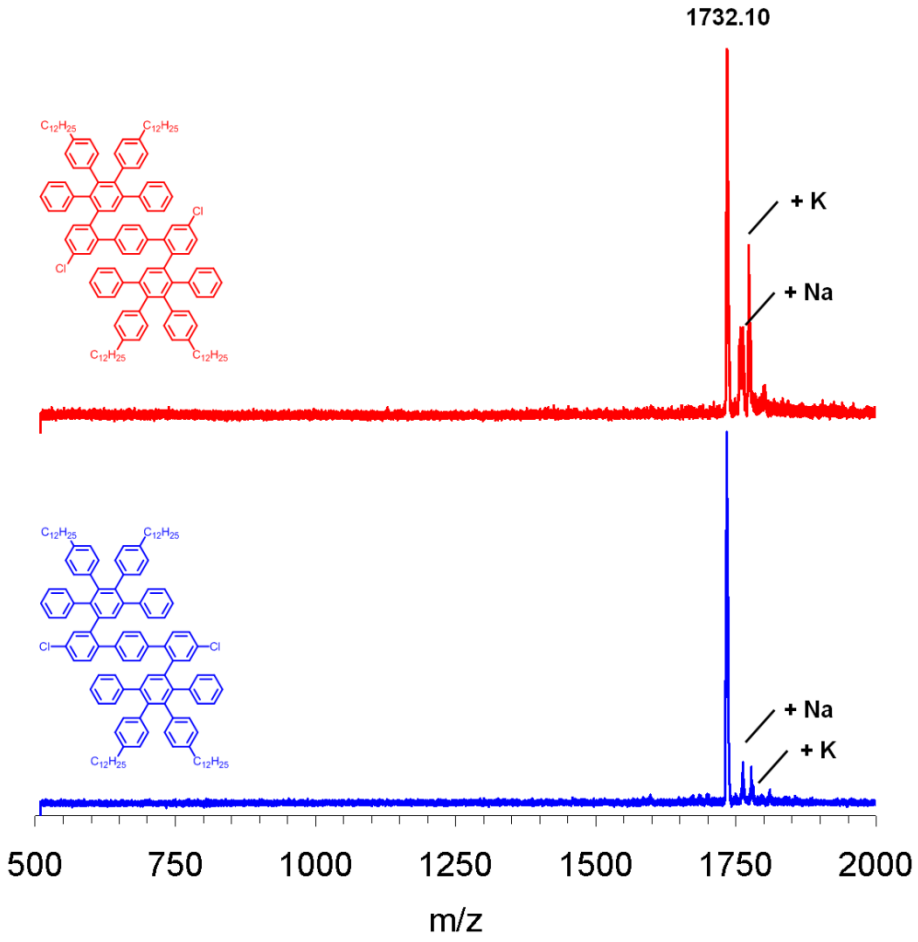

Figure 4-41: MALDI-TOF spectra of **4-37** (bottom) and **4-38** (top).

4.5.2 Model Compound

The new *para*-terphenyl geometry of monomers **4-37** and **4-38** has not been reported in the preparation of nanographene materials so far. Intuitively, one would expect the two dendrons to be easily cyclodehydrogenated as they can be drawn as to individual HBC precursors sharing the central benzene ring of the terphenyl backbone. An analogous connectivity of the benzene units has been found suitable for cyclodehydrogenation in the HBC case in the past.[106] However, it was initially unclear whether the whole molecule can be planarized and to what degree the free rotation of the two dendrons is affected by the central benzene unit of the terphenyl backbone. From *para*-terphenyls it is known that an alternating arrangement of the benzene units is favorable since steric interactions between neighboring protons can thus be minimized. Taking into account the two dendrons attached to the two peripheral benzene rings of the *para*-terphenyl skeleton of monomers **4-37** and **4-38** this would result in a strong decrease of their rotation and a nearly coplanar arrangement of these

units. It is apparent that the conversion of the oligophenylene scaffold to the final graphene species will be facilitated if a certain degree of planarity is already present prior to the actual cyclodehydrogenation step.[54,55]

In order to verify this assumption the synthesis of a model compound with an identical arrangement of the benzene units as for monomers **4-37** and **4-38** was envisaged. Based on the results from the previously investigated hexa-substituted **C84**, two more alkyl chains need to be attached in order to guarantee for full solubility of the PAH after cyclodehydrogenation.

Another motivation for the introduction of additional peripheral alkyl chains is the examination of the two- and three-dimensional self-assembly behavior of the final **C78** disc which should be driven by the microphase separation of the hard aromatic core and the soft alkyl substituents. It was hoped that the direct *Cl*-alkylation of **4-37** by a nickel(II) mediated *Kumada* coupling with dodecyl magnesium bromide would yield the desired oligophenylene **4-39**.[107,108] However, several attempts to directly attach the two dodecyl chains using this approach failed. Results from FD mass spectroscopy indicated that dehalogenization occurred to a significant degree as a side reaction resulting in a complex mixture in which **4-39** was only detected in minor amounts.

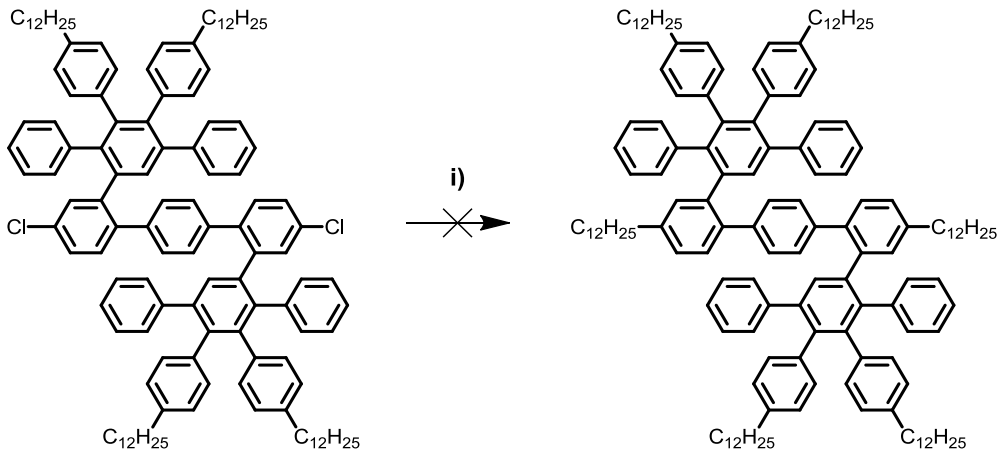

4-37 **4-39**

Figure 4-42: Attempted *Cl*-alkylation of **4-37**; conditions: i) dodecyl magnesium bromide, $Ni(dppf)_2Cl_2$, Et_2O, reflux.

It was then envisaged to introduce the dodecyl chains prior to the oligophenylene formation following the synthetic route which was successful for the build-up of monomers **4-37** and **4-38**. The modified bisacetylene **4-46** was prepared in six steps as shown in Figure 4-43. The initial *Suzuki-Miyaura* coupling was more challenging in this case as the coupling partner 1,4-dibromo-2-nitrobenzene **4-40** is in principle reactive at both bromine sites. By carefully adjusting the temperature to 80 °C and monitoring the

course of the reaction for several days by FD mass spectroscopy and thin layer chromatography, 4,4''-dibromo-2,2''-dinitro-1,1':4',1''-terphenyl **4-41** was obtained in 51 % yield. In the next step, the alkyl chains were introduced *via* double *Sonogashira-Hagihara* cross-coupling with dodec-1-yne. Both, the acetylene and the nitro groups were reduced in one step by reduction with hydrogen gas in the presence of palladium(0). Diazotation, followed by addition of potassium iodide was used for the synthesis of the diiodo derivative **4-44**.

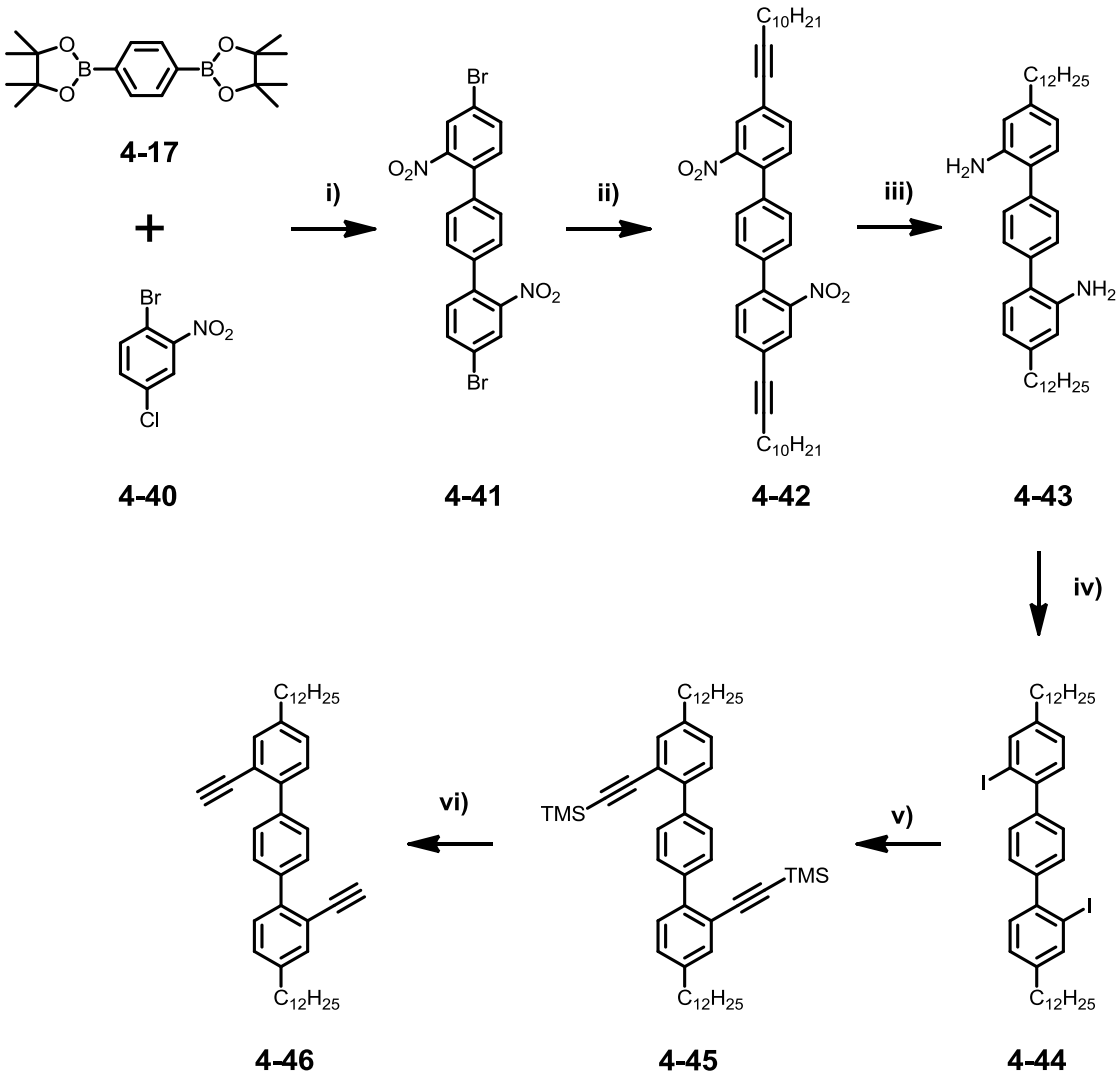

Figure 4-43: Synthetic route to the dodecyl-functionalized bisacetylene **4-46**; conditions: i) $Pd(PPh_3)_4$, K_2CO_3, toluene, 50 °C, 51 %; ii) dodec-1-yne, $Pd(PPh_3)_2Cl_2$/CuI, NEt_3; room temperature, 88 %; iii) H_2, Pd/C, RT, 91 %; iv) $NaNO_2$, Cl/H_2O, then KI, - 5 °C, 31 %; v) trimethylsilyl acetylene, $Pd(PPh_3)_2Cl_2$/CuI, NEt_3; room temperature, 71 % vi) K_2CO_3, THF/MeOH, room temperature, 72 %.

This compound was transformed into the corresponding bisacetylene **4-46** by a second *Sonogashira-Hagihara* cross-coupling with trimethylsilyl acetylene followed by deprotection with potassium carbonate in a 1/1 mixture of methanol and THF.
The microwave-assisted *Diels-Alder* reaction between 4,4''-didodecyl-2,2''-diethynyl-1,1':4',1''-terphenyl **4-46** and the functionalized tetraphenylcyclopentadienone unit **4-11b** proceeded smoothly in *ortho*-xylene at 160 °C yielding the desired model compound **4-39** in 81 % as a colorless oil.

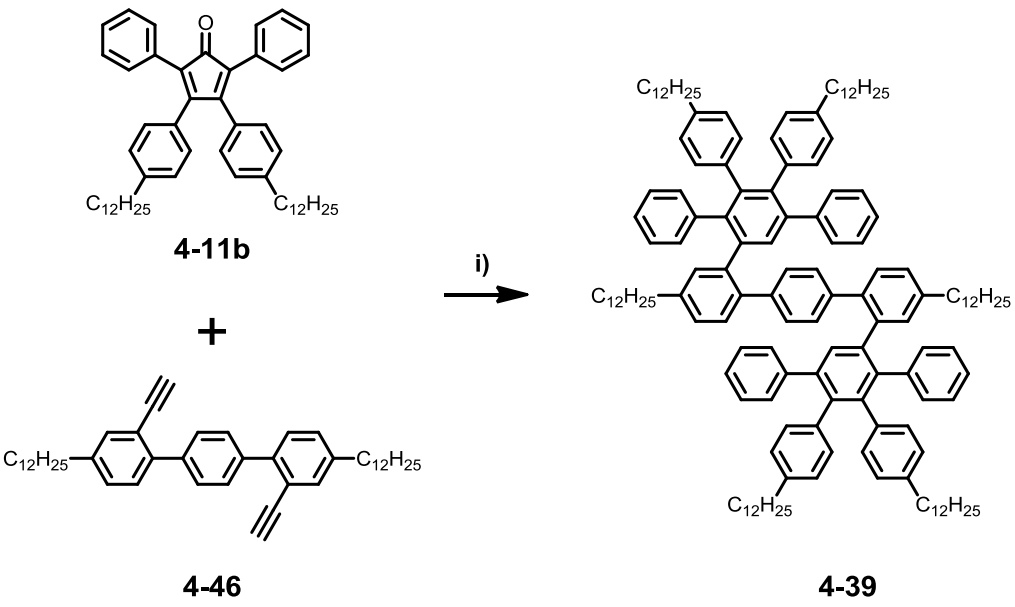

Figure 4-44: Synthesis of model compound **4-39** *via Diels-Alder* reaction; conditions: i) *ortho*-xylene, 160 °C, µW, 300 W, 81 %.

4.5.3 Polymer Synthesis and Characterization

With the monomers **4-37** and **4-38** available their polycondensation was attempted using the standard *Yamamoto* protocol (Figure 4-45).[47,48] The reaction was carried out in an overall 3/1 mixture of toluene/DMF at a monomer concentration of $1.4 \cdot 10^{-2}$ M. The catalyst was prepared under glove-box conditions from a stoichiometric mixture of bis(cyclooctadiene)nickel(0), 1,5-cyclooctadiene and 2,2'-bipyridine in toluene/DMF. The deep-purple catalyst solution was subsequently activated at 80 °C for 30 minutes in the dark. The monomer solution was added subsequently and the reaction was allowed to proceed for two days in the dark.

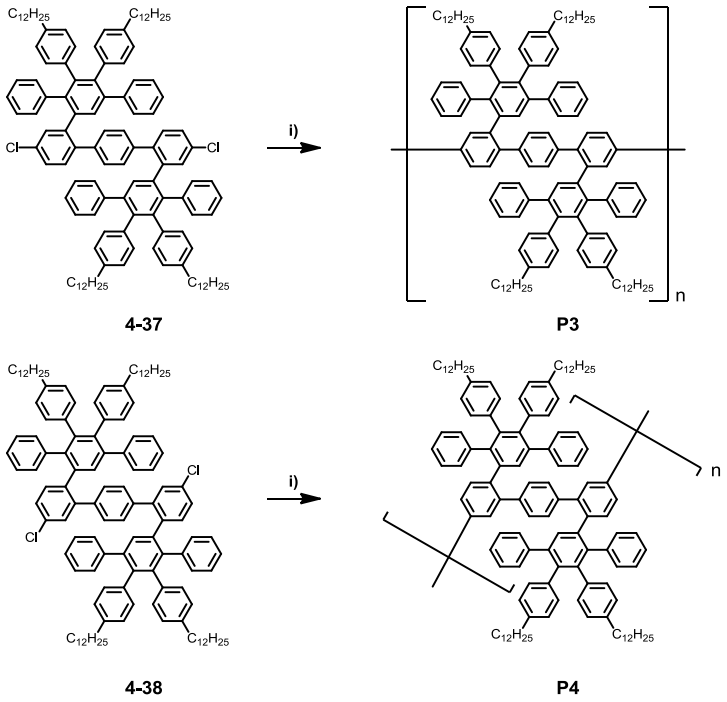

Figure 4-45: Synthesis of the laterally extended poly(*para*-phenylene) precursors **P3+4**; conditions: i) bis(cycloocta-(1,5)-diene)nickel(0), cycloocta-(1,5)-diene, 2,2'-bipyridine, toluene/DMF, 80 °C, quantitative.

Then, excess chlorobenzene was introduced as capping agent and the reaction was continued for another 24 h.

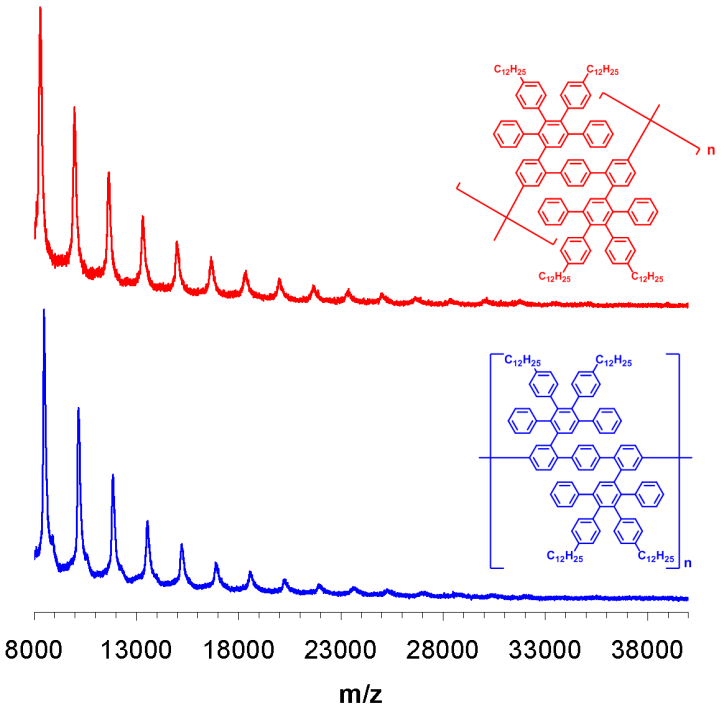

Figure 4-46: MALDI-TOF spectra of **P3** and **P4**.

The quenching of the reaction and the decomposition of nickel residues was achieved by carefully dropping the reaction mixture into dilute methanolic hydrochloric acid. A white precipitate instantly formed which was collected by filtration. The material was re-dissolved in DCM, filtered and re-precipitated as described above for two more times.
Initial analysis of **P3** and **P4** by MALDI-TOF spectroscopy indicated the presence of a regular pattern which extended up to molecular weights of 35000 - 40000 g/mol. The number of repeat units was between 20 and 24 for both polymers. Due to the rigid poly(*para*-phenylene) backbone, a length between 22 nm and 27 nm can be derived for the longest chains of the mixture.

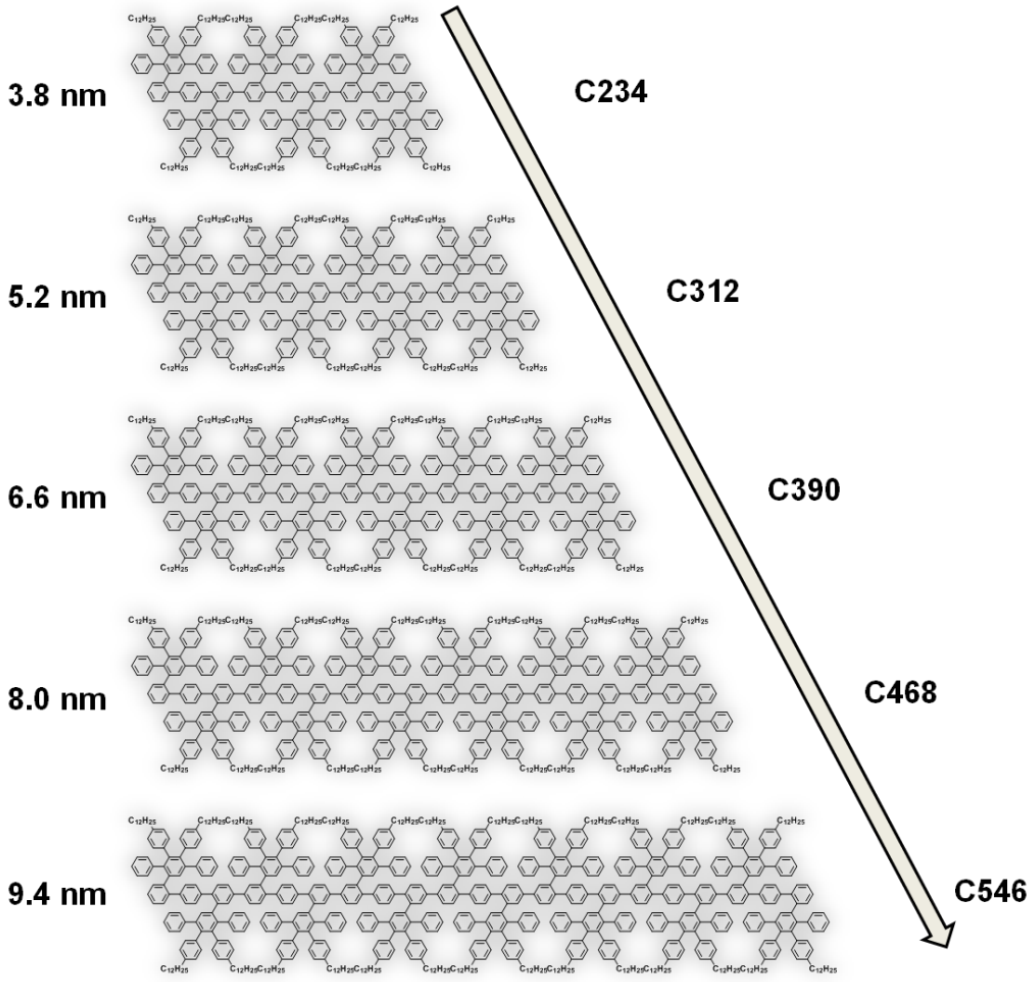

Figure 4-47: Schematic representation of a series of oligomers with the corresponding number of carbon atoms and the length as derived from computational analysis (MMFF94s).

Figure 4-46 shows the results for both polymers reflecting the power of the polymerization approach. In the case of **P3** and **P4** already the heptamer is composed of 546 regularly arranged aromatic carbon atoms and 91 benzene rings. As illustrated

in Figure 4-47 a high number of carbon-carbon bonds are pre-formed upon synthesis of the polymeric precursors and prior to the actual cyclodehydrogenation step.

It can be concluded at this point that one major goal of this study, namely the maximization of the molecular weight by changing from the A_2B_2-type *Suzuki* polycondensation to the *AA*-type Yamamoto approach, has been met. The molecular weights achieved for **P3+4** by the *Yamamoto* method are approximately 50 % higher than for the *Suzuki-Miyaura* samples **P1+2 thus** illustrating the effect of circumventing the limiting aspect of stoichiometry.

For the future design of polymeric precursors in the context of GNR synthesis *AA*-type functionalization should be chosen as the length of the polymer directly translates into the longitudinal extension of the final GNR. This is important for potential applications such as field-effect transistors that require a minimum channel width.[20] Also for nanoscale integrated circuits a certain length of the carbon structure is imperative.[23]

In general, MALDI-TOF spectra are obtained in the so-called “linear mode” which however leads to broad signals preventing their detailed investigation. For **P4** it was possible to obtain also the “reflector mode” spectrum which is characterized by a narrow signal width which renders end-group analysis possible. The result of this measurement is shown in Figure 4-48 illustrating the difference between the two device setups.

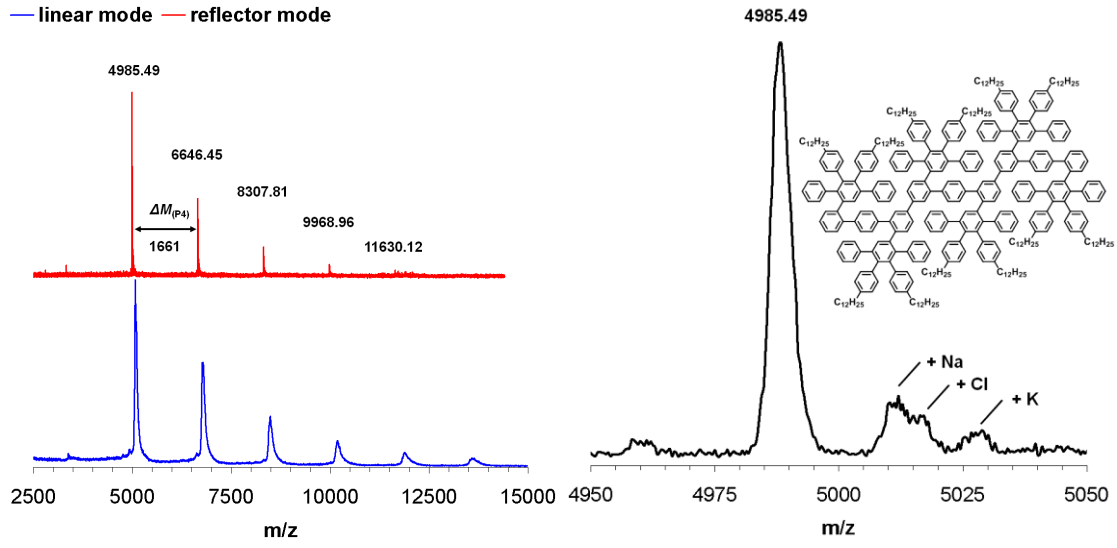

Figure 4-48: Comparison of the MALDI-TOF spectrum of **P4** as obtained from linear and reflector mode (left), analysis of the peak composition for the trimeric unit (right).

Well-resolved signals up to the mass of the heptamer (M = 11630.12 g/mol) were detected. For all peaks, the calculated mass fully corresponded to the experimental

value. A closer look on the peak of the trimer (M = 4985.49 g/mol) shows that almost no chlorine atoms are left after polymerization and capping, respectively (Figure 4-48). Only a small shoulder at 5017.18 g/mol gives evidence for unreacted functional groups. Two other signals might be ascribed to the sodium and potassium adducts, a phenomenon frequently encountered in MALDI-TOF spectroscopy.

The ^{1}H NMR spectra for the monomers and polymers recorded in THF-d_8 were subsequently compared to each other on a qualitative basis. As it can be seen in Figure 4-49 and Figure 4-50, the spectra are of high complexity making the full assignment of all signals difficult. This is due to the fact that many protons of the molecules are virtually identical as far as their chemical environment is concerned leading to pronounced overlapping and significant line broadening effects.

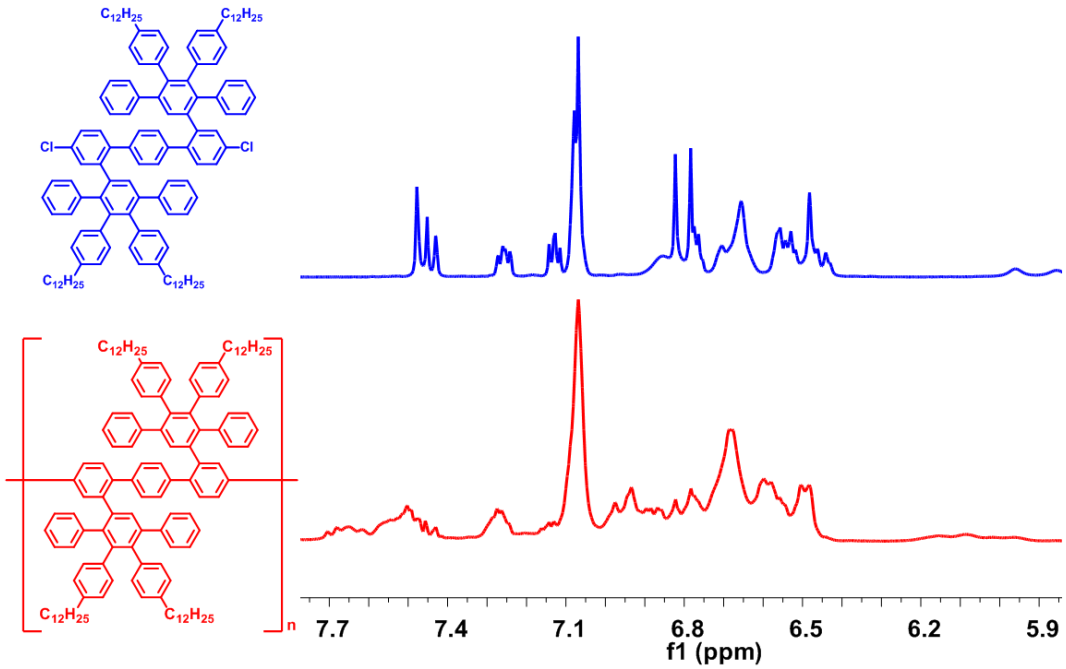

Figure 4-49: Aromatic section of the ^{1}H NMR spectra of monomer **4-37** and **P3** in THF-d_8 at 25 °C.

Importantly, the integration of the signals is in perfect accordance with the actual molecular structure which in addition to the MALDI-TOF results confirms the purity of the compounds. After *Yamamoto* polycondensation the ^{1}H NMR spectra of the corresponding polymers preserve the characteristic features seen in the spectra of the two oligophenylene monomers **4-37** and **4-38**. Also, the chemical shifts are little affected by the build-up of polymeric structures and the integration is in agreement with the expected values.

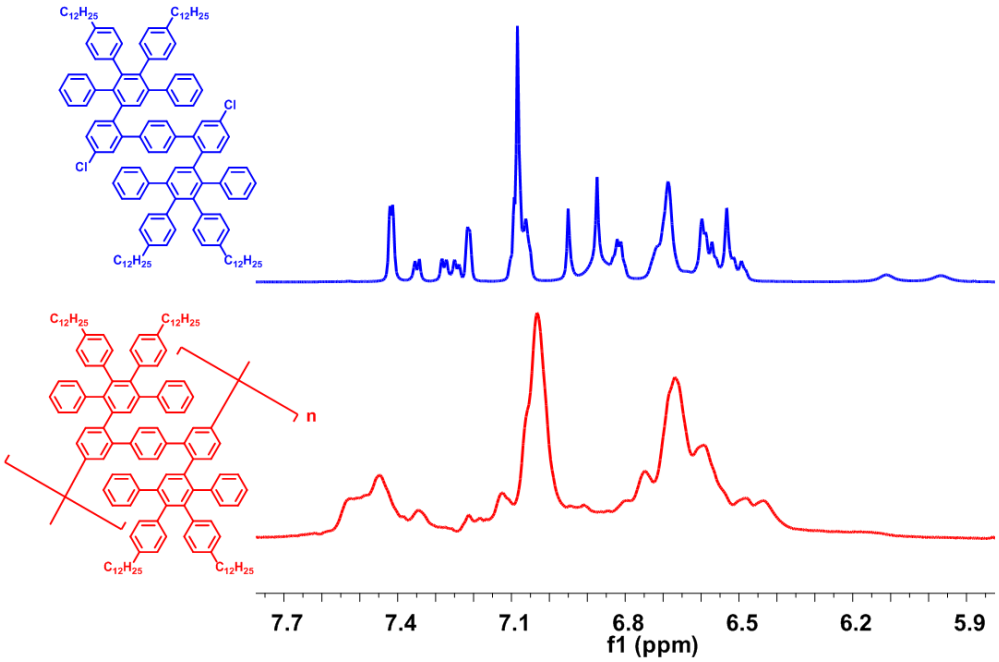

Figure 4-50: Aromatic section of the ^{1}H NMR spectra of monomer **4-38** and **P4** in THF-d_8 at 25 °C.

Subsequently, the analysis of the molecular weight of polymers **P3** and **P4** was carried out by analytical GPC (Figure 4-51).

For **P3**, a continuous curve is observed from which a number average molecular weight M_n of 76900 g/mol can be derived that equals 46 repeat units, much more than that seen in the MALDI-TOF spectrum of the polymer (Figure 4-46).

In the case of **P4**, the curve follows a bimodal distribution although the course is also rather continuous for this sample. It can be seen that the area of the high molecular weight peak is much larger than that of the lower molecular weight fraction. If the whole curve is used for the determination of the molecular weight, a M_n value of 11400 g/mol is obtained. By using only the high molecular weight peak of the elugram for the analysis the value amounts to 29700 g/mol corresponding to a degree of polymerization X_n of 18.

Additionally, the elution curve was also recorded for the two monomers **4-37** and **4-38** in order to correct the molecular weights derived from the PS calibration. The average mass determined from the PS curve was in remarkably good agreement with the actual molecular weight (1743 g/mol) of the two compounds. In the case of **4-37** a value of 1544 g/mol was experimentally found, for **4-38** 1437 g/mol were obtained. Compared to biphenyl monomer **4-13a** used for the *Suzuki-Miyaura* systems the detected value is more accurate and the error within 10 - 20 %.

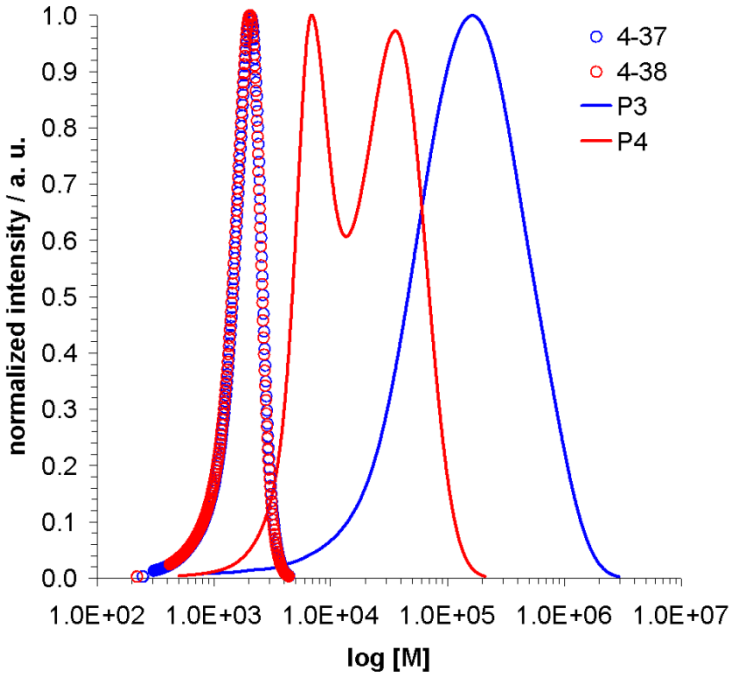

Figure 4-51: GPC traces of **P3** and **P4** and the monomers **4-37** and **4-38** as derived from the UV-vis signal.

Further evidence for the successful build-up of an extended conjugated structure was also provided by optical spectroscopy. The UV-vis absorption spectrum of model compound **4-39** was compared to the data of **P3** and **P4** (Figure 4-52). Both polymer spectra exhibit a significant bathochromic shift which can be ascribed to the larger π-system in their case. The different connectivity of **P3** and **P4** has also a strong impact on the structure of the absorption. It can be expected that the *para*-connectivity of **P3** promotes conjugation along the polymer chain whereas the *meta*-pattern of **P4** is likely to interrupt the communication between the terphenyl units. In fact, the absorption band extends to almost 370 nm in the case of **P3** whereas **P4** only absorbs until roughly 340 nm. It has to be kept in mind that the difference in molecular weight between **P3** and **P4** seen in GPC might also contribute to this difference. However, the similarity between the spectrum of model compound **4-39** and **P4** and the small bathochromic shift for this pair is another indication for limited conjugation. It appears that for *meta*-connected **P4** the repeat units act as decoupled fluorophores and not as a conjugated chain like in the case of **P3**.

Further analysis was performed on the basis of the corresponding fluorescence data (Figure 4-52). For both polymers and the model compound **4-39** a continuous emission centered in the blue-region of the spectrum was found.

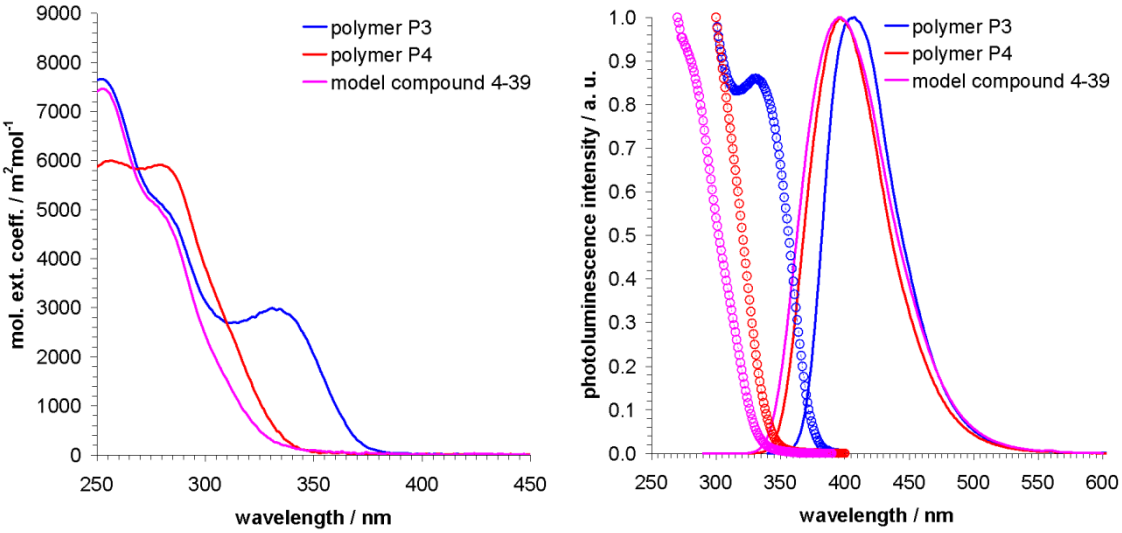

Figure 4-52: UV-vis absorption spectra of **P3**, **P4** and model compound **4-39** in chloroform at 10^{-5} M (left), normalized fluorescence emission and excitation spectra of **P3**, **P4** and model compound **4-39** in chloroform at 10^{-5} M (right).

Again, the band location is very similar for **4-39** and **P4** with the maxima located at virtually identical wavelengths of 396 nm and 397 nm, respectively. Despite the polymeric structure of **P4** it is noteworthy, that there is no stronger bathochromic shift. For **P3** the red shift is more pronounced as the emission maximum is found at 408 nm for this polymer.

4.6 Synthesis and Characterization of the C78 disc

4.6.1 Solution Cyclodehydrogenation

In order to determine optimum conditions for the cyclodehydrogenation of the GNRs derived from **P3** and **P4**, preliminary experiments were carried out on model compound **4-39**. As seen in Figure 4-53, the planarization of this oligophenylene precursor would yield a hexa-substituted **C78$_{hexa}$** disc with a maximum lateral extension of 1.72 nm and the peripheral carbon atoms of the terphenyl backbone separated by 1.12 nm. The PAH contains 13 aromatic benzene units, one less than the related **C84** disc which has been previously presented. As **4-39** is decorated with six linear dodecyl chains, mesophase behavior induced by microphase separation and *π*-*π*-stacking is expected for the molecule if the full planarization of the aromatic core can be achieved by cyclodehydrogenation.

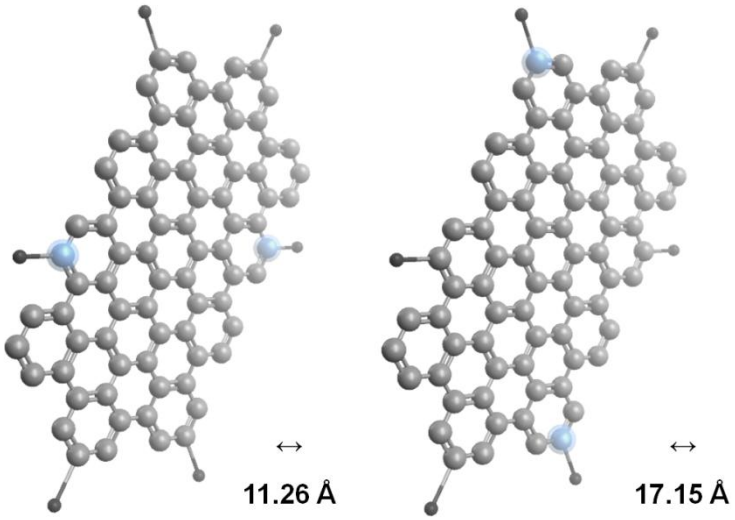

Figure 4-53: Geometric dimensions of the **C78** core as derived from computational analysis (MMFF94s).

Early attempts towards the synthesis of non-substituted **C78** by *Müller* are to be mentioned which however made use of an alternative oligophenylene not reflecting the connectivity of the benzene moieties in the present case.[56,57] Unlike **4-39** (transversal terphenyl backbone), the oligophenylene of this synthetic approach was built from a quinquephenyl unit which extends along the longitudinal axis of precursor **4-42** (indicated in red in Figure 4-54). The cyclodehydrogenation of this compound was achieved by applying a mixture of copper(II) triflate and aluminum(III) chloride in carbon disulfide. However, the structural analysis of the compound was strongly limited by the

sparse solubility of the PAH which did not bear any solubilizing groups. Owing to this, the supramolecular properties could not be studied either.

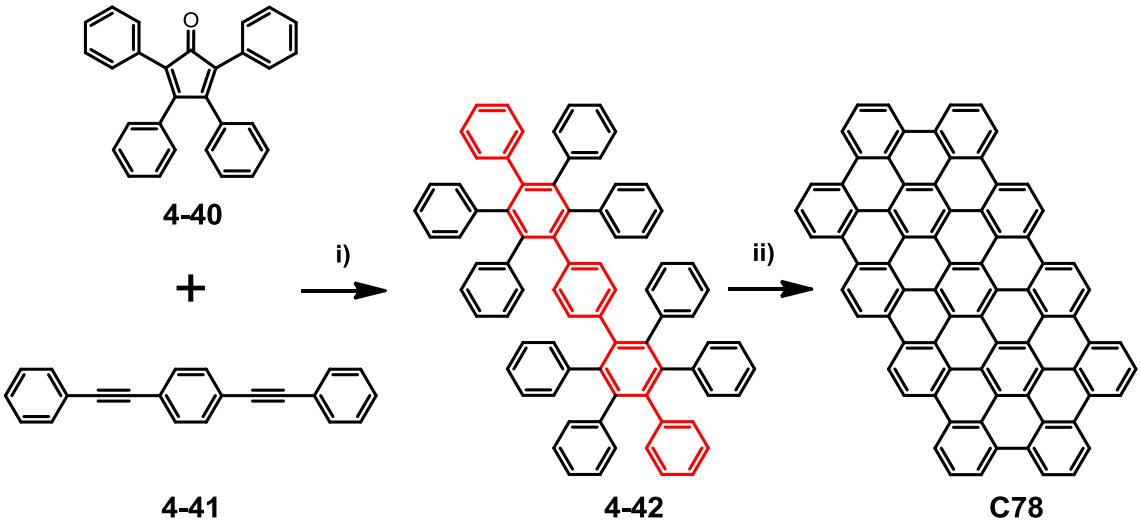

Figure 4-54: Synthesis of non-substituted **C78** *via* the route of *Müller*;[56] conditions: i) Ph_2O, 240 °C, 98 %; ii) $Cu(OTf)_2/AlCl_3$, CS_2, RT, quantitative.

Later on, an alternative pathway towards the synthesis of **C78$_{deca}$** was developed by *Simpson* (Figure 4-55).[58,59] The cyclodehydrogenation was realized by treatment of precursor **4-45** with ferric chloride in DCM.

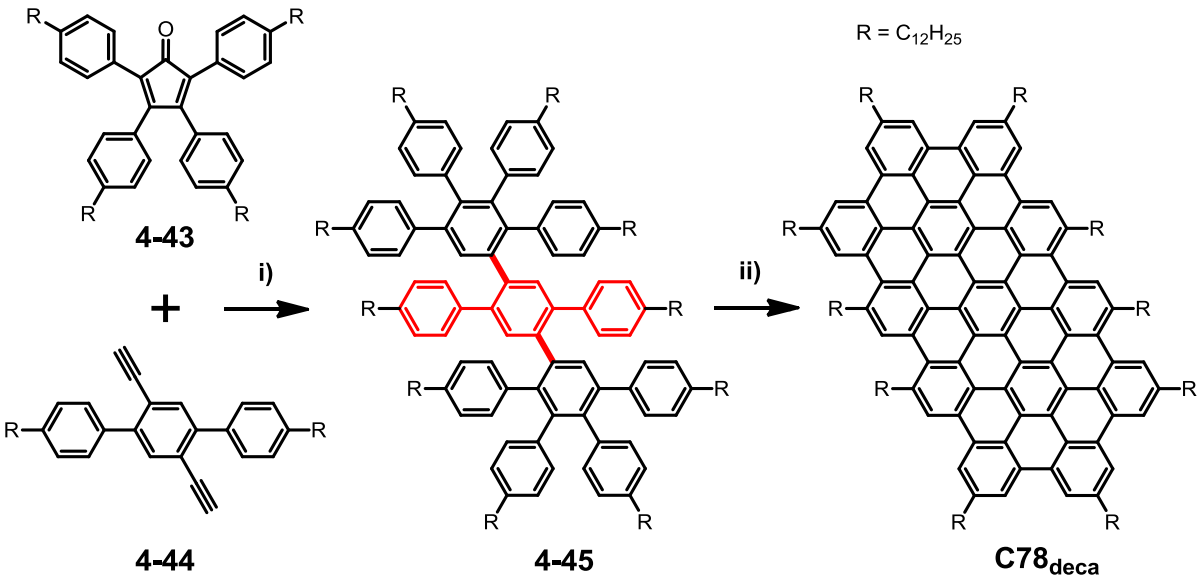

Figure 4-55: Synthesis of deca-substituted **C78$_{deca}$** *via* the route of *Simpson*;[59] conditions: i) Ph_2O, 200 °C, 90 %; ii) $FeCl_3$, DCM, RT, 83 %.

This derivative is characterized by its extensive alkyl substitution on the periphery. In total, ten linear dodecyl chains were attached to the molecular backbone enabling access to solution-based analytical tools. In contrast to the previous case, the molecular backbone of precursor **4-45** is formed by a terphenyl, on whose central benzene ring the two lateral dendrons are attached (indicated in red in Figure 4-55). The optical properties and the self-assembly behavior on surfaces could be investigated in detail for this PAH.[59]

In view of these two literature examples the different topology of precursor **4-39** needs to be emphasized. This concerns on the one hand the arrangement of the benzene units which reflect the connectivity of **P3** and **P4** and permit the treatment of **4-39** as a model case for the cyclodehydrogenation reaction. On the other hand, the substitution pattern on the molecular backbone of **4-39** is different and should greatly affect the expected self-assembly of **C78$_{hexa}$**.

For the determination of optimum reaction conditions, experiments with three different oxidants were performed on **4-39** (Figure 4-56). Moreover, the necessary amount for complete cyclodehydrogenation was determined by running the reaction in the presence of variable amounts of the corresponding oxidant. Also, the influence of the reaction time was investigated.

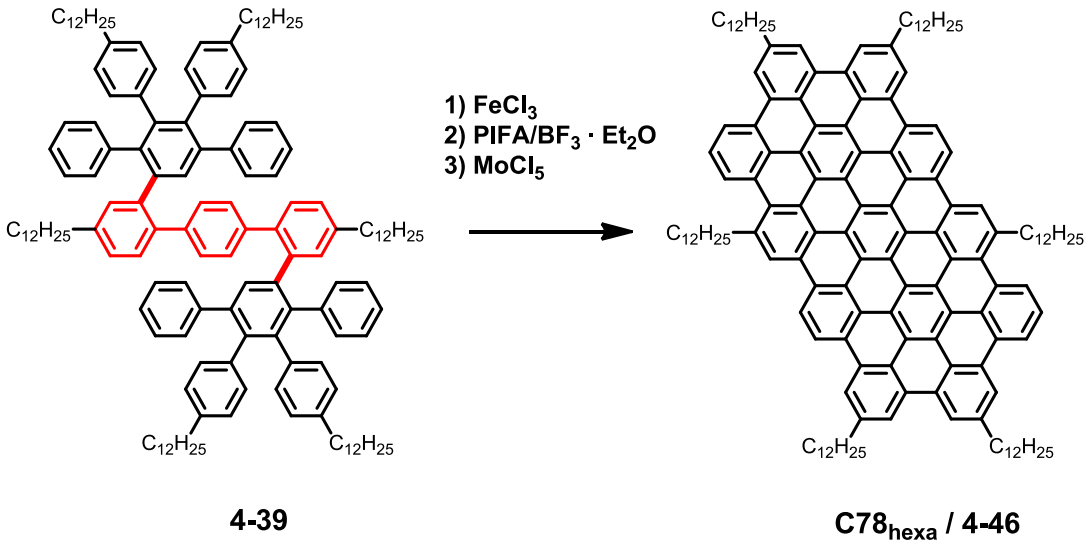

Figure 4-56: Successful synthesis of hexa-substituted **C78$_{hexa}$** *via* three different oxidant systems.

The most widely applied oxidizing system in the synthesis of extended PAHs is ferric chloride ($FeCl_3$) in a mixture of DCM and nitromethane.[51,52,55,59-61,63,64] Taking into account the successful conditions determined for the **C84** disc, initial trials were carried out using a similar excess of ferric chloride (7.50 equivalents per bond). The reaction

was allowed to proceed for 12 h with argon bubbling during the early stage of the cyclodehydrogenation. Quenching was achieved by treatment of the reaction mixture with excess methanol upon which **C78$_{hexa}$** precipitated as a red-brown powder. The compound was collected by filtration and thoroughly washed in order to remove residual ferric chloride and by-products of the reaction. As the compound showed high solubility in polar solvents like DCM and THF, it could be re-dissolved and was precipitated into methanol for two more times.

Remarkably, MALDI-TOF indicated full conversion of the precursor **4-39** without any significant chlorination which is frequently observed as an undesired side-reaction (Figure 4-57).

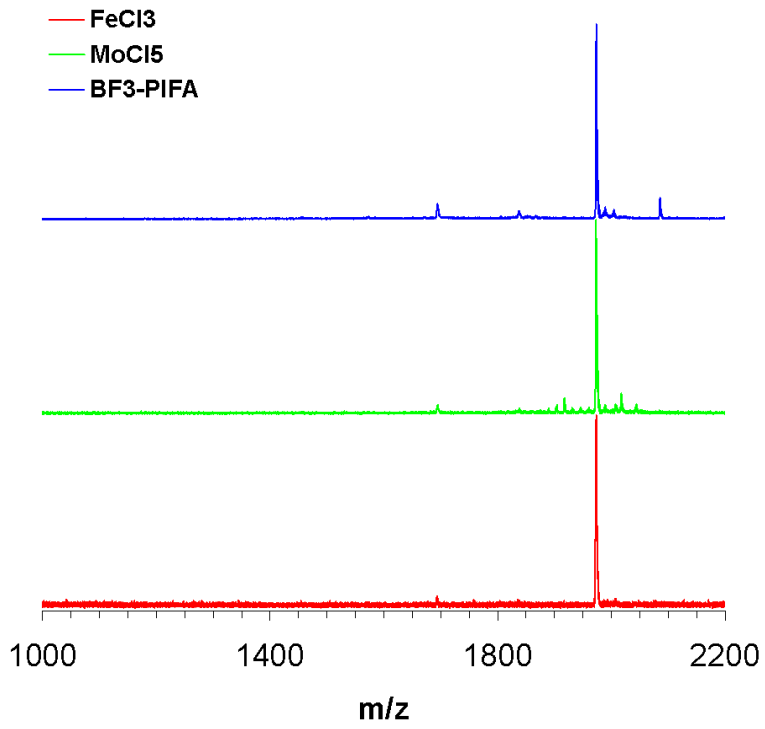

Figure 4-57: MALDI-TOF analysis of **C78$_{hexa}$** obtained *via* three different oxidant systems.

Furthermore, the isotopic pattern of the target peak fully matched the predicted isotopic composition of **C78$_{hexa}$** thus proving the high efficiency of the cyclodehydrogenation under these conditions (Figure 4-58). Also, neither the starting compound nor any partially fused reaction intermediates were detected by MALDI-TOF. It was thus decided to successively decrease the amount of ferric chloride in order to define the minimum amount of equivalents necessary for full conversion of oligophenylene **4-39** into the **C78$_{hexa}$** disc. Indeed, the reaction still performed well, when the amount of oxidant was decreased to one half of the previous value, thus 3.75 equivalents per bond. Also in this case, quantitative conversion was derived from the corresponding

MALDI-TOF spectra after 12 h indicating an identical degree of purity as seen in the previous case. Further reducing the number of bond equivalents to 2.00 did however only result in the formation of partially fused species even when the reaction time was extended to one week.

The independent structure proof *via* NMR spectroscopy was possible for **C78$_{hexa}$** derived from the experiments with ferric chloride and will be discussed in the following section.

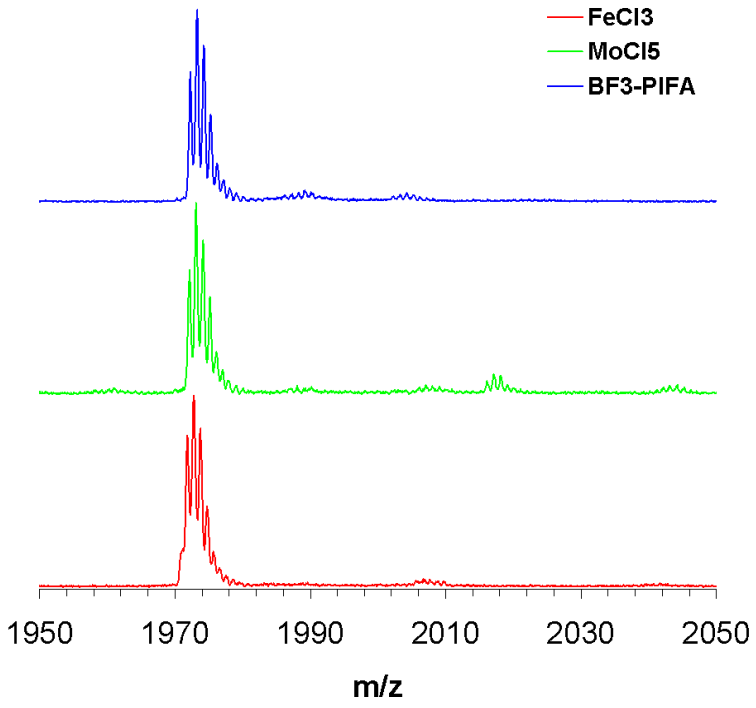

Figure 4-58: Magnified MALDI-TOF spectra of **C78$_{hexa}$** obtained *via* three different oxidant systems.

The second oxidative system that was tested for the synthesis of **C78$_{hexa}$** consisted of a mixture of phenyliodine(III) bis(trifluoroacetate) (PIFA) and boron trifluoride etherate $BF_3 \cdot Et_2O$ in DCM.[90] It has been discussed in the context of **GNR1+2** that PIFA efficiently mediates aryl-aryl bond formation in the presence of a *Lewis* acid.[42,43,91]

The cyclodehydrogenation of precursor **4-39** was successfully achieved in the presence of 2.50 bond equivalents of this oxidant. The reaction can be easily controlled by temperature which is in strong contrast to the ferric chloride system. Typically, the oxidant was added to the precursor solution at - 60 °C and the reaction mixture was then kept at this temperature level for 2 h. During this period the color of the reaction system slowly turned from yellow to dark green. Then, the temperature was slowly raised to -10 °C during additional 2 h and the reaction was stopped by addition of methanol and water to yield a dark red precipitate which was collected and further

purified by repeated dissolution and precipitation as described above. MALDI-TOF spectroscopy revealed the formation of the desired product and indicated virtually quantitative conversion of the starting compound to the **C78$_{hexa}$** disc. The significance of this result is that by application of PIFA the troublesome chlorination of the target molecule can be ruled out as no hydrochloric acid is formed. So far, the synthesis of HBC represented the largest example for the preparation of a PAH by this method.[43] **C78$_{hexa}$** exceeds the dimensions of HBC by a factor of almost two. The same holds for the number of bonds which have to be established upon planarization. This illustrates the high potential of the PIFA method for the future preparation of largest PAHs.

Another *Lewis* acid known to promote the oxidative *Scholl* reaction is molybdenum pentachloride ($MoCl_5$). This oxidant is frequently applied to selective single bond formation between aryl units but has been scarcely applied to larger multi-bond precursors.[42,43,109-112] Little is known about the stoichiometry or the mechanism of the reaction of molybdenum pentachloride with aromatic rings. This concerns in particular the question whether the reaction is a two- or one-electron transfer process.[42,112] However, previous studies illustrated the milder character of molybdenum pentachloride suggesting slower kinetics of the *Scholl* reaction for this reagent.[113,114] It was therefore chosen as a suitable candidate to study the underlying reaction mechanism during the formation of **C78$_{hexa}$**.

The strength of the oxidative system was progressively increased for the molybdenum pentachloride series. First trials were carried out with 2.00 equivalents of molybdenum pentachloride per bond and the reaction time was set to 48 h with argon bubbling during the first stage of the reaction. After quenching of this reaction, a complex mixture was detected by MALDI-TOF spectroscopy which contained only traces of **C78$_{hexa}$** but a number of partially fused intermediates which however shed light on the course of the reaction.

From previous studies by *Dötz* it is known that panel formation of the dendritic 2,3,4,5-tetraphenylbenzene subunits occurs firstly due to their favorable geometrical conformation (Figure 4-59).[54,83] This is evidenced by the model case study on compound **4-47** which could be efficiently converted into **C30**. However, the cyclodehydrogenation also proceeded smoothly for the analogous 2,3,4,5,6-pentaphenylbenzene precursor **4-49** leading to the **C36** disc upon planarization (Figure 4-59).

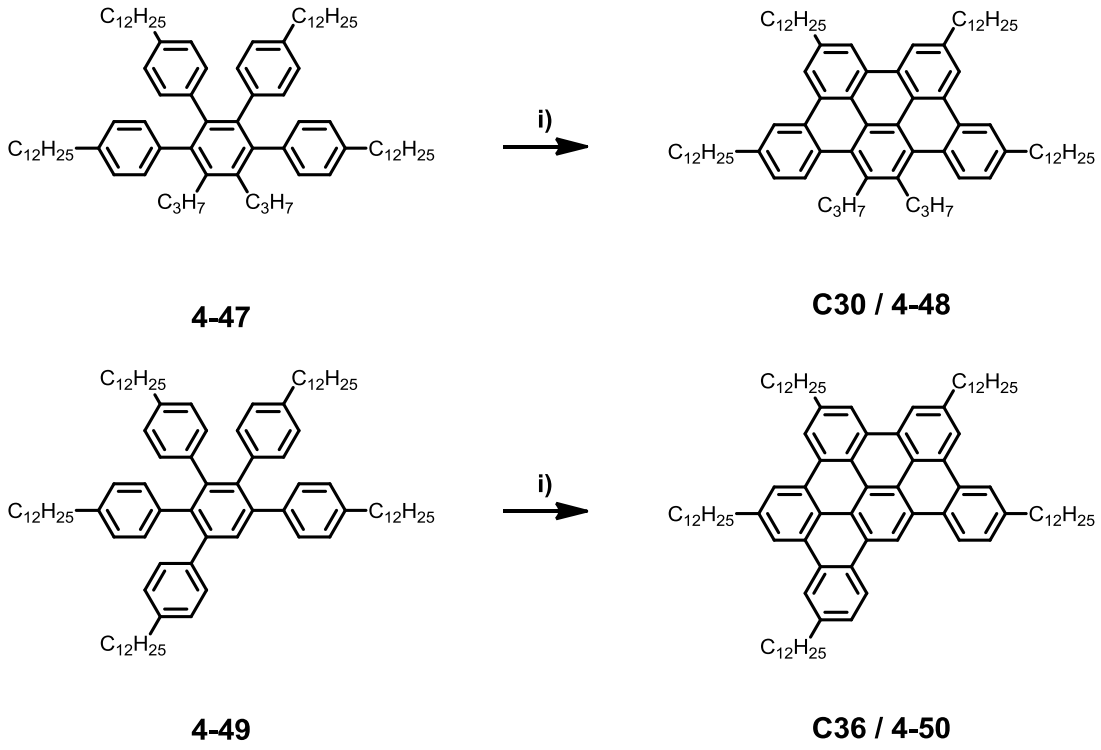

Figure 4-59: Synthesis of **C30** and **C36** as shown by *Dötz*;[83] conditions: i) $FeCl_3$, DCM, RT, 24 - 53 %.

Due to their extensive alkyl chain substitution, both PAHs, **C30** and **C36**, could be fully characterized by means of MALDI-TOF and NMR spectroscopy at the time.

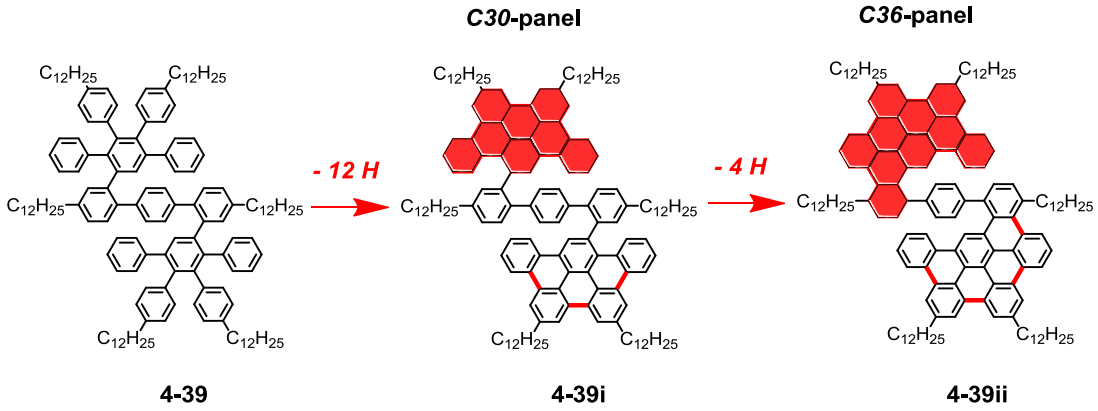

Figure 4-60: Proposed formation of **C30** and **C36** panels during the cyclodehydrogenation of **4-39** at low concentration of molybdenum pentachloride.

Due to the geometrical conformity of the two 2,3,4,5,6-pentaphenylbenzene dendrons of oligophenylene **4-39** with the substitution pattern of **4-47** and **4-49**, it appears justified to assume a similar pathway during the synthesis of **$C78_{hexa}$**. In the case of **4-39** the formation of **C30** and **C36** panels would correspond to the build-up of six and

eight bonds, respectively, resulting in the intermediate structures **4-39i** and **4-39ii** (Figure 4-60). Whereas the resulting tribenzo-[b,n,pqr]perylene moieties are able to freely rotate around the single bond connecting them to the *para*-terphenyl backbone of **4-39i** a lower degree of conformational freedom is retained in intermediate **4-39ii**.

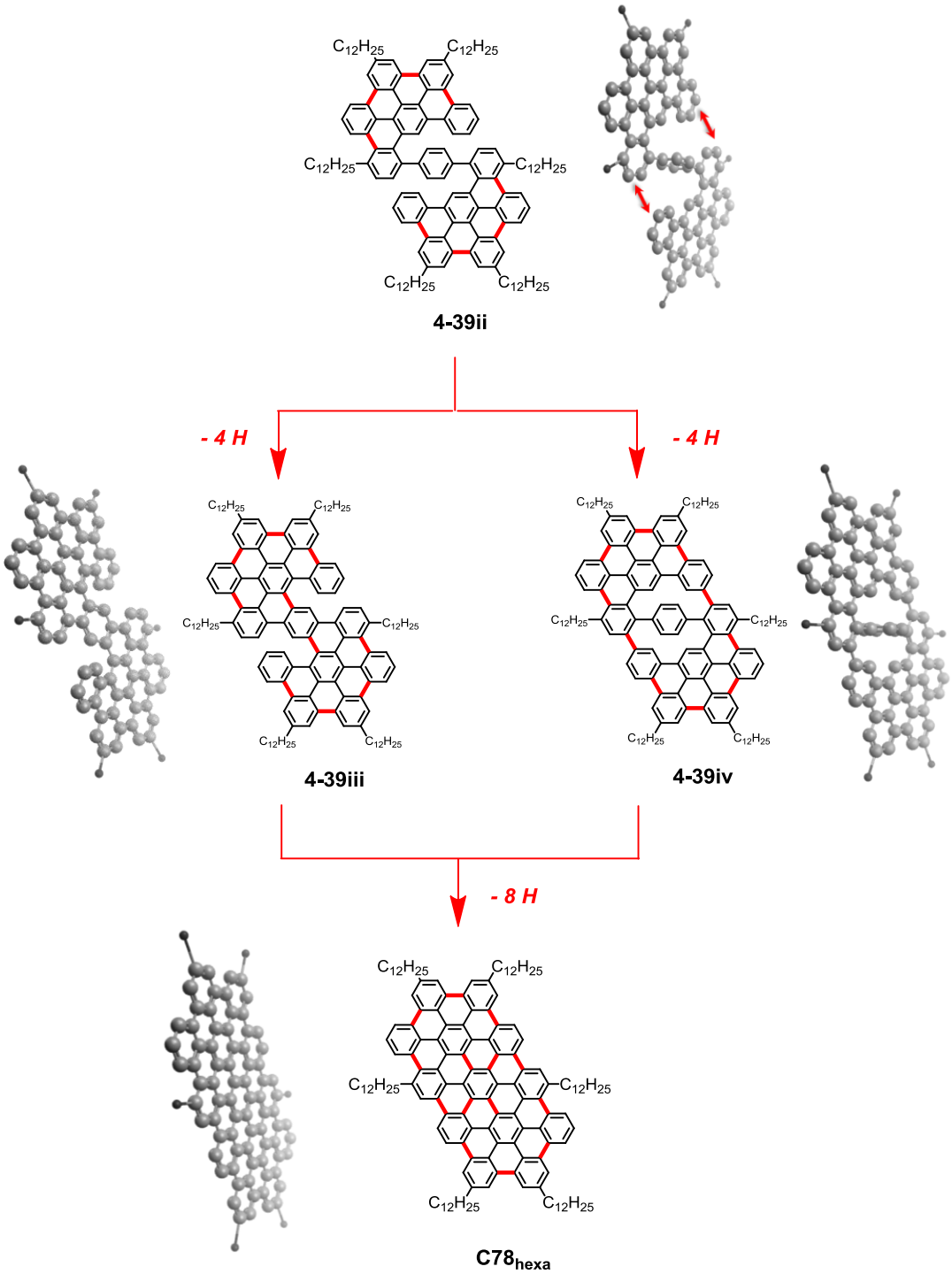

Figure 4-61: Proposed pathway for the cyclodehydrogenation of **4-39** and computational analysis of the possible intermediates (MMFF94s).

Surprisingly, the intermediate **4-39i** was however only present in negligible amounts after quenching the reaction carried out in the presence of 2.00 bond equivalents of molybdenum pentachloride. In contrast, the main peak of the MALDI-TOF spectrum was found at 1983.42 g/mol for which intermediate **4-39ii** is likely to account (Figure 4-62). The importance of this finding lies in the fact that for **4-39ii** the two panels are already connected to the peripheral benzene rings of the linear molecular backbone. *Para*-terphenyl and its higher homologues are known to adopt an alternating, twisted conformation between the benzene units in order to minimize the steric repulsion of the hydrogen atoms as seen in the crystal structures depicted in Figure 4-38 and 4-39.

A similar effect can be intuitively predicted for intermediate **4-39ii** and molecular simulations indeed confirm this assumption (Figure 4-61). The two **C36** panels are twisted by 70 ° with respect to the central benzene ring of the terphenyl unit and are orientated in a coplanar fashion.

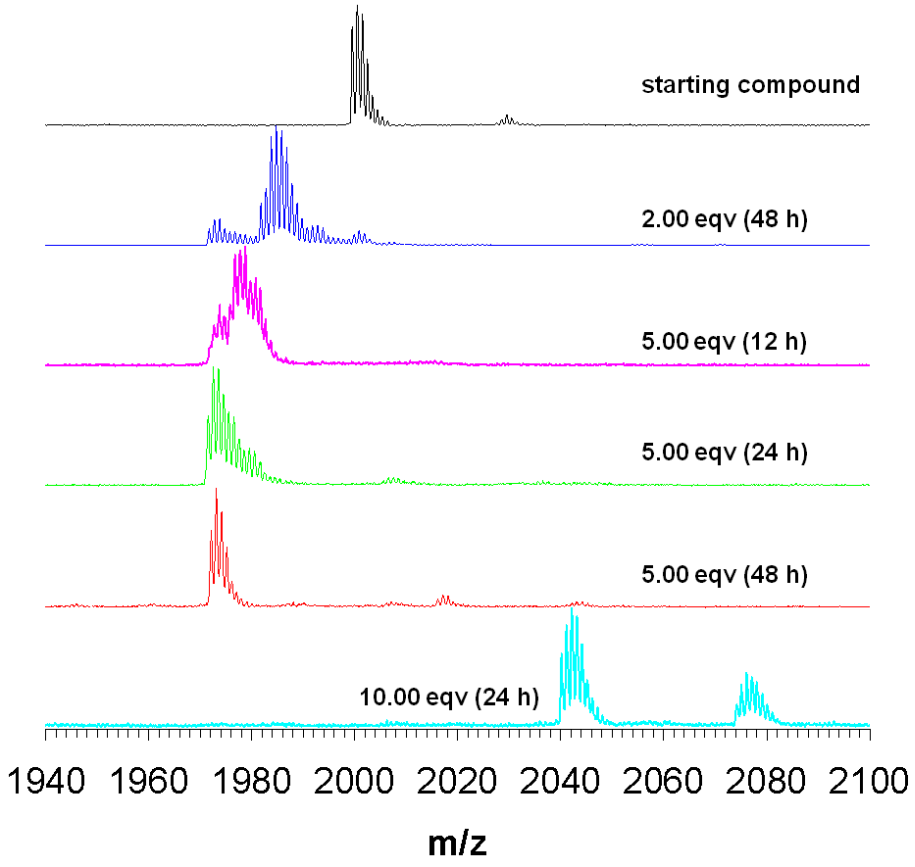

Figure 4-62: MALDI-TOF spectra obtained during the cyclodehydrogenation of **4-39** with molybdenum pentachloride.

In order to push the *Scholl* reaction to higher conversion, the amount of molybdenum pentachloride was increased to 5.00 bond equivalents in the following experiment and

quenching was carried out after 12, 24 and 48 h, respectively. The corresponding MALDI-TOF spectra reveal the progress of the reaction as compared to the previous case. However, after 12 h and 24 h the conversion of **4-39** into **C78$_{hexa}$** was not yet complete resulting in the formation of various partially fused intermediates (Figure 4-62).

Starting from intermediate **4-39ii** its conformational situation has to be considered in order to identify the next two bonds to be closed. The paralleled orientation of the two **C36** panels brings also their peripheries into close contact as indicated by the red arrows in Figure 4-61. For the formation of the following linkages, two alternative possibilities exist which particularly affect the conformation adopted by the *para*-terphenyl backbone.

In the first case, the two **C36** units are fused to the central benzene ring resulting in intermediate **4-39iii**. By this route, the free rotation of the *para*-terphenyl is prevented and severe steric crowding is revealed by molecular simulation that results in a bent conformation at the periphery of the lateral panels.

The second pathway leaves the central benzene ring untouched resulting in the attachment of the two panels in a fashion as shown for **4-39iv**. In this molecule, the central benzene ring still maintains a maximum distance to the surrounding hydrogen atoms by adopting a nearly orthogonal orientation. Due to the full connection of the benzene rings along the molecule's rim, the planarity of the **C78$_{hexa}$** disc is already prepared. The computational analysis of these two alternative conformations revealed an energy difference of 13 kJ/mol between **4-39iii** and **4-39iv** suggesting a preferential pathway *via* the second route (MMFF94s).

Full conversion of **4-39** to the final PAH is achieved after additional 24 h reaction time in the presence of 5.00 bond equivalents of the oxidant (Figure 4-62). In this case, **C78$_{hexa}$** is detected at a mass of 1972.33 g/mol as exclusive species with its isotopic pattern being identical to the theoretic prediction.

In a last experiment, it was tested whether the reaction time could be shortened by an even higher excess of molybdenum pentachloride corresponding to 10.0 bond equivalents. It became however obvious after only 24 h reaction time that in this case chlorination of **C78$_{hexa}$** was unavoidable. Two large peaks at 2074.22 g/mol and 2040.26 g/mol can be ascribed to the triple and double chlorinated **C78$_{hexa}$** disc, respectively (Figure 4-62).

4.6.2 NMR Analysis

In view of the good solubility of the **C78$_{hexa}$** disc attempts were undertaken to obtain NMR data of this extended PAH. The NMR analysis of non-substituted **C78** was prevented by the insolubility of the compound in the past which was a frequent obstacle hampering early spectroscopic studies on this class of compounds.[56,57] But also, for the well-soluble **C78$_{deca}$** disc it was not possible to obtain resolved spectra despite the testing of a set of solvents at elevated temperatures. This is due to a second major problem frequently encountered in the NMR analysis of large PAHs.[58,59] They tend to form columnar aggregates in solution that might persist even upon strong dilution and at high temperature. The self-association is a consequence of the strong *inter*molecular interaction of neighboring *π*-surfaces that typically results in a loss of the NMR signature of the aromatic protons.

In the present case initial trials proved unsuccessful as well. Neither mixtures of carbon disulfide with polar solvents such as DCM-d_2 or THF-d_8 which were efficiently used for the examination of **C72**,[54,55] nor measurements at elevated temperatures in TCE-d_2 gave the desired spectrum. In all cases only the alkyl chains were detected whereas the aromatic region did not contain signals due to the aforementioned increased molecular aggregation. It was then decided to use an aromatic solvent which would on the one hand intercalate and thus disrupt the supposed aggregates of **C78$_{hexa}$** and on the other hand allow for an NMR measurement at elevated temperature. Dissolution of **C78$_{hexa}$** was easily achieved in *ortho*-dichlorobenzene (*o*-DCB-d_4) having a boiling point of 180 °C. Above a temperature level of 140 °C, the ^{1}H NMR spectrum disclosed the expected signals of the aromatic core of the molecule. This was in sharp contrast to the poor result in TCE-d_2 at the identical temperature.

The ^{1}H NMR spectrum of **C78$_{hexa}$**, recorded at 170 °C in *o*-DCB-d_4 is depicted in Figure 4-63. The first remarkable feature is the strong deep-field shift of the aromatic protons which are found in the region of δ = 8.0 - 9.5 ppm.

The distinct shift of the signals is a consequence of the extended aromatic system and corresponds well to ^{1}H NMR results obtained for **C60**[51] and **C72**[54,55] in the past. The good resolution of the spectrum allows for the partial assignment of the signals even though the high number of protons of similar chemical environment leads to partial overlap in the aromatic region of **C78$_{hexa}$**. Integration of the signals and comparison of the peak intensities reveals the expected ratio between aromatic and aliphatic protons further highlighting the good purity of the compound.

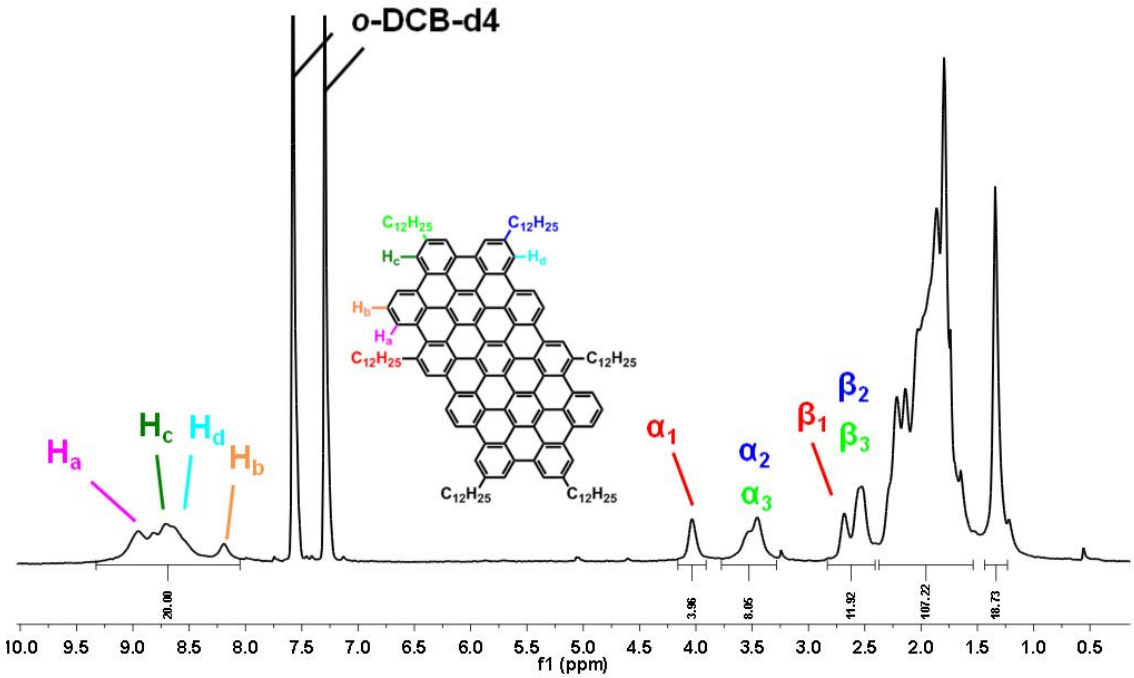

Figure 4-63: ^{1}H NMR spectrum of the **C78$_{hexa}$** disc in *o*-DCB-d$_4$ at 170 °C.

The decreased symmetry of the **C78$_{hexa}$** disc translates into a set of three chemically different dodecyl chains on the aromatic backbone. This is reflected by the splitting of the resonances emerging from the *alpha*-CH_2 and *beta*-CH_2 protons into two groups of signals of an integral ratio of 1:2 in each case. The two dodecyl chains located in the *bay*-position suffer from an increased deshielding as compared to the four other chains leading to a downfield shift of the *alpha*-CH_2 resonance by 0.55 ppm. A similar effect, even though less pronounced, is observed for the *beta*-CH_2 protons which are shifted by 0.15 ppm (Figure 4-63).

Whereas ^{1}H-^{1}H-COSY NMR experiments did not lead to resolved cross-signals, the NOESY measurement of **C78$_{hexa}$** could be used for the unambiguous assignment of a number of aromatic peaks. As it can be seen in Figure 4-64, the alkyl chains commute with the neighboring protons of the aromatic backbone. Strong cross-signals arise from the *alpha*-CH_2 (δ = 4.04 ppm) and *beta*-CH_2 protons (δ = 2.70 ppm) of the two dodecyl chains located in the *bay*-position of the molecule. Thus, the aromatic signal at δ = 8.95 ppm can be attributed to the proton of the opposite *bay*-position (H_a). A strong down-field shift of this proton is also to be expected from its spatial confinement.

On the contrary, the up-field shifted signal of H_b at δ = 8.20 ppm reflects its exposed position on the aromatic core. With the help of peak integration this signal can be undoubtedly assigned to H_b. Still further information concerning the other four alkyl chains is contained in the NOESY spectrum of **C78$_{hexa}$**. Also for these chains, a cross-

signal of the peak centered at δ = 3.47 ppm with the aromatic region is found (Figure 4-64).

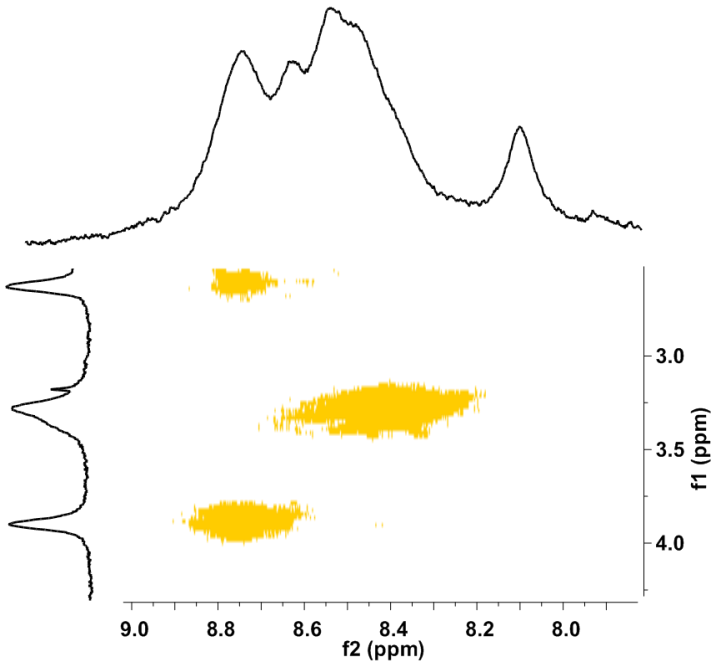

Figure 4-64: Detail of the NOESY spectrum of the **C78$_{hexa}$** disc in *o*-DCB-d$_4$ at 130 °C.

Whereas the peak intensity reflects the higher number of eight surrounding protons, the exact position of the resonances originating from H_c and H_d is prevented by the missing resolution of the spectral data in the aromatic region. It can be assumed that despite the elevated temperature, aggregates of the disc still exist.

However, in combination with the results from MALDI-TOF analysis discussed in detail above, it can be concluded that the cyclodehydrogenation towards **C78$_{hexa}$** can indeed serve as a model reaction for the preparation of the larger GNRs. This is due to the fact that precursor **4-39** exactly reflects the arrangement of the benzene rings found in the repeat unit of polymers **P3+4**. Additionally, the successful NMR characterization of the **C78$_{hexa}$** disc highlights that the structure proof for largest PAHs with molecular dimensions in the nanometer range can still be achieved under ideal experimental conditions (solvent and temperature). The well-resolved ^{1}H NMR spectrum of **C78$_{hexa}$** is important for future PAH characterization as no coherent NMR data on bigger discs is currently available.

4.6.3 Optical Spectroscopy

In view of the facile dissolution of the PAH in common polar solvents, the optical properties of the **C78$_{hexa}$** disc were subsequently analyzed in solution.

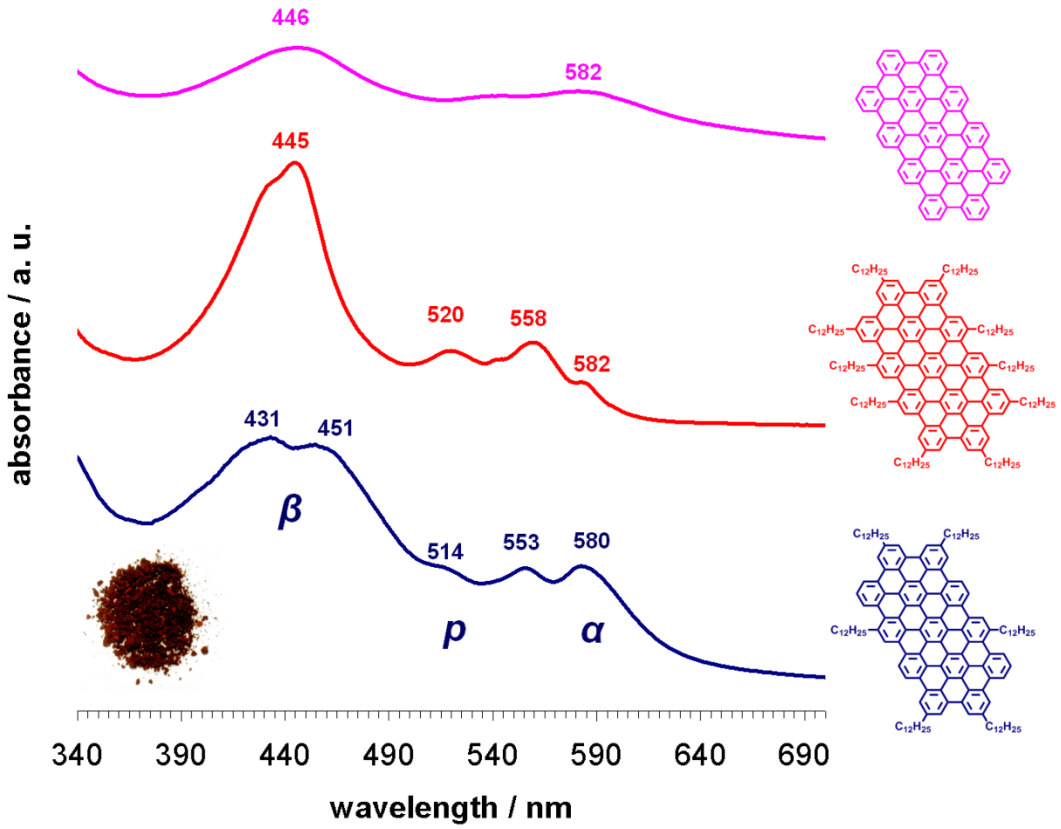

Figure 4-65: Normalized UV-vis absorption spectra of **C78$_{hexa}$** and **C78$_{deca}$** in THF at $5 \cdot 10^{-6}$ M and thin film spectrum of non-substituted **C78**.

The results were compared to the data of the oligophenylene precursor **4-39**. Furthermore, they were correlated to the results obtained for the previously synthesized **C78**[56,57] and **C78$_{deca}$**[58,59] systems. Solutions of **C78$_{hexa}$** generally appear orange to dark red depending on the concentration of the PAH. UV-vis spectroscopy revealed a strongly structured spectrum for **C78$_{hexa}$** covering almost the whole visible range. In comparison to the oligophenylene precursor **4-39** (Figure 4-52), a red-shift of the absorption maximum by nearly 200 nm is observed which is indicative for the formation of an extended aromatic system. In the spectrum of **C78$_{hexa}$**, the two main absorption bands are located at 431 and 451 nm, respectively, and can be attributed to the *β*-bands of the compound.[59] The small shoulder resolved at 514 nm was previously identified as *p*-band.[59] A remarkably well-resolved *α*-band is seen at a wavelength of 580 nm. Compared to triphenylene, HBC and other highly symmetric PAHs, the

intensity of this symmetry-forbidden band is relatively high which can be ascribed to the decreased symmetry of **C78$_{hexa}$**.

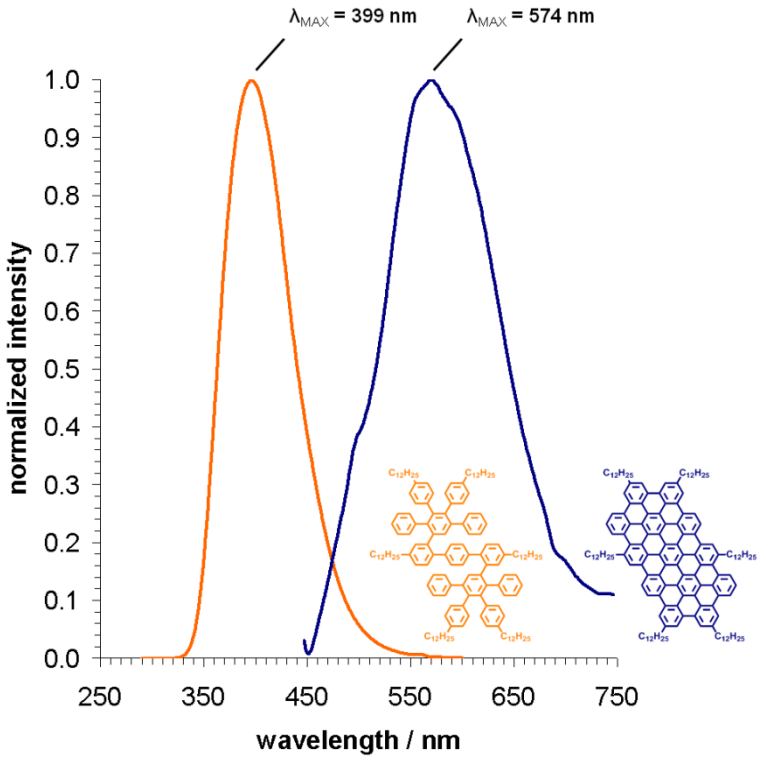

Figure 4-66: Normalized fluorescence emission spectra of **4-39** and **C78$_{hexa}$** in THF at 5 · 10-5 M.

When compared to the solid-state spectrum of non-substituted **C78** (recorded as a thin film on quartz) and the solution spectrum of **C78$_{deca}$** a high degree of similarity is noticed. Even though the solid-state spectrum appears broadened the main bands are still visible. The band positions in the spectrum of **C78$_{deca}$** are virtually identical and apparently not affected by the number and different substitution of the alkyl chains.

These findings provide a further indication for the successful formation of **C78$_{hexa}$** by the newly developed route *via* precursor **4-39**. A comparison to the two literature examples and the **C72**[53-55] and **C84** case previously discussed allows for important conclusions regarding the design of future PAH precursors.

A continuous and highly rigid longitudinal backbone as in the case of **4-42** guarantees a suitable arrangement of the benzene units that are easily fused upon cyclodehydrogenation (Figure 4-54). Secondly, the attachment of lateral dendrons to the same phenyl unit as in the case of precursor **4-45** is another possibility as this prevents the latter to rotate independently (Figure 4-55). Thirdly, the backbone structure realized for the newly developed precursor **4-39** leads to a favorable coplanar

orientation of the two dendrons thus minimizing the steric repulsions among the *para*-terphenyl core (Figure 4-56).

In contrast to these three examples, the attachment of the dendrons to two neighboring units as seen in the biphenyl backbone of the **C72**[53] and **C84** precursors renders the planarization difficult due to the strong steric strain that drives the adoption of a twisted three-dimensional conformation.

Further analysis of **C78$_{hexa}$** was directed towards the luminescence behavior of the PAH (Figure 4-66). The fluorescence spectrum of the PAH is dominated by a broad emission centered at 574 nm. This confirms the observation from the UV-vis measurements where the *α*-bands are found in the same spectral region (580 nm).

For a PAH, the highest wavelength absorption reflects the transition from the lowest vibrational energy level of the ground state to the lowest vibrational energy state of the exited state.[85] Thus, the corresponding energy difference is a versatile estimate of the HOMO-LUMO energy gap of the compound. For the band gap of **C78$_{hexa}$** a value of 2.1 eV can be derived.[58,59] When this value is brought into relation to other extended PAHs, the **C78** core integrates well into the experimentally found correlation depicted in Figure 4-67.[115,116] The band gaps of various PAHs narrow down from a value of 4.74 eV for parent benzene to 1.43 eV for giant **C222** with its 37 aromatic sextets.[64]

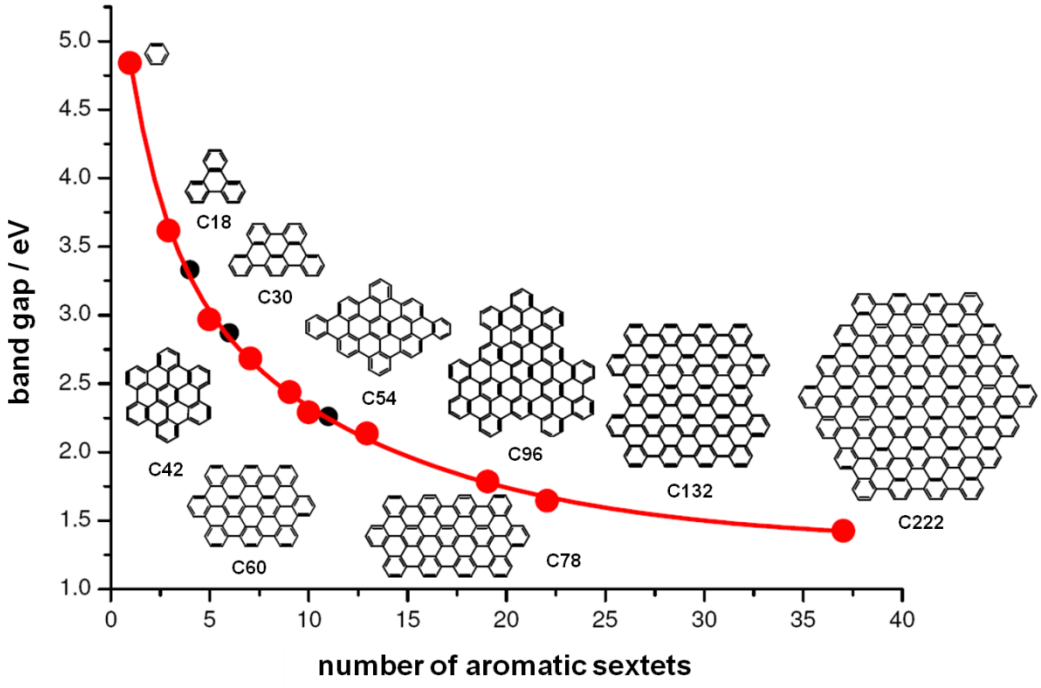

Figure 4-67: Correlation between the optical band gap and the number of aromatic sextets of various PAHs.

4.6.4 Self-Assembly

Discotic PAHs frequently assemble into well-organized superstructures due to the microphase separation between the soft alkyl periphery and the hard aromatic core of the molecules. Weak *π-π* interactions contribute to the face-to-face stacking of the molecules.[87,88]

The phase forming properties of the **C78** core remain, however, to be elucidated. Therefore, a combination of DSC and 2D-WAXS analysis was performed on **C78$_{hexa}$** with the help of *A. Mavrinskiy and Dr. W. Pisula* (MPI-P Mainz, Germany).

The thermal analysis of hexa-substituted **C78$_{hexa}$** indicated an endothermic phase transition at 46.5 °C which reoccurred upon cooling at 33.2 °C (Figure 4-68). No further phase transitions were observed prior to the thermal decomposition of the sample.

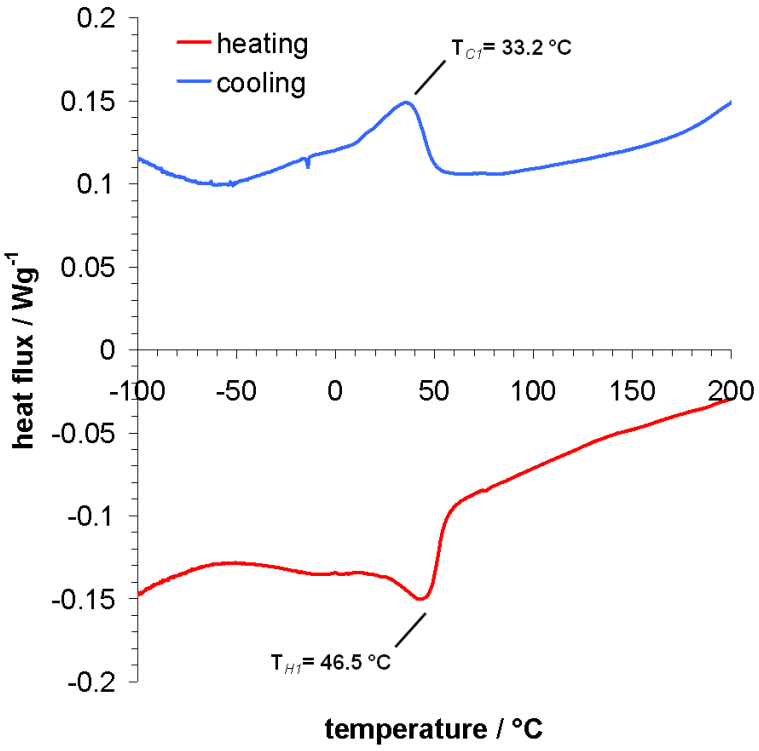

Figure 4-68: DSC trace of the **C78$_{hexa}$** disc upon second heating (red) and cooling (blue).

A subsequent analysis of the temperature-dependent phase behavior of the disc was performed by 2D-WAXS experiments (Figure 4-69).

In a mechanically extruded fiber of **C78$_{hexa}$**, [88] the discs are found to be self-organized in a columnar liquid crystalline phase above the temperature of the phase transition. At 160 °C, the *π*-stacking distance between the building blocks as derived from the meridional reflections equals p = 0.35 nm. The equatorial reflections correspond to the

*inter*columnar organization which is described by a hexagonal unit cell exhibiting a packing parameter of a_{hex} = 3.20 nm. This value corresponds well to the molecular dimensions of the disc when interdigitation of lateral alkyl chains from adjacent molecules is taken into account.[55] Also, the dimensions of the unit cell are identical to the results obtained by the 2D-WAXS analysis of the **C84** disc (Figure 4-23) reflecting the close similarity of both PAHs concerning molecular dimension and their hexa-fold dodecyl substitution on the aromatic core.

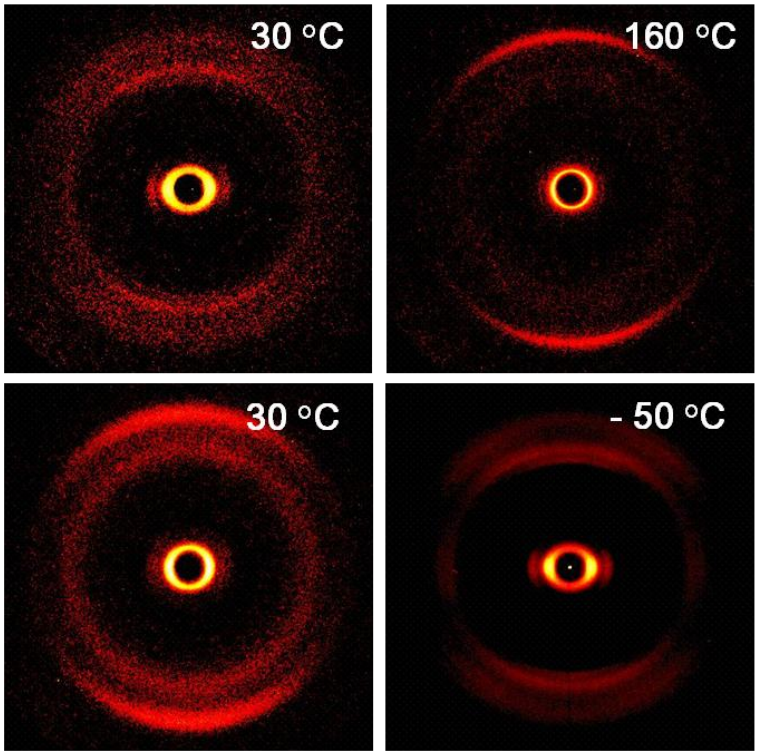

Figure 4-69: Temperature-dependent 2D-WAXS patterns of the **C78$_{hexa}$** disc.

Upon cooling, **C78$_{hexa}$** forms a crystalline state from the LC phase as seen in the pattern obtained at - 50 °C (Figure 4-69). Characteristically, the molecules are tilted towards the columnar axis. The hexagonal unit cell is conserved, but with a slightly smaller parameter of a_{hex} = 2.81 nm.

STM analysis of **C78$_{hexa}$** was successfully performed in cooperation with the group of *de Feyter* (KU Leuven, Belgium). For these experiments the PAH could be processed from 1,2,4-trichlorobenzene. A solution with a concentration of $5 \cdot 10^{-6}$ M was dropcasted on a highly ordered pyrolytic graphite (HOPG) surface and the compound was successfully visualized at the liquid-solid interface. The aromatic cores of the molecules can be assigned to areas of high tunneling currents which appear bright in the images (Figure 4-70). The darker regions can be attributed to the alkyl chains

which exhibit a significantly lower tunneling probability. The geometric dimensions as seen by STM are in agreement with the calculated values and also the characteristic shape of **C78$_{hexa}$** is reflected by the images. The ordered monolayer is characterized by its unit cell (a = 3.59 ± 0.02 nm, b = 2.62 ± 0.05 nm, α = 85.4 ± 0.2 °) and stretches over large areas of the substrate as seen from the low magnification image.

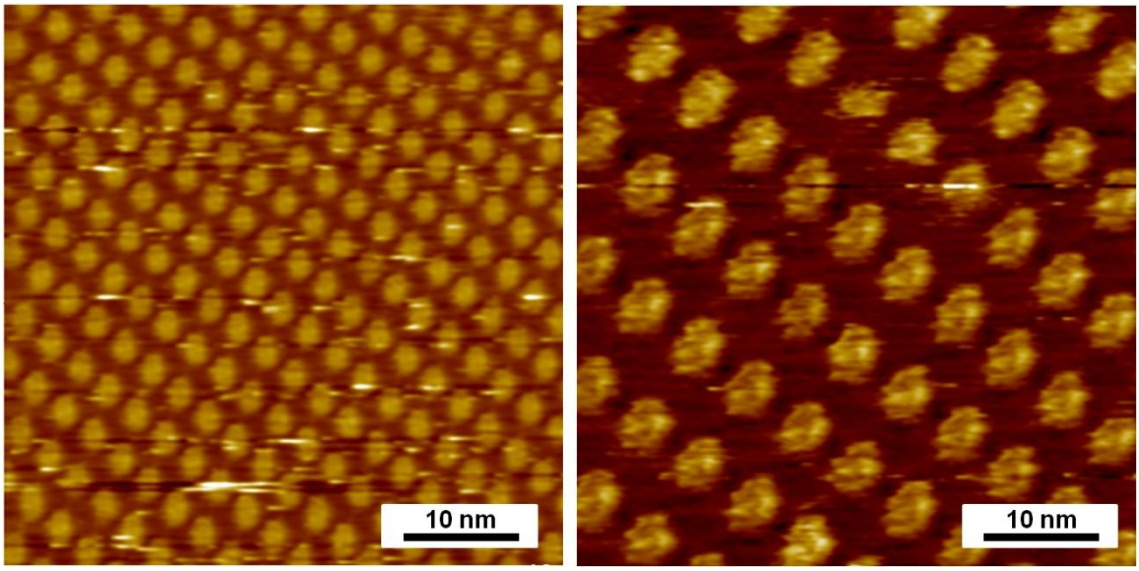

Figure 4-70: STM images of the **C78$_{hexa}$** disc at the liquid-solid interface of TCB/HOPG.

Whereas the quality of the images of **C78$_{hexa}$** is comparable to previous STM investigations of large PAHs in the past, [50-53,59,63] the deposition and visualization of the same compound on a Au(111) surface revealed interesting details regarding the self-assembly. This is due to the exceptionally high quality of the images which are shown in Figure 4-71 allowing for the investigation of the molecular arrangement in the two-dimensional lattice. A valuable feature of the STM images is their submolecular resolution allowing for the exact identification of the alkyl chain packing and the assessment of the electron density of the aromatic core.

The unit cell of **C78$_{hexa}$** on the gold surface exhibits slightly different dimensions as compared to the previous case and is defined by a = 3.4 ± 0.1 nm, b = 4.3 ± 0.2 nm, α = 88 ± 2 °. Concerning the angles of the alkyl chains with respect to the reconstruction lines of the substrate the values are β_1 = 94 ± 2 ° and β_2 = 39 ± 2 °. The six alkyl chains split thus into two groups that consist of four and two chains, respectively. The packing model of **C78$_{hexa}$** derived from the images is depicted in Figure 4-72. It reveals that the arrangement of four discs creates *inter*molecular voids which cannot be fully covered by the dodecyl chains of **C78$_{hexa}$** due its substitution pattern. This situation leads to the filling of the cavities with four guest molecules that

appear as small bright spots (indicated by blue circles in Figure 4-71). Most probably these correspond to entrapped 1,2,4-trichlorobenzene molecules which are co-adsorbed within the monolayer of the PAH.

As mentioned above, the resolution of most STM images that have been previously obtained in the analysis of large PAHs is too low and often allows only for the determination of the unit cell parameters. This is best evidenced by the **C78$_{hexa}$** case on HOPG for which the *inter*molecular space appears unstructured and featureless (Figure 4-70). Even though it is generally accepted that "empty" space creates a thermodynamically unfavorable state within two-dimensional monolayers,[117,118] the example of **C78$_{hexa}$** on Au(111) provides a true experimental insight into the structural response provided by the system. As the dimensions of **C78$_{hexa}$** and the substitution pattern of the dodecyl groups do not allow for a higher interdigitation of the side chains well resolved solvent molecules have to be entrapped in between neighboring discs. It is also clearly seen that the two peripheral alkyl chains have to adopt a kinked conformation in order to assure their parallelization.

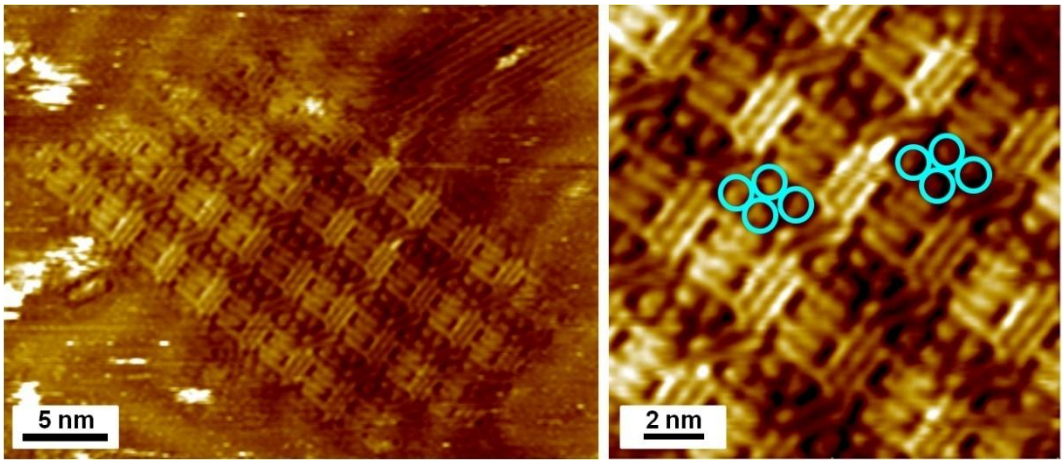

Figure 4-71: STM images of the **C78$_{hexa}$** disc at the liquid-solid interface of TCB/Au(111).

As to the aromatic cores of **C78$_{hexa}$** the molecular dimensions of the disc obtained from the STM analysis are in good agreement with the calculated values (Figure 4-53). The molecule has an apparent length of 2.3 ± 0.1 nm and a width of 1.4 ± 0.1 nm. Again, only the high resolution of the images makes a precise measurement possible.

The spatial requirement of **C78$_{hexa}$** is in excellent agreement to the provided space of the unit cell, illustrating the tight molecular packing in the monolayer promoted by the interdigitation of the alkyl substituents.

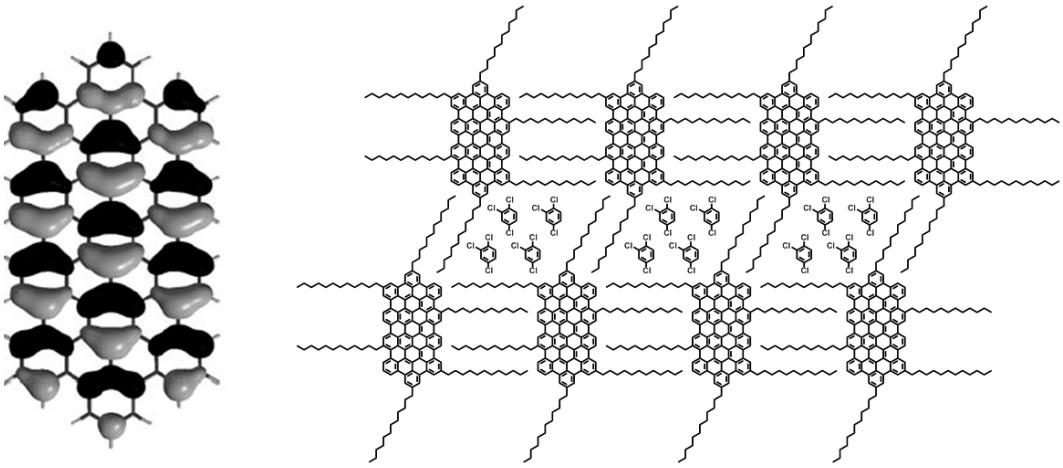

Figure 4-72: Wave functions of the HOMO of the **C78** core (left),[59] packing model for the monolayer formed by the **C78$_{hexa}$** disc at the TCB/Au(111) interface (right).

Interestingly, the aromatic cores are characterized by three bright linear stripes that correspond to an increased tunneling probability at these positions. This finding confirms the previously determined electron densities and location of the HOMO for **C78$_{deca}$** (Figure 4-72).[59] It also provides a qualitative prove that despite the geometric differences of the two oligophenylene precursors **4-39** and **4-45** the same PAH is accessible *via* oxidative cyclodehydrogenation.

The measured distance between two adjacent rows ranges between 0.4 nm and 0.5 nm. A similar line pattern characterized by an identical spacing has been observed for **C60**[51] and **C78$_{deca}$**[59] in the past.

4.7 Yamamoto-Based Graphene Nanoribbons

4.7.1 Solution-based Approaches

The preparation of GNRs from the two high-molecular weight precursors **P3** and **P4**, was performed according to the results from the cyclodehydrogenation studies on the **C78$_{hexa}$** disc. The corresponding materials will be referred to as **GNR3** and **GNR4** in the following.

Using ferric chloride (7.50 bond equivalents) as oxidant in a mixture of DCM and nitromethane, graphitic insoluble materials were obtained in quantitative yield. The application of PIFA/ $BF_3 \cdot Et_2O$ (3.00 bond equivalents) as described for the synthesis of **GNR1+2** lead to comparable results.

The MALDI-TOF analysis will be exemplified on the basis of **GNR3** as the best spectral resolution was obtained for these samples.

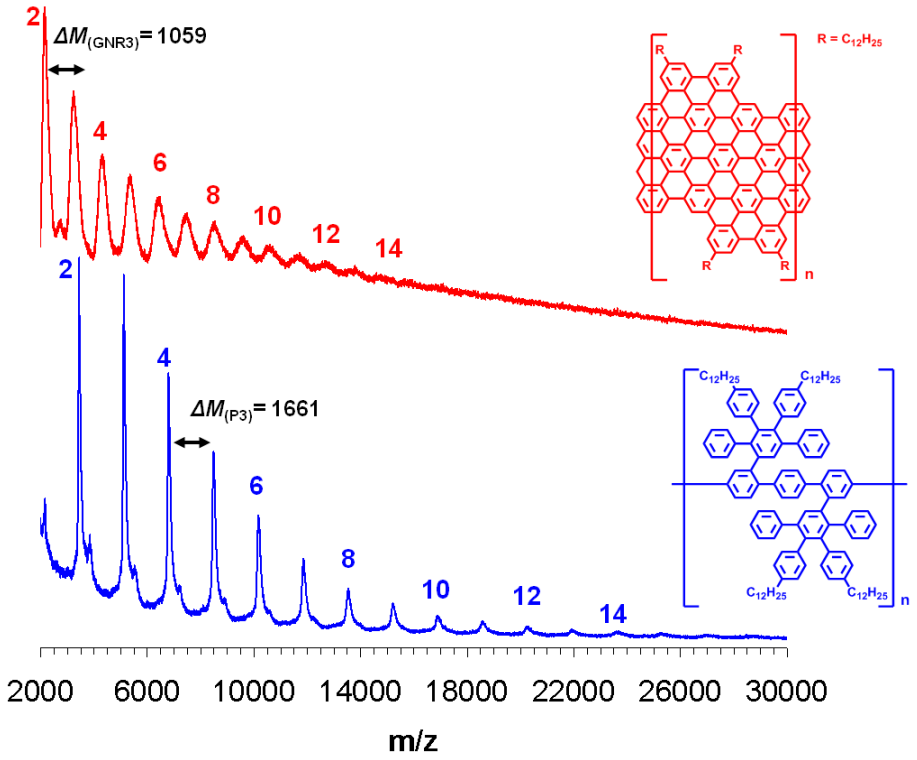

Figure 4-73: MALDI-TOF spectra of **GNR3** (red) and precursor polymer **P3** (blue).

Usage of a solid state preparation (TCNQ) was necessary for desorption of the graphene material from the sample holder and lead to the recording of the spectrum shown in Figure 4-73. Although a similar number of repeat units with respect to the

precursor (up to 14) is observed for **GNR3**, the distance between the peaks does not correspond to the expected mass loss of the cyclodehydrogenation reaction. Since the successful formation of the **C78** core has been demonstrated under different synthetic conditions and was proven by NMR analysis, it seems highly unlikely that decomposition at the aromatic units of the molecule occurs. On the other hand, the loss of alkyl chains during oxidative treatment with ferric chloride has never been reported in the literature and was also not observed during the planarization of model compound **4-39**. The observed phenomenon seems thus to originate from the MALDI-TOF measurement itself and could be related to the chopping of the alkyl chains by the laser pulse. Indeed, if all dodecyl chains of **GNR3** are reduced to a benzylic unit high agreement between theoretic and experimental masses is found.

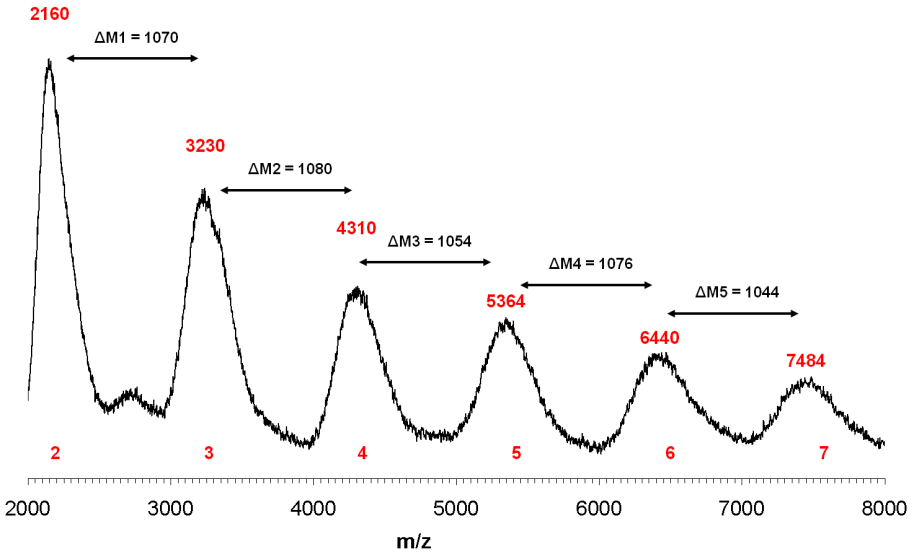

Figure 4-74: Detailed view on the MALDI-TOF spectrum of **GNR3**.

It appears as if the laser-induced fragmentation of the complete dodecyl side chains is unfavorable due to the special stabilization of the methylene group attached to the aromatic backbone. Neither by decreasing of the laser power nor by variation of the matrix this effect could be suppressed. It is noteworthy that a similar phenomenon has been observed in the past during the controlled pyrolysis of dodecyl-substituted HBC molecules. Also in this case, the degradation of the alkyl periphery resulted in the formation of the benzylic motif.[119]

Upon amplification, the signal width of **GNR3** becomes evident making detailed conclusions about degree and efficiency of the cyclodehydrogenation difficult (Figure 4-74). It can be noted, however, that the peaks are separated by a constant value that ranges between 1040 - 1080 mass units.

No significant chlorination seems to have taken place during the oxidative treatment with ferric chloride which is in analogy to the observations made during the preparation of **C78$_{hexa}$** under identical experimental conditions. Due to the complex fragmentation phenomenon seen during MALDI-TOF measurements, other analytical tools are of particular interest for the analysis of **GNR3** and **GNR4**.

Firstly, FTIR spectroscopy can be used to prove the presence of alkyl groups in the GNRs (Figure 4-75 and Figure 4-76). Indeed, the spectra before and after cyclodehydrogenation indicate the conservation of the side chains as seen by the strong aliphatic C-H stretching vibrations at 2920 cm^{-1} and 2850 cm^{-1}.

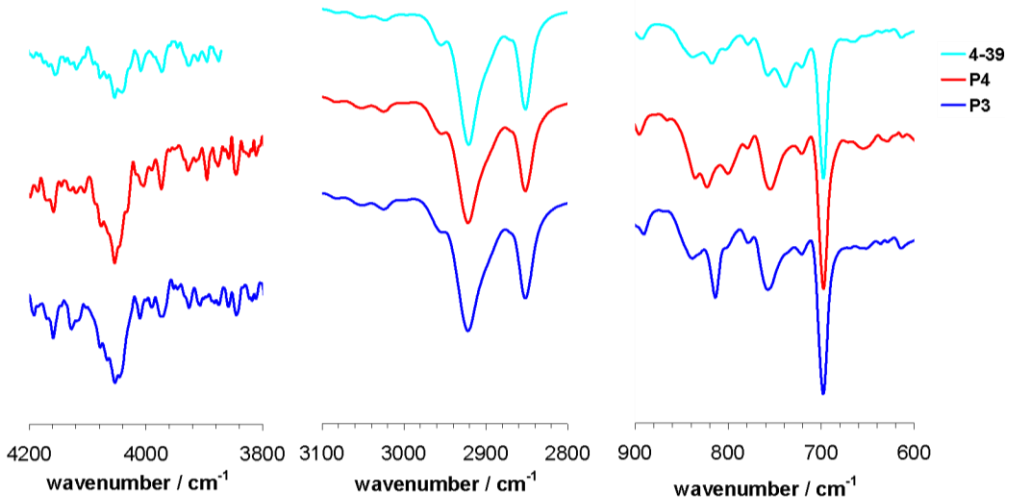

Figure 4-75: Representative regions of the FTIR spectra of **P3**, **P4** and model compound **4-39** before cyclodehydrogenation.

The spectral data of **C78$_{hexa}$** is shown for comparison and shows the same trends in this region of the spectrum as the bigger graphitic homologues.

As shown for **GNR1**, the FTIR analysis of the fully insoluble materials provides also qualitative information about the cyclodehydrogenation itself. Thus, the band originating from the rotation of free benzene units at 4050 cm^{-1} is detected for all three oligophenylene precursors (Figure 4-75).[36,92] Consequently, due to the fusion of the aromatic units during the oxidative treatment no signals are detected for **GNR3**, **GNR4** and **C78$_{hexa}$**, respectively. Furthermore, the triad at 3030 cm^{-1}, 3060 cm^{-1} and 3090 cm^{-1} characteristic for aromatic C-H stretching vibrations is strongly decreased in signal strength and lacks the initial fine structure.[73] In the fingerprint region of the spectra the sharp band at 699 cm^{-1} can be used to further estimate the efficiency of the oxidative treatment. Both, position and intensity of this signal are highly sensitive to the presence of monosubstituted benzene rings which are numerously present in the

oligophenylene precursors. The successful annelation of the aromatic units leads to a strong attenuation of this band in all spectra upon reaction with ferric chloride (Figure 4-76).

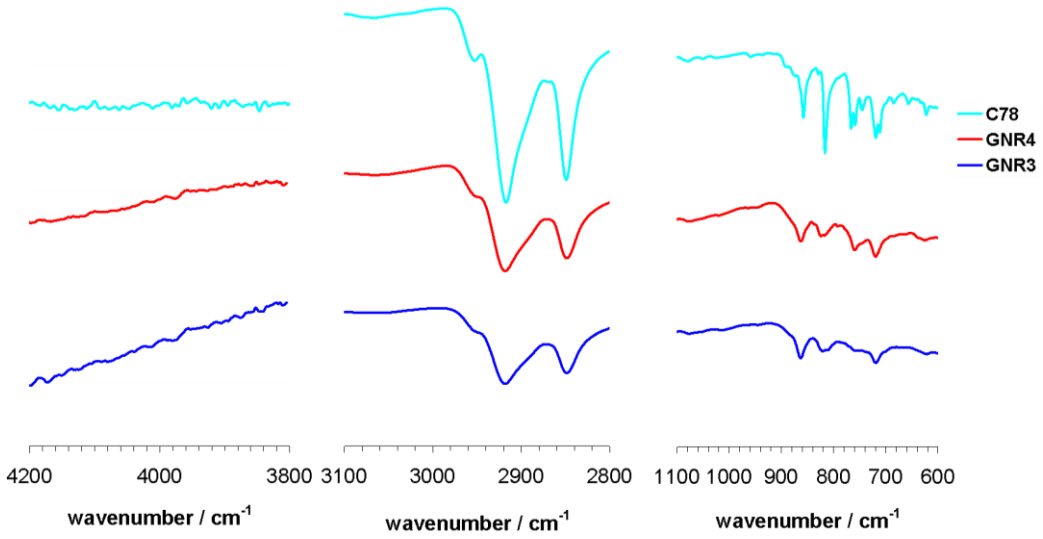

Figure 4-76: Representative regions of the FTIR spectra of **GNR3**, **GNR4** and the **C78$_{hexa}$** disc after cyclodehydrogenation.

Also, the overall fine structure of this spectral region is strongly reduced which is in accordance with the formation of large aromatic systems.

The importance of Raman spectroscopy to the analysis of graphene materials has already been highlighted in the context of **GNR1+2**.[92-95] Comparison of experimentally obtained spectra to theoretic predictions can be used as an important structural proof in the analysis of molecules that are difficult to process as a result of their intrinsic graphitic nature.[39]

Characteristic spectral features are the G band or graphite-band (1580 cm^{-1}) and the D band or disorder-band (1350 cm^{-1}). As the D and D' bands arise from defect sites they can be used to estimate the quality of graphene materials. In the present case, incomplete cyclodehydrogenation would give contributions to these bands. However, the edges of smaller nanographenes and GNRs also appear as defect sites and are responsible for most of the D band contributions.[94,95]

The Raman analysis performed on **GNR3** and **GNR4** revealed characteristic signals which are in agreement with a nanoribbon-type graphitic structure (Figure 4-77). The G and D peaks are found at 1304 cm^{-1} and 1583 cm^{-1} for **GNR3** and at 1292 cm^{-1} and 1593 cm^{-1} for **GNR4**, respectively.[94,95]

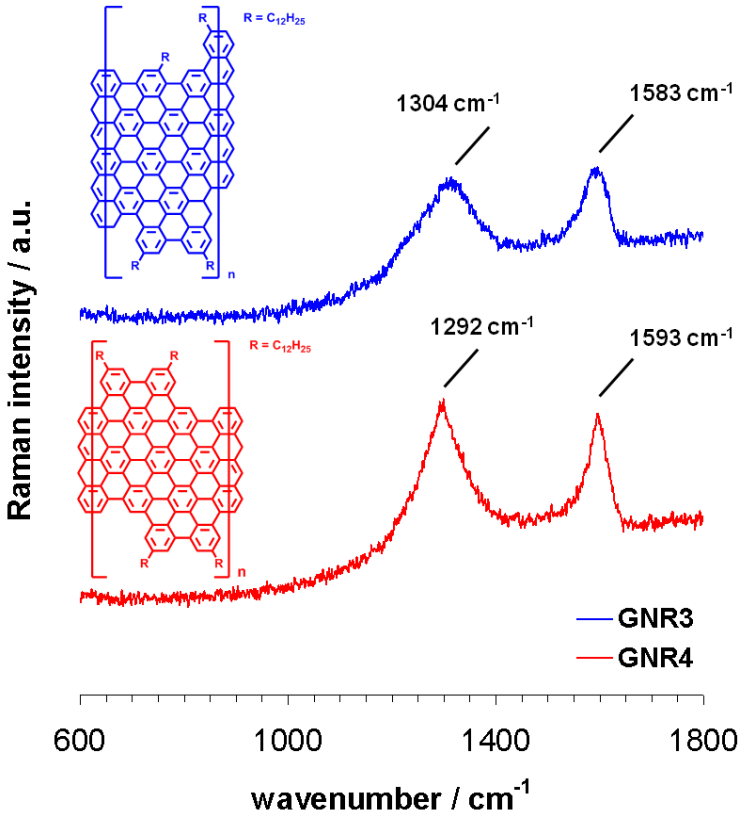

Figure 4-77: Raman spectra of **GNR3** and **GNR4**.

Solid state UV-vis spectroscopy (Figure 4-78) was then used to study the optical properties of the GNRs and revealed significant differences between **GNR3** and **GNR4**. As compared to the thin film spectrum of **C78** (Figure 4-65), the spectra of the GNRs lack a significant fine structure and are strongly red-shifted. The plateau-like absorption covers the whole visible range for both materials and extends to 800 nm in the case of *para*-connected **GNR3**. For *meta*-connected **GNR4** the absorption edge can be located at a wavelength of approximately 1000 nm reflecting a larger aromatic system for this compound. The effect could originate from a higher degree of polymerization as compared to **GNR3** or to the larger π-surface of **GNR4** which has been detailed previously. Furthermore, possible differences between type and degree of conjugation of the two nanoribbons might contribute to the experimental result. This assumption could be possibly verified by a computational analysis of the optoelectronic properties of the two GNRs.

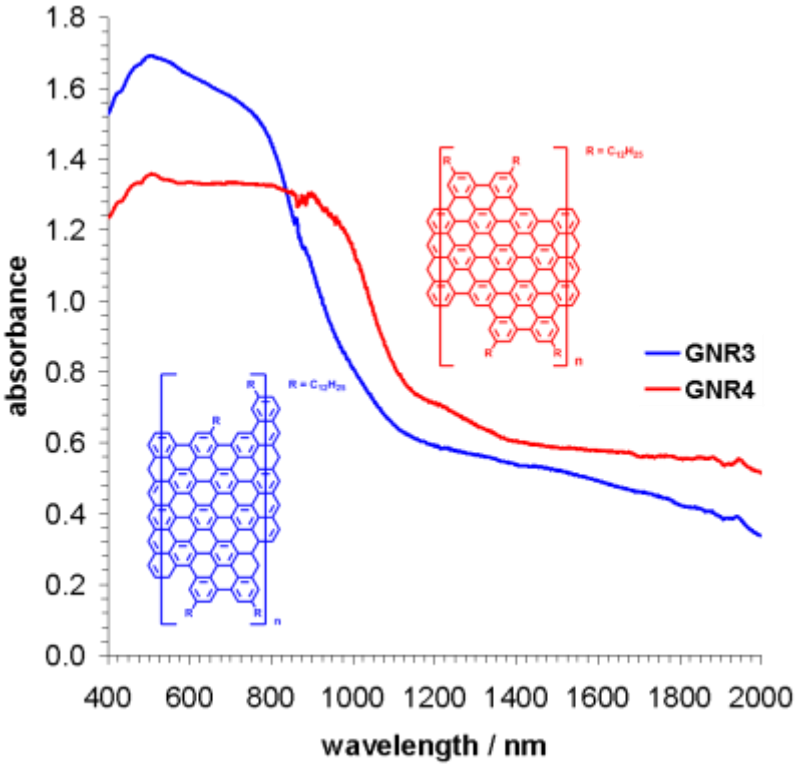

Figure 4-78: Solid-state UV-vis spectra of **GNR3** and **GNR4**.

In conclusion, the combined results of solid-state analytical tools such as MALDI-TOF, FTIR, Raman and SSUV spectroscopy are in agreement with the expected outcome of the cyclodehydrogenation reaction towards **GNR3** and **GNR4**. Moreover, this reaction has been verified for the previously discussed **C78$_{hexa}$** model case.

One of the advantages of the chemical bottom-up approach is the possibility to fully characterize the tailor-made precursor polymer and compare its data to the information available on the final GNRs. As such the detailed MALDI-TOF and FTIR study of the material before and after cyclodehydrogenation and the comparison of the data are of particular significance. Since the issue of limited or missing solubility is a common problem in the field of GNR research independently of the way of fabrication, the distinct advantage of this approach shall be once more emphasized: Only the presented chemical method allows for the reproducible production of structurally well-defined graphene materials allowing for the precise control over their promising electronic properties. Still, new answers to the problem of processability are indispensable in order to promote the technical application of GNRs. One potential solution, the surface-assisted fabrication of GNRs, will be discussed in the following part.

4.7.2 Surface-Assisted Approaches

Covalently bonded two-dimensional molecular arrays have attracted considerable scientific interest and can be efficiently studied by STM techniques.[120,121] Examples of surface-confined covalent bond formation involve *Ullmann* coupling[122], imidization[123,124], crosslinking of porphyrins[125,126] and oligomerization of heterocyclic carbenes[127] and polyamines.[128] A chemistry-driven protocol for the direct growth of GNRs[39] and graphene networks on surfaces[40,41] has been very recently established by the groups of *Müllen* (MPI-P Mainz, Germany) and *Fasel* (EMPA Dübendorf, Switzerland). From these studies it is known that the nanoribbon formation on the metal surface proceeds *via* a radical pathway.[39,40] After deposition of the functionalized monomer on the surface *via* UHV sublimation instant dehalogenation is believed to occur. This generates biradical species that diffuse on the surface and couple to each other resulting in the formation of carbon-carbon bonds.[126,129] These radical addition reactions proceed at intermediate thermal levels (200 °C) and are the prerequisite for the subsequent cyclodehydrogenation at higher temperatures (400 °C). Only if polymeric species of sufficient molecular weight are formed during the first stage, the full graphitization of the molecules will proceed subsequently with the thermal desorption of the material from the surface being avoided.

For UHV STM-assisted surface polymerization and cyclodehydrogenation, functional monomers of high rigidity and planarity are needed which assist in the flat orientation on the metal substrate. Also, the method allows for the topological tailoring of the GNRs as their shape it is determined by the functionality pattern and geometry of the precursor monomers.[39]

Based on the design of monomers **4-37** and **4-38** used for the solution-based fabrication of **GNR3** and **GNR4**, two analogous oligophenylene monomers **4-51** and **4-52** were conceived (Figure 4-79). The use of the rigid building block phencyclone **4-12** in the *Diels-Alder* reaction with the bisacetylenes **4-31** and **4-36** results in the formation of pre-planarized dendrons that contain a triphenylene moiety.[75] As described above, the decrease of conformational flexibility is one of the requirements for the surface-assisted approach and was thus conferred to the molecular design of the two monomers. The two oligophenylenes **4-51** and **4-52** were obtained by the established *Diels-Alder* route in 76 % and 85 %, respectively. After standard column chromatography both monomers were thoroughly purified by means of rGPC. The purity was confirmed by MALDI-TOF and NMR spectroscopy (Figure 4-80).

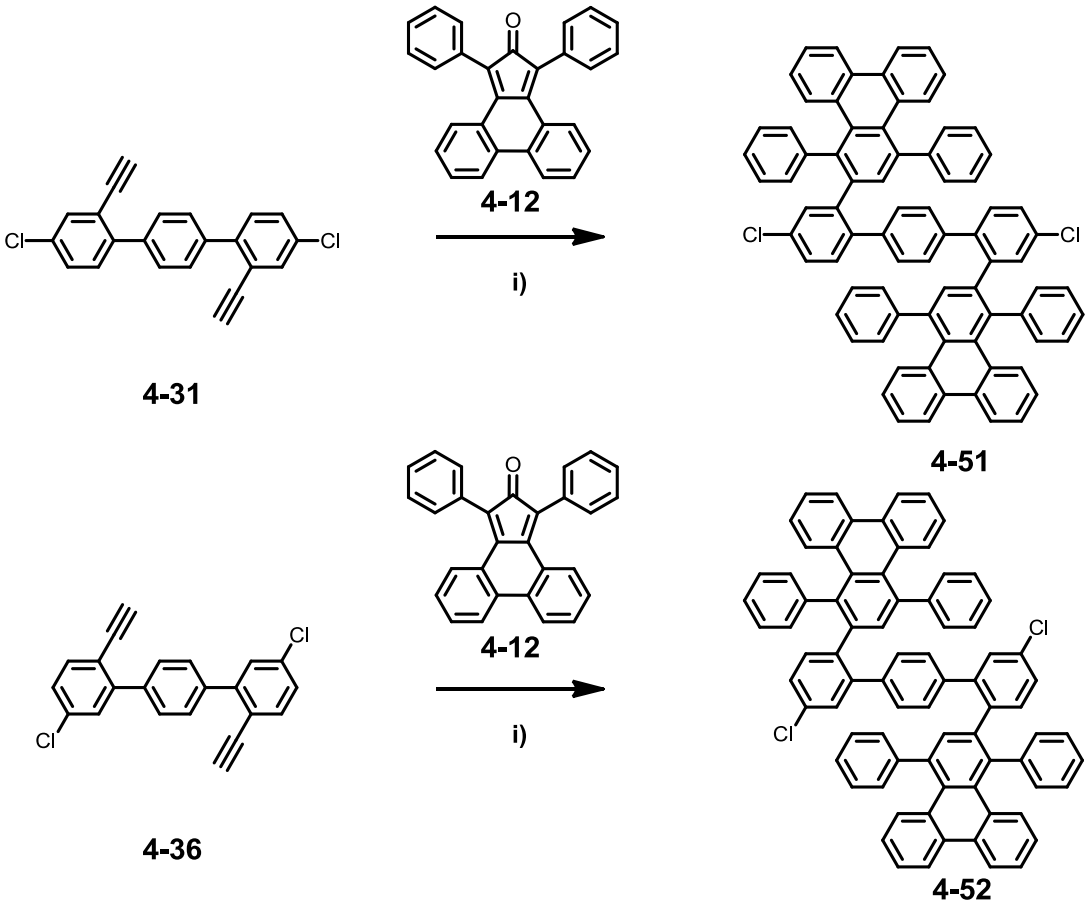

Figure 4-79: Synthesis of monomers **4-51** and **4-52** for surface-assisted experiments; conditions: i) *ortho*-xylene, 160 °C, µW, 300 W, 76 - 85 %.

With their considerable molecular weights of 1056 g/mol it was initially uncertain whether sublimation would be possible for the precursors **4-51** and **4-52**.

However, both molecules could be successfully deposited on various metal substrates at a temperature of 330 °C. Figure 4-81 depicts the STM images for *para*-functionalized monomer **4-51**. The images shown in Figure 4-81A and Figure 4-81B were obtained after annealing of the compound on Au(111) at temperatures of up to 400 °C. Even though polymeric structures were unambiguously formed, the degree of planarization seems to be rather low. The analysis under these conditions is further obstructed by the mobility of the oligomeric species on the substrate which prevented higher STM resolution.

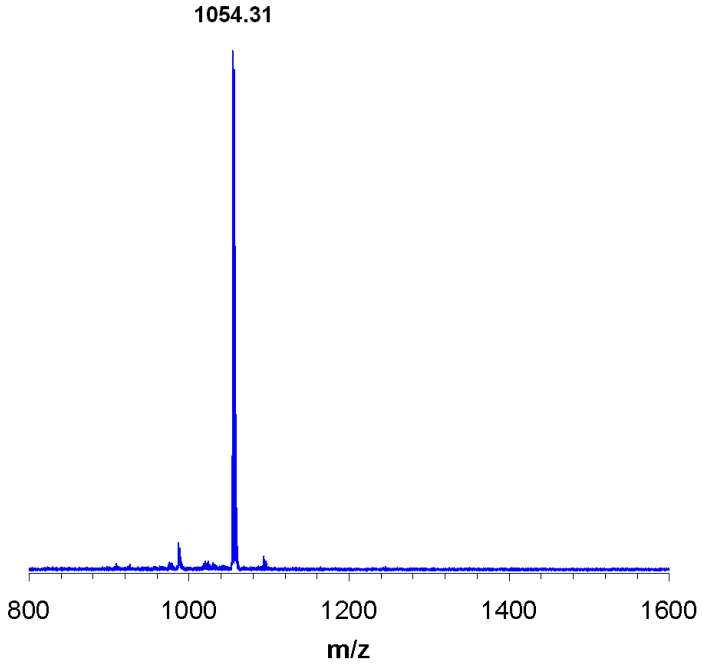

Figure 4-80: MALDI-TOF spectrum of **4-51**.

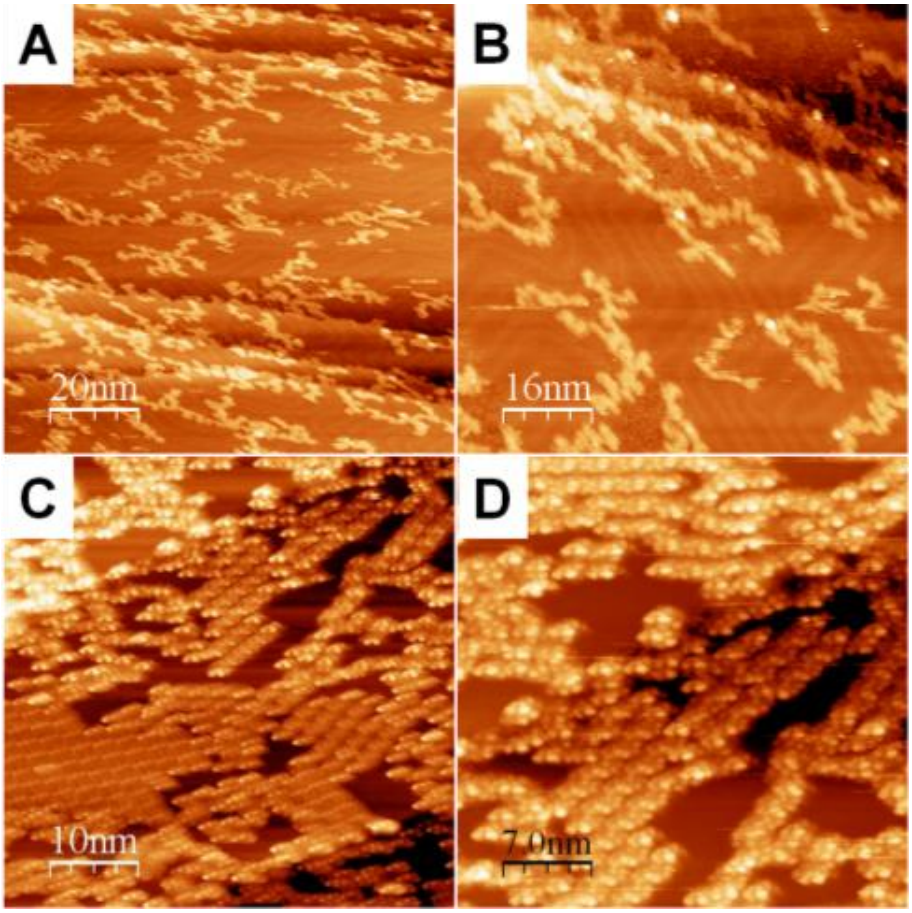

Figure 4-81: STM images of **4-51** after deposition and annealing at 400 °C on Au(111) (top) and Cu(111) (bottom).

Using a Cu(111) surface leads to a better quality of the images as evidenced by the results depicted in Figure 4-81C and Figure 4-81D for the same monomer. Linear chains are distributed over the whole area of the image and closely pack into larger clusters and islands. Their lengths exceed 15 nm and the lateral extension is around 2 nm which is in good agreement with the predicted value. However, also in this case the annealing procedure could not be driven to the full planarization of the molecules.

The STM tip was used to perform a line profile analysis on the surface-confined polymeric structures (Figure 4-82). The measurements revealed the absence of a continuous course as this would be expected for a fully flattened GNR.[39] On the contrary, the periodic protrusions seen in the STM image correspond to distinct steps in the corresponding profile curve. The separation between two adjacent peaks is 2.6 nm, a distance that is in good agreement with twice the diameter of the repeat unit (1.1 nm).

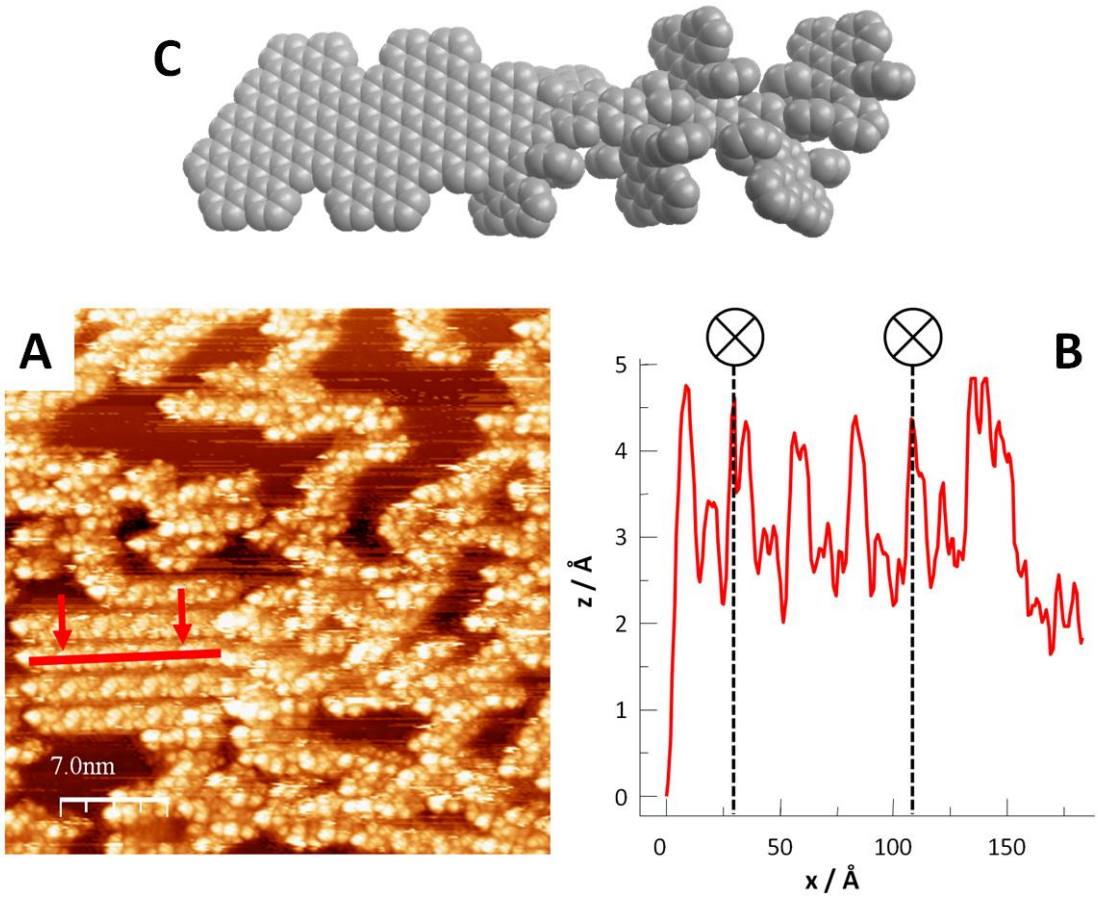

Figure 4-82: STM images of **4-51** on Cu(111) (A), height profile corresponding to the red line (B) and computational visualization of the planar and non-planar surface conformation (C, MMFF94s).

It appears that the polymeric species adopt a twisted, even though regular conformation on the examined surfaces that does not allow for complete planarization (Figure 4-82C). Taking into account the free rotatability of the polymeric chain an alternating up-down arrangement of the dendrons would explain the observed periodicity in the line profile. The deviation from planarity also explains the apparent height of approximately 0.4 nm which is much larger than to be expected for a fully planarized ribbon (Figure 4-82).[39]

For the *meta*-functionalized building block **4-52** analogous results were obtained (Figure 4-84). Also for this oligophenylene monomer, polymeric arrays form on the metal substrate but cannot be fully converted to the final GNR. Furthermore, the effect of the different substitution pattern is reflected by the strongly twisted chains which seem to have coupled at random sites. Both Au(111) and Ag(111) were tested for this sample but gave a similar result (Figure 4-83).

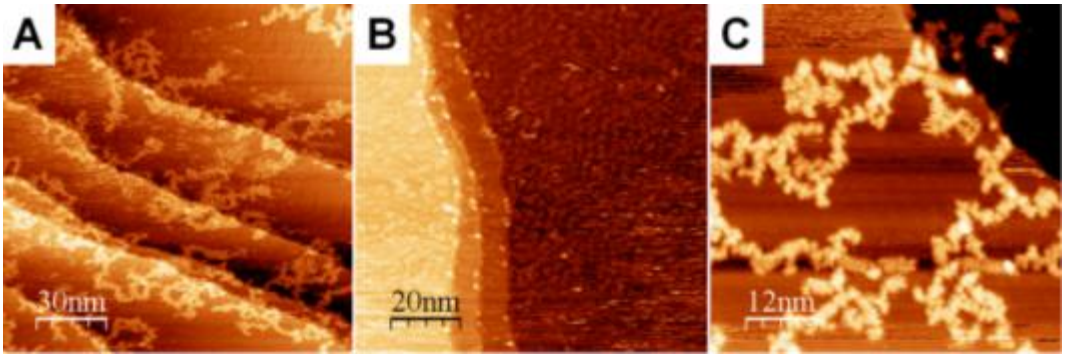

Figure 4-83: STM images of **4-52** after deposition and annealing at 400 °C on Au(111) (A + B) and Ag(111) (C).

The results of the experiments carried out with the two chlorine-functionalized monomers suggested that increasing the halogen reactivity might lead to a more efficient polymerization and thereby result in an increase of the molecular weight. It has been discussed previously that one of the key steps of the surface protocol is the formation of a radical at the moment where the monomer contacts the metal substrate from the gas phase. It can be assumed that decreasing the strength of the carbon-halogen bond will efficiently support the formation of the active site and thus lead to a more efficient polymerization. Additionally, high molecular weight species will progressively lose their surface mobility which could also be beneficial for the successive planarization of the polymeric structure. Based on these considerations it became therefore necessary to exchange the two chlorine atoms of **4-51** by two bromine atoms (Figure 4-84).

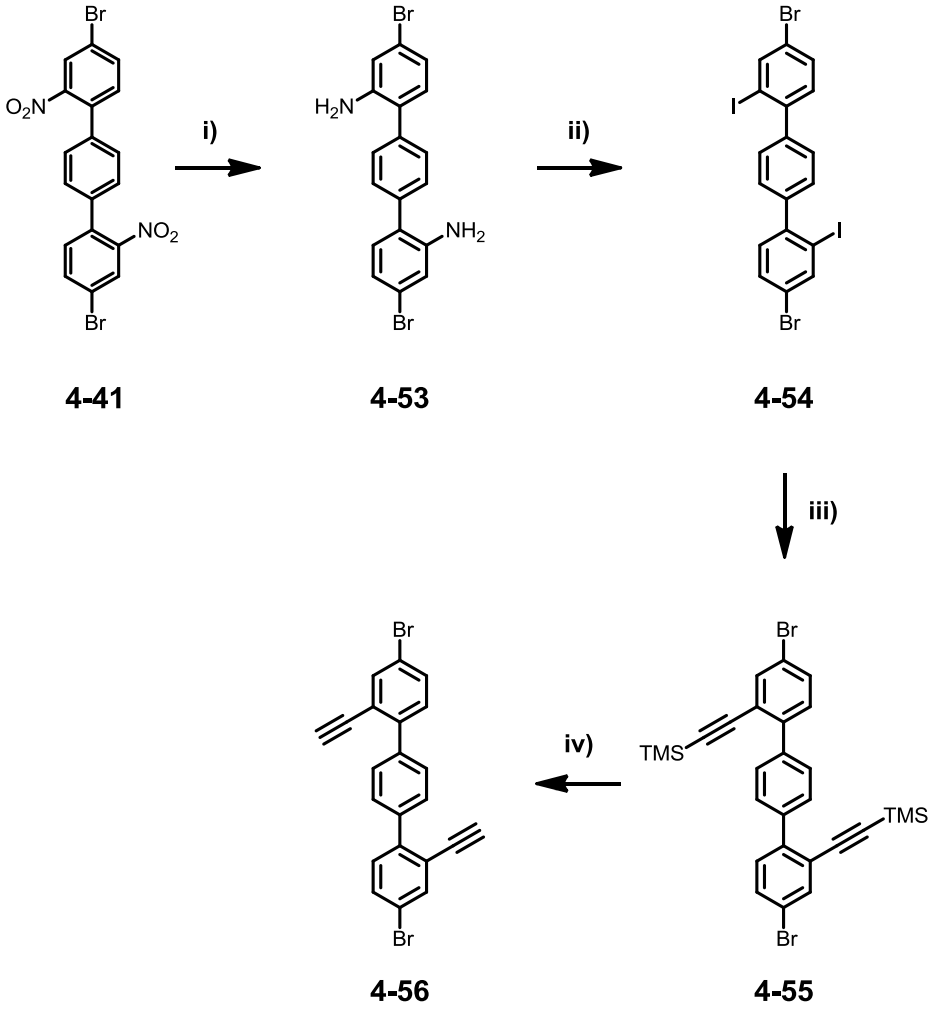

Figure 4-84: Synthetic route to the functionalized bisacetylene **4-56**; conditions: i) H_2, Pd/C, RT, 94 % ii) $NaNO_2$, Cl/H_2O, then KI, - 10 °C, 42 %; iii) trimethylsilyl acetylene, $Pd(PPh_3)_2Cl_2/CuI$, NEt_3; room temperature, 72 % iv) K_2CO_3, THF/MeOH, room temperature, 60 %.

With 4,4''-dibromo-2,2''-dinitro-1,1':4',1''-terphenyl **4-41** already available from the aforementioned synthesis of model compound **4-39**, the synthesis of the functionalized bisacetylene **4-56** was achieved using the established synthetic route (Figure 4-84).

In the case of **4-56**, the regioselective *Sonogashira-Hagihara* cross-coupling with trimethylsilyl acetylene represented the major synthetic challenge in order to avoid isomeric mixtures. However, the difference in reactivity of the iodine and bromine atoms of **4-54** at room temperature made the synthesis of the protected bisacetylene **4-55** possible.

Even though partial triple substitution could not be fully suppressed, column chromatography after deprotection of the acetylene groups allowed for the efficient isolation of 4,4''-dibromo-2,2''-diethynyl-1,1':4',1''-terphenyl **4-56** in 60 %.

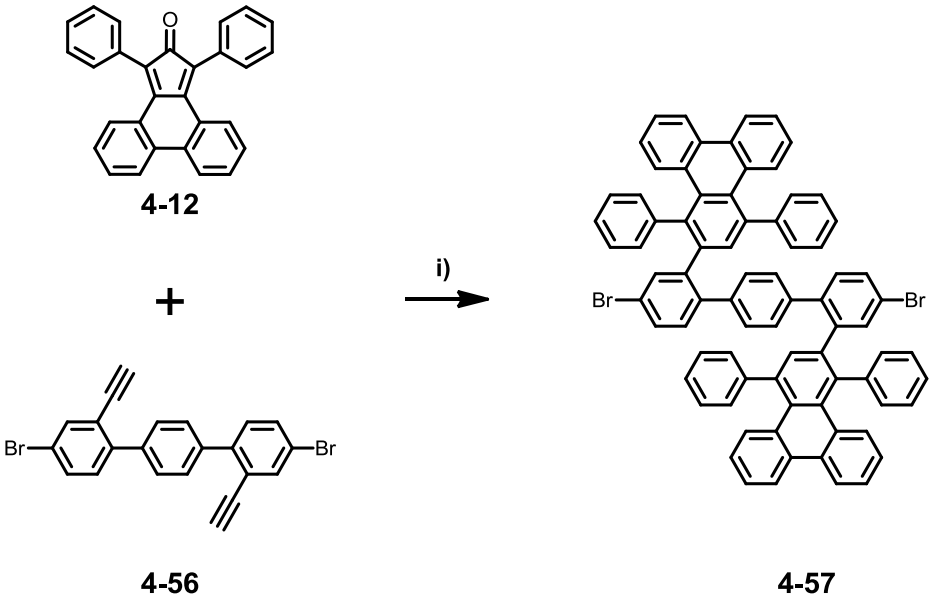

Figure 4-85: Synthesis of monomer **4-57**; conditions: i) *ortho*-xylene, 160 °C, µW, 300 W, 90 %.

The bisacetylene **4-56** was then again reacted with phencyclone **4-12** to give the rigidified oligophenylene precursor **4-57** in 90 % for which an enhanced reactivity towards surface polymerization was expected (Figure 4-85).

The molecular weight of this compound (M = 1145.02 g/mol) is still higher than in the previous two cases. UHV sublimation of this large oligophenylene was realized at a temperature of 380 °C. The STM results obtained from monomer **4-57** suggested the successful formation of laterally extended GNR. All images shown in Figure 4-86 were obtained on Au(111) after various temperature treatments.

As it can be seen in particular from Figure 4-86B and Figure 4-86C, the metal substrate is densely covered with linear ribbon-type structures that formed from monomer **4-57** and reach maximum lengths of 30 nm to 40 nm. For the polymerization and cyclodehydrogenation the pathway which is schematically depicted in Figure 4-87 has been previously proposed.[39] After contacting the metal substrate, dehalogenation instantly occurs resulting in the formation of a surface-stabilized biradical.

Furthermore, for efficient polymerization to occur this radical species needs to be stabilized into a horizontal geometry as this has been recently demonstrated by the surface-assisted preparation of graphene structures from a set of functional monomers. [39-41]

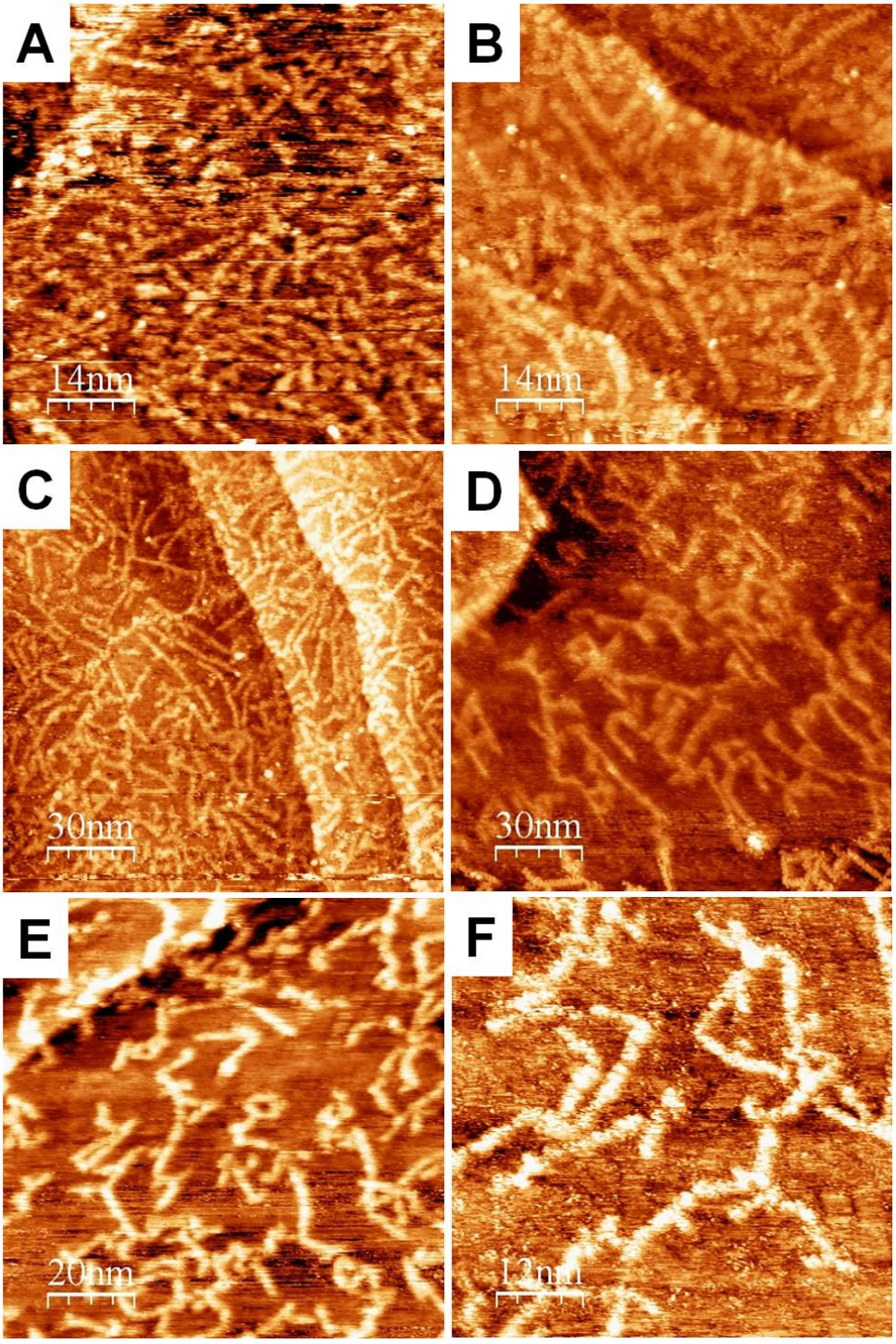

Figure 4-86: STM images of **4-57** after deposition and annealing at 380 °C (**A**), 450 °C (**B**), 500 °C (**C-F**) on Au(111).

Comparison of the length of the surface-bound GNR structures suggests that the polymerization proceeded to higher degree in the case of bromine-functionalized **4-57** as compared to chlorine-functionalized monomers **4-51** and **4-52**.

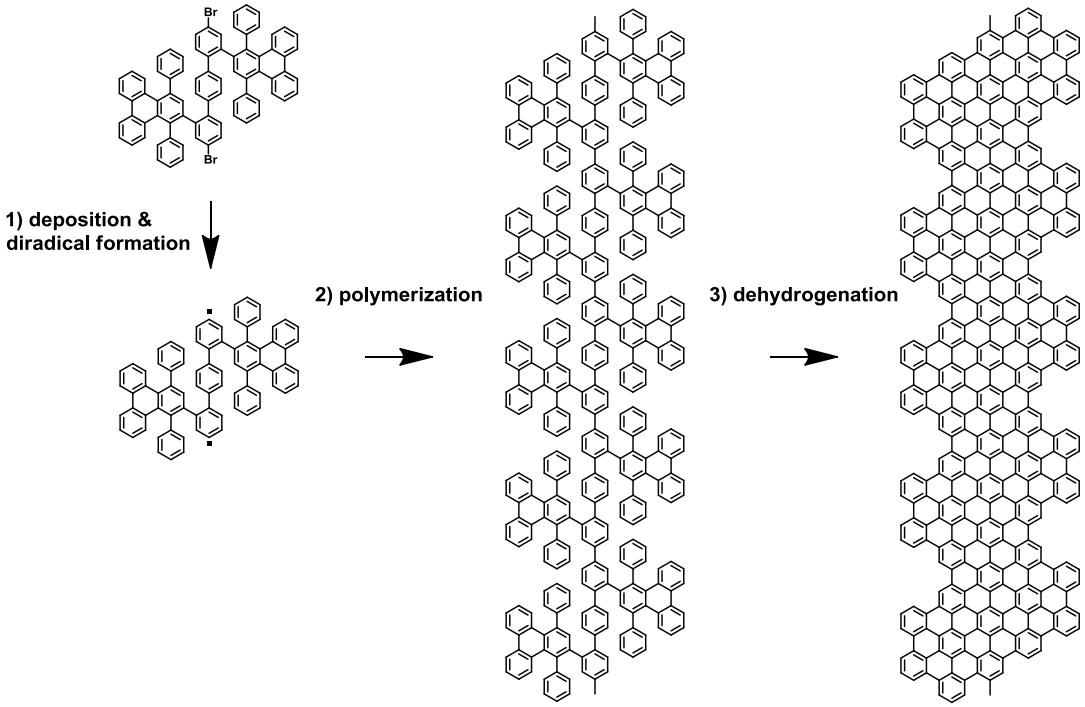

Figure 4-87: Mechanistical representation of the surface-assisted polymerization and cyclodehydrogenation of **4-57**.

The fully aromatic GNR is then produced in the third step by annealing at elevated temperatures of 350 - 500 °C resulting in the *intra*molecular cyclodehydrogenation of the polymeric structures. From the results obtained for **4-57** the extent of this step cannot be definitely judged as the resolution of the STM images does not allow for a final answer. Still, the GNRs appear to be significantly more flat that the structures seen from the processing of precursors **4-51** and **4-52**. It has to be kept in mind, that the precursor polymer can in principle adopt a twisted structure on the substrate and that the planarization involves the bond formation between multiple benzene units which is in contrast to the smaller literature-known examples.[39] The formation of defect sites along the axis of the GNRs built from **4-57** is thus likely to occur.

Nevertheless, the results obtained thus far give motivation to optimize this experimental system within the scope of future studies in the group of *Fasel* (EMPA Dübendorf, Switzerland). Also, the improvement of the molecular design by additional rigidification of the core region of the precursor can be envisaged. Substitution with four bromine atoms at the periphery of the molecule could also open an alternative pathway towards the recently reported fabrication of two-dimensional graphene surface networks.[40,41]

4.8 Summary

At present, the delivery of chemically defined graphene materials to material science and electronics remains an unsolved challenge. In this chapter various attempts towards the bottom-up synthesis of laterally extended GNRs have been presented. Based on initial studies making use of the *Suzuki-Miyaura* protocol the preparation of dendronized poly(*para*-phenylene) precursors was rationally optimized in the following by application of an alternative *Yamamoto* approach. In the context of chemical fabrication of GNRs, this method has been used for the first time as a polymerization tool and allowed for the significant increase of the molecular weight which can be directly correlated to the length of the final GNR.

The *AA*-type *Yamamoto* polycondensation avoids the stoichiometry problem of A_2B_2-type reaction systems and should be applied in future studies. Despite the bulky nature of the oligophenylene monomers, considerable degrees of polymerization reaching 20 to 24 repeat units could be realized. The *Yamamoto* systems described herein also expands the portfolio of synthetic protocols applicable to the chemical build-up of GNRs which is so far dominated by *Diels-Alder*[36,38] and *Suzuki*[37] approaches. By way of example the concept of chemical tailoring has been presented. Simple variation of the halogen substitution from a *para*- to a *meta*-pattern resulted in GNRs of different width and edge structure.

As the characterization and processing of GNRs from solution remains difficult even when a high number of lateral alkyl chains are introduced, it is imperative to prove the cyclodehydrogenation reaction on a smaller scale. Therefore, **C78** and **C84** discs were prepared from oligophenylenes which exactly reflect the structural design of the larger polymeric GNR precursors. Various oxidant systems have been successfully evaluated including the typical ferric chloride protocol but also less frequently encountered oxidants like molybdenum pentachloride and PIFA. Since chlorination is a frequently observed side reaction when ferric chloride and molybdenum pentachloride are used, the successful cyclodehydrogenation with PIFA offers an attractive possibility to circumvent this problem.

The structure proof *via* NMR spectroscopy was possible in the case of **C78** which is the largest PAH that has ever been characterized by this analytical method. As the use of discotic nanographenes for molecular electronics is a promising field of application in itself, the two- and three-dimensional self-assembly of **C78** and **C84** was studied in detail. The enhanced resolution of STM images obtained in the case of **C78** also allowed for the examination of the supramolecular packing and the structure of the

PAH on the molecular level. By means of 2D-WAXS the typical liquid-crystalline character of alkyl-substituted discotic PAHs could be confirmed for both compounds. In the past, various techniques such as dip-coating and zone-casting have been used to create ordered PAH superstructures that were examined with respect to their semiconducting and charge transport properties. In most cases, HBC served as the functional molecule. Both, **C78** and **C84** are significantly larger but remain well-processable from solution and the melt so that their application in devices could be probed to elucidate new structure-property relationships.

In the next step, the reaction conditions obtained from the experimental studies on **C78** and **C84** were transferred to the synthetic protocol applied to the preparation of the larger GNRs. It is believed that these materials will find numerous applications in the future as only chemistry allows for the precise tailoring of geometry, width and edge structure. A combination of various solid-state analytics was used to investigate these unique graphitic materials derived from the solution-based synthesis. Results from mass spectroscopy as well as studies making use of vibrational spectroscopy indicate in all cases a high extent of the cyclodehydrogenation reaction. Still, the processing of GNRs remains an important challenge to be resolved.

Concerning the surface-based routes, the comparison between chlorine- and bromine-functionalized monomers indicated that the chlorine group is not sufficiently activated to promote an efficient growth of GNRs on a metal surface. On the contrary, for the bromine-functionalized oligophenylene monomer the partial formation of laterally extended GNRs is likely to have taken place. Despite the incorporation of the triphenylene motif into the two dendrons, further rigidification at the central core of the monomer would be certainly beneficial for future surface studies. This could be achieved by incorporation of planar triphenylene or pyrene units into the molecular backbone as this has been proven successful for the solution-based synthesis of **C72** in the past.

Still, important questions regarding the mechanisms of this surface chemistry need to be addressed, too. This concerns for example the design of the precursor both regarding the ideal arrangement of benzene units and the placement of the functional groups on the molecular backbone. Even though classical bond formation reactions are possible in two-dimensional space, the validity of *Carother*'s law for step-growth polymerizations under these exotic reaction conditions needs to studied as well in order to shift the degree of polymerization yet to higher values.

4.9 Bibliography

(1) Boehm, H. P. *Angew. Chem. Int. Ed.* **2010**, *49*, 9332-9335.
(2) Novoselov, K. S.; Geim, A. K.; Morozov, S. V.; Jiang, D.; Zhang, Y.; Dubonos, S. V.; Grigorieva, I. V.; Firsov, A. A. *Science* **2004**, *306*, 666.
(3) Berger, C.; Song, Z.; Li, T.; Li, X.; Ogbazghi, A. Y.; Feng, R.; Dai, Z.; Marchenkov, A. N.; Conrad, E. H.; First, P. N.; de Heer, W. A. *J. Phys. Chem. B* **2004**, *108*, 19912-19916.
(4) Geim, A. K.; Novoselov, K. S. *Nat. Mater.* **2007**, *6*, 183-191.
(5) Geim, A. K. *Science* **2009**, *324*, 1530-1534.
(6) Zhu, Y.; Murali, S.; Cai, W.; Li, X.; Suk, J. W.; Potts, J. R.; Ruoff, R. S. *Adv. Mater.* **2010**, *22*, 3906-3924.
(7) Orlita, M.; Faugeras, C.; Plochocka, P.; Neugebauer, P.; Martinez, G.; Maude, D. K.; Barra, A. L.; Sprinkle, M.; Berger, C.; De Heer, W. A. *Phys. Rev. Lett.* **2008**, *101*, 267601.
(8) Castro Neto, A. H.; Guinea, F.; Peres, N. M. R.; Novoselov, K. S.; Geim, A. K. *Rev. Mod. Phys.* **2009**, *81*, 109.
(9) Novoselov, K. S.; Jiang, Z.; Zhang, Y.; Morozov, S. V.; Stormer, H. L.; Zeitler, U.; Maan, J. C.; Boebinger, G. S.; Kim, P.; Geim, A. K. *Science* **2007**, *315*, 1379.
(10) Wang, X.; Zhi, L.; Mullen, K. *Nano Lett.* **2008**, *8*, 323-327.
(11) Kim, K. S.; Zhao, Y.; Jang, H.; Lee, S. Y.; Kim, J. M.; Ahn, J. H.; Kim, P.; Choi, J. Y.; Hong, B. H. *Nature* **2009**, *457*, 706-710.
(12) Stoller, M. D.; Park, S.; Zhu, Y.; An, J.; Ruoff, R. S. *Nano Lett.* **2008**, *8*, 3498-3502.
(13) Pang, S.; Tsao, H. N.; Feng, X.; Müllen, K. *Adv. Mater.* **2009**, *21*, 3488-3491.
(14) Han, M. Y.; Özyilmaz, B.; Zhang, Y.; Kim, P. *Phys. Rev. Lett.* **2007**, *98*, 206805.
(15) Özyilmaz, B.; Jarillo-Herrero, P.; Efetov, D.; Kim, P. *Appl. Phys. Lett.* **2007**, *91*, 192107.
(16) Jia, X.; Hofmann, M.; Meunier, V.; Sumpter, B. G.; Campos-Delgado, J.; Romo-Herrera, J. M.; Son, H.; Hsieh, Y. P.; Reina, A.; Kong, J. *Science* **2009**, *323*, 1701.
(17) Kosynkin, D. V.; Higginbotham, A. L.; Sinitskii, A.; Lomeda, J. R.; Dimiev, A.; Price, B. K.; Tour, J. M. *Nature* **2009**, *458*, 872-876.
(18) Shimizu, T.; Haruyama, J.; Marcano, D. C.; Kosinkin, D. V.; Tour, J. M.; Hirose, K.; Suenaga, K. *Nat. Nanotechnol.* **2011**, *6*, 45-50.
(19) Li, X.; Wang, X.; Zhang, L.; Lee, S.; Dai, H. *Science* **2008**, *319*, 1229-1232.
(20) Schwierz, F. *Nat. Nanotechnol.* **2010**, *5*, 487-496.
(21) Chen, Z.; Lin, Y. M.; Rooks, M. J.; Avouris, P. *Physica E* **2007**, *40*, 228-232.
(22) Tzalenchuk, A.; Lara-Avila, S.; Kalaboukhov, A.; Paolillo, S.; Syvajarvi, M.; Yakimova, R.; Kazakova, O.; Janssen, T. J. B. M.; Fal'ko, V.; Kubatkin, S. *Nat. Nanotechnol.* **2010**, *5*, 186-189.
(23) Wei, Z.; Wang, D.; Kim, S.; Kim, S. Y.; Hu, Y.; Yakes, M. K.; Laracuente, A. R.; Dai, Z.; Marder, S. R.; Berger, C. *Science* **2010**, *328*, 1373-1376.
(24) Mativetsky, J. M.; Treossi, E.; Orgiu, E.; Melucci, M.; Veronese, G. P.; Samori, P.; Palermo, V. *Journal of the American Chemical Society* **2010**, *132*, 14130-14136.
(25) Barone, V.; Hod, O.; Scuseria, G. E. *Nano Lett.* **2006**, *6*, 2748-2754.
(26) Yang, L.; Park, C.-H.; Son, Y.-W.; Cohen, M. L.; Louie, S. G. *Phys. Rev. Lett.* **2007**, *99*, 186801.
(27) Radovic, L. R.; Bockrath, B. *J. Am. Chem. Soc.* **2005**, *127*, 5917-5927.
(28) Enoki, T.; Kobayashi, Y.; Fukui, K. I. *Int. Rev. Phys. Chem.* **2007**, *26*, 609-645.
(29) Oeiras, R. Y.; Araújo-Moreira, F. M.; da Silva, E. Z. *Phys. Rev. B* **2009**, *80*, 73405.
(30) Shimizu, A.; Kubo, T.; Uruichi, M.; Yakushi, K.; Nakano, M.; Shiomi, D.; Sato, K.; Takui, T.; Hirao, Y.; Matsumoto, K.; Kurata, H.; Morita, Y.; Nakasuji, K. *J. Am. Chem. Soc.* **2010**, *132*, 14421-14428.
(31) Konishi, A.; Hirao, Y.; Nakano, M.; Shimizu, A.; Botek, E.; Champagne, B.; Shiomi, D.; Sato, K.; Takui, T.; Matsumoto, K.; Kurata, H.; Kubo, T. *J. Am. Chem. Soc.* **2010**, *132*, 11021-11023.
(32) Tsuda, A.; Furuta, H.; Osuka, A. *Angew. Chem. Int. Ed.* **2000**, *39*, 2549-2552.
(33) Tsuda, A.; Osuka, A. *Science* **2001**, *293*, 79-82.
(34) Ikeda, T.; Aratani, N.; Osuka, A. *Chem. Asian J.* **2009**, *4*, 1248-1256.
(35) Crossley, M. J.; Burn, P. L. *J. Chem. Soc., Chem. Commun.* **1991**, 1569-1571.
(36) Wu, J.; Gherghel, L.; Watson, M. D.; Li, J.; Wang, Z.; Simpson, C. D.; Kolb, U.; Müllen, K. *Macromolecules* **2003**, *36*, 7082-7089.
(37) Yang, X.; Dou, X.; Rouhanipour, A.; Zhi, L.; Räder, H. J.; Müllen, K. *J. Am. Chem. Soc.* **2008**, *130*, 4216-4217.
(38) Fogel, Y.; Zhi, L.; Rouhanipour, A.; Andrienko, D.; Räder, H. J.; Müllen, K. *Macromolecules* **2009**, *42*, 6878-6884.
(39) Cai, J.; Ruffieux, P.; Jaafar, R.; Bieri, M.; Braun, T.; Blankenburg, S.; Muoth, M.; Seitsonen, A. P.; Saleh, M.; Feng, X.; Müllen, K.; Fasel, R. *Nature* **2010**, *466*, 470-473.
(40) Bieri, M.; Treier, M.; Cai, J.; Aït-Mansour, K.; Ruffieux, P.; Gröning, O.; Gröning, P.; Kastler, M.; Rieger, R.; Feng, X.; Müllen, K.; Fasel, R. *Chem. Commun.* **2009**, *2009*, 6919-6921.
(41) Bieri, M.; Nguyen, M. T.; Gröning, O.; Cai, J.; Treier, M.; Aït-Mansour, K.; Ruffieux, P.; Pignedoli, C. A.; Passerone, D.; Kastler, M.; Müllen, K.; Fasel, R. *J. Am. Chem. Soc.* **2010**, *132*, 16669–16676.

(42) King, B. T.; Kroulik, J.; Robertson, C. R.; Rempala, P.; Hilton, C. L.; Korinek, J. D.; Gortari, L. M. *J. Org. Chem.* **2007**, *72*, 2279-2288.
(43) Rempala, P.; Kroulík, J.; King, B. T. *J. Org. Chem.* **2006**, *71*, 5067-5081.
(44) Schlüter, A. D.; Wegner, G. *Acta Polym.* **1993**, *44*, 59-69.
(45) Schlüter, A. D. *J. Polym. Sci. B, Polym. Lett.* **2001**, *39*, 1533-1556.
(46) Kotha, S.; Lahiri, K.; Kashinath, D. *Tetrahedron* **2002**, *58*, 9633-9695.
(47) Yamamoto, T. *Progr. Polym. Sci.* **1992**, *17*, 1153-1205.
(48) Yamamoto, T. *Bull. Chem. Soc. Jpn.* **1999**, *72*, 621-638.
(49) Müller, M.; Mauermann-Düll, H.; Wagner, M.; Enkelmann, V.; Müllen, K. *Angew. Chem. Int. Ed.* **1995**, *34*, 1583-1586.
(50) Müller, M.; Petersen, J.; Strohmaier, R.; Günther, C.; Karl, N.; Müllen, K. *Angew. Chem. Int. Ed.* **1996**, *35*, 886-888.
(51) Iyer, V. S.; Yoshimura, K.; Enkelmann, V.; Epsch, R.; Rabe, J. P.; Müllen, K. *Angew. Chem. Int. Ed.* **1998**, *37*, 2696-2699.
(52) Feng, X.; Wu, J.; Ai, M.; Pisula, W.; Zhi, L.; Rabe, J. P.; Müllen, K. *Angew. Chem. Int. Ed.* **2007**, *46*, 3033-3036.
(53) Müller, M.; Kübel, C.; Morgenroth, F.; Iyer, V. S.; Müllen, K. *Carbon* **1998**, *36*, 827-831.
(54) Wasserfallen, D. *Synthetical Engineering of Supramolecular Properties of Large Polycyclic Aromatic Hydrocarbons*; PhD Thesis: Mainz, **2006**.
(55) Wasserfallen, D.; Kastler, M.; Pisula, W.; Hofer, W. A.; Fogel, Y.; Wang, Z.; Müllen, K. *J. Am. Chem. Soc.* **2006**, *128*, 1334-1339.
(56) Müller, M.; Iyer, V. S.; Kübel, C.; Enkelmann, V.; Müllen, K. *Angew. Chem. Int. Ed.* **1997**, *36*, 1607-1610.
(57) Morgenroth, F.; Kübel, C.; Müller, M.; Wiesler, U. M.; Berresheim, A. J.; Wagner, M.; Müllen, K. *Carbon* **1998**, *36*, 833-837.
(58) Simspon, C. *Nanoscale Polycyclic Aromatic Hydrocarbons: Synthesis and Characterization*; PhD Thesis: Mainz, **2003**.
(59) Böhme, T.; Simpson, C.; Müllen, K.; Rabe, J. *Chem. Eur. J.* **2007**, *13*, 7349-7357.
(60) Simpson, C. D.; Wu, J.; Watson, M. D.; Müllen, K. *J. Mater. Chem.* **2004**, *14*, 494-504.
(61) Iyer, V. S.; Wehmeier, M.; Brand, J. D.; Keegstra, M. A.; Müllen, K. *Angew. Chem. Int. Ed.* **1997**, *36*, 1604-1607.
(62) Tomovic, Z.; Watson, M. D.; Müllen, K. *Angew. Chem. Int. Ed.* **2004**, *43*, 755-758.
(63) Samori, P.; Severin, N.; Simpson, C. D.; Müllen, K.; Rabe, J. P. *J. Am. Chem. Soc.* **2002**, *124*, 9454-9457.
(64) Simpson, C. D.; Brand, J. D.; Berresheim, A. J.; Przybilla, L.; Räder, H. J.; Müllen, K. *Chem. Eur. J.* **2002**, *8*, 1424-1429.
(65) Treier, M.; Pignedoli, C. A.; Laino, T.; Rieger, R.; Müllen, K.; Passerone, D.; Fasel, R. *Nat. Chem.* **2011**, *3*, 61-67.
(66) Miyaura, N.; Suzuki, A. *Chem. Rev.* **1995**, *95*, 2457-2483.
(67) Suzuki, A. *J. Organomet. Chem.* **1999**, *576*, 147-168.
(68) Sonntag, M.; Strohriegl, P. *Chem. Mater* **2004**, *16*, 4736-4742.
(69) Diels, O.; Alder, K. *Justus Liebigs Ann. Chem.* **1928**, *460*, 98-122.
(70) Dilthey, W.; Quint, F. *J. Prakt. Chem.* **1930**, *128*, 139-149.
(71) Dilthey, W.; Hurtig, G. *Ber. Dtsch. Chem. Ges.* **1934**, *67*, 2004-2007.
(72) Ogliaruso, M. A.; Romanelli, M. G.; Becker, E. I. *Chem. Rev.* **1965**, *65*, 261-367.
(73) Shifrina, Z. B.; Averina, M. S.; Rusanov, A. L.; Wagner, M.; Müllen, K. *Macromolecules* **2000**, *33*, 3525-3529.
(74) Ito, S.; Wehmeier, M.; Brand, J. D.; Kübel, C.; Epsch, R.; Rabe, J. P.; Müllen, K. *Chem. Eur. J.* **2000**, *6*, 4327-4342.
(75) Qin, T.; Zhou, G.; Scheiber, H.; Bauer, R. E.; Baumgarten, M.; Anson, C. E.; List, E. J. W.; Müllen, K. *Angew. Chem. Int. Ed.* **2008**, *47*, 8292-8296.
(76) Carothers, W. H. *Trans. Faraday Soc.* **1936**, *32*, 39-49.
(77) Odian, G. G. *Principles of Polymerization*; J. Wiley & Sons: Hoboken, **2004**.
(78) Kreyenschmidt, M.; Baumgarten, M.; Tyutyulkov, N.; Müllen, K. *Angew. Chem. Int. Ed.* **1994**, *33*, 1957-1959.
(79) Kawano, S.; Yang, C.; Ribas, M.; Baluschev, S.; Baumgarten, M.; Müllen, K. *Macromolecules* **2008**, *41*, 7933-7937.
(80) Kastler, M.; Schmidt, J.; Pisula, W.; Sebastiani, D.; Müllen, K. *J. Am. Chem. Soc.* **2006**, *128*, 9526-9534.
(81) Shabangi, M.; Flowers, R. A. *Tetrahedron Lett.* **1997**, *38*, 1137-1140.
(82) Molander, G. A.; Harris, C. R. *Chem. Rev.* **1996**, *96*, 307-338.
(83) Dötz, F.; Brand, J. D.; Ito, S.; Gherghel, L.; Müllen, K. *J. Am. Chem. Soc.* **2000**, *122*, 7707-7717.
(84) Rieger, R.; Müllen, K. *J. Phys. Org. Chem.* **2010**, *23*, 315-325.
(85) Clar, E. *The Aromatic Sextet*; J. Wiley & Sons: London, **1972**.
(86) Fetzer, J. C. *Large (C >= 24) Polycyclic Aromatic Hydrocarbons: Chemistry and Analysis*; Wiley Interscience: New York, **2000**.
(87) Fischbach, I.; Pakula, T.; Minkin, P.; Fechtenkötter, A.; Müllen, K.; Spiess, H. W.; Saalwächter, K. *J. Phys. Chem. B* **2002**, *106*, 6408-6418.
(88) Pisula, W.; Tomovic, Z.; Simpson, C.; Kastler, M.; Pakula, T.; Müllen, K. *Chem. Mater.* **2005**, *17*, 4296-4303.

(89) Weiss, K.; Beernink, G.; Dötz, F.; Birkner, A.; Müllen, K.; Wöll, C. H. *Angew. Chem. Int. Ed.* **1999**, *38*, 3748-3752.
(90) Pohnert, G. *J. Prakt. Chem.* **2000**, *342*, 731-734.
(91) Takada, T.; Arisawa, M.; Gyoten, M.; Hamada, R.; Tohma, H.; Kita, Y. *J. Org. Chem.* **1998**, *63*, 7698-7706.
(92) Centrone, A.; Brambilla, L.; Renouard, T.; Gherghel, L.; Mathis, C.; Müllen, K.; Zerbi, G. *Carbon* **2005**, *43*, 1593-1609.
(93) Dresselhaus, M. S.; Dresselhaus, G.; Saito, R.; Jorio, A. *Phys. Rep.* **2005**, *409*, 47-99.
(94) Pimenta, M. A.; Dresselhaus, G.; Dresselhaus, M. S.; Cancado, L. G.; Jorio, A.; Saito, R. *Phys. Chem. Chem. Phys.* **2007**, *9*, 1276-1290.
(95) Malard, L. M.; Pimenta, M. A.; Dresselhaus, G.; Dresselhaus, M. S. *Phys. Rep.* **2009**, *473*, 51-87.
(96) Tuinstra, F.; Koenig, J. L. *J. Chem. Phys.* **1970**, *53*, 1126.
(97) Sinitskii, A.; Dimiev, A.; Kosynkin, D. V.; Tour, J. M. *ACS Nano* **2010**, *4* 5405-5413.
(98) Yang, L.; Park, C. H.; Son, Y. W.; Cohen, M. L.; Louie, S. G. *Phys. Rev. Lett.* **2007**, *99*, 186801.
(99) Yamamoto, T.; Ito, T.; Sanechika, K.; Hishinuma, M. *Synth. Met.* **1988**, *25*, 103-107.
(100) Yamamoto, T.; Morita, A.; Maruyama, T. *Polymer J.* **1990**, *22*, 187-190.
(101) Kanbara, T.; Saito, N.; Yamamoto, T.; Kubota, K. *Macromolecules* **1991**, *24*, 5883-5885.
(102) Yamamoto, T.; Morita, A.; Miyazaki, Y.; Maruyama, T.; Wakayama, H.; Zhou, Z. H.; Nakamura, Y.; Kanbara, T.; Sasaki, S.; Kubota, K. *Macromolecules* **1992**, *25*, 1214-1223.
(103) Yamamoto, T.; Maruyama, T.; Zhou, Z. H.; Ito, T.; Fukuda, T.; Yoneda, Y.; Begum, F.; Ikeda, T.; Sasaki, S. *J. Am. Chem. Soc.* **1994**, *116*, 4832-4845.
(104) Chmil, K.; Scherf, U. *Makromol. Chem., Rapid Commun.* **1993**, *14*, 217-222.
(105) Blouin, N.; Michaud, A.; Wakim, S.; Boudreault, P. T.; Leclerc, M.; Vercelli, B.; Zecchin, S.; Zotti, G. *Macromol. Chem. Phys.* **2006**, *207*, 166-174.
(106) Feng, X.; Wu, J.; Enkelmann, V.; Müllen, K. *Org. Lett* **2006**, *8*, 1145-1148.
(107) Mohr, B.; Enkelmann, V.; Wegner, G. *J. Org. Chem.* **1994**, *59*, 635-638.
(108) Usta, H.; Facchetti, A.; Marks, T. J. *J. Am. Chem. Soc.* **2008**, *130*, 8580-8581.
(109) Kovacic, P.; Jones, M. B. *Chem. Rev.* **1987**, *87*, 357-379.
(110) Waldvogel, S. R.; Aits, E.; Holst, C.; Fröhlich, R. *Chem. Commun.* **2002**, *2002*, 1278-1279.
(111) Kramer, B.; Fröhlich, R.; Waldvogel, S. *Eur. J. Org. Chem.* **2003**, *2003*, 3549-3554.
(112) Rempala, P.; Kroulík, J.; King, B. T. *J. Am. Chem. Soc.* **2004**, *126*, 15002-15003.
(113) Brown, I. D.; Skowron, A. *J. Am. Chem. Soc.* **1990**, *112*, 3401-3403.
(114) Kobayashi, S.; Busujima, T.; Nagayama, S. *Chem. Eur. J.* **2000**, *6*, 3491-3494.
(115) Watson, M. D.; Fechtenkötter, A.; Müllen, K. *Chem. Rev* **2001**, *101*, 1267-1300.
(116) Wu, J.; Pisula, W.; Müllen, K. *Chem. Rev.* **2007**, *107*, 718-747.
(117) Rabe, J. P.; Buchholz, S. *Science* **1991**, *253*, 424-427.
(118) Elemans, J. A. A. W.; Lei, S.; de Feyter, S. *Angew. Chem. Int. Ed.* **2009**, *48*, 7298-7332.
(119) Gherghel, L.; Kübel, C.; Lieser, G.; Räder, H. J.; Müllen, K. *J. Am. Chem. Soc.* **2002**, *124*, 13130-13138.
(120) Gourdon, A. *Angew. Chem. Int. Ed.* **2008**, *47*, 6950-6953.
(121) Perepichka, D. F.; Rosei, F. *Science* **2009**, *323*, 216-217.
(122) Lipton-Duffin, J. A.; Ivasenko, O.; Perepichka, D. F.; Rosei, F. *Small* **2009**, *5*, 592-597.
(123) Treier, M.; Richardson, N. V.; Fasel, R. *J. Am. Chem. Soc.* **2008**, *130*, 14054-14055.
(124) Treier, M.; Fasel, R.; Champness, N. R.; Argent, S.; Richardson, N. V. *Phys. Chem. Chem. Phys.* **2009**, *11*, 1209-1214.
(125) Veld, M. I.; Iavicoli, P.; Haq, S.; Amabilino, D. B.; Raval, R. *Chem. Commun.* **2008**, *2008*, 1536-1538.
(126) Grill, L.; Dyer, M.; Lafferentz, L.; Persson, M.; Peters, M. V.; Hecht, S. *Nat. Nanotechnol.* **2007**, *2*, 687-691.
(127) Matena, M.; Riehm, T.; Stöhr, M.; Jung, T. A.; Gade, L. H. *Angew. Chem. Int. Ed.* **2008**, *120*, 2448-2451.
(128) Weigelt, S.; Busse, C.; Bombis, C.; Knudsen, M. M.; Gothelf, K. V.; Lægsgaard, E.; Besenbacher, F.; Linderoth, T. R. *Angew. Chem. Int. Ed.* **2008**, *47*, 4406-4410.
(129) Hla, S.-W.; Bartels, L.; Meyer, G.; Rieder, K.-H. *Phys. Rev. Lett.* **2000**, *85*, 2777-2780.

5 Three-Dimensional Polymer and Carbon Networks

5.1 Introduction

The bottom-up synthesis of a three-dimensional interconnected network structure, porous or non-porous, requires the presence of a crosslinker, that is a molecule containing three or more functional groups.[1]

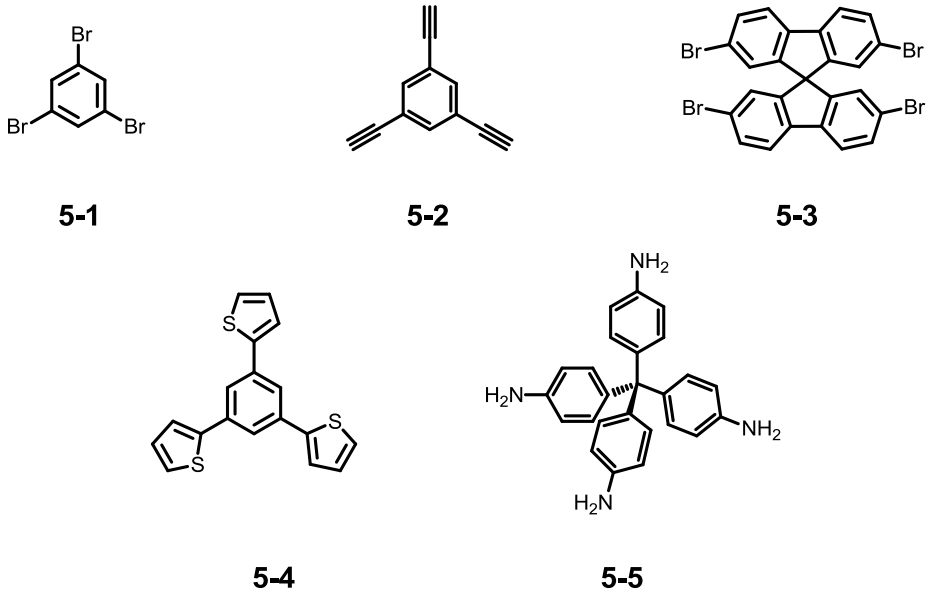

Figure 5-1: Examples of tri- and tetravalent crosslinkers applied to the synthesis of microporous polymer networks.

A number of literature examples used for the synthesis of microporous polymer networks are depicted in Figure 5-1 illustrating the broad chemical variety of structure and functionality. Molecules like **5-1**, **5-2** and **5-3** which are characterized by halogen or ethinyl functions have been used for transition-metal mediated approaches such as the

Sonogashira-Hagihara[2-7], the *Glaser*,[8] the *Suzuki-Miyaura*[7] and the *Yamamoto* reaction.[9-11] For the synthesis of networks, a second complementary monomer component is frequently applied even though the crosslinker can in principal be reacted with itself. This is illustrated by 1,3,5-tri(thiophen-2-yl)benzene **5-4** where the addition of ferric chloride leads to the oxidative *auto*-polymerization of the trivalent molecule.[12] Whereas these approaches all rely on irreversible bond formation, the application of reversible condensation reactions has only been reported very recently. In this respect, amine-functionalized crosslinkers such as **5-5** can be used for the build-up of covalent organic frameworks (COFs) through imine chemistry resulting in materials of high structural order and perfection.[13]

Melamine (2,4,6-triamino-1,3,5-triazine) **5-6** is a heterocyclic aromatic compound that fulfills the requirements needed for a crosslinking unit. The molecule contains three activated amine groups which readily undergo a number of condensation reactions (Figure 5-2). A common example involves the treatment of melamine with formaldehyde **5-7** resulting in resins also known as amino plastics (**MF**, Figure 5-2). Under appropriate reaction conditions melamine can even act as a hexavalent crosslinker since every amine group can undergo two nucleophilic substitutions as illustrated by hexamethylolmelamine **5-8** (Figure 5-2). These type of condensations are often run in the bulk state and the products thus obtained find numerous large-scale applications due to the good mechanical properties and their enhanced thermal and chemical robustness.[14,15]

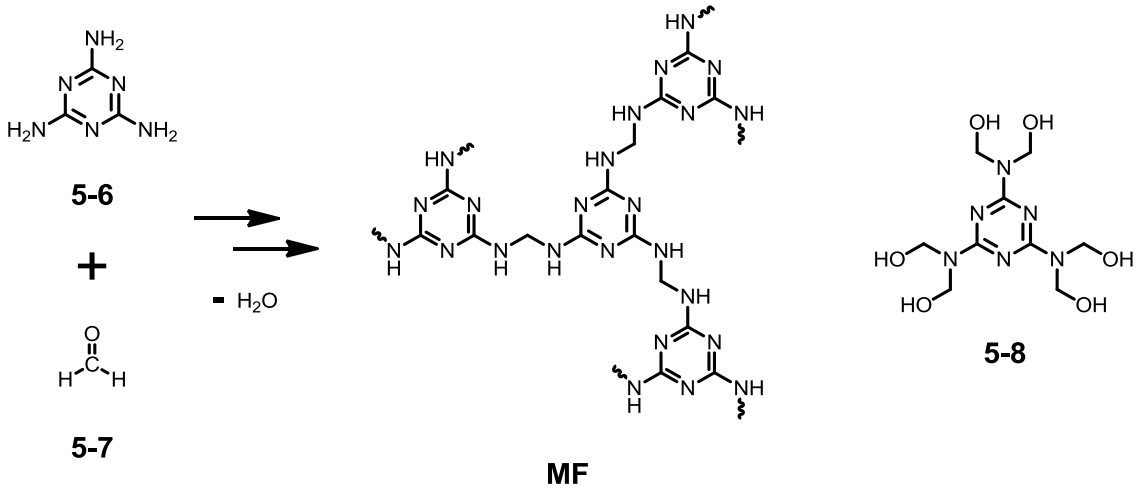

Figure 5-2: Condensation of melamine and formaldehyde leading to the formation of a melamine resin (left), chemical structure of hexamethylolmelamine **5-8** (right).

Melamine-formaldehyde resins are used in laminates, adhesives, fire retardants, molding compounds, coatings, and concrete plasticizers.[16-18] Foams made from these polymers are used as thermal insulators and abrasive cleaners.

The annularly production capacity exceeds one million tons (2003) illustrating the importance of melamine as one of the major monomers of the plastic industry.[18] The good availability and low pricing of the compound also make it an attractive candidate for new applications in material science. An appealing feature of melamine is given by its intrinsic nitrogen content of 66.7 wt% resulting in the formation of nitrogen-rich materials if the molecule is integrated in new synthetic routes.

No microporous polymers based on melamine as a crosslinker are known so far even though the molecule constitutes an ideal and interesting starting point for synthetic approaches. The reactive amine sites of melamine are for example a suitable scaffold for *Schiff* base reactions with di- and trivalent aldehyde components.[19,20] The outcome of this approach will be presented in the present chapter which will also address alternative pathways for the synthesis of imine-linked networks. Based on a number of aromatic aldehydes the chemical portfolio of these materials will be discussed as well as their porous properties. Finally, controlled pyrolysis of the polymer networks can give rise to nitrogen-rich carbons which were examined with respect to their potential in electrochemical applications.

5.2 Poly(aminal) Networks

5.2.1 Synthetic Procedures

The synthesis of a microporous polymer material is generally achieved in solution. For bottom-up approaches, both components react with each other leading to the formation of larger oligomeric units. The progressive crosslinking of these units results in precipitation. It is believed that crosslinking and addition reactions still continue once a heterogeneous reaction system has been formed as a consequence of the high local concentration of the reaction partners. This is due to the fact that the analysis of microporous polymer networks frequently indicates only a very low content of non-reacted functional groups. Nevertheless, both components need to be well-soluble at early stages of the reaction in order to guarantee for the stoichiometric balance of the reactive sites.

Melamine is known for its notoriously low solubility in most organic solvents at neutral pH values. Only highly polar protic solvents are able to dissolve significant amounts of

the compound. Preliminary testing under various temperatures was carried out in order to identify a suitable reaction medium. The solubility testing involved a number of solvents such as acetonitrile, phenyl ether, DMF, DMA and NMP. It turned however out, that only DMSO was able to dissolve sufficient amounts of melamine at temperatures higher than 100 °C. Furthermore, its elevated boiling point of 189 °C offers the possibility to thermally drive the equilibrium of a polycondensation reaction to the desired product side. As an insoluble polymer network is to be formed, the removal of a high-boiling solvent such as DMSO can be easily achieved by filtration or centrifugation.

A first series of materials termed *Schiff* base networks (**SNW**) was obtained from aldehyde components that are either di- or trivalent and purely C/H-containing (Figure 5-3). Thus, terephthalaldehyde **5-8**, biphenyl-4,4'-dicarbaldehyde **5-9**, isopthalaldehyde **5-10**, 1,3,5-tris(4-formylphenyl)benzene **5-11**,[21] naphthalene-2,6-dicarbaldehyde **5-12**[22] and benzene-1,3,5-tricarbaldehyde **5-13**[23] were applied to the network synthesis.

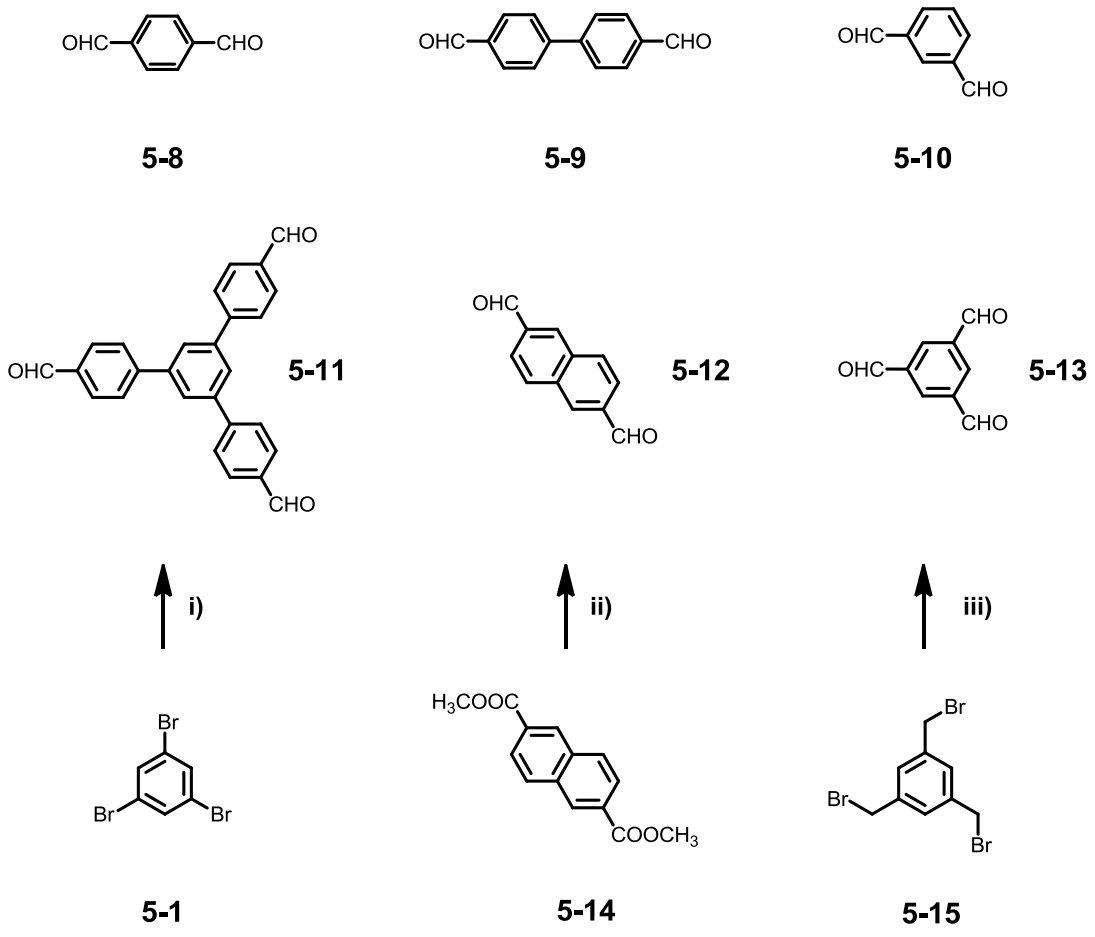

Figure 5-3: Pure C/H-containing aldehyde components and synthetic routes; conditions: i) 4-formylphenylboronic acid, $Pd(Ph_3)_4$, K_2CO_3, toluene, Aliquat 336, reflux, 78 %; ii) sodium bis(2-methoxyethoxy)aluminumhydride (Red-Al), N-methylpiperazine, toluene, 5 °C, 81 %; iii) NMO, molecular sieves, MeCN, reflux, 56 %.

Several of these aldehydes are like melamine large-scale industrial chemicals; the others are accessible on gram scale through straightforward synthetic routes which are depicted in Figure 5-3.

The experimental procedure successfully applied to the network synthesis is exemplified for terephthalaldehyde **5-8** which was reacted under an inert atmosphere with melamine **5-6** at 180 °C in DMSO to give **SNW-1** in 61 % (Figure 5-4).

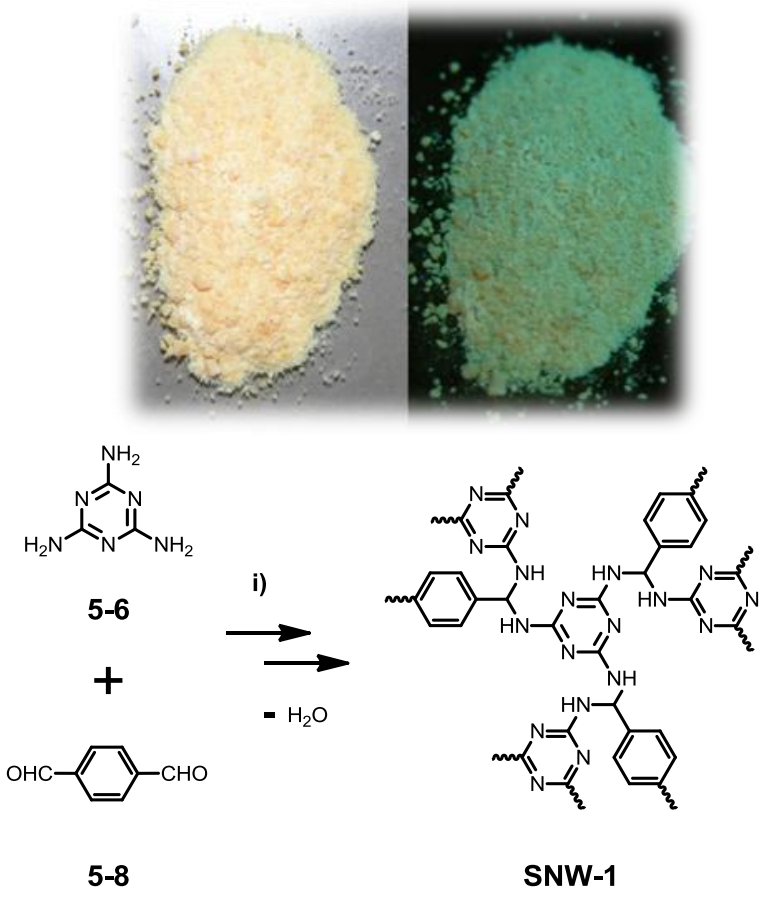

Figure 5-4: Synthesis of **SNW-1**; conditions: i) DMSO, 180 °C, 72 h, 61 % (bottom); photograph of the polymer with and without UV irradiation (top).

To ensure consistency between syntheses and in order to exclude concentration effects, the **SNW** materials were synthesized at a fixed overall molar concentration of 0.4 M and a molar ratio of amine to aldehyde groups of 1:1. Typically, the reaction mixture was held at the elevated temperature level for three days. After 24 h, turbidity slowly began to occur, but only after 48 h visible precipitation of a white voluminous solid set in. After 72 h and cooling to room temperature the precipitate was isolated by filtration and washed with excess acetone, THF and DCM. Subsequently, *Soxhlet* extraction with THF was carried out during 24 h. The solvents were then removed

under vacuum at room temperature to afford the materials as finely divided off-white powders. A photograph of the as-synthesized **SNW-1** material is shown in Figure 5-4. Upon irradiation with a UV lamp operating at 366 nm the polymer emits a pale turquoise fluorescence.

It was then examined to what degree heterocyclic aldehyde components are tolerated by the reaction protocol. The incorporation of such co-monomers would allow for the precise "doping" of the networks with heteroatoms. Also, metal-chelating sites could be introduced *via* pyridine motifs. Thus, pyridine-2,6-dicarbaldehyde **5-16**, 2,2'-bipyridine-5,5'-dicarbaldehyde **5-21**, thiophene-2,5-dicarbaldehyde **5-17** and furan-2,5-dicarbaldehyde **5-18** were applied to the same synthetic protocol as described above (Figure 5-5). Again, most components were commercially available, only 2,2'-bipyridine-5,5'-dicarbaldehyde **5-21** had to be synthesized in a two-step synthesis from the corresponding dimethyl-derivative **5-19**.[24]

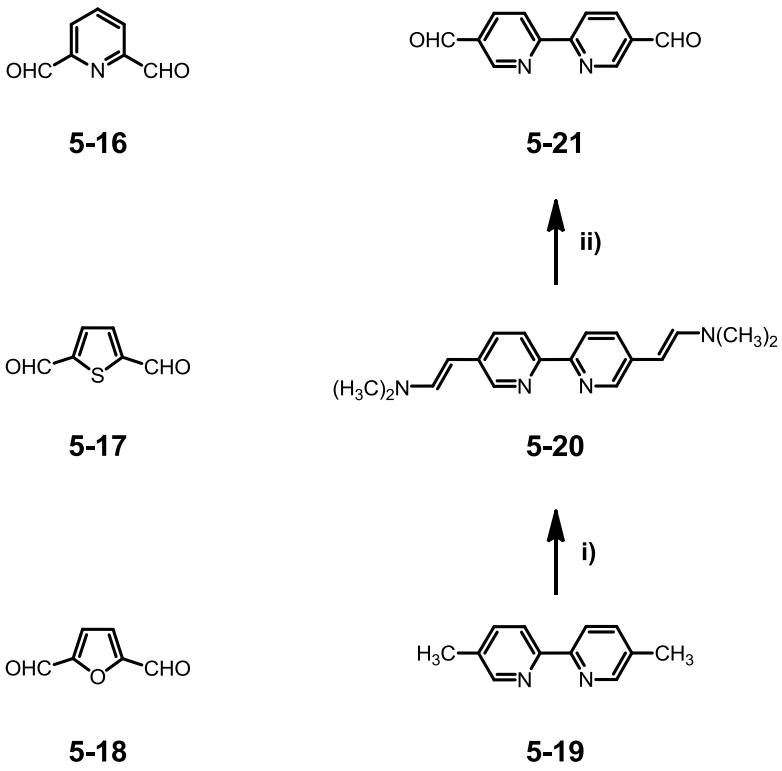

Figure 5-5: Heteroatom-containing aldehyde components and synthetic routes; conditions: i) *tert*-butoxy bis(dimethylamino)methane, DMF, 120 °C, 66 %; ii) $NaIO_4$, THF/H_2O, room temperature, 69 %.

Finally, the roles of the two components were "inverted" by switching from melamine **5-6** to 1,3,5-triazine-2,4-diamine **5-22** which bears only two amine groups (Figure 5-6). In contrast to the results from the C/H-containing aldehyde components, all reactions proceeded significantly faster in this case. The materials precipitated shortly after

launching the synthesis which may be ascribed to the activated functional groups of the heterocyclic aldehydes. Also, the products of the reaction were darker in color.
Therefore, the two trivalent aldehydes 1,3,5-tris(4-formylphenyl)benzene **5-11** and benzene-1,3,5-tricarbaldehyde **5-13** were applied as crosslinkers in this case. The reactions proceeded in a similar fashion as described for the C/H-containing aldehyde components, but the yields were significantly lower (46 - 52 wt%).

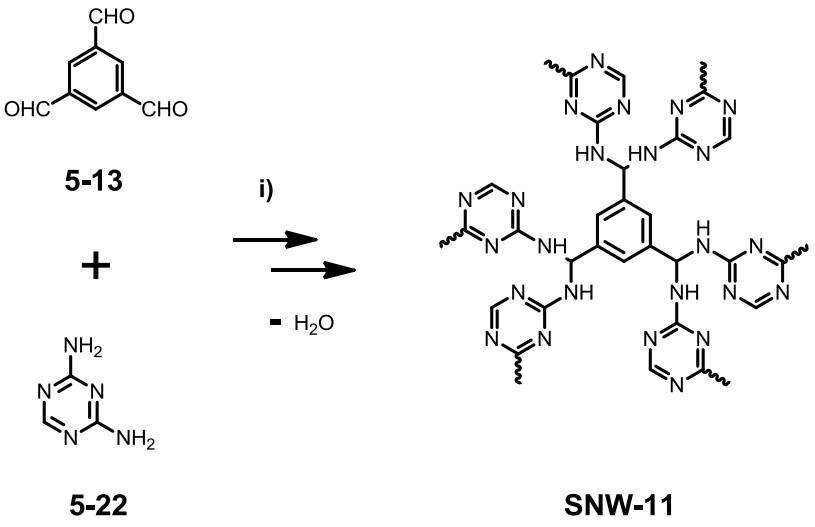

Figure 5-6: Synthesis of **SNW-11**; conditions: i) DMSO, 180 °C, 72 h, 52 %.

5.2.2 Structural Characterization

The complete insolubility of all twelve **SNW** materials and the precipitation during synthesis gave initial evidence for the formation of a highly crosslinked polymeric structure. The chemical nature of the materials was examined by *Fourier* transform infrared (FTIR) spectroscopy and compared to the spectra of the molecular precursors. As a first important finding, the FTIR spectra of all **SNW** materials indicate high conversion of the functional groups that were initially present in the monomers. Bands which can be attributed to the primary amine group of melamine at 3470 cm^{-1} and 3420 cm^{-1} (symmetric NH_2 stretching), at 3335 cm^{-1} and 3125 cm^{-1} (asymmetric NH_2 stretching) and at 1650 cm^{-1} (NH_2 deformation) are absent or strongly attenuated in the spectra of the networks (Figure 5-7).[25] The same is true for the signals of the carbonyl function of the aldehydes at 2870 cm^{-1} (C-H stretching) and 1690 cm^{-1} (C=O stretching). On the contrary, distinct bands corresponding to quadrant (1540 cm^{-1})[25-27] and semicircle stretching (1470 cm^{-1})[25-27] as well as to breathing modes (1350 cm^{-1})[28,29] of the triazine ring are observed in all spectra of the **SNW** materials

thus proving the successful incorporation of melamine (Figure 5-7). No bands that may be attributed to imine linkages such as the C=N stretching vibration around 1600 cm^{-1} are found in the FTIR spectra. Additionally, the aromatic out-of-plane (815 cm^{-1}) and in-plane (988 cm^{-1}) deformation vibrations of the aldehyde components are clearly resolved. The signal at 815 cm^{-1} overlaps however with a vibration seen at the identical position for the triazine ring of melamine.[25]

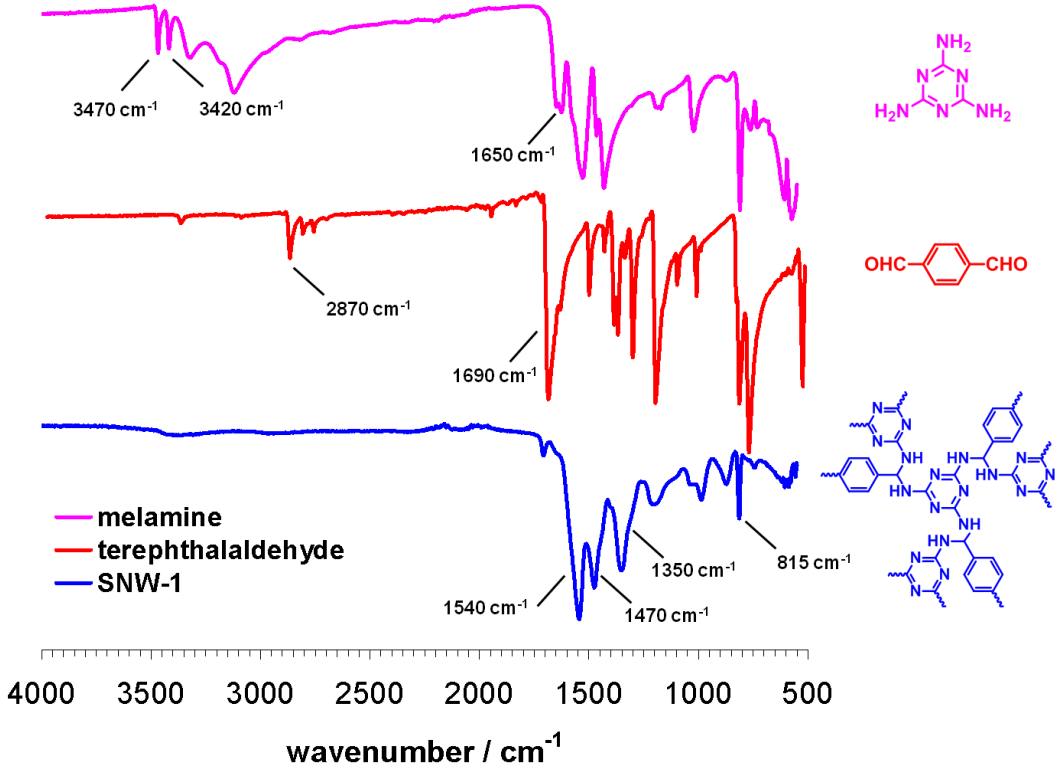

Figure 5-7: FTIR spectra of melamine **5-6**, terephthalaldehyde **5-8** and **SNW-1**.

The final proof for the proposed poly(aminal) structure was given by a combination of $^{13}C[^{1}H]$ and $^{15}N[^{1}H]$ cross-polarization (CP) magic angle spinning (MAS) NMR spectroscopy.

The ^{13}C CP-MAS NMR spectrum of **SNW-1** is shown in Figure 5-8. Three principal resonances are found at δ = 167.1 ppm, δ = 129.5 ppm, and δ = 55.2 ppm, respectively. The first can be undoubtedly assigned to the carbon atoms present in the triazine ring of melamine,[30] whereas the signal at δ = 129.5 ppm originates from the aromatic carbons of the benzene units. The resonance at δ = 55.2 ppm can be correlated to the tertiary carbon atoms formed upon the addition of the primary amine group of melamine to a newly formed carbon-nitrogen double bond resulting in an aminal.[31,32] Typically, aliphatic carbon atoms of aminal groups are found in this spectral region.[33,34]

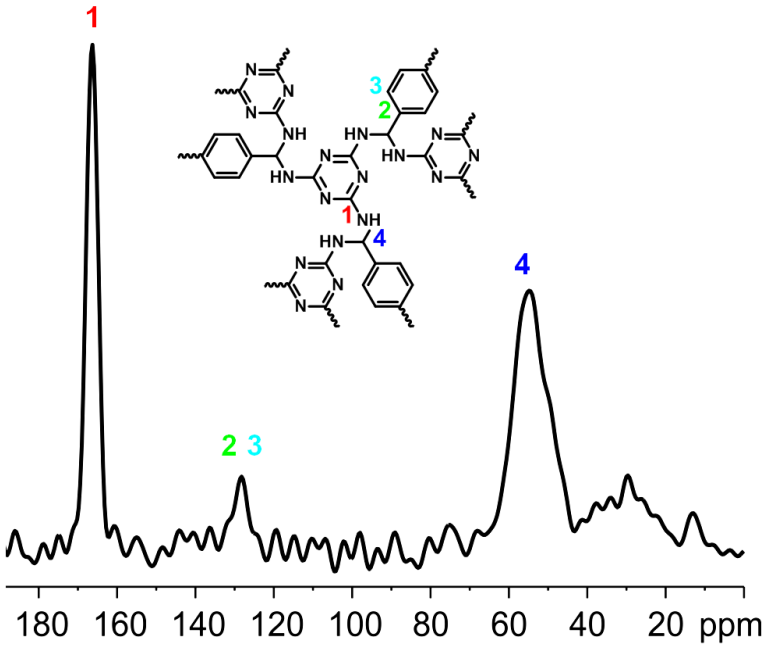

Figure 5-8: ^{13}C CP-MAS NMR spectrum of **SNW-1**.

In addition to the results from the ^{13}C CP-MAS NMR analysis, the ^{15}N CP-MAS NMR spectrum of **SNW-1** (Figure 5-9) shows two major resonances at δ = - 205 ppm and δ = - 283 ppm, respectively.

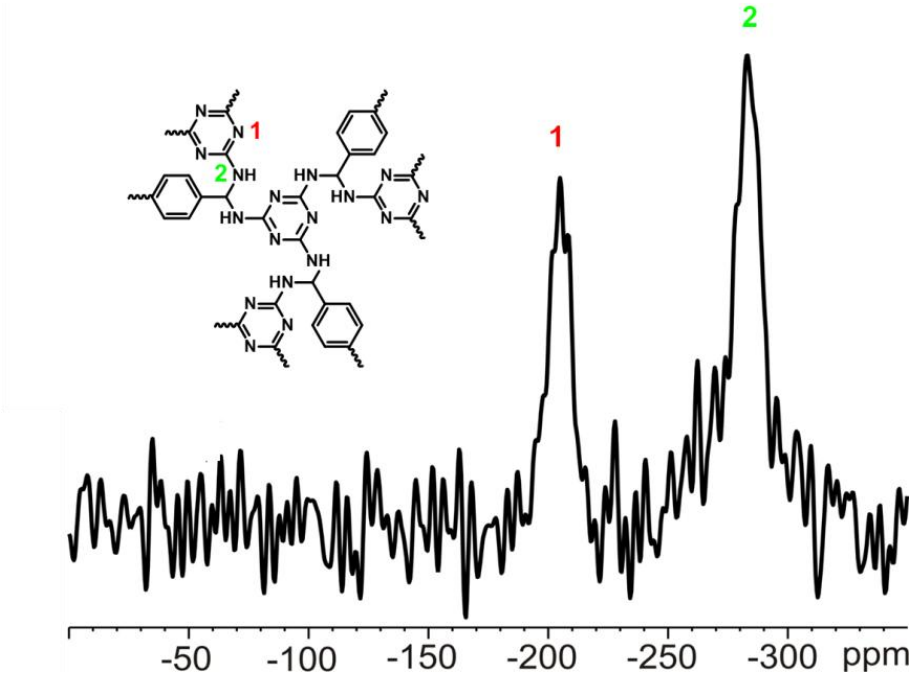

Figure 5-9: ^{15}N CP-MAS NMR spectrum of **SNW-1**.

The first signal is assigned to the nitrogen atoms of the triazine ring, whereas the latter can be attributed to the secondary amine present in the aminal group.[35] Again, no

resonance around δ = - 55 ppm is found which would correspond to imine-type nitrogen atoms. In accordance with the results from the FTIR analysis, no signals of unreacted aldehyde or primary amine groups can be detected in the solid state NMR spectra of **SNW-1** indicating a high efficiency of the crosslinking reaction.

Figure 5-10 illustrates the proposed reaction pathway for the bond formation during the build-up of the polymeric networks. In a first step, the primary amine groups of melamine **5-6** and the aldehyde functions of terephthalaldehyde **5-8** react with each other to form an intermediate imine species **5-23**. It is well-known that the imine bond is highly susceptible to further addition reactions with partners bearing active hydrogen.[19,20] Thus, the addition of a second melamine species **5-6** results in the formation of the aminal **5-24**. This reaction can be considered as a secondary crosslinking step whose importance for the generation of rigidity and porosity will be detailed in the following chapter.

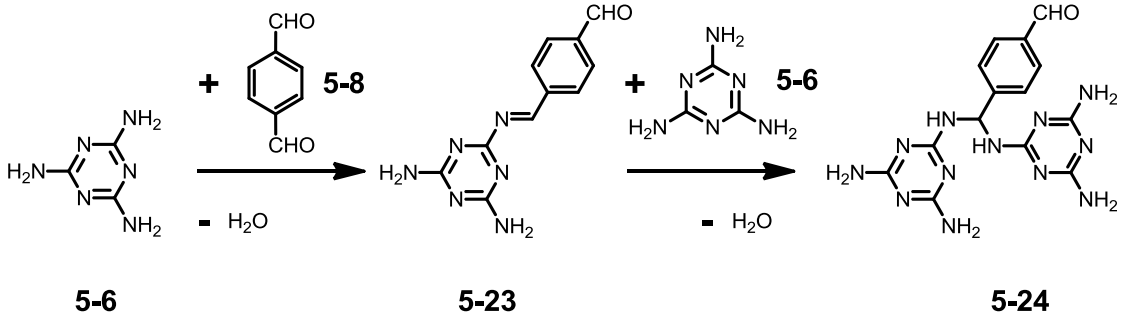

Figure 5-10: Proposed reaction pathway during the formation of the **SNW** materials.

Solid state NMR measurements are also a versatile tool to monitor the incorporation of the heterocyclic aldehyde components into the materials as these show up at characteristic resonances in the ^{13}C CP-MAS NMR spectra.

This is evidenced for heteroatom-containing **SNW-7** and **SNW-9** which were obtained from the condensation of melamine **5-6** with pyridine-2,6-dicarbaldehyde **5-16** and thiophene-2,5-dicarbaldehyde **5-17**, respectively.

In the first case (Figure 5-11), the resolution of the NMR spectrum allows for the exact peak assignment of the carbon atoms on the pyridine ring. Thus, the two signals at δ = 120.1 ppm and δ = 137.4 ppm originate from the aromatic carbons in the 3,5 and 4-position of the pyridine backbone, whereas the substituted 2,6-position gives rise to the resonance at δ = 158.6 ppm. The resonance at 166.5 ppm can be ascribed to the carbon atoms of the triazine ring and the signal at δ = 62.9 ppm is attributed to the tertiary carbon atom of the characteristic aminal motif. The downfield shift of this

resonance with respect to **SNW-1** can be rationalized in terms of the electron-withdrawing effect of the neighboring pyridine unit.

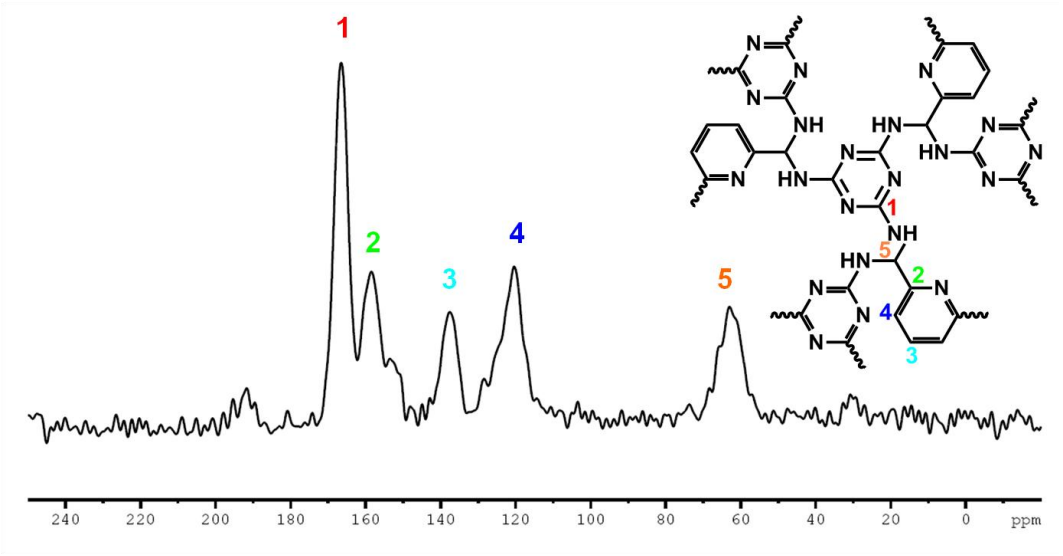

Figure 5-11: ^{13}C CP-MAS NMR spectrum of **SNW-7**.

In the case of **SNW-9** (Figure 5-12) the ^{13}C CP-MAS NMR spectrum also reflects the chemical nature of the polymeric network.

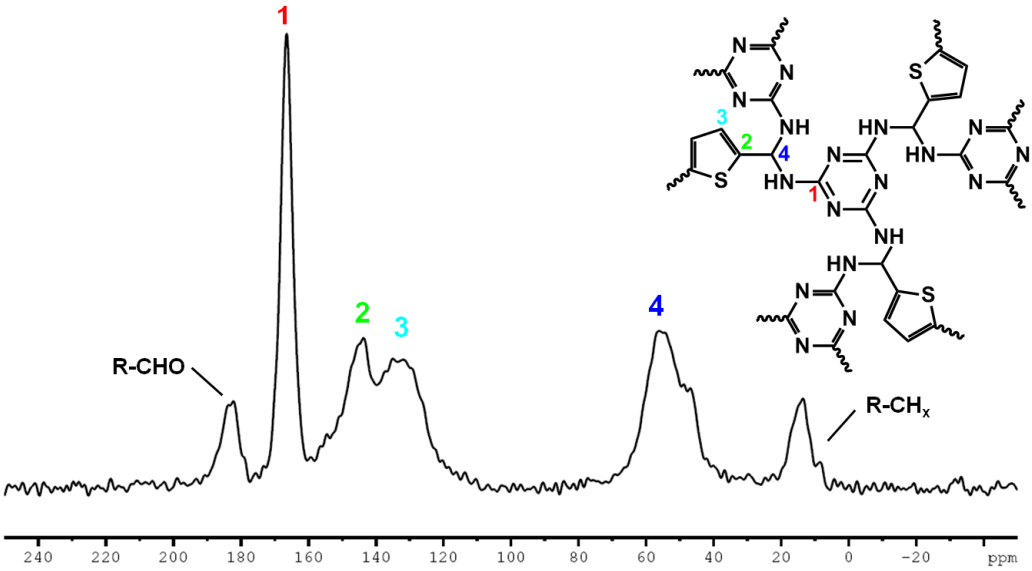

Figure 5-12: ^{13}C CP-MAS NMR spectrum of **SNW-9**.

Again, the carbon atoms of the triazine ring give rise to a strong signal at δ = 167.2 ppm. The signals corresponding to the two carbon atoms of the thiophene moiety are detected at δ = 146.3 ppm and δ = 131.1 ppm whereas the aminal group

gives rise to the resonance at δ = 59.8 ppm. The spectrum contains two additional resonances at δ = 186.8 ppm and δ = 18.2 ppm. Whereas the first can be attributed to some residual aldehyde groups of the starting compound thiophene-2,5-dicarbaldehyde **5-17**, the latter corresponds to methyl- or methylene-type carbons.

A characteristic feature of the **SNW** series is the incorporation of the melamine motif resulting in high intrinsic nitrogen levels. Melamine with its unique nitrogen to carbon ratio of 2.33 leads to nitrogen contents varying between 25 wt% and 45 wt% as determined by elemental combustion analysis (ECA).

A comparative representation of the elemental compositions can be found in Figure 5-13. For some networks (**SNW-9**, **SNW-11**, **SNW-12**) the nitrogen content even exceeds the carbon content of the sample (Table 1). For the other materials both values are found at similar levels. In general, all samples exceed by far the nitrogen contents reported for hypercrosslinked poly(aniline)[36,37] and poly(pyrrole)[38] or poly(aryltriazine) networks.[29,39]

	aldehyde component	C / wt%	H / wt%	N / wt%	S / wt%
SNW-1	terephthalaldehyde	38.60	4.32	38.02	1.52
SNW-2	biphenyl-4,4'-dicarbaldehyde	40.31	4.57	35.94	3.44
SNW-3	isophtalalydehyde	41.31	4.77	40.42	3.85
SNW-4	1,3,5-tris(4-formylphenyl)benzene	46.57	4.41	41.73	0.60
SNW-5	naphthalene-2,6-dicarbaldehyde	37.91	4.41	35.88	0.80
SNW-6	benzene-1,3,5-tricarbaldehyde	41.78	4.65	33.49	2.21
SNW-7	pyridine-2,6-dicarbaldehyde	42.50	4.50	37.93	0.23
SNW-8	2,2'-bipyridine-5,5'-dicarbaldehyde	38.50	4.17	35.96	3.84
SNW-9	thiophene-2,5-dicarbaldehyde	43.33	3.80	43.77	13.89
SNW-10	furan-2,5-dicarbaldehyde	45.92	4.02	23.89	5.24
SNW-11*	benzene-1,3,5-tricarbaldehyde	39.75	4.66	44.60	1.40
SNW-12*	1,3,5-tris(4-formylphenyl)benzene	36.49	2.98	37.86	1.90

*based on 1,3,5-triazine-2,4-diamine

Table 5-1: The elemental composition of the **SNW** materials as determined by elemental combustion analysis.

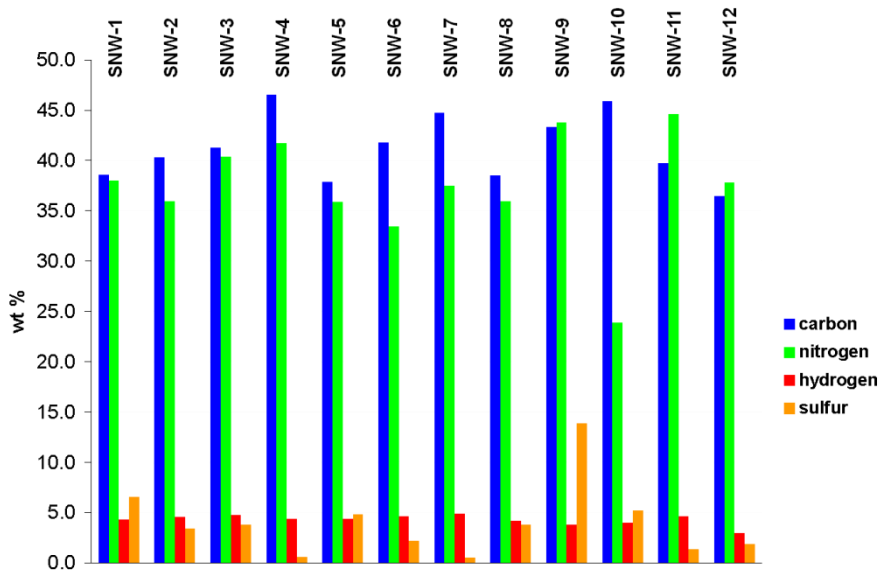

Figure 5-13: Elemental composition of the **SNW** materials as determined by elemental combustion analysis.

Thermogravimetric analysis (TGA) of the **SNW** materials revealed decomposition temperatures higher than 400 °C for all samples independently of the chemical nature of the aldehyde component.

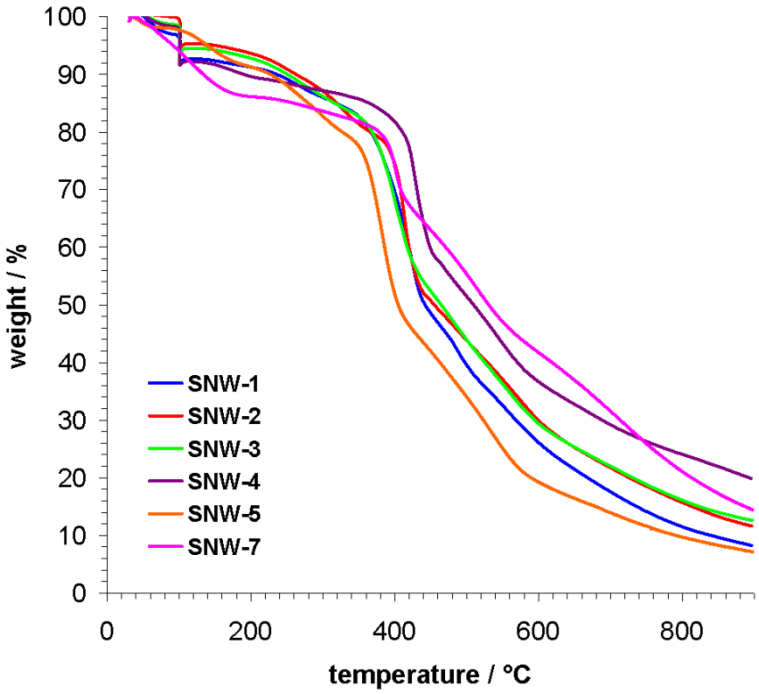

Figure 5-14: Thermogravimetric analysis of the **SNW** materials under nitrogen.

This is reflected by the curves in Figure 5-14 which correspond to the networks built from terephtalaldehyde (**SNW-1**), biphenyl-4,4'-dicarbaldehyde (**SNW-2**),

isophtalalydehyde (**SNW-3**), 1,3,5-tris(4-formylphenyl)benzene (**SNW-4**), naphthalene-2,6-dicarbaldehyde **SNW-5**) and pyridine-2,6-dicarbaldehyde (**SNW-7**).

After a first degradation step affecting 30 wt% of the sample, further decomposition proceeds only slowly. This behavior is a consequence of the high resistivity of the triazine ring to thermal degradation mainly accounting for the use of melamine-based flame-retardants.[16,17] Even at temperatures of 900 °C, **SNW-7** still retains 20 % of its original mass.

5.2.3 Porosity

The porous properties of the **SNW** materials were subsequently analyzed by nitrogen physisorption at 77 K. In order to empty the pores prior to the analysis the polymer material was outgassed at 100 °C for 24 h under high vacuum. For each sample, the sorption analysis was performed directly after this activation procedure.

Two typical examples for sorption isotherms of the poly(aminal) networks are shown in Figure 5-15 for microporous **SNW-1** and in Figure 5-17 for mesoporous **SNW-7**, respectively.

For **SNW-1**, derived from terephtalaldehyde **5-8**, the isotherm shows a steep gas uptake at low relative pressures and a nearly flat course in the intermediate pressure regime (plateau).

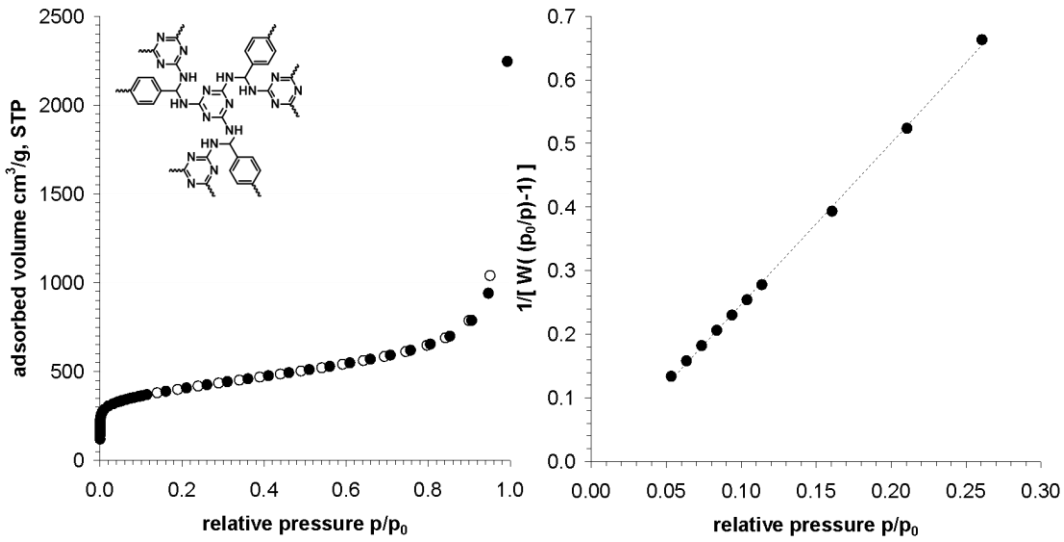

Figure 5-15: Nitrogen sorption isotherm of **SNW-1** (left) and corresponding BET plot (right) measured at 77 K.

The type I shape of this isotherm is typically observed for microporous materials[40-42] for which the pore diameter is by definition below 2.0 nm.

The mechanism schematically illustrated in Figure 5-16 has been proposed for the filling of the pores and can be used to explain the characteristic shape of the sorption isotherm. At very low relative pressures of $p/p_0 = 10^{-6}$ - 10^{-5} the adsorption will start within the smallest micropores of the material. During this primary filling, pores with diameters below 1.0 nm (also termed ultramicropores) are the preferential site for gas molecules due to the overlap of the adsorption potentials from opposite pore walls.[41,42]
For **SNW-1**, the semi-logarithmic representation of the sorption isotherm (Figure 5-19) reveals that already at the beginning of the measurement, at a relative pressure of $p/p_0 = 10^{-5}$, a significant fraction of the pore volume has been filled. The adsorption of 140 g/cm^3 at this extremely low relative pressure level proves the presence of ultramicropores within the polymer network.

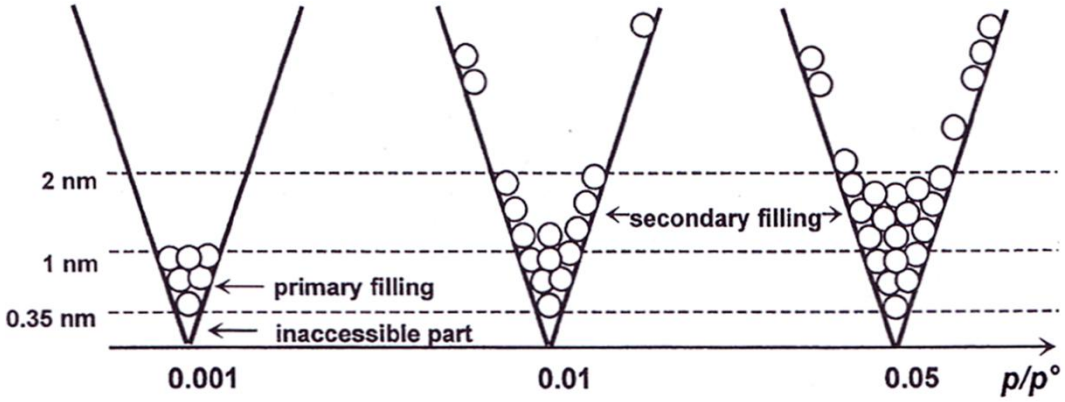

Figure 5-16: Main steps of the successive filling of micropores during adsorption as seen for **SNW-1**.[41]

As it can be seen in Figure 5-16, monolayer adsorption in the remaining larger micropores with diameters up to 2.0 nm is progressively completed in the relative pressure regime p/p_0 of 10^{-4} to 10^{-2} (secondary filling).[43] At a relative pressure of p/p_0 = 0.1 all micropores are considered to be occupied by the gas molecules. For this reason the adsorbed gas volume is converted into the corresponding liquid volume which equals the overall micropore volume (MPV) of the sample. For **SNW-1** an enhanced MPV of 0.56 cm^3/g is found. This number is in good agreement to the corresponding value of 0.41 cm^3/g derived from non-local density functional theory (NLDFT).
At higher relative pressures, the sample adsorbs only minor gas amounts resulting in a weak slope of the isotherm (Figure 5-15). In this pressure range, mesopores and small macropores of the sample are filled. Upon approaching the saturation pressure at p/p_0 = 1.0 a strong gas uptake is again observed which is due to the condensation of nitrogen in large macropores, *inter*particular voids and the external surface of the material. In order to suppress this effect, the total pore volume of the sample is usually

calculated at a relative pressure of p/p_0 = 0.8 as described above. For **SNW-1** a PV of 1.01 cm^3/g is found by this method. In agreement with the classification of **SNW-1** as a microporous material no hysteresis is found upon desorption. The isotherm exhibits full reversibility (Figure 5-15).

The surface areas of porous materials are frequently calculated using the *Brunauer-Emmett-Teller* (BET) model which was developed in 1938 and takes multilayer adsorption into account.[41,42,44] This is in contrast to the classical *Langmuir* theory which is based on the assumption of pure monolayer adsorption.[41,42,45] In fact, it has to be considered that at prefential sites such as narrow pores, edges and grooves multilayer adsorption sets in prior to the completion of a closed monolayer. In the BET model the adsorbed model is thus not considered to be of uniform thickness but rather to be made of random stacks of gas molecules.

The BET equation requires a linear plot that for most solids, using nitrogen as the analysis gas, is restricted to a limited region of the adsorption isotherm which is usually found in the p/p_0 range of 0.05 to 0.35:

$$\frac{1}{[W((p/p_0)-1)]} = \frac{1}{W_m + C} + \frac{C-1}{W_m C}(p/p_0)$$

Herein, W is the weight of gas adsorbed at a given relative pressure p/p_0 and W_m is the weight of adsorbate constituting a monolayer of surface coverage. The term C (BET constant) is related to the energy of adsorption in the first adsorbed layer.

Thus, from the slope s and the intercept i of the BET plot the weight of the monolayer can be calculated:

$$s = \frac{C-1}{W_m C}$$

$$i = \frac{1}{W_m + C}$$

Combining both equations yields the desired equation for W_m:

$$W_m = \frac{1}{s+1}$$

From this value, the total surface area S_T can be derived using the molecular cross-sectional area A_{CS} of nitrogen (16.2 $Å^2$):

$$S_T = \frac{W_m A_{CS} N_A}{M}$$

In this equation N_A is *Avogadro*'s number and M is the molecular weight of the adsorbate. In order to compare the surface area of different samples, the value of the specific surface area S_{BET} is usually given, which is obtained by division of S_T by the weight w of the sample:

$$S_{BET} = \frac{S_T}{w}$$

The BET plot of **SNW-1** is shown in Figure 5-15 and reveals a virtually linear fit to the experimental data. The surface area S_{BET} calculated as described above is 1377 m^2/g for this sample. In comparison to other microporous polymer networks this number is high but does not reach the best cases reported. Values of up to 2100 m^2/g have been measured for hypercrosslinked polymer networks obtained by multiple *Friedel-Crafts* alkylation.[46-48] Very recently, an unprecedented surface area of 5600 m^2/g has been claimed for a polymer network prepared *via* the nickel-mediated coupling of tetraphenylmethane.[10]

The porosity of **SNW-7** (pyridine-2,6-dicarbaldehyde) differs significantly from the previous case. The most striking feature of the isotherm which is depicted in Figure 5-17 is the irreversible sorption behavior resulting in a pronounced hysteresis loop upon desorption.

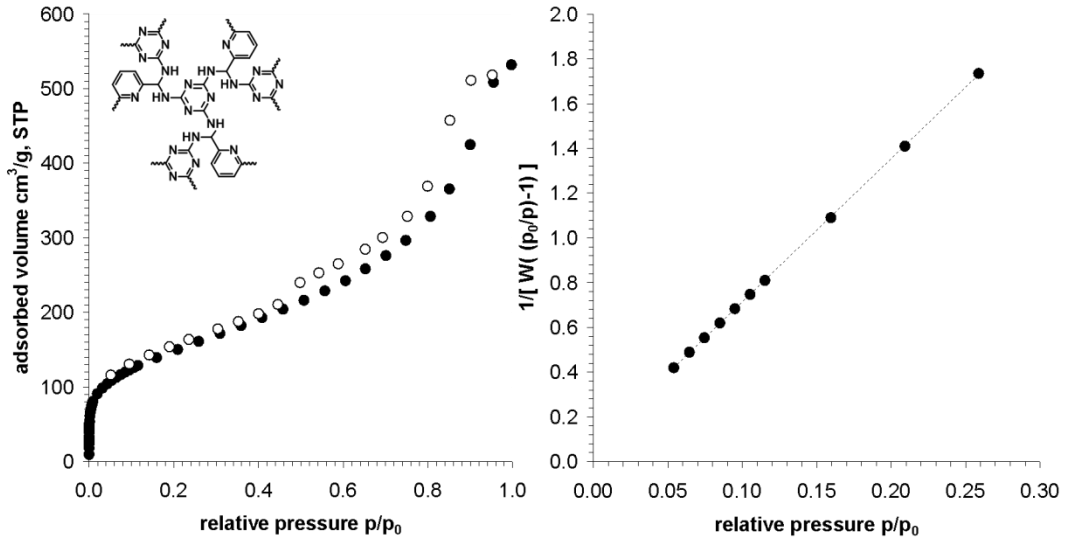

Figure 5-17: Nitrogen sorption isotherm of **SNW-7** (left) and corresponding BET plot (right) measured at 77 K.

Only at a relative pressure of p/p_0 = 0.45 both branches of the isotherm meet again. This value is close to the lower theoretical limit at p/p_0 = 0.42.[41,42] The isotherm of **SNW-7** can thus be classified as type IV.[40]

The observed hysteresis phenomenon is typical of mesoporous materials and related to the capillary effect that occurs upon condensation in the multilayer regime (Figure 5-18). Typically, pores with diameters between 3.0 nm and 7.0 nm are affected by this phenomenon.[41] As it can be seen in Figure 5-18 the characteristic processes set in at relative pressures higher than p/p_0 = 0.1 for mesoporous analytes which is in contrast to the microporous case described above.

The characteristic evolution of a meniscus is believed to be the reason for the hysteresis effect (Figure 5-18). A meniscus represents a curved surface for which the equilibrium saturation pressure is different than in the case of a planar surface. The consequence is capillary condensation which leads to a transition from the gas-like state to the liquid-like state at relative pressures p/p_0 which are far below the actual saturation pressure at p/p_0 = 1.00.

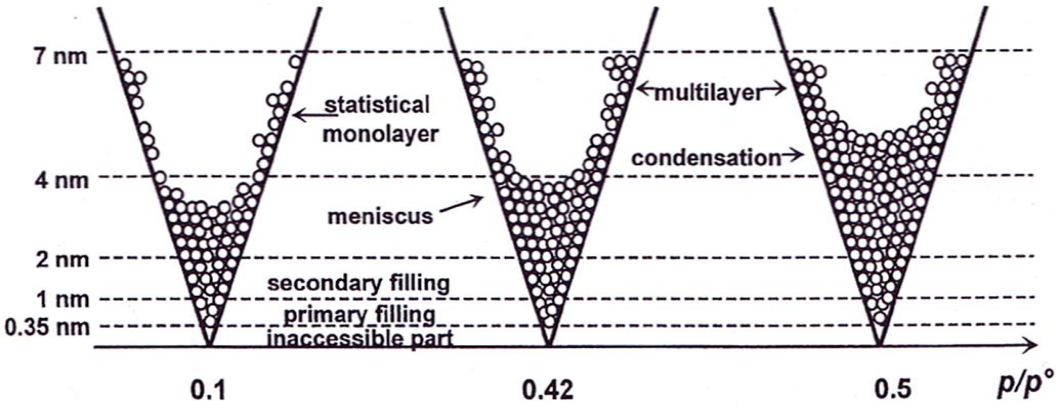

Figure 5-18: Main steps of the successive filling of mesopores during adsorption as seen for **SNW-7**.[41]

Conversely, an adsorbed film remains on the pore walls during desorption when evaporation of the center core takes place. The appearance of partial irreversibility during the sorption analysis is thus related to metastable states which cause the adsorbate to be entrapped upon desorption. The exact assessment of the hysteresis behavior of mesoporous materials remains however under discussion until today.[41,42]

The observed lower specific surface area S_{BET} of 541 m^2/g for **SNW-7** as well as the decreased pore volume PV of 0.51 cm^3/g are in accordance with the predominance of mesopores in the material. The direct and template-free generation of mesoporosity as in the case of **SNW-7** is a special feature which is not frequently encountered in the field of porous polymer materials.[49]

As it is seen in Table 5-2, the specific surface areas of the **SNW** family determined by the BET method vary between 199 m^2/g (**SNW-12**) and 1377 m^2/g (**SNW-1**). These two samples also posses the lowest (0.22 cm^3/g) and highest pore volume (1.01 cm^3/g) of the series.

The difference in porosity between the samples is best seen in the semi-logarithmic representation of the nitrogen adsorption isotherm (Figure 5-19). Those samples exhibiting high surface areas and a pronounced microporosity such as **SNW-1**, **SNW-3**, **SNW-4** and **SNW-5** significantly exceed the other samples as far as the adsorbed gas volume at a particular relative pressure p/p_0 is concerned. Mesoporous samples such as **SNW-7**, **SNW-9** and **SNW-11** exhibit lower adsorption values and moderate surface areas.

	aldehyde component	**S_{BET} $[m^2g^{-1}]$**	**PV $[cm^3g^{-1}]$**	**MPV $[cm^3g^{-1}]$**
SNW-1	terephthalaldehyde	1377	1.01	0.56
SNW-2	biphenyl-4,4'-dicarbaldehyde	842	0.62	0.36
SNW-3	isophtalalydehyde	1133	0.84	0.48
SNW-4	1,3,5-tris(4-formylphenyl)benzene	1213	0.69	0.48
SNW-5	naphthalene-2,6-dicarbaldehyde	1032	0.73	0.43
SNW-6	benzene-1,3,5-tricarbaldehyde	639	0.57	0.24
SNW-7	pyridine-2,6-dicarbaldehyde	541	0.51	0.19
SNW-8	2,2'-bipyridine-5,5'-dicarbaldehyde	730	0.67	0.28
SNW-9	thiophene-2,5-dicarbaldehyde	216	0.22	0.09
SNW-10	furan-2,5-dicarbaldehyde	251	0.22	0.06
SNW-11*	benzene-1,3,5-tricarbaldehyde	220	0.25	0.08
SNW-12*	1,3,5-tris(4-formylphenyl)benzene	199	0.21	0.07

*based on 1,3,5-triazine-2,4-diamine

Table 5-2: Porous parameters of the **SNW** materials as determined by nitrogen physisorption at 77K.

Remarkably, the highest specific surface areas of 1377 m^2/g and 1213 m^2/g were obtained in the case of **SNW-1** and **SNW-4**, respectively (Table 5-2). These two materials possess similar network geometries although they were derived from two different monomer combinations. This is due to the fact that tris(4-formylphenyl)benzene **5-11** itself can act as a trivalent crosslinker. Also in this case,

the semi-logarithmic plot of the low pressure regime as well as the corresponding MPV of 0.56 and 0.48 cm^3/g illustrate the similar microporosity of **SNW-1** and **SNW-4**.

When comparing the data of the networks derived from different *para*-functionalized monomers the modular nature of the porosity in the case of the **SNW** materials becomes apparent. Thus, the surface area of **SNW-1** (terephtalaldehyde, 1377 m^2/g) significantly exceeds the values of **SNW-2** (biphenyl-4,4'-dicarbaldehyde, 842 m^2/g) and **SNW-8** (2,2'-bipyridine-5,5'-dicarbaldehyde, 730 m^2/g). This can be rationalized in terms of the additional aromatic ring in the latter case which leads to a bigger separation of the crosslinking triazine units and an increased conformational flexibility of the whole network.

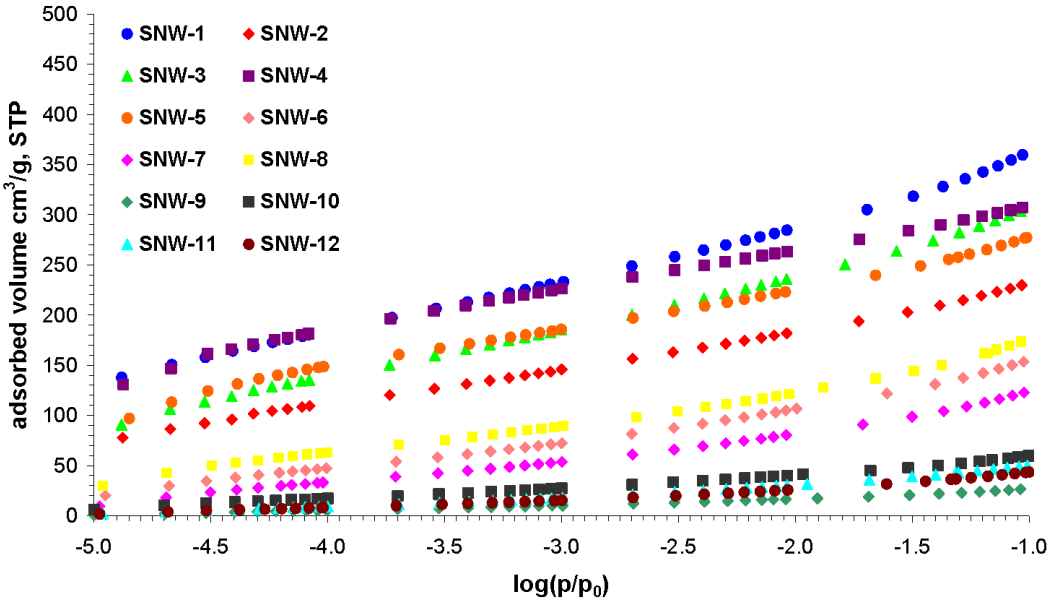

Figure 5-19: Semi-logarithmic representation of the nitrogen adsorption isotherms of the **SNW** series.

The surface area of **SNW-5** (naphthalene-2,6-dicarbaldehyde, 1032 m^2/g) ranges somewhat in between the two extremes which is in agreement with the intermediate separation of the functional groups on the naphthalene backbone. The possibility to "tune" the porous characteristics by variation of the monomer dimensions is well-known for crystalline zeolites[50,51] and metal-organic frameworks (MOFs).[52,53] Also, for highly ordered covalent-organic frameworks (COFs) this effect has been reported.[54] However, for fully disordered polymer networks such as the **SNW** materials a tunable microporosity via modification of the monomer strut length has only scarcely been observed.[2]

As to the two "inverted" networks **SNW-11** and **SNW-12** for which melamine was replaced by divalent 1,3,5-triazine-2,4-diamine **5-22** the importance of a rigid, densely

reticulated network structures becomes evident. It appears that the exchange of the crosslinker has a negative impact on the porosity of the materials since the corresponding surface areas of 220 m^2/g and 199 m^2/g are among the lowest of the entire series. Their counterparts from the crosslinking with melamine, **SNW-4** and **SNW-6** reach values of 1213 m^2/g and 639 m^2/g, respectively. A similar trend is found for the corresponding pore volumes.

In summary, the unique porosity of the **SNW** materials in combination with their broad chemical variety induced by the choice of the aldehyde component enables the synthesis of tailor-made porous polymer networks (microporous or mesoporous) which contain optimized porous properties for particular applications that will be presented in the following paragraphs.

5.2.4 Gas Storage

For physisorptive gas storage, the combination of enhanced specific surface area and high microporosity is often considered the primary requisite for high uptake capacities. Consequently, the highest storage capacities for hydrogen[10,46,48,55] and methane[55,56] that have been reported so far were achieved by HCPs with surface areas exceeding 2000 m^2/g. In comparison to other microporous adsorbents such as zeolites,[57] carbons,[58] MOFs[59-61] and COFs[39,62] suitable for the physisorptive storage of gases, microporous polymer networks have distinct advantages. They can be precisely designed by means of chemical synthesis and they exhibit excellent chemical resistivity and thermal stability combined with low density. Also, scalability and pricing are important factors from an economical point of view as the filling of an automotive tank will possibly require kilo amounts of gas storage material. Within the scope of this work the **SNW** materials showing the highest porosities were evaluated as adsorbents both for physisorptive methane and hydrogen storage. Furthermore, the hydrophilicity was examined by water adsorption measurements. The gas uptake experiments have been carried out in the cooperation with the group of *Kaskel* (Technical University Dresden, Germany).

In the recent past, there is a growing demand for vehicles driven with methane. Natural gas whose main constituent is methane offers a considerable advantage over conventional fossil fuels both from an environmental point of view and due to the natural resources. The combustion of methane releases the smallest amount of carbon dioxide per unit of heat produced but results in similar heats of combustion. The combination of high methane pressures and vessels containing a storage medium that

contributes to the overall gas uptake *via* physisorption is believed to greatly enhance the operating distance of gas-driven vehicles.[57,63,64]

For the methane measurements of the **SNW** materials, all samples were outgassed prior to the analysis by heating in vacuum to 150 °C until the weight was constant. The methane excess adsorption of the samples was measured gravimetrically at pressures of up to 150 bar at room temperature using a magnetic suspension balance integrated within an experimental setup that was previously described.[65,66]

The excess adsorption isotherms depicted in Figure 5-20 reveal a strong influence of the porosity on the final storage performance even though all materials exhibit a similar shape of the isotherm.

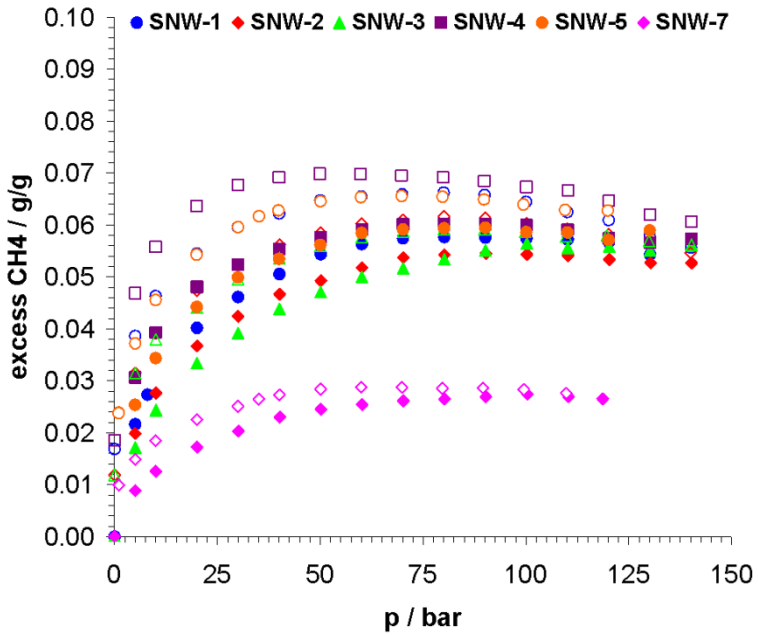

Figure 5-20: Gravimetric methane excess sorption isotherms of the **SNW** materials measured at 298 K.

At lower pressure a progressive mass uptake is observed with pressure. Upon further increasing the pressure the slope of the isotherms decreases and is approaching a maximum.

Above pressures of approximately 100 bar, the slope of the isotherms is negative. This finding is typical of excess adsorption isotherms as the density of the surrounding gas phase increases at higher pressures whereas from a certain point the pores are completely filled and cannot accommodate more gas molecules.[65,66] A slight hysteresis is observed for all materials during desorption. The value of 5.4 wt% found for **SNW-4** is among the highest storage capacities so far reported for HCPs at 35 bar and 298 K (Table 5-3).[56] The gas uptake of **SNW-4** is of the same order of magnitude as the value

determined for zeolite 5A.[57] It is noteworthy, that the uptake at a much higher pressure level of 100 bar of 6.0 wt% is only slightly higher thus indicating the efficient filling of the pores at lower pressures.

	S_{BET} [m^2g^{-1}]	PV [cm^3g^{-1}]	CH_4 (35 bar) [g/g]	CH_4 (100 bar) [g/g]	H_2 (1 bar) [wt%]
SNW-1	1377	1.01	0.048	0.057	0.97
SNW-2	842	0.62	0.044	0.054	0.39
SNW-3	1133	0.84	0.041	0.056	0.71
SNW-4	1213	0.69	0.054	0.060	0.86
SNW-5	1032	0.73	0.052	0.059	-
SNW-7	541	0.51	0.021	0.027	-

Table 5-3: Porous parameters and gas uptake performance of the **SNW** materials.

As it can be seen from the sorption isotherms in Figure 5-21 the **SNW** materials are also suitable candidates for the physisorptive storage of hydrogen.

The chemical energy per mass of hydrogen exceeds by a factor of three the corresponding parameter of liquid hydrocarbons.[67] Once produced, hydrogen is a clean synthetic fuel as the combustion with oxygen results in the formation of water. However, for the development of hydrogen-driven vehicles efficient methods for the safe and affordable on-board storage must be developed.[67-69] As in the case of methane storage, microporous solids are needed that offer enhanced and accessible inner surface areas. In this context, microporous polymer networks have been investigated as storage materials, too.[46-48,55,70]

The hydrogen sorption isotherm of the **SNW** samples, measured at a temperature of 77 K, reveals a fully reversible course which is important in order to guarantee for the complete delivery of the stored gas (Figure 5-21). The uptake of the materials reaches 0.95 wt% at a pressure of 1 bar for **SNW-1**. However, the experimental setup used did not allow for the recording of the high-pressure isotherms which are needed to estimate the saturation uptake of porous adsorbents. Due to the slope of the isotherm, a higher value can be however expected once all pores are filled with hydrogen. Compared to other microporous sorbents the uptake capacities of the poly(aminal) networks adopt intermediate values.[46-48,55,70] Still, this performance is obtained from a low-cost material which could be easily produced on a technical scale.

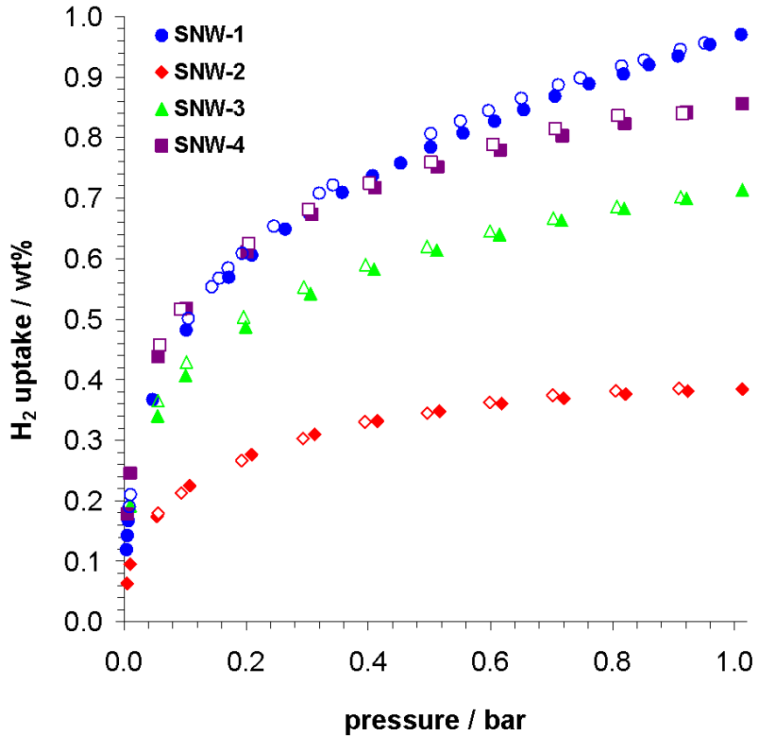

Figure 5-21: Hydrogen sorption isotherm of the **SNW** materials measured at 77 K.

The affinity towards the adsorption of water vapor was subsequently studied for microporous **SNW-1** and mesoporous **SNW-7**. The two samples were selected due to the different nature of the aldehyde component and their difference in porosity.

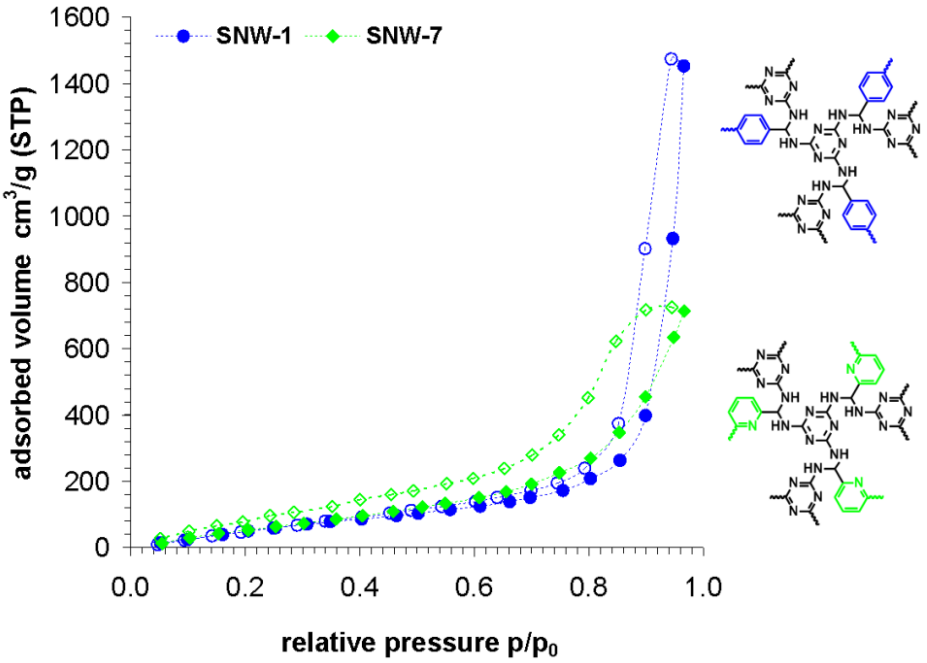

Figure 5-22: Water vapor physisorption isotherms for **SNW-1** and **SNW-7** measured at 298 K.

Whereas the microporous **SNW-1** contains phenyl rings, polar pyridine moieties are present in the mesoporous network **SNW-7**.

The lone pair of the pyridine ring should be a favorable site for the adsorption of water molecules through formation of hydrogen bonds. Indeed, the two sorption isotherms of the polymer samples reflect the different chemical composition of the materials. Being in general typical of a hydrophobic material such as carbon[71] pronounced differences in the course of the isotherm become apparent at relative pressures p/p_0 higher than 0.70 and during desorption. Despite the lower specific surface area of **SNW-7**, the sample adsorbs slightly higher amounts of water at a given relative pressure p/p_0 which is indicative for the increased hydrophilicity of this material. The steep increase of the isotherms close to the saturation pressure is caused by the "bridging effect".[72]

Also, during desorption the hysteresis loop is much more pronounced as compared to **SNW-1** illustrating the strong affinity of the sample to the vapor phase. Contributions to the hysteresis might also arise from the mesoporous nature of the material owing to the different mechanism during desorption which has been previously discussed in the context of nitrogen physisorption.

5.2.5 Morphology Control

The control of morphology through templating constitutes an important aspect of polymer science. Most popular are emulsion techniques which allow for the tailored fabrication of polymer particles of uniform size and precise morphology.[73-76] Furthermore, by emulsion polymerization the heat management of the synthetic process is facilitated and thermal hotspots can be avoided. Also, the viscosity remains virtually constant during the entire process thus ensuring the homogeneity of the reactive system. A textbook example for heterophase polymerization is the free radical copolymerization of styrene with butadiene in an oil-in-water (O/W) emulsion resulting in the formation of styrene-1,3-butadiene rubber latices.[1,77] Polymer nanoparticles are of high interest since they have been used as materials in different fields of application ranging from pharmaceutics[78-80] to catalysis.[81,82]

However, many polymerization approaches are highly sensitive to the presence of water and thus need to be performed under anhydrous conditions. This is in particular true for reactive systems in which the presence of water leads to undesired side-reactions as in the case of poly(urethanes)[1,83] or an unfavorable shift of the reaction equilibrium as seen during poly(ester)[1,84] or poly(amide) formation.[1,85] Metallocene-catalyzed polymerization techniques suffer from the destruction of the catalyst if water is present.[86]

Therefore, a number of anhydrous oil-in-oil (O/O) systems have been developed[83-90] which rely on the immiscibility of certain organic solvents and the development of special block-copolymer surfactants.[89,90] By this approach, a number of polymerizations could be successfully transferred to non-aqueous emulsion[83-88] and miniemulsion[73,91-94] protocols.

The typical morphology of microporous polymer networks is a consequence of their mode of synthesis. Formed upon precipitation from the reaction mixture, electron microscopy reveals the typical “cauliflower-type” nanostructure of hypercrosslinked polymers.[36,47,95] This is seen in the images of **SNW-1** obtained from scanning-electron (SEM) and transition electron microscopy (TEM).

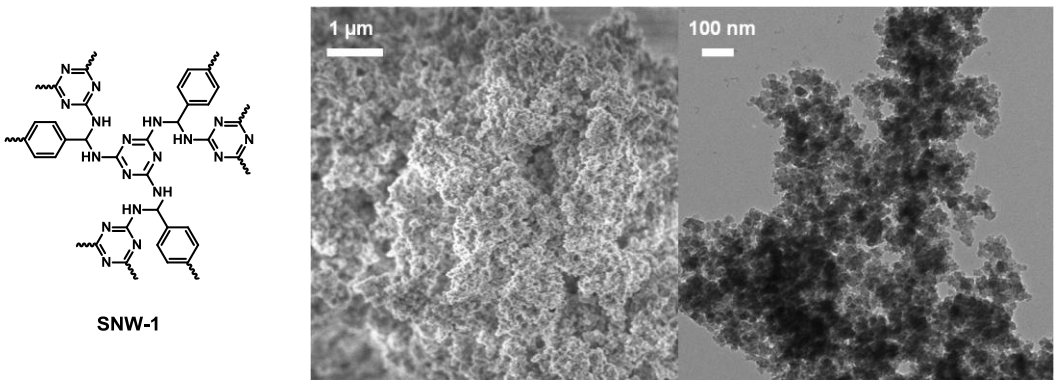

Figure 5-23: Scanning-electron micrograph (left) and transition-electron micrograph of **SNW-1** (right).

The SEM micrograph which is shown in Figure 5-23 represents a several micrometer large flake which itself is composed of numerous small primary particles. The diameter of the smaller particles can be estimated to range between 10 nm and 20 nm. Although some larger pores are clearly visible, the nanoscale micropores that account for most of the surface area are smaller than the resolution of the microscope. The corresponding TEM image is in accordance with the observations of the SEM analysis. The primary particles are well-resolved and of uniform size but suffer from random morphology and agglomeration.

From the electron micrographs it is obvious that there is great potential for the control of the morphology of the **SNW** materials and microporous polymer networks in general. As the extensive crosslinking is at the heart of the preparation, a homogenous course of the reaction can only be achieved by the transfer of the synthetic protocol into an emulsion process. This would efficiently circumvent the aforementioned drawbacks frequently observed during the build-up of microporous polymer networks. Furthermore, full control of morphology would be achievable by polymerization within

the droplet phase of an emulsion. In the case of the **SNW** materials, a potential emulsion recipe needs however to fulfill several major criteria:

- DMSO is the reaction solvent of choice
- a reaction temperature of 180 °C is needed for high conversions
- the same holds for the extended reaction time of 72 h
- water needs to be strictly excluded due to the reversibility of the polycondensation

Based on these considerations, the development of a high-temperature non-aqueous inverse O/O emulsion process for the fabrication of microporous **SNW-1** nanoparticles was envisaged. Furthermore, a miniemulsion approach was chosen in which small droplets of high stability are created by applying strong shear forces.[73] By this, micelle formation as in the case of classical emulsion polymerization can be avoided since this would constitute a further challenge at temperature levels above 100 °C.
However, also miniemulsions tend to become unstable at high temperature. For this reason, a special block copolymer emulsifier **P(B/E-b-EO)** consisting of a poly(butylene-co-ethylene) block and a poly(ethyleneoxide) block has been recently developed and was successfully applied to miniemulsion polymerizations at elevated temperatures (Figure 5-24).[93,94,96]
The same surfactant, provided by the group of *Landfester* (MPI-P Mainz, Germany) was also chosen in the present case as it is capable to stabilize DMSO/paraffin systems.[93] DMSO and paraffin oils are not miscible which is mandatory for the formation of a stable O/O emulsion. In the experiments carried out the concentration of the DMSO monomer phase as well as the amount of **P(B/E-b-EO)** were systematically varied in order to determine optimum reaction conditions. Table 5-4 summarizes the experimental conditions for the polymerizations carried out. The fundamental steps of the high-temperature miniemulsion process are schematically depicted in Figure 5-24.
Thus, in a typical experiment 1.0 ml of a DMSO solution containing melamine **5-6** and terephthalaldehyde **5-8** were mixed with 4.0 ml of a high-boiling paraffin (Isopar M) containing the surfactant **P(B/E-b-EO)**. It is well-known that the homogenization step during miniemulsion formation is of high importance since fairly monodisperse droplets need to be obtained at the beginning of the process.[75,76,97] Therefore, the two-phase DMSO-paraffin system was miniemulsified by ultrasonication using a sonifier equipped with a high-intensity tip. During this procedure, the mixture was cooled by an ice bath in order to prevent thermal degradation. Homogenous white latices instantly formed in all experiments and were transferred to a *Schlenk* tube in which the polymerization was

carried out at 180 °C for 72 h under vigorous stirring and under an inert atmosphere. The latices remained stable over the whole time period with the color of the emulsion progressively changing from white to beige.

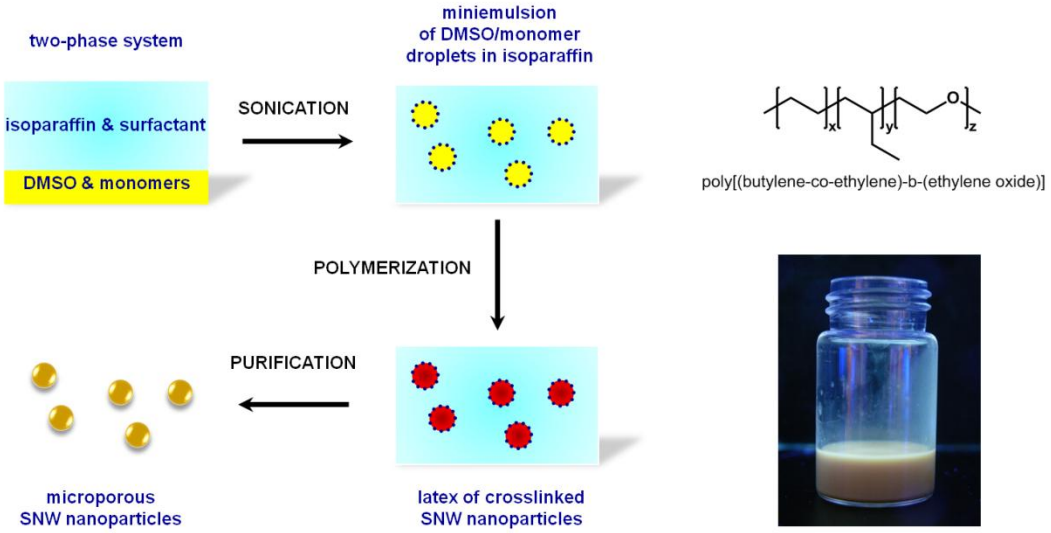

Figure 5-24: Schematic representation of the miniemulsion process applied to the synthesis of microporous **SNW-1** nanoparticles (left), structure of the block copolymer emulsifier **P(B/E-b-EO)** (top right), photograph of the **SNW-1** latex after polymerization (bottom right).

It is noteworthy that the mixture appeared fully homogenous to the eye and that only a negligible amount of precipitate was found on the walls of the reaction vessel. Also, the stability of the latices was preserved upon cooling down from 180 °C to room temperature. The stability of the emulsion after polymerization is evidenced by the photographs shown in Figure 5-24. The viscosity was not found to be increased either as compared to the start of the polymerization.

run	C_{total} [mol/l]	$C_{surfactant}$ [wt%]	S_{BET} [m^2/g]	Yield [%]
1	0.4 M	20	-	10.9
2	0.6 M	20	-	8.7
3	1.1 M	10	349	34.3
4a	1.1 M	20	297	29.4
4b	1.1 M	20	256	48.9
5	1.1 M	30	148	42.1

Table 5-4: Experimental parameters and results of the **SNW-1** nanoparticle synthesis.

The work-up was achieved by slowly dropping the latices into excess cold acetone which enabled the efficient removal of the high-boiling solvents and the surfactant **P(B/E-b-EO)**. The precipitate that quickly formed could be collected by centrifugation and was subsequently passed to *Soxhlet* extraction with chloroform in order to remove residual emulsifier. A light brown, finely divided powder was obtained as the reaction product after drying of the material.

In the first experiments towards the synthesis of microporous **SNW-1** nanoparticles similar conditions as in the case of the bulk system were applied (Table 5-4, run 1 & 2). The overall monomer concentration in the DMSO phase was set to 0.4 M and 0.6 M, respectively, with the ratio of amine and aldehyde groups being equal. A surfactant concentration of 20 wt% with respect to the paraffin phase was used. The analysis of the morphology by electron microscopy revealed that spherical particles were formed in both cases which however did not show a homogenous size distribution. Also, the particles appeared agglomerated in the SEM micrographs and virtually translucent to the electron beam in the TEM analysis (Figure 5-25A&C). This outcome may be attributed to the low polymer content of the particles which also accounted for the moderate yield preventing the analysis of the specific surface area for these two samples.

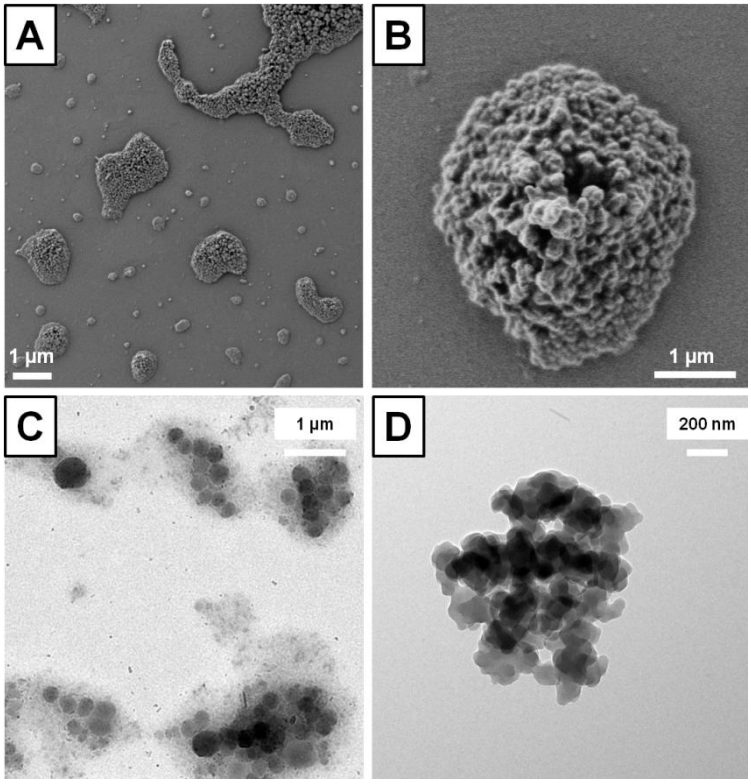

Figure 5-25: SEM and TEM images of **SNW-1** nanoparticles obtained for low monomer (A, C / run 1) and low surfactant concentrations (B, D / run 3).

As a consequence from the results of the initial two trials, the concentration of the monomers was significantly raised to 1.1 M for the following experiments (Table 5-4, run 3 - 5). In order to examine the role of the surfactant, the concentration was varied between 10 wt% and 30 wt%. For this series, the yield as determined by mass was higher and allowed for the subsequent characterization of the porous properties. For all three runs, the analysis by SEM and TEM confirmed the build-up of spherical particles. At a lower concentration of **P(B/E-b-EO)** (10 wt%, run 3) the material is rather inhomogeneous in nature and particles of irregular shape and diameter are observed. Even though micron-sized particles are clearly visible, magnification reveals that they are composed of smaller spheres, an observation which is in analogy to the discussion of the **SNW-1** material prepared by bulk synthesis (Figure 5-25B&D). It can be concluded, that the amount of surfactant was too low in this case to guarantee for the efficient stabilization of individual droplets as seen for the first two runs.

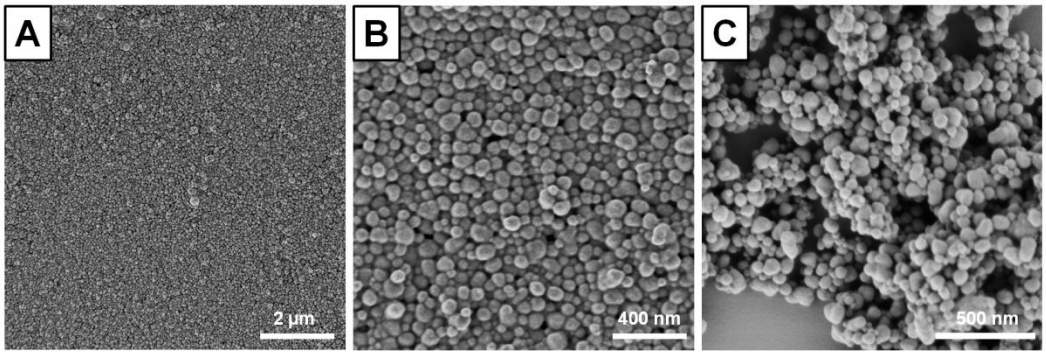

Figure 5-26: SEM images of **SNW-1** nanoparticles obtained at intermediate surfactant concentration before (A, B / run 4a) and after (C / run 4a) extraction with chloroform.

Increasing the amount of **P(B/E-b-EO)** by a factor of two (20 wt%, run 4a & 4b) finally lead to a better stabilization of the miniemulsion as evidenced by the results from electron microscopy. The SEM images obtained indicate the presence of numerous spherical particles. The size of the nanoparticles appears very uniform and ranges between 50 nm and 150 nm. Only few larger particles are seen in the micrographs further illustrating the high stability and homogeneity of the emulsion system (Figure 5-26). Importantly, the particles are not agglomerated but well-separated indicating their formation within individual nanoreactors of the emulsion system. The TEM imaging of these particles further supports the results of the SEM analysis. All particles are nearly spherical and of very uniform size (50 – 100 nm). The contrast is significantly improved as compared to the initial low-concentration runs. Interestingly, the particles appear to be covered by a thin translucent outer layer which may originate

from the surfactant. In some cases clusters of particles seem to be “wrapped” by a continuous shell that extends over the whole outer perimeter of the group (Figure 5-27C).

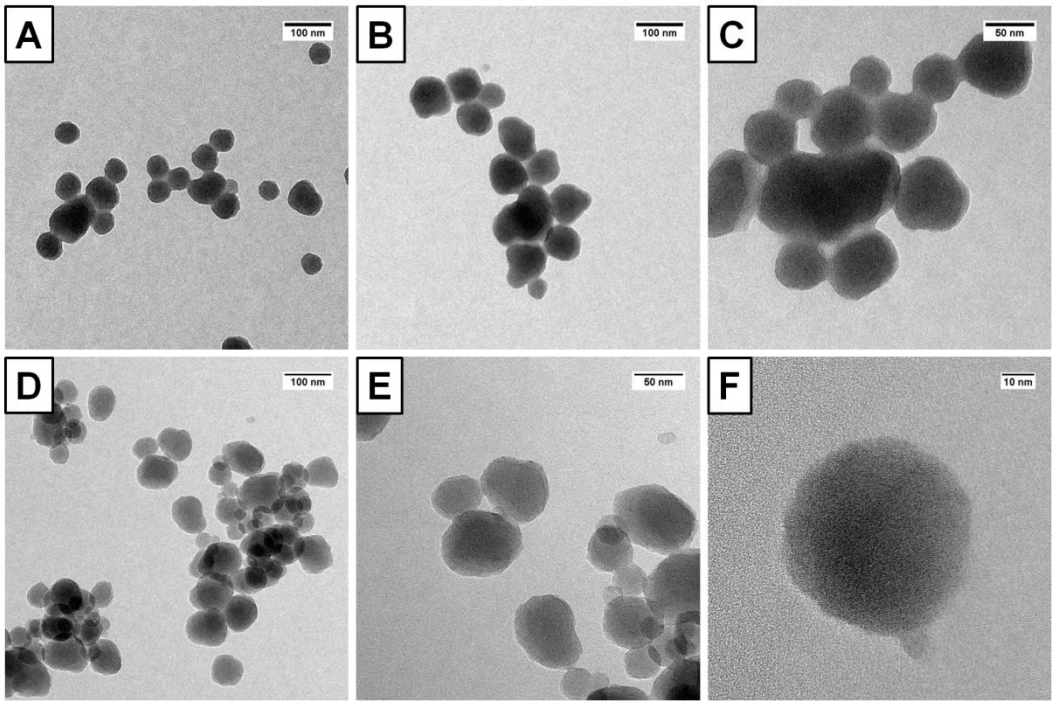

Figure 5-27: TEM images of **SNW-1** nanoparticles obtained at intermediate surfactant concentration before (A, B, C / run 4a) and after (D, E, F / run 4a) extraction with chloroform.

However, once the material has been extracted with chloroform the outer layer disappears and the nanoparticles tend to be more separated from each other (Figure 5-26C, Figure 5-27D&E). In high-resolution TEM images the internal morphology of the **SNW-1** nanoparticles becomes visible. The inner structure is very uniform and the intrinsic porosity shows up as an interconnected network of channels and pores which are found on the expected size regime (Figure 5-27F).

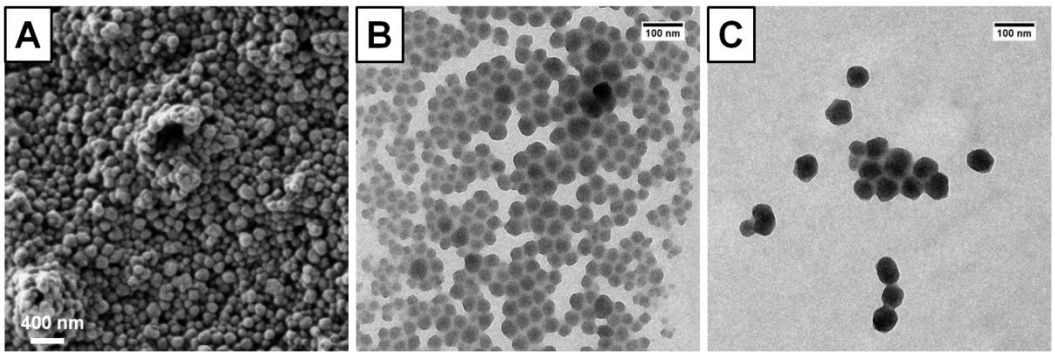

Figure 5-28: SEM (A / run 5) and TEM (B, C / run 5) images of **SNW-1** nanoparticles obtained at high surfactant concentration.

For the emulsion polymerization carried out in the presence of the highest amount of **P(B/E-b-EO)** (30 wt%, run 5) the morphology analysis by means of electron microscopy gave a similar result which confirms the need for high levels of emulsifier in this miniemulsion (Figure 5-28A-C).

The information from electron microscopy concerning the size of the **SNW-1** nanoparticles was subsequently correlated to measurements of the particle size regime carried out by dynamic light scattering (DSL) on the polymerized latices.

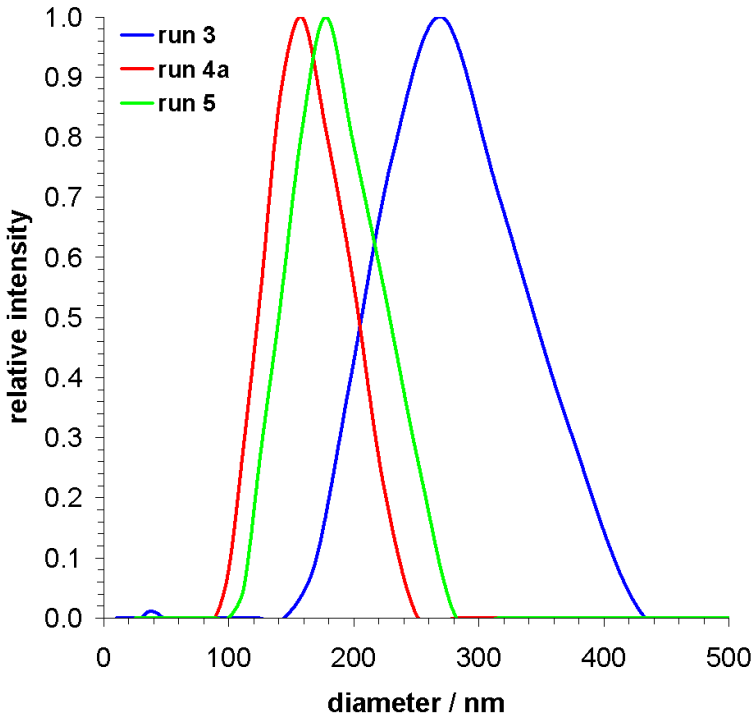

Figure 5-29: DLS particle size distribution of **SNW-1** nanoparticles (intensity weight).

As seen in Figure 5-29, the amount of **P(B/E-b-EO)** strongly governs the location and shape of the particle size distribution curve. For the system obtained at low surfactant concentration (run 3), the curve is very broad and extends from 150 nm to 450 nm with the maximum located at 282 ± 132 nm. This finding reflects the presence of aggregates which are also seen on the corresponding electron micrographs (Figure 5-25).

For intermediate (run 4a) and high (run 5) amounts of the emulsifier an essentially different result was obtained. Firstly, both curves are shifted to smaller particle diameters with the maxima centered at 167 ± 64 nm (run 4a) and 190 ± 75 nm (run 5). In view of the large error margin of the analytical method both curves can be in principal considered similar. Secondly, the particle size distribution is significantly more narrow than in the previous case and only covers a range of 150 nm in total. This

clearly indicates the localization of the reaction partners within the DMSO droplets which are of uniform size after the initial sonication.

Comparing the size of the **SNW-1** nanoparticles to the dimensions found by SEM and TEM indicates larger particle diameters in solution. As the samples were dried upon preparation for electron microscopy the shrinkage of the polymer is a possible explanation for the observed aberrance.

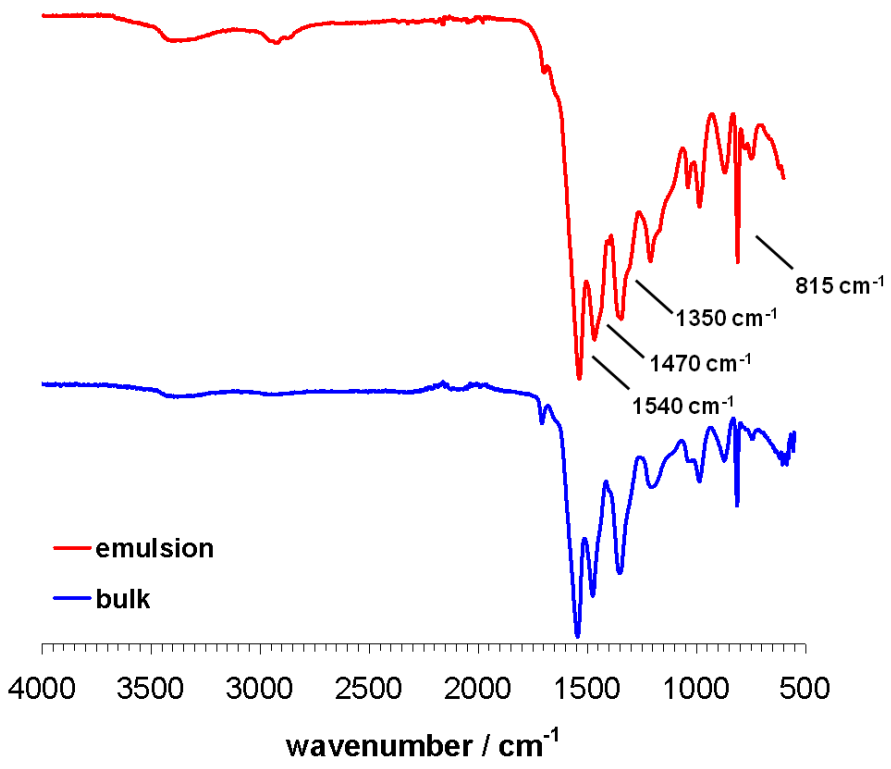

Figure 5-30: FTIR spectra of the **SNW-1** bulk material (blue) and the **SNW-1** nanoparticles (red).

The chemical nature of the materials (run 4a) was then examined by FTIR spectroscopy and compared to that of the **SNW-1** material obtained from bulk synthesis. As it can be derived from Figure 5-30 the structure of the spectra and the positions of the main bands are identical for both samples. In particular the signals of the triazine ring at 1540 cm^{-1},[26,27] 1470 cm^{-1},[26,27] and 1350 cm^{-1} [28,29] are well-resolved. Also, the conversion appears to be virtually complete as only minor bands of the initial functional groups are detected. Importantly, no additional signals which could originate from entrapping of **P(B/E-b-EO)** were detected proving the efficient removal of the surfactant during the *Soxhlet* extraction step with chloroform. The FTIR results further illustrate the successful transfer of the **SNW** bulk synthesis to the miniemulsion process yielding a material of identical chemical nature.

In the next step, the porosity of the **SNW-1** nanoparticles was investigated by nitrogen physisorption. As seen in Figure 5-31, the materials preserve the microporous character of the parent **SNW-1** bulk material. All isotherms are characterized by a steep gas uptake in the low pressure regime and a rather flat course in the intermediate section. All sorption isotherms can thus be classified as type I according to the IUPAC recommendation.[40-42]

Concerning the specific surface areas S_{BET} a strong dependency on the amount of the emulsifier **P(B/E-b-EO)** is found. Hence, the material obtained from run 3 (10 wt% surfactant) reaches a value of 349 m^2/g but lacks however a defined morphology as revealed by the electron microscopy study. For the two systems, run 4a and 4b, obtained by polymerization in the presence of 20 wt% **P(B/E-b-EO)** values of 297 m^2/g and 256 m^2/g are found illustrating the good reproducibility of the miniemulsion method. Lastly, for the highest surfactant amount of 30 wt% applied to run 5, a surface area of 148 m^2/g is derived by the BET method. The pore volumes of the nanoparticles obtained at a relative pressure of p/p_0 = 0.8 by converting the gas volume into the corresponding liquid volume range between 0.11 cm^3/g and 0.25 cm^3/g.

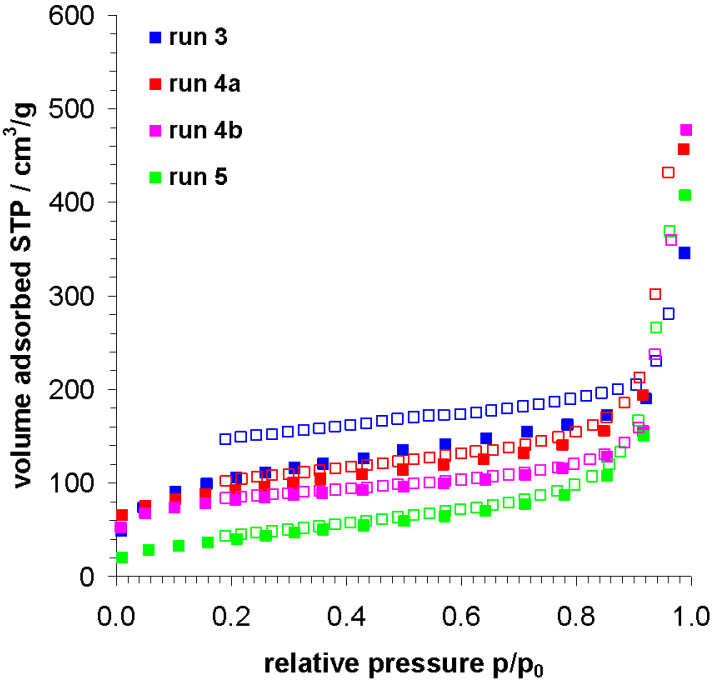

Figure 5-31: Nitrogen sorption isotherms of the **SNW-1** nanoparticles obtained at different surfactant concentrations.

When comparing the specific surface area of the **SNW-1** nanoparticles to the value of the bulk **SNW-1** system (1377 m^2/g), the decrease in porosity has to be considered. This effect is possibly due to the fact that the monomer concentration had to be raised for the emulsion systems owing to the difficulties and irregular morphologies

encountered during the initial trials based on the original synthetic conditions. The **SNW-1** nanoparticles obtained for a **P(B/E-b-EO)** concentration of 20 wt% represent a compromise of full morphology control and an elevated porosity of up to 300 m^2/g. Despite the fact that no evidence for residual surfactant was found by FTIR spectroscopy, it cannot be ruled out that the access to the inner volume of the nanoparticles is partially blocked. Even trace amounts of the surfactant located at the outer surface of the particles would strongly interfere with the full assessment of the pore volume by the gas molecules during nitrogen physisorption.

In conclusion, these experiments represent the first example for the successful preparation of a microporous polymer network within the droplet phase of a non-aqueous emulsion. In view of the harsh conditions regarding reaction temperature and time, the parameters for a stable non-aqueous emulsion system suitable for the synthesis of highly monodisperse **SNW-1** nanoparticles could be defined. In comparison to the bulk system (Figure 5-23) a defined morphology is now fully achievable also enabling better control of the process parameters during the preparation of these highly crosslinked and intrinsically insoluble materials. For a possible up-scaling of the synthetic protocol this aspect is of high importance.

5.2.6 Catalysis

The direct low-temperature oxidation of methane to methanol constitutes one of the major challenges in catalytic research. On an industrial scale, methanol is produced from gas mixtures containing varying amounts of carbon monoxide and hydrogen (synthesis gas). The reaction is carried out at 200 - 300 °C and elevated pressure in the presence of a catalyst typically composed of copper, zinc oxide, and alumina.[18]

Recently, molecular catalysts derived from platinum bipyrimidine complexes (*Periana* catalysts) have been introduced (Figure 5-32).[98,99] By this, the selective low-temperature oxidation of methane could be demonstrated at temperatures around 200 °C using concentrated sulfuric acid as a reaction medium.

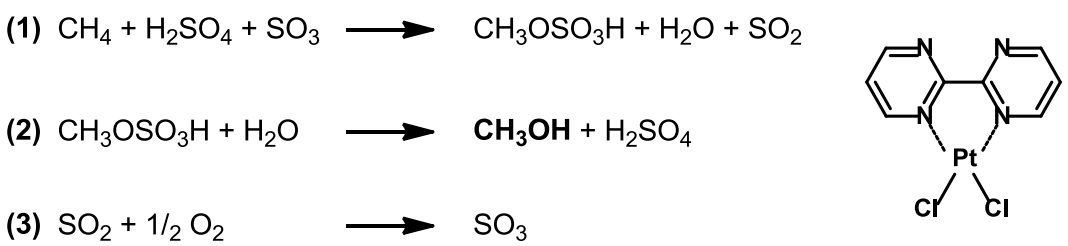

Figure 5-32: Fundamental steps of the *Periana* process (left) and structure of the molecular catalyst (right).

Figure 5-32 depicts the fundamental reaction steps and the structure of the molecular *Periana* catalyst species. Despite the promising results regarding activity, recovery and recycling of the precious metal species constitute a major drawback of this approach. For this reason, the development of solid catalysts for the *Periana* process would be highly desirable.[100,101] Microporous polymer networks with their enhanced surface areas are ideal candidates for catalyst supports.[12,102] They need however to offer suitable binding sites for the platinum species and must withstand the harsh conditions of the catalytic process. In principle, the **SNW** materials fulfill the requirements. They contain a high number of nitrogen species with lone pairs that should efficiently stabilize the catalytic centre. Also, their surface areas and pore volumes guarantee for an enhanced loading with the platinum species. For this reason, **SNW-1** with its surface area of 1377 m^2/g and a pore volume of 1.01 cm^3/g was evaluated as a solid catalyst support for the direct oxidation of methane to methanol. The catalysis experiments have been carried out in cooperation with the group of *Schüth* (MPI-KF Mülheim, Germany).

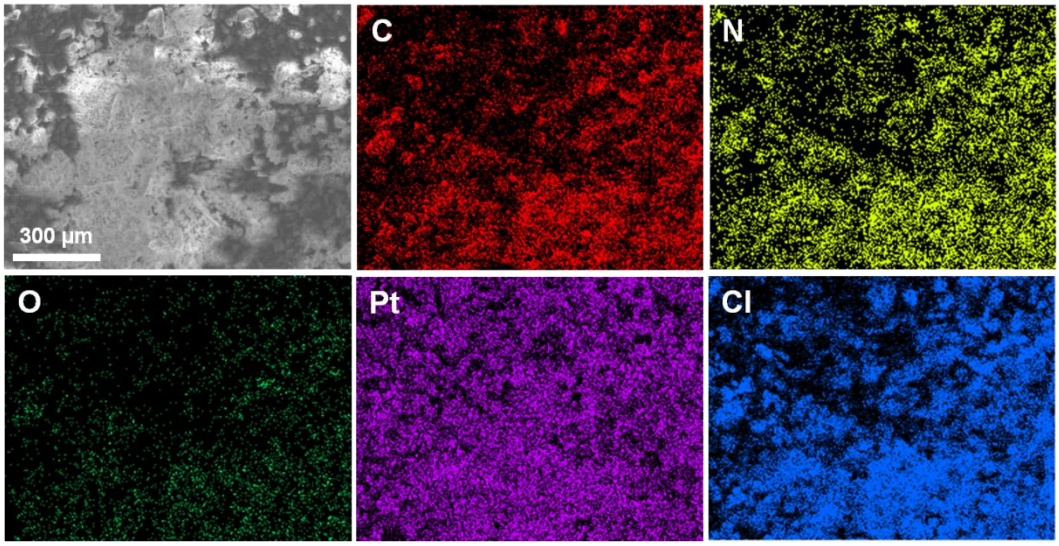

Figure 5-33: SEM micrograph of the platinum loaded **SNW-1** material and corresponding EDX elemental mapping of the sample.

In a first step, the polymer network was impregnated with the platinum species. This was achieved by treatment of **SNW-1** with an aqueous solution of potassium tetrachloroplatinate(II). The material thus obtained was dried and analyzed by SEM and energy-dispersive X-ray spectroscopy (EDX). As it can be clearly seen in Figure 5-33 the material is very homogenously doped with platinum after the impregnation procedure. No larger particles are visible suggesting that the metal is indeed

coordinated on the molecular level. The platinum level was found to be 31.1 wt% corresponding to 3.1 atom%. The values obtained for chlorine are 7.02 wt% and 3.88 atom%, respectively. In view of the atomic platinum/chlorine ratio of 0.25 of the precursor potassium tetrachloroplatinate(II) and the increased value of 0.78 found for the impregnated **SNW-1** network the coordination of the platinum(II) species is likely to have occurred. This is due to the fact that the coordination is accompanied by an elimination of chlorine as a reaction by-product in the form of potassium chloride. Hence, the platinum/chlorine ratio increases resulting in a theoretic value of 0.50 if the *Periana* species is formed (Figure 5-32). The experimental result for **SNW-1** indicates, however, that other complexes might have been formed since true chelating sites such as 2,2'-bipyrine or bipyrimidine are not encountered in the network structure. Alternatively, the metal species could be stabilized by the nitrogen lone pairs found in the aminal groups or the triazine units as indicated in Figure 5-33.

The EDX mapping was also performed to analyze the elemental composition of the polymer support. For carbon and nitrogen, values of 29.2 wt% and 29.9 wt% were found. This equals 47.6 atom% and 41.9 atom%, respectively. Also, the oxygen level which is not accessible by elemental combustion analysis could be quantified by this method (2.84 wt%, 3.48 atom%). The numbers and the corresponding ratio are in good agreement with the values obtained from elemental combustion analysis (Table 5-1).

For the catalyst testing a standardized reaction protocol was applied.[98] The platinum-loaded **SNW-1** material (50.0 mg) was placed in an autoclave which was filled with 15.0 ml of oleum containing 30 wt% of sulphur trioxide. The reactor was flushed with argon, pressurized with 40.0 bar methane and heated to 215 °C for 2.5 h.

During the course of the reaction the pressure in the vessel gradually decreased indicating the consumption of methane. The reaction mixture was subsequently analyzed by means of HPLC in order to quantify the amount of methanol produced. The turn over numbers (TON) can be calculated using the ratio of produced methanol and the platinum content of the catalyst as derived from EDX spectroscopy.

In the case of platinum-loaded **SNW-1** a TON of 157 was found which is below the TON of 357 for the molecular *Periana* catalyst (Figure 5-34). Possibly, this can be ascribed to a non-ideal coordination of the platinum(II) cation on the polymeric backbone as described above. Future experiments should address the influence of catalyst supports in which a precise coordination site is already preformed. A possible candidate in this respect would be **SNW-8** that is characterized by the 2,2'-bipyridine motif.

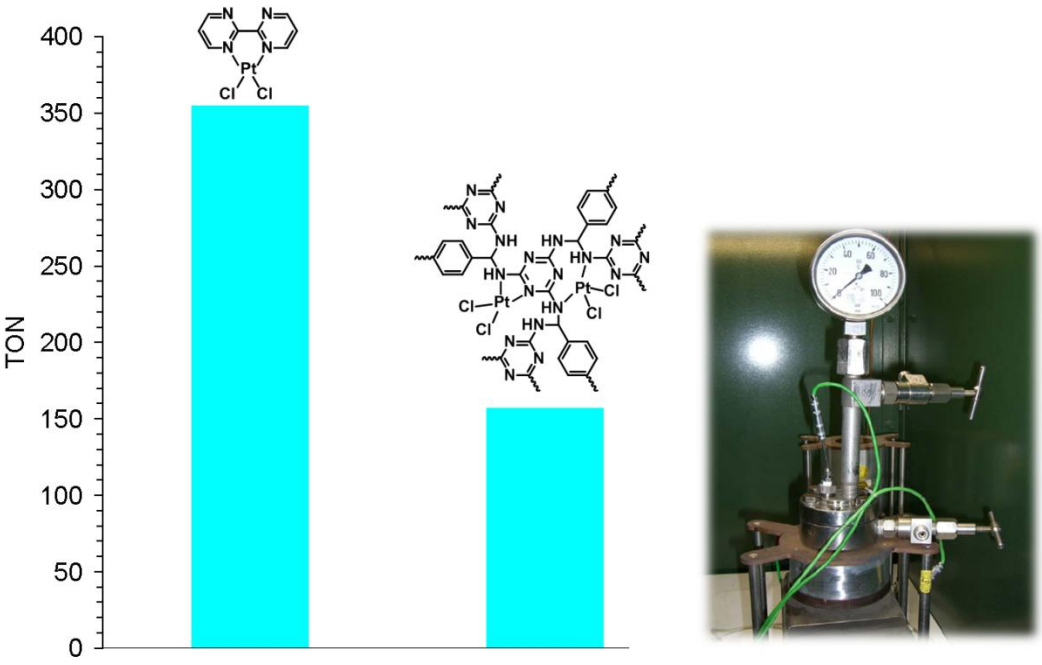

Figure 5-34: Catalytic activity of platinum loaded **SNW-1** in the direct oxidation of methane to methanol (left), photograph of the experimental setup.

It was also found difficult to fully recover the polymer material which was partially degraded under the strongly oxidizing conditions of the catalytic process. This is in contrast to recent results regarding microporous triazine networks that lack groups containing active hydrogen such as amines which are possible starting points of degradation.[100,101] Still, the aforementioned benefits of solid catalysts have to be considered which will be further evaluated in future studies on the **SNW** series.

5.3 Poly(azomethine) Networks

It is well-known that the condensation of aldehydes with primary amines leads to the formation of azomethines (imines) under mild reaction conditions and in high yield.[19] The versatility of linear A_2B_2-type poly(azomethines)[103-106] derived from difunctional building blocks has been demonstrated for applications in organic electronic devices[105,107-109] and liquid crystals (LC).[110,111] Also, the C=N linkage was applied to the construction of hyperbranched[112] and dendritic[113,114] poly(azomethine) structures. The reversibility of the imine formation was also beneficial for the preparation of elaborated cage-like molecules.[115-117]

Three-dimensional A_3B_2- or A_4B_2-type poly(azomethine) network structures, constructed from crosslinkers such as **5-5**, are however less frequently encountered and were only scarcely studied with respect to their porous properties.[13,118]

Due to their extended π-conjugated systems in combination with band levels matching the redox window of water[105,107-109,119,120] poly(azomethines) are believed to be suitable semiconductors for applications in the field of heterogeneous photocatalysis. For organic materials, however, the long-time stability of the photocatalyst constitutes a major criterion. In order to guarantee for high chemical and thermal resistivity conjugated A_3B_2-type poly(azomethine) networks are needed for which enhanced chemical and thermal robustness can be expected due to their highly crosslinked nature. Furthermore, as seen in the case of the poly(aminal) networks, the crosslinking approach leads to insoluble materials which are required for a heterogeneous catalytic process.[119,120]

In a further step, the preparation of porous A_4B_2-type poly(azomethine) materials was envisaged for which the synthesis was based on a novel anthracene-based crosslinker. Also in this case, the catalyst-free *Schiff* base condensation approach would lead to a novel class of porous polymer networks for which a number of applications in the field of material science can be thought of.

5.3.1 Synthetic Procedures

In principal, the classical *Schiff* base reaction between a primary amine and an aldehyde can be achieved by simply mixing and heating both components in a suitable solvent.[19,20] In some cases the reaction even works in the solid state.[121,122] However, the formation of the imine can be significantly accelerated if an acid catalyst is added. This is why in the present case a solution-based synthetic pathway in the presence of

acetic acid was chosen. The A_3-type crosslinker 1,3,5-tris(4-aminophenyl)benzene **5-25** was reacted with difunctional (B_2) aromatic aldehydes to give a series of novel poly(azomethine) networks denominated as **ANW**.

The aromatic core between the two aldehyde groups was expanded from terephthalaldehyde (**5-8**), naphthalene-2,6-dicarbaldehyde **5-12**[22] to anthracene-2,6-dicarbaldehyde (**5-27**) leading to extended *π*-systems in the resulting polymeric networks. For the anthracene core, regioisomer anthracene-9,10-dicarbaldehyde (**5-28**),[123] was chosen with the objective to compare the influence of different substitution patterns (Figure 5-35).

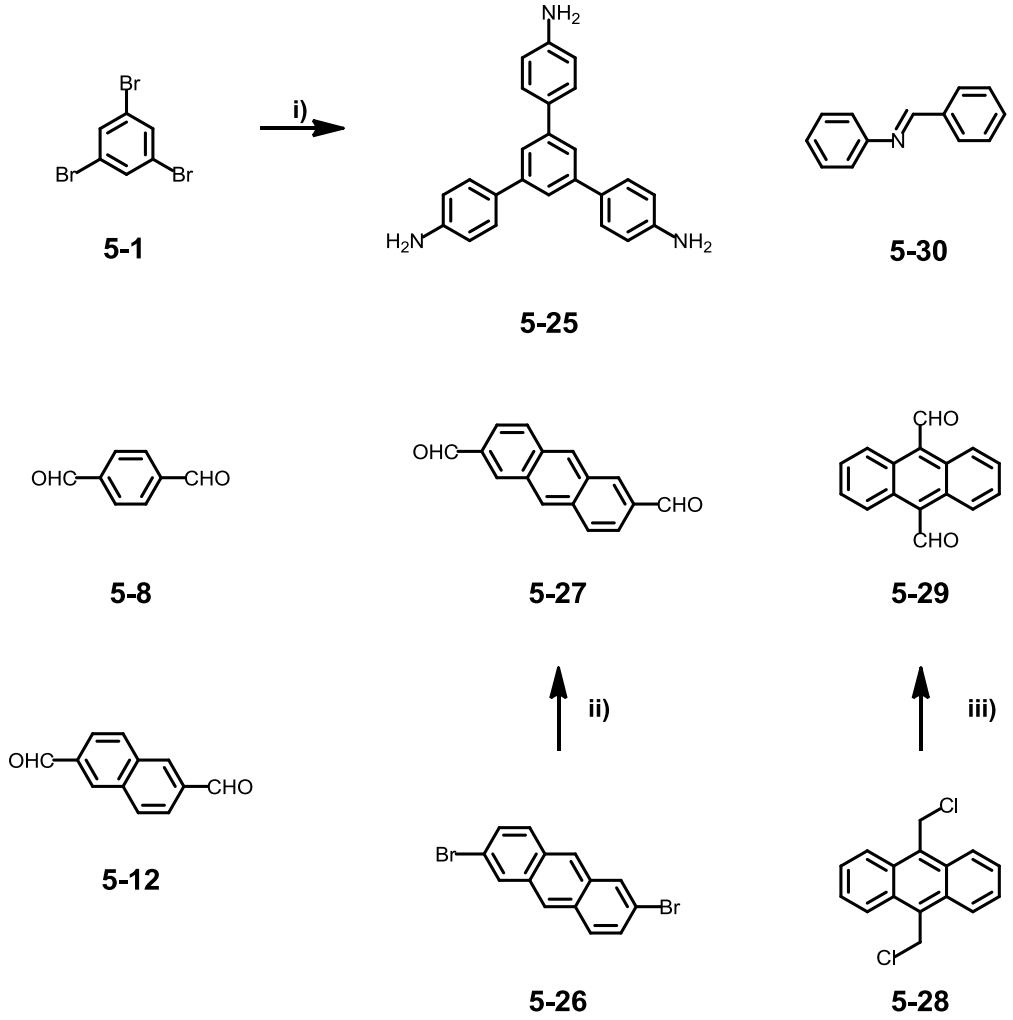

Figure 5-35: Chemical structure of the building units for non-porous **ANW** materials and model compound *N*-benzylideneaniline **5-30**; conditions: i) 4-aminophenylboronic acid, $Pd(Ph_3)_4$, K_2CO_3, toluene, Aliquat 336, reflux, 62 %; ii) *n*-BuLi, then DMF, THF, - 78 °C, 61 %; iii) sodium, 2-nitropropane, DMSO/EtOH, room temperature, 54 %.

Whereas all components are either commercially available or accessible *via* reported one-step routes, a novel synthesis had to be established for the preparation of

unreported anthracene-2,6-dicarbaldehyde **5-27**. The double-lithiation of 2,6-dibromoanthracene and a subsequent treatment with excess DMF was found suitable for the introduction of the two aldehyde groups. Compound **5-27** was thus obtained in 61 % yield.

For the network formation (Figure 5-36), both monomers were dissolved in a dioxane/acetic acid mixture which was then heated to reflux for 72 h. All networks were synthesized at a fixed molar ratio of amine to aldehyde groups of 1.15 / 1.00 to allow for efficient crosslinking.

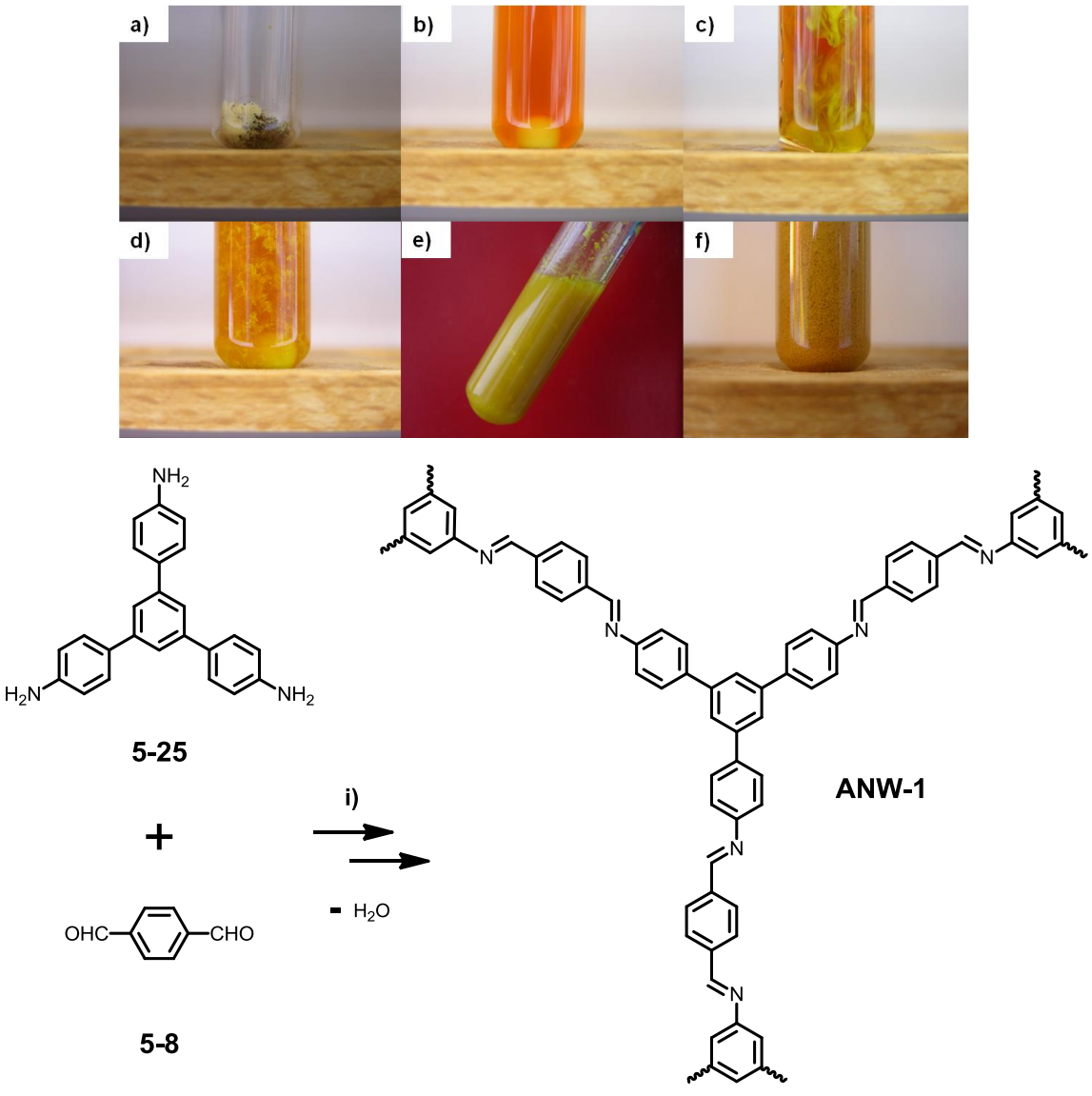

Figure 5-36: Synthesis of **ANW-1**; conditions: i) dioxane/acetic acid, reflux, 72 h, 82 % (bottom) and photograph illustrating the different steps of the synthesis (top).

In all cases, yellow-orange powders precipitated which could be easily collected by filtration (Figure 5-36).

Soxhlet extraction of the materials with THF for 24 h was used to remove low-molecular weight by-products. The yield, as determined gravimetrically, was between 70 wt% and 80 wt% in all experiments. The materials showed fully insoluble in all common organic solvents.

5.3.2 Structural Characterization

Fourier transform infrared (FTIR) spectroscopy was used to investigate the chemical nature of the materials as well as to monitor the conversion of the functional groups after the reaction (Figure 5-37). Bands arising from the NH_2 stretching (3400 cm^{-1}) and NH_2 deformation (1650 cm^{-1}) vibrations of the primary amine group of the crosslinker are virtually absent in the spectra of all **ANW** materials. Also, the strongly attenuated signals from the aldehyde groups at 2870 (C-H stretching) and 1690 cm^{-1} (C=O stretching) indicate high conversion of the functional groups initially present.

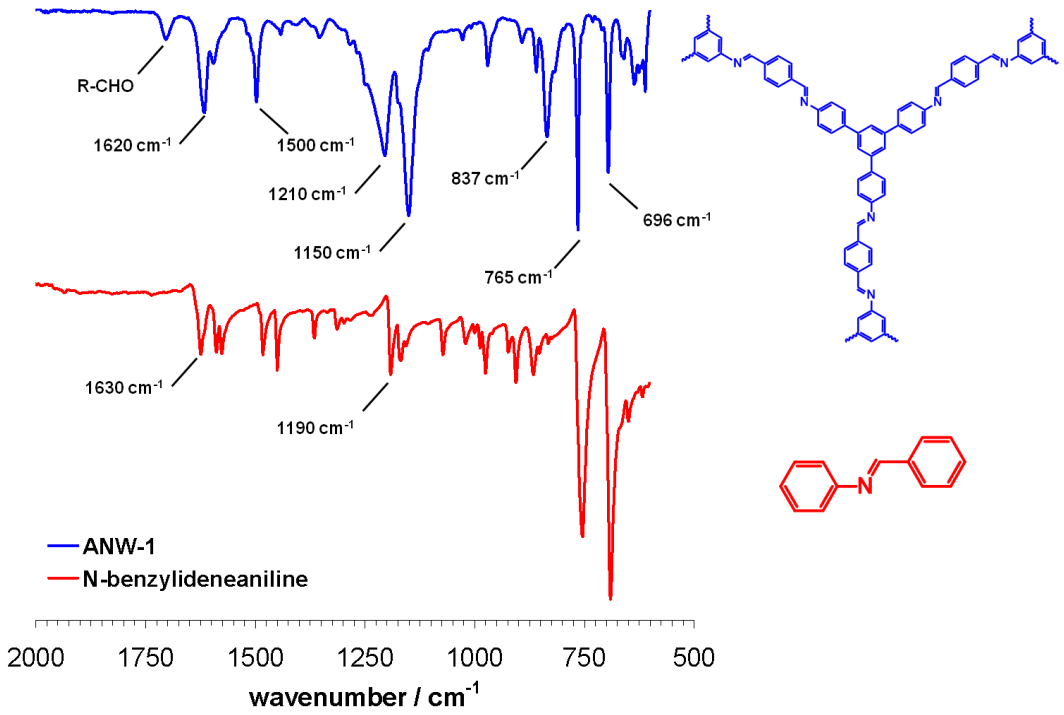

Figure 5-37: FTIR spectra of model compound *N*-benzylideneaniline **5-30** and **ANW-1**.

However, a prominent band appears at 1620 cm^{-1} and can be assigned to the C=N stretching vibration of the imine linkages within the newly formed networks.[13,103-105,107-

[109,118] Furthermore, the signal at 1210 cm^{-1} can be attributed to the C-C=N-C stretching of the imines.[13]

N-Benzylideneaniline **5-30** (Figure 5-35) represents a suitable model compound which allows for the facile comparison of the imine band position. In the FTIR spectrum of this molecule the two aforementioned signals show up at 1630 cm^{-1} and 1190 cm^{-1}, respectively (Figure 5-37). The good agreement to the spectrum obtained for **ANW-1** further confirms the presence of the C=N motif in the network.

Several signals arising from the numerous benzene rings of the material are located at 1500 cm^{-1}, 1150 cm^{-1}, 837 cm^{-1}, 765 cm^{-1} and 696 cm^{-1}. The band at 1500 cm^{-1} is characteristic for the aromatic C-C ring stretching of phenylene-dimethylidene-type rings such as those situated in between of the imine linkages in **ANW-1**.[13] The aromatic in-plane and out-of-plane deformation vibrations correspond to the signals seen at 1150 cm^{-1}, 837 cm^{-1} and 765 cm^{-1}, respectively. The well-resolved band at 696 cm^{-1} is typical for the out-of-plane deformation vibration of 1,3,5-substituted benzene rings. In general, the very strong intensity of all these signals perfectly reflects the chemical nature of the aromate-rich network. A closer look on the molecular structure was subsequently carried out by means of $^{13}C[^{1}H]$ and $^{15}N[^{1}H]$ solid-state NMR spectroscopy.

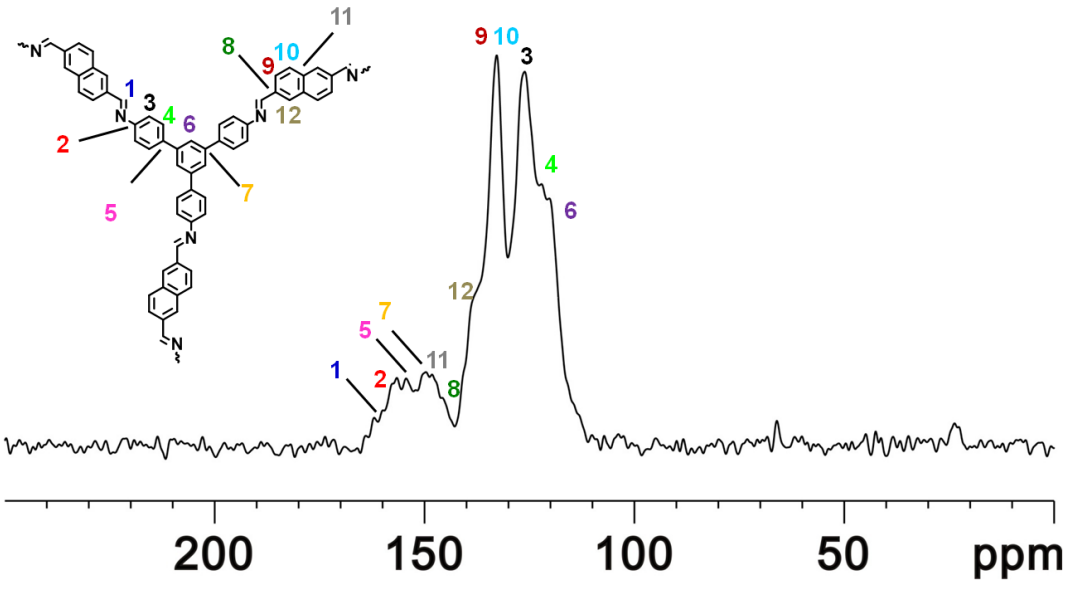

Figure 5-38: ^{13}C CP-MAS NMR spectrum of **ANW-2**.

Hence, the ^{13}C CP-MAS NMR spectrum of naphthalene-based **ANW-2** (Figure 5-38) shows a characteristic signal at δ = 158 ppm which can be attributed to the carbon atom of the imine bond.[13,118]

The resonance of the aromatic carbon neighboring the nitrogen of the C=N group is detected at δ = 153 ppm. The quaternary aromatic carbon atoms of the triphenylbenzene and naphthalene moiety give rise to signal group around δ = 150 ppm. The tertiary aromatic carbon atoms of the naphthalene ring are found at δ = 133 ppm and the ones from the remaining benzene rings as a broad peak between δ = 115 ppm and δ = 125 ppm. No resonance corresponding to the carbon atoms of the aldehyde groups is found proving a high conversion of the functional sites.

In accordance with the expected structure of **ANW-2**, the ^{15}N CP-MAS NMR spectrum of the material contains only one signal at δ = - 50 ppm which is characteristic for imine-type nitrogen atoms (Figure 5-39). No nitrogen atoms of unreacted amine groups are detected.

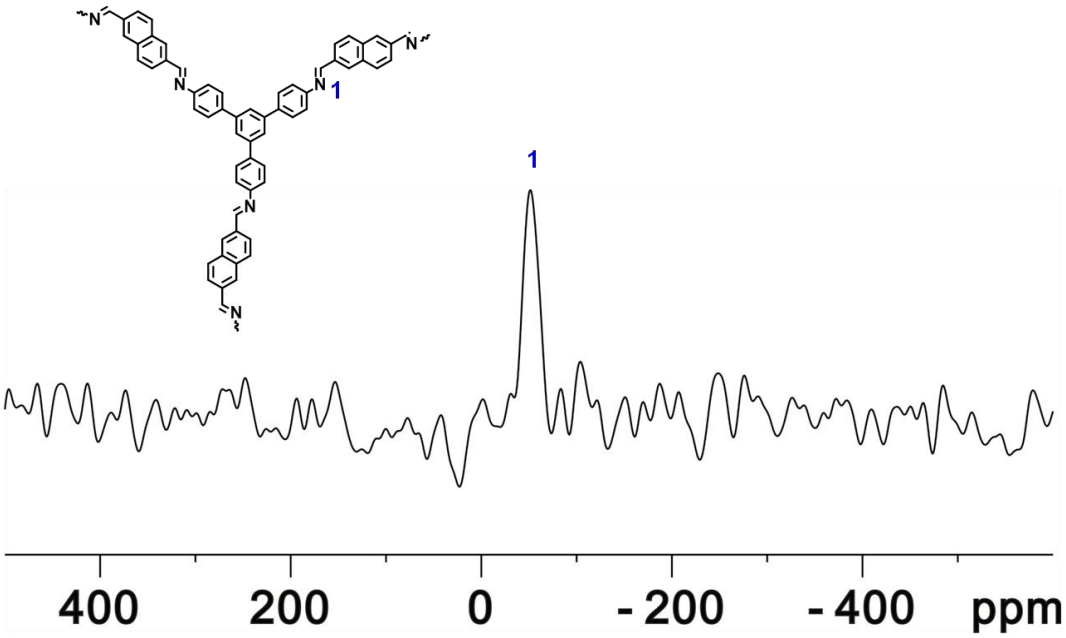

Figure 5-39: ^{15}N CP-MAS NMR spectrum of **ANW-2**.

The thermal stability of the **ANW** materials was investigated by thermogravimetric analysis and revealed a high stability of the materials with decomposition temperatures of 400 - 500 °C for all samples (Figure 5-40).

Interestingly, **ANW-4** containing anthracene-9,10-dicarbaldehyde **5-28** as comonomer, showed the lowest degradation temperature which may be ascribed to the different substitution pattern of the aldehyde groups for this sample.

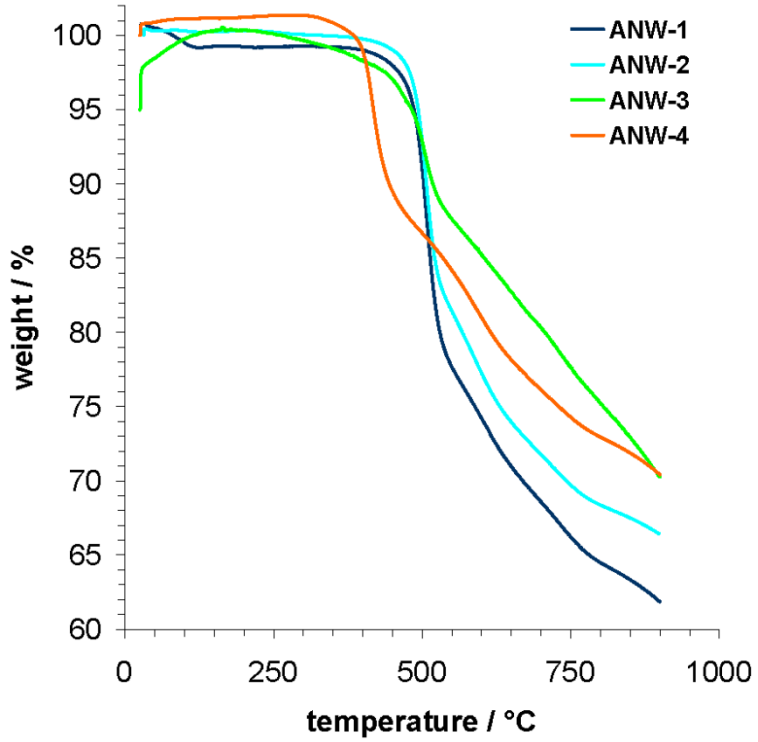

Figure 5-40: Thermogravimetric analysis of the **ANW** materials under nitrogen.

5.3.3 Optoelectronic Properties

In semiconductor-mediated photocatalysis, excitons (electron-hole pairs) are generated through light absorption and dissociate into free charge carriers inducing redox reactions such as water splitting, CO_2 fixation and organic mineralization. The width of the band gap along with the levels of conduction and valence band represent crucial factors in order to make the photocatalytic process favorable.[119,120] Therefore, the optoelectronic properties of the **ANW** materials were firstly analyzed by solid state UV-vis spectroscopy (SSUV) (Figure 5-41).

For all four networks, a sharp absorption edge is observed, whose location is found to be dependent on the nature of the B_2 component and which ranges between 504 nm (**ANW-2**) and 632 nm (**ANW-4**). Using the corresponding cut-off wavelength λ_{max} the energy of the optical band gap E_g^{OPT} was calculated (Table 5-5).

The values which were found are in close agreement to band gaps that have been calculated using the similar procedure for linear A_2B_2-type poly(azomethine) systems. Typically, the band gap ranges between 2.20 eV and 2.30 eV for these structurally related polymeric materials.[105]

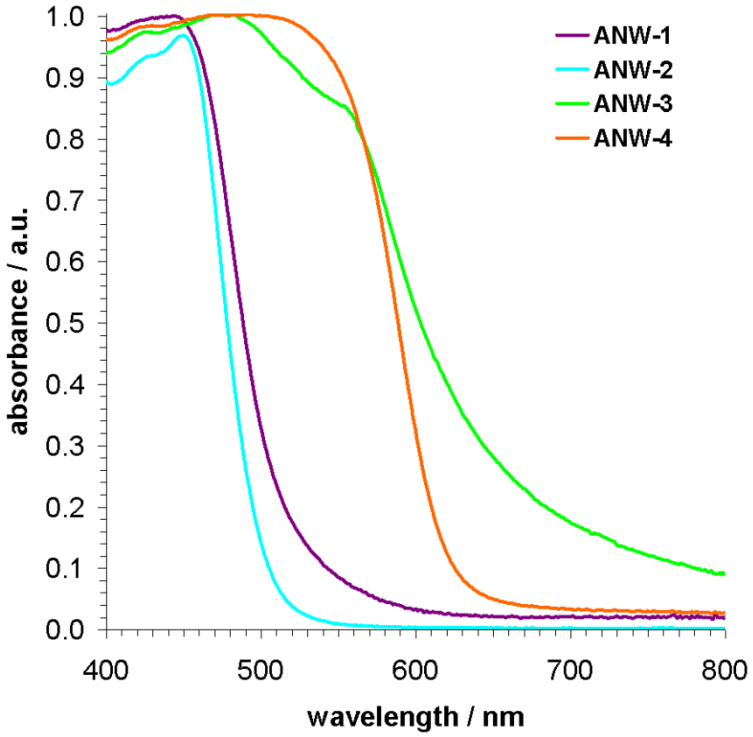

Figure 5-41: Solid state UV-Vis absorption spectra of the **ANW** materials.

In order to gain further insight into to the electronic and conformational details of the poly(azomethine) networks, gas phase DFT calculations (B3LYP, 6-311G**) were performed on representative cutouts of the network structure (Figure 5-42, Table 5-5). The structural motif of all **ANW** materials consists of rigid struts comprising two C=N-linkages which are connected to 1,3,5-substituted benzene nodes. The calculations on these model segments reveal that the frontier orbitals are centered on the B_2 parts of the strut, rationalizing their choice for modification.

	aldehyde component	**λ_{max} [nm]**	**E_g^{OPT} [eV]**	**E_g^{DFT} [eV]**	**H_2^{4h} [µmol]**
ANW-1	terephthalaldehyde	522	2.38	3.36	6.0
ANW-2	naphthalene-2,6-dicarbaldehyde	504	2.46	3.26	26.7
ANW-3	anthracene-2,6-dicarbaldehyde	591	2.10	2.87	24.6
ANW-4	anthracene-9,10-dicarbaldehyde	632	1.96	2.73	2.8

Table 5-5: Chemical composition, optoelectronic properties and photocatalytic activity of the **ANW** materials.

In line with this observation, the HOMO-LUMO gap E_g^{DFT} of the model strand narrows with increasing B_2 core size thus opening a larger window for absorbed radiation.

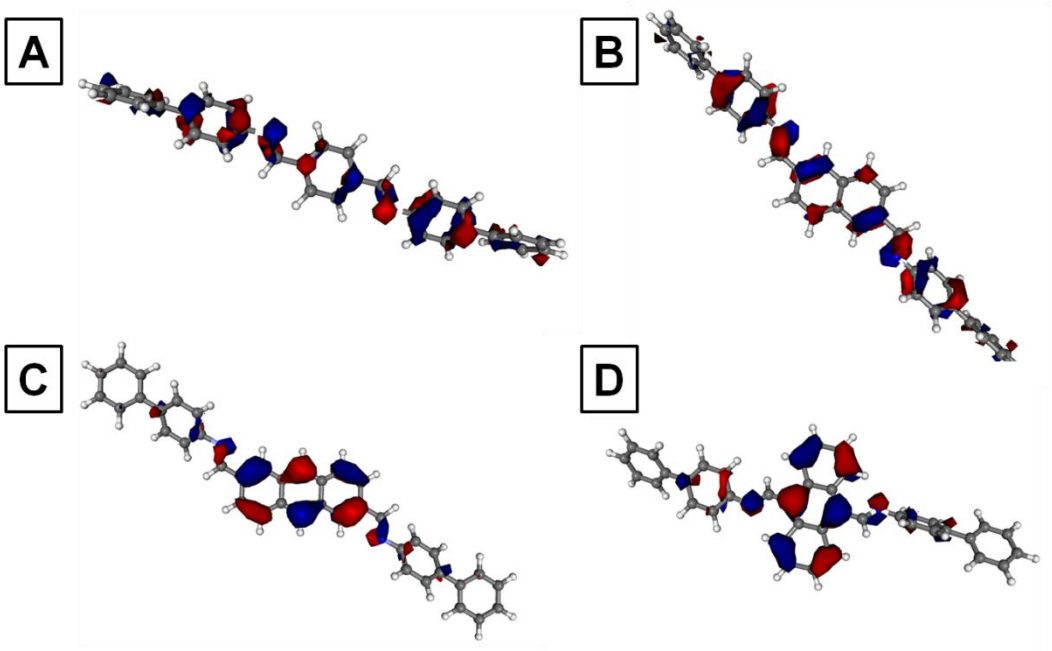

Figure 5-42: Graphical HOMO representation of the model segments from **ANW-1** (A), **ANW-2** (B), **ANW-3** (C) and **ANW-4** (D) as obtained by geometry-optimized DFT calculations (B3LYP, 6-311G**).

As to the two anthracene monomers **5-27** and **5-29**, the 9,10-substitution of **5-29** gives rise to a substantially increased torsion angle (< 2° for **ANW-3** and ~ 30° for **ANW-4**) between the imine group and the neighboring aromatic core. Steric crowding caused by the *alpha*-protons of the anthracene unit would be intuitively predicted in this case and is believed to hamper the conjugation along the polymeric backbone.

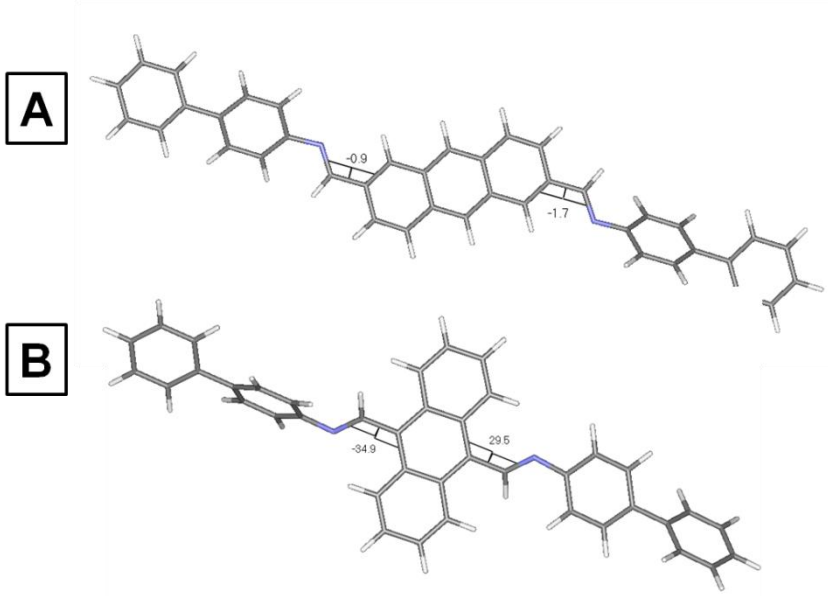

Figure 5-43: DFT geometry optimization and torsion angels of the model segments of **ANW-3** (A) and **ANW-4** (B) (B3LYP, 6-311G**).

Interestingly, although following a common trend, the E_g^{OPT} and E_g^{DFT} values differ substantially. This finding may be reflective of a π-conjugated system that significantly exceeds the length of the model segments which have been used for the DFT calculations. Furthermore, effects of the actual network equilibrium structure and the three-dimensional overlap of aromatic units are not covered by the gas-phase DFT model contrary to the SSUV measurements. It should be noted that the fragments may be heavily distorted in the network formed upon polymerization.

5.3.4 Photocatalysis

After analysis of the optoelectronic parameters, photocatalytic experiments were carried out with the water-insoluble **ANW** powders (Figure 5-44). The measurements were realized in cooperation with the group of *Antonietti* (MPI-KG Golm, Germany).
The materials were modified by 3.0 wt% platinum as co-catalyst. As it can be seen in Figure 5-44, all four samples shortly reached steady hydrogen production from water containing 10.0 vol% triethanolamine as an electron donor. The evolution rate upon irradiation with UV light (λ > 300 nm) was found to be strongly dependent on the core size of the B_2-unit of the network and continuously increased from **ANW-1**, **ANW-3** to a maximum of 7.0 µmol H_2/h in the case of **ANW-2** (Table 5-5).

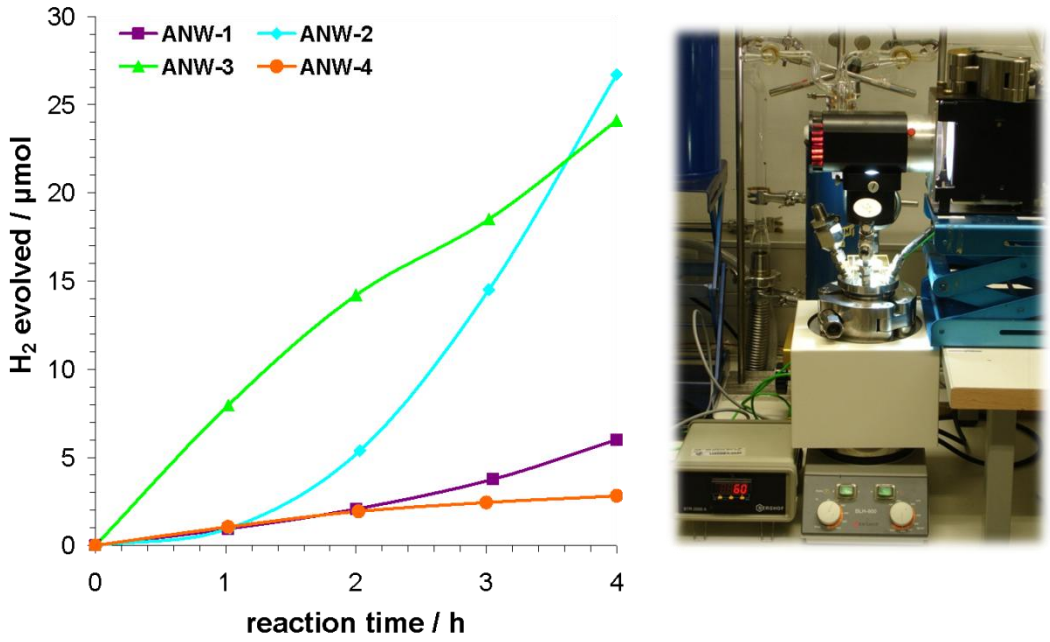

Figure 5-44: Time course of hydrogen production through **ANW** networks from water containing 10.0 vol% triethanolamine as electron donor (λ > 300 nm) (left), photograph of the experimental setup for photocatalytic experiments (right).

On the contrary, no reaction occurred in the dark in the presence of the networks. The catalytic performance of the **ANW** materials is significantly higher than previously reported for poly(*para*-phenylene) (1.0 - 3.0 µmol H_2/h)[124,125] and poly-(phenyleneethynylene) (1.0 µmol H_2/h)[126] systems. Importantly, there was no obvious deactivation of **ANW-2** when the sample was subjected to four consecutive photochemical runs over a period of 20 h (Figure 5-45). In addition, the ^{13}C CP-MAS NMR spectrum of this sample was virtually unaffected by the experiments thus confirming a high stability of the organic poly(azomethine) backbone in the photocatalytic process being. Long-term stability is usually considered a major advantage of inorganic semiconductors.[119,120,127,128] Therefore, the outcome of this test is important to prove the competitiveness of the ANW system and organic networks in general.

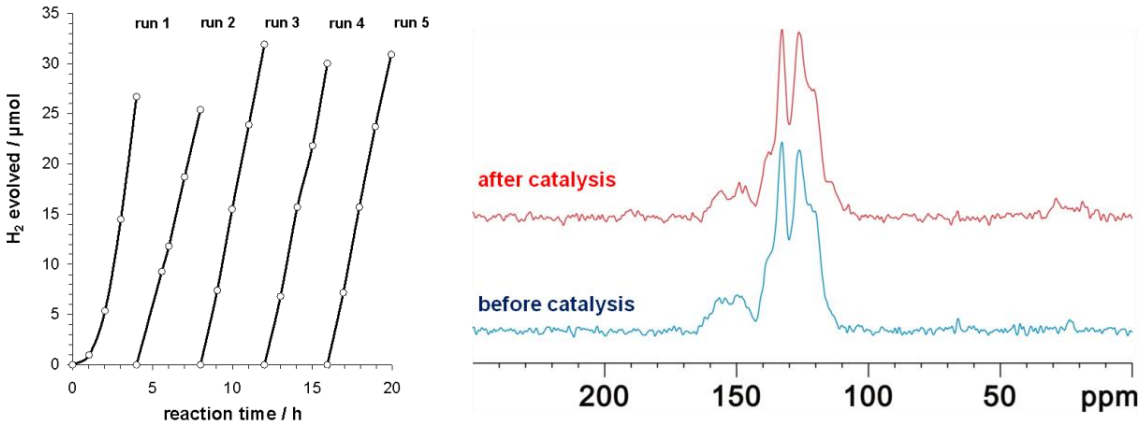

Figure 5-45: Long-time photocatalytic experiment with **ANW-2** over a time period of 20 h (left), ^{13}C CP-MAS NMR spectra of the same sample before and after catalysis (right).

Remarkably, **ANW-4** showed the lowest photocatalytic activity of the series even though it exhibited a similar band gap as **ANW-3** (Table 5-5). This observation can be attributed to the aforementioned distortion of the network structure (Figure 5-43) induced by the incorporation of anthracene-9,10-dicarbaldehyde **5-29**. The efficient transport of charge carriers through the material is interrupted by a strong deviation from planarity in the connecting struts thus resulting in an overall decrease of the catalytic efficiency.

In summary, a modular approach towards the application of purely organic and structurally well-defined semiconductors for photocatalytic hydrogen production has been presented. The **ANW** materials benefit from a cheap and straight-forward polycondensation which is in contrast to the elaborate high-temperature protocols that are typically applied to the preparation of inorganic materials.[119,120,127,128] The catalysis

results as well as recent studies on carbon nitride structures suggest that polymer chemistry with its broad synthetic variety will be beneficial for further development of organic photocatalysts based on polymeric networks.[129,130] Even though the **ANW** series does not yet reach the performance of carbon nitrides (50 - 100 µmol H_2/h)[129,130] and benchmark inorganic photocatalysts (> 100 µmol H_2/h)[119,127,128] the high potential of organic semiconducting materials in this field of application is apparent.

5.3.5 Porosity

For the **ANW** materials described in the previous paragraph only minor porosity was determined by nitrogen physisorption. This is surprising as the concept of combining an A_3-type crosslinker and a B_2-type comonomer was successfully applied to various microporous polymer networks in the past.[2-8]

Still, only very few imine-linked porous networks are known, among them a three-dimensional crystalline COF material.[13,118] This new class of materials is typically created by linking organic building units into predetermined structures using the concept of reticular chemistry.[131] It was successfully demonstrated that the crystallization of two- and three-dimensional periodic covalent structures is indeed possible if the building blocks and their conditions for assembly are carefully chosen.[13,29,39,132-142] Whereas the reversibility of the underlying condensation reactions is important to the build-up of ordered structures, it can be supposed that strong *intra*molecular hydrogen-bonding forces between the C=N units oppose the efficient separation of neighboring chain segments in the case of imine-type polymer networks. Linear poly(azomethines) are known for their outstanding chemical and thermal stability albeit poor solubility which is related to this phenomenon.[103-106]

In view of the above considerations it was decided to substitute the trivalent 1,3,5-tris(4-aminophenyl)benzene crosslinker **5-25** by the tetrafunctional crosslinker **5-32** (Figure 5-46). The bulky anthracene unit in the centre of the molecule should assist in expanding the network structure by preventing *intra*molecular contact sites. On the other hand it confines a defined geometric orientation to the growing network which is a prerequisite for high structural perfection. It is hoped that by this porosity and order can be introduced into the **ANW** materials. Furthermore, the reactivity during network synthesis is now inverted by switching from amine groups to aldehyde functions on the crosslinking unit.

The novel tetravalent crosslinker 5,5'-(anthracene-9,10-diyl)diisophthalaldehyde **5-32** was obtained by double *Suzuki-Miyaura* cross-coupling of 9,10-dibromoanthracene **5-31** with commercially available 3,5-diformylphenylboronic acid (Figure 5-46). The

desired compound precipitated during the course of the reaction and was purified by recrystallization from acetone (69 %). The purity of the compound was verified by FD mass spectroscopy and NMR analysis. The ^{1}H NMR spectrum of **5-35** recorded in DCM-d_2 (Figure 5-47) is in agreement with the highly symmetric structure.

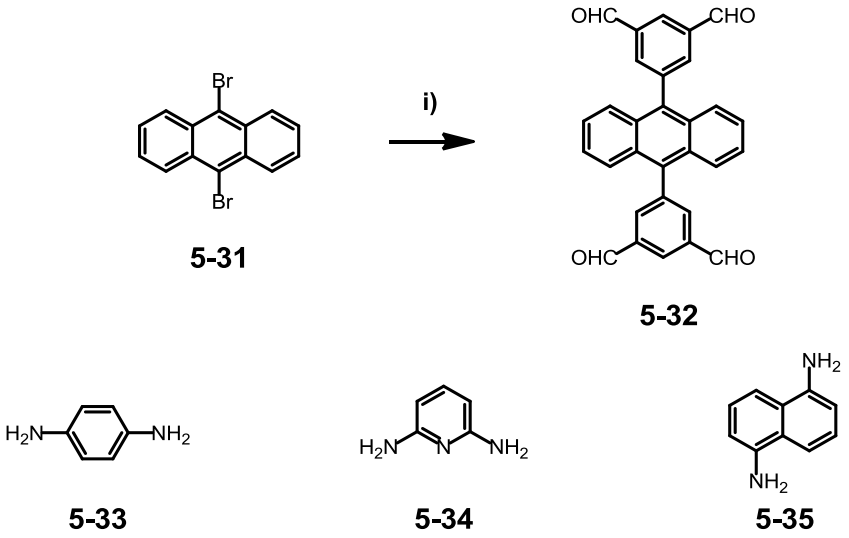

Figure 5-46: Chemical structure of the building units for the synthesis of porous **ANW** materials and the synthetic route to the tetravalent crosslinker **5-31**; conditions: i) 3,5-diformylphenylboronic acid, $Pd(Ph_3)_4$, K_2CO_3, dioxane, Aliquat 336, reflux, 69 %.

Thus, the singlet at δ = 10.25 ppm is assigned to the protons of the aldehyde group (H_a). The triplet at δ = 8.61 ppm (H_b) and the doublet at δ = 8.28 ppm (H_c) are easily distinguished by the corresponding peak integration and the ratio of 1/2 for the two signals.

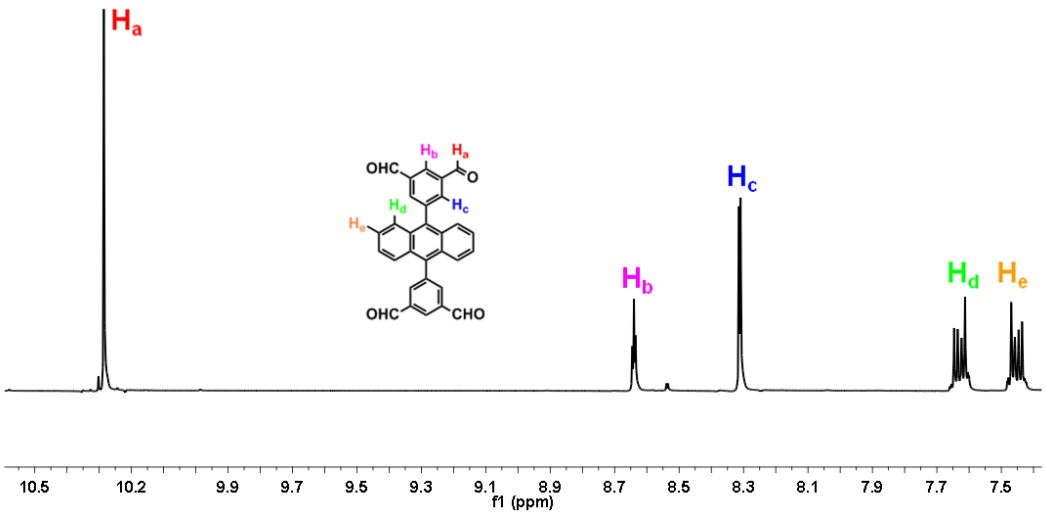

Figure 5-47: Aromatic region of the ^{1}H NMR spectrum of **5-31** in DCM-d_2 at 25 °C.

The two sets of doublets seen at δ = 7.60 ppm (H_d) and δ = 7.42 (H_e) originate from the two chemically different protons on the anthracene backbone.

The synthesis of the **ANW** networks using the newly designed crosslinker **5-35** was then achieved in a similar fashion as described for the first set of networks derived from 1,3,5-tris(4-aminophenyl)benzene **5-25**. Three aromatic amines, namely benzene-1,4-diamine **5-33**, pyridine-2,6-diamine **5-34** and naphthalene-1,5-diamine **5-35** were chosen as co-monomers for this series. They differ in their chemical nature and the substitution pattern of the amine groups on the molecular backbone (Figure 5-46).

In a typical experiment, crosslinker and comonomer were dissolved in a dioxane/acetic acid mixture which was then heated to reflux for 72 h. A fixed molar ratio of aldehyde to amine groups of 1.15 / 1.00 was used to guarantee for complete crosslinking. A greenish-yellow precipitate was formed during the reaction which was collected and purified by *Soxhlet* extraction with THF during 24 h. The yield, as determined gravimetrically, was between 70 wt% and 80 wt% for the three networks.

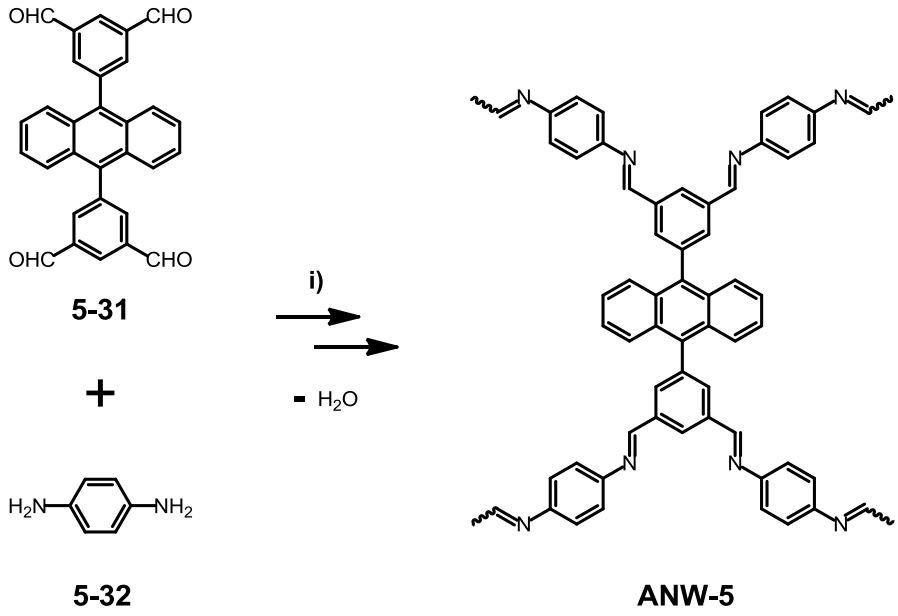

Figure 5-48: Synthesis of **ANW-5**; conditions: i) dioxane/acetic acid, reflux, 72 h, 73 %.

The formation of imine linkages in the **ANW** series was confirmed by FTIR and solid state NMR studies. As exemplified on the basis of **ANW-5** (Figure 5-49), the FTIR spectrum shows a complex structure in the fingerprint region for which the incorporation of the anthracene unit accounts. Nevertheless, the build-up of a poly(azomethine) network can be unambiguously proven by the identification of the characteristic C=N stretching band at 1620 cm^{-1} [13,103-105,107-109,118] and the C-C=N-C- stretching band at 1210 cm^{-1} [13] which are both well-resolved.

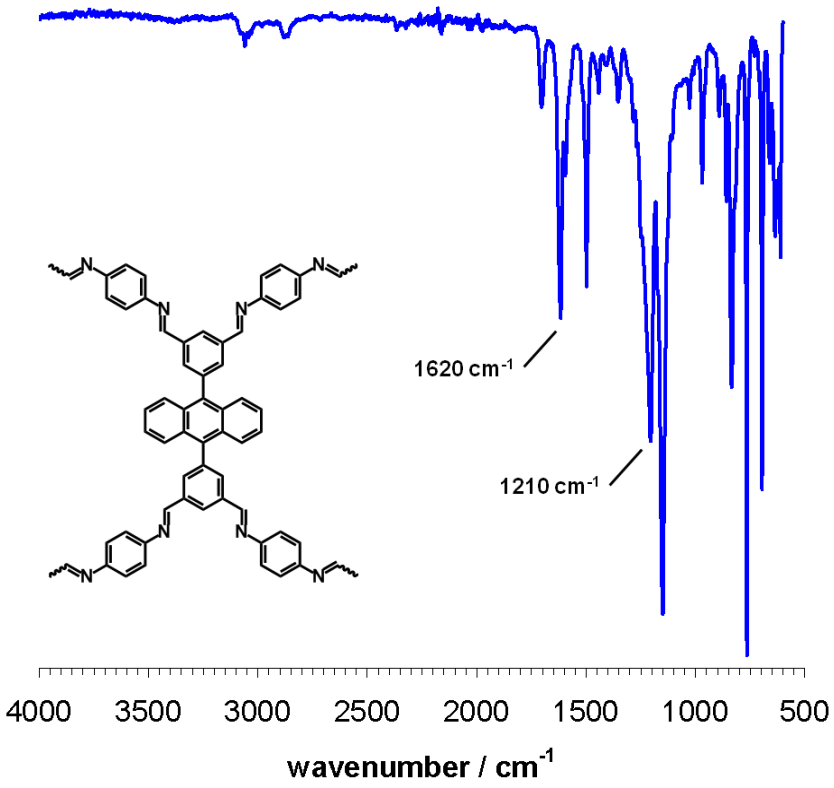

Figure 5-49: FTIR spectrum of **ANW-5**.

Only a marginal signal from unreacted aldehyde groups is found at 1710 cm^{-1} most probably originating from the slight excess of aldehyde groups over amine functions.

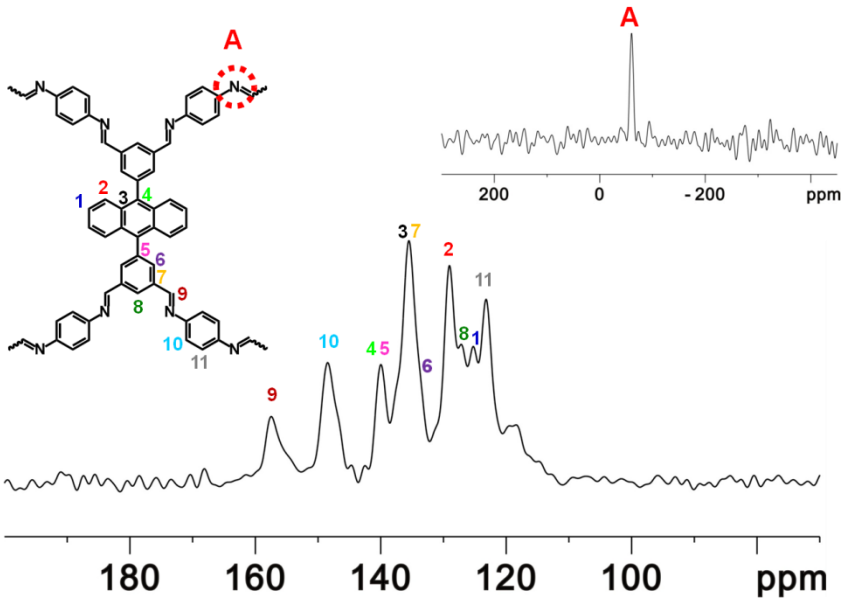

Figure 5-50: ^{13}C CP-MAS NMR spectrum of **ANW-5**; the inset shows the ^{15}N CP-MAS NMR spectrum.

The view on the chemical nature of **ANW-5** was completed by a combination of $^{13}C[^{1}H]$ and $^{15}N[^{1}H]$ solid-state NMR spectroscopy. The ^{13}C CP-MAS NMR spectrum of the network shows a characteristic signal at δ = 159 ppm which is typical of the carbon atom of the imine bond (Figure 5-50).[13,118] Also, the resonance of the aromatic carbon neighboring the nitrogen of the C=N group gives rise to an isolated peak at δ = 148 ppm. The other signals were assigned as indicated in Figure 5-50. No peak corresponding to the carbon atoms of the aldehyde groups of starting compound **5-31** can be detected indicating the high conversion of the functional sites also by this analysis. This finding is in line with the result of FTIR spectroscopy discussed above (Figure 5-49).

The examination of the **ANW** materials by means of nitrogen physisorption at 77 K revealed a high porosity for each sample (Figure 5-50, Table 5-6). The highest specific surface area S_{BET} was, however, found in the case of **ANW-5**. The network reaches a value of 701 m^2/g and a pore volume of 0.51 m^3/g. The corresponding sorption isotherm shows an overall type I character but exhibits a small hysteresis loop that indicates the partial presence of larger pores (Figure 5-51).

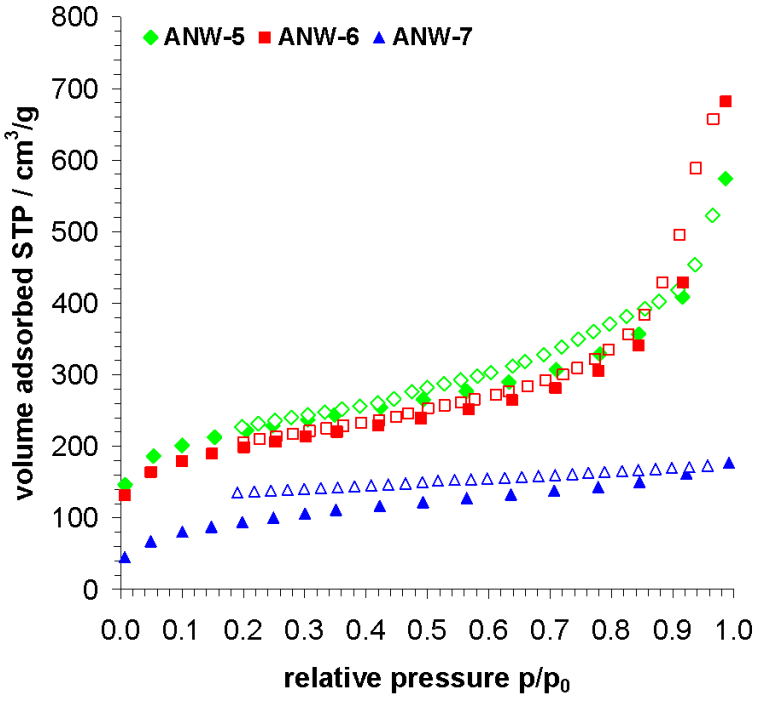

Figure 5-51: Nitrogen sorption isotherms of the **ANW** materials measured at 77 K.

The lowest porosity of the three samples is seen for **ANW-7** (327 m^2/g) which can be explained with the kinks induced by the 1,5-substiuted naphthalene moieties. Pyridine-containing **ANW-6** exhibits an intermediate surface area of 635 m^2/g.

	amine component	S_{BET} [m^2g^{-1}]	$PV_{0.8}$ [cm^3g^{-1}]	$MPV_{0.1}$ [cm^3g^{-1}]	PV_{DFT} [cm^3g^{-1}]	d_{DFT} [nm]
ANW-5	benzene-1,4-diamine	701	0.51	0.31	0.75	0.58
ANW-6	pyridine-2,6-diamine	635	0.47	0.28	0.96	1.54
ANW-7	naphthalene-1,5-diamine	327	0.22	0.12	0.25	2.31

Table 5-6: Porous parameters of the **ANW** materials as determined by nitrogen physisorption.

A similar correlation between the three materials is found when the pore size distributions of the samples as derived from NLDFT modeling are compared (Figure 5-52, Table 5-6). The maxima follow the same trend that is observed for the specific surface area and the pore volume. Consequently, the smallest average pore diameter d_{DFT} of 0.58 nm is found for **ANW-5** which is in accordance with the predominance of micropores in this sample (Table 5-6).

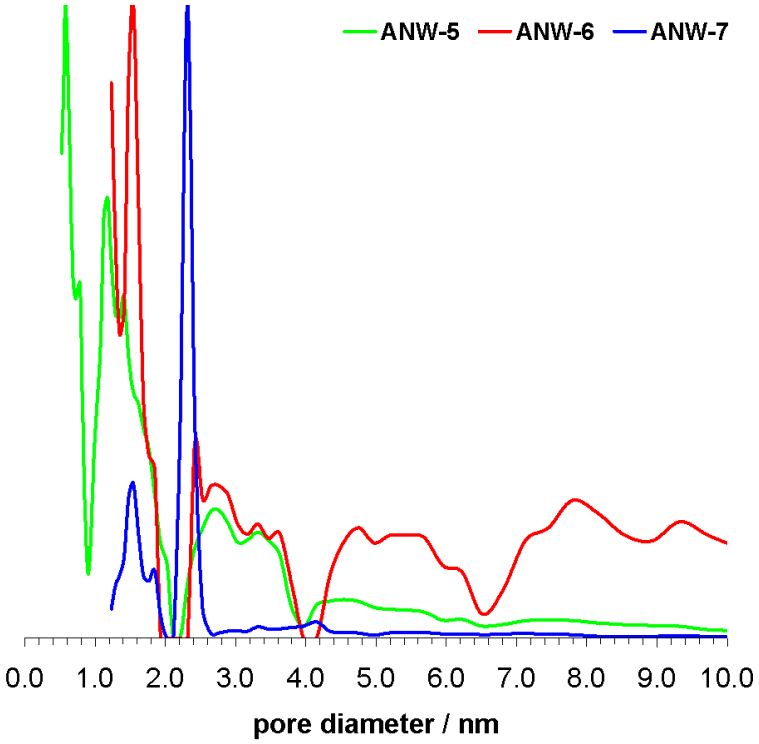

Figure 5-52: Normalized pore size distributions of the **ANW** materials.

The materials presented herein are thus rare examples of porous poly(azomethine) networks. A crystalline COF material that has been previously described showed a specific surface area of 1360 m^2/g.[13] Values of up to 1500 m^2/g were reported for fully amorphous three-dimensional imine-linked polymers.[118]

In the next step, the phase purity of the materials was confirmed by SEM imaging of the samples. As it can be seen for **ANW-5** in Figure 5-53, only one type of morphology is found for the network. The homogenous material is composed of small particles with a diameter of roughly 150 nm.

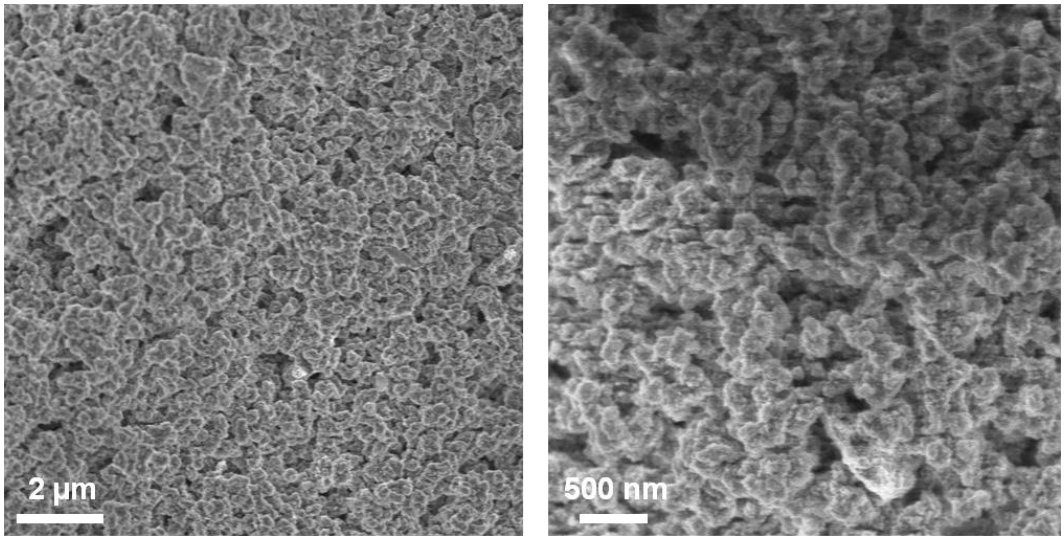

Figure 5-53: SEM images of **ANW-5**.

Powder X-ray diffraction was subsequently carried out in order to investigate the degree of structural order within the poly(azomethine) networks. Whereas **ANW-6** and **ANW-7** gave rise to featureless patterns that indicated a mostly amorphous character, the diffractogram of **ANW-5** revealed a high degree of crystallinity within the sample (Figure 5-54). Since the analysis by FTIR and NMR spectroscopy did not give any evidence for the presence of unreacted starting compounds (Figure 5-49 and Figure 5-50), the reflections seen in the diffractogram must originate from the polymeric material itself.

The pronounced difference between the three samples can be explained by the substitution pattern on the amine components. Only in the case of benzene-1,4-diamine **5-33**, the linear *para*-substitution allows for a strain-free connection to the anthracene-based cross-linking units in analogy to the cutout from the proposed network structure depicted in Figure 5-55. It has been previously highlighted that the *Schiff* base reaction is of fully reversible nature thus offering the possibility for the efficient “healing” of structural defects during network formation.

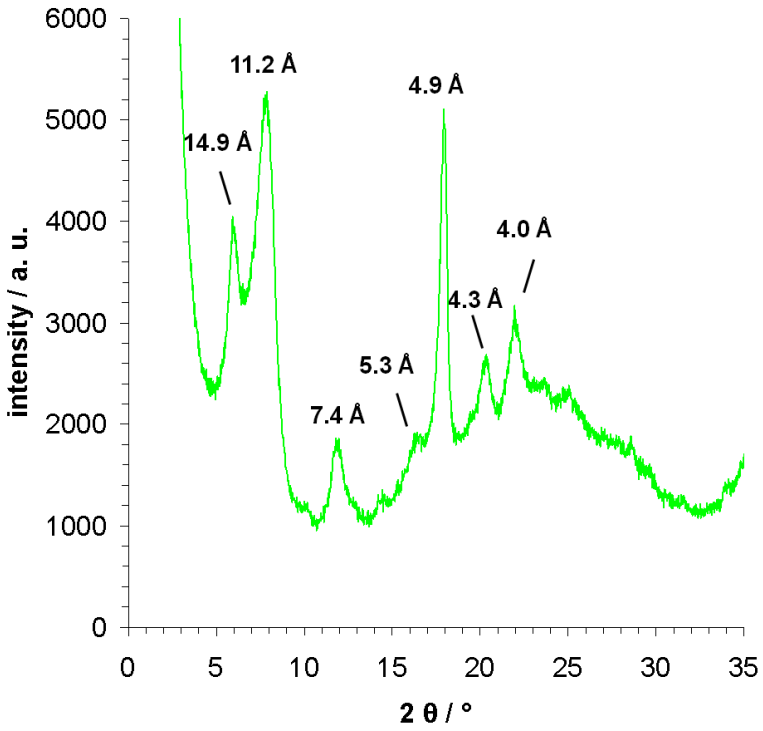

Figure 5-54: Powder X-ray pattern of **ANW-5** and characteristic distances.

A possible outcome of the network formation would be a planar layered structure with the 9,10-substituted anthracene cores orientated perpendicular to the sheet axis resulting from the steric crowding caused by their *alpha*-protons (Figure 5-55).

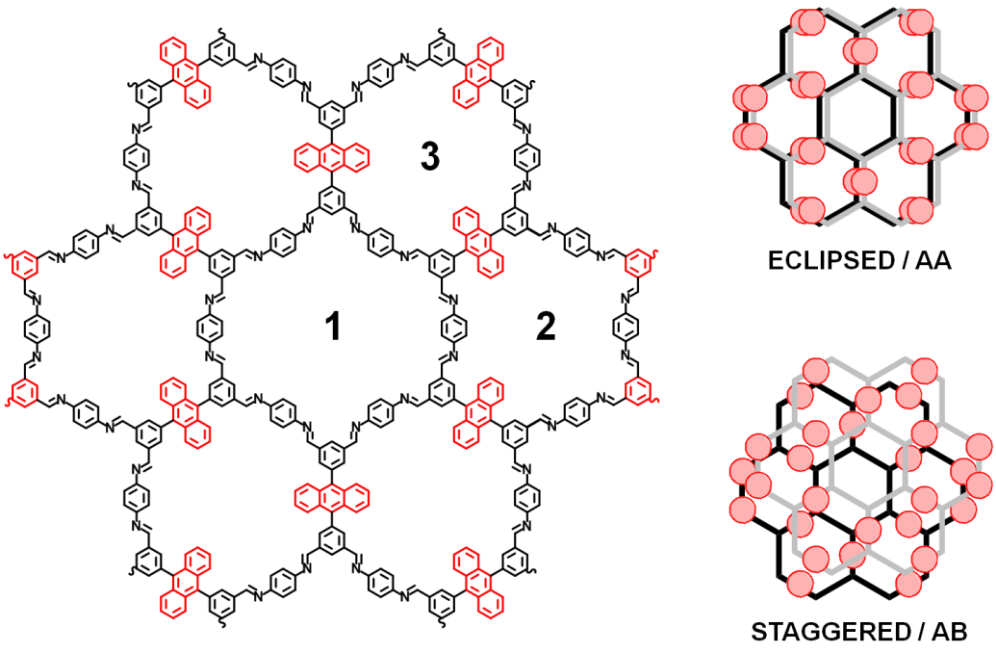

Figure 5-55: Cutout of the proposed network structure of **ANW-5** (left); possible *AA*- and *AB*-type packing models for a layered structure (right).

As these “spikes” point to the interspace between two adjacent sheets it appears likely that the sheets adopt a staggered graphite-type *AB*-type packing and no eclipsed *AA*-conformation (Figure 5-55).[132] An *AB*-type stacked layers could furthermore enable favorable *π*-*π*-interactions of the anthracene units of **ANW-5**. In the past, a similar *AB*-alternating arrangement has been observed for a COF synthesized *via* boroxine ring formation.[132] The structure of the powder X-ray diffractogram of **ANW-5** (Figure 5-54) further supports this assumption due to the high number of distinct reflections. In general, the diffractograms of *AA*-packed COF materials display fewer reflections owing to their higher degree of symmetry.[39,132,134,135] Nevertheless, a computational analysis should be performed in order to provide a definite answer to the question regarding the mode of packing.

The characteristic distances *d* of pores, cavities, channels and between atomic layers in a crystal can be calculated using *Bragg*’s law:

$$n \cdot \lambda = 2 \cdot d \cdot \sin(\theta)$$

where *n* is an integer, *λ* is the wavelength of the X-ray beam and *θ* denotes the diffraction angle between the incident ray and the scattering planes.

Application of this equation to the diffractogram of **ANW-5** reveals characteristic geometric parameters of the material (Figure 5-54). Hence, at small angles values of 14.9 Å, 11.2 Å and 7.4 Å can be derived which are most probably caused by the pores within the layers of the network. As indicated in Figure 5-55, the proposed structure model of **ANW-5** is characterized by three different types of pores which are all defined by an individual diameter. Taking into account a staggered *AB*-type arrangement, the pore appears smaller since it is partially covered by the adjacent layers.[134] This explains why the pore diameters obtained are smaller than to be expected from the model.

Another strong reflection is seen at a 2*θ* value of 17.92 ° (Figure 5-54). Transformation of this angle into the corresponding *d*-value leads to a distance of 4.9 Å which might correspond to the *intra*layer separation of **ANW-5**. Indeed, the perpendicularly orientated anthracene units should increase the spacing between adjacent sheets which is typically found at values between 3.3 Å and 3.5 Å for COF materials made up of planar sheets. [39,132,134,135]

5.4 Nitrogen-Enriched Mesoporous Carbons

The unique character of the **SNW** series makes them suitable precursors for controlled pyrolysis trials for the fabrication of nitrogen-rich carbon materials. The polymer networks combine a superior nitrogen content, ranging between 25 wt% and 45 wt% (Table 5-1), with an enhanced primary porosity of up to 1377 m^2/g (Table 5-2). Furthermore, the porosity of the **SNW** materials can be either of microporous or mesoporous origin and should thus affect the nanotexture and porosity of the resulting carbon materials.

For the fabrication of nitrogen-enriched carbons a variety of different precursors have been used in the past. Examples of (liquid) molecular sources involve acetonitrile,[143,144] pyridine[145] and quinoline.[146] Representative polymer-based precursors are melamine-formaldehyde resins,[147-152] poly(acrylonitrile)[153-155] and poly(vinylpyridine).[156] Also, the nitrogen-doping of the material can be achieved by a post-treatment with ammonia[148,157] or nitric acid.[158]

A number of different species can be formed when the carbon atoms of the underlying lattice are replaced by nitrogen.[148,159] As depicted in Figure 5-56, the lone pair of nitrogen can fully participate in the delocalized electronic system of the carbon matrix. Usually, a trend towards quaternization and oxidation is seen at high pyrolysis temperatures. The nitrogenated functionalities are frequently located at the periphery of graphene sheets within the carbon material. The type and amount of nitrogen can be identified by X-ray photoelectron spectroscopy (XPS). Some typical electron binding energies of the N1s core level are indicated in Figure 5-56.

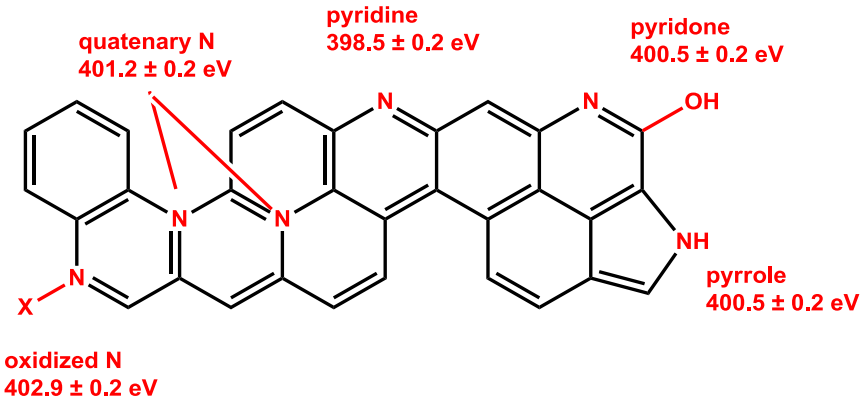

Figure 5-56: Typical nitrogen species and corresponding N1s electron binding energies of nitrogen-enriched carbons.[159]

5.4.1 Synthetic Procedures

Among the twelve **SNW** materials, **SNW-1**, **SNW-5** and **SNW-7** were chosen for the pyrolysis experiments as the aromatic aldehydes used during the network synthesis differ substantially (Figure 5-57). For terephthalaldehyde (**5-8**), naphthalene-2,6-dicarbaldehyde (**5-12**) and pyridine-2,6-dicarbaldehyde (**5-16**) the different size, chemical nature and substitution pattern should allow for a detailed investigation of structure-property relationships.

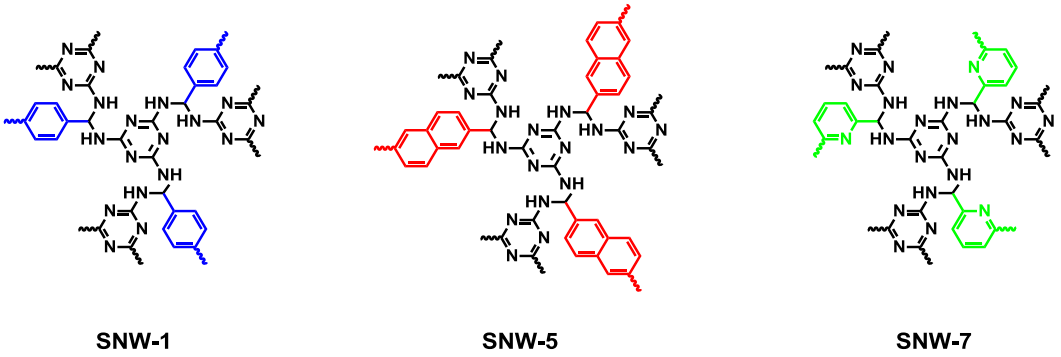

Figure 5-57: Network structure of the **SNW** materials used for pyrolysis experiments.

The same holds for the type of porosity which the **SNW** materials exhibit. Whereas **SNW-1** (1377 m^2/g) and **SNW-5** (1032 m^2/g) are microporous, nitrogen physisorption analysis clearly revealed the mesoporous nature and lower specific surface area of **SNW-7** (540 m^2/g). Also, micropore volume and overall pore volume vary for the three precursors (Table 5-7).

	C [wt%]	H [wt%]	N [wt%]	S_{BET} [m^2g^{-1}]	$PV_{0.8}$ [cm^3g^{-1}]	$MPV_{0.1}$ [cm^3g^{-1}]
SNW-1	38.60	4.32	38.02	1377	0.56	1.01
SNW-5	37.91	4.41	35.88	1032	0.43	0.73
SNW-7	42.50	4.50	37.93	541	0.19	0.51

Table 5-7: Elemental composition and porous parameters of the **SNW** materials used for pyrolysis experiments.

For the high-temperature treatment, the polymeric materials were used as synthesized by the method previously described. An amount of 120.0 mg was placed in a quartz boat and heated to the selected temperature at a heating rate of 2 ^oC/min under a

constant flow of argon (99,998 vol%, 3 vol. ppm oxygen). The sample was held at the corresponding temperature level for 1 h. After cooling, black powders were recovered in all cases and characterized without further treatment.

SNW-1 was the first sample to be investigated and was pyrolized at 400 °C, 600 °C, 800 °C and 1200 °C. The corresponding carbon materials are denominated as **SNW-1-400**, **SNW-1-600**, **SNW-1-800** and **SNW-1-1200**, respectively. According to the same procedure, carbon samples derived from **SNW-5** and **SNW-7** were obtained after pyrolysis at 800 °C and 1200 °C corresponding to **SNW-5-800**, **SNW-5-1200**, **SNW-7-800** and **SNW-7-1200**, respectively.

5.4.2 Porosity and Structural Characterization

Firstly, the progressive evolution of porosity as a function of the pyrolysis temperature was studied for carbon samples prepared from the **SNW** precursors (Table 5-8).

For **SNW-1-400** and **SNW-1-600**, the structural rearrangement of the network leads to broad pore size distributions and a drop of the porosity as compared to the pristine polymer network. This is seen by the low specific surface areas (219 m^2/g and 678 m^2/g) and pore volumes (0.08 cm^3/g and 0.31 cm^3/g) of the two materials. However, the shape of the sorption isotherms (Type I)[40] still reflects the original microporous character of the material which suggests a structural transition state in this temperature regime (Figure 5-58).

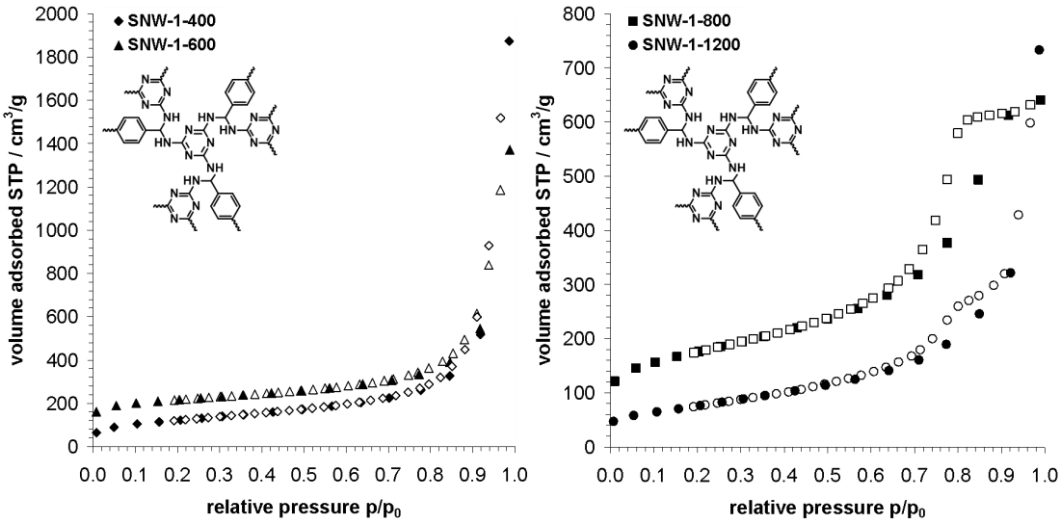

Figure 5-58: Nitrogen sorption isotherms of **SNW-1-400** and **SNW-1-600** (left) and **SNW-1-800** and **SNW-1-1200** (right) measured at 77 K.

A remarkable evolution towards mesoporosity is then found at higher pyrolysis temperatures. For **SNW-1-800** (Figure 5-58), a characteristic type IV adsorption-desorption curve[40] and a narrow *Barret-Joyner-Halenda* (BJH)[160] pore size distribution with a maximum at 9.0 nm are observed (Figure 5-60). The characteristic hysteresis loops are clearly seen for both samples. In comparison to **SNW-1-400**, a nearly threefold increase both in terms of specific surface area (585 m^2/g) and pore volume (0.24 cm^3/g) is obtained for **SNW-1-800**. Further increasing the pyrolysis temperature does not significantly alter the pore dimensions, while the available surface area again decreases to a value of 275 m^2/g for **SNW-1-1200**.

For naphthalene-based **SNW-5-800** and **SNW-5-1200** (Figure 5-57), both specific surface areas (699 m^2/g and 643 m^2/g) and pore volumes (0.60 cm^3/g and 0.55 cm^3/g) do not suffer from an evident decline, indicating that the pore structure seems to be irreversibly fixed at high temperatures. Whereas in the previous case a very narrow pore size distribution evolved at the same temperature level, a broad, rather unstructured BJH pore size distribution is seen for **SNW-5-800** and **SNW-5-1200**. The average pore diameter is significantly larger and shifted to an average value of 28.0 nm for the two samples (Figure 5-60).

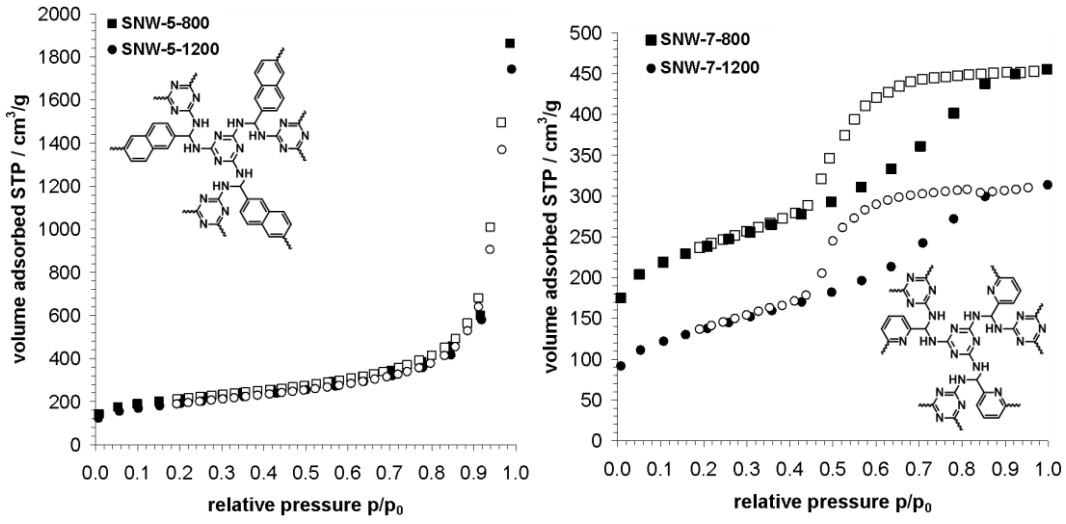

Figure 5-59: Nitrogen sorption isotherms of **SNW-5-800** and **SNW-5-1200** (left) and **SNW-7-800** and **SNW-7-1200** (right) measured at 77 K.

In the case of **SNW-7-800** and **SNW-7-1200**, derived from the pyridine-containing precursor **SNW-7**, the increase of the pyrolysis temperature from 800°C to 1200 °C leads to a decrease both of specific surface area from 748 m^2/g to 454 m^2/g and pore volume from 0.34 cm^3/g to 0.19 cm^3/g, respectively (Table 5-7). Interestingly, the intrinsic mesoporous nature of **SNW-7** is conserved during pyrolysis throughout the

whole temperature range (Figure 5-59). Consequently, **SNW-7-800** and **SNW-7-1200** possess the narrowest pore dimensions of the whole pyrolysis series. In this case, the mesopore distribution is centered on pore diameters of 4.0 nm as revealed by the BJH analysis (Figure 5-60).

A comparison of the BJH pore size distributions of the samples obtained at 800 °C and 1200 °C is found in Figure 5-60. Apart from the information on the pore diameters the volumetric fraction of a certain pore size is also seen. Whereas almost the entire pore volume is well-defined for the samples derived from **SNW-1** and **SNW-7**, the **SNW-5** carbons appear much less structured. The pore volume is distributed over a wide range of pore sizes for both samples.

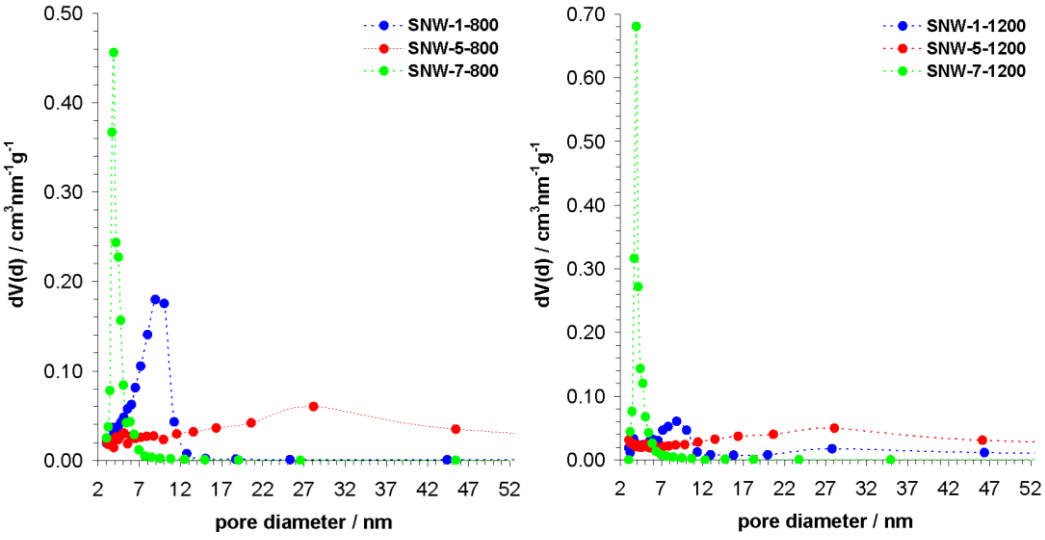

Figure 5-60: BJH pore size distributions for the carbons obtained at 800 °C (left) and 1200 °C (right).

In Table 5-8, the porous parameters as obtained from nitrogen physisorption at 77 K are summarized. It can be seen that by pyrolysis of the three polymer networks the whole range of mesopores is covered. Per definition, these are found on length scales between 2.0 nm and 50.0 nm.[40-42] Very small mesopores are present in the **SNW-5** carbons, intermediate pore diameters are found for the **SNW-1** series and the **SNW-7** materials exhibit the largest pore dimensions.

The template-free formation of a defined, regular mesopore structure of the **SNW** carbons is remarkable as most fabrication pathways for NEMCs rely on the use of either exo- or endotemplates. Hence, a number of nitrogen-rich carbons were prepared using various types of inorganic structured materials such as mica,[147,149,151] zeolites[144] or SBA-15[143,146,161] whose mesoporous topology is transferred to the carbon material. However, the template needs to be impregnated with a nitrogen-rich precursor prior to

the pyrolysis. Also, the inorganic matrix needs to be again removed after the heat-treatment by etching or dissolution. It is apparent that the involvement of multiple and tedious preparative steps greatly limits the large-scale manufacture of these materials. Also, contamination of the carbon surface with inorganic or metallic residues cannot be fully avoided contrary to the catalyst- and template-free synthetic approach developed for the formation of the mesoporous **SNW** carbons.

	S_{BET} [m^2g^{-1}]	$PV_{0.8}$ [cm^3g^{-1}]	$MPV_{0.1}$ [cm^3g^{-1}]	d_{BJH} [nm]	PV_{BJH} [cm^3g^{-1}]
SNW-1-400	219	0.08	0.21	16.75	1.46
SNW-1-600	678	0.31	0.52	20.16	1.91
SNW-1-800	585	0.24	0.58	8.94	0.90
SNW-1-1200	275	0.10	0.29	7.45	0.86
SNW-5-800	699	0.29	0.60	28.17	2.17
SNW-5-1200	643	0.26	0.55	28.08	2.55
SNW-7-800	748	0.34	0.62	3.89	0.51
SNW-7-1200	454	0.19	0.42	3.93	0.52

Table 5-8: Porous parameters of the **SNW** carbons.

The morphology of the **SNW** carbon samples was further examined by high-resolution transmission electron microscopy (HRTEM). The images confirm the mesoporous nature of **SNW-1-800**, **SNW-5-800** and **SNW-7-800**.

For all three samples, a regular pore structure extends throughout the whole carbon matrix. Due to the high degree of porosity and pore walls made up of extremely thin carbon sheets, **SNW-1-800** appears highly translucent under the electron beam (Figure 5-59A&B). The average pore diameter can be roughly estimated to be around 5.0 - 10.0 nm which is in accordance with the aforementioned results from the nitrogen physisorption analysis.

Typical HRTEM images of **SNW-5-800** are shown in Figure 5-61C&D, clearly reflecting the presence of a bimodal mesoporous texture. The larger particles contain pores with diameters above 20.0 nm, while the smaller ones possess pores in the lower nanometer range of 2.0 nm. In the case of **SNW-7-800** (Figure 5-61E&F), distinct dense layers of carbon sheets are detected while mesopores with a size of less than 5.0 nm manifest.

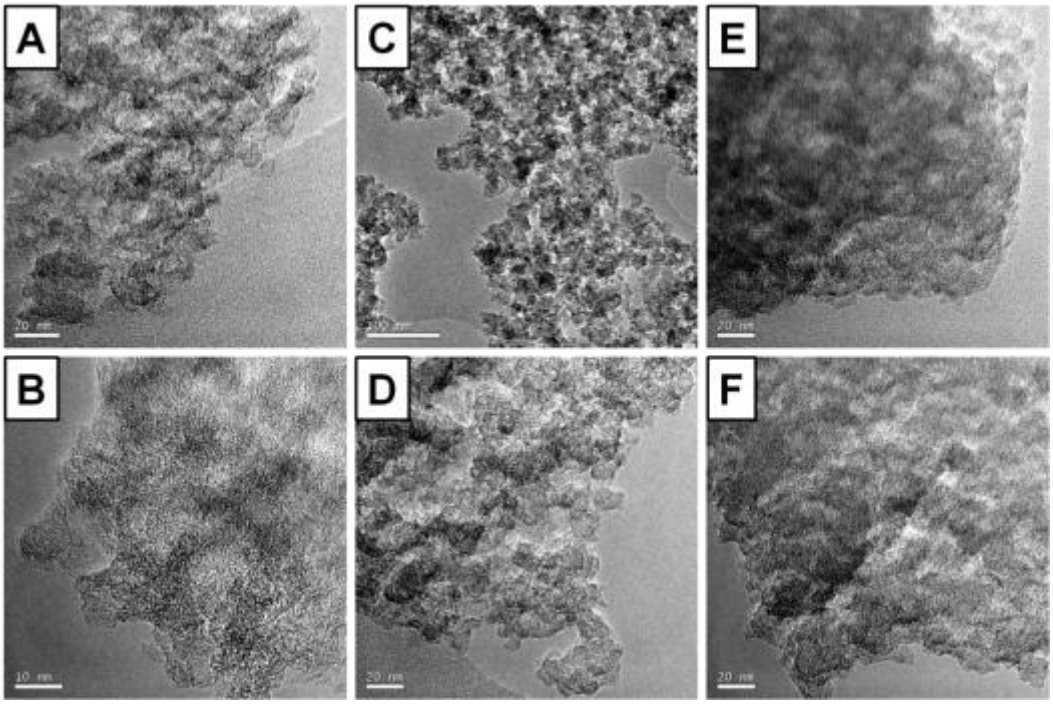

Figure 5-61: HR-TEM images of **SNW-1-800** (A, B), **SNW-5-800** (C, D) and **SNW-7-800** (E, F).

In summary, the HRTEM results in combination with the pore analysis illustrate how the variation of the precursor polymer network will govern both morphology and porosity of the **SNW** carbon materials.

5.4.3 Chemical Characterization

Following the examination of the structural properties, the mechanistical details of the pyrolysis process as well as the chemical nature of the resulting carbon materials derived from the **SNW** polymer scaffolds were studied. At lower pyrolysis temperatures, spectroscopic tools can be still used and are helpful in revealing information on the chemical composition of **SNW-1-400** and **SNW-1-600**. These two carbon samples are considered to be also representative for the pyrolysis of the other two networks **SNW-5** and **SNW-7**.

Both FTIR (Figure 5-62) and ^{13}C CP MAS NMR data (Figure 5-63) reveal that at a temperature of 400 °C the chemical character of the precursor network is partially preserved. Even though a significant broadening of the IR bands is observed, the peaks at 1540 cm^{-1} and 1470 cm^{-1} prove the conservation of the triazine rings at this temperature level.[26,27,29] The presence of the signals at 988 cm^{-1} and 815 cm^{-1} can be attributed to the out-of-plane and in-plane deformation vibrations of the benzene units

for **SNW-1-400**, respectively. The peak positions in the spectrum of the carbon material are virtually identical with those of the parent **SNW-1** polymer material.

In the corresponding ^{13}C CP MAS NMR spectrum of the sample (Figure 5-63), two distinct peaks located at δ = 166 ppm and δ = 130 ppm, assignable to the triazine and benzene carbons, are detected. The complete disappearance of the aminal signal at δ = 55 ppm indicates that the thermal degradation of the material starts at the tertiary carbon atoms of the amine groups within **SNW-1**. Furthermore, the breaking of these bonds might result in the formation of new NH-containing moieties leading to the prominent band between 3000 cm^{-1} and 3500 cm^{-1} emerging in the FTIR spectrum of **SNW-1-400** (Figure 5-62).

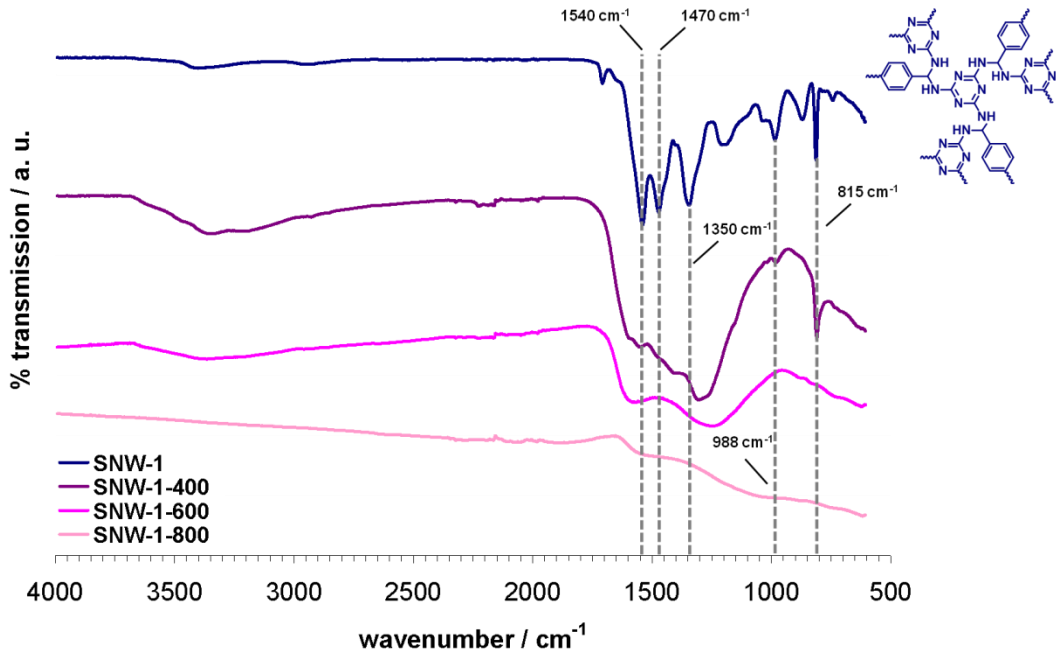

Figure 5-62: FTIR spectra of **SNW-1**, **SNW-1-400**, **SNW-1-600** and **SNW-1-800**.

Results from elemental combustion analysis (ECA, Table 5-9) are in agreement with the spectroscopic investigation. The nitrogen content stays relatively constant at 400 °C (41.21 wt%) as compared to the precursor (38.02 wt%). On the contrary, the hydrogen content at this temperature (2.96 wt%) is decreased by approximately 30.0 % with respect to the starting material (4.32 wt%). It is known for melamine-based flame retardants that triazine-based condensation products form at elevated temperatures on the expense of ammonia elimination (deamination).[16,17,25] It can thus be deduced that for the **SNW** materials the nitrogen-rich triazine rings also withstand the thermal conditions while the elimination of the aminal group is reflected by the loss of hydrogen and the pronounced spectroscopic changes.

Raising the pyrolysis temperature to 600 °C results in a lower signal resolution for both FTIR and ^{13}C CP MAS NMR spectra. The onset of graphitization of **SNW-1-600** leads to the complete loss of signals from the pristine network in the FTIR spectrum (Figure 5-62). However, the onset of adsorption is located at 1500 - 1600 cm^{-1} where characteristic C=N stretching vibrations of nitrogen-containing heterocycles such as pyridines are typically found.

Additionally, the ^{13}C CP MAS NMR spectrum of **SNW-1-600**, obtained by single pulse excitation (Figure 5-63), reveals the decomposition of the triazine unit in this temperature regime as the corresponding resonance at δ = 166 ppm is no longer detected. Instead, the broad signal extending from δ = 100 to δ = 170 ppm is indicative of the presence of different aromatic carbon species. However, the contribution from δ = 140 to δ = 170 ppm to this signal unambiguously validates the presence of aromatic carbon atoms with at least one neighboring nitrogen atom causing a pronounced down-field NMR shift.

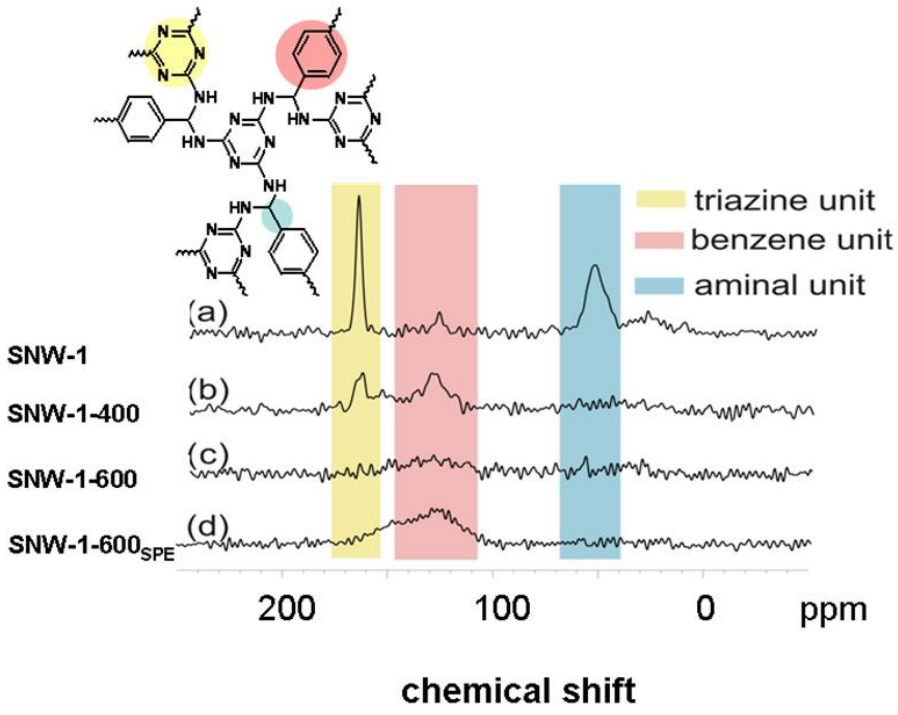

Figure 5-63: ^{13}C CP MAS spectra of **SNW-1** (a), **SNW-1-400** (b) and **SNW-1-600** (c). The CP contact times are 3.0 ms (a, b) and 4.0 ms (c). Single pulse excitation (SPE) spectrum of **SNW-1-600** with 8.0 s relaxation delay (d).

X-ray photoelectron spectroscopy (XPS) analysis performed on the N1s region[148,159] of **SNW-1-600** (Figure 5-64) complements the view on the chemical nature of the materials at these intermediate pyrolysis temperatures. The local state of the nitrogen atoms is mainly pyridinic which can be derived from the signal at 398.6 eV. However,

the smaller peak at 400.8 eV indicates that the exchange of carbon by nitrogen starts already at this temperature resulting in quaternary nitrogen species which are fully embedded into the surrounding carbon matrix (Figure 5-56).

The proposed degradation pathway as reflected by the combination of FTIR, ^{13}C CP MAS NMR and XPS spectroscopy is consistent with the drop in specific surface area and the occurrence of broad pore size distributions previously discussed (Table 5-8). It is well-known that the porosity of microporous polymer networks is esseantially established by the presence of numerous crosslinking points and the connection of stiff aromatic groups.[2-12] The early elimination of the aminal units in the pyrolysis of the **SNW** materials followed by the decomposition of the triazine rings must therefore inevitably result in the loss of the original porosity.

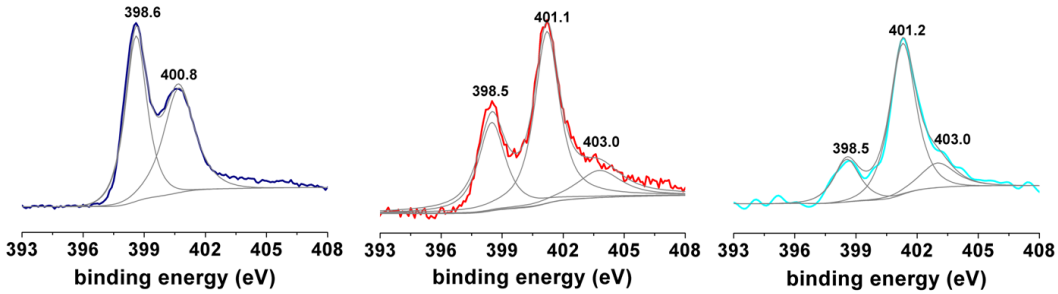

Figure 5-64: XPS spectra of the N1s regions: **SNW-1-600**, **SNW-1-800** and **SNW-1-1200**.

The chemical analysis on the **SNW** carbons obtained at higher pyrolysis temperature was continued on the basis of ECA and XPS data. As seen in Figure 5-62 the FTIR spectrum of **SNW-1-800** is composed of a mostly featureless absorption which is not suitable for a well-founded interpretation. Elemental analysis (Table 5-9, Figure 5-65) of the samples prepared at 800 °C indicates a characteristic depletion of the nitrogen and hydrogen content for all samples of the series. The nitrogen level for **SNW-1-800**, **SNW-5-800** and **SNW-7-800** is found to be 7.11, 5.63 and 6.05 wt%, respectively. These numbers prove that significant amounts of nitrogen are still present at 800 °C. On the contrary, hydrogen-rich functional groups are mostly absent since nitrogen is fully incorporated in pyridine or quaternary arrangements that are not containing hydrogen (Figure 5-56).[157] The progressive dehydrogenation of the sample is confirmed by the XPS spectrum of **SNW-1-800** (Figure 5-64) which contains characteristic signals of pyridinic (398.5 eV) and quaternary (401.1 eV) nitrogen species. Compared to the XPS spectrum recorded for the samples obtained at 600 °C the peak intensities are now reversed.

At the highest pyrolysis temperature of 1200 °C, the signals of the corresponding XPS spectrum of **SNW-1-1200** are further shifted to higher binding energies. The spectrum is dominated by the quaternary nitrogen peak at 401.2 eV and only minor amounts of other nitrogenated species are present. The small peak located at 403.0 eV is commonly attributed to nitrogen oxide but may also result from the electrostatic charging of the sample (Figure 5-64).[148,159] It has to be noted that even after severe thermal treatment at 1200 °C the **SNW** carbons still show residual nitrogen levels of up to 1.93 wt% (Table 5-9, Figure 5-65).

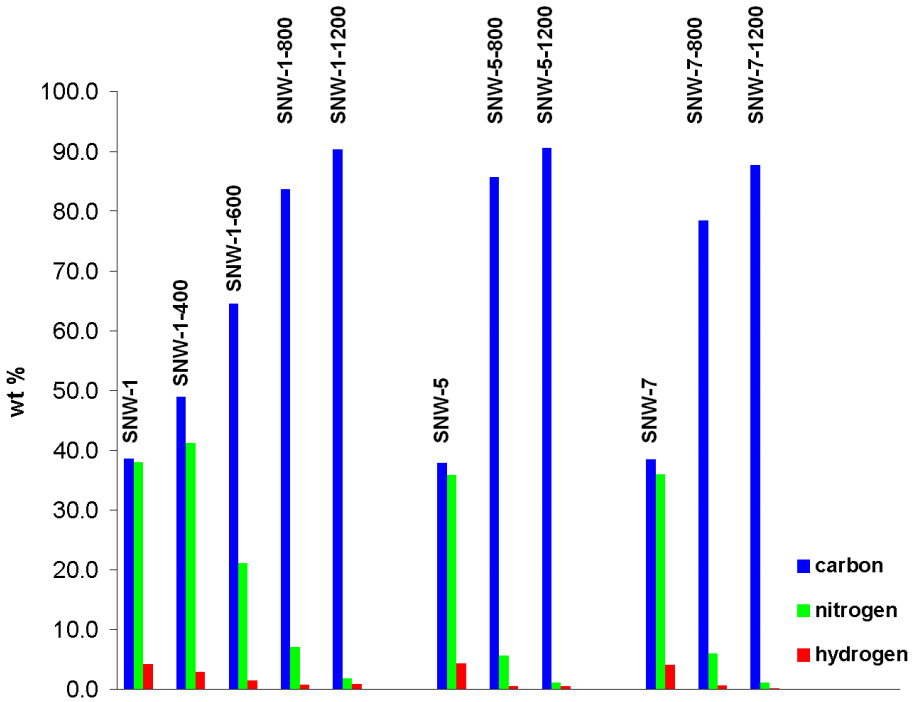

Figure 5-65: Elemental composition of the **SNW** carbons as determined by elemental combustion analysis.

In view of the porosity evolution between 800 and 1200 °C (Table 5-8), these results suggest a complex reassembly of smaller fragments into thermally stable, extended nitrogen-containing ring systems. The opening of the triazine rings at 600 °C seems to be the prerequisite for a high-temperature crosslinking step that irreversibly connects smaller subunits. The secondary increase in specific surface area along with the occurrence of mesoporosity is in accordance with an efficient self-organizing reaction that leads to surprisingly well-defined porosity.

	C [wt%]	H [wt%]	N [wt%]	C/H ratio	C/N ratio
SNW-1	38.60	4.32	38.02	8.94	1.02
SNW-1-400	48.95	2.96	41.21	16.54	1.19
SNW-1-600	64.53	1.54	21.19	41.90	3.05
SNW-1-800	83.74	0.82	7.11	102.12	11.78
SNW-1-1200	90.32	0.96	1.93	94.08	46.80
SNW-5	37.91	4.41	35.88	8.60	1.06
SNW-5-800	85.73	0.54	5.63	158.76	15.23
SNW-5-1200	90.63	0.62	1.13	146.18	80.20
SNW-7	42.50	4.50	37.93	9.44	1.12
SNW-7-800	78.42	0.66	6.05	85.13	12.96
SNW-7-1200	87.74	0.235	1.18	373.36	74.36

Table 5-9: Elemental composition of the **SNW** carbons as determined by elemental combustion analysis.

5.4.4 Electrochemical Characterization

Electrochemical energy as a clean power source has sparked great fundamental and industrial interest. Electrochemical double-layer capacitors (EDLC) are electrical devices that store and release energy by nanoscopic charge separation at the interface of a high-surface-area electrode and an electrolyte (Figure 5-66).[162-166]

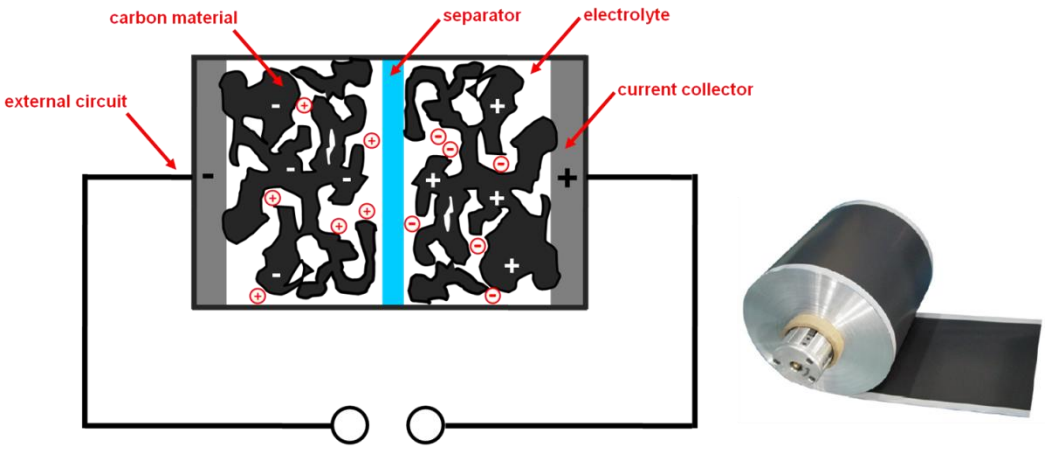

Figure 5-66: Schematic representation of an EDLC device (left) and technical realization in roll form (right).

They can be used to complement or replace battery systems when high power uptake or delivery is needed.[167-169] The extraordinary cycling stability, wide thermal operation range, low weight and flexible packaging of EDLC are unattainable in traditional energy storage systems. For a single charge, EDLC are able to deliver higher power densities than conventional batteries because the storage mechanism is not governed by chemical redox processes but relies on pure physical charge storage. Despite the aforementioned advantages, EDLC still suffer from one major drawback which is their lower energy density compared to batteries as observed in the *Ragone* plot (Figure 5-67).[162,164,169] Thus, the optimal discharge time of EDLC is limited to less than a minute. For their widespread use as self-contained devices in applications ranging from portable electronics to large industrial equipment, this parameter needs to be significantly improved.

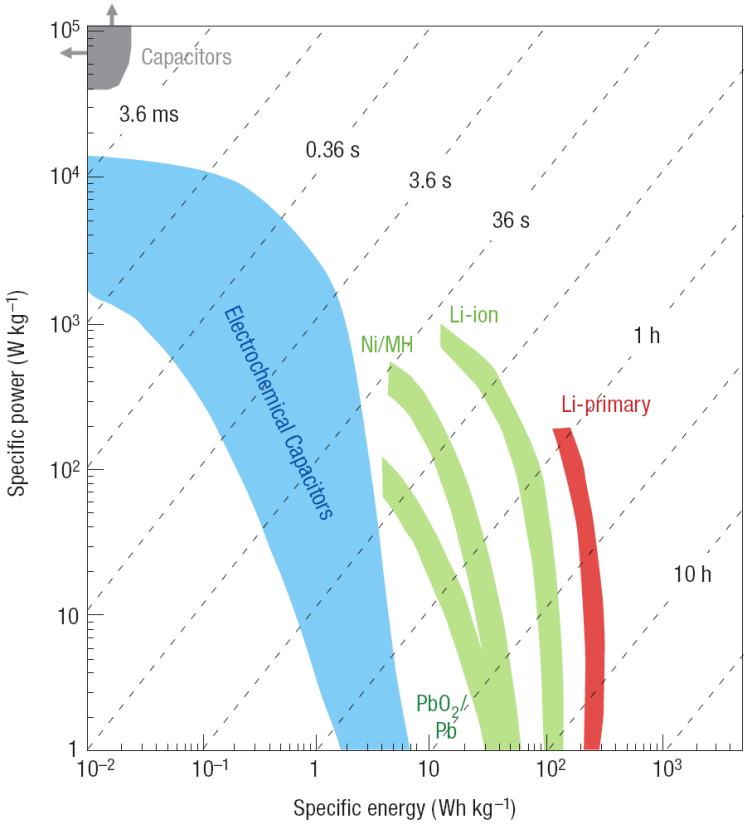

Figure 5-67: *Ragone* plot for various electrical energy storage devices. The diagonal lines represent the time constants of the devices and are obtained by dividing the energy density by the power.[169]

The performance of ultracapacitors is largely determined by the electrode material. Thus, the energy densities of EDLC can be in principle increased by construction of electrode materials with enhanced capacitive performances. The most frequently applied electrode materials are porous carbons owing to their high surface area, open porosity, nearly ideal polarization, easy availability and low pricing.[170] A high specific

surface area is considered as a primary requirement for achieving prominent capacitance,[162,171] while experiments with activated carbons (AC),[171] carbon nanotubes (CNT),[145,154,172] and carbide-derived carbons (CDC)[173-175] highlight the importance of defined porosity. Fully microporous carbon materials usually suffer from severe kinetic limitations for fast charging and discharging.[175,176]

In this context, nitrogen-enriched mesoporous carbons (NEMC) have been recently identified as a novel class of promising electrode materials.[143,144,147,149,158] On the one hand, they possess significant amounts of open and accessible pores on the mesoscale that offer convenient transport pathways for electrolytes. Still, micropores are also present in the material as seen from the nitrogen sorption isotherms and the corresponding pore size distributions.

On the other hand, NEMC contain nitrogen-enriched surfaces that can improve the capacitive performance of EDLC. The importance of nitrogen sites is given by electrochemical processes occurring at the surface of the carbon material resulting in *pseudo*-capacitance behaviour.[152,162] Pyridinic, quaternary and oxidized nitrogen groups located at the periphery of graphene sheets are believed to be particularly active in promoting the underlying electrochemical process (Figure 5-56).[144,147,149,158]. Hence, for a NEMC the overall capacitance is composed of classical double-layer contributions and the *pseudo*-capacitive effect of the nitrogen species.

The presence of regular mesoporosity in addition to enhanced nitrogen levels discussed for the **SNW** carbons match well the theoretic and experimental expectations for carbon materials to be used in electrochemical energy storage. As seen for the samples obtained at 800 °C, the nitrogen content ranges between 5.0 and 7.0 wt%. Furthermore, the mesoporosity of the samples is regular and can be tuned by the choice of the precursor network. For this reason, the **SNW** carbons were investigated in detail as electrode materials for EDLC devices in cooperation with *Dr. Y. Liang* (MPI-P Mainz, Germany).

For the **SNW-1** series, the evaluation of the electrochemical properties as seen by the CV curves discloses that elevation of the pyrolysis temperature (from 400 °C to 800 °C) continuously improves the capacitive performance both in 1 M H_2SO_4 and 1 M KOH electrolytes. This is reflected by the diagrams which are shown in Figure 5-68. Changing the electrolyte does neither significantly alter the appearance of the curves nor does it affect the order of the samples based on their performance. The curves exhibit rather symmetrical, rectangular shapes which are typical of double-layer capacitance originating from nanoscopic charge separation. This process seems to dominate the overall capacitance. **SNW-1-800** and **SNW-1-1200** exhibit the best

electrochemical performance. This is why the thermal treatment for **SNW-5** and **SNW-7** was directly performed at temperatures of 800 and 1200 °C, respectively.

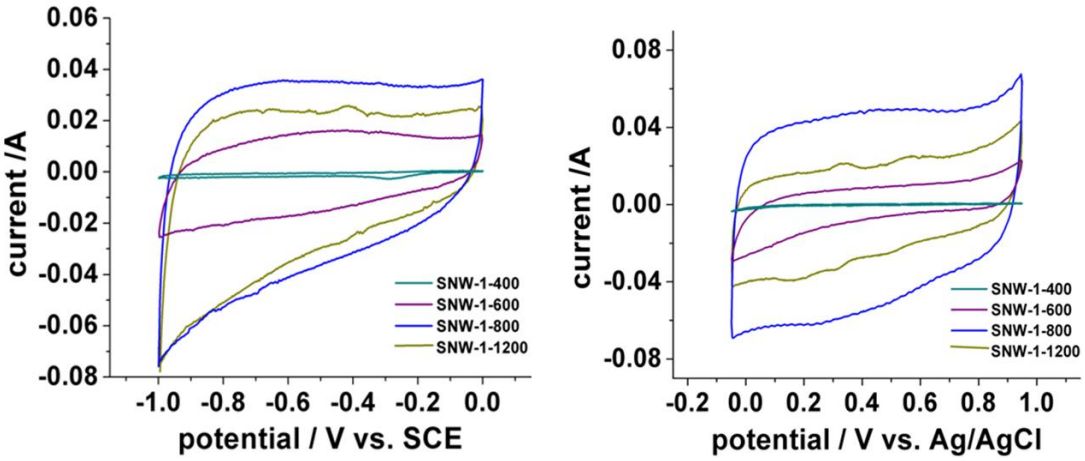

Figure 5-68: Cyclic voltammograms of the **SNW-1** carbons at a sweep rate of 50 mV/s in 1M KOH (left) and 1 M H_2SO_4 electrolyte (right).

The CV curves of the **SNW** carbon materials obtained at 800 °C are shown in Figure 5-69. Also for the other samples rectangular-shaped voltammograms are observed which differ however in the surface they comprise. Under alkaline conditions partial polarization is observed at a potential close to - 1.0 V (Figure 5-69).

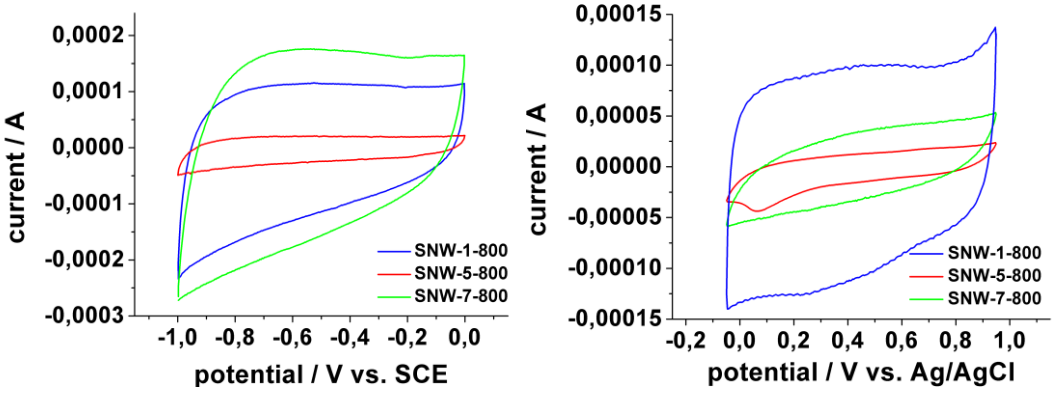

Figure 5-69: Cyclic voltammograms of **SNW-1-800**, **SNW-5-800** and **SNW-7-800** at a sweep rate of 50 mV/s in a 1M KOH (left) and 1 M H_2SO_4 electrolyte (right).

Galvanostatic charge-discharge measurements were then applied in order to investigate the capacitive performance at a set of current densities ranging between 2.0 A/g and 10.0 A/g (Figure 5-70 and Figure 5-71). In principle, smaller current densities (less than 0.5 A/g) generate more capacitive contribution from microporous carbons, however, at the expense of power density of the whole capacitor

system.[155,164,165] As a result, a minimum current density of 2.0 A/g was used in the present case.

Normalized gravimetric capacitance values C_g were calculated from the galvanostatic discharge curves measured in a three-electrode cell using the following equation:[177]

$$C_g = \frac{I \cdot t}{m \cdot \Delta V}$$

Herein, *I* is the specific discharge current density, *t* is the overall discharge time, *ΔV* is the potential range and *m* is the mass of electrode material. The corresponding specific C_s values are obtained by dividing C_g by the BET surface area S_{BET} of the **SNW** carbons determined from nitrogen physisorption (Table 5-8).

Using an alkaline environment of 1 M KOH **SNW-1-800** and **SNW-7-800** exhibit superior capacitive values. The specific gravimetric capacitances C_g at a current rate of 2.0 A/g reaches values of 301 F/g and 351 F/g. The corresponding specific capacitances C_s, calculated by applying the specific surface area of the samples, are 51 µF/cm^2 and 43 µF/cm^2, respectively (Table 5-10).

	2.0 A/g		5.0 A/g		10.0 A/g	
	C_g [F/g]	C_s [µF/cm^2]	C_g [F/g]	C_s [µF/cm^2]	C_g [F/g]	C_s [µF/cm^2]
SNW-1-800[a]	301	51	285	48	220	37
SNW-5-800[a]	86	12	75	11	66	12
SNW-7-800[a]	351	43	302	37	244	31
SNW-1-800[b]	381	72	339	60	253	47
SNW-5-800[b]	80	11	68	10	55	8
SNW-7-800[b]	184	26	171	23	142	19

[a]in a 1 M KOH electrolyte [b]in a 1 M H_2SO_4 electrolyte

Table 5-10: The gravimetric and specific capacitance values of **SNW-1-800**, **SNW-5-800** and **SNW-7-800** as derived from galvanostatic charge-discharge measurements at constant current densities of 2.0 A/g, 5.0 A/g and 10.0 A/g.

In contrast, **SNW-5-800** exhibits gravimetric and specific capacitance values of only 86 F/g and 12 µF/cm^2; much lower than those of **SNW-1-800** and **SNW-7-800**. It appears that the lack of defined mesoporosity and the presence of too large pores greatly restrict the utilization of **SNW-5-800** for energy storage applications.

Upon changing the electrolyte to 1 M H_2SO_4, **SNW-1-800** shows the best capacitive activities of 381 F/g and 72 µF/cm^2 among the experimental series (Table 5-10).

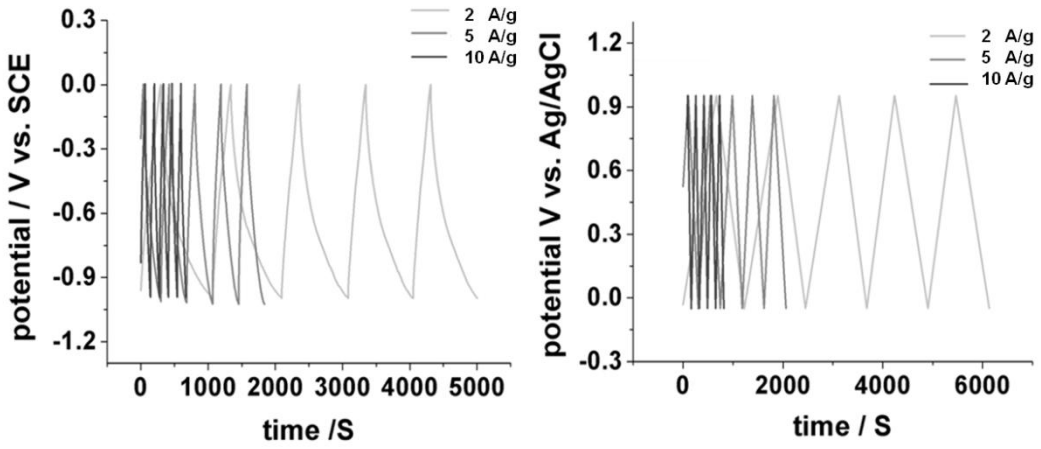

Figure 5-70: Galvanostatic charge-discharge curves of **SNW-1-800** at constant currents of 2.0 A/g, 5.0 A/g and 10.0 A/g in 1M KOH (left) and 1 M H_2SO_4 electrolyte (right).

The lower capacitive values for **SNW-7-800** (184 F/g and 26 µF/cm^2) in acid environment could be related to the change in size of the ions. Whereas hydrated OH^- has an estimated diameter of 0.13 nm, the H_3O^+ species has a diameter of 0.28 nm. Again, the results for **SNW-5-800** (80 F/g and 11 µF/cm^2) fall short of the values obtained for the other two samples.

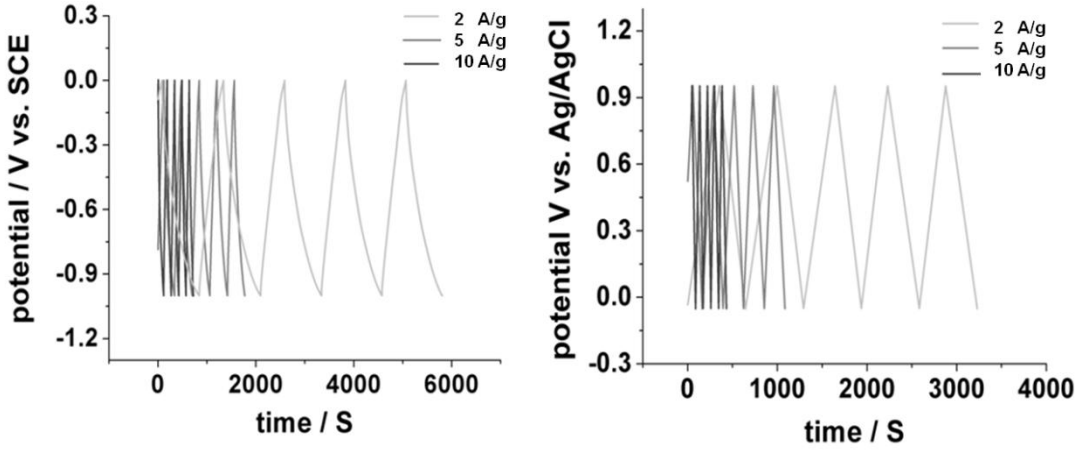

Figure 5-71: Galvanostatic charge-discharge curves of **SNW-7-800** at constant currents of 2.0 A/g, 5.0 A/g and 10.0 A/g in 1M KOH (left) and 1 M H_2SO_4 electrolyte (right).

Ideally, an EDLC should be able to deliver the same energy under any operational conditions. It is therefore important to study the capacitance retention at higher current

loads. However, the capacitive value of **SNW-1-800** still retains 339 F/g and 253 F/g at high current densities of 5.0 A/g and 10.0 A/g, respectively, illustrating the good performance of the **SNW** carbons (Table 5-10).

The long-time performance was tested for the best sample **SNW-1-800** (Figure 5-72). Capacity fading was not observed even after 4500 cycles at a current density of 2.0 A/g. The charge-discharge curves of the initial and final cycles were almost identical in shape. This result also suggests perfect reversibility of the *pseudo*-capacitive interactions which are believed to contribute to the overall performance of the samples. After the long-time experiment, **SNW-1-800** shows an enhanced gravimetric capacitance of 425 F/g which might originate from a progressive activation process of the carbon material.[178]

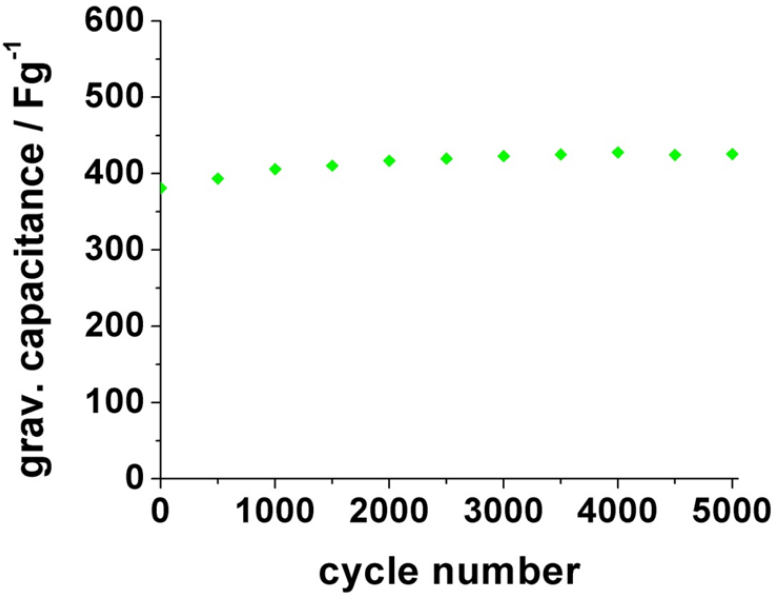

Figure 5-72: Cycle life test of **SNW-1-800** in 1M H_2SO_4 electrolyte at a constant current of 2.0 A/g.

It has been discussed above, that for nitrogen-rich carbon materials the capacitance behavior is significantly enhanced by *pseudo*-faradaic charge transfer involving nitrogen functionalities. In previous studies, significant gravimetric capacitance values C_g of 100 - 200 F/g were even reported for carbon materials exhibiting minor[151] or no[148] mesoporosity illustrating the role of the surface functions.

In the present case, polar hydrophilic nitrogen groups also enhance the surface wettability for the aqueous electrolyte thus ensuring a complete utilization of the exposed surface for charge storage. Furthermore, the materials additionally benefit from defined and accessible mesoporosity, whose importance is seen by considering the similar surface area and nitrogen content of **SNW-1-800** and **SNW-7-800**,

respectively (Table 5-8 and Table 5-9). The difference in the final capacitive performance of both materials may thus be attributed to the individual pore size distribution of each sample.[179]

Furthermore, **SNW-1-800** with its specific surface area of 548 m^2/g reaches or even outperforms the best reported cases both in acid and basic conditions.[148] This is remarkable as the surface areas of carbon materials obtained *via* alternative preparative routes can significantly exceed the porosity determined for the **SNW** series. This leads to the conclusion that the optimized mesoporosity and surface chemistry discussed above is at the heart of the superior performance of **SNW-1-800**.

Still, it is important to compare the specific capacitance values C_s of the **SNW** carbons to state-of-the-art literature examples. By this, the actual contribution of the nitrogenated surface can be estimated as this capacitance value has been normalized with respect to the specific surface area of the sample. Hence, the value of 72 $\mu F/cm^2$ for **SNW-1-800** under acidic conditions is on the same level as the best reported cases obtained using similar analytic conditions.[154,171] It has been highlighted that the device setup, e. g. a two- or a three-electrode cell, will also have an impact on the final capacitive value that is determined.[177] In general, measurements carried out using a three-electrode cell as in the present case deliver higher capacitance values which has to be kept in mind upon comparison of different experimental series.

5.5 Summary

In summary, it could be shown that the use of *Schiff* base chemistry for the build-up of polymer networks opens new versatile routes to functional polymer networks. It turns out that three-dimensional poly(aminal) (**SNW**) as well as poly(azomethine) networks (**ANW**) can be used for a variety of applications ranging from energy storage to catalysis.

It has been demonstrated that the high-temperature condensation of melamine with di- and trivalent aromatic aldehydes is an efficient method for the preparation of porous polymer networks. The catalyst-free synthesis relies on cheap and abundant starting materials which render the process scalable. Furthermore, owing to the incorporation of the melamine units, unprecedented nitrogen levels of up to 40 wt% have been reached. Having at hand a set of twelve poly(aminal) networks, porosity and gas uptake performance of the samples was analyzed in detail and correlated to the nature and structure of the monomeric building units. A number of physisorptive measurements using nitrogen, hydrogen, methane and water were applied to the analysis of the materials. It could be demonstrated how the monomer combination can be used to tailor type and degree of porosity. Thus, microporous and mesoporous polymer **SNW** networks can be selectively produced comprising surfaces areas between 200 m^2/g and 1400 m^2/g. Also, the enhanced values obtained from hydrogen and high-pressure methane sorption experiments illustrate the potential application of the poly(aminal) networks as gas storage materials.

As the formation of interconnected, strongly crosslinked networks in solution will inevitably result in the heterogenization of the process, the newly developed synthetic route towards poly(aminal) networks was successfully transferred to a non-aqueous miniemulsion protocol. By careful tuning of reaction conditions and surfactant, the synthesis of microporous **SNW** nanoparticles was achieved. The morphology control of porous polymer networks was demonstrated for the first time within the scope of this work and should provide access to new fields of application involving catalysis, drug delivery or chemoselective chromatography. Furthermore, a potential up-scaling of the synthetic process will benefit from this emulsion protocol as it allows for efficient heat management, control over viscosity and mass transport as well as facile post-processing.

Closely related to the poly(aminal) synthesis is the preparation of porous and non-porous poly(azomethine) networks which were obtained by a related synthetic approach. It was shown how the imine bond can be equally used for the construction of

extended aromate-rich **ANW** materials. These networks are fully conjugated in nature and were found suitable for experiments regarding the photocatalytic production of hydrogen. In these experiments, a homologous series of poly(azomethine) networks was used to investigate structure-property relationships of organic photocatalysts. Hence, the degree of conjugation along the linear struts of the network was correlated to the experimentally determined catalytic activity. By designing a suitable anthracene-based crosslinker it was also possible to prepare a covalent organic poly(azomethine) framework for which a surface area of 700 m^2/g was obtained and a high degree of crystallinity confirmed.

Through controlled pyrolysis of the melamine-based poly(aminal) networks nitrogen-enriched mesoporous carbon materials were prepared. Despite the absence of a template, the carbons thus produced revealed a surprisingly well-defined mesoporosity. It was possible to link type and porosity of the precursor network to the structure and chemical composition of the final carbonaceous material. Also, the effect of the pyrolysis temperature could be correlated to the properties of the samples.

With respect to state-of-the-art carbon materials, the electrochemical characterization of the **SNW** carbons revealed a high potential for their use in electrochemical double-layer capacitors. Maximum capacitance values of 381 F/g and 351 F/g were determined under alkaline and acidic conditions, respectively.

5.6 Bibliography

(1) Odian, G. G. *Principles of Polymerization*; J. Wiley & Sons: Hoboken, **2004**.
(2) Jiang, J. X.; Su, F.; Trewin, A.; Wood, C. D.; Campbell, N. L.; Niu, H.; Dickinson, C.; Ganin, A. Y.; Rosseinsky, M. J.; Khimyak, Y. Z.; Cooper, A. I. *Angew. Chem. Int. Ed.* **2007**, *46*, 8574-8578.
(3) Jiang, J. X.; Su, F.; Trewin, A.; Wood, C. D.; Niu, H.; Jones, J. T. A.; Khimyak, Y. Z.; Cooper, A. I. *J. Am. Chem. Soc.* **2008**, *130*, 7710-7720.
(4) Jiang, J. X.; Trewin, A.; Su, F.; Wood, C. D.; Niu, H.; Jones, J. T. A.; Khimyak, Y. Z.; Cooper, A. I. *Macromolecules* **2009**, *42*, 2658-2666.
(5) Dawson, R.; Laybourn, A.; Clowes, R.; Khimyak, Y. Z.; Adams, D. J.; Cooper, A. I. *Macromolecules* **2009**, 675-683.
(6) Stöckel, E.; Wu, X.; Trewin, A.; Wood, C. D.; Clowes, R.; Campbell, N. L.; Jones, J. T. A.; Khimyak, Y. Z.; Adams, D. J.; Cooper, A. I. *Chem. Commun.* **2009**, *2009*, 212-214.
(7) Weber, J.; Thomas, A. *J. Am. Chem. Soc.* **2008**, *130*, 6334-6335.
(8) Jiang, J. X.; Su, F.; Niu, H.; Wood, C. D.; Campbell, N. L.; Khimyak, Y. Z.; Cooper, A. I. *Chem. Commun.* **2008**, *2008*, 486-488.
(9) Schmidt, J.; Werner, M.; Thomas, A. *Macromolecules* **2009**, *42*, 4426-4429.
(10) Ben, T.; Ren, H.; Ma, S.; Cao, D.; Lan, J.; Jing, X.; Wang, W.; Xu, J.; Deng, F.; Simmons, J. M. *Angew. Chem. Int. Ed.* **2009**, *48*, 9457-9460.
(11) Trewin, A.; Cooper, A. I. *Angew. Chem. Int. Ed.* **2010**, *49*, 1533-1535.
(12) Schmidt, J.; Weber, J.; Epping, J. D.; Antonietti, M.; Thomas, A. *Adv. Mater.* **2009**, *21*, 702-705.
(13) Uribe-Romo, F. J.; Hunt, J. R.; Furukawa, H.; Klöck, C.; O'Keeffe, M.; Yaghi, O. M. *J. Am. Chem. Soc.* **2009**, *131*, 4570-4571.
(14) Kay, M.; Price, A. F.; Lavery, I. *J. Fire Retardant Chem.* **1979**, *6*, 69-91.
(15) Broadbent, J. R. A.; Hirschler, M. M. *Eur. Polym. J.* **1984**, *20*, 1087-1093.
(16) Costa, L.; Camino, G.; Luda di Cortemiglia, M. P. *ACS Symposium Series, Fire and Polymers*; American Chemical Society: Washington, DC, **1990**.
(17) Weil, E. D.; Zhu, W. *ACS Symposium Series, Fire and Polymers II*; American Chemical Society: Washington, DC, **1995**.
(18) Arpe, H. J. *Industrielle Organische Chemie: Bedeutende Vor-und Zwischenprodukte*; Wiley-VCH: Weinheim, **2007**.
(19) Layer, R. W. *Chem. Rev.* **1963**, *63*, 489-510.
(20) Patai, S. *The Chemistry of the Carbon-Nitrogen Double Bond*; Interscience Publishers: London and New York, **1970**.
(21) Kotha, S.; Shah, V. R. *Synthesis* **2008**, *23*, 3653-3658.
(22) Hagiya, K.; Mitsui, S.; Taguchi, H. *Synthesis* **2003**, *6*, 823-828.
(23) Tullberg, E.; Frejd, T. *Synth. Commun.* **2007**, *37*, 237-245.
(24) Hodačova, J.; Buděšínský, M. *Org. Lett.* **2007**, *9*, 5641-5643.
(25) Costa, L.; Camino, G. *J. Therm. Anal. Calorim.* **1988**, *34*, 423-429.
(26) Devallencourt, C.; Saiter, J. M.; Fafet, A.; Ubrich, E. *Thermochim. Acta* **1995**, *259*, 143-151.
(27) Larkin, P. J.; Makowski, M. P.; Colthup, N. B.; Flood, L. A. *Vib. Spectrosc.* **1998**, *17*, 53-72.
(28) Manecke, G.; Wöhrle, D. *Makromol. Chem.* **1968**, *120*, 176-191.
(29) Bojdys, M. J.; Jeromenok, J.; Thomas, A.; Antonietti, M. *Adv. Mater.* **2010**, *22*, 2202-2205.
(30) Schindlbauer, H.; Anderer, J. *Angew. Makromol. Chem.* **1979**, *79*, 157-162.
(31) Forlani, L. S., M.; Todesco, P. E. *Gazz. Chim. Ital.* **1986**, *116*, 229-232.
(32) Musumarra, G.; Sergi, C. *Heterocycles* **1994**, *37*, 1033-1039.
(33) Lee, T.-K.; Choi, J.-H.; Byun, J.-W.; Lee, Y.-S. *Tetrahedron Lett.* **2008**, *49*, 5380-5382.
(34) Selvam, N. P.; Saranya, S.; Perumal, P. T. *Can. J. Chem.* **2008**, *86*, 32-38.
(35) Philbrook, A.; Blake, C. J.; Dunlop, N.; Easton, C. J.; Keniry, M. A.; Simpson, J. S. *Polymer* **2005**, *46*, 2153-2156.
(36) Germain, J.; Fréchet, J. M. J.; Svec, F. *J. Mater. Chem.* **2007**, *17*, 4989-4997.
(37) Germain, J.; Svec, F.; Fréchet, J. M. J. *Chem. Mater.* **2008**, *20*, 7069-7076.
(38) Germain, J.; Fréchet, J. M. J.; Svec, F. *Chem. Commun.* **2009**, *2009*, 1526-1528.
(39) Kuhn, P.; Antonietti, M.; Thomas, A. *Angew. Chem. Int. Ed.* **2008**, *47*, 3450-3453.
(40) Sing, K. S. W.; Everett, D. H.; Haul, R. A. W.; Moscou, L.; Pierotti, R. A.; Rouquerol, J.;

Siemieniewska, T. *Pure Appl. Chem.* **1985**, *57*, 603–619.
(41) Rouquerol, F.; Rouquerol, J.; Sing, K. *Adsorption by Powders and Porous Solids. Principles, Methodology and Applications*; Academic Press: New York, **1999**.
(42) Lowell, S.; Shields, J. E.; Thomas, M. A.; Thommes, M. *Characterization of Porous Solids and Powders: Surface Area, Pore Size, and Density*; Kluwer Academic Publishers: Dordrecht, **2004**.
(43) Ansón, A.; Benham, M.; Jagiello, J.; Callejas, M. A.; Benito, A. M.; Maser, W. K.; Züttel, A.; Sudan, P.; Martínez, M. T. *Nanotechnology* **2004**, *15*, 1503.
(44) Brunauer, S.; Emmett, P. H.; Teller, E. *J. Am. Chem. Soc.* **1938**, *60*, 309-319.
(45) Langmuir, I. *J. Am. Chem. Soc.* **1918**, *40*, 1361-1403.
(46) Ahn, J. H.; Jang, J. E.; Oh, C. G.; Ihm, S. K.; Cortez, J.; Sherrington, D. C. *Macromolecules* **2006**, *39*, 627-632.
(47) Germain, J.; Hradil, J.; Fréchet, J. M. J.; Svec, F. *Chem. Mater.* **2006**, *18*, 4430-4435.
(48) Wood, C. D.; Tan, B.; Trewin, A.; Niu, H.; Bradshaw, D.; Rosseinsky, M. J.; Khimyak, Y. Z.; Campbell, N. L.; Kirk, R.; Stöckel, E.; Cooper, A. I. *Chem. Mater.* **2007**, *19*, 2034-2048.
(49) Dawson, R.; Su, F.; Niu, H.; Wood, C. D.; Jones, J. T. A.; Khimyak, Y. Z.; Cooper, A. I. *Macromolecules* **2008**, *41*, 1591-1593.
(50) Weitkamp, J. *Solid State Ion.* **2000**, *131*, 175-188.
(51) Ma, Y.; Tong, W.; Zhou, H.; Suib, S. L. *Microporous Mesoporous Mater.* **2000**, *37*, 243-252.
(52) Eddaoudi, M.; Kim, J.; Rosi, N.; Vodak, D.; Wachter, J.; O'Keeffe, M.; Yaghi, O. M. *Science* **2002**, *295*, 469-472.
(53) Kitagawa, S.; Kitaura, R.; Noro, S. *Angew. Chem. Int. Ed.* **2004**, *43*, 2334-2375.
(54) Mastalerz, M. *Angew. Chem. Int. Ed.* **2008**, *47*, 445-447.
(55) Schwab, M. G.; Lennert, A.; Pahnke, J.; Jonschker, G.; Koch, M.; Senkovska, I.; Rehahn, M.; Kaskel, S. *J. Mater. Chem.* **2011**, *21*, 2131-2135.
(56) Wood, C. D.; Tan, B.; Trewin, A.; Su, F.; Rosseinsky, M. J.; Bradshaw, D.; Sun, Y.; Zhou, L.; Cooper, A. I. *Adv. Mater.* **2008**, *20*, 1916-1921.
(57) Menon, V. C.; Komarneni, S. *J. Porous Mater.* **1998**, *5*, 43-58.
(58) Celzard, A.; Albiniak, A.; Jasienko-Halat, M.; Mareché, J. F.; Furdin, G. *Carbon* **2005**, *43*, 1990-1999.
(59) Bourrelly, S.; Llewellyn, P. L.; Serre, C.; Millange, F.; Loiseau, T.; Ferey, G. *J. Am. Chem. Soc.* **2005**, *127*, 13519-13521.
(60) Eddaoudi, M.; Kim, J.; Rosi, N.; Vodak, D.; Wachter, J.; O'Keeffe, M.; Yaghi, O. M. *Science* **2002**, *295*, 469.
(61) Ma, S.; Sun, D.; Simmons, J. M.; Collier, C. D.; Yuan, D.; Zhou, H. C. *J. Am. Chem. Soc.* **2008**, *130*, 1012-1016.
(62) Furukawa, H.; Yaghi, O. M. *J. Am. Chem. Soc.* **2009**, *131*, 8875-8883.
(63) Wegrzyn, J.; Gurevich, M. *Appl. Energy* **1996**, *55*, 71-83.
(64) Sun, Y.; Liu, C.; Su, W.; Zhou, Y.; Zhou, L. *Adsorption* **2009**, *15*, 133-137.
(65) Frère, M. G.; de Weireld, G. F. *Journal of Chemical & Engineering Data* **2002**, *47*, 823-829.
(66) Senkovska, I.; Kaskel, S. *Microporous Mesoporous Mater.* **2008**, *112*, 108-115.
(67) Schlapbach, L.; Züttel, A. *Nature* **2001**, *414*, 353-358.
(68) Züttel, A. *Mater. Today* **2003**, *6*, 24-33.
(69) Zhou, L. *Renewable Sustainable Energy Rev.* **2005**, *9*, 395-408.
(70) Schwab, M. G.; Senkovska, I.; Rose, M.; Klein, N.; Koch, M.; Pahnke, J.; Jonschker, G.; Schmitz, B.; Michael, H.; Kaskel, S. *Soft Matter* **2009**, *5*, 1055-1059.
(71) Pires, J.; Pinto, M. L.; Carvalho, A.; de Carvalho, M. B. *Adsorption* **2003**, *9*, 303-309.
(72) Müller, E. A.; Gubbins, K. E. *Carbon* **1998**, *36*, 1433-1438.
(73) Lovell, P. A.; El-Aasser, M. S. *Emulsion Polymerization and Emulsion Polymers*; J. Wiley & Sons: Chichester, **1997**.
(74) Bibette, J.; Calderon, F. L.; Poulin, P. *Rep. Prog. Phys.* **1999**, *62*, 969.
(75) Landfester, K. *Annu. Rev. Mater. Res.* **2006**, *36*, 231-279.
(76) Landfester, K. *Angew. Chem. Int. Ed.* **2009**, *48*, 4488-4507.
(77) Vandenberg, E. J.; Hulse, G. E. *Ind. Eng. Chem.* **1948**, *40*, 932-937.
(78) Ilium, L.; Davis, S. S.; Wilson, C. G.; Thomas, N. W.; Frier, M.; Hardy, J. G. *Int. J. Pharmacol.* **1982**, *12*, 135-146.
(79) Roy, K.; Mao, H.-Q.; Huang, S. K.; Leong, K. W. *Nat. Med.* **1999**, *5*, 387.
(80) Taton, T. A.; Mirkin, C. A.; Letsinger, R. L. *Science* **2000**, *289*, 1757-1760.
(81) Koch, M.; Stork, M.; Klapper, M.; Mullen, K.; Gregorius, H. *Macromolecules* **2000**, *33*, 7713-7717.

(82) Koch, M.; Falcou, A.; Nenov, N.; Klapper, M.; Müllen, K. *Macromol. Rapid Commun.* **2001**, *22*, 1455-1462.
(83) Müller, K.; Klapper, M.; Müllen, K. *Colloid. Polym. Sci.* **2007**, *285*, 1157-1161.
(84) Müller, K.; Klapper, M.; Müllen, K. *J. Polym. Sci. B, Polym. Lett.* **2007**, *45*, 1101-1108.
(85) Klapper, M.; Nenov, S.; Haschick, R.; Müller, K.; Müllen, K. *Acc. Chem. Res.* **2008**, *41*, 1190-1201.
(86) Nenov, S.; Clark Jr, C. G.; Klapper, M.; Müllen, K. *Macromol. Chem. Phys.* **2007**, *208*, 1362-1369.
(87) Müller, K.; Klapper, M.; Müllen, K. *Macromol. Rapid Commun.* **2006**, *27*, 586-593.
(88) Müller, K.; Park, M. K.; Klapper, M.; Knoll, W.; Müllen, K. *Macromol. Chem. Phys.* **2007**, *208*, 1394-1401.
(89) Periard, J.; Banderet, A.; Riess, G. *J. Polym. Sci. B, Polym. Lett.* **1970**, *8*, 109-114.
(90) Riess, G. *Progr. Polym. Sci.* **2003**, *28*, 1107-1170.
(91) Landfester, K.; Willert, M.; Antonietti, M. *Macromolecules* **2000**, *33*, 2370-2376.
(92) Crespy, D.; Stark, M.; Hoffmann-Richter, C.; Ziener, U.; Landfester, K. *Macromolecules* **2007**, *40*, 3122-3135.
(93) Crespy, D.; Landfester, K. *Polymer* **2009**, *50*, 1616-1620.
(94) Crespy, D.; Landfester, K. *Macromolecules* **2005**, *38*, 6882-6887.
(95) Lee, J. Y.; Wood, C. D.; Bradshaw, D.; Rosseinsky, M. J.; Cooper, A. I. *Chem. Commun.* **2006**, *2006*, 2670-2672.
(96) Schlaad, H.; Kukula, H.; Rudloff, J.; Below, I. *Macromolecules* **2001**, *34*, 4302-4304.
(97) Landfester, K. *Adv. Mater.* **2001**, *13*, 765-768.
(98) Periana, R. A.; Taube, D. J.; Gamble, S.; Taube, H.; Satoh, T.; Fujii, H. *Science* **1998**, *280*, 560.
(99) Conley, B. L.; Tenn Iii, W. J.; Young, K. J. H.; Ganesh, S. K.; Meier, S. K.; Ziatdinov, V. R.; Mironov, O.; Oxgaard, J.; Gonzales, J.; Goddard Iii, W. A. *J. Mol. Catal. A* **2006**, *251*, 8-23.
(100) Palkovits, R.; Antonietti, M.; Kuhn, P.; Thomas, A.; Schüth, F. *Angew. Chem. Int. Ed.* **2009**, *48*, 6909-6912.
(101) Palkovits, R.; von Malotki, C.; Baumgarten, M.; Müllen, K.; Baltes, C.; Antonietti, M.; Kuhn, P.; Weber, J.; Thomas, A.; Schüth, F. *Chem. Sus. Chem.* **2009**, *3*, 277-282.
(102) Zhang, Y.; Riduan, S. N.; Ying, J. Y. *Chem. Eur. J.* **2008**.
(103) Yang, C. J.; Jenekhe, S. A. *Chem. Mater.* **1991**, *3*, 878-887.
(104) Yang, C. J.; Jenekhe, S. A. *Macromolecules* **1995**, *28*, 1180-1196.
(105) Tsai, F. C.; Chang, C. C.; Liu, C. L.; Chen, W. C.; Jenekhe, S. A. *Macromolecules* **2005**, *38*, 1958-1966.
(106) Iwan, A.; Sek, D. *Progr. Polym. Sci.* **2008**, *33*, 289-345.
(107) Sek, D.; Iwan, A.; Jarzabek, B.; Kaczmarczyk, B.; Kasperczyk, J.; Mazurak, Z.; Domanski, M.; Karon, K.; Lapkowski, M. *Macromolecules* **2008**, *41*, 6653-6663.
(108) Niu, H.; Huang, Y.; Bai, X.; Li, X.; Zhang, G. *Mater. Chem. Phys.* **2004**, *86*, 33-37.
(109) Liou, G. S.; Lin, H. Y.; Hsieh, Y. L.; Yang, Y. L. *J. Polym. Sci. A, Polym. Chem.* **2007**, *45*, 4921-4932.
(110) Adell, J. M.; Alonso, M. P.; Barbera, J.; Oriol, L.; Pinol, M.; Serrano, J. L. *Polymer* **2003**, *44*, 7829-7841.
(111) Choi, E. J.; Ahn, J. C.; Chien, L. C.; Lee, C. K.; Zin, W. C.; Kim, D. C.; Shin, S. T. *Macromolecules* **2004**, *37*, 71-78.
(112) Song, L.; Tu, C.; Shi, Y.; Qiu, F.; He, L.; Jiang, Y.; Zhu, Q.; Zhu, B.; Yan, D.; Zhu, X. *Macromol. Rapid Commun.* **2010**, *31*, 443-448.
(113) Higuchi, M.; Shiki, S.; Ariga, K.; Yamamoto, K. *J. Am. Chem. Soc.* **2001**, *123*, 4414-4420.
(114) Yamamoto, K.; Higuchi, M.; Shiki, S.; Tsuruta, M.; Chiba, H. *Nature* **2002**, *415*, 509-511.
(115) Tozawa, T.; Jones, J. T. A.; Swamy, S. I.; Jiang, S.; Adams, D. J.; Shakespeare, S.; Clowes, R.; Bradshaw, D.; Hasell, T.; Chong, S. Y.; Tang, C.; Thompson, S.; Parker, J.; Trewin, A.; Bacsa, J.; Slawin, A. M. Z.; Steiner, A.; Cooper, A. I. *Nat. Mater.* **2009**, *8*, 973-978.
(116) Hasell, T.; Wu, X.; Jones, J. T. A.; Bacsa, J.; Steiner, A.; Mitra, T.; Trewin, A.; Adams, D. J.; Cooper, A. I. *Nat. Chem.* **2010**, *2*, 750-755.
(117) Holst, J. R.; Trewin, A.; Cooper, A. I. *Nat. Chem.* **2010**, *2*, 915-920.
(118) Pandey, P.; Katsoulidis, A. P.; Eryazici, I.; Wu, Y.; Kanatzidis, M. G.; Nguyen, S. B. T. *Chem. Mater.* **2010**, *22*, 4974–4979.
(119) Kudo, A.; Miseki, Y. *Chem. Soc. Rev.* **2009**, *38*, 253-278.
(120) Mills, A.; Hunte, S. L. *J. Photochem. Photobiol., A* **1997**, *108*, 1-36.
(121) Hamza, S. M.; Ramiz, M. M. M.; Aly, I. M. *J. Therm. Anal. Calorim.* **1994**, *42*, 1231-1239.
(122) Khrushcheva, N. S.; Loim, N. M.; Sokolov, V. I. *Russ. Chem. Bull.* **1997**, *46*, 1952-1955.

(123) Kim, H. S.; Moon, K. S.; Jang, D. O. *Supramol. Chem.* **2006**, *18*, 97-101.
(124) Yanagida, S.; Kabumoto, A.; Mizumoto, K.; Pac, C.; Yoshino, K. *J. Chem. Soc., Chem. Commun.* **1985**, *1985*, 474-475.
(125) Shibata, T.; Kabumoto, A.; Shiragami, T.; Ishitani, O.; Pac, C.; Yanagida, S. *J. Phys. Chem.* **1990**, *94*, 2068-2076.
(126) Jiang, D. L.; Choi, C. K.; Honda, K.; Li, W. S.; Yuzawa, T.; Aida, T. *J. Am. Chem. Soc.* **2004**, *126*, 12084-12089.
(127) Osterloh, F. E. *Chem. Mater.* **2008**, *20*, 35-54.
(128) Maeda, K.; Domen, K. *J. Phys. Chem. C* **2007**, *111*, 7851-7861.
(129) Wang, X.; Maeda, K.; Thomas, A.; Takanabe, K.; Xin, G.; Carlsson, J. M.; Domen, K.; Antonietti, M. *Nat. Mater.* **2009**, *8*, 76-80.
(130) Zhang, J.; Chen, X.; Takanabe, K.; Maeda, K.; Domen, K.; Epping, J. D.; Fu, X.; Antonietti, M.; Wang, X. *Angew. Chem. Int. Ed.* **2009**, *49*, 441-444.
(131) Yaghi, O. M.; O'Keeffe, M.; Ockwig, N. W.; Chae, H. K.; Eddaoudi, M.; Kim, J. *Nature* **2003**, *423*, 705-714.
(132) Coté, A. P.; Benin, A. I.; Ockwig, N. W.; O'Keeffe, M.; Matzger, A. J.; Yaghi, O. M. *Science* **2005**, *310*, 1166-1170.
(133) Côté, A. P.; El-Kaderi, H. M.; Furukawa, H.; Hunt, J. R.; Yaghi, O. M. *J. Am. Chem. Soc.* **2007**, *129*, 12914-12915.
(134) Wan, S.; Guo, J.; Kim, J.; Ihee, H.; Jiang, D. *Angew. Chem. Int. Ed.* **2008**, *47*, 8826-8830.
(135) Wan, S.; Guo, J.; Kim, J.; Ihee, H.; Jiang, D. *Angew. Chem. Int. Ed.* **2009**, *48*, 5439 - 5442.
(136) Hunt, J. R.; Doonan, C. J.; LeVangie, J. D.; Co te, A. P.; Yaghi, O. M. *J. Am. Chem. Soc.* **2008**, *130*, 11872-11873.
(137) Tilford, R. W.; Gemmill, W. R.; zur Loye, H. C.; Lavigne, J. J. *Chem. Mater.* **2006**, *18*, 5296-5301.
(138) Tilford, R. W.; Mugavero Iii, S. J.; Pellechia, P. J.; Lavigne, J. J. *Adv. Mater.* **2008**, *20*, 2741-2746.
(139) Kuhn, P.; Thomas, A.; Antonietti, M. *Macromolecules* **2009**, *42*, 319-326.
(140) Kuhn, P.; Krüger, K.; Thomas, A.; Antonietti, M. *Chem. Commun.* **2008**, *2008*, 5815-5817.
(141) Zwaneveld, N. A. A.; Pawlak, R.; Abel, M.; Catalin, D.; Gigmes, D.; Bertin, D.; Porte, L. *J. Am. Chem. Soc.* **2008**, *130*, 6678-6679.
(142) El-Kaderi, H. M.; Hunt, J. R.; Mendoza-Cortes, J. L.; Cote, A. P.; Taylor, R. E.; O'Keeffe, M.; Yaghi, O. M. *Science* **2007**, *316*, 268-272.
(143) Xia, Y.; Mokaya, R. *Adv. Mater.* **2004**, *16*, 1553-1558.
(144) Yang, Z.; Xia, Y.; Sun, X.; Mokaya, R. *J. Phys. Chem. B* **2006**, *110*, 18424-18431.
(145) Zhang, Y.; Liu, C.; Wen, B.; Song, X.; Li, T. *Mater. Lett.* **2011**, *65*, 49-52.
(146) Kim, W.; Joo, J. B.; Kim, N.; Oh, S.; Kim, P.; Yi, J. *Carbon* **2009**, *47*, 1407-1411.
(147) Hulicova, D.; Yamashita, J.; Soneda, Y.; Hatori, H.; Kodama, M. *Chem. Mater.* **2005**, *17*, 1241-1247.
(148) Hulicova-Jurcakova, D.; Kodama, M.; Shiraishi, S.; Hatori, H.; Zhu, Z. H.; Lu, G. Q. *Adv. Funct. Mater.* **2009**, *19*, 1800-1809
(149) Hulicova, D.; Kodama, M.; Hatori, H. *Chem. Mater.* **2006**, *18*, 2318-2326.
(150) Li, W.; Chen, D.; Li, Z.; Shi, Y.; Wan, Y.; Huang, J.; Yang, J.; Zhao, D.; Jiang, Z. *Electrochem. Commun.* **2007**, *9*, 569-573.
(151) Kodama, M.; Yamashita, J.; Soneda, Y.; Hatori, H.; Nishimura, S.; Kamegawa, K. *Mater. Sci. Eng. B* **2004**, *108*, 156-161.
(152) Lota, G.; Frackowiak, E. *Fuel Cells* **2010**, *10*, 848-855.
(153) Pels, J. R.; Kapteijn, F.; Moulijn, J. A.; Zhu, Q.; Thomas, K. M. *Carbon* **1995**, *33*, 1641-1653.
(154) Béguin, F.; Szostak, K.; Lota, G.; Frackowiak, E. *Adv. Mater.* **2005**, *17*, 2380-2384.
(155) Frackowiak, E.; Lota, G.; Machnikowski, J.; Vix-Guterl, C.; Béguin, F. *Electrochim. Acta* **2006**, *51*, 2209-2214.
(156) Kyotani, T.; Sonobe, N.; Tomita, A. *Nature* **1988**, *331*, 331-333.
(157) Mangun, C. L.; Benak, K. R.; Economy, J.; Foster, K. L. *Carbon* **2001**, *39*, 1809-1820.
(158) Hulicova-Jurcakova, D.; Seredych, M.; Lu, G. Q.; Bandosz, T. J. *Adv. Funct. Mater.* **2009**, *19*, 438-447.
(159) Raymundo-Piñero, E.; Cazorla-Amorós, D.; Linares-Solano, A.; Find, J.; Wild, U.; Schlögl, R. *Carbon* **2002**, *40*, 597-608.
(160) Barrett, E. P.; Joyner, L. G.; Halenda, P. P. *J. Am. Chem. Soc.* **1951**, *73*, 373-380.
(161) Paraknowitsch, J. P.; Zhang, J.; Su, D.; Thomas, A.; Antonietti, M. *Adv. Mater.* **2010**, *22*, 87-92.
(162) Conway, B. E. *Electrochemical Supercapacitors: Scientific Fundamentals and Technological Aspects*, **1999**.

(163) Aricò, A. S.; Bruce, P.; Scrosati, B.; Tarascon, J. M.; van Schalkwijk, W. *Nat. Mater.* **2005**, *4*, 366-377.
(164) Burke, A. *J. Power Sources* **2000**, *91*, 37-50.
(165) Kötz, R.; Carlen, M. *Electrochim. Acta* **2000**, *45*, 2483-2498.
(166) Zhang, L. L.; Zhao, X. S. *Chem. Soc. Rev.* **2009**, *38*, 2520-2531.
(167) Simon, P.; Miller, J. R. *Science* **2006**, *321*, 651-652.
(168) Winter, M.; Brodd, R. J. *Chem. Rev* **2004**, *104*, 4245-4270.
(169) Gogotsi, Y.; Simon, P. *Nat. Mater.* **2008**, *7*, 845-854.
(170) Lee, J.; Kim, J.; Hyeon, T. *Adv. Mater.* **2006**, *18*, 2073-2094.
(171) Raymundo-Piñero, E.; Kierzek, K.; Machnikowski, J.; Béguin, F. *Carbon* **2006**, *44*, 2498-2507.
(172) An, K. H.; Kim, W. S.; Park, Y. S.; Choi, Y. C.; Lee, S. M.; Chung, D. C.; Bae, D. J.; Lim, S. C.; Lee, Y. H. *Adv. Mater.* **2001**, *13*, 497-500.
(173) Chmiola, J.; Yushin, G.; Gogotsi, Y.; Portet, C.; Simon, P.; Taberna, P. L. *Science* **2006**, *313*, 1760-1763.
(174) Chmiola, J.; Largeot, C.; Taberna, P. L.; Simon, P.; Gogotsi, Y. *Angew. Chem. Int. Ed.* **2008**, *120*, 3440-3443.
(175) Korenblit, Y.; Rose, M.; Kockrick, E.; Borchardt, L.; Kvit, A.; Kaskel, S.; Yushin, G. *ACS Nano* **2010**, *4*, 1337-1344.
(176) Levi, M. D.; Salitra, G.; Levy, N.; Aurbach, D.; Maier, J. *Nat. Mater.* **2009**, *8*, 872-875.
(177) Stoller, M. D.; Ruoff, R. S. *Energy Environ. Sci.* **2010**, *3*, 1294-1301.
(178) Kajdos, A.; Kvit, A.; Jones, F.; Jagiello, J.; Yushin, G. *J. Am. Chem. Soc.* **2010**, *132*, 3252-3253.
(179) Largeot, C.; Portet, C.; Chmiola, J.; Taberna, P. L.; Gogotsi, Y.; Simon, P. *J. Am. Chem. Soc.* **2008**, *130*, 2730-2731.

6 Conclusion and Outlook

6.1 Macrocycles

Within the scope of the first part of this work, three macrocyclic molecular triangles were successfully synthesized by the *Yamamoto* macrocyclization method (Figure 6-1). The build-up was achieved by cyclotrimerization of shape-persistent precursors which are characterized by a common 120 ° substitution pattern of the halogen groups. From these results it can be judged that other precursors which fulfill the geometric requirement are equally applicable. The range of candidates is greatly extended by the successful macrocyclization of a functional *ortho*-terphenyl as demonstrated in the case of cylco-*nona*-phenylene. Despite the increased flexibility of the starting compound the macrocyclization selectively yielded the target compound. Thus, *ortho*-attachment of benzene-, pyridine- or pyrimidine-units to any desired functional precursor easily creates the 120 ° angle which represents the prerequisite for the success of this method. Possible backbones with interesting properties would be benzo-1,10-phenanthrolines, pyrenes or even larger PAHs such as perylene and HBC.

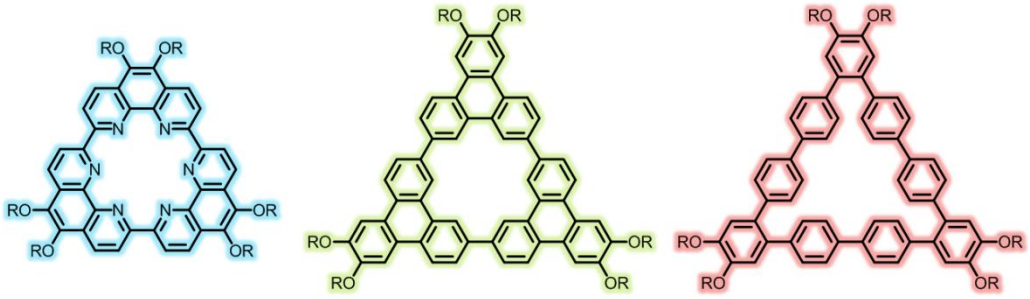

Figure 6-1: The chemical structure of the three macrocycles obtained by *Yamamoto* macrocyclization.

The molecular self-organization of these cyclic trimers was studied and can be correlated to the individual nature of each macrocycle. Hence, in the case of the cyclo-2,9-tris-1,10-phenanthroline macrocycles, the metal sequestration behavior of the hexaaza cavity was investigated in the context of two- and three-dimensional self-assembly. The incorporation of large cationic metal guests with electron-rich counteranions leads to an improved order in the bulk state and greatly determines the supramolecular structures in the two-dimensional case. However, single-crystal analysis of these macrocycles would provide a deeper understanding of the stabilizing role the guest species plays on the *inter*columnar arrangement. Selective transformation of the metal guest into a neutral species by means of chemical or electrochemical reduction offers on the one hand the possibility for the template-assisted fabrication of metallic nanostructures or the addressing of single metal complexes in the context of molecular data storage. The studies presented herein greatly extend the understanding of toroidal macrocycles which are versatile ligands that combine a unique shape and metal sequestration behavior.

The benefits of an increased *π*-surface have been highlighted *via* the introduction of the triphenylene motif. For this discotic macrocycle, strong *inter*molecular packing is a characteristic feature that dominates both the self-assembly in solution and the liquid crystallinity of the mesophase. The tendency towards aggregation was found to be on the same level as seen for HBC derivatives. Still, the cyclo-7,10-tris-triphenylene macrocycle offers interesting optoelectronic properties which have been studied with respect to parent triphenylene and a model compound. It was found that despite the high degree of conjugation the typical signature of monomeric triphenylene reappeared in the spectrum of the macrocycle.

As mentioned above, the successful formation of the cylco-*nona*-phenylene greatly expands the catalogue of possible precursors for the *Yamamoto* macrocyclization. It should also be noted that the macrocycle is accessible through an extremely short and straightforward synthetic route that involves not more than three steps and delivers the cyclic oligoarylene in high yield. The self-assembly of this important class of macrocycles is poorly recognized at present so that the investigations carried out in this study provide a first insight into their supramolecular character.

In the future, the *ortho*-terphenyl design could be easily extended to functionalized *ortho*-quinquephenyls and *ortho*-heptaphenyls in a modular fashion. The resulting triangular macrocycles with their long linear sides would be fascinating model compounds for the understanding of parent poly(*para*-phenylene) and its derivatives. Furthermore, the increased cavity size of such giant cyclic systems would offer the

efficient accommodation of a number of guest species in two-dimensional self-assembly studies

6.2 Graphene Nanoribbons

The application of structurally perfect GNRs to the development of graphene-based electronics is currently widely investigated. The approaches presented in the second part aim at the synthetic bottom-up fabrication of well-defined GNRs both in solution and on surfaces.

Two distinct polycondensation protocols, namely the *Suzuki-Miyaura* and the *Yamamoto* reaction, have been successfully evaluated for the build-up of dendronized poly(*para*-phenylene) precursors and GNRs derived thereof (Figure 6-2). It was found that the *AA*-type *Yamamoto* system is superior to the A_2B_2-type *Suzuki-Miyaura* approach in terms of molecular weight and reproducibility.

This fact is to be considered upon designing new oligophenylene monomers in the future. The laterally extended polymer structures described herein add to the portfolio of solution-based systems which are so far dominated by GNRs of smaller width obtained either by *Diels-Alder* or *Suzuki-Miyaura* approaches.

With respect to the macrocycle synthesis discussed above, the polycondensation results also highlight the enormous synthetic flexibility of the nickel(0) mediated *Yamamoto* cross-coupling protocol.

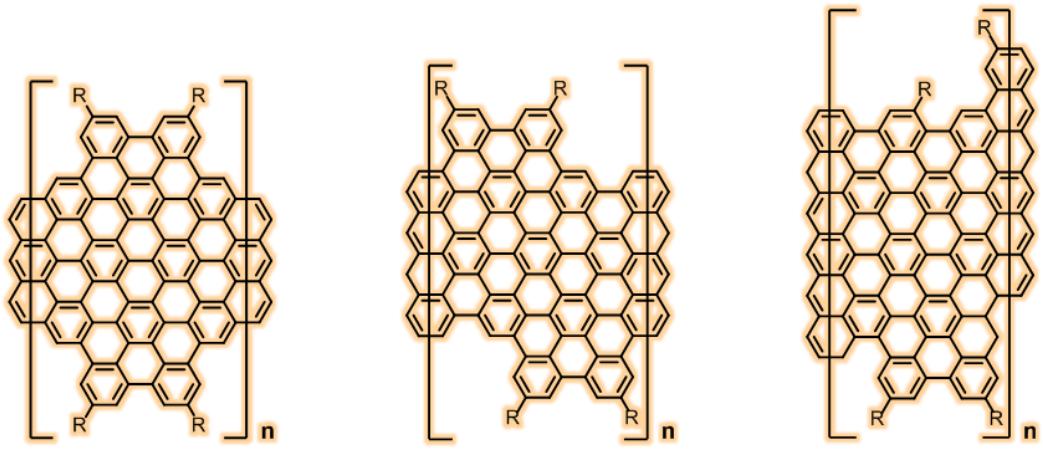

Figure 6-2: The chemical structure of the *Suzuki*- and *Yamamoto*-based GNRs.

As characterization and processing of graphene materials from solution still suffer from their inherent insolubility, other strategies of structure proof need to be established. In this respect, the synthesis of large PAHs with aromatic cores that

exactly correspond to the spatial arrangement of the benzene units of the parent polymeric precursors was found a powerful tool. Following this concept, well-soluble **C78** and **C84** discs could be prepared and characterized (Figure 6-3). On a smaller scale traditional solution-based analytical methods can be applied even though the exceptional importance of the NMR proof in the case of the **C78** disc shall be emphasized.

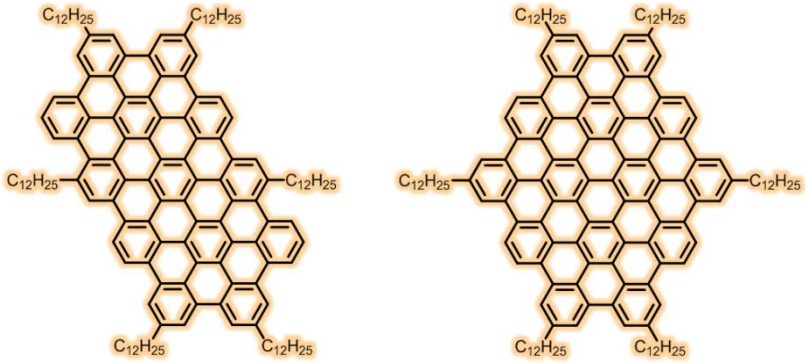

Figure 6-3: The chemical structure of the **C78** and **C84** discs.

Inspired by the design of the solution-based monomers, rigidified oligophenylene precursors were synthesized and subjected to an STM-controlled surface polymerization and cyclodehydrogenation protocol. The results obtained suggest that the surface-assisted *in-situ* fabrication of atomically-precise GNRs has the potential to further spur the application of graphene materials in physics and material science. For this, however, the transfer of the process to a non-conductive support constitutes an important task to be addressed.

Regarding the design and properties of the GNRs themselves a number of synthetic challenges remain. Band gap tuning can be achieved by the control of the width of the nanoribbons. Thus, still larger oligophenylene monomers can be thought of that would rely on G2-type dendrons. On the other hand smaller poly(acene)- or poly(*peri*acene)-type GNRs need to be developed. Also the introduction of heteroatoms such as boron or nitrogen will greatly affect the type of semi-conductor that is obtained. In the present case exchange of biphenyl by bipyridine would allow for the synthesis of identical structures that contain however heteroatoms at precise positions and in defined amounts. Routes towards the synthesis of GNRs and nanographenes with zigzag-peripheries will open new fields of graphene chemistry.

However, all these intriguing properties can only be accessed if novel ways of processing are introduced into the field of GNR synthesis. Large-scale device manufacturing will only be possible if a poorly soluble graphene material that has

been created either in solution or on a surface can be efficiently transferred to the desired substrate.

6.3 Networks

The build-up of three-dimensional polymer networks through *Schiff* base reactions was studied in the last chapter of the work. Derived from a catalyst-free condensation approach, the materials obtained by reaction of amines with aldehydes are not contaminated with inorganic reaction by-products or remains and are structurally well-defined as evidenced by solid-state spectroscopy (Figure 6-4).

When melamine was used as a crosslinker, poly(aminal) networks were obtained which were found to exhibit an enhanced intrinsic porosity reaching 1400 m^2/g for the best sample. Taking into account the good availability of the starting compounds, true "low-cost" materials are accessible which allow for a possible large-scale application of these novel high-surface networks. The same argument holds for the transfer of the network synthesis to a high-temperature non-aqueous miniemulsion approach that allows for the efficient management of process parameters such as heat and viscosity that become relevant upon up-scaling. At the same time an unprecedented control over the morphology of microporous polymer networks has been demonstrated. The significant challenges met during the transfer of the bulk synthesis to an emulsion protocol could be overcome by carefully tailoring the process parameters. In principle, this approach could now be applied to other water-sensitive protocols suitable for the bulk synthesis of highly crosslinked porous polymers. Possible examples involve network formation through *Sonogashira-Hagihara* or *Friedel-Crafts* chemistry.

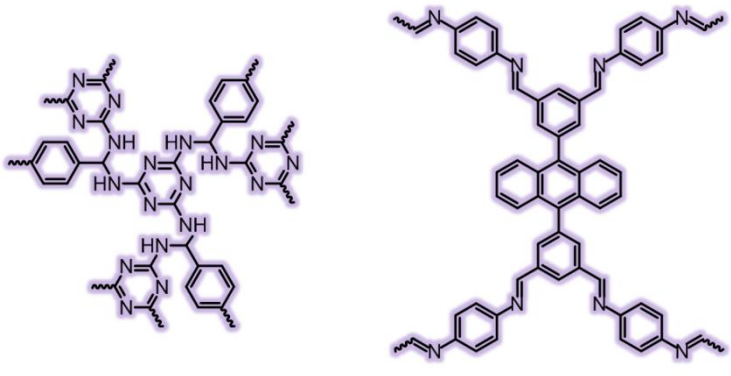

Figure 6-4: Representative structures of the poly(aminal) and poly(azomethine) networks.

The high versatility of the microporous poly(aminal) networks is highlighted by studies addressing their gas uptake behavior and the use of their amine-decorated surfaces for catalyst immobilization. These basic sites offer further potential if the material is applied as a filter in the removal of acidic species such as hydrogen cyanide or phosgene from exhaust streams. The surface-bound acid-base pairs thus formed would lead to an immobilization of the toxic species. Once the adsorbent has been saturated with the acidic guest it could be regenerated *via* controlled outgassing at elevated temperature.

Furthermore, the poly(aminal) networks can be utilized as a precursor for the template-free fabrication of nitrogen-enriched mesoporous carbons which showed outstanding electrochemical performance during capacitive testing. A gravimetric capacitance of 381 F/g was measured which remained constant upon long-term testing. Apart from the high nitrogen content, the chemical nature of the nitrogen sites has a strong impact on the final performance of the material. The results obtained in this study suggest that the carbons derived from the poly(aminal) precursor could also be used as metal-free catalysts in the reduction of oxygen in fuel cell applications or as electrode component in battery systems. Future studies must reveal the exact nature of the nitrogen sites which are embedded into the carbon matrix. The tracking of the nitrogen atoms could be easily done by introducing isotope-labeled melamine into the synthesis of the polymeric poly(aminal) precursor.

Yet another class of polymer networks accessible by *Schiff* base chemistry are three-dimensional poly(azomethines). These were synthesized from the condensation of multivalent aromatic amines and aldehydes. Due to their fully conjugated backbone, these materials were evaluated as truly organic catalysts in the photocatalytic production of hydrogen. In this experimental study it could be illustrated how the electronic properties of a conjugated polymer network can be adjusted to the redox window of water *via* systematic variation of the co-monomer component. Taking into account that the number of organic semiconductors in photocatalysis is mainly limited to structurally poorly defined carbon nitride structures, the enhanced catalytic activity of the poly(azomethine) networks constitutes an important step forward. In this case precise chemical tailoring can be used to further enhance the catalytic activity which is still lower than that of benchmark inorganic semiconductors.

The same holds for the generation of porosity in imine-linked polymer networks. Only few literature examples are known due to the difficulty to prevent the re-aggregation of the chain segments. However, the reversibility of the underlying condensation reaction in principle enables the pathway towards enhanced structural perfection. This could be confirmed in the present case when a specially developed anthracene-

crosslinker allowed for the build-up of a highly crystalline covalent organic poly(azomethine) framework. A unique porous sheet-like structure could be confirmed by a set of analytical tools. However, computer modeling would provide a definite answer regarding the type of packing adopted by the material.

7 Experimental Part

7.1 General Methods

7.1.1 Chemicals and Solvents

All chemicals and solvents used were obtained from the companies ABCR, Acros, Aldrich, Alpha-Aesar, Fluka, Lancaster, Merck and Strem. Unless otherwise mentioned, they were used as obtained.

7.1.2 Chromatography

Preparative column chromatography was performed on silica gel from Merck with a grain size of 63.0 - 200.0 µm (silica gel) or 40.0 - 63.0 µm (flash silica gel).
For analytical thin layer chromatography (TLC), silica gel coated substrates (60 F254) from Merck were used. Compounds were detected by fluorescence quenching at 254 nm, self-fluorescence at 366 nm or staining in an iodine vapor chamber. For eluents, analytically pure solvents were used.
Recycling gel permeation chromatography (rGPC) was performed on a JAI LC-9101 equipped with JAI PS GPC columns using chloroform as eluent at room temperature.

7.1.3 Inert Atmosphere

Oxygen or moisture sensitive reactions were carried out in an argon atmosphere (grade 4.8, Westfalen AG). If not mentioned specifically, reactions were degassed by bubbling a stream of argon through the reaction mixture.

7.2 Analytical Techniques

7.2.1 Mass Spectroscopy (MS/MALDI-TOF)

Field-desorption mass spectra were obtained on a VG Instruments ZAB 2-SE-FPD spectrometer.
MALDI-TOF spectroscopy was conducted on a Bruker Reflex II-TOF spectrometer, utilizing a 337 nm nitrogen laser. If not specifically mentioned, tetracyanoquinodimethane (TCNQ) was used as the matrix substance for solid state preparation. Else, the samples were directly measured from chloroform or THF by drop-casting the solution on the sample holder.

7.2.2 NMR Spectroscopy

^{1}H-NMR, ^{13}C-NMR, H,H-COSY, C,H-COSY and NOESY experiments were recorded in the listed deuterated solvents on a Bruker DPX 250, Bruker AMX 300, Bruker DRX 500 or a Bruker DRX 700 spectrometer. The deuterated solvent was used as an internal standard, CD_2Cl_2 was set to δ_H = 5.32 ppm and δ_C = 54.00 ppm, THF to δ_H = 3.58 ppm and δ_C = 67.57 ppm, $CDCl_3$ to δ_H = 7.24 ppm and δ_C = 77.23 ppm and $C_2D_2Cl_4$ to δ_H = 5.91 ppm and δ_C = 74.20 ppm.[1]

7.2.3 Solid State NMR Spectroscopy

Solid-state ^{13}C[^{1}H] cross-polarization (CP) NMR spectra were recorded on a Bruker DSX instrument equipped with a 11.4 T wide bore magnet and a commercial 2.5 mm MAS double ^{1}H-X probe operating at a ^{13}C *Larmor* frequency of 125.7 MHz, 25.0 kHz magic angle spinning (MAS) frequency and 3.0 ms CP contact time.
The ^{15}N[^{1}H] cross-polarization spectra were obtained on a Bruker Avance II console operating at a ^{15}N *Larmor* frequency of 30.4 MHz, 10.0 kHz angle spinning (MAS) and 7.0 ms CP contact time.
The samples were packed in zirconia rotors with 4.0 mm outer diameter.
Both, ^{13}C and ^{15}N NMR spectra were referenced with respect to tetramethyl silane[2] using adamantane[3] (^{13}C, 29.456 ppm) and nitromethane[4] (^{15}N, - 358.4 ppm) as secondary standards. All spectra were acquired at room temperature accumulating 6000 (for ^{13}C) and 30000 (for ^{15}N) scans.

7.2.4 Elemental Combustion Analysis (ECA)

Elemental analysis of solid samples was carried out on a Foss Heraeus Vario EL at the Institute for Organic Chemistry (Johannes Gutenberg University Mainz).
All samples were exhaustively dried under high vacuum prior to the analysis in order to remove possible remains of solvents and humidity. Still, minor aberrations from the theoretic value were observed in particular for those samples bearing liquid-like alkyl or alkoxy substituents and those containing a dendritic oligophenylene backbone. The entrapment of solvent molecules, in particular *ortho*-xylene, is a common phenomenon in the analysis of these substances.[5]

7.2.5 Optical Spectroscopy

Solution UV-vis spectra were recorded at room temperature on a Perkin-Elmer Lambda 100 spectrophotometer. The molar extinctions are given in the unit $M^{-1}cm^{-1}$ or were normalized for better comparison of different samples. Solvents of spectroscopic grade were employed. The baseline was corrected by substracting a measurement of the cuvette filled with pure solvent used for the measurement. Solution photoluminescence spectra were recorded at room temperature on a SPEX-Fluorolog II (212) spectrometer. Solutions of different concentration were compared to study the aggregation behavior. Solvents of spectroscopic grade were employed.

7.2.6 Infrared Spectroscopy (FTIR)

Infrared spectroscopy was measured on a Nicolet 730 FT-IR spectrometer equipped with an attenuated total reflection (ATR) setup. The samples were deposited as pristine material on the diamond crystal and pressed on it with a stamp. Measurements with a scan number of 128 were recorded for each sample, the background was subtracted.

7.2.7 Raman Spectroscopy

Raman spectra were recorded on a Bruker RFS100/s using a laser wavelength of 1066 nm (400 mW).

7.2.8 Analytical Gel Permeation Chromatography (GPC)

Analytical gel permeation chromatography (GPC) was performed on SDV PSS GPC columns using THF as eluent at a temperature of 303 K. The refractive index was determined on a RI ERC 7512 detector (ERMA). Absorbance was determined on a UV S-3702 detector (SOMA) at a fixed wavelength of 270 nm. The samples were referenced with respect to standard PS and PPP calibration curves.

7.2.9 Two-Dimensional Wide-Angle X-Ray Scattering (2D-WAXS)

The two-dimensional wide-angle X-ray diffraction experiments of orientated filaments were performed by means of a rotating anode (Rigaku 18 kW) X-ray beam with a pinhole collimation and a 2D Siemens detector with a beam diameter of 1.0 mm. A double graphite monochromator for the Cu-K_α radiation (λ = 0.154 nm) was used. The patterns were recorded with vertical orientation of the filament axis and with the beam perpendicular to the filament.

7.2.10 Single Crystal X-Ray Analysis

The single crystal analysis was performed on a Nonius-KCCD diffractometer with a Mo-K_α (λ = 0.072 nm, graphite monochromatized) at a temperature of 150 K. The structures were solved by direct methods (Shelxs) and refined with anisotropic temperature factors for all non-hydrogen atoms. The hydrogen atoms were refined with fixed isotropic temperature factors in the riding mode.

7.2.11 Polarized optical microscopy (POM)

Optical textures were investigated using a Zeiss polarizing optical microscope (equipped with digital temperature control system UNKAM TMS 591. The samples were sandwiched between glass slides to form a thin film and were afterwards heated above the melting point using a heating stage. The images were recorded between cross-polarizers.

7.2.12 Thermogravimetric analysis (TGA)

Thermogravimetric analysis data was acquired on a Mettler TGA/SDTA 851e at a heating rate of 10 K/min under a nitrogen atmosphere.

7.2.13 Differential Scanning Calorimetry (DSC)

Differential scanning calorimetry (DSC) was measured on a Mettler DSC 30 with heating and cooling rates of 10 K/min. The peak values of the second heating cycle were given to exclude influences from the thermal history.

7.2.14 Scanning Electron Microscopy (SEM)

The measurements were performed on Zeiss LEO 1530 or Hitachi SU8000 field emission scanning electron microscopes.

7.2.15 Transition Electron Microscopy (TEM)

The measurements were carried out on Philips EM 420 or Philips Tecnai F20 transmission electron microscopes.

7.2.16 Nitrogen Adsorption

Nitrogen adsorption experiments and micropore analysis were conducted at 77 K using an Autosorb-1 from Quantachrome. Prior to the measurements, the samples were degassed at 423 K for 12 h. BET surface areas, NLDFT and BJH pore-size distributions were determined using the Quadrawin software. Pore volumes at $p/p_0 = 0.1$ and $p/p_0 = 0.8$ were converted into the corresponding liquid volumes using a nitrogen density of $1.25 \cdot 10^{-3}$ g/cm^3 (gaseous) and $8.10 \cdot 10^{-1}$ g/cm^3 (liquid).

7.2.17 Hydrogen Adsorption

Hydrogen adsorption experiments were conducted at 77 K using an Autosorb 1C from Quantachrome. Prior to the measurements, the samples were degassed at 423 K for 12 h. Gravimetric storage capacities were calculated using a hydrogen density of $8.99 \cdot 10^{-5}$ g/cm^3 (gaseous).

7.2.18 Methane Adsorption

High-pressure methane adsorption measurements were conducted at room temperature using a Rubotherm magnetic suspension balance. Prior to the

measurements, the samples were degassed at 423 K for 12 h. The buoyancy correction was performed according to the literature.[6]

7.2.19 Water Adsorption

Water adsorption isotherms were conducted at room temperature using a Quantachrome Hydrosorb 1000. Prior to the measurements, the samples were degassed at 423 K for 12 h.

7.2.20 Photocatalytic Measurements

The photocatalytic reactions were carried out in a Pyrex top-irradiation reaction vessel connected to a glass closed gas circulation system. H_2 production was performed by dispersing 100.0 mg of the polymer material in 100.0 ml of an aqueous solution containing triethanolamine (10 vol%). For the deposition of platinum, an appropriate amount of H_2PtCl_6 was dissolved in the catalyst solution. The solution was evacuated several times to remove air completely prior to irradiation under a 300 W xenon lamp and a water filter. The wavelength of the incident light ($\lambda > 300$ nm) was controlled by using a cut-off filter. The temperature of the reactant solution was maintained at room temperature by a flow of cooling water during the reaction. The evolved gases were analyzed by gas chromatography.

7.2.21 Electrochemical Measurements

Electrochemical characterizations were conducted on an EG&G potentiostat/galvanostat Model 2273 advanced electrochemical system. A conventional cell with a three-electrode configuration was employed. The working electrode was prepared by mixing the **SNW** carbon material with carbon black (Mitsubishi Chemicals) in an agate mortar until a homogeneous black powder was obtained. Then, a PTFE binder (60 % in water, Sigma-Aldrich) was added. The weight ratio of the three components was set to 80:10:10 based on the solid content. After brief evaporative drying in air, the resulting paste was pressed at 5.0 MPa to a nickel mesh (KOH electrolyte) or stainless steel gauze (H_2SO_4 electrolyte) with a stainless wire for electric connection. The electrode assembly was dried for 16 h at 80 °C in air. Each electrode contained 3.0 - 5.0 mg active material on a surface area of about 1.0 cm^2. A platinum foil was applied as a counter electrode with a standard calomel electrode or an Ag/AgCl electrode as a reference electrode. The experiments were carried out in

nitrogen saturated 1 M H_2SO_4 or 1 M KOH solutions. Cyclic voltammetry (CV) was performed by polarizing the working electrode between - 1.00 V to 0.00 V (SCE) or - 0.05 to + 0.95 V (Ag/AgCl) at different scan rates between 10 - 200 mV/s. Prior to the CV measurements, the working electrode was kept at the open potential for 30 min. The galvanostatic charging-discharging of the working electrodes was measured in a potential range between - 1.00 to 0.00 V (SCE) or - 0.05 to + 0.95 V (Ag/AgCl) at different current densities (2.0 - 10.0 A/g), which were calculated on the basis of the weight of each electrode. All measurements were performed at room temperature.

7.3 Macrocycle Synthesis

7.3.1 6,7-Dihydro-5H-[1,4]diazepino[1,2,3,4-lmn][1,10]phenanthroline-4,8-diium dibromide (3-6)[7]

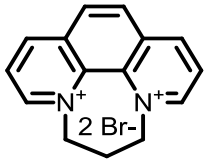

5.00 g (27.75 mmol) 1,10-phenanthroline were dissolved in 25.51 g (123.82 mmol) of 1,3-dibromopropane and heated to 120 °C for 4 h. The yellow precipitate was dissolved in water and washed three times with DCM in order to remove residues of the starting compounds. The aqueous phase was evaporated under reduced pressure to yield 10.02 g (26.36 mmol) of a yellow powder in 95 %. **3-6** was used for the next step without further purification.

^{1}H-NMR (250 MHz, D_2O): δ 9.65 (d, J = 5.8, 2H), 9.44 (d, J = 8.5, 2H), 8.58 (s, 2H), 8.53 (dd, J = 8.5, 5.6, 2H), 5.14 (t, J = 6.9, 4H), 3.42 (p, J = 7.0, 2H).

^{13}C-NMR (75 MHz, D_2O): δ 164.23, 150.85, 147.33, 134.09, 130.23, 127.30, 60.37, 30.89.

Elemental Analysis: found 46.40 % C, 3.75 % H, 7.45 % N - calc. 47.15 % C, 3.69 % H, 7.33 % N.

7.3.2 6,7-Dihydro-3H-[1,4]diazepino[1,2,3,4-lmn][1,10]phenanthroline-3,9(5H)-dione (3-7)[7]

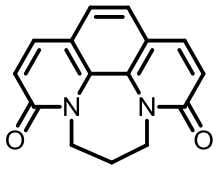

70.82 g (210.78 mmol) of potassium ferricyanide and 32.35 g (0.79 mol) of sodium hydroxide were mixed with 120.0 ml of H_2O after what the resulting red-brown suspension was cooled to 0 °C. 9.00 g (23.55 mmol) of **3-6** suspended in 80.0 ml of

water were added drop-wise under continuous stirring keeping the temperature of the mixture below 5 °C. After 2 h, the reaction mixture was carefully neutralized with concentrated hydrochloric acid and the resulting precipitate was collected. The aqueous phase was removed under reduced pressure. The inorganic residue was extracted with THF for 72 h to yield in total 2.44 g (9.66 mmol) of **3-7** as a yellow powder in 41 %.

^{1}H-NMR (250 MHz, CD_2Cl_2): δ 7.72 (d, J = 9.5, 2H), 7.36 (s, 2H), 6.73 (d, J = 9.4 Hz, 2H), 4.27 (t, J = 6.4, 4H), 2.38 (p, J = 6.6, 2H).

^{13}C-NMR (75 MHz, CD_2Cl_2): δ 162.94, 139.27, 132.78, 123.46, 123.34, 123.09, 46.07, 26.30.

MS (FD, 8kV): m/z (%) = 252.8 (100.0 %, M^+), (calc. $C_{15}H_{12}N_2O_2$ = 252.27 g/mol).

Elemental Analysis: found 66.98 % C, 4.94 % H, 11.24 % N - calc. 71.42 % C, 4.79 % H, 11.10 % N.

7.3.3 2,9-Dichloro-1,10-phenanthroline (3-8)[7]

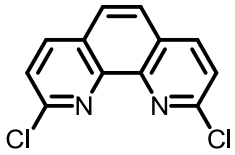

1.50 g (5.95 mmol) of **3-7** and 2.65 g (12.73 mmol) of phosphorus pentachloride were dispersed in 18.0 ml of phosphoryl chloride. The turbid mixture was heated to reflux for 8 h to yield a brown solution. After cooling, the reaction mixture was slowly added to 150.0 ml of an acidified ice/water mixture. After complete hydrolysis, the aqueous phase was brought to pH = 14 by slow addition of NaOH. The resulting precipitate was collected and the aqueous phase extracted several times with DCM. The crude product was purified by column chromatography (ethyl acetate/hexane = 1/1) to yield 1.19 g (4.78 mmol) of **3-8** as an off-white powder in 82 %.

^{1}H-NMR (250 MHz, CD_2Cl_2): δ 8.26 (d, J = 8.4, 2H), 7.87 (s, 2H), 7.66 (d, J = 8.4, 2H).
^{13}C-NMR (75 MHz, CD_2Cl_2): δ 151.90, 145.42, 139.54, 128.46, 126.84, 125.18.

MS (FD, 8kV): m/z (%) = 250.1 (100.0 %, M^+), (calc. $C_{12}H_6Cl_2N_2$ = 249.10 g/mol).

Elemental Analysis: found 57.94 % C, 2.39 % H, 11.35 % N - calc. 57.86 % C, 2.43 % H, 11.25 % N.

7.3.4 2,9-Dichloro-1,10-phenanthrolin-5,6-dione (3-9)[8]

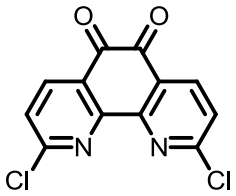

1.00 g (5.85 mmol) of **3-8** and 4.77 g (40.08 mmol) of potassium bromide were mixed and cooled in a flask with gas outlet to - 5 °C. 14.0 ml of concentrated H_2SO_4 were added slowly always keeping the temperature of the mixture below 0 °C. To the orange viscous mixture were slowly added 7.0 ml of concentrated nitric acid. Subsequently, the reaction mixture was heated to 80 °C for 3 h. Bromine vapours were passed through a 10 % solution of sodium thiosulfate. After cooling, the reaction mixture was added to 200.0 ml of an ice/water mixture and stirred for 2 h at room temperature. The yellow-orange precipitate was collected and washed with H_2O and treated with an aqueous solution of sodium thiosulfate. 1.43 g (5.15 mmol) of **3-9** were obtained and used for the next step without further purification (88 %).

^{1}H-NMR (250 MHz, CD_2Cl_2): δ 8.42 (d, J = 8.2, 2H), 7.63 (d, J = 8.2, 2H).

^{13}C-NMR (75 MHz, CD_2Cl_2): δ 177.83, 159.06, 158.21, 152.76, 140.16, 127.70.

MS (FD, 8kV): m/z (%) = 278.8 (100.0 %, M^+), (calc. $C_{12}H_4Cl_2N_2O_2$ = 279.08 g/mol).

7.3.5 2,9-Dichloro-5,6-bis(octyloxy)-1,10-phenanthroline (3-10a)

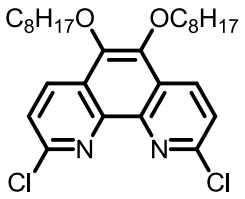

To a mixture of 10.0 ml water and 10.0 ml THF 0.50 g (1.81 mmol) of **3-9**, 0.38 g (1.17 mmol) tetra-*n*-butylammonium bromide and 1.89 g (10.83 mmol) sodium dithionite were added. Then, 1.15 g (6.00 mmol) octyl bromide was added to the mixture. A solution of 1.50 g (27.07 mmol) of potassium hydroxide in 10.0 ml water was subsequently added after what the reaction mixture turned black. The reaction mixture was stirred for 48 h at 40 °C. After dilution with water, the reaction mixture was extracted with ethyl acetate. The crude product was purified by column chromatography (DCM/ethyl acetate = 50:1) to yield 0.55 g (1.09 mmol) of **3-10a** in 60 % as a light yellow powder.

^{1}H-NMR (300 MHz, CD_2Cl_2): δ 8.53 (d, J = 8.6, 2H), 7.64 (d, J = 8.6, 2H), 4.23 (t, J = 6.7, 4H), 1.86 (p, J = 6.8, 2H), 1.62 - 1.22 (m, 20H), 0.88 (t, J = 6.9, 6H).

^{13}C-NMR (75 MHz, CD_2Cl_2): δ 150.81, 143.21, 143.08, 134.30, 126.44, 124.93, 74.78, 32.40, 30.85, 29.99, 29.82, 26.69, 23.23, 14.43.

MS (FD, 8kV): m/z (%) = 503.8 (100.0 %, M^+), (calc. $C_{28}H_{38}Cl_2N_2O_2$ = 505.52 g/mol).

7.3.6 2,9-Dichloro-5,6-bis(dodecyloxy)-1,10-phenanthroline (3-10b)

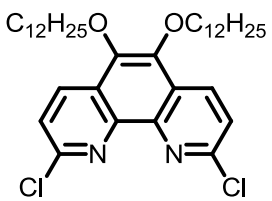

To a mixture of 10.0 ml water and 10.0 ml THF 1.00 g (3.61 mmol) of **3-9**, 0.75 g (2.33 mmol) tetra-*n*-butylammonium bromide and 3.77 g (21.66 mmol) sodium dithionite were added. Then, 3.0 g (12.0 mmol) dodecyl bromide was added to the

mixture. A solution of 3.0 g (54.15 mmol) of potassium hydroxide in 20.0 ml water was subsequently added after what the reaction mixture turned black. The reaction mixture was stirred for 48 h at 40 °C. After dilution with water, the reaction mixture was extracted with ethyl acetate. The crude product was purified by column chromatography (DCM/ethyl acetate = 50:1) to yield 1.49 g (2.41 mmol) of **3-10b** in 67 % as a light yellow powder.

^{1}H-NMR (250 MHz, CD_2Cl_2): δ = 8.53 (d, J = 8.6, 2H), 7.64 (d, J = 8.6, 2H), 4.22 (t, J = 6.7, 4H), 1.86 (p, J = 7.0, 4H), 1.61 - 1.10 (m, 36H), 0.87 (t, J = 6.9, 6H).

^{13}C-NMR (75 MHz, CD_2Cl_2): δ 150.79, 143.19, 143.07, 134.27, 126.41, 124.91, 74.76, 32.51, 30.86, 30.27, 30.24, 30.21, 30.19, 30.05, 29.95, 26.71, 23.28, 14.46.

MS (FD, 8kV): m/z (%) = 616.1 (100.0 %, M^+), (calc. $C_{36}H_{54}Cl_2N_2O_2$ = 617.73 g/mol).

Elemental Analysis: found 67.58 % C, 9.98 % H, 4.13 % N - calc. 70.00 % C, 8.81 % H, 4.53 % N (see general remarks "7.2.4 Elemental Combustion Analysis").

7.3.7 2,9-Dichloro-5,6-bis(hexadecyloxy)-1,10-phenanthroline (3-10c)

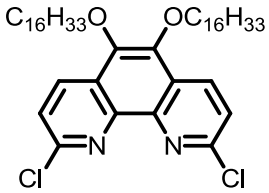

To a mixture of 8.0 ml water and 8.0 ml THF 0.40 g (1.43 mmol) of **3-9**, 0.30 g (0.93 mmol) tetra-*n*-butylammonium bromide and 1.50 g (8.60 mmol) sodium dithionite were added. Then, 1.46 g (4.76 mmol) hexadecyl bromide was added to the mixture. A solution of 1.19 g (21.50 mmol) of potassium hydroxide in 8.0 ml water was subsequently added after what the reaction mixture turned black. The reaction mixture was stirred for 48 h at 40 °C. After dilution with water, the reaction mixture was extracted with ethyl acetate. The crude product was purified by column chromatography (DCM/ethyl acetate = 50:1) to yield 0.71 g (0.97 mmol) of **3-10c** in 68 % as a light yellow powder.

^{1}H-NMR (300 MHz, CD_2Cl_2): δ 8.53 (d, J = 8.6, 2H), 7.64 (d, J = 8.6, 2H), 4.22 (t, J = 6.7, 4H), 1.88 (p, J = 7.0, 4H), 1.60 - 1,12 (m, 52H), 0.87 (t, J = 6.9, 6H).

^{13}C-NMR (75 MHz, CD_2Cl_2): δ 150.81, 143.21, 143.09, 134.30, 126.43, 124.93, 74.78, 32.50, 30.85, 30.28, 30.25, 30.24, 30.20, 30.17, 30.03, 29.94, 26.69, 23.27, 14.45.
MS (FD, 8kV): m/z (%) = 728.0 (100.0 %, M^+), (calc. $C_{44}H_{70}Cl_2N_2O_2$ = 729.94 g/mol).

7.3.8 6,9-Dichloro-2,2-dimethyl-[1,3]dioxolo[4,5-f][1,10] phenanthroline (3-11)[9]

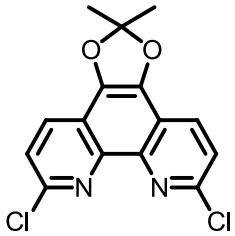

1.00 g (3.58 mmol) of **3-9** and 3.20 g (34.8 mmol) of 2-nitropropane were dissolved in 300.0 ml of acetonitrile. Then, 300.0 of an aqueous solution containing 3.00 g (2.31 mmol) of potassium carbonate was added. The reaction mixture was degassed by argon bubbling and heated to 55 °C for 24 h under an inert atmosphere. After cooling, the mixture was extracted with DCM and the crude product was purified by column chromatography (hexane/ethyl acetate = 1:1) to yield 0.75 g (2.33 mmol) of **3-11** in 65 % as yellow-greenish powder.

^{1}H-NMR (300 MHz, CD_2Cl_2): δ 8.22 (d, J = 8.6, 2H), 7.63 (d, J = 8.6, 2H), 1.86 (s, 6H).
^{13}C-NMR (75 MHz, CD_2Cl_2): δ 148.67, 140.47, 137.05, 131.08, 124.27, 121.88, 117.12, 25.74.

MS (FD, 8kV): m/z (%) = 320.1 (100.0 %, M^+), (calc. $C_{15}H_{10}Cl_2N_2O_2$ = 321.16 g/mol).

Elemental Analysis: found 56.20 % C, 3.33 % H, 9.38 % N - calc. 56.10 % C, 3.14 % H, 8.72 % N.

7.3.9 5,6-Bis(dodecyloxy)-1,10-phenanthroline (3-17)

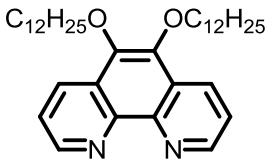

To a mixture of 13.0 ml water and 13.0 ml THF 0.50 g (2.38 mmol) of 1,10-phenanthroline-5,6-dione, 0.49 g (1.54 mmol) tetra-*n*-butylammonium bromide and 2.48 g (14.27 mmol) sodium dithionite were added. Then, 1.98 g (7.91 mmol) dodecyl bromide was added to the mixture. A solution of 1.98 g (35.68 mmol) of potassium hydroxide in 13.0 ml water was subsequently added after what the reaction mixture turned deep red. The reaction mixture was stirred for 48 h at 40 °C. After dilution with water, the reaction mixture was extracted with ethyl acetate. The crude product was purified by column chromatography (DCM/ethyl acetate = 50:1) to yield 0.49 g (0.91 mmol) of **3-17** in 59 % as a light yellow powder.

^{1}H-NMR (250 MHz, CD_2Cl_2): δ 9.04 (dd, J = 1.7, 4.3, 2H), 8.57 (d, J = 8.3, 2H), 7.71 (dd, J = 4.3, 8.3, 2H), 4.23 (t, J = 6.7, 4H), 1.89 (p, J = 6.8, 4H), 1.61 - 1.10 (m, 36H), 0.88 (t, J = 6.6, 6H).

^{13}C-NMR (75 MHz, CD_2Cl_2): δ 149.41, 144.98, 142.84, 130.77, 127.01, 123.35, 74.52, 32.52, 30.96, 30.66, 30.27, 30.24, 30.22, 30.09, 29.95, 26.78, 23.28, 14.45.

MS (FD, 8kV): m/z (%) = 548.1 (100.0 %, M^+), (calc. $C_{36}H_{56}N_2O_2$ = 548.84 g/mol).

7.3.10 2,2-Dimethyl-[1,3]dioxolo[4,5-f][1,10]phenanthroline (3-18)[9]

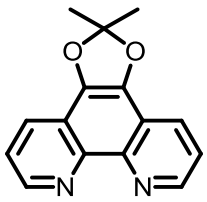

0.30 g (1.42 mmol) of 1,10-phenanthroline-5,6-dione was suspended in 300.0 ml of acetonitrile. Then 0.53 g (6.04 mmol) of 2-nitropropane was added. The mixture was degassed by argon bubbling and then 3.0 ml of a methanolic tetrabutylammonium

hydroxide solution (25 wt%) was added. The resulting mixture was heated to 60 °C for 72 h under an inert atmosphere. After removal of the solvent under reduced pressure the crude product was purified by column chromatography (ethyl acetate/methanol = 9/1) to yield 0.22 g (0.87 mmol) of **3-18** in 61 % as yellow solid.

^{1}H-NMR (300 MHz, CD_2Cl_2): δ 9.01 (dd, J = 1.8, 4.3, 2H), 8.24 (dd, J = 1.8, 8.2, 2H), 7.61 (dd, J = 4.3, 8.2, 2H), 1.86 (s, 6H).

^{13}C-NMR (75 MHz, CD_2Cl_2): δ 148.23, 143.07, 136.94, 128.23, 123.22, 121.41, 119.01, 26.32.

MS (FD, 8kV): m/z (%) = 251.9 (100.0 %, M^+), (calc. $C_{15}H_{12}N_2O_2$ = 252.27 g/mol).

7.3.11 Cyclo-2,9-tris-(5,6)-bisoctyloxy-1,10-phenanthroline (3-19a)

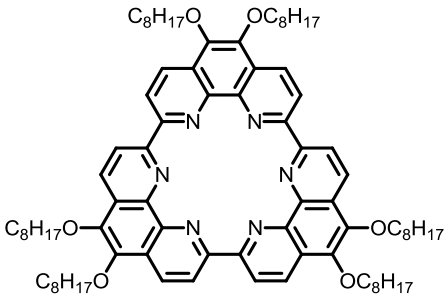

The catalyst solution was prepared inside the glove box by adding 12.0 ml DMF and 24.0 ml toluene to a mixture of 0.26 g (0.95 mmol) bis(cyclooctadiene)nickel(0), 0.15 g (0.95 mmol) 2,2'-bipyridine and 0.12 ml (0.95 mmol) cyclooctadiene. The resulting solution was stirred for 30 min at 60 °C. Then, a solution of 0.20 g (0.40 mmol) of **3-10a** in 12.0 ml toluene was added dropwise over 30 min. The reaction mixture was stirred for 72 h at 60 °C under the exclusion of light. After cooling, the mixture was diluted with diethyl ether and washed with diluted hydrochloric acid (2 M). The crude product was pre-purified by column chromatography on silica (DCM/methanol = 10/1). Further purification was achieved by preparative gel permeation chromatography (chloroform) to yield 28 mg (0.021 mmol) of **3-19a** in 16 % as an orange waxy solid.

^{1}H-NMR (500 MHz, CD_2Cl_2): δ 8.98 (d, J = 8.7, 6H), 8.75 (d, J = 8.8, 6H), 4.37 (t, J = 6.6, 12H), 1.98 (p, J = 7.0, 12H), 1.81 - 1.22 (m, 60H), 0.92 (t, J = 7.0, 18H).

^{13}C-NMR (126 MHz, CD_2Cl_2): δ 153.58, 144.50, 143.36, 133.65, 128.21, 123.07, 74.96, 32.45, 30.96, 30.06, 29.89, 26.78, 23.27, 14.46.

MS (MALDI-TOF): m/z (%) = 1325.96 (100.0 %), 1326.96 (95.5 %), 1327.96 (49.4 %), 1328.26 (20.5 %), (calc. $C_{84}H_{114}N_6NaO_6$ = 1326.83 g/mol - isotop. distr.: 1325.87 (100.0 %), 1326.87 (93.3 %), 1327.88 (42.2 %), 1328.98 (20.9 %)).

7.3.12 Cyclo-2,9-tris-(5,6)-bisdodecyloxy-1,10-phenanthroline (3-19b)

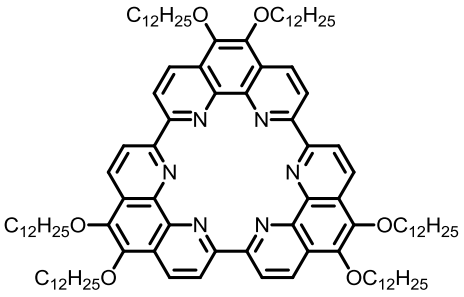

The catalyst solution was prepared inside the glove box by adding 20.0 ml DMF and 40.0 ml toluene to a mixture of 0.43 g (1.55 mmol) bis(cyclooctadiene)nickel(0), 0.24 g (1.55 mmol) bipyridine and 0.19 ml (1.55 mmol) cyclooctadiene. The resulting solution was stirred for 30 min at 60 °C. Then, a solution of 0.40 g (0.65 mmol) of **3-10b** in 20.0 ml toluene was added dropwise over 30 min. The reaction mixture was stirred for 72 h at 60 °C under the exclusion of light. After cooling, the mixture was diluted with diethyl ether and washed with diluted hydrochloric acid (2 M). The crude product was pre-purified by column chromatography on silica (DCM/methanol = 10/1). Further purification was achieved by preparative gel permeation chromatography (chloroform) to yield 67 mg (0.041 mmol) of **3-19b** in 19 % as an orange waxy solid.

^{1}H-NMR (500 MHz, CD_2Cl_2): δ 8.98 (d, J = 8.7, 6H), 8.79 (d, J = 8.8, 6H), 4.37 (t, J = 6.6, 12H), 1.86 (p, J = 7.0, 12H), 1.75 - 1.10 (m, 108H), 0.89 (t, J = 6.9, 18H).

^{13}C-NMR (126 MHz, CD_2Cl_2): δ 153.81, 144.63, 143.01, 133.20, 127.53, 123.01, 74.91, 32.56, 31.11, 30.37, 30.34, 30.24, 30.01, 26.89, 23.31,14.47.

MS (MALDI-TOF): m/z (%) = 1663.24 (100.0 %), 1662.25 (82.3 %), 1664.25 (62.4 %), 1665.26 (29.5 %), (calc. $C_{108}H_{162}N_6NaO_6$ = 1663.47 g/mol - isotop. distr.: 1663.25 (100.0 %), 1662.25 (84.1%), 1664.25 (62.2 %), 1665.26 (22.9 %)).

7.3.13 Cyclo-2,9-tris-(5,6)-bishexadecyloxy-1,10-phenanthroline (3-19c)

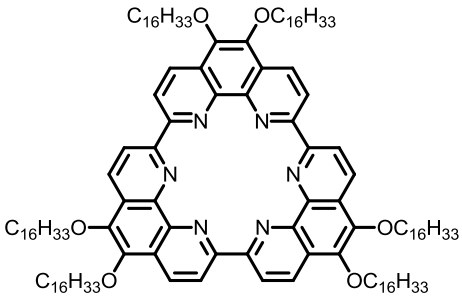

The catalyst solution was prepared inside the glove box by adding 10.0 ml DMF and 20.0 ml toluene to a mixture of 0.23 g (0.82 mmol) bis(cyclooctadiene)nickel(0), 0.13 g (0.82 mmol) bipyridine and 0.10 ml (0.82 mmol) cyclooctadiene. The resulting solution was stirred for 30 min at 60 °C. Then, a solution of 0.25 g (0.34 mmol) of **3-10c** in 10.0 ml toluene was added dropwise over 30 min. The reaction mixture was stirred for 72 h at 60 °C under the exclusion of light. After cooling, the mixture was diluted with diethyl ether and washed with diluted hydrochloric acid (2 M). The crude product was pre-purified by column chromatography on silica (DCM/methanol = 10/1). Further purification was achieved by preparative gel permeation chromatography (chloroform) to yield 27 mg (0.041 mmol) of **3-19c** in 12 % as an orange waxy solid.

^{1}H-NMR (500 MHz, CD_2Cl_2): δ 8.98 (d, J = 8.6, 6H), 8.76 (d, J = 8.8, 6H), 4.33 (t, J = 6.6, 12H), 1.98 (p, J = 7.0, 12H), 1.84 - 1.05 (m, 156H), 0.88 (t, J = 6.9, 18H).

^{13}C-NMR (126 MHz, CD_2Cl_2): δ 153.77, 144.59, 143.37, 133.73, 128.21, 123.11, 74.97, 32.51, 30.97, 30.32, 30.27, 30.13, 29.95, 26.80, 23.27, 14.45.

MS (MALDI-TOF): m/z (%) = 1999.02 (100.0 %), 2000.02 (73.5 %), 1999.02 (72.5 %), 2001.02 (46.0 %), (calc. $C_{132}H_{210}N_6NaO_6$ = 2000.11 g/mol - isotop. distr.: 1999.62 (100.0 %), 2000.63 (73.2 %), 1998.62 (69.0 %), 2001.63 (35.8 %), 2002.63 (13.1 %)).

7.3.14 Cyclo-2,9-tris-(5,6)-dimethyl-[1,3]dioxolo[4,5-f]-1,10-phenanthroline (3-20)

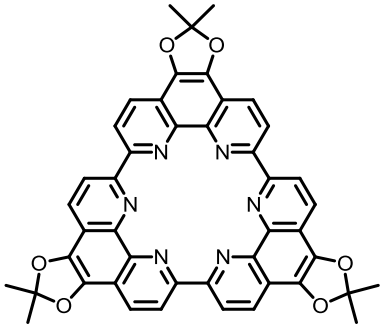

The catalyst solution was prepared inside the glove box by adding 9.0 ml DMF and 18.0 ml toluene to a mixture of 0.21 g (0.75 mmol) bis(cyclooctadiene)nickel(0), 0.12 g (0.75 mmol) 2,2'-bipyridine and 0.10 ml (0.75 mmol) cyclooctadiene. The resulting solution was stirred for 30 min at 60 °C. Then, a solution of 0.10 g (0.31 mmol) of **3-11** in 10.0 ml toluene was added dropwise over 30 min. The reaction mixture was stirred for 72 h at 60 °C under the exclusion of light. After cooling, the mixture was diluted with diethyl ether and washed with diluted hydrochloric acid (2 M). The crude product was pre-purified by column chromatography on silica (DCM/methanol = 10/1). Further purification was achieved by preparative gel permeation chromatography (chloroform) to yield 15 mg (0.020 mmol) of **3-20** in 19 % as an orange solid.

^{1}H-NMR (700 MHz, CD_2Cl_2): δ 8.72 (6H, d, J = 8.42 Hz), 8.59 (6H, d, J = 8.89 Hz), 1.96 (s, 18H).

^{13}C-NMR (176 MHz, CD_2Cl_2): δ 152.54, 142.37, 138.20, 130.84, 123.19, 122.85, 118.94, 26.20.

MS (MALDI-TOF): m/z (%) = 773.14 (100.0 %), 774.16 (55.8 %), 775.16 (22.2 %), 776.14 (14.6 %), (calc. $C_{45}H_{30}N_6NaO_6$ = 773.75 g/mol - isotop. distr.: 773.21 (100.0%), 774.22 (49.2%), 775.22 (13.1%), 776.22 (2.7%).

7.3.15 1,2-Dibromo-4,5-bis(dodecyloxy)benzene (3-22a)[10]

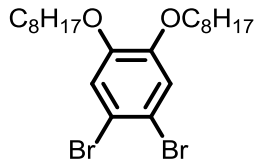

3.00 g (11.20 mmol) 4,5-dibromobenzene-1,2-diol were dissolved in 30.0 ml DMF. Then, 4.32 g (22.38 mmol) of dodecyl bromide and 3.09 g (22.38 mmol) potassium carbonate were added. The mixture was heated to 100 °C for 24 h. After cooling, the reaction mixture was extracted with diethyl ether and the crude product was purified by column chromatography (hexane) to yield 4.41 g (8.96 mmol) of **3-22a** as a white solid in 80 %.

^{1}H-NMR (300 MHz, CD_2Cl_2): δ 7.17 (s, 2H), 3.76 (t, J = 6.6, 4H), 1.67 (p, 4H), 1.51 – 1.15 (m, 20H), 0.92 (t, J = 6.7, 6H).

^{13}C-NMR (75 MHz, CD_2Cl_2): δ 147.98, 119.01, 115.43, 72.56, 32.85, 30.38, 29.91, 29.21, 26.50, 20.30, 14.48.

MS (FD, 8kV): m/z (%) = 491.9 (100.0 %, M^+), (calc. $C_{22}H_{36}Br_2N_2O_2$ = 492.33 g/mol).

7.3.16 1,2-Dibromo-4,5-bis(dodecyloxy)benzene (3-22b)[10]

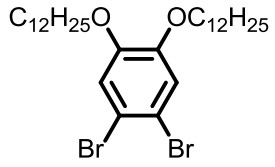

10.00 g (37.32 mmol) 4,5-dibromobenzene-1,2-diol were dissolved in 100.0 ml DMF. Then, 18.61 g (74.65 mmol) of dodecyl bromide and 10.32 g (74.65 mmol) potassium carbonate were added. The mixture was heated to 100 °C for 24 h. After cooling, the reaction mixture was extracted with diethyl ether and the crude product was purified by column chromatography (hexane) to yield 19.17 g (31.72 mmol) of **3-22b** as a white waxy solid in 83 %.

^{1}H-NMR (300 MHz, CD_2Cl_2): δ 7.08 (s, 2H), 3.93 (t, J = 6.6, 4H), 1.77 (p, 4H), 1.51 – 1.15 (m, 36H), 0.88 (t, J = 6.7, 6H).

^{13}C-NMR (75 MHz, CD_2Cl_2): δ 149.86, 118.71, 115.03, 70.28, 32.55, 30.30, 30.27, 30.22, 30.21, 29.98, 29.95, 29.72, 26.54, 23.30, 14.48.

MS (FD, 8kV): m/z (%) = 603.9 (100.0 %, M^+), (calc. $C_{30}H_{52}Br_2N_2O_2$ = 604.54 g/mol).

Elemental Analysis: found 62.05 % C, 9.28 % H - calc. 59.60 % C, 8.67 % H (see general remarks "7.2.4 Elemental Combustion Analysis").

7.3.17 4',5'-Bis(dodecyloxy)-1,1':2',1''-terphenyl (3-23)[11]

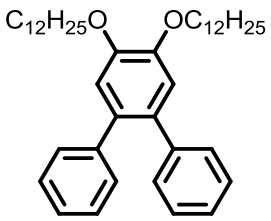

6.00 g (9.92 mmol) of **3-22b** and 3.63 g (29.77 mmol) of phenylboronic acid were dissolved in 150.0 ml of toluene. Then, 40.0 ml of aqueous potassium carbonate solution (2 M) and a few drops of Aliquat 336 werde added. After degassing by argon bubbling, 2.29 g (1.98 mmol) of tetrakis(triphenylphosphine)palladium(0) were added and the resulting mixture was heated to reflux for 24 h. The precipitate that was formed during the reaction was collected by filtration, washed with methanol and used for the next step without further purification. 5.17 g (8.63 mmol) of **3-23** were obtained as a white solid in 87 %.

^{1}H-NMR (300 MHz, CD_2Cl_2): δ 7.24 - 7.08 (m, 10H), 6.93 (s, 2H), 4.04 (t, J = 6.6, 4H), 1.82 (p, 4H), 1.56 – 1.18 (m, 36H), 0.88 (t, J = 6.7, 6H).

^{13}C-NMR (75 MHz, CD_2Cl_2): δ 149.08, 142.32, 133.75, 130.57, 128.36, 126.71, 116.94, 70.11, 32.56, 30.33, 30.27, 30.05, 29.99, 26.69, 23.31, 14.49.

MS (FD, 8kV): m/z (%) = 595.0 (100.0 %, M^+), (calc. $C_{42}H_{62}O_2$ = 598.94 g/mol).

2,3-Bis(dodecyloxy)triphenylene (3-24)[11]

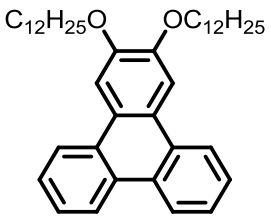

0.50 g (0.83 mmol) **3-23** and 0.23 g iodine (0.91 mmol) were dissolved in 120.0 ml toluene. Then 0.4 ml (5.72 mmol) of propylene oxide was added. The solution was irradiated with 300 nm (40 W) for 48 h at room temperature. The crude product was purified by column chromatography (hexane/ethyl acetate = 20/1) to yield 0.36 g (0.61 mmol) of **3-24** as a white solid in 73 %.

^{1}H-NMR (300 MHz, CD_2Cl_2): δ 8.66 (d, J = 8.6, 2H), 8.52 (d, J = 8.7, 2H), 8.03 (s, 2H), 7.70 – 7.57 (m, 4H), 4.24 (t, J = 6.6, 4H), 1.93 (p, 4H), 1.65 - 1.18 (m, 36H), 0.88 (t, J = 6.6, 6H).

^{13}C-NMR (75 MHz, CD_2Cl_2): δ 150.33, 130.14, 129.61, 127.61, 126.78, 124.67, 123.89, 123.38, 107.31, 69.88, 32.53, 30.67, 30.32, 30.27, 30.08, 29.98, 26.74, 23.29, 14.46.

MS (FD, 8kV): m/z (%) = 593.5 (100.0 %, M^+), (calc. $C_{42}H_{60}O_2$ = 596.92 g/mol).

Elemental Analysis: found 87.21 % C, 10.98 % H - calc. 84.51 % C, 10.13 % H (see general remarks "7.2.4 Elemental Combustion Analysis").

7.3.18 7,10-Dibromo-2,3-bis(dodecyloxy)triphenylene (3-25)[11]

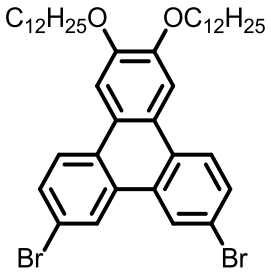

1.00 g (1.68 mmol) **3-24** were dissolved in 18.0 ml DCM and a catalytic amount of iron powder and iodine was added. Then, 7.2 ml of a DCM solution containing 1.08 g (6.76 mmol) bromine was added dropwise at a temperature of - 5 °C. The reaction was allowed to proceed at this temperature for 3 h after what it was stopped by the addition of a 10 % solution of sodium thiosulfate. The crude product was recrystallized from DCM to yield 0.84 g (1.11 mmol) of **3-25** as a white crystalline solid in 66 %.

^{1}H-NMR (300 MHz, THF): δ 8.83 (s, 2H), 8.50 (d, J = 8.8, 2H), 8.03 (s, 2H), 7.73 (d, J = 8.7, 2H), 4.23 (t, J = 6.1, 4H), 1.89 (p, 4H), 1.43 (m, 36H), 0.89 (t, J = 6.6, 6H).

^{13}C-NMR (75 MHz, THF): δ 151.68, 131.51, 130.90, 130.17, 127.34, 126.13, 124.77, 121.45, 107.68, 69.98, 33.06, 30.92, 30.87, 30.82, 30.62, 30.51, 27.34, 23.74, 14.60.

MS (FD, 8kV): m/z (%) = 754.2 (100.0 %, M^+), (calc. $C_{42}H_{60}O_2$ = 754.72 g/mol).

Elemental Analysis: found 64.19 % C, 5.12 % H - calc. 66.84 % C, 7.75 % H (see general remarks "7.2.4 Elemental Combustion Analysis").

7.3.19 Cyclo-7,10-tris-(2,3)-bisdodecyloxy-triphenylene (3-26)

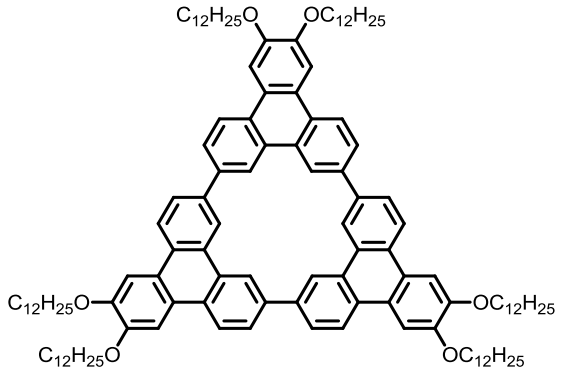

The catalyst solution was prepared inside the glove box by adding 6.0 ml DMF and 12.0 ml toluene to a mixture of 0.12 g (0.47 mmol) bis(cyclooctadiene)nickel(0), 0.07 g (0.47 mmol) 2,2'-bipyridine and 0.05 ml (0.47 mmol) cyclooctadiene. The resulting solution was stirred for 30 min at 60 °C. Then, a solution of 0.15 g (0.20 mmol) of **3-25** in 4.0 ml toluene was added dropwise over 30 min. The reaction mixture was stirred for 12 h at 60 °C under the exclusion of light. After cooling, the mixture was diluted with diethyl ether and washed with diluted hydrochloric acid (2 M). The crude product was pre-purified by column chromatography on silica (DCM/methanol = 10/1). Further purification was achieved by preparative gel permeation chromatography (chloroform) to yield 25 mg (0.014 mmol) of **3-22** in 21 % as a white solid.

^{1}H-NMR (300 MHz, $CDCl_3$): δ 7.95 (s, 6H), 7.35 (d, J = 7.6, 6H), 7.16 (d, J = 8.1, 6H), 7.03 (s, 6H), 3.75 (t, J = 4.1, 12H), 1.79 (p, 12H), 1.55 - 1.28 (m, 108H), 0.91 (t, J = 6.7, 18H).

^{13}C-NMR (75 MHz, $CDCl_3$): δ 148.33, 133.18, 128.21, 127.95, 123.18, 122.10, 121.90, 117.66, 105.41, 68.41, 31.81, 29.71, 29.64, 29.33, 29.29, 26.08, 22.54, 13.93.

MS (MALDI-TOF): m/z (%) = 1783.39 (100.0 %), 1782.81 (71.3 %), 1782.49 (67.5 %), 1784.35 (66.5 %), 1783.72 (64.3 %), (calc. $C_{126}H_{174}O_6$ = 1784.73 g/mol - isotop. distr.: 1784.33 (100.0%), 1783.33 (73.4%), 1785.34 (70.7%), 1786.34 (33.0%), 1787.34 (10.9%), 1788.35 (3.2%), 1784.34 (1.6%)).

7.3.20 (4',5'-Bis(octyloxy)-[1,1':2',1''-terphenyl]-4,4''-diyl)bis (trimethylsilane) (3-30)

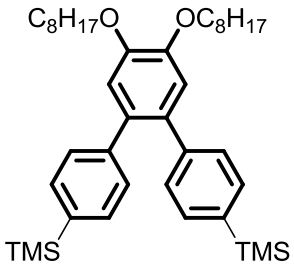

2.03 g (4.12 mmol) **3-22a** and 2.00 g (10.30 mmol) 4-(trimethylsilyl)phenylboronic acid were dissolved in 100.0 ml of dioxane. Then, 20.0 ml of aqueous potassium carbonate solution (2 M) and a few drops of Aliquat 336 werde added. After degassing by argon bubbling, 0.47 g (0.41 mmol) of tetrakis(triphenylphosphine)palladium(0) were added and the resulting mixture was heated to 100 °C for 24 h. After removal of the solvent, the crude product was filtered over a silica pad (hexane) and recrystallized from DCM to yield 2.52 g (4.00 mmol) of **3-30** as colorless crystals in 97 %.

^{1}H-NMR (300 MHz, CD_2Cl_2) δ 7.38 (d, J = 8.1, 4H), 7.14 (d, J = 8.1, 4H), 6.92 (s, 2H), 4.04 (t, J = 6.6, 4H), 1.83 (p, 4H), 1.38 (m, 20H), 0.90 (t, J = 6.8, 6H), 0.26 (s, 18H).

^{13}C-NMR (75 MHz, CD_2Cl_2) δ 148.97, 142.69, 138.47, 133.53, 133.44, 129.78, 116.93, 70.00, 32.44, 30.19, 29.88, 26.62, 23.27, 14.46, 1.01.

MS (FD, 8kV): m/z (%) = 629.7 (100.0 %, M^+), (calc. $C_{40}H_{62}O_2Si_2$ = 631.09 g/mol).

7.3.21 4,4''-Dibromo-4',5'-bis(octyloxy)-1,1':2',1''-terphenyl (3-31)

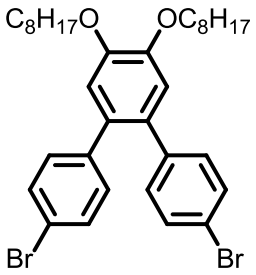

0.5 g (0.79 mmol) of **3-30** and 0.70 g (3.95 mmol) *N*-bromosuccinimide were dissolved in a mixture of 10.0 ml THF and 15.0 ml methanol. Then, 0.41 g (3.95 mmol) sodium

bromide was added and the reaction mixture was heated to 45 °C for 24 h under an inert atmosphere. The reaction was monitored by thin-layer chromatography. The crude product was purified by column chromatography (hexane/ethyl acetate = 20/1) to yield 0.38 g (0.59 mmol) of **3-31** as a white solid in 75 %.

^{1}H-NMR (300 MHz, CD_2Cl_2) δ 7.35 (d, J = 8.6, 4H), 7.00 (d, J = 8.5, 4H), 6.89 (s, 2H), 4.03 (t, J = 6.6, 4H), 1.82 (p, 4H), 1.53 – 1.21 (m, 20H), 0.88 (t, J = 6.9, 6H).

^{13}C-NMR (75 MHz, CD_2Cl_2) δ 149.35, 140.92, 132.27, 132.22, 131.63, 120.98, 116.48, 70.03, 32.43, 29.96, 29.88, 26.62, 23.27, 14.46.

MS (FD, 8kV): m/z (%) = 644.1 (100.0 %, M^+), (calc. $C_{34}H_{44}Br_2O_2$ = 644.52 g/mol).

Elemental Analysis: found 64.62 % C, 7.95 % - calc. 63.36 % C, 6.88 % H (see general remarks "7.2.4 Elemental Combustion Analysis").

7.3.22 Hexa(octyloxy)cyclo-*nona*-phenylene (3-32)

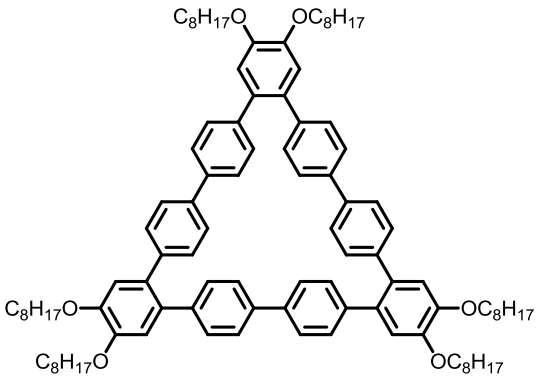

The catalyst solution was prepared inside the glove box by adding 6.0 ml DMF and 12.0 ml toluene to a mixture of 0.12 g (0.47 mmol) bis(cyclooctadiene)nickel(0), 0.07 g (0.47 mmol) 2,2'-bipyridine and 0.05 ml (0.47 mmol) cyclooctadiene. The resulting solution was stirred for 30 min at 60 °C. Then, a solution of 0.13 g (0.20 mmol) of **3-31** in 4.0 ml toluene was added dropwise over 30 min. The reaction mixture was stirred for 24 h at 60 °C under the exclusion of light. After cooling, the mixture was diluted with diethyl ether and washed with diluted hydrochloric acid (2 M). The crude product was pre-purified by column chromatography on silica (DCM/methanol = 10/1). Further purification was achieved by preparative gel permeation chromatography (chloroform) to yield 25 mg (0.017 mmol) of **3-32** in 22 % as a white crystalline solid.

^{1}H-NMR (700 MHz, THF): δ 7.48 (d, J = 8.3, 12H), 7.11 (d, J = 8.2, 12H), 7.01 (s, 6H), 4.06 (t, J = 6.4, 12H), 1.83 (p, 12H), 1.55 (p, 12H), 1.45 – 1.27 (m, 5H), 0.91 (t, J = 6.8, 18H).

^{13}C-NMR (176 MHz, THF): δ 150.30, 142.00, 138.58, 134.51, 131.31, 126.37, 116.88, 70.23, 33.02, 30.67, 30.54, 30.50, 27.28, 23.75, 14.63.

MS (MALDI-TOF): m/z (%) = 1453.73 (100.0 %), 1452.63 (84.0 %), 1454.60 (64.6 %), 1455.64 (25.5 %), 1456.87 (9.9 %), (calc. $C_{102}H_{132}O_6$ = 1454.14 g/mol - isotop. distr.: 1454.01 (100.0%), 1453.00 (89.2%), 1455.01 (56.6%), 1456.01 (20.7%), 1457.02 (5.5%), 1458.02 (1.4%)).

7.4 Graphene Nanoribbon Synthesis

7.4.1 4,4'-Dibromo-2,2'-dinitro-1,1'-biphenyl (4-2)[12]

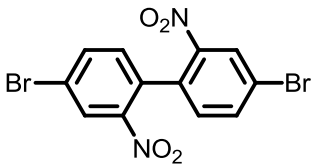

A mixture of 20.0 g (69.78 mmol) 1,4-dibromo-2-nitrobenzene and 10.0 g (155.78 mmol) copper powder were placed in a *Schlenk* flask which was evacuated and refilled with argon for three times. Then, the mixture was heated to 190 °C for 12 h under vigorous stirring. The crude product was purified by column chromatography (DCM/hexane = 1:1) to yield 6.87 g (17.09 mmol) of **4-2** in 49 % as a yellow-orange powder.

^{1}H NMR (300 MHz, CD_2Cl_2): δ 8.39 (d, J = 2.0, 2H), 7.87 (dd, J = 2.0, 8.2, 2H), 7.20 (d, J = 8.2, 2H).

^{13}C NMR (75 MHz, CD_2Cl_2): δ 147.98, 137.30, 132.76, 132.62, 128.51, 123.34.

MS (FD, 8kV): m/z (%) = 402.9 (100.0 %, M^+), (calc. $C_{12}H_6Br_2N_2O_4$ = 402.00 g/mol).

Elemental Analysis: found 35.87 % C, 1.50 % H, 6.90 % N - calc. 35.85 % C, 1.50 % H, 6.97 % N.

7.4.2 4,4'-Dibromo-[1,1'-biphenyl]-2,2'-diamine (4-3)[12]

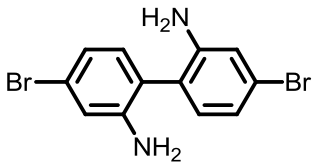

5.5 g (13.68 mmol) of **4-2** were suspended in 70.0 ml of ethanol. Then, 34.0 ml of concentrated hydrochloric acid were slowly added. Under continuous stirring 6.50 g (54.76 mmol) of tin powder were added in small amounts. The reaction was run under reflux for 2 h. During the reaction the mixture progressively turned yellow-white. After cooling, the reaction mixture was carefully neutralized by the slow addition of sodium hydroxide. After extraction with diethyl ether and removal of the solvent under reduced pressure 4.38 g (12.81 mmol) of **4-3** were obtained as a yellow solid in 95 %. The substance was used without further purification for the next step.

^{1}H NMR (300 MHz, CD_2Cl_2): δ 8.90 (d, J = 2.1, 2H), 8.48 (d, J = 8.7, 2H), 8.05 (dd, J = 2.0, 8.8, 2H), 3.81 (s, 4H).

^{13}C NMR (75 MHz, CD_2Cl_2): δ 146.32, 132.85, 123.05, 122.70, 121.89, 118.52.

MS (FD, 8kV): m/z (%) = 342.0 (100.0 %, M^+), (calc. $C_{12}H_{10}Br_2N_2$ = 342.03 g/mol).

Elemental Analysis: found 42.51 % C, 2.95 % H, 8.18 % N - calc. 42.14 % C, 2.95 % H, 8.19 % N.

7.4.3 4,4'-Dibromo-2,2'-diiodo-1,1'-biphenyl (4-4)

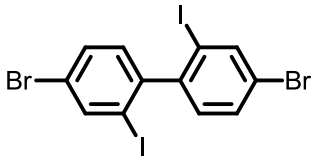

4.38 g (12.81 mmol) of **4-3** were suspended in 20.0 ml of water. Then, 16.0 ml of concentrated hydrochloric acid were added under cooling. At a temperature of - 5 °C, 10.0 ml of an aqueous solution containing 2.21 g (31.74 mmol) sodium nitrite

were added dropwise. During this procedure, the color of the reaction mixture changed from yellow to dark brown. Subsequently, 40.0 ml of an aqueous solution containing 21.49 g (128.19 mmol) potassium iodide were added dropwise while maintaining the temperature below 0 °C. After the addition, the reaction was allowed to proceed for 1 h at room temperature. After extraction with DCM, treatment with an aqueous solution of sodium thiosulfate and removal of the solvent under reduced pressure the crude product was purified by column chromatography (hexane) to yield 2.41 g (4.28 mmol) of **4-4** in 34 % as an off-white solid.

^{1}H NMR (300 MHz, CD_2Cl_2): δ 8.12 (d, J = 1.9, 2H), 7.58 (dd, J = 2.0, 8.2, 2H), 7.06 (d, J = 8.2, 2H).

^{13}C NMR (75 MHz, CD_2Cl_2): δ 147.46, 141.53, 131.96, 131.43, 122.90, 100.34.

MS (FD, 8kV): m/z (%) = 565.2 (100.0 %, M^+), (calc. $C_{12}H_6Br_2I_2$ = 563.79 g/mol).

Elemental Analysis: found 26.07 % C, 1.06 % H - calc. 25.56 % C, 1.07 % H.

7.4.4 4,4'-Dibromo-2,2'-diethynyl-1,1'-biphenyl (4-6)

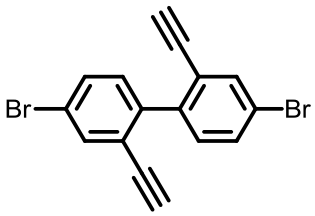

1.00 g (1.77 mmol) of **4-4** were mixed with 40.0 mg (0.21 mmol) of copper(II) iodide and 15.0 ml of triethylamine. After degassing by argon bubbling, 80.0 mg (0.11 mmol) of bis(triphenylphosphine)palladium(II) dichloride and 0.54 ml (3.72 mmol) of (trimethylsilyl)acetylene were added. The reaction mixture was stirred at room temperature for 12 h under an inert atmosphere and monitored by thin-layer chromatography. The reaction mixture was filtered over a silica pad (hexane) to remove inorganic residues.

The product thus obtained (0.55 g, 1.09 mmol, 62 %) was then dissolved in a mixture of 50.0 ml THF and 50.0 ml methanol. After degassing by argon bubbling, 0.80 g (5.79 mmol) of potassium carbonate were added to the mixture and the reaction was run at room temperature for 12 h and monitored by thin-layer chromatography. The crude

product was purified by column chromatography (hexane) to yield 0.32 g (0.89 mmol) of **4-6** as a white crystalline solid in 75 %.

^{1}H NMR (300 MHz, CD_2Cl_2): δ 7.75 (d, J = 2.0, 2H), 7.55 (dd, J = 2.1, 8.3, 2H), 7.26 (d, J = 8.3, 2H), 3.10 (s, 2H).

^{13}C NMR (75 MHz, CD_2Cl_2): δ 141.56, 136.14, 132.22, 132.07, 123.94, 121.99, 82.37, 81.28.

MS (FD, 8kV): m/z (%) = 360.2 (100.0 %, M^+), (calc. $C_{16}H_8Br_2$ = 360.04 g/mol).

Elemental Analysis: found 53.34 % C, 3.50 % H - calc. 53.37 % C, 2.24 % H.

7.4.5 1,2-Bis(4-(3,7-dimethyloctyl)phenyl)ethyne (4-8)[13]

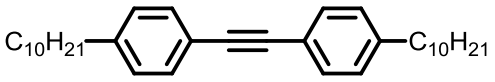

3.30 g (135.62 mmol) of freshly ground magnesium coils were washed with diethyl ether, thoroughly dried and placed in a *Schlenk* flask. The flask was evacuated and flushed with argon several times. Then, 15.00 g (67.81 mmol) 1-bromo-3,7-dimethyloctane dissolved in 60.0 ml THF were slowly added under vigorous stirring. The liquid phase turned grayish and was subsequently heated to 60 °C for 3 h.
In a second flask 7.22 g (20.83 mmol) 1,2-bis(4-bromophenyl)ethyne were suspended in 10.0 ml THF and 1.70 g (2.083 mmol) bis(diphenylphosphino)ferrocene-palladium(II)dichloride was added. Then, the solution containing the *Grignard* reagent was slowly transferred by means of a double cannula. All operations were carried out under an inert atmosphere and the reaction mixture was heated to 60 °C for 24 h. The crude product was purified by column chromatography (hexane/DCM = 20/1) to yield 9.08 g (19.79 mmol) of **4-8** as a yellowish oil in 95 %.

^{1}H NMR (300 MHz, CD_2Cl_2): δ 7.43 (d, J = 8.2, 4H), 7.19 (d, J = 8.2, 4H), 2.62 (t, J = 6.8, 4H), 1.72 - 1.03 (m, 20H), 0.90 (m, 18 H).

^{13}C NMR (75 MHz, CD_2Cl_2): δ 144.2, 131.7, 128.9, 120.9, 89.2, 39.7, 39.1, 37.5, 33.8, 32.9, 28.4, 25.1, 22.8, 22.7, 19.7.

MS (FD, 8kV): m/z (%) = 456.3 (100.0 %, M^+), (calc. $C_{34}H_{50}$ = 458.76 g/mol).

7.4.6 1,2-Bis(4-alkylphenyl)ethane-1,2-dione (4-9a+b)[13]

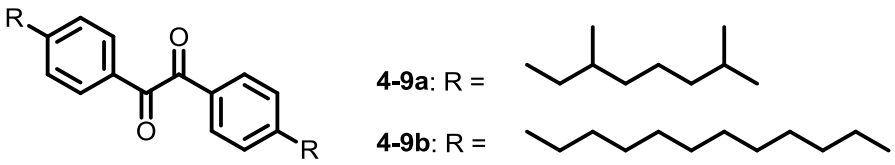

4-9a

2.47 g (9.71 mmol) iodine and 9.00 g (19.62 mmol) of **4-8** were dissolved in 70.0 ml DMSO. After degassing by argon bubbling the reaction mixture was heated to 155 °C for 24 h under an inert atmosphere. After cooling, the reaction mixture was treated with an aqueous solution of sodium thiosulfate and extracted with DCM. The crude product was purified by column chromatography (hexane/DCM = 1/1) to yield 7.89 g (16.09 mmol) of **4-9a** in 82 %.

^{1}H NMR (300 MHz, CD_2Cl_2): δ 7.86 (d, J = 8.2, 4H), 7.34 (d, J = 8.2, 4H), 2.69 (t, J = 7.6, 4H), 1.73 - 1.00 (m, 20H), 0.88 (m, 18H).

^{13}C NMR (75 MHz, CD_2Cl_2): δ 195.0, 151.9, 131.2, 130.3, 129.4, 39.7, 38.8, 37.4, 34.1, 32.9, 28.4, 25.0, 22.8, 22.7, 19.7.

MS (FD, 8kV): m/z (%) = 490.1 (100.0 %, M^+), (calc. $C_{34}H_{50}O_2$ = 490.38 g/mol).

4-9b

12.80 g (76.04 mmol) of 1-dodecene were placed in a *Schlenk* flask and 167.4 ml of a 9-borabicyclo[3.3.1]nonane solution (9-BBN, 0.5 M in THF) were added slowly under an inert atmosphere. The resulting mixture was stirred at room temperature. After 12 h, 20.0 ml of aqueous sodium hydroxide solution (3 M) were added. Subsequently, 7.00 g (19.0 mmol) of 1,2-bis(4-bromophenyl)ethyne and 0.78 g (0.96 mmol) of bis(diphenylphosphino)ferrocenepalladium(II)-dichloride were added. The resulting mixture was stirred at room temperature for additional 12 h. After cooling, the reaction mixture was extracted with DCM. The crude product was purified by column chromatography (hexane/DCM = 7/3) to yield 7.27 g (13.30 mmol) of **4-9b** in 70 %.

^{1}H NMR (300 MHz, CD_2Cl_2): δ 7.85 (d, J = 8.4, 4H), 7.33 (d, J = 8.4, 4H), 2.67 (t, J = 7.7, 4H), 1.75 - 1.10 (m, 40H), 0.88 (t, J = 6.7, 6H).

^{13}C NMR (75 MHz, CD_2Cl_2): δ 195.0, 151.6, 131.2, 130.3, 129.5, 36.5, 32.3, 31.4, 30.0, 29.9, 29.8, 29.7, 29.6, 23.1, 14.3.

MS (FD, 8kV): m/z (%) = 546.1 (100.0 %, M^+), (calc. $C_{38}H_{58}O_2$ = 546.87 g/mol).

7.4.7 3,4-Bis(4-alkylphenyl)-2,5-diphenylcyclopenta-2,4-dienone (4-11a+b)[13]

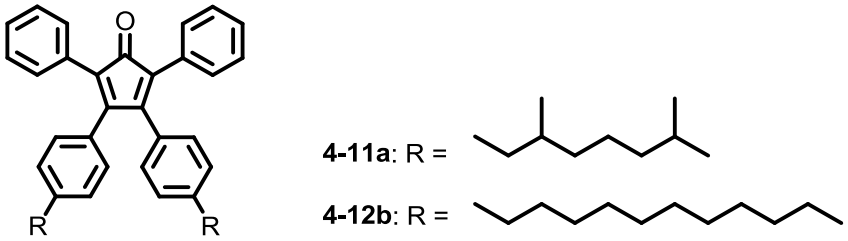

12.24 mmol of the corresponding 1,2-bis(4-alkylphenyl)ethane-1,2-dione **4-9a+b**, 3.09 g (14.69 mmol) of 1,3-diphenylpropan-2-one were dissolved in 42.0 ml of tert-buthanol. The mixture was heated to 80 °C after what 7.4 ml (7.34 mmol) of tetrabutylammonium hydroxide in methanol (1 M) were added. The reaction mixture turned dark red instantly and was stirred at the same temperature for 30 min. The crude product was purified by column chromatography (hexane/ethyl acetate = 9/1) to yield **4-11a+b** in 45 - 55 % as dark red oils which solidified upon standing.

4-11a

^{1}H NMR (300 MHz, CD_2Cl_2): 7.22 (m, 10H), 7.00 (d, *J* = 8.1, 4H), 6.83 (d, *J* = 8.2, 4H), 2.58 (t, *J* = 7.3, 4H), 1.78 - 1.01 (m, 20H), 0.89 (m, 18H).

^{13}C NMR (75 MHz, CD_2Cl_2): δ 200.8, 155.4, 144.4, 131.7, 130.8, 130.5, 129.7, 128.3, 128.2, 127.6, 125.5, 39.7, 38.9, 37.5, 33.6, 32.8, 28.4, 25.1, 22.8, 22.7, 19.7.

MS (FD, 8kV): m/z (%) = 664.7 (100.0 %, M^+), (calc. $C_{49}H_{60}O$ = 665.00 g/mol).

4-11b

^{1}H NMR (300 MHz, CD_2Cl_2): 7.24 (m, 10H), 7.02 (d, *J* = 8.1, 4H), 6.77 (d, *J* = 8.3, 4H), 2.58 (t, *J* = 7.2, 4H), 1.78 - 1.01 (m, 40H), 0.89 (m, 6H).
^{13}C NMR (75 MHz, CD_2Cl_2): δ 200.3, 156.3, 145.2, 132.5, 131.9, 130.9, 130.7, 129.9, 128.8, 124.8, 122.3, 40.1, 39.3, 37.9, 34.1, 33.3, 28.8, 25.5, 22.8, 22.7, 19.7.

MS (FD, 8kV): m/z (%) = 719.9 (100.0 %, M^+), (calc. $C_{53}H_{68}O$ = 721.11 g/mol).

7.4.8 4'',5'-Dibromo-2,2''',5,5'''-tetraphenyl-3,3''',4,4'''-tetra(4-alkyl)-1,1':2',1'':2'',1'''-quaterphenyl (4-13a+b)

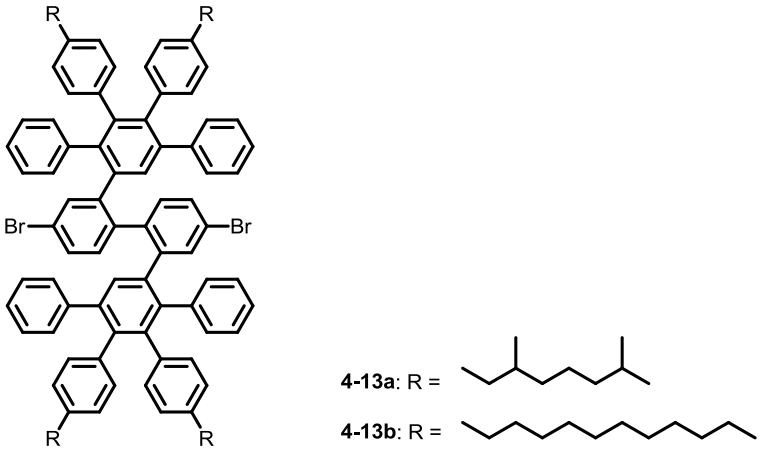

0.20 g (0.56 mmol) **4-6** and 2.22 mmol of the corresponding 3,4-bis(4-alkyl)-2,5-diphenylcyclopenta-2,4-dienone **4-11a+b** were placed in a microwave vessel. Then, 8.0 ml of *ortho*-xylene were added and the reaction mixture was degassed by argon bubbling. The reaction vessel was sealed, placed in a microwave reactor and heated to 160 °C at 300 W for 24 h with activated cooling. The crude product was pre-purified by column chromatography (hexane/ethyl acetate = 9/1). Further purification was achieved by preparative gel permeation chromatography (chloroform) to yield **4-13a+b** in 77 - 81 % as transparent oils.

4-13a

^{1}H NMR (500 MHz, $C_2Cl_4D_2$, 140 °C) δ 7.30 (s, 2H), 7.12 (s, 2H), 7.06 (s, 6H), 6.87 (s, 4H), 6.76 (s, 9H), 6.69 (s, 9H), 6.60 (s, 9H), 6.57 - 6.49 (m, 3H), 2.40 (m, 8H), 1.65 - 0.86 (m, 64H), 0.84 (m, 12H).

^{13}C NMR (75 MHz, THF): δ 143.58, 142.63, 141.49, 141.04, 140.83, 140.63, 138.81, 138.40, 134.45, 132.55, 131.12, 128.25, 127.71, 127.36, 126.99, 126.70, 121.35, 40.50, 39.73, 38.27, 33.89, 33.80, 33.34, 33.19, 29.09, 23.26, 23.18, 20.14.

MS (FD, 8kV): m/z (%) = 1634.4 (100.0 %, M^+), (calc. $C_{112}H_{128}Br_2$ = 1634.02 g/mol).

Elemental Analysis: found 79.31 % C, 8.93 % H - calc. 82.32 % C, 7.90 % H (see general remarks "7.2.4 Elemental Combustion Analysis").

4-13b

^{1}H NMR (500 MHz, THF): δ 7.35 (s, 2H), 7.15 (d, J = 7.7, 3H), 7.03 (s, 7H), 6.79 (m, 12H), 6.63 (m, 20H), 2.37 (d, J = 6.8, 4H), 2.33 (d, J = 6.9, 4H), 1.41 (m, 8H), 1.35 - 1.04 (m, 72H), 0.89 (t, J = 6.7, 12H).

^{13}C NMR (126 MHz, THF) δ 143.41, 142.41, 141.25, 141.05, 140.61, 140.17, 138.50, 138.20, 136.25, 134.05, 132.24, 130.85, 127.94, 127.44, 127.11, 126.69, 126.43, 121.05, 36.05, 32.72, 31.94, 30.46, 30.29, 30.14, 29.70, 23.39, 14.26.

MS (FD, 8kV): m/z (%) = 1744.9 (100.0 %, M^+), (calc. $C_{120}H_{144}Br_2$ = 1746.24 g/mol).

Elemental Analysis: found 82.20 % C, 8.63 % H - calc. 82.54% C, 8.31 % H (see general remarks "7.2.4 Elemental Combustion Analysis").

7.4.9 Polymer 1 / Polymer 2

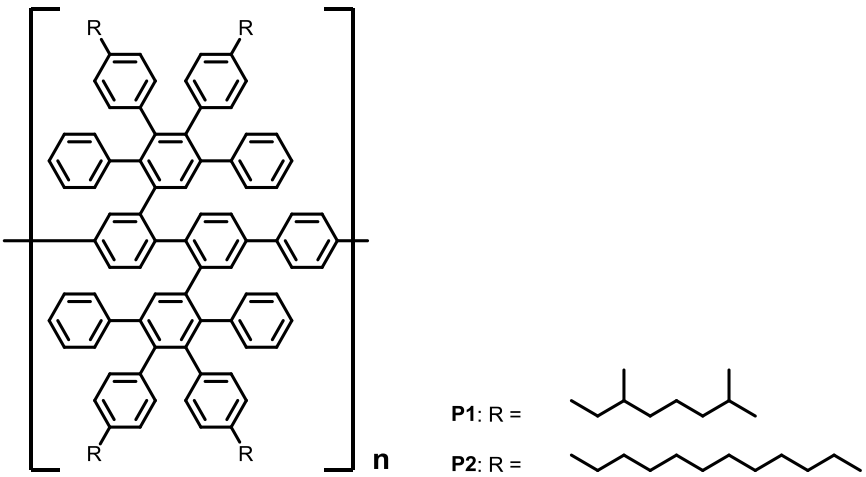

All monomers used were thoroughly dried under reduced pressure prior to the polymerizations. In a typical experiment, 0.061 mmol of **4-13a+b** and 20.13 mg (0.061 mmol) of 1,4-phenyldiboronic acid bis(pinacol) ester were placed in a *Schlenk* tube. Then, 4.0 ml of toluene and 2.0 ml of an aqueous potassium carbonate solution (2 M) and a few drops of Aliquat 336 werde added. The mixture was degassed by three freeze-pump-thaw cycles. Then, 10.00 mg (8.66 µmol) of tetrakis(triphenylphosphine)-

palladium(0) was added in a counterstream of argon followed by three freeze-pump-thaw cycles. The polymerization was carried out at reflux for 72 h. Then, excess bromobenzene and 5.00 mg (4.33 µmol) of tetrakis(triphenylphosphine)palladium(0) dissolved in 1.0 ml of toluene were added and the reaction was continued for 12 h. Subsequently, excess phenylboronic acid and 5.00 mg (4.33 µmol) of tetrakis(triphenylphosphine)palladium(0) dissolved in 1.0 ml toluene were added and the reaction was allowed to proceed for additional 12 h. After cooling, the reaction mixture was slowly dropped into dilute methanolic hydrochloric acid. The white precipitate which formed was collected by filtration, re-dissolved in DCM and precipitated as described above for two more times to yield **P1+2** as off-white powders in 70 - 75 %.

GPC: 7000 g/mol (PS; P1); 6130 g/mol (PS; P2).

FTIR: 3087 cm^{-1}, 3055 cm^{-1}, 3027 cm^{-1}, 2952 cm^{-1}, 2929 cm^{-1}, 1599 cm^{-1}, 1520 cm^{-1}, 1464 cm^{-1}, 1436 cm^{-1}, 1377 cm^{-1}, 1258 cm^{-1}, 1198 cm^{-1}, 1119 cm^{-1}, 1028 cm^{-1}, 1004 cm^{-1}, 901 cm^{-1}, 841 cm^{-1}, 814 cm^{-1}, 766 cm^{-1}, 723 cm^{-1}, 702 cm^{-1}, 667 cm^{-1}.

7.4.10 2-(4-Dodecylphenyl)-4,4,5,5-tetramethyl-1,3,2-dioxaborolane (4-16)

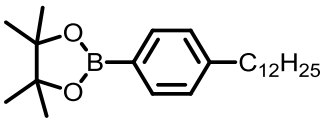

5.00 g (15.37 mmol) 1-bromo-4-dodecylbenzene, 15.61 g (61.48 mmol) bis(pinacolato)diboron and 15.00 g (152.72 mmol) of anhydrous potassium acetate were dissolved in 500.0 ml dioxane. Then, 2.00 g (2.46 mmol) of 1,1'-bis(diphenylphosphino)ferrocene-palladium(II)dichloride were added. The reaction mixture was heated to 100 °C and stirred under an inert atmosphere for 12 h. After cooling, the crude product was extracted with dichloromethane and then purified by column chromatography (hexane/ethyl acetate = 9/1) to yield 4.75 g (12.76 mmol) of **4-16** in 83 % as a colorless oil which solidified upon standing.

^{1}H NMR (300 MHz, CD_2Cl_2): δ 7.65 (d, J = 8.0, 2H), 7.18 (d, J = 7.9, 2H), 2.61 (t, J = 7.2, 2H), 1.66 - 1.55 (m, 2H), 1.38 - 1.19 (m, 30H), 0.88 (t, J = 6.7, 3H).

^{13}C NMR (75 MHz, CD_2Cl_2): δ 147.10, 135.22, 128.45, 84.18, 36.70, 32.53, 31.97, 30.27, 30.25, 30.18, 30.18, 30.08, 30.08, 29.95, 29.91, 29.91, 25.46, 25.26, 23.29, 14.46.

MS (FD, 8kV): m/z (%) = 370.2 (100.0 %, M^+), (calc. $C_{24}H_{41}BO_2$ = 372.39 g/mol).

Elemental Analysis: found 74.16 % C, 12.32 % H - calc. 77.41 % C, 11.10 % H (see general remarks "7.2.4 Elemental Combustion Analysis").

7.4.11 4'',5'-Bis(4-dodecylphenyl)-2,2''',5,5'''-tetraphenyl-3,3''',4,4'''-tetra(4-dodecylphenyl)-1,1':2',1'':2'',1'''-quaterphenyl (4-17)

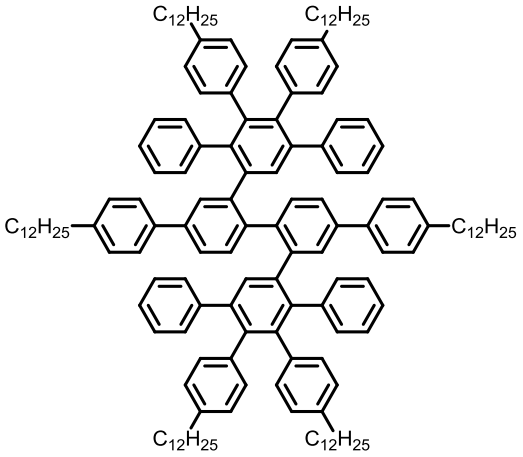

0.20 g (0.11 mmol) **4-13b** and 0.10 g (0.34 mmol) **4-16** were dissolved in 20.0 ml toluene. Then, 4.0 ml of aqueous potassium carbonate solution (2 M) and a few drops of Aliquat 336 werde added. After degassing by argon bubbling, 0.05 g (0.04 mmol) of tetrakis(triphenylphosphine)palladium(0) were added and the resulting mixture was heated to reflux for 24 h. After removal of the solvent, the crude product was was pre-purified by column chromatography (hexane/ethyl acetate = 9/1). Further purification was achieved by preparative gel permeation chromatography (chloroform) to yield 0.18 g (0.09 mmol) of **4-17** in 76 % as a colorless oil.

^{1}H-NMR (300 MHz, THF): δ 7.59 (t, J = 5.3, 2H), 7.30 (t, J = 7.3, 6H), 7.19 (d, J = 7.4, 4H), 7.05 (d, J = 7.0, 4H), 7.02 - 6.77 (m, 16H), 6.68 (m, 10H), 6.62 - 6.34 (m, 8H), 6.34 - 5.98 (m, 2H), 2.62 (m, 4H), 2.36 (m, 8H), 1.68 (m, 12H), 1.34 - 1.01 (m, 108H), 0.88 (m, 18H).

^{13}C-NMR (75 MHz, THF): δ 143.39, 142.97, 142.75, 141.60, 141.16, 140.87, 140.56, 140.47, 140.16, 140.07, 139.25, 138.80, 138.26, 135.96, 132.73, 132.62, 131.23, 129.53, 129.29, 128.11, 128.05, 127.82, 127.68, 126.73, 126.42, 126.07, 125.05, 36.61, 36.35, 33.05, 32.68, 32.33, 30.81, 30.50, 30.09, 30.03, 29.88, 23.73, 14.62.

MS (FD, 8kV): m/z (%) = 387.6 (100.0 %, M^+), (calc. $C_{156}H_{202}$ = 2077.27 g/mol).
Elemental Analysis: found 89.25 % C, 10.64 % H - calc. 90.20 % C, 9.80 % H (see general remarks "7.2.4 Elemental Combustion Analysis").

7.4.12 Cyclodehydrogenation of 4-22 / C84 disc

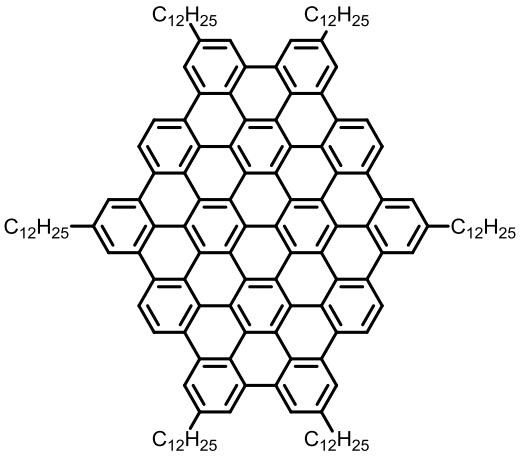

10.0 mg (4.81 µmol) of **4-17** were dissolved in 10.0 ml DCM. Then, 188.0 mg (1.16 mmol, 7.5 eqv./H) ferric chloride, dissolved in 1.0 ml nitromethane were added. Through the reaction mixture was passed for 2 h a stream of argon saturated with DCM in order to prevent evaporation of the reaction solvent. The reaction was stirred at room temperature for 24 h and monitored by MALDI-TOF spectroscopy. Then, excess methanol was added and the precipitate that formed was collected by filtration and washed with water and methanol. After drying, 9.0 mg (4.41 µmol) of a reddish brown solid were obtained in 91 %.

MS (MALDI-TOF): m/z (%) = 2044.45 (100.0 %), 2045.41 (85.9 %), 2043.44 (59.4 %), 2046.45 (50.2 %), 2047.48 (23.6 %), 2048.51 (14.8 %), 2049.48 (9.8 %), (calc. $C_{156}H_{170}$ = 2045.02 g/mol - isotop. distr.: 2044.33 (100.0%), 2045.34 (85.8%), 2043.33 (59.3%), 2046.34 (48.2%), 2047.34 (19.3%), 2048.35 (6.7%), 2049.35)).

7.4.13 Graphene Nanoribbons GNR 1 / GNR 2

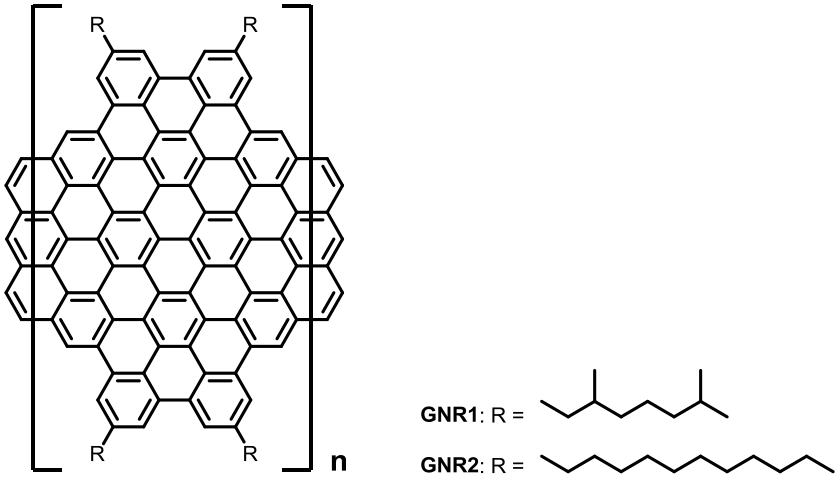

Method 1 ($FeCl_3$)

In a typical experiment, 25.0 mg of **P1+2** were dissolved in 25.0 ml DCM. The equivalents of ferric chloride were calculated on the basis of the mass of the repeating unit. 0.58 g (3.55 mmol, 7.5 eqv./H) ferric chloride, dissolved in 2.5 ml nitromethane were added. Through the reaction mixture was passed for 2 h a stream of argon saturated with DCM in order to prevent evaporation of the reaction solvent. The reaction was stirred at room temperature for 24 h. Then, excess methanol was added and the precipitate that formed was collected by filtration and washed with water and methanol. After drying, 23.0 mg of a black solid were obtained in 88 - 91 %.

Method 2 ($PIFA/BF_3$)

In a typical experiment 25.0 mg of **P1+2** were dissolved in 8.0 ml anhydrous DCM. The equivalents of $PIFA/BF_3$ were calculated on the basis of the mass of the repeating unit. Then, 254.0 mg phenyliodine(III) bis(trifluoroacetate (PIFA, 0.59 mmol, 2.5 eqv./bond) and 83.0 mg (0.074 ml, 0.45 mmol, 2.5 eqv./bond) boron trifluoride etherate dissolved in 2.5 ml anhydrous DCM were added at a temperature of - 60 °C (chloroform/dry ice). The reaction was stirred under an inert atmosphere at this temperature for 2 h and at a room temperature for additional 24 h. Then, excess methanol and water was added and the precipitate that formed was collected by filtration and washed with methanol. After drying, 21.0 mg of a black solid were obtained in 89 %.

FTIR: 2924 cm^{-1}, 2849 cm^{-1}, 1611 cm^{-1}, 1592 cm^{-1}, 1461 cm^{-1}, 1310 cm^{-1}, 1203 cm^{-1}, 1115 cm^{-1}, 866 cm^{-1}, 822 cm^{-1}, 762 cm^{-1}, 727 cm^{-1}, 698 cm^{-1}.

Raman: 1585 cm^{-1}, 1310 cm^{-1}.

7.4.14 2,2'-(4,4'-Dibromo-[1,1'-biphenyl]-2,2'-diyl)bis(1,4-diphenyltriphenylene) (4-23)

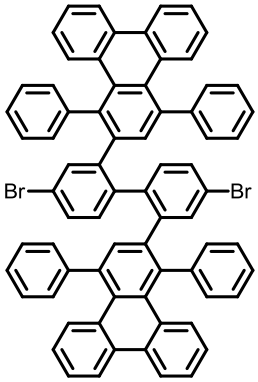

0.20 g (0.56 mmol) **4-6** and 0.85 g (2.22 mmol) phencyclone were placed in a microwave vessel. Then, 15.0 ml of *ortho*-xylene were added and the reaction mixture was degassed by argon bubbling. The reaction vessel was sealed, placed in a microwave reactor and heated to 160 °C at 300 W for 24 h with activated cooling. The crude product was purified by column chromatography (hexane/ethyl acetate = 7/3) to yield 0.48 g (0.45 mmol) of **4-23** in 81 % as an off-white solid.

^{1}H-NMR (300 MHz, THF): δ 8.53 (d, 4H), 7.80 - 7.50 (m, 3H), 7.45 (t, J = 6.4, 4H), 7.36 (t, J = 7.4, 4H), 7.20 (d, J = 8.3, 6H), 7.05 (t, J = 6.7, 7H), 6.92 (s, 3H), 6.85 (t, J = 8.9, 5H), 5.87 (s, 8H).

^{13}C-NMR (75 MHz, THF): δ 151.73, 144.94, 144.34, 141.49, 140.31, 139.72, 139.24, 138.99, 138.16, 137.22, 135.07, 133.75, 133.36, 132.09, 131.80, 131.46, 131.43, 130.48, 130.14, 129.90, 129.00, 128.18, 127.87, 126.84, 126.61, 126.38, 125.14, 124.92, 124.60, 122.98.

MS (FD, 8kV): m/z (%) = 1069.7 (100.0 %, M^+), (calc. $C_{72}H_{44}Br_2$ = 1068.93 g/mol).

Elemental Analysis: found 75.68 % C, 5.16 % H - calc. 80.90 % C, 4.15 % H (see general remarks "7.2.4 Elemental Combustion Analysis").

7.4.15 2'',3'-Bis(1,4-diphenyltriphenylen-2-yl)-1,1':4',1'':4'',1'''-quaterphenyl (4-24)

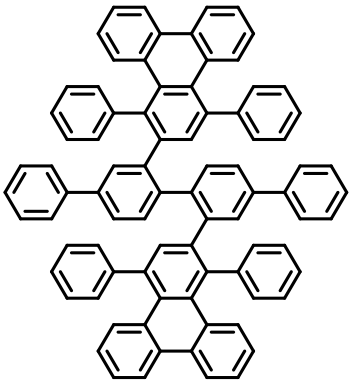

150.0 mg (0.14 mmol) **4-23** and 70.0 mg (0.56 mmol) phenylboronic acid were dissolved in 15.0 ml toluene. Then, 4.0 ml of aqueous potassium carbonate solution (2 M) and a few drops of Aliquat 336 werde added. After degassing by argon bubbling, 30.0 mg (0.03 mmol) of tetrakis(triphenylphosphine)palladium(0) were added and the resulting mixture was heated to reflux for 24 h. After removal of the solvent, the crude product was pre-purified by column chromatography (hexane/DCM = 7/3). Further purification was achieved by preparative gel permeation chromatography (chloroform) to yield 91.0 mg (0.09 mmol) of **4-24** in 61 % as a white solid.

^{1}H-NMR: (500 MHz, $C_2Cl_4D_2$, 130 °C) δ 8.49 (t, J = 7.4, 4H), 7.71 (t, J = 8.0, 2H), 7.56 (d, J =8.0, 2H), 7.39 (d, J = 8.9, 4H), 7.30 - 7.21 (m, 8H), 7.21 - 7.11 (m, 10H), 7.11 - 7.02 (m, 8H), 6.99 (d, J = 7.5, 8H), 6.95 - 6.74 (m, 8H).

^{13}C-NMR: (126 MHz, $C_2Cl_4D_2$, 130 °C) δ 150.45, 143.13, 143.08, 142.19, 141.78, 140.55, 139.14, 138.12, 138.10, 137.76, 137.38, 136.27, 135.20, 133.75, 133.02, 132.56, 132.01, 131.81, 131.77, 131.47, 130.72, 130.21, 130.14, 129.90, 128.97, 128.11, 127.71, 126.85, 126.39, 126.20, 125.01, 124.87, 124.61, 121.22.
MS (MALDI-TOF): m/z (%) = 1062.45 (100.0 %), 1063.45 (97.8 %), 1064.46 (54.5 %), 1065.42 (23.9 %), 1066.30 (7.3 %), (calc. $C_{84}H_{54}$ = 1063.33 g/mol - isotop. distr.: 1062.42 (100.0%), 1063.43 (91.5%), 1064.43 (41.3%), 1065.43 (12.1%), 1066.44 (2.7%)).

7.4.16 4,4''-Dichloro-2,2''-dinitro-1,1':4',1''-terphenyl (4-27)[14]

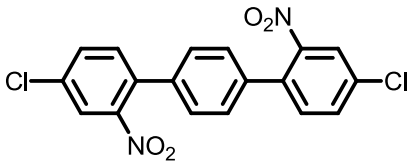

15.00 g (63.44 mmol) 1-bromo-4-chloro-2-nitrobenzene and 5.00 g (30.17 mmol) 1,4-phenyldiboronic acid were dissolved in 215.0 ml of dioxane. Then, a few drops of Aliquat 336 and 85.0 ml of an aqueous K_2CO_3 (2 M) were added. After degassing by argon bubbling, 0.70 g (0.61 mmol) of tetrakis(triphenylphosphine)palladium(0) were added. The reaction mixture was heated to reflux for 24 h. After cooling, the reaction mixture was poured on ice. 10.35 g (26.55 mmol) of a yellow precipitate which formed were collected, washed with methanol and used without further purification for the next step (88 %).

^{1}H NMR (250 MHz, CD_2Cl_2): δ 7.92 (d, J = 2.1, 2H), 7.67 (dd, J = 2.2, 8.3, 2H), 7.48 (d, J = 8.3, 2H), 7.38 (s, 4H).

^{13}C NMR (75 MHz, CD_2Cl_2): δ 149.89, 137.36, 134.88, 134.60, 133.79, 133.27, 128.89, 124.98.

MS (FD, 8kV): m/z (%) = 387.1 (100.0 %, M^+), (calc. $C_{18}H_{10}Cl_2N_2O_4$ = 389.91 g/mol).

Elemental Analysis: found 56.56 % C, 3.09 % H, 6.53 % N - calc. 55.55 % C, 2.59 % H, 7.20 % N.

7.4.17 4,4''-Dichloro-[1,1':4',1''-terphenyl]-2,2''-diamine (4-28)

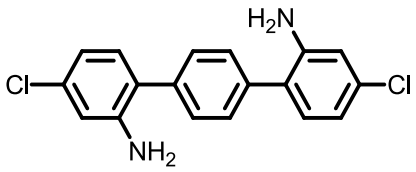

5.00 g (12.85 mmol) **4-27** and 0.70 g of palladium on carbon (10 wt%) were suspended in 200.0 ml of THF. The reaction mixture was evacuated after what a balloon filled with hydrogen gas was connected. The reaction mixture was heated to 50 °C for 24 h under vigorous stirring and monitored by thin-layer chromatography. With the consumption of the starting compound the reaction mixture turned homogenous. The crude product was purified by column chromatography (hexane/ethyl acetate = 7/3) to yield 3.89 g (11.82 mmol) of **4-28** as a yellow solid in 92 %.

^{1}H NMR (300 MHz, CD_2Cl_2): δ 7.40 (s, 4H), 6.96 (d, J = 6.4, 2H), 6.69 (dd, J = 2.0, 6.5, 4H), 3.88 (s, 4H).

^{13}C NMR (75 MHz, CD_2Cl_2): δ 145.66, 138.21, 134.42, 132.00, 130.04, 125.98, 118.82, 115.57.

MS (FD, 8kV): m/z (%) = 327.3 (100.0 %, M^+), (calc. $C_{18}H_{10}Cl_2N_2O_4$ = 329.22 g/mol).

Elemental Analysis: found 63.87 % C, 4.39 % H, 7.15 % N - calc. 65.67 % C, 4.29 % H, 8.51 % N.

7.4.18 4,4''-Dichloro-2,2''-diiodo-1,1':4',1''-terphenyl (4-29)

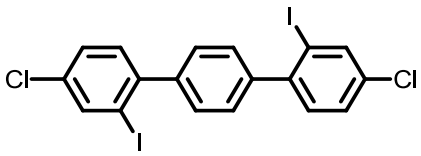

3.00 g (9.11 mmol) of **4-28** were suspended in 20.0 ml of water. Then, 12.0 ml of concentrated hydrochloric acid were added under cooling. At a temperature of - 5 °C, 10.0 ml of an aqueous solution containing 1.56 g (22.58 mmol) sodium nitrite were added dropwise. During this procedure, the color of the reaction mixture changed from yellow to dark brown. Subsequently, 30.0 ml of an aqueous solution containing 15.29 g (91.18 mmol) potassium iodide were added dropwise while maintaining the temperature below 0 °C. After the addition, the reaction was allowed to proceed for 1 h at room temperature. After extraction with DCM, treatment with an aqueous solution of sodium thiosulfate and removal of the solvent under reduced pressure the crude product was purified by column chromatography (hexane/ethyl acetate = 20/1) to yield 1.96 g (3.55 mmol) of **4-29** in 39 % as a yellowish solid

^{1}H NMR (300 MHz, CD_2Cl_2): δ 8.00 (d, J = 2.1, 2H), 7.43 (dd, J = 2.0, 8.5, 2H), 7.40 (s, 4H), 7.31 (d, J = 8.2, 2H).

^{13}C NMR (75 MHz, CD_2Cl_2): δ 145.27, 143.16, 139.39, 134.20, 131.21, 129.53, 128.99, 98.77.

MS (FD, 8kV): m/z (%) = 549.1 (100.0 %, M^+), (calc. $C_{18}H_{10}Cl_2I_2$ = 550.99 g/mol).

Elemental Analysis: found 40.55 % C, 2.13 % H - calc. 39.24 % C, 1.83 % H.

7.4.1 4,4''-Dichloro-2,2''-diethynyl-1,1':4',1''-terphenyl (4-31)

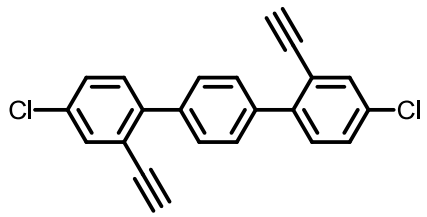

0.50 g (0.91 mmol) of **4-29** were mixed with 20.0 mg (0.11 mmol) of copper(II) iodide and 15.0 ml of triethylamine. After degassing by argon bubbling, 40.0 mg (0.06 mmol) of bis(triphenylphosphine)palladium(II) dichloride and 0.27 ml (1.36 mmol) of (trimethylsilyl)acetylene were added. The reaction mixture was stirred at room temperature for 24 h under an inert atmosphere and monitored by thin-layer chromatography. The reaction mixture was filtered over a silica pad (DCM) to remove inorganic residues.

The product thus obtained (0.40 g, 0.82 mmol, 90 %) was then dissolved in a mixture of 50.0 ml THF and 50.0 ml methanol. Then, 0.70 g (5.07 mmol) potassium carbonate was added and the reaction mixture was stirred at room temperature for 24 h. The crude product was purified by column chromatography (hexane/ethyl acetate = 9/1) to yield 0.18 g (0.53 mmol) of **4-31** in 64 %.

^{1}H NMR (300 MHz, CD_2Cl_2): δ 7.65 (s, 4H), 7.63 (d, J = 1.8, 2H), 7.44 (dd, J = 2.1, 8.4, 2H), 7.39 (dd, J = 0.5, 8.4, 2H), 3.20 (s, 2H).

^{13}C NMR (75 MHz, CD_2Cl_2): δ 142.82, 139.19, 134.04, 133.51, 131.50, 129.95, 129.48, 122.51, 82.24, 81.99.

MS (FD, 8kV): m/z (%) = 345.5 (100.0 %, M^+), (calc. $C_{22}H_{12}Cl_2$ = 347.24 g/mol).

Elemental Analysis: found 75.79 % C, 4.26 % H - calc. 76.10 % C, 3.48 % H.

7.4.2 5,5''-Dichloro-[1,1':4',1''-terphenyl]-2,2''-diamine (4-33)

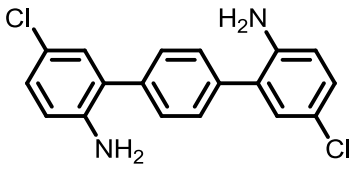

4.20 g (20.34 mmol) 2-bromo-4-chloroaniline and 3.05 g (9.25 mmol) 1,4-phenyldiboronic acid bis(pinacol) ester were dissolved in 180.0 ml of dioxane. Then, a few drops of Aliquat 336 and 75.0 ml of an aqueous K_2CO_3 (2 M) were added. After degassing by argon bubbling, 0.35 g (0.30 mmol) of tetrakis-(triphenylphosphine)palladium(0) were added. The reaction mixture was heated to reflux for 24 h. The crude product was purified by column chromatography (hexane/ethyl acetate = 7/3) to yield 2.41 g (7.31 mmol) of **4-33** as a yellow solid in 79 %.

^{1}H NMR (300 MHz, CD_2Cl_2): δ 7.52 (s, 4H), 7.12 (dd, J = 2.1, 10.1, 4H), 6.72 (dd, J = 0.9, 7.9, 2H), 3.88 (s, 4H).

^{13}C NMR (75 MHz, CD_2Cl_2): δ 143.21, 138.25, 130.36, 130.01, 128.81, 128.77, 123.30, 117.27.

MS (FD, 8kV): m/z (%) = 327.3 (100.0 %, M^+), (calc. $C_{18}H_{10}Cl_2N_2O_4$ = 329.22 g/mol).

Elemental Analysis: found 65.65 % C, 4.57 % H, 7.76 % N - calc. 65.67 % C, 4.29 % H, 8.51 % N.

7.4.3 5,5''-Dichloro-2,2''-diiodo-1,1':4',1''-terphenyl (4-34)

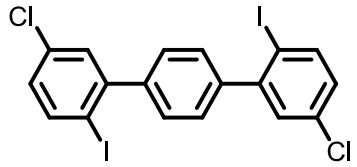

2.00 g (6.07 mmol) of **4-33** were suspended in 15.0 ml of water. Then, 8.0 ml of concentrated hydrochloric acid were added under cooling. At a temperature of - 5 °C, 7.0 ml of an aqueous solution containing 1.04 g (15.05 mmol) sodium nitrite were added dropwise. During this procedure, the color of the reaction mixture changed from yellow to dark brown. Subsequently, 20.0 ml of an aqueous solution containing 10.19 g (60.79 mmol) potassium iodide were added dropwise while maintaining the temperature below 0 °C. After the addition, the reaction was allowed to proceed for 1 h at room temperature. After extraction with DCM, treatment with an aqueous solution of sodium thiosulfate and removal of the solvent under reduced pressure the crude product was purified by column chromatography (hexane/ethyl acetate = 8/2) to yield 1.40 g (3.55 mmol) of **4-34** in 42 % as a yellowish solid

^{1}H NMR (300 MHz, CD_2Cl_2): δ 7.91 (d, J = 8.5, 2H), 7.41 (s, 4H), 7.39 (d, J = 2.5, 2H), 7.08 (dd, J = 2.6, 8.5, 2H).

^{13}C NMR (75 MHz, CD_2Cl_2): δ 148.20, 143.29, 141.26, 135.03, 130.62, 129.65, 129.49, 96.09.

MS (FD, 8kV): m/z (%) = 549.1 (100.0 %, M^+), (calc. $C_{18}H_{10}Cl_2I_2$ = 550.99 g/mol).

Elemental Analysis: found 40.60 % C, 2.22 % H - calc. 39.24 % C, 1.83 % H.

7.4.4 5,5''-Dichloro-2,2''-diethynyl-1,1':4',1''-terphenyl (4-36)

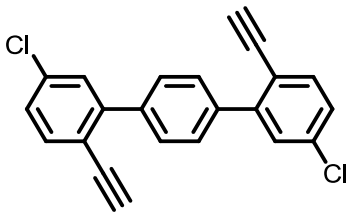

2.00 g (3.64 mmol) of **4-34** were mixed with 80.0 mg (0.44 mmol) of copper(II) iodide and 30.0 ml of triethylamine and 10.0 ml of toluene. After degassing by argon bubbling, 160 mg (0.24 mmol) of bis(triphenylphosphine)palladium(II) dichloride and 1.50 ml (7.56 mmol) of (trimethylsilyl)acetylene were added. The reaction mixture was stirred at room temperature for 24 h under an inert atmosphere and monitored by thin-layer chromatography. The reaction mixture was filtered over a silica pad (DCM) to remove inorganic residues. The product thus obtained (1.52 g, 3.09 mmol, 85 %) was then dissolved in a mixture of 100.0 ml THF and 100.0 ml methanol. Then, 3.00 g (21.74 mmol) potassium carbonate was added and the reaction mixture was stirred at room temperature for 24 h. The crude product was purified by column chromatography (hexane/ethyl acetate = 9/1) to yield 0.73 g (2.10 mmol) of **4-36** in 68 %.

^{1}H NMR (300 MHz, CD_2Cl_2): δ 7.67 (s, 4H), 7.58 (d, J = 8.3, 2H), 7.46 (d, J = 2.2, 2H), 7.33 (dd, J = 2.2, 8.3, 2H), 3.19 (s, 2H).

^{13}C NMR (75 MHz, CD_2Cl_2): δ 145.84, 139.27, 135.76, 135.48, 130.21, 129.51, 127.99, 119.56, 82.49, 81.78.

MS (FD, 8kV): m/z (%) = 345.5 (100.0 %, M^+), (calc. $C_{22}H_{12}Cl_2$ = 347.24 g/mol).

Elemental Analysis: found 75.90 % C, 4.08 % H - calc. 76.10 % C, 3.48 % H.

7.4.5 4'''',5'-Dichloro-2,2'''',5,5''''-tetraphenyl-3,3'''',4,4''''-tetra(4-dodecylphenyl)-1,1':2',1'':4'',1''':2''',1''''-quinquephenyl (4-37)

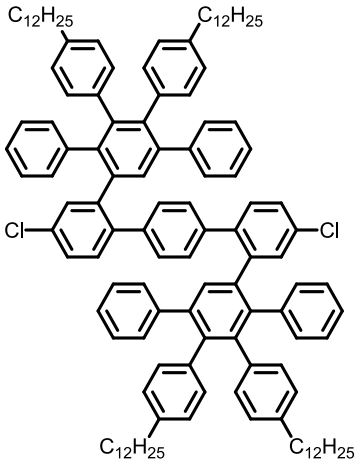

0.14 g (0.40 mmol) **4-31** and 0.70 g (0.97 mmol) **4-11b** were placed in a microwave vessel. Then, 8.0 ml of *ortho*-xylene were added and the reaction mixture was degassed by argon bubbling. The reaction vessel was sealed, placed in a microwave reactor and heated to 160 °C at 300 W for 24 h with activated cooling. The crude product was pre-purified by column chromatography (hexane/ethyl acetate = 9/1). Further purification was achieved by preparative gel permeation chromatography (chloroform) to yield 0.59 g (0.34 mmol) of **4-37** in 85 % as a transparent oil which solidified upon standing.

^{1}H NMR (700 MHz, THF): δ 7.50 - 7.40 (m, 4H), 7.25 (t, J = 12.2, 2H), 7.13 (t, J = 7.5, 2H), 7.07 (m, 10H), 6.92 - 6.40 (m, 29H), 6.01 - 5.80 (d, J = 73.9, 1H), 2.38 (t, J = 7.5, 4H), 2.28 (t, J = 7.3, 4H), 1.43 (p, 4H), 1.36 (p, 4H), 1.32 - 1.06 (m, 72H), 0.89 (t, J = 7.1, 12H).

^{13}C NMR (75 MHz, THF): δ 143.24, 142.98, 141.66, 141.16, 140.86, 140.74, 140.32, 140.18, 139.91, 139.79, 139.72, 138.69, 138.51, 133.23, 132.49, 132.33, 132.09, 130.94, 129.98, 128.41, 128.24, 127.86, 127.52, 127.37, 127.07, 126.20, 36.36, 36.29, 33.05, 32.38, 32.32, 30.86, 30.80, 30.65, 30.50, 30.03, 29.95, 29.83, 23.62, 14.65.

MS (FD, 8kV): m/z (%) = 1731.6 (100.0 %, M^+), (calc. $C_{126}H_{148}Cl_2$ = 1733.43 g/mol).

Elemental Analysis: found 85.16 % C, 9.21 % H - calc. 87.30 % C, 8.61 % H (see general remarks "7.2.4 Elemental Combustion Analysis").

7.4.6 4',5'''-Dichloro-2,2'''',5,5''''-tetraphenyl-3,3'''',4,4''''-tetra(4-dodecylphenyl)-1,1':2',1'':4'',1''':2''',1''''-quinquephenyl (4-38)

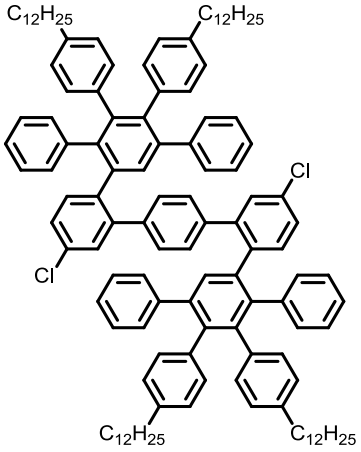

0.14 g (0.40 mmol) **4-36** and 0.70 g (0.97 mmol) **4-11b** were placed in a microwave vessel. Then, 8.0 ml of *ortho*-xylene were added and the reaction mixture was degassed by argon bubbling. The reaction vessel was sealed, placed in a microwave reactor and heated to 160 °C at 300 W for 24 h with activated cooling. The crude product was pre-purified by column chromatography (hexane/ethyl acetate = 9/1). Further purification was achieved by preparative gel permeation chromatography (chloroform) to yield 0.51 g (0.29 mmol) of **4-38** in 74 % as a transparent oil which solidified upon standing.

^{1}H NMR (700 MHz, THF): δ 7.42 (d, J = 4.9, 3H), 7.35 (d, J = 8.1, 1H), 7.32 – 7.23 (m, 2H), 7.22 (s, 2H), 7.08 (t, J = 10.6, 10H), 6.91 (d, J = 53.1, 7H), 6.82 (s, 3H), 6.69 (s, 9H), 6.55 (m, 10H), 6.11 (s, 1H), 2.40 (t, J = 7.5, 4H), 2.32 (t, J = 7.1, 4H), 1.47 (p, 4H), 1.39 (p, 4H), 1.35 - 1.03 (m, 72H), 0.91 (t, J = 6.9, 12H).

^{13}C NMR (176 MHz, THF): δ 144.06, 143.93, 143.71, 142.36, 142.28, 141.72, 141.64, 141.43, 141.35, 141.31, 141.17, 141.06, 140.57, 139.44, 139.22, 135.19, 135.09, 134.48, 134.24, 134.03, 133.20, 132.77, 131.59, 131.18, 130.81, 129.13, 128.54, 128.32, 127.77, 126.97, 37.07, 33.78, 33.09, 31.59, 31.56, 31.37, 31.28, 30.74, 24.47, 15.37.

MS (FD, 8kV): m/z (%) = 1730.9 (100.0 %, M^+), (calc. $C_{126}H_{148}Cl_2$ = 1733.43 g/mol).

Elemental Analysis: found 84.91 % C, 8.95 % H - calc. 87.30 % C, 8.61 % H (see general remarks "7.2.4 Elemental Combustion Analysis").

7.4.7 4,4''-Dibromo-2,2''-dinitro-1,1':4',1''-terphenyl (4-41)

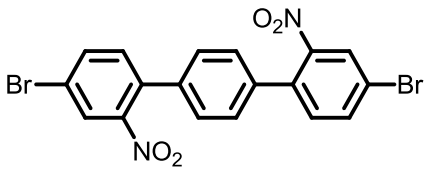

4.93 g (17.55 mmol) 1,4-dibromo-2-nitrobenzene and 2.20 g (6.66 mmol) 1,4-phenyldiboronic acid bis(pinacol) ester were dissolved in 80.0 ml of toluene. Then, a few drops of Aliquat 336 and 10.0 ml of an aqueous K_2CO_3 (2 M) were added. After degassing by argon bubbling, 0.25 g (0.22 mmol) of tetrakis-(triphenylphosphine)palladium(0) were added. The reaction mixture was heated to reflux for 72 h. After cooling, the reaction mixture was poured on a mixture of ice and methanol. 10.35 g (3.37 mmol) of a yellow precipitate which formed were collected, washed with methanol and used without further purification for the next step (51 %).

^{1}H NMR (300 MHz, CD_2Cl_2): δ 8.06 (d, J = 2.0, 2H), 7.81 (dd, J = 2.0, 8.3, 2H), 7.41 (d, J = 8.3, 2H), 7.39 (s, 4H).

^{13}C NMR (75 MHz, CD_2Cl_2): δ 149.96, 137.39, 136.23, 135.01, 133.96, 128.82, 127.80, 122.27.

MS (FD, 8kV): m/z (%) = 477.6 (100.0 %, M^+), (calc. $C_{18}H_{10}Br_2N_2O_4$ = 478.09 g/mol).

7.4.8 4,4''-Di(dodec-1-yn-1-yl)-2,2''-dinitro-1,1':4',1''-terphenyl (4-42)

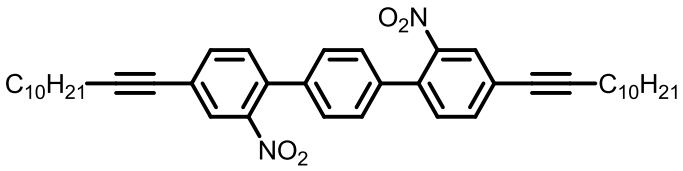

2.60 g (5.43 mmol) of **4-41** were mixed with 80.0 mg (0.44 mmol) of copper(II) iodide and 50.0 ml of triethylamine. After degassing by argon bubbling, 160 mg (0.24 mmol) of bis(triphenylphosphine)palladium(II) dichloride and 2.70 g (16.31 mmol) of dodec-1-yne were added. The reaction mixture was stirred at room temperature for 24 h. The crude product was purified by column chromatography (hexane/ethyl acetate = 9/1) to yield 3.11 g (4.78 mmol) of **4-42** in 88 %.

^{1}H NMR (300 MHz, CD_2Cl_2): δ 7.87 (d, J = 1.6, 2H), 7.64 (dd, J = 1.7, 8.0, 2H), 7.43 (d, J = 8.0, 2H), 7.37 (s, 4H), 2.45 (t, J = 7.0, 4H), 1.56 (p, 4H), 1.51 – 1.22 (m, 28H), 0.92 – 0.84 (t, J = 6.4, 6H).

^{13}C NMR (75 MHz, CD_2Cl_2): δ 149.59, 137.79, 135.73, 134.80, 132.53, 128.80, 127.54, 125.69, 94.87, 78.68, 32.52, 30.18, 30.12, 29.92, 29.72, 29.52, 29.10, 23.28, 19.95, 14.46.

MS (FD, 8kV): m/z (%) = 649.1 (100.0 %, M^+), (calc. $C_{42}H_{52}N_2O_4$ = 648.87 g/mol).

7.4.9 4,4''-Didodecyl-[1,1':4',1''-terphenyl]-2,2''-diamine (4-43)

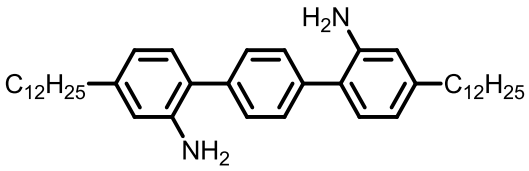

2.40 g (3.71 mmol) **4-42** and 0.30 g of palladium on carbon (10 wt%) were suspended in 90.0 ml of THF. The reaction mixture was evacuated after what a balloon filled with hydrogen gas was connected. The reaction mixture was heated to 50 °C for 24 h under vigorous stirring and monitored by thin-layer chromatography. The crude product was purified by filtration to yield 1.82 g (3.38 mmol) of **4-43** as a yellow oil in 91 %.

^{1}H NMR (300 MHz, CD_2Cl_2): δ 7.51 (s, 4H), 7.06 (d, J = 7.7, 2H), 6.66 (dd, J = 1.6, 7.7, 2H), 6.61 (d, J = 1.4, 2H), 3.83 (s, 4H), 2.55 (t, J = 6.8, 4H), 1.63 (m, 4H), 1.47 – 1.17 (m, 36H), 0.89 (t, J = 6.7, 6H).

^{13}C NMR (75 MHz, CD_2Cl_2): δ 144.28, 144.23, 138.91, 130.77, 129.96, 125.16, 119.43, 116.18, 68.36, 36.33, 32.56, 32.08, 30.71, 30.56, 30.09, 29.98, 26.19, 23.31, 14.49.

MS (FD, 8kV): m/z (%) = 595.5 (100.0 %, M^+), (calc. $C_{42}H_{64}N_2$ = 596.97 g/mol).

7.4.10 4,4''-Didodecyl-2,2''-diiodo-1,1':4',1''-terphenyl (4-44)

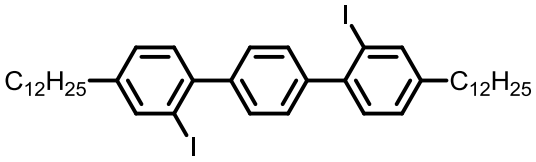

1.50 g (2.51 mmol) of **4-43** was suspended in a mixture of 7.0 ml of water and 1.0 ml of THF. Then, 4.0 ml of concentrated hydrochloric acid were added under cooling. At a temperature of - 5 °C, 4.0 ml of an aqueous solution containing 0.50 g (7.06 mmol) sodium nitrite were added dropwise. During this procedure, the color of the reaction mixture changed from yellow to dark brown. Subsequently, 12.0 ml of an aqueous solution containing 5.00 g (28.52 mmol) potassium iodide were added dropwise while maintaining the temperature below 0 °C. After the addition, the reaction was allowed to proceed for 1 h at room temperature. After extraction with DCM, treatment with an aqueous solution of sodium thiosulfate and removal of the solvent under reduced pressure the crude product was purified by column chromatography (hexane) to yield 0.64 g (0.78 mmol) of **4-44** in 31 % as a yellowish oil.

^{1}H NMR (300 MHz, CD_2Cl_2): δ 7.83 (d, J = 1.2, 2H), 7.39 (s, 4H), 7.28 (d, J = 7.8, 2H), 7.25 (dd, J = 1.2, 4.7, 2H), 2.61 (t, J = 6.8, 4H), 1.63 (m, 4H), 1.45 - 1.15 (m, 36H), 0.89 (t, J = 6.7, 6H).
^{13}C NMR (75 MHz, CD_2Cl_2): δ 144.88, 144.00, 143.73, 140.10, 130.48, 129.56, 129.06, 98.71, 35.55, 32.54, 31.93, 30.29, 30.19, 30.08, 29.97, 29.89, 23.31, 14.49.

MS (FD, 8kV): m/z (%) = 816.7 (100.0 %, M^+), (calc. $C_{42}H_{60}I_2$ = 818.73 g/mol).

7.4.11 4,4''-Didodecyl-2,2''-diethynyl-1,1':4',1''-terphenyl (4-46)

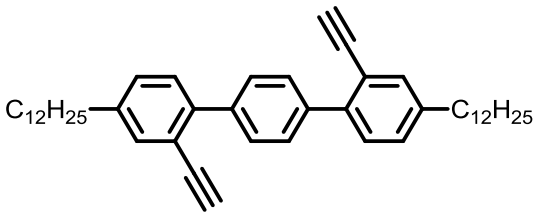

0.50 g (0.61 mmol) of **4-44** were mixed with 15.0 mg (0.09 mmol) of copper(II) iodide and 5.0 ml of triethylamine. After degassing by argon bubbling, 30 mg (0.05 mmol) of bis(triphenylphosphine)palladium(II) dichloride and 0.4 ml (2.00 mmol) of (trimethylsilyl)acetylene were added. The reaction mixture was stirred at room temperature for 24 h under an inert atmosphere and monitored by thin-layer chromatography. The reaction mixture was filtered over a silica pad (hexane) to remove inorganic residues. The product thus obtained (0.33 g, 0.43 mmol, 71 %) was then dissolved in a mixture of 20.0 ml THF and 20.0 ml Methanol. Then, 0.27 g (1.96 mmol) potassium carbonate was added and the reaction mixture was stirred at room temperature for 24 h. The crude product was purified by column chromatography (hexane) to yield 0.19 g (0.31 mmol) of **4-46** in 72 %.

^{1}H NMR (300 MHz, CD_2Cl_2): 7.66 (s, 4H), 7.48 (d, J = 1.6, 2H), 7.37 (d, J = 7.9, 2H), 7.28 (dd, J = 1.8, 8.0, 2H), 3.13 (s, 2H), 2.65 (t, J = 7.2, 4H), 1.66 (p, 4H), 1.32 (m, 36H), 0.89 (t, J = 6.7, 6H).

^{13}C NMR (75 MHz, CD_2Cl_2): δ 142.83, 141.81, 139.85, 134.49, 130.11, 129.45, 127.37, 120.54, 84.06, 80.29, 35.84, 32.55, 31.91, 30.30, 30.21, 29.98, 29.90, 23.31, 14.50.

MS (FD, 8kV): m/z (%) = 613.0 (100.0 %, M^+), (calc. $C_{46}H_{62}$ = 614.98 g/mol).

Elemental Analysis: found 90.02 % C, 10.01 % H - calc. 89.84 % C, 10.16 % H.

7.4.12 4''',5'-didodecyl-2,2'''',5,5''''-tetraphenyl-3,3'''',4,4''''-tetra(4-dodecylphenyl)-1,1':2',1'':4'',1''':2''',1''''-quinquephenyl (4-39)

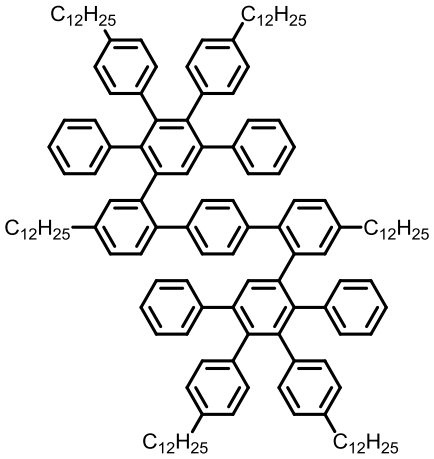

0.25 g (0.33 mmol) **4-46** and 0.75 g (1.05 mmol) **4-11b** were placed in a microwave vessel. Then, 8.0 ml of *ortho*-xylene were added and the reaction mixture was degassed by argon bubbling. The reaction vessel was sealed, placed in a microwave reactor and heated to 160 °C at 300 W for 24 h with activated cooling. The crude product was pre-purified by column chromatography (hexane/ethyl acetate = 9/1). Further purification was achieved by preparative gel permeation chromatography (chloroform) to yield 0.51 g (0.27 mmol) of **4-39** in 81 % as a transparent oil.

^{1}H NMR (500 MHz, THF): δ 7.41 (d, J = 10.9, 2H), 7.18 (d, J = 22.4, 2H), 7.12 – 7.00 (m, 12H), 6.85 (d, J = 19.8, 5H), 6.74 (s, 3H), 6.69 (d, J = 8.1, 8H), 6.58 (s, 5H), 6.47 (d, J = 14.6, 4H), 6.31 - 5.77 (m, 1H), 2.56 (s, 4H), 2.37 (t, J = 7.4, 4H), 2.29 (t, J = 7.1, 4H), 1.57 (s, 4H), 1.51 - 1.03 (m, 122H), 0.89 (t, J = 6.5, 18H).

^{13}C NMR (126 MHz, THF): δ 143.28, 143.25, 142.98, 142.91, 141.84, 141.50, 141.25, 141.10, 140.97, 140.90, 140.45, 140.12, 140.08, 139.26, 139.14, 139.04, 138.77, 133.59, 133.36, 133.10, 133.00, 132.57, 132.47, 132.19, 130.66, 130.56, 129.96, 128.32, 127.86, 127.75, 127.51, 127.41, 126.87, 125.91, 36.44, 36.37, 33.06, 32.56, 32.41, 32.35, 30.86, 30.81, 30.71, 30.67, 30.52, 30.49, 30.31, 30.04, 29.97, 25.98, 25.81, 25.65, 25.49, 25.33, 25.17, 23.75, 21.50, 14.64.
MS (FD, 8kV): m/z (%) = 2002.1 (100.0 %, M^{+}), (calc. $C_{150}H_{198}$ = 2001.18 g/mol).

Elemental Analysis: found 90.29 % C, 9.48 % H - calc. 90.03 % C, 9.97 % H.

7.4.13 Polymer 3

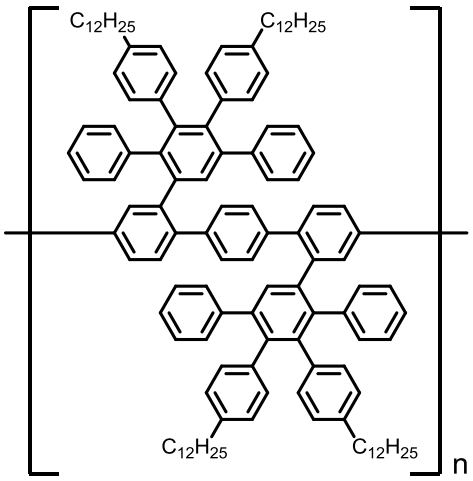

The catalyst solution was prepared inside the glove box by adding 0.5 ml DMF and 2.0 ml toluene to a mixture of 55.0 mg (0.19 mmol) bis(cyclooctadiene)nickel(0), 29.0 mg (0.19 mmol) 2,2'-bipyridine and 0.05 ml (0.19 mmol) cyclooctadiene. The resulting solution was stirred for 30 min at 60 °C. Then, a solution of 100.0 mg (0.06 mmol) of **4-37** dissolved in 1.0 ml toluene and 0.5 ml DMF was added. The reaction mixture was stirred for 72 h at 80 °C under the exclusion of light. Then, excess chlorobenzene (anhydrous) was added and the mixture was stirred for additional 12 h. After cooling, the reaction mixture was slowly dropped into dilute methanolic hydrochloric acid. The white precipitate which formed was collected by filtration, re-dissolved in DCM and precipitated as described above for two more times to yield **P3** as an off-white powder in 83 %.

GPC: 76900 g/mol (PS).

FTIR: 3087 cm^{-1}, 3055 cm^{-1}, 3025 cm^{-1}, 2921 cm^{-1}, 1600 cm^{-1}, 1514 cm^{-1}, 1465 cm^{-1}, 1440 cm^{-1}, 1407 cm^{-1}, 1376 cm^{-1}, 1155 cm^{-1}, 1117 cm^{-1}, 1073 cm^{-1}, 1023 cm^{-1}, 1004 cm^{-1}, 839 cm^{-1}, 814 cm^{-1}, 757 cm^{-1}, 698 cm^{-1}, 614 cm^{-1}.

Polymer 4

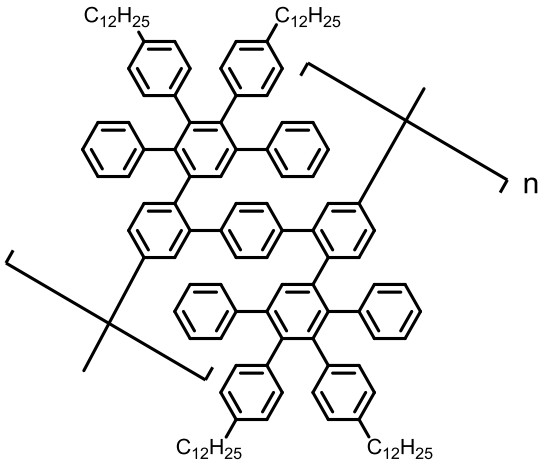

The catalyst solution was prepared inside the glove box by adding 0.5 ml DMF and 2.0 ml toluene to a mixture of 55.0 mg (0.19 mmol) bis(cyclooctadiene)nickel(0), 29.0 mg (0.19 mmol) 2,2'-bipyridine and 0.05 ml (0.19 mmol) cyclooctadiene. The resulting solution was stirred for 30 min at 60 °C. Then, a solution of 100.0 mg (0.06 mmol) of **4-38** dissolved in 1.0 ml toluene and 0.5 ml DMF was added. The reaction mixture was stirred for 72 h at 80 °C under the exclusion of light. Then, excess chlorobenzene (anhydrous) was added and the mixture was stirred for additional 12 h. After cooling, the reaction mixture was slowly dropped into dilute methanolic hydrochloric acid. The white precipitate which formed was collected by filtration, re-dissolved in DCM and precipitated as described above for two more times to yield **P4** as an off-white powder in 81 %.

GPC: 11400 g/mol (PS).

FTIR: 3083 cm^{-1}, 3056 cm^{-1}, 3025 cm^{-1}, 2922 cm^{-1}, 2852 cm^{-1}, 1601 cm^{-1}, 1514 cm^{-1}, 1465 cm^{-1}, 1439 cm^{-1}, 1407 cm^{-1}, 1377 cm^{-1}, 1261 cm^{-1}, 1074 cm^{-1}, 1023 cm^{-1}, 1008 cm^{-1}, 896 cm^{-1}, 823 cm^{-1}, 801 cm^{-1}, 755 cm^{-1}, 721 cm^{-1}, 698 cm^{-1}, 655 cm^{-1}.

7.4.14 Cyclodehydrogenation of 4-39 / C78 disc

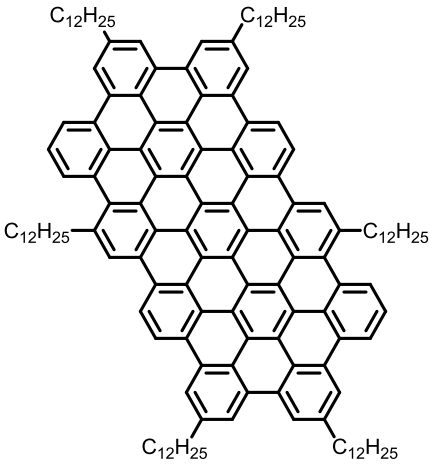

Method 1 ($FeCl_3$)

25.0 mg (12.51 µmol) of **4-39** were dissolved in 30.0 ml DCM. Then, 426.0 mg (2.62 mmol, 7.5 eqv./H) ferric chloride dissolved in 2.0 ml nitromethane were added. Through the reaction mixture was passed for 2 h a stream of argon saturated with DCM in order to prevent evaporation of the reaction solvent. The reaction was stirred at room temperature for 24 h and monitored by MALDI-TOF spectroscopy. Then, excess methanol was added and the precipitate that formed was collected by filtration and washed with water and methanol. After drying, 23.0 mg (11.61 µmol) of a reddish brown solid were obtained in 93 %.

Method 2 ($PIFA/BF_3$)

25.0 mg (12.51 µmol) of **4-39** were dissolved in 10.0 ml DCM. Then, 193.0 mg phenyliodine(III) bis(trifluoroacetate (PIFA, 0.45 mmol, 2.5 eqv./bond) and 63.0 mg (0.056 ml, 0.45 mmol, 2.5 eqv./bond) boron trifluoride etherate dissolved in 2.0 ml DCM were added at a temperature of - 60 °C (chloroform/dry ice). The reaction was stirred under an inert atmosphere at this temperature for 2 h and at a temperature of - 10 °C for additional 1.5 h. Then, excess methanol and water was added and the precipitate that formed was collected by filtration and washed with methanol. After drying, 20.0 mg (10.14 µmol) of a reddish brown solid were obtained in 81 %.

Method 3 ($MoCl_5$)

25.0 mg (12.51 µmol) of **4-39** were dissolved in 10.0 ml DCM. Then, 250.0 mg (0.88 mol, 5.0 eqv./bond) molybdenum pentachloride dissolved in 5.0 ml DCM were added. Through the reaction mixture was passed for 2 h a stream of argon saturated with DCM in order to prevent evaporation of the reaction solvent. The reaction was stirred at room temperature for 48 h and monitored by MALDI-TOF spectroscopy. Then, excess methanol was added and the precipitate that formed was collected by filtration and washed with water and methanol. After drying, 22.0 mg (11.16 µmol) of a reddish brown solid were obtained in 89 %.

^{1}H NMR (500 MHz, *o*-DCB, 170 °C): δ 8.67 (s, 4H), 8.55 (m, 4H), 8.43 (m, 4H), 8.36 (m, 4H), 7.92 (s, 4H), 3.75 (t, 4H), 3.08 (s, 4H), 3.17 (t, J = 7.4, 4H), 2.40 (t, J = 7.1, 4H), 2.26 (m, 8H), 2.08 - 1.09 (m, 108H), 1.06 (t, J = 6.1, 18H).

MS (MALDI-TOF): m/z (%) = 1973.29 (100.0 %), 1974.25 (81.2 %), 1972.27 (67.7 %), 1975.21 (44.5 %), 1976.17 (19.8 %), 1977.14 (11.6 %), 1978.00 (7.1 %), (calc. $C_{150}H_{170}$ = 1972.95 g/mol - isotop. distr.: 1972.33 (100.0%), 1973.34 (82.5%), 1971.33 (61.6%), 1974.34 (44.6%), 1975.34 (17.1%), 1976.35 (5.7%), 1977.35 (1.5%)).

7.4.15 Graphene Nanoribbon GNR3

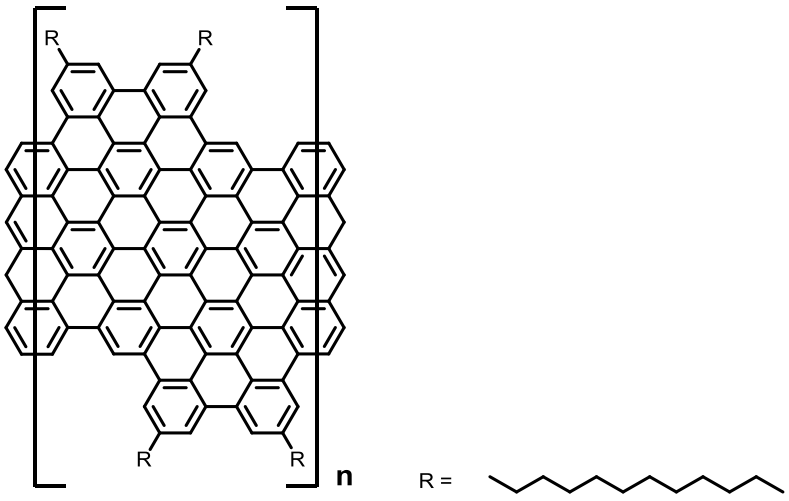

Method 1 ($FeCl_3$)

In a typical experiment, 25.0 mg of **P3** was dissolved in 30.0 ml DCM. Then, 0.51 g (3.16 mmol, 7.5 eqv./H) ferric chloride, dissolved in 2.0 ml nitromethane were

added. Through the reaction mixture was passed for 2 h a stream of argon saturated with DCM in order to prevent evaporation of the reaction solvent. The reaction was stirred at room temperature for 24 h. Then, excess methanol was added and the precipitate that formed was collected by filtration and washed with water and methanol. After drying, 23.0 mg of a black solid were obtained in 91 %.

Method 2 ($PIFA/BF_3$)

In a typical experiment 25.0 mg of **P3** was dissolved in 20.0 ml anhydrous DCM. Then, 200.0 mg phenyliodine(III) bis(trifluoroacetate (PIFA, 0.45 mmol, 2.1 eqv./bond) and 63.0 mg (0.056 ml, 0.45 mmol, 2.1 eqv./bond) boron trifluoride etherate dissolved in 2.0 ml anhydrous DCM were added at a temperature of - 60 °C (chloroform/dry ice). The reaction was stirred under an inert atmosphere at this temperature for 2 h and at room temperature for additional 24 h. Then, excess methanol and water was added and the precipitate that formed was collected by filtration and washed with methanol. After drying, 24.0 mg of a black solid were obtained in 95 %.

FTIR: 3063 cm^{-1}, 2920 cm^{-1}, 2849 cm^{-1}, 1718 cm^{-1}, 1603 cm^{-1}, 1587 cm^{-1}, 1452 cm^{-1}, 1302 cm^{-1}, 1215 cm^{-1}, 1076 cm^{-1}, 1012 cm^{-1}, 870 cm^{-1}, 818 cm^{-1}, 723 cm^{-1}, 620 cm^{-1}.

Raman: 1593 cm^{-1}, 1292 cm^{-1}.

7.4.16 Graphene Nanoribbon GNR4

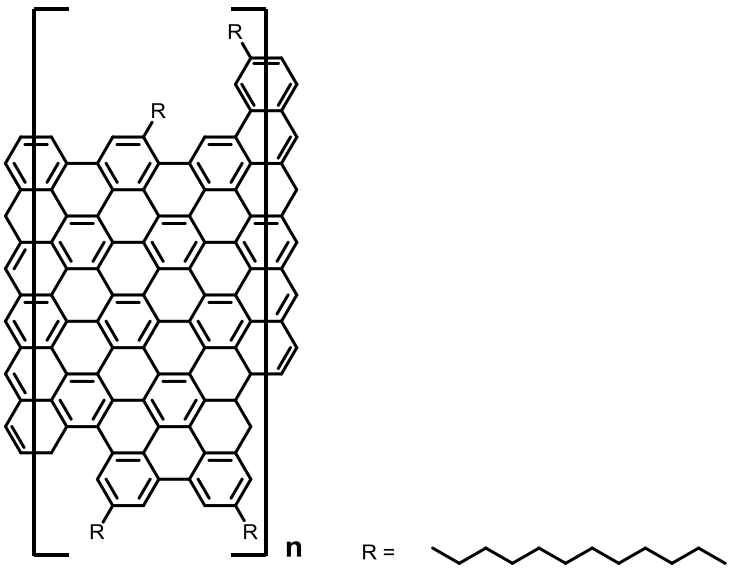

Method 1 ($FeCl_3$)

In a typical experiment, 25.0 mg of **P4** was dissolved in 30.0 ml DCM. Then, 0.51 g (3.16 mmol, 7.5 eqv./H) ferric chloride, dissolved in 2.0 ml nitromethane were added. Through the reaction mixture was passed for 2 h a stream of argon saturated with DCM in order to prevent evaporation of the reaction solvent. The reaction was stirred at room temperature for 24 h. Then, excess methanol was added and the precipitate that formed was collected by filtration and washed with water and methanol. After drying, 23.5 mg of a black solid were obtained in 92 %.

Method 2 ($PIFA/BF_3$)

In a typical experiment 25.0 mg of **P4** was dissolved in 20.0 ml anhydrous DCM. Then, 200.0 mg phenyliodine(III) bis(trifluoroacetate (PIFA, 0.45 mmol, 2.1 eqv./bond) and 63.0 mg (0.056 ml, 0.45 mmol, 2.5 eqv./bond) boron trifluoride etherate dissolved in 2.0 ml anhydrous DCM were added at a temperature of - 60 °C (chloroform/dry ice). The reaction was stirred under an inert atmosphere at this temperature for 2 h and at room temperature for additional 24 h. Then, excess methanol and water was added and the precipitate that formed was collected by filtration and washed with methanol. After drying, 20.0 mg of a black solid were obtained in 85 %.

FTIR: 3065 cm^{-1}, 2919 cm^{-1}, 2850 cm^{-1}, 1724 cm^{-1}, 1604 cm^{-1}, 1582 cm^{-1}, 1452 cm^{-1}, 1367 cm^{-1}, 1337 cm^{-1}, 1305 cm^{-1}, 1208 cm^{-1}, 1150 cm^{-1}, 1078 cm^{-1}, 861 cm^{-1}, 822 cm^{-1}, 760 cm^{-1}, 718 cm^{-1}, 624 cm^{-1}.

Raman: 1583 cm^{-1}, 1294 cm^{-1}.

7.4.17 2,2'-(4,4''-Dichloro-[1,1':4',1''-terphenyl]-2,2''-diyl)bis(1,4-diphenyltriphenylene) (4-51)

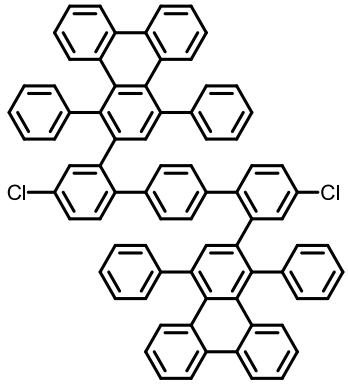

0.15 g (0.43 mmol) **4-31** and 0.50 g (1.30 mmol) phencyclone were placed in a microwave vessel. Then, 8.0 ml of *ortho*-xylene were added and the reaction mixture was degassed by argon bubbling. The reaction vessel was sealed, placed in a microwave reactor and heated to 160 °C at 300 W for 24 h with activated cooling. The crude product was pre-purified by column chromatography (hexane/ethyl acetate = 9/1). Further purification was achieved by preparative gel permeation chromatography (chloroform) to yield 0.27 g (0.26 mmol) of **4-51** in 76 % as a colorless solid.

^{1}H NMR (700 MHz, THF) δ 8.45 (dd, J = 7.9, 25.4, 1H), 8.37 (dd, J = 7.9, 42.3, 3H), 7.89 (s, 1H), 7.74 (dd, J = 8.1, 41.0, 2H), 7.54 (s, 2H), 7.53 - 7.48 (m, 3H), 7.48 - 7.22 (m, 14H), 7.19 (dd, J = 2.3, 8.5, 2H), 7.17 (d, J = 8.2, 2H), 7.12 (dt, J = 4.7, 12.0, 2H), 7.04 (t, J = 7.2, 1H), 7.02 - 6.91 (m, 4H), 6.89 (d, J = 8.5, 2H), 6.82 (m, 3H), 6.70 (t, J = 7.2, 1H), 6.32 (d, J = 383.1, 1H), 6.38 (s, 1H), 6.22 (s, 1H), 5.99 (d, J = 413.2 , 2H).

^{13}C NMR (75 MHz, CD_2Cl_2): δ 145.61, 145.50, 142.99, 142.69, 142.31, 142.04, 140.18, 139.72, 139.19, 137.79, 137.71, 134.32, 134.21, 133.37, 133.09, 132.89, 132.48, 132.37, 132.25, 132.03, 131.74, 131.43, 130.98, 130.81, 130.01, 129.25, 128.10, 127.70, 127.31, 127.11, 126.87, 126.32, 126.07, 125.90, 124.35, 124.16, 124.06.
MS (FD, 8kV): m/z (%) = 1053.9 (100.0 %, M^+), (calc. $C_{78}H_{48}Cl_2$ = 1056.12 g/mol).

Elemental Analysis: found 85.07 % C, 4.88 % H - calc. 88.71 % C, 4.58 % H (see general remarks "7.2.4 Elemental Combustion Analysis").

7.4.18 2,2'-(5,5''-Dichloro-[1,1':4',1''-terphenyl]-2,2''-diyl)bis(1,4-diphenyltriphenylene) (4-52)

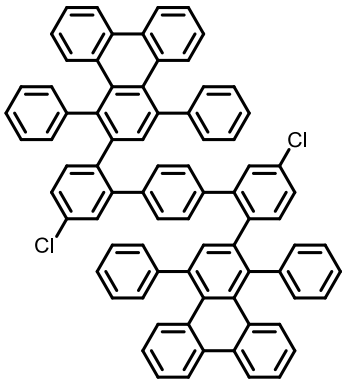

0.20 g (0.58 mmol) **4-36** and 0.55 g (1.44 mmol) phencyclone were placed in a microwave vessel. Then, 8.0 ml of *ortho*-xylene were added and the reaction mixture was degassed by argon bubbling. The reaction vessel was sealed, placed in a microwave reactor and heated to 160 °C at 300 W for 24 h with activated cooling. The crude product was pre-purified by column chromatography (hexane/ethyl acetate = 9/1). Further purification was achieved by preparative gel permeation chromatography (chloroform) to yield 0.52 g (0.49 mmol) of **4-52** in 85 % as a colorless solid.

^{1}H NMR (500 MHz, THF) δ 8.44 (dd, J = 8.0, 12.8, 1H), 8.40 (d, J = 7.9, 1H), 8.34 (d, J = 7.8, 1H), 7.88 (s, 1H), 7.71 (dd, J = 8.3, 40.1, 2H), 7.50 (s, 2H), 7.46 - 7.21 (m, 18H), 7.21 - 7.15 (m, 2H), 7.10 (t, J = 7.7, 2H), 7.05 - 6.95 (m, 3H), 6.93 (dd, J = 2.1, 11.3, 3H), 6.86 (t, J = 7.4, 2H), 6.70 (t, J = 7.8, 2H), 6.55 (s, 1H), 6.30 (s, 4H), 5.74 (s, 1H).

^{13}C NMR (126 MHz, THF) δ 146.72, 144.43, 143.69, 143.24, 140.88, 140.18, 138.88, 136.20, 136.05, 135.89, 134.93, 134.78, 134.59, 134.22, 134.00, 133.57, 132.77, 132.47, 132.12, 131.70, 131.32, 131.17, 131.03, 130.65, 130.42, 129.75, 129.34, 129.01, 128.64, 128.03, 127.63, 127.36, 126.74, 126.35, 126.03, 125.75, 124.78, 124.50.

MS (FD, 8kV): m/z (%) = 1054.8 (100.0 %, M^+), (calc. $C_{78}H_{48}Cl_2$ = 1056.12 g/mol).
Elemental Analysis: found 85.53 % C, 5.59 % H - calc. 88.71 % C, 4.58 % H (see general remarks "7.2.4 Elemental Combustion Analysis").

7.4.19 4,4''-Dibromo-[1,1':4',1''-terphenyl]-2,2''-diamine (4-53)

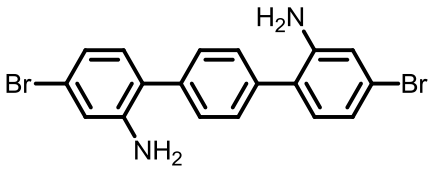

1.47 g (3.08 mmol) **4-41** and 0.20 g of palladium on carbon (10 wt%) were suspended in 50.0 ml of THF. The reaction mixture was evacuated after what a balloon filled with hydrogen gas was connected. The reaction mixture was heated to 50 °C for 24 h under vigorous stirring and monitored by thin-layer chromatography. With the consumption of the starting compound the reaction mixture turned homogenous. The crude product was purified by filtration to yield 1.21 g (2.89 mmol) of **4-53** as an orange solid in 94 %.

^{1}H NMR (300 MHz, CD_2Cl_2): δ 7.51 (s, 4H), 7.19 (tt, J = 7.1, 13.9, 4H), 6.95 (m, 2H), 4.03 (s, 4H).

^{13}C NMR (75 MHz, CD_2Cl_2): δ 145.87, 138.29, 132.27, 130.02, 126.44, 122.58, 121.80, 118.53.

MS (FD, 8kV): m/z (%) = 417.8 (100.0 %, M^+), (calc. $C_{18}H_{14}Br_2N_2$ = 418.13 g/mol).

7.4.20 4,4''-Dibromo-2,2''-diiodo-1,1':4',1''-terphenyl (4-54)

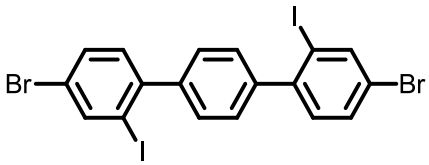

1.20 g (2.85 mmol) of **4-53** was suspended in 7.0 ml of water. Then, 4.0 ml of concentrated hydrochloric acid were added under cooling. At a temperature of - 5 °C, 4.0 ml of an aqueous solution containing 0.50 g (7.06 mmol) sodium nitrite were added dropwise. During this procedure, the color of the reaction mixture changed from yellow to dark brown. Subsequently, 12.0 ml of an aqueous solution containing 5.00 g (28.52 mmol) potassium iodide were added dropwise while maintaining the temperature below 0 °C. After the addition, the reaction was allowed to proceed for 1 h at room temperature. After extraction with DCM, treatment with an aqueous solution of

sodium thiosulfate and removal of the solvent under reduced pressure the crude product was purified by column chromatography (hexane/ethyl acetate = 8/2) to yield 0.77 g (1.20 mmol) of **4-54** in 42 % as an orange solid.

^{1}H NMR (300 MHz, CD_2Cl_2): δ 8.15 (d, J = 2.0, 2H), 7.57 (dd, J = 2.0, 8.2, 2H), 7.39 (s, 4H), 7.25 (d, J = 8.2, 2H).

^{13}C NMR (75 MHz, CD_2Cl_2): δ 145.72, 143.22, 142.06, 131.96, 131.62, 129.48, 122.19, 99.27.

MS (FD, 8kV): m/z (%) = 639.9 (100.0 %, M^+), (calc. $C_{18}H_{10}Br_2I_2$ = 639.89 g/mol).

7.4.21 4,4''-Dibromo-2,2''-diethynyl-1,1':4',1''-terphenyl (4-56)

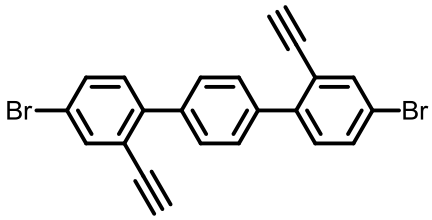

0.60 g (0.99 mmol) of **4-54** was mixed with 25.0 mg (0.14 mmol) of copper(II) iodide and 10.0 ml of triethylamine. After degassing by argon bubbling, 50 mg (0.08 mmol) of bis(triphenylphosphine)palladium(II) dichloride and 0.40 ml (2.01 mmol) of (trimethylsilyl)acetylene were added. The reaction mixture was stirred at room temperature for 24 h under an inert atmosphere and monitored by thin-layer chromatography. The reaction mixture was filtered over a silica pad (DCM) to remove inorganic residues.
The product thus obtained (0.41 g, 0.71 mmol, 72 %) was then dissolved in a mixture of 20.0 ml THF and 20.0 ml methanol. Then, 0.55 g (3.95 mmol) potassium carbonate was added and the reaction mixture was stirred at room temperature for 24 h. The crude product was purified by column chromatography (hexane/ethyl acetate = 9/1) to yield 0.19 g (0.43 mmol) of **4-56** in 60 %.

^{1}H NMR (300 MHz, CD_2Cl_2): δ 7.79 (d, J = 2.1, 2H), 7.65 (s, 4H), 7.58 (dd, J = 2.1, 8.4, 2H), 7.33 (d, J = 8.4, 2H), 3.19 (s, 2H).

^{13}C NMR (75 MHz, CD_2Cl_2): δ 143.28, 139.27, 136.96, 132.90, 131.70, 129.46, 122.86, 121.35, 82.11, 68.34.

MS (FD, 8kV): m/z (%) = 436.0 (100.0 %, M^+), (calc. $C_{22}H_{12}Br_2$ = 436.14 g/mol).

Elemental Analysis: found 68.12 % C, 6.60 % H - calc. 60.59 % C, 2.77 % H.

7.4.22 2,2'-(4,4''-Dibromo-[1,1':4',1''-terphenyl]-2,2''-diyl)bis(1,4-diphenyltriphenylene) (4-57)

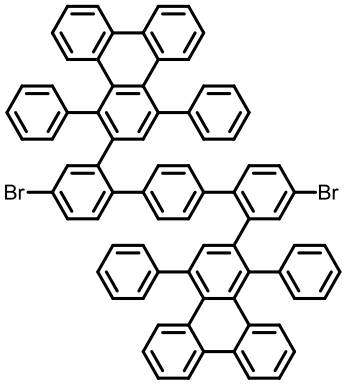

0.15 g (0.34 mmol) **4-56** and 0.33 g (0.86 mmol) phencyclone were placed in a microwave vessel. Then, 3.0 ml of *ortho*-xylene were added and the reaction mixture was degassed by argon bubbling. The reaction vessel was sealed, placed in a microwave reactor and heated to 160 °C at 300 W for 24 h with activated cooling. The crude product was pre-purified by column chromatography (hexane/ethyl acetate = 9/1). Further purification was achieved by preparative gel permeation chromatography (chloroform) to yield 15 mg (0.31 mmol) of **4-57** in 90 % as an off-white solid.

^{1}H-NMR (700 MHz, THF): δ 8.45 (dd, J = 8.0, 25.6, 1H), 8.37 (dd, J = 7.9, 42.2, 2H), 7.89 (s, 1H), 7.74 (dd, J = 8.1, 41.1, 2H), 7.66 (d, J = 2.1, 1H), 7.54 (d, J = 3.0, 2H), 7.49 (s, 1H), 7.43 (dt, J = 7.6, 15.9, 3H), 7.38 - 7.29 (m, 10H), 7.27 (dd, J = 5.0, 13.1, 2H), 7.16 (d, J = 8.3, 2H), 7.12 (t, J = 7.7, 2H), 7.04 (t, J = 7.2, 1H), 7.02 - 6.90 (m, 4H), 6.83 (t, J = 7.1, 4H), 6.75 (d, J = 8.5, 1H), 6.70 (t, J = 7.7, 1H), 6.37 (s, 1H), 6.24 (s, 1H), 6.22 (s, 4H), 6.09 - 5.99 (m, 1H), 5.65 (s, 1H).
^{13}C-NMR (176 MHz, THF): δ 145.65, 145.55, 143.34, 143.03, 142.33, 142.07, 140.85, 140.64, 139.68, 139.33, 139.24, 137.83, 137.75, 135.66, 135.31, 134.39, 134.28, 132.92, 132.69, 132.60, 132.53, 132.32, 131.22, 131.03, 130.96, 130.82, 129.25,

128.16, 127.76, 127.36, 126.92, 126.44, 126.37, 126.05, 125.95, 124.41, 124.22, 124.12, 121.49.

MS (MALDI-TOF): m/z (%) = 1144.23 (100.0 %), 1145.35 (87.4 %), 1146.25 (77.9 %), 1147.20 (49.8 %), 1143.28 (40.9 %), 1142.24 (40.5 %), 1148.15 (20.73 %), (calc. $C_{78}H_{48}Br_2$ = 1145.02 g/mol - isotop. distr.: 1144.21 (100.0%), 1145.21 (84.4%), 1142.21 (51.4%), 1146.21 (48.6%), 1143.22 (43.6%), 1147.21 (41.3%), 1146.22 (35.6%)).

Elemental Analysis: found 87.37 % C, 4.03 % H - calc. 81.82 % C, 4.23 % H (see general remarks "7.2.4 Elemental Combustion Analysis").

7.5 Network Synthesis

7.5.1 Tris(4-formylphenyl)benzene (5-11)[15]

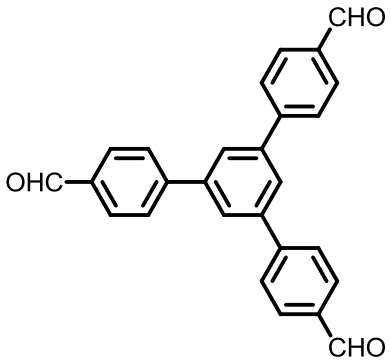

3.50 g (11.12 mmol) 1,3,5-tribromobenzene and 10.00 g (66.69 mmol) 4-formylphenylboronic acid were dissolved in 350.0 ml toluene. Then, 90.0 ml of aqueous potassium carbonate solution (2 M) and a few drops of Aliquat 336 were added. After degassing by argon bubbling, 1.90 g (1.64 mmol) of tetrakis(triphenylphosphine)palladium(0) were added and the resulting mixture was heated to reflux for 72 h. After removal of the solvent, the crude product was filtered over a silica pad (DCM/methanol = 9/1) and recrystallized from a DCM/methanol mixture to yield 3.39 g (8.67 mmol) of **5-11** as colorless crystals in 78 %.

^{1}H-NMR (300 MHz, CD_2Cl_2): δ 10.09 (s, 3H), 8.02 (d, 6H, J = 8.5), 7.97 (s, 3H), 7.91 (d, 6H, J = 8.4).

^{13}C-NMR (75 MHz, CD_2Cl_2): δ 195.32, 146.76, 142.04, 136.42, 130.80, 128.51, 127.01.

MS (FD, 8kV): m/z (%) = 387.6 (100.0 %, M^+), (calc. $C_{27}H_{18}O_3$ = 390.43 g/mol).
Elemental Analysis: found 84.38 % C, 5.32 % H - calc. 83.06 % C, 4.65 % H.

7.5.2 Naphthalene-2,6-dicarbaldehyde (5-12)[16]

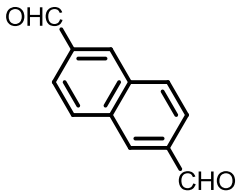

Prior to the synthesis the reducing agent was prepared as follows. To 6.1 ml (20.46 mmol) of sodium bis(2-methoxyethoxy)aluminumhydride (*Red-Al*, 65 % in toluene) were added 10.0 ml dry toluene. Afterwards, 2.5 ml (22.61 mmol) *N*-methylpiperazine were added dropwise below 10 ºC, and the resulting mixture was stirred for 30 min to give a clear solution.
Then, 2.0 g (8.19 mmol) of dimethyl naphthalene-2,6-dicarboxylate were mixed with 40.0 ml dry toluene and the solution was degassed by argon bubbling. To the resulting slurry the solution of the reducing agent was slowly added maintaining the temperature below 5 °C. The reaction mixture progressively turned yellow with the starting material being slowly dissolved. The reaction was allowed to proceed for 1 h after what it was stopped by the addition of water. The crude product was extracted with ethyl acetate and the solvent was removed under reduced pressure. Recrystallization from acetone yielded 1.22 g (6.63 mmol) of **5-12** as colorless crystals in 81 %.

^{1}H-NMR (300 MHz, CD_2Cl_2): δ 10.21 (s, 2H), 8.41 (d, J = 0.8, 2H), 8.16 (s, 2H), 8.04 (dd, J = 1.3, 8.5, 2H).

^{13}C-NMR (75 MHz, CD_2Cl_2): δ 191.68, 137.22, 135.59, 133.30, 128.56, 124.11.

MS (FD, 8kV): m/z (%) = 184.1 (100.0 %, M^+), (calc. $C_{12}H_8O_2$ = 184.19 g/mol).

Elemental Analysis: found 78.05 % C, 4.76 % H - calc. 78.25 % C, 4.38 % H.

7.5.3 Benzene-1,3,5-tricarbaldehyde (5-13)[17]

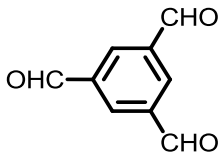

4.55 g (33.66 mmol) *N*-methylmorpholine oxide and 40.0 g crushed molecular sieves were added to a stirred solution of 2.0 g (5.60 mmol) 1,3,5-tris-bromomethylbenzene in 200 ml acetonitrile. The resulting slurry was heated to reflux for 12 h. After cooling and filtration, the solvent was removed under reduced pressure. The crude product was purified by column chromatography (hexane/ethyl acetate = 1:1) to yield 0.51 g (3.14 mmol) of **5-13** in 56 % as an off-white solid.

^{1}H-NMR (300 MHz, CD_2Cl_2): δ 10.19 (s, 3H), 8.62 (s, 3H).

^{13}C-NMR (75 MHz, CD_2Cl_2): δ 190.62, 138.43, 135.15.

MS (FD, 8kV): m/z (%) = 160.8 (100.0 %, M^+), (calc. $C_{12}H_8O_2$ = 162.14 g/mol).

Elemental Analysis: found 68.97 % C, 5.28 % H - calc. 66.67 % C, 3.73 % H.

7.5.4 5,5'-Bis(2-dimethylaminovinyl)-2,2'-bipyridine (5-20)[18]

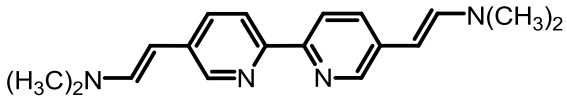

To 1.00 g (5.43 mmol) 5,5'-dimethyl-2,2'-bipyridine in 10.0 ml anhydrous DMF 10.0 ml (48.43 mmol) *tert*-butoxy bis(dimethylamino)methane (*Bredereck*'s reagent) were added. The reaction mixture was heated to 120 °C for 5 days under an inert atmosphere. The yellow crystals which were formed upon cooling were collected by filtration and washed with diethyl ether to yield 1.05 g (3.58 mmol) of **5-20** in 66 %. The crude product was used without further purification for the next step.

^{1}H NMR (300 MHz, CD_2Cl_3): δ 8.43 (d, J = 2.4 Hz, 2H), 8.12 (d, J = 8.5 Hz, 2H), 7.54 (dd, J = 8.4, 2.4, 2H), 6.86 (d, J = 13.6 Hz, 2H), 5.11 (d, J = 13.8, 2H), 2.85 (s, 12H).

^{13}C NMR (75 MHz, CD_2Cl_3): δ 151.21, 144.34, 141.47, 134.89, 128.99, 121.12, 93.48, 40.16.

MS (FD, 8kV): m/z (%) = 293.9 (100.0 %, M^+), (calc. $C_{18}H_{22}N_4$ = 294.39 g/mol).

7.5.5 2,2'-Bipyridine-5,5'-dicarbaldehyde (5-21)[18]

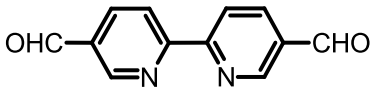

1.00 g (3.40 mmol) of **5-20** were dissolved in 45.0 ml DCM and 150.0 ml THF. Then, a solution of 5.53 g (25.85 mmol) sodium periodate 30.0 ml water was added. The mixture was stirred at room temperature for 24 h. The solvent was removed under reduced pressure. The crude product was purified by column chromatography (DCM/methanol = 20:1) to yield 0.49 g (2.35 mmol) of **5-21** in 69 % as light yellow solid.

^{1}H NMR (300 MHz, CD_2Cl_2): δ 10.18 (s, 2H), 9.15 (d, J = 1.6, 2H), 8.72 (d, J = 8.2, 2H), 8.32 (dd, J = 2.1, 8.2, 2H).

^{13}C NMR (75 MHz, CD_2Cl_2): δ 191.08, 159.70, 152.02, 137.72, 132.34, 122.78.

MS (FD, 8kV): m/z (%) = 211.5 (100.0 %, M^+), (calc. $C_{12}H_8N_2O_2$ = 212.20 g/mol).

Elemental Analysis: found 71.59 % C, 4.03 % H, 13.93 % N - calc. 67.92 % C, 3.80 % H, 13.20 % N.

7.5.6 General Procedure for the Synthesis of SNW Networks

Melamine systems:

300 mg (2.38 mmol) melamine and the aldehyde component (see table below) were placed in a flame-dried *Schlenk* flask and dissolved in the corresponding amount of DMSO (see table below). After degassing by argon bubbling the mixture was heated to 180 °C for 72 h under an inert atmosphere. After cooling to room temperature the precipitated material was collected by filtration and purified by *Soxhlet* extraction with THF for 24 h. The material was then dried under reduced pressure at room temperature.

	aldehyde component	**mg**	**mmol**	**ml DMSO**	**% yield**
SNW-1	terephthalaldehyde	479	3.57	14.9	61
SNW-2	biphenyl-4,4'-dicarbaldehyde	750	3.57	14.9	62
SNW-3	isophtalalydehyde	479	3.57	14.9	62
SNW-4	1,3,5-tris(4-formylphenyl)benzene	929	2.38	11.9	66
SNW-5	naphthalene-2,6-dicarbaldehyde	657	3.57	14.9	66
SNW-6	benzene-1,3,5-tricarbaldehyde	386	2.38	11.9	68
SNW-7	pyridine-2,6-dicarbaldehyde	482	3.57	14.9	75
SNW-8	2,2'-bipyridine-5,5'-dicarbaldehyde	757	3.57	14.9	60
SNW-9	thiophene-2,5-dicarbaldehyde	500	3.57	14.9	62
SNW-10	furan-2,5-dicarbaldehyde	443	3.57	14.9	58

1,3,5-Triazine-2,4-diamine systems:

250 mg (2.25 mmol) 1,3,5-triazine-2,4-diamine and the aldehyde component (see table below) were placed in a flame-dried *Schlenk* flask and dissolved in the corresponding amount of DMSO (see table below). After degassing by argon bubbling the mixture was heated to 180 °C for 72 h under an inert atmosphere. After cooling to room temperature the precipitated material was collected by filtration and purified by *Soxhlet* extraction with THF for 24 h. The material was then dried under reduced pressure at room temperature.

	aldehyde component	**mg**	**mmol**	**ml DMSO**	**% yield**
SNW-11	benzene-1,3,5-tricarbaldehyde	365	2.25	11.2	52
SNW-12	1,3,5-tris(4-formylphenyl)benzene	878	2.25	11.2	46

7.5.7 1,3,5-Tris(4-aminophenyl)benzene (5-25)

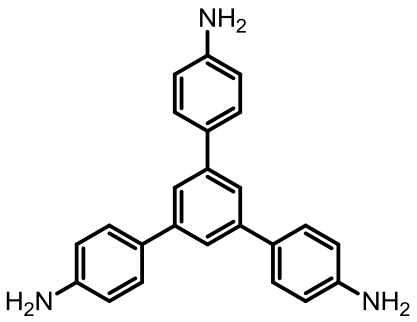

2.00 g (6.35 mmol) of 1,3,5-tribromobenzene and 4.61 g (33.66 mmol) 4-aminophenylboronic acid were dissolved in 50.0 ml of dioxane. Then, a few drops of Aliquat 336 and 15.0 ml of an aqueous K_2CO_3 (2 M) were added. After degassing by argon bubbling, 0.11 g (0.095 mmol) of tetrakis(triphenylphosphine)palladium(0) were added. The reaction mixture was heated to 100 °C for 24 h. The crude product was purified by column chromatography (hexane/ethyl acetate 7/3) to yield 1.38 g (3.937 mmol) of **5-25** in 62 % as an off-white solid.

^{1}H NMR (300 MHz, CD_2Cl_2): δ 7.59 (s, 3H), 7.51 (dd, *J* = 2.1, 8.7, 6H), 6.77 (dd, *J* = 2.2, 8.7, 6H), 3.82 (s, 6H).

^{13}C NMR (75 MHz, CD_2Cl_2): δ 146.79, 142.32, 131.69, 128.39, 122.80, 115.49.

MS (FD, 8kV): m/z (%) = 350.8 (100.0 %, M^+), (calc. $C_{24}H_{21}N_3$ = 351.17 g/mol).

7.5.8 Anthracene-2,6-dicarbaldehyde (5-27)

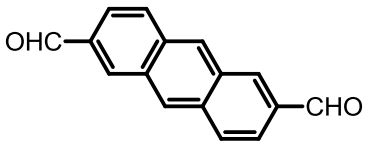

0.50 g (1.48 mmol) of 2,6-dibromoanthracene was placed in a flame-dried *Schlenk* tube which was subsequently evacuated and refilled with argon for three times. 15.0 ml of dry THF were added and the mixture was cooled to - 78 °C. Then, 21.4 mmol ml of *n*-butyllithium (1.6 M in hexane) was added and the reaction was allowed to proceed for 1 h at this temperature. 10.0 ml of anhydrous DMF were added and the mixture was stirred for 1 h. The mixture was slowly brought to room temperature and quenched by the addition of methanol/water. The crude product was purified by column

chromatography (hexane, hexane/ethyl acetate 7/3) and recrystallized from toluene/ethanol to yield 0.22 g (0.94 mmol) of **5-27** in 61 % as a yellow crystalline solid.

^{1}H NMR (300 MHz, CD_2Cl_2): δ 10.21 (s, 2H), 8.72 (s, 2H), 8.58 (s, 2H), 8.18 (d, *J* = 9.1, 2H), 7.97 (d, *J* = 8.8, 2H).

^{13}C NMR (176 MHz, CD_2Cl_2): δ 192.16, 136.78, 135.43, 134.23, 132.76, 130.15, 129.70, 122.15.

MS (FD, 8kV): m/z (%) = 233.2 (100.0 %, M^+), (calc. $C_{16}H_{10}O_2$ = 234.25 g/mol).

7.5.9 Anthracene-9,10-dicarbaldehyde (5-29)[19]

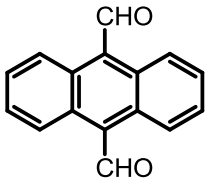

1.00 g (3.63 mmol) of 9,10-bis-(chloromethyl)anthracene was dissolved in 20.0 ml anhydrous DMSO. To this solution was added a solution of 1.3 ml (14.5 mmol) 2-nitropropane and 0.33 g (14.5 mmol) sodium in 12.0 ml of dry ethanol. The reaction mixture was stirred under an inert atmosphere for 5 h at room temperature. The reaction was quenched by the addition of water
and extracted with DCM. The crude product was recrystallized from toluene to yield 0.46 g (1.96 mmol) of **5-29** as a red-orange solid in 54 %.

^{1}H NMR (300 MHz, CD_2Cl_2): δ 11.44 (s, 2H), 8.71 (dd, J = 3.3, 6.9, 4H), 7.69 (dd, J = 3.3, 6.9, 4H).

^{13}C NMR (75 MHz, CD_2Cl_2): δ 194.89, 132.74, 130.96, 128.97, 125.02.

MS (FD, 8kV): m/z (%) = 233.8 (100.0 %, M^+), (calc. $C_{16}H_{10}O_2$ = 234.07 g/mol).

7.5.10 5,5'-(Anthracene-9,10-diyl)diisophthalaldehyde (5-31)

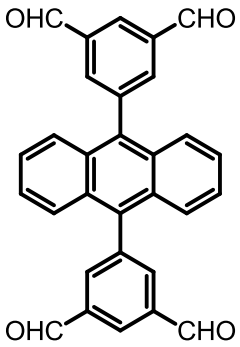

0.53 g (1.57 mmol) of 9,10-dibromoanthracene and 0.75 g (4.21 mmol) of 3,5-diformylphenylboronic acid were dissolved in 20 ml dioxane. Then, 4.0 ml of an aqueous potassium carbonate solution (2 M) and a few drops of Aliquat 336 were added. After degassing by argon bubbling, 0.18 g (0.16 mmol) of tetrakis(triphenylphosphine)palladium(0) were added and the resulting mixture was heated to reflux for 24 h. After cooling, the crude product was collected by filtration and recrystallized from acetone to yield 0.49 g (1.10 mmol) of **5-31** as a greenish solid in 69 %.

^{1}H NMR (300 MHz, CD_2Cl_2) δ 10.25 (s, 4H), 8.61 (t, J = 1.6, 2H), 8.28 (d, J = 1.6, 4H), 7.60 (dd, J = 3.2, 6.9, 4H), 7.42 (dd, J = 3.3, 6.8, 4H).

^{13}C NMR (75 MHz, CD_2Cl_2) δ 191.58, 141.61, 138.17, 137.89, 135.58, 130.34, 130.31, 126.85, 126.63.

MS (FD, 8kV): m/z (%) = 440.8 (100.0 %, M^+), (calc. $C_{30}H_{18}O_4$ = 442.46 g/mol).

Elemental Analysis: found 84.70 % C, 4.25 % H - calc. 81.44 % C, 4.10 % H.

7.5.11 General Procedure for the Synthesis of ANW Networks

1,3,5-Tris(4-aminophenyl)benzene systems:

250 mg (0.71 mmol) of 1,3,5-tris(4-aminophenyl)benzene and the aldehyde component (see table below) were placed in a flame-dried *Schlenk* tube. Then, 10.0 ml of dioxane and 2.2 ml of acetic acid (3 M) were added and the mixture was degassed by argon bubbling. The reaction mixture was heated to reflux for 72 h. The yellow precipitate was

collected by filtration and subjected to *Soxhlet* extraction with THF for 24 h to yield the materials as yellow powders.

	aldehyde component	**mg**	**mmol**	**% yield**
ANW-1	terephthalaldehyde	125	0.93	82
ANW-2	naphthalene-2,6-dicarbaldehyde	171	0.93	76
ANW-3	anthracene-2,6-dicarbaldehyde	218	0.93	70
ANW-4	anthracene-9,10-dicarbaldehyde	218	0.93	72

Elemental Analysis:

ANW-1: found 82.06 % C, 3.55 % H, 7.70 % N - calc. for $C_{72}H_{42}N_6$ 87.25 % C, 4.27 % H, 8.48 % N.
ANW-2: found 84.63 % C, 4.28 % H, 6.98 % N - calc. for $C_{84}H_{48}N_6$ 88.40 % C, 4.24 % H, 7.36 % N.
ANW-3: found 81.55 % C, 5.23 % H, 6.21 % N - calc. for $C_{96}H_{54}N_6$ 89.28 % C, 4.21 % H, 6.51 % N.
ANW-4: found 85.10 % C, 3.66 % H, 5.52 % N - calc. for $C_{96}H_{54}N_6$ 89.28 % C, 4.21 % H, 6.51 % N.

5,5'-(Anthracene-9,10-diyl)diisophthalaldehyde systems:

80 mg (0.18 mmol) of 5,5'-(anthracene-9,10-diyl)diisophthalaldehyde and the amine component (see table below) were placed in a flame-dried *Schlenk* tube. Then, 3.4 ml of dioxane and 0.7 ml of acetic acid (3 M) were added and the mixture was degassed by argon bubbling. The reaction mixture was heated to reflux for 72 h. The precipitate was collected by filtration and subjected to *Soxhlet* extraction with THF for 24 h to yield the materials as yellow-brown powders.

	amine component	**mg**	**mmol**	**% yield**
ANW-5	benzene-1,4-diamine	34	0.32	76
ANW-6	pyridine-2,6-diamine	35	0.32	82
ANW-7	naphthalene-1,5-diamine	50	0.32	75

Elemental Analysis:

ANW-5: found 74.91 % C, 2.53 % H, 7.95 % N - calc. for $C_{42}H_{22}N_4$ 86.58 % C, 3.81 % H, 9.62 % N.

ANW-6: found 67.03 % C, 4.51 % H, 12.15 % N - calc. for $C_{40}H_{20}N_6$ 82.18 % C, 3.45 % H, 14.38 % N.

ANW-7: found 83.38 % C, 3.73 % H, 7.47 % N - calc. for $C_{50}H_{26}N_4$ 87.96 % C, 3.84 % H, 8.21 % N.

7.6 Crystal Structures

7.6.1 2,9-dichloro-5,6-bis(dodecyloxy)-1,10-phenanthroline (3-10b)

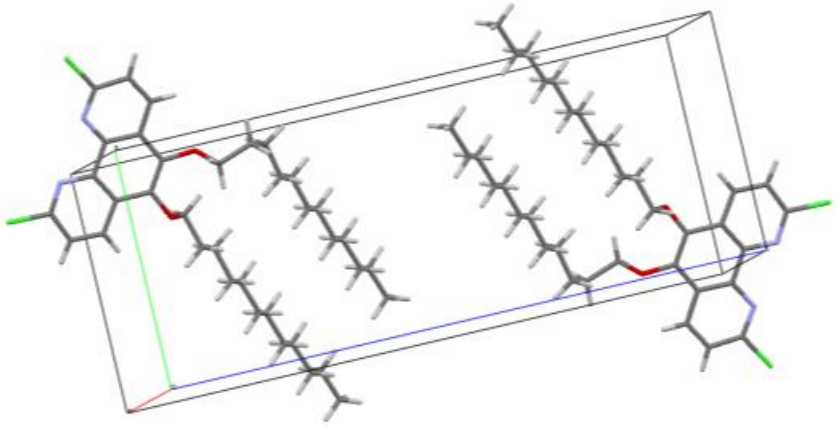

$C_{36}H_{54}Cl_2N_2O_2$, M = 617.73 g/mol, triclinic, space group *P-1*, a = 7.2700(2) Å, b = 10.1780(5) Å, c = 25.3170(12) Å, α = 85.0580(18) °, β = 88.256(2) °, γ = 77.211(2) °, V = 1819.92 Å^3.

7.6.2 4,4''-Dichloro-2,2''-diethynyl-1,1':4',1''-terphenyl (4-31)

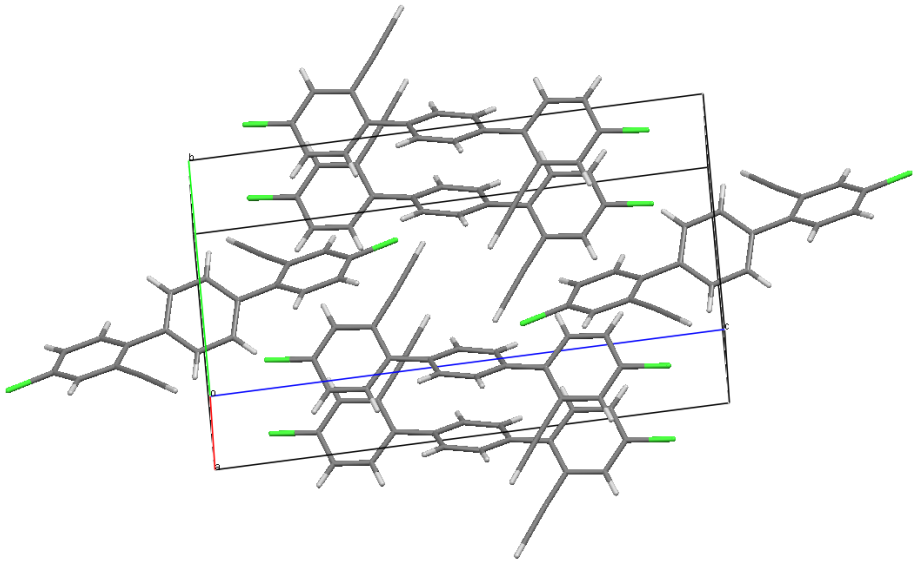

$C_{11}H_6Cl$, M = 347.24 g/mol, monoclinic, space group $P2_1/n$, a = 3.84150(10) Å, b = 11.5774(5) Å, c = 18.4847(8) Å, β = 94.252(2), V = 819.837 Å^3.

7.6.3 5,5''-Dichloro-2,2''-diethynyl-1,1':4',1''-terphenyl (4-36)

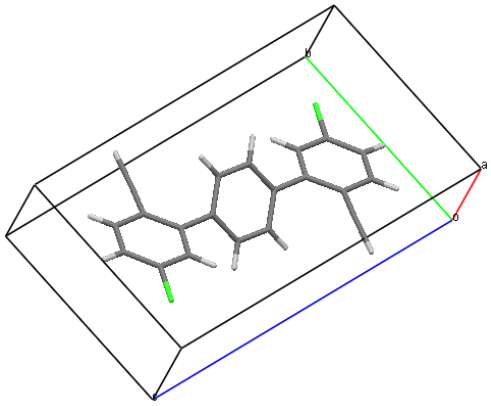

$C_{11}H_6Cl$, M = 347.24 g/mol, triclinic, space group *P-1*, a = 3.91990(10) Å, b = 7.6994(4) Å, c = 14.3414(8) Å, α = 79.388(3) °, β = 86.908(3) °, γ = 78.607(3) °,
V = 416.98 $Å^3$.

7.7 Bibliography

(1) Gottlieb, H. E.; Kotlyar, V.; Nudelman, A. *J. Org. Chem.* **1997**, *62*, 7512-7515.
(2) Muntean, J. V.; Stock, L. M.; Botto, R. E. *J. Magn. Reson.* **1988**, *76*, 540-542.
(3) Morkombe, C. R.; Zilm, K. *J. Magn. Reson.* **2003**, *162*, 479-486.
(4) Goward, G. R.; Schnell, I.; Spiess, H. W. *Magn. Reson. Chem.* **2001**, *39*, S5-S17.
(5) Weil, T. *Biologisch Inspirierte Polyphenylen-Dendrimere*; PhD Thesis: Mainz, **2001**.
(6) Senkovska, I.; Kaskel, S. *Microporous Mesoporous Mater.* **2008**, *112*, 108-115.
(7) Yamada, M.; Nakamura, Y.; Kuroda, S.; Shimao, I. *Bull. Chem. Soc. Jpn.* **1990**, *63*, 2710-2712.
(8) Yamada, M.; Tanaka, Y.; Yoshimoto, Y.; Kuroda, S.; Shimao, I. *Bull. Chem. Soc. Jpn.* **1992**, *65*, 1006-1011.
(9) Frey, J.; Kraus, T.; Heitz, V.; Sauvage, J. P. *Chem. Eur. J.* **2007**, *13*, 7584-7594.
(10) Li, Z.; Lieberman, M. *Inorg. Chem.* **2001**, *40*, 932-939.
(11) Meier, H.; Rose, B. *Journal Prakt. Chem.* **1998**, *340*, 536-543.
(12) Sonntag, M.; Strohriegl, P. *Chem. Mater* **2004**, *16*, 4736-4742.
(13) Ito, S.; Wehmeier, M.; Brand, J. D.; Kübel, C.; Epsch, R.; Rabe, J. P.; Müllen, K. *Chem. Eur. J.* **2000**, *6*, 4327-4342.
(14) Blouin, N.; Michaud, A.; Wakim, S.; Boudreault, P. T.; Leclerc, M.; Vercelli, B.; Zecchin, S.; Zotti, G. *Macromol. Chem. Phys.* **2006**, *207*, 166-174.
(15) Kotha, S.; Shah, V. R. *Synthesis* **2008**, *23*, 3653-3658.
(16) Hagiya, K.; Mitsui, S.; Taguchi, H. *Synthesis* **2003**, *6*, 823-828.
(17) Tullberg, E.; Frejd, T. *Synth. Commun.* **2007**, *37*, 237-245.
(18) Hodačova, J.; Buděšínský, M. *Org. Lett.* **2007**, *9*, 5641-5643.
(19) Kim, H. S.; Moon, K. S.; Jang, D. O. *Supramol. Chem.* **2006**, *18*, 97-101.

8 List of Publications

8.1 Scientific Publications

1) Schwab, M. G.; Senkovska, I.; Rose, M.; Koch, M.; Pahnke J.; Jonschker, G.; Kaskel, S. „MOF@PolyHIPEs“, *Adv. Eng. Mat.* **2008**, *10*, 1151-1155.

2) Schwab, M. G.; Senkovska, I.; Rose, M.; Klein, N.; Koch, M.; Pahnke, J.; Jonschker, G.; Schmitz, B.; Hirscher, M.; Kaskel, S. „High surface area polyHIPEs with hierarchical pore system”, *Soft Matter* **2009**, *5*, 1055-1059.

3) Schwab, M. G.; Fassbender, B.; Spiess, H. W.; Thomas, A.; Feng, X.; Müllen, K. „Catalyst-free Preparation of Melamine-Based Microporous Polymer Networks through Schiff Base Chemistry“, *J. Am. Chem. Soc.* **2009**, *131*, 7216-7217.

4) Liang, Y.; Schwab, M. G.; Zhi, L.; Mugnaioli, E.; Kolb, U.; Feng, X.; Müllen, K. „Direct Access to Metal or Metal Oxide Nanocrystals Integrated with One-Dimensional Nanoporous Carbons for Electrochemical Energy Storage”, *J. Am. Chem. Soc.* **2010**, *132*, 15030-15037.

5) Schwab, M. G.; Hamburger, M.; Feng, X.; Shu, J.; Spiess, H. W.; Wang, X.; Antonietti, M.; Müllen, K. „Photocatalytic Hydrogen Evolution Through Fully Conjugated Poly(azomethine) Networks”, *Chem. Commun.* **2010**, *46*, 8932-8934.

6) Schwab, M. G.; Lennert, A.; Pahnke, J.; Jonschker, G.; Koch, M.; Senkovska, I.; Rehahn, M.; Kaskel, S. „Nanoporous Copolymer Networks Through Multiple Friedel-Crafts-Alkylation - Studies on Hydrogen and Methane Storage”, *J. Mater. Chem.* **2011**, *21*, 2131-2135.

7) Liang, Y.; Schwab, M. G.; Shu, J.; Graf, R.; Spiess, H. W.; Feng, X.; Müllen, K. „Template-Free Fabrication of Nitrogen-Enriched Mesoporous Carbons from Schiff Base Networks for High-Performance Electrochemical Capacitors", *submitted*.

8) Schwab, M. G.; Takase, M.; Mavrinskiy, A.; Pisula, W.; Wu, D.; Feng, X.; Mali, K.; de Feyter, S.; Müllen, K. „Torands revisited - Metal Sequestration and Self-Assembly of Cyclo-2,9-tris-1,10-phenanthroline Hexaaza Macrocycles", *in preparation*.

9) Schwab, M. G.; Qin, T.; Mavrinskiy, A.; Pisula, W.; Feng, X.; Baumgarten, M.; Mali, K.; de Feyter, S.; Kim, H.; Laquai, F.; Sax, S.; List, E.; Müllen, K. „Molecular Triangles: Synthesis, Self-Assembly and Blue Emission of Cyclic Triphenylene Trimers", *in preparation*.

10) Schwab, M. G.; Mavrinskiy, A.; Pisula, W.; Feng, X.; Mali, K.; Balandina, T.; Sankarapillai, M.; de Feyter, S.; Cai, J.; Fasel, R.; Müllen, K. „Structurally Well-Defined Graphene Nanoribbons of Exceptional Width and Length", *in preparation*.

11) Schwab, M. G.; Crespy, D.; Landfester, K.; Feng, X.; Müllen, K. „The Preparation of Microporous Melamine-based Polymer Networks in the Droplet Phase of an Anhydrous High-Temperature Miniemulsion", *in preparation*.

8.2 Patents

1) Koch, M.; Pahnke, J.; Jonschker, G.; Schwab, M. „Monolithische Polymermaterialien zur Gasspeicherung" DE 10 **2008** 006 874 A1.

2) Jonschker, G.; Koch, M.; Pahnke, J.; Schwab, M. „Polykondensations-netzwerke zur Gasspeicherung" DE 10 **2008** 011 189 A1.

3) Schwab, M. G., Liang, Y.; Müllen, K.; Ivanovici, S.; „Template-Free Fabrication of Nitrogen-Enriched Mesoporous Carbons", *patent pending*.